

Bottom-up Syntheses of Zigzag-edged Nanographenes and Nanographene-Porphyrin Conjugates

Kumulative Dissertation

zur Erlangung des Grades

„Doktor Der Naturwissenschaften“

im Promotionsfach Chemie

im Fachbereich Chemie, Pharmazie, und Geowissenschaften der
Johannes Gutenberg---Universität Mainz und in Kooperation mit dem
Max-Planck-Institut für Polymerforschung Mainz

vorgelegt von

Qiang Chen

geboren in Shandong / China

Mainz, 2019

Dekan: Prof. Dr. [REDACTED]

1. Berichterstatter: Prof. Dr. [REDACTED]

2. Berichterstatter: Prof. Dr. [REDACTED]

Tag der mündlichen Prüfung: 21. Nov. 2019

Die vorliegende Arbeit wurde in der Zeit von Mai 2015 bis März 2019 im Max-Planck-Institut für Polymerforschung in Mainz unter der Betreuung von Prof. Dr. [REDACTED] durchgeführt.

Ich danke Prof. Dr. [REDACTED] für seine wissenschaftliche und persönliche Unterstützung sowie für seine ständige Diskussionsbereitschaft.

To my family

Table of Content

Abbreviations	II
Chapter 1. Introduction.....	1
1.1 Graphene.....	1
1.2 Polycyclic Aromatic Hydrocarbons (PAHs) and Nanographene Molecules (GMs).....	5
1.2.1 GMs with Full Armchair Periphery	8
1.2.2 GMs with Both Armchair and Zigzag Periphery	11
1.2.3 GMs with Full Zigzag Periphery.....	17
1.3 π -System Extended Porphyrins	23
1.4 Motivation	29
References	34
Chapter 2. Synthesis of Dibenzo[<i>hi, st</i>]ovalene and Its Amplified Spontaneous Emission in a Polystyrene Matrix	44
Chapter 3. Dibenzo[<i>hi, st</i>]ovalene as Highly Luminescent Nanographene: Efficient Synthesis <i>via</i> Photochemical Cyclodehydroiodination, Opto-electronic Properties and Single Molecule Spectroscopy.....	73
Chapter 4. Synthesis and Supramolecular Organization of Discotic Liquid Crystalline Dibenzo[<i>hi, st</i>]ovalene with Long-Range Helical Packing	124
Chapter 5. Regioselective Bromination and Functionalization of Dibenzo[<i>hi, st</i>]ovalene as Highly Luminescent Nanographene with Zigzag Edges	148
Chapter 6. Synthesis of Circumpyrene: Nanographene with a Full Zigzag Periphery.....	173
Chapter 7. Synthesis of Triply Fused Porphyrin-Nanographene Conjugates.....	210
Chapter 8. Summary and Outlook	270
Acknowledgements	278
List of Publications.....	280
Curriculum Vitae	283

Abbreviations

0D zero-dimensional	FET field-effect transistor
1D one-dimensional	FWHM full width at half maximum
2D two-dimensional	GM nanographene molecule
3D three-dimensional	GNR graphene nanoribbon
ACID anisotropy of the induced current density	GO graphene oxide
AGNR armchair-edged graphene nanoribbon	GQD graphene quantum dot
APEX annulative π -extension	HBC hexa- <i>peri</i> -hexabenzocoronone
ASE amplified spontaneous emission	HOMO highest occupied molecular orbital
BAHA tris(4-bromo-phenyl)aminium hexachloroantimonat	HOPG highly oriented pyrolyzed graphite
BODIPY boron-dipyrromethene	HPB hexaphenylbenzene
CNT carbon nanotube	HR-MS high-resolution mass spectrometry
COSY correlation spectroscopy	ISC intersystem crossing
CP cyclopentadienone	LC liquid crystal
CV cyclic voltammetry	LDA lithium diisopropylamide
CVD chemical vapor deposition	LQE liquid-phase exfoliation
D-A Diels-Alder reaction	LUMO lowest unoccupied molecular orbital
DBOV dibenzo[<i>hi,st</i>]ovalene	MALDI-MS matrix-assisted laser desorption ionization mass spectrometry
DCM dichloromethane	MS mass spectrometry
DDQ 2,3-dichloro-5,6-dicyano-1,4-benzoquinone	MeOH methanol
DLC discotic liquid crystal	MP melting point
4-DMAP 4-(dimethylamino)-pyridine	MS mass spectrometry
DMF dimethyl formamide	NICS nucleus-independent chemical shift
DNA deoxyribonucleic acid	NIR near-infrared
EA ethylacetate	NMR nuclear magnetic resonance
ESI electrospray ionization	NOESY nuclear Overhauser enhancement and exchange spectroscopy
EPR electron paramagnetic resonance	OLED organic light-emitting diode
	OSC organic semiconductor

PA photoinduced absorption	TCB 1,2,4-trichlorobenzene
PB photobleaching	TCNQ tetracyanoquinodimethane
PAH polycyclic aromatic hydrocarbon	TDOP 3,4,5-tris(dodecyloxy)phenyl
PCC pyridinium chlorochromate	TEA triethylamine
PCDHI photochemical cyclodehydroiodination	TfOH trifluoromethanesulfonic acid
PDT photodynamic therapy	THF tetrahydrofuran
PLQY photoluminescence quantum yield	TIPS triisopropylsilyl
PS poly(styrene)	TLC thin-layer chromatography
PTSA <i>p</i> -toluenesulfonic acid	TMS trimethylsilyl
rGO reduced graphene oxide	TOF time of flight
r.t. room temperature	TP triphenylene
SE stimulated emission	UHV ultrahigh vacuum
SiC silicon carbide	UV-vis ultraviolet-visible (absorption spectroscopy)
STM scanning tunneling microscopy	ZGNR zigzag-edged graphene nanoribbon
TA transient absorption	ZPL zero-phonon line
TBAF tetra- <i>n</i> -butylammonium fluoride	

Chapter 1. Introduction

1.1 Graphene

Graphene is a flat single-atom-thick monolayer of graphite. It is composed of all sp^2 -hybridized carbon atoms that are covalently bonded to each other in a planar hexagonally-packed configuration (Figure 1-1). Other carbon materials could theoretically be made from graphene fragments. For example, they can be wrapped into zero-dimensional (0D) fullerenes,¹ one-dimensional (1D) cylinder carbon nanotubes (CNT), or accumulated to form multilayer three-dimensional (3D) graphite.²

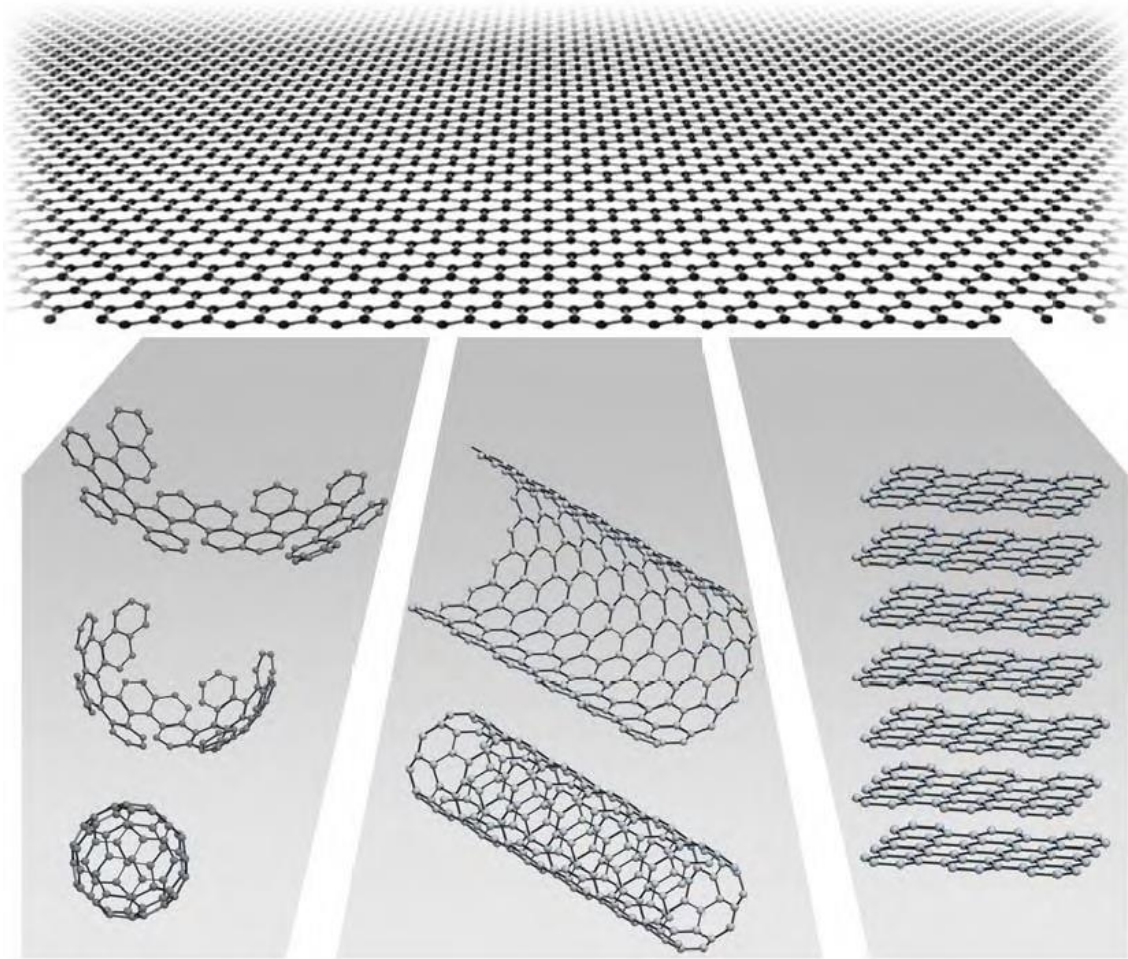


Figure 1-1. Schematic diagram of monolayer graphene and its relationship to other carbon allotropes, including fullerene, carbon nanotube, and graphite. Ref. ² Copyright: 2007, Nature publishing group.

Graphene is one of the most important milestones in the history of two-dimensional (2D) materials. However, separated 2D crystals were thought to be non-existent because of their thermal instability,^{3, 4} before the experimental isolation and discovery of pristine, high-

quality, and stable single-layer to few-layer graphene by Geim's group in 2004, who adopted the peeling of graphene sheets from highly oriented pyrolyzed graphite (HOPG).⁵ Following this simple fabrication protocol, many researchers from all over the world successfully replicated their experiments to obtain graphene. Subsequently, it was found that mono-layer graphene offered fantastic properties, such as room temperature quantum Hall effect,⁶ high intrinsic electron mobility up to $200,000 \text{ cm}^2/(\text{V}\cdot\text{s})$,⁷ which could benefit its electronic applications. Other exceptional physical properties have also been discovered, such as high thermal conductivity of $3,000\text{--}5,000 \text{ W}/(\text{m}\cdot\text{K})$ at room temperature⁸ and transmission of 97.7% incident light over a broad wavelength range.⁹ For their breakthrough contribution in graphene research, Geim and Novoselov were awarded the Nobel Prize in physics in 2010.¹⁰

11

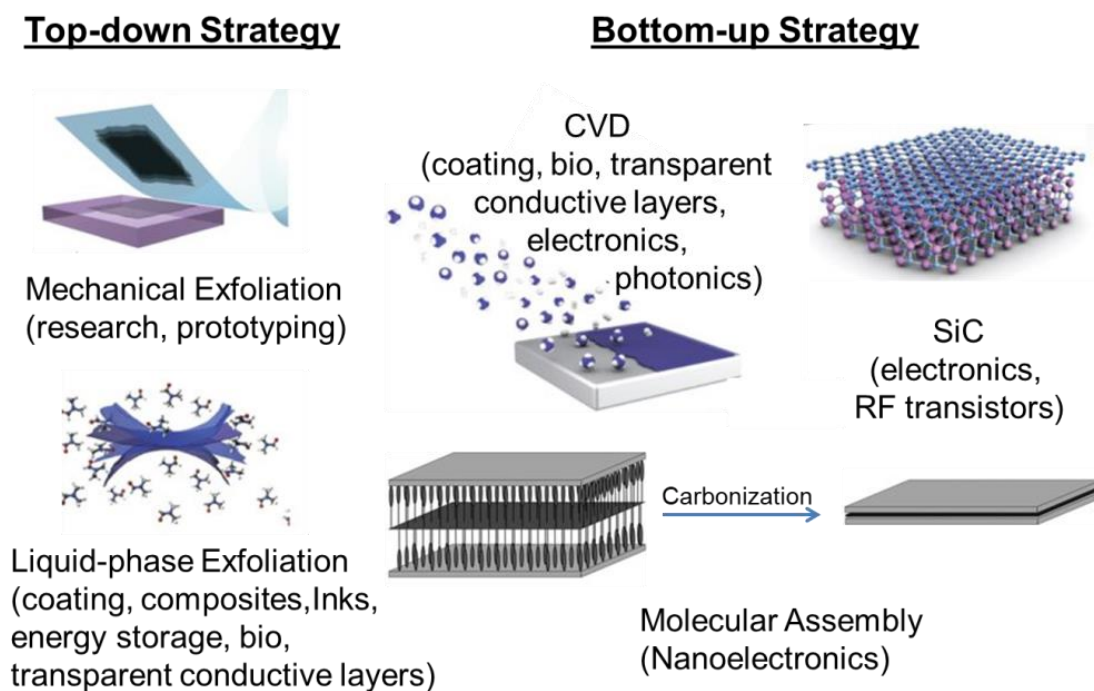


Figure 1-2. Two main strategies used for the preparation of graphene. Ref. ¹² Copyright: 2012, Nature publishing group. Ref. ¹³ Copyright: 2009, WILEY - VCH Verlag GmbH & Co. KGaA, Weinheim.

The experimental discovery of the outstanding physical properties of graphene defined a high demand for its mass production, because of its wide potential applications, especially as active components of (opto)electronic devices.¹⁴ Generally, two main strategies have been used to synthesize graphene: one is called as “top-down” strategy, represented by exfoliation of graphite with tapes (Figure 1-2).⁵ In addition, several other exfoliation techniques have been developed during the past several decades, such as liquid-phase exfoliation (LQE),¹⁵

electrochemical exfoliation in aqueous¹⁶ or non-aqueous media,¹⁷ and supercritical fluid exfoliation.¹⁸ These methods have the advantage to allow the synthesis of less defective graphene in large quantity. The other widely used protocol is chemical oxidation/exfoliation of graphene to graphene oxide (GO) followed by reduction to remove oxygen groups,¹⁹ which is low-cost and simple to operate. However, graphene made by this method always contains ample defects, which decrease its performance when incorporated into electronic devices. The “bottom-up” strategy has also been employed to produce graphene, including growth of graphene on metal surfaces (Cu, Ni, etc.) using small molecule sources by a chemical vapor desorption (CVD) method,²⁰ thermal decomposition of SiC at high temperature²¹ and polymerization of assembled single molecule layer.¹³

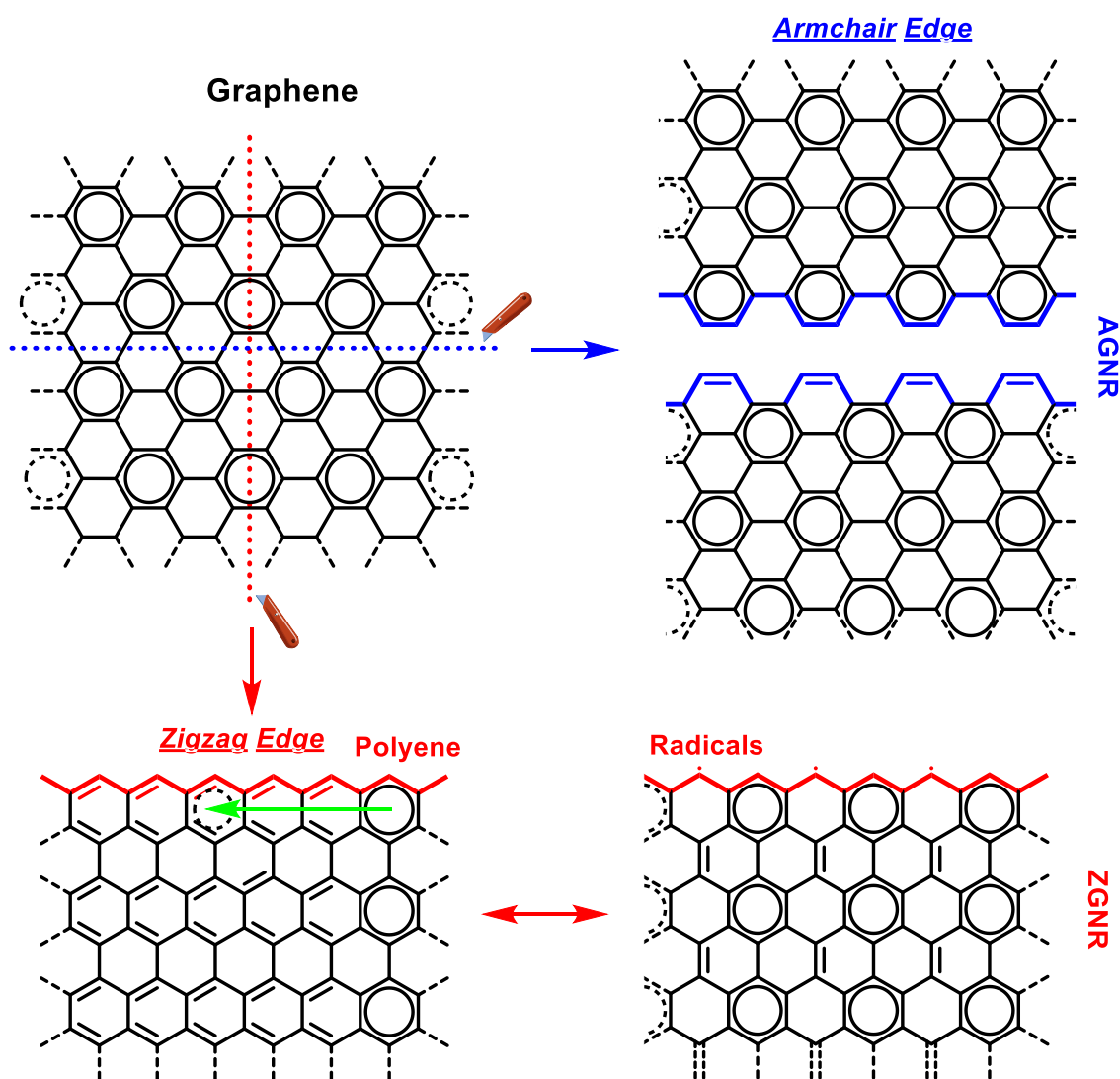


Figure 1-3. Formation of armchair and zigzag edges in infinite graphene by cutting along two different crystallographic directions: the blue one (top) indicates formation of armchair edges and the red one (bottom) indicates formation of zigzag edges.

The extraordinary electronic, thermal and mechanical properties of graphene, together with improved large-scale production technology, make this fantastic material widely used in many areas, such as electronics, sensing, catalysis, and energy storage and conversion.²² Amongst all characteristics of graphene, its high charge-carrier mobility is one of the most important because it makes graphene promising to exhibit excellent performance in field-effect transistors (FETs). However, this advantage is compromised due to the intrinsic zero-bandgap feature of pristine graphene, which prohibits on/off switching of the current through the FETs fabricated with this material. Therefore, unless the application demands a switch that is never “off”, a bandgap opening is required. According to the quantum confinement effect, when limiting the dimensional of graphene into 0D graphene quantum dots (GQDs) or 1D graphene nanoribbons (GNRs), its bandgap can be opened.²³ These nanosized graphene fragments can thus utilize the electronic advantages of the pristine graphene structure and offer a controlled, finite bandgap to generate a new family of carbon-based semiconductor materials. On the other hand, opening of bandgap also renders these materials with tunable and novel photophysical properties for use in photonic devices and imaging.²⁴

When breaking the covalent bonds connecting adjacent carbon atoms and the π -conjugation in pristine graphene network, edges could be produced, which will subsequently change the electronic properties of graphene.²⁵ Depending on the crystallographic orientation of the graphene lattice, two different edges will be generated (Figure 1-3): armchair edge and zigzag edge, and each type of edge is characterized by unique electronic properties and specific chemical reactivity. Full armchair and full zigzag edged GNRs (AGNR and ZGNR) are the simplest examples to discuss the effect of edge structures on the electronic and chemical properties of graphene, which have been intensively investigated both theoretically and experimentally.²⁶⁻²⁸ As demonstrated in Figure 1-3, AGNRs can be depicted as either fully benzenoid structures or benzenoid structures with partially appended double bonds, depending on their width. Determined by these resonance structures, AGNRs exhibit semiconductor properties and high chemical stability, while for ZGNRs, limited number of disjoint benzenoid rings can be drawn in their Kekulé structures, leaving the zigzag edges decorated with highly reactive polyene. As a consequence, ZGNRs have metallic electron transport properties and high intrinsic reactivity on their edges.²⁹ The property differences between armchair and zigzag edges come from the incompatibility of zigzag edges with fully benzenoid structures, which results in the presence of highly reactive localized double bonds and unpaired electrons (radicals).

1.2 Polycyclic Aromatic Hydrocarbons (PAHs) and Nanographene Molecules (GMs)

Polycyclic aromatic hydrocarbons (PAHs) are hydrocarbon compounds consisting of more than two fused benzene rings. They belong to the most abundant organic compounds in nature, and could be found in air, water, soil and interstellar space.³⁰ Some of them are produced during combustion of organic materials or metabolization of organic compounds in microorganism and plants. PAHs were first discovered in fossil fuels (coal and oil) and coal tar in the 19th century, which arise from slow chemical conversion of steroids, proteins and lipids contained in plants, phytoplankton, and zooplankton.³¹ Nowadays, human beings significantly rely on petro industry and the combustion of fossil fuels releases a large amount of PAHs into the environment, some of which can be harmful to human beings and animals.³² For example, benzo[*a*]pyrene is the most harmful PAH since it can form carcinogenic and mutagenic metabolites, which can intercalate into DNA and interfere with transcription.³³

Although all PAHs are composed of sp^2 -hybridized carbon atoms and terminated with hydrogens, which are seemingly all the same, their chemical and optical properties are dramatically different depending on the mode of connection of these fused benzene rings, which gives rise to different edge structures. Figure 1-4 shows three different PAHs consisting of four benzene rings. Linearly fused tetracene (**1-1**) with four benzene rings in one row is not stable in air and could be easily oxidized by oxygen at the L-region (zigzag edges) when exposed to air. It also exhibits intense absorption in the long wavelength range (~500 nm).³⁴ On the contrary, *peri*-condensed pyrene (**1-2**) has two carbon atoms located in its center and displays relatively higher chemical stability. The K-regions (convex armchair edge) have double bond character and could undergo chemical reactions, such as oxidation to diketone derivatives and annulative π -extension (APEX).^{35, 36} Different from tetracene, the maximum UV-vis absorption wavelength of pyrene is located at around 330 nm. The angularly fused triphenylene molecule (**1-3**) with three bay-regions (armchair edges) is extremely stable against oxidation reactions and has a relatively high optical energy gap with maximum absorption wavelength appearing at around 260 nm.³⁷

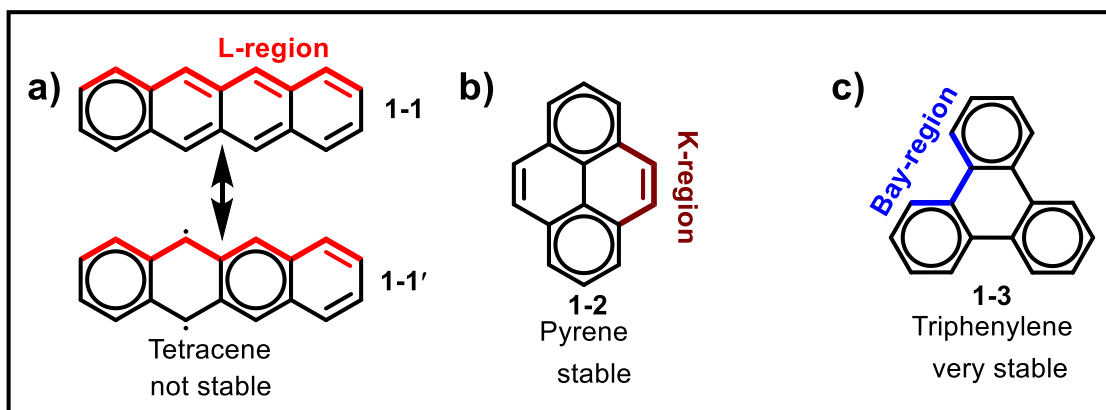


Figure 1-4. Possible chemical structures of three PAHs consisting of four fused benzene rings.

Clar's π -sextet rule has been the most successful model to explain the different stability of these polycyclic aromatic hydrocarbon systems, which was formulated in 1972.³⁸ It states that the Kekulé resonance structures of PAHs with the maximum amount of disjoint aromatic π -sextets, e.g. benzene-like units, are essentially determining their properties. Here, the aromatic π -sextets are defined as six π -electrons delocalized through a single six-membered ring separated from each other by C-C single bonds. This rule can be used to explain the chemical reactivity and optoelectronic property differences for the PAHs in Figure 1-4. Application of this rule to tetracene indicates that resonance structure **1-1'** is more important than **1-1** with only one Clar's sextet ring. Therefore, the rings at the head and tail of tetracene are expected to have higher stability than the inner rings, which has been proven by different measures of aromaticity³⁹ and could explain the fact that the inner rings possess a high tendency toward oxidation or bromination reactions. Triphenylene (**1-3**) possesses three Clar's aromatic π -sextets in its backbone without any isolated double bonds, so it demonstrates the highest chemical stability.

One important application of PAHs is their use as active materials in optoelectronic devices due to their attractive optical and electronic properties arising from delocalized π -conjugation structures. The delocalized electrons bring about decreased energy gaps and strong tendency to self-assemble into supramolecular structures through π - π interactions. These properties could be further tuned by their molecular shapes, sizes, and edge structures. For example, rylene derivatives are commercially available and have been used as dyes because of their intense absorption in the visible light region and high chemical and photochemical stability.⁴⁰ Unsubstituted pentacene exhibits a fairly high charge carrier mobility of 2–3 cm²/(V·s),

because of the tense mode of packing in the solid state, and has been used as active layer material in organic field-effect transistors.^{41, 42}

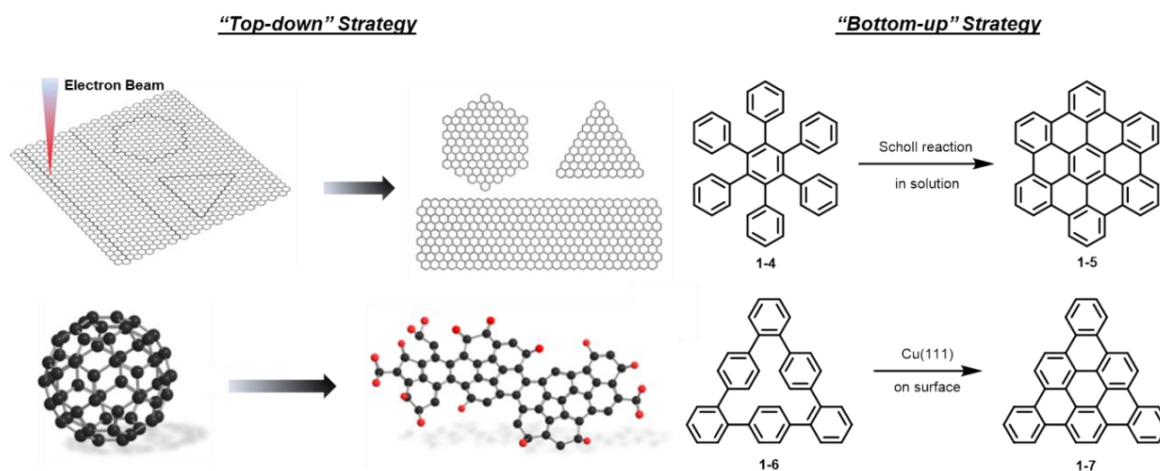


Figure 1-5. Synthesis of GMs through “top-down” and “bottom-up” methods. Ref.⁴³ Copyright: 2017, Nature publishing group. Ref.⁴⁴ Copyright: 2015 American Chemical Society.

Nanographene molecules (GMs) are large PAHs with sizes of 1–5 nm, which can be regarded as nanosized fragments of infinite graphene.⁴⁵ Similar to the synthesis of graphene, GMs could also be made through both “top-down” and “bottom-up” strategies (Figure 1-5). The “top-down” method, such as cutting down of graphene^{23, 46} and unzipping of fullerene,^{44, 47} have benefits to provide GMs in large quantity, but cannot precisely control the structures of obtained GMs, which have a critical effect on their (opto)electronic properties, as discussed above. However, the “bottom-up” synthesis, which mostly relies on solution or surface-mediated organic reactions, can provide GMs with atomic precision through rational design of precursors.^{48, 49}

In recent years, various GMs have been synthesized to open the bandgap of infinite graphene. These GMs have exhibited unique electronic structures, interesting photophysical and self-assembly properties, which are vital for their practical applications. The properties of these GMs, for example, the energy gaps and electronic absorption spectra, are strongly dependent on their molecule shapes, sizes, edge structures and peripheral substituents. For GMs with similar shapes and sizes, their edge structures could be different and will bring them new properties. According to their edge types, GMs could be further classified into three main categories: a) GMs with full armchair edge, which have high stability, represented by hexa-*peri*-hexabenzocoronene (HBCs); b) GMs with both armchair and zigzag edge, such as periacenes and anthenes; and c) GMs with full zigzag edge, such as ovalene and

circumanthracene. In the sections below, I will further discuss the syntheses, properties and applications of each type of GMs.

1.2.1 GMs with Full Armchair Periphery

Full armchair edged GMs by far have received the most attention. They could be depicted in a fully benzenoid pattern, meaning that their structures are composed of only benzenoid rings, e.g. aromatic π -sextets, which are interconnected by C-C single bonds, without any extra double bonds. In their molecular backbones, all the carbon atoms are included in an isolated aromatic π -sextet. So, GMs of this type usually exhibit a wide energy gap and consequently high chemical stability.

At the beginning of the 20th century, fundamental contributions to the synthesis of PAHs were made by Roland Scholl and Erich Clar,^{38, 50-52} who developed drastic conditions to synthesize and characterize a lot of PAH molecules. Their synthesis method involves the application of high temperature and strong oxidation/acid conditions, which are known as Scholl reaction and some are still used by chemists today to make larger nanographene molecules.

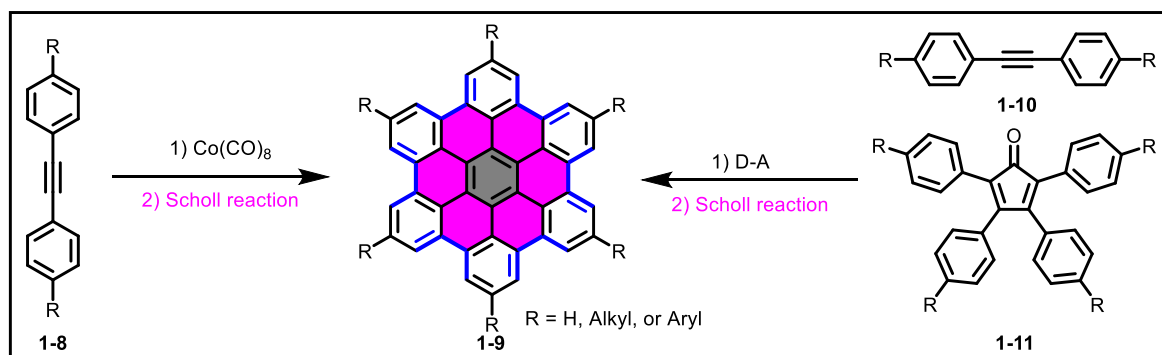


Figure 1-6. Two representative methods to synthesize HBCs with high and low symmetry: left, cyclotrimerization of diphenylacetylene catalyzed by $\text{Co}(\text{CO})_8$ followed by Scholl reaction; right, Diels-Alder cycloaddition of diphenylacetylene with tetraphenylcyclopentadienone followed by Scholl reaction.

Hexa-*peri*-hexabenzocoronene (HBC) is the most prominent and widely studied fully armchair-edged GMs (Figure 1-6). Its synthetic method was firstly reported by Clar's group in 1958 and great improvements were made by Müllen's group in 1995.^{48, 53} These early investigations in the preparation of HBCs paved the way for the bottom-up synthesis of GMs, which have been widely studied and found various applications in material science today. The improved synthetic method depends on cyclodehydrogenation (Scholl reaction) of substituted hexaphenylbenzene (HPB) with FeCl_3 or a combination of AlCl_3 and $\text{Cu}(\text{OTf})_2$ as Lewis acid

and oxidants, respectively. Highly symmetric HBCs could be made using $\text{Co}(\text{CO})_8$ catalyzed trimerization of substituted diphenylacetylene followed by cyclodehydrogenation with FeCl_3 ,⁴⁸ while less symmetric HBCs could be achieved by Diels-Alder (D-A) cycloaddition reaction of tetraphenylcyclopentadienone (CP) with (substituted) diphenylacetylene and subsequent cyclodehydrogenation.⁵⁴

The Scholl reaction has become an important tool in modern synthetic carbon chemistry, while the real mechanism is still under many controversial discussions (Figure 1-7): King *et al.* proposed an arenium cation mechanism based on their experimental and theoretical evidence,^{55,56} which was supported by the discovery of phenyl group rearrangement during an intramolecular Scholl reaction by Müllen's group in 2007,⁵⁷ while a cation-radical reaction mechanism process was suggested by Rathore's group.⁵⁸⁻⁶⁰ The actual reaction mechanism might be something in between these two mechanisms and dependent on the ability of the substrate to be protonated or oxidized, as well as reagents used for reaction.

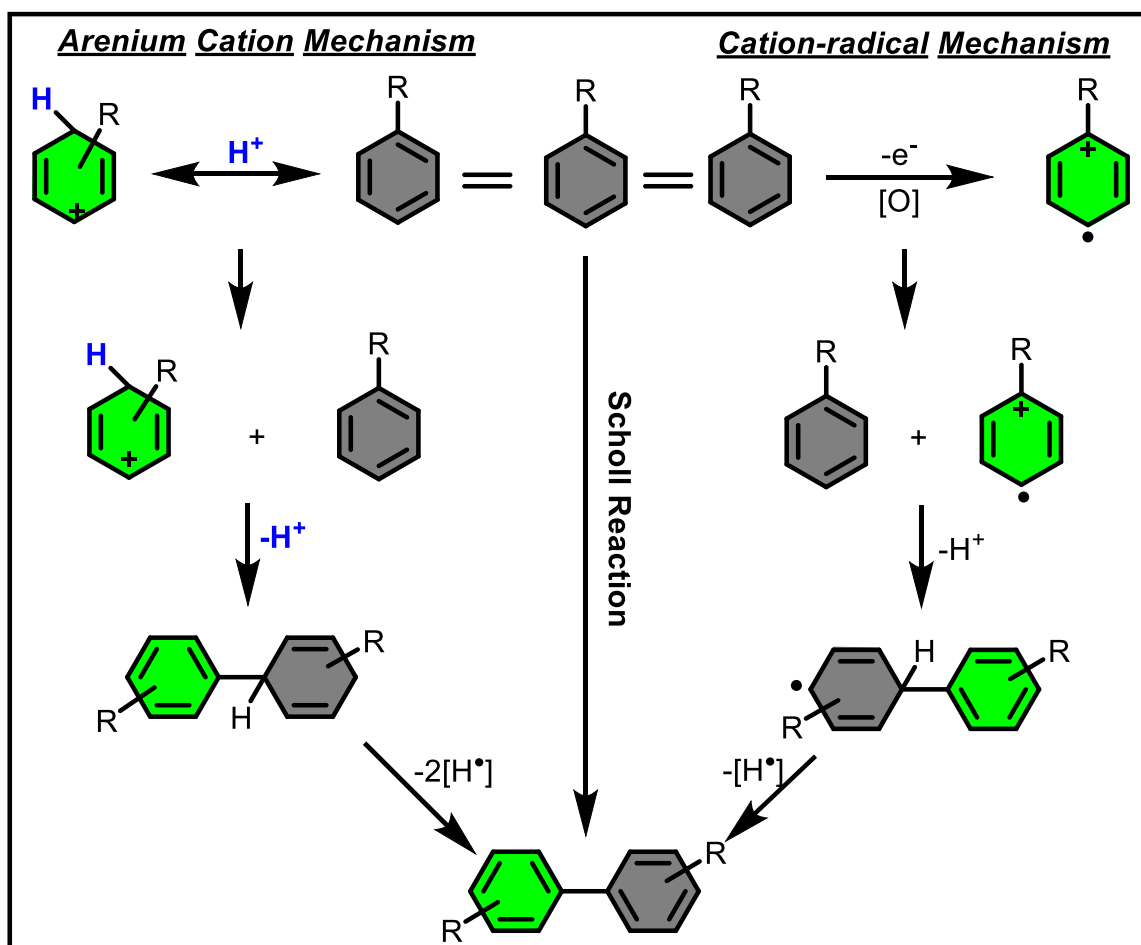


Figure 1-7. Two possible reaction mechanisms proposed for the Scholl reaction: left, arenium cation mechanism; right, cation-radical mechanism.

One ultimate goal for the bottom-up synthesis of GMs is to make structurally well-defined model compounds of graphene to investigate their structure-property relationship and facilitate their practical applications. For discotic liquid crystals, enlarging the core sizes will raise the order of columnar supramolecular structures due to increased intermolecular overlapping area.⁶¹ Moreover, the increased intermolecular π - π interaction is beneficial to improve the charge carrier mobility along the columnar direction, which is vital for their applications in electronic devices. In this context, the synthesis concept discussed above, e.g. D-A addition of CPs with ethynyl to produce polyphenylenes followed by Scholl reaction with FeCl_3 or combination of AlCl_3 and $\text{Cu}(\text{OTf})_2$, was further applied to larger systems and resulted in the formation of armchair-edged nanographenes with different shapes and sizes, such as supernaphthalene (**1-13**),⁶² supertriphenylene (**1-15**)⁶³ (Figure 1-8). By now, the largest GM ever synthesized through wet chemistry techniques and unambiguously characterized has a total of 222 carbon atoms in the aromatic core (**1-17**, supercoronene).⁶⁴ These achievements are just a small part of the results obtained by organic chemists, which can compete with the top-down method widely applied by physicists.

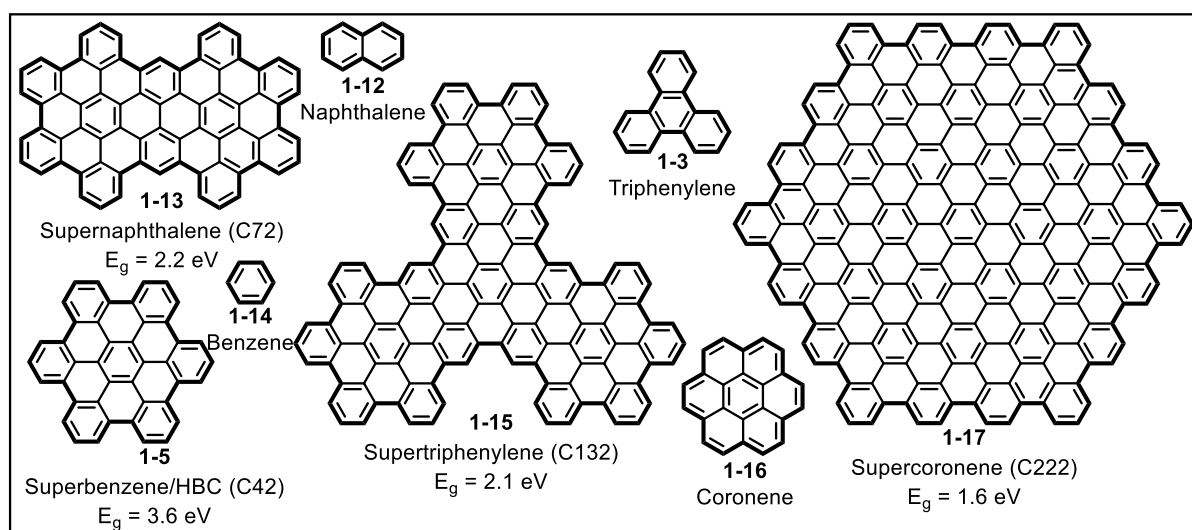


Figure 1-8. Structures of extended armchair-edged nanographene molecules with different sizes and corresponding HOMO-LUMO gaps calculated from onsets of their UV-vis absorption spectra.

While keeping the edge types unchanged, increasing the core sizes of GMs results in gradual shrinking of their energy gaps because the π -electrons could be delocalized over a larger area. Taking the relatively large systems HBC (C_{42}), supernaphthalene (C_{72}), supertriphenylene (C_{132}), and supercoronene (C_{222}) as examples, their highest occupied molecular orbital (HOMO) - lowest unoccupied molecular orbital (LUMO) gaps calculated from their respective UV-vis absorption peaks converge from 3.6 eV for C_{42} to 1.6 eV for C_{222} . These

characteristics make large GMs potentially applicable in organic photovoltaics, which demands intense absorption in the long wavelength range and broad UV-vis absorption band. However, increasing core sizes of GMs also inevitably brings some drawbacks, for example decreased solubility, which prohibits their characterization and solution processing. As a consequence, other strategies, which can alleviate this problem, are in high demand to tune the (opto)electronic properties of GMs.

1.2.2 GMs with Both Armchair and Zigzag Periphery

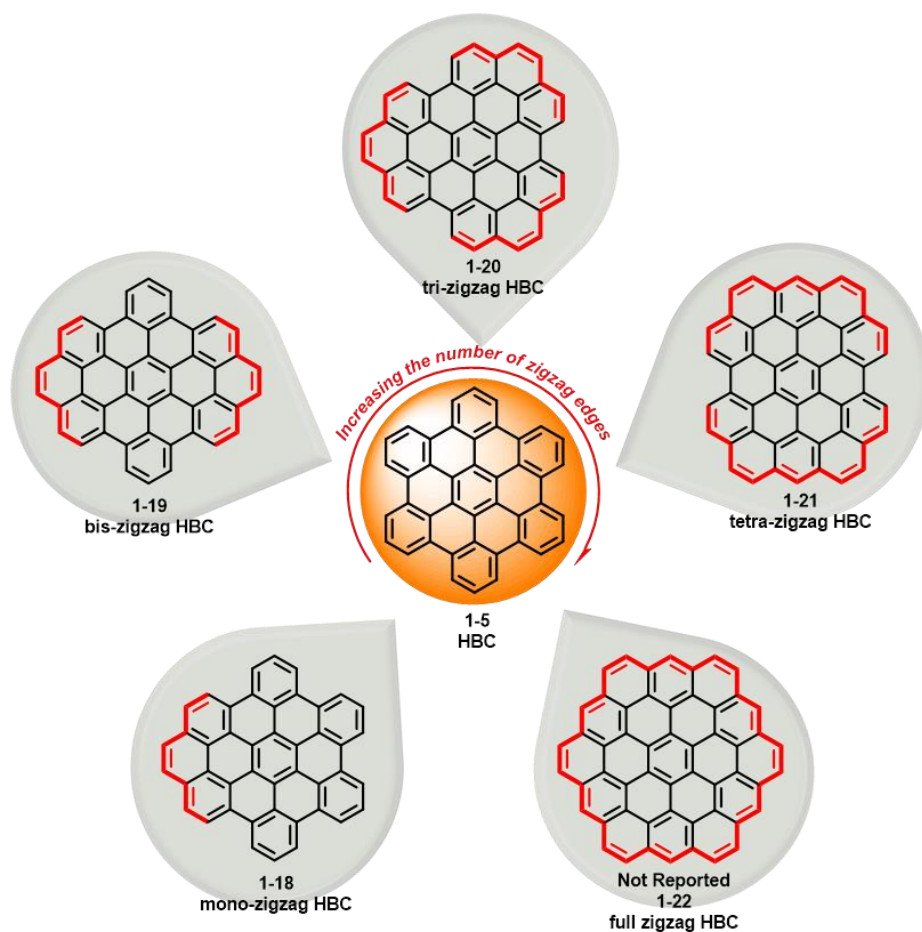


Figure 1-9. Chemical structures of HBC, mono-zigzag HBC, bis-zigzag HBC, tri-zigzag HBC, tetra-zigzag HBC and full zigzag HBC.

Fusing one C=C bond to the bay region of full armchair edged GMs will give rise to zigzag edge. However, these two extra π -electrons in the C=C bond cannot be included in any aromatic π -sextets and will not contribute to increase the total number of Clar's aromatic π -sextets in the new GM. For example, annulation of one, two or three C=C bonds to fully benzenoid HBC at each bay position produces HBC derivatives with partial zigzag edges, namely mono-zigzag HBC **1-18**, bis-zigzag HBC **1-19**, tri-zigzag HBC **1-20**, and tetra-zigzag

HBC **1-21**, respectively (Figure 1-9).⁶⁵⁻⁶⁷ Fully zigzag-edged HBC **1-22**, also named as circumcoronene, has attracted enormous interests in the past several years. However, the synthesis of circumcoronene has never been achieved in spite of many dedicated efforts.^{68, 69} Incorporation of zigzag edges is expected to alter not only the electronic and photophysical properties of HBC but also to furnish interesting chemical reactivity as well as self-assembly behavior in 2D and 3D.

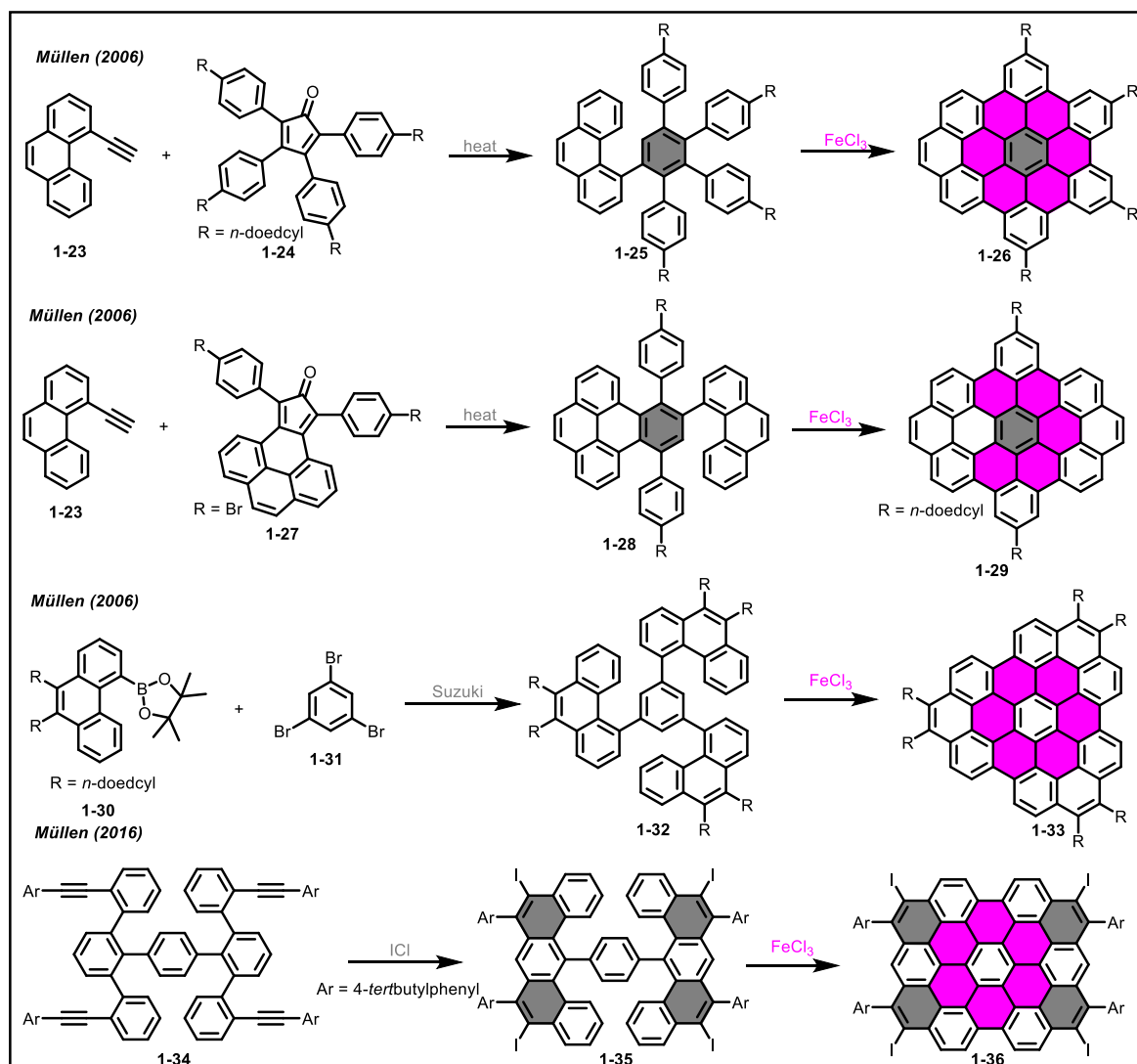


Figure 1-10. Synthetic methods toward mono-zigzag HBC, bis-zigzag HBC, tri-zigzag HBC and tetra-zigzag HBC derivatives.

The synthetic methods toward partially zigzag-edged HBCs are shown in Figure 1-10. Firstly, D-A cycloaddition of 4-ethynyl phenanthrene (**1-23**) with tetraphenylcyclopentadienone **1-24** and **1-27** gave polyphenylene intermediates **1-25** and **1-28** in 95% and 75% yield, respectively.⁶⁶ C_3 symmetric polyphenylene intermediate **1-32** with high steric hindrance was obtained by three-fold Suzuki coupling of phenanthrene borate ester **1-30** with

tribromobenzene (**1-31**) under strong base condition. Finally, these three intermediates were planarized with iron (III) chloride as oxidants to give mono- to tri-zigzag HBCs in good yield. Stable tetra-zigzag-edged HBC derivative was recently synthesized as a novel non-fully benzenoid PAH.⁶⁷ The key intermediate **1-35** with two pre-installed benzo[*m*]tetraphene units was prepared by ICl promoted four-fold iodination benzoannulation reactions to introduce extra zigzag edge, which subsequently underwent cyclodehydrogenation to give the target product **1-36** in good yield. In order to increase the stability of tetra-zigzag HBC, four phenyl groups were introduced to kinetically block the most reactive zigzag positions.

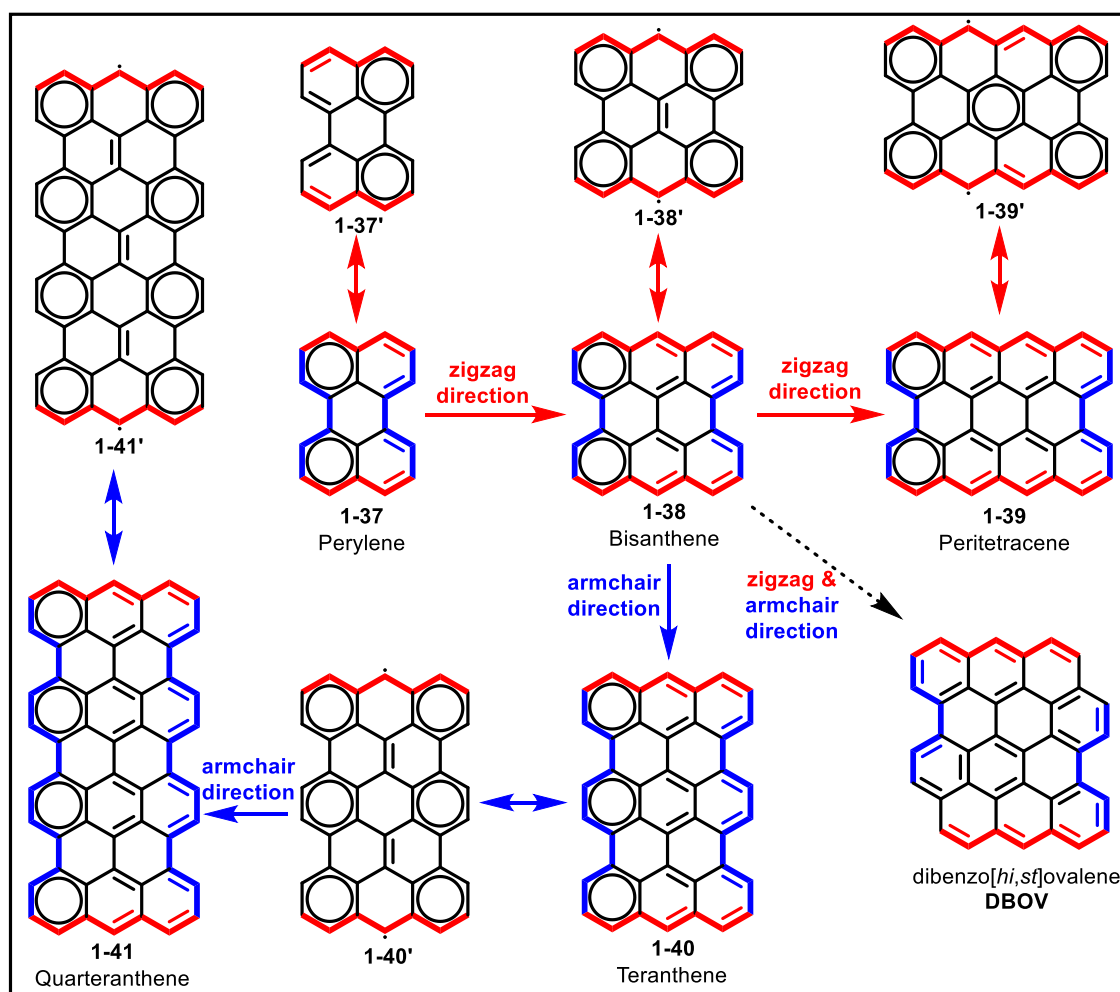


Figure 1-11. Chemical structures and respective resonance structures of GMs with both zigzag and armchair edge.

Periacenes and anthene derivatives are another type of GMs with both zigzag and armchair edges having rectangular shape (Figure 1-11). In their fully conjugated Kekulé resonance structures, only one Clar's aromatic π -sextet could be drawn for each row of acene, leaving the other six-membered rings with two conjugated C=C bonds. This structural character

endows their zigzag edges with olefinic characteristics and increases their chemical reactivity, such as tendency to undergo oxidation at L-regions and D-A reaction at bay regions, and decreased energy gap in comparison with the fully armchair-edged GMs. For example, perylene, as the smallest member of the periacene family, has intense maximum absorption wavelength locates at 440 nm. However, triphenylene, which is composed of four benzene rings with two electrons less than perylene, does not show any absorption above 300 nm. Rylene and its imide derivatives have shown obvious advantages, such as high chemical, thermal and photo stability and their photophysical properties and applications have been widely investigated.^{70, 71} The size of the perylene (**1-37**) core can be extended along zigzag, armchair or both zigzag and armchair directions. Extension of the armchair edges produces higher order rylenes (such as quaterrylene, pentarylene, hexarylene derivatives), which show narrow energy gaps, near-infrared (NIR) absorption and strong visible light emission properties.⁷²

Lateral extension of perylene along zigzag edges gives rise to higher periacenes (Figure 1-11). The name was used to describe rectangular shaped GMs with two parallel armchair edges and zigzag edges, which are the most representative members of GMs with both armchair and zigzag edges. They could be named as bisanthene (**1-38**), peritetracene (**1-39**), peripentacene, respectively, according to the length of their zigzag edges (Figure 1-11). Theoretical calculations indicate that, with extension along zigzag edges, the change from a nonmagnetic phase to an antiferromagnetic phase will occur starting from peritetracene (**1-39**), which has four fused benzene rings along the zigzag edge, inducing an open-shell ground state character.^{73, 74} Since only two Clar's aromatic π -sextets can be drawn for high order periacenes (zigzag benzene rings >3) and more could be obtained for their open-shell forms, they have high chemical reactivity and are prone to react with oxygen or water in the air, which make the synthesis, isolation and characterization of high-order periacenes very challenging.

The parent bisanthene (**1-38**) has been known for many years. It was firstly synthesized by Clar⁷⁵ and later improved by Scott's and Wu's groups.^{76, 77} Unsubstituted bisanthene is not stable because of its high HOMO level, which can easily undergo addition with singlet oxygen in air at its most reactive *meso*-positions. Therefore, several measures were taken to solve this problem, for example, 1) introduction of electron-withdrawing dicarboxylic imide (**1-44**) to its zigzag edges to decrease corresponding HOMO level;⁷⁸ 2) introducing bulky functional groups to kinetically block the most reactive positions (**1-45**), which also increases

its solubility in organic solution;⁷⁹ 3) construction of quinoidal structures on the backbone of bisanthene (**1-46**).⁸⁰ In addition to enhanced stability and solubility in organic solutions after structural functionalization, they also exhibit intense absorption and emission in the NIR region as well as amphoteric redox behavior.

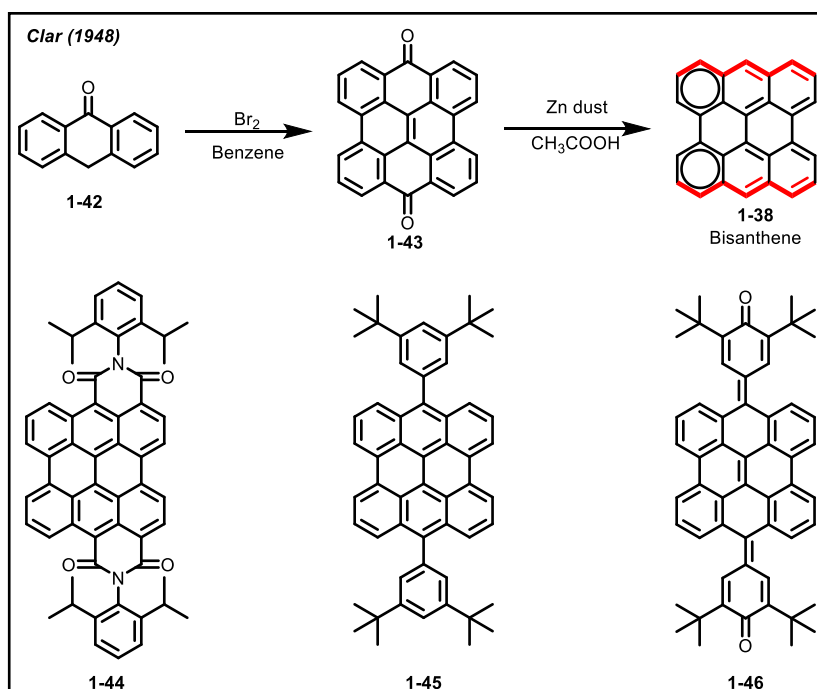


Figure 1-12. First synthesis of bisanthene by Clar's group in 1948 and structures of bisanthene derivatives with increased stability.

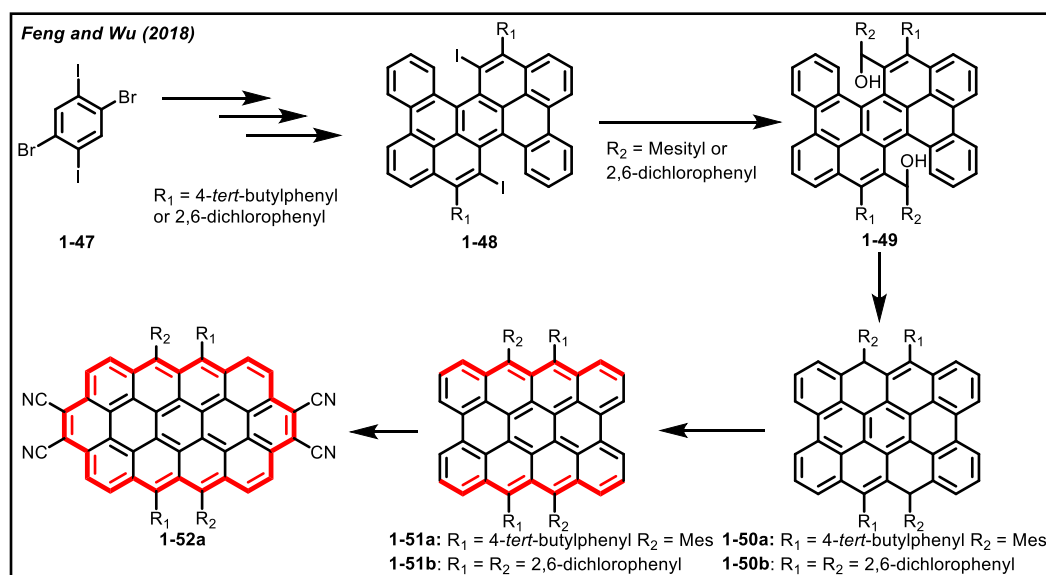


Figure 1-13. Syntheses of substituted peritetracenes by Feng's and Wu's groups and its Diels-Alder addition reaction with DDQ.

Peritetracene, as the next member of the periacene family, is a “star” molecule and its synthesis has drawn a lot of interests during the past decades,⁸¹ because of its antiferromagnetic property with an open-shell ground state predicted by theoretical calculations.⁷³ Successful syntheses and characterization of peritetracene derivatives (**1-51**) were achieved by Feng’s and Wu’s groups recently (Figure 1-13).^{82, 83} Both methods rely on the synthesis of diiodo intermediates **1-48** with 1,4-dibromo-2,5-diiodobenzene (**1-47**) as starting material, followed by lithiation and nucleophilic addition with aldehyde to give diol precursor **1-49**, which further undergoes intramolecular Friedel–Crafts ring-closure reaction to give dihydroperitetracene **1-50**. For the dehydrogenation step, Feng’s group used slightly excess amount of 2,3-dichloro-5,6-dicyano-1,4-benzoquinone (DDQ) to treat **1-50a** in toluene solution, which provided peritetracene **1-51a** in quantitative amount. The sterically hindered bulky mesityl (Mes-) groups and 4-*tert*-butylphenyl groups help to increase the stability and solubility of the resulting peritetracene (**1-51a**). Significant biradical character was proven by variable-temperature NMR measurements. Interestingly, the obtained peritetracene **1-51a** underwent D-A addition with excess DDQ in the reaction mixture to give tetracyano substituted fully zigzag-edged circumanthracene **1-52a**. On the other hand, in Wu’s case, DDQ oxidation of intermediate **1-50b** did not work most probably because of the electron-deficient nature of the core, induced by four electron-withdrawing dichlorophenyl groups. Nevertheless, **1-50b** could be deprotonated with a strong base of KO*t*Bu to afford a dianion, which was in-situ oxidized with *p*-chloranil to give the target peritetracene **1-51b**. Its half-life time was measured to be 7 h in tetrahydrofuran (THF) solution under ambient condition and light, monitored by UV-vis absorption spectroscopy. This time is much longer than that of **1-51a** reported by Feng’s group, indicating the important role of dichlorophenyl for the stabilization of such compounds with biradical properties. Further extension to larger periacenes than peritetracene has not been achieved by now, because they are predicted to suffer from high reactivity.⁸⁴

Alternatively, extension along the armchair edges of bisanthene core produces higher order anthenes. For example, Kubo’s group reported successful syntheses of teranthene **1-56** and quarteranthene **1-60** by fusing one and two extra anthryl units to the zigzag edge of bisanthene, respectively (Figure 1-14).^{85, 86} In order to obtain stable and soluble anthenes in solution, they introduced bulky *tert*-butyl and mesityl groups to kinetically block the most reactive positions. As shown in Figure 1-14, the key steps for their syntheses are partial cyclization with KOH/quinolone (dehydrochlorination) and full cyclodehydrogenation was accomplished under harsh conditions with DDQ/Sc(OTf)₃ as oxidants at high temperature.

Teranthene **1-56** was obtained as green dark solid after crystallization from dichloromethane and hexane under argon flow. By using UV-vis absorption spectroscopy, the half-life time of teranthene in toluene solution under ambient condition was measured to be 3 days. By using a similar method, quateranthene **1-60** was obtained as bluish-black solid. However, its half-life time was determined to be only 15 h under the same measuring condition, in accordance with its more pronounced biradical character.

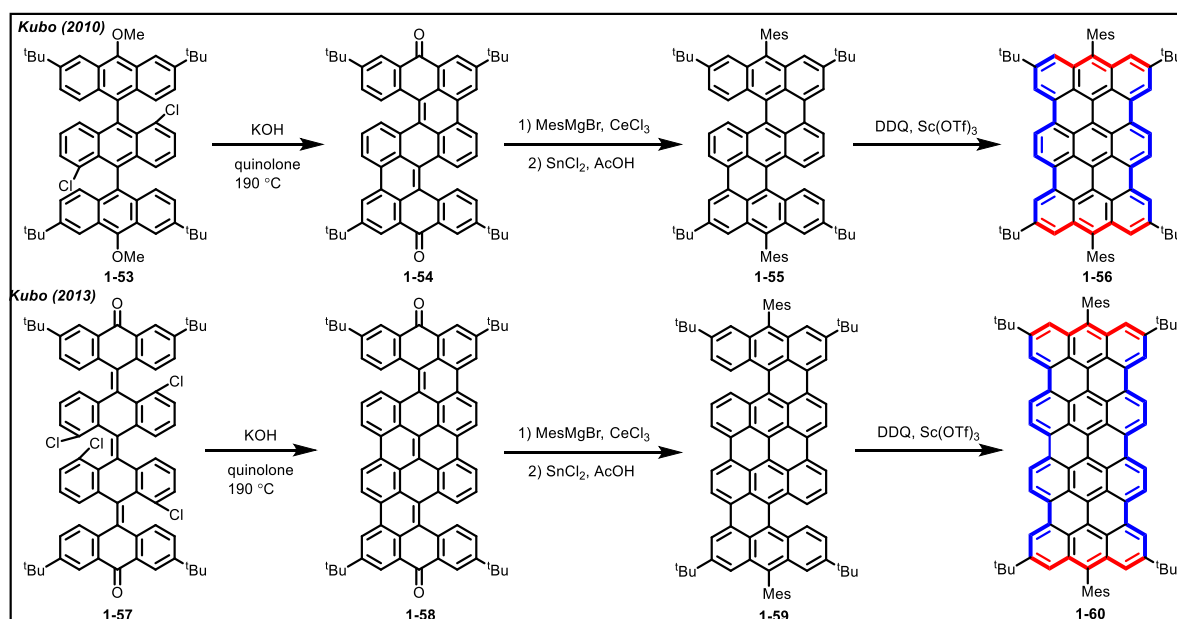


Figure 1-14. Synthetic scheme toward teranthene and quateranthene.

As already discussed above, the size of the bisanthene core could be expanded either along its zigzag edges to give high order periacenes or armchair edges to produce anthenes by fusing extra anthryl units (Figure 1-11), both of which greatly alter its electronic and photophysical properties and provide enhanced biradical properties. However, extension along both armchair and zigzag directions simultaneously have not been tried due to lack of proper synthetic methods. This will provide a possible way to build new nanographene species with novel (opto)electronic properties.

1.2.3 GMs with Full Zigzag Periphery

When cutting infinite graphene along its zigzag directions into small fragments, fully zigzag-edged PAHs and GMs will be obtained. Depending on the number of zigzag edges, different geometries and shapes can be achieved, such as triangle, diamond, parallelogram, hexagon, etc. According to their core structures, they could be further classified into two categories. Some of them belong to non-Kekulé polynuclear aromatic hydrocarbons with one or more

unpaired electrons in their corresponding conjugation system. Consequently, they exhibit open-shell characters and are of high interest both theoretically and experimentally. Phenalenyl radical (**1-61**) is the smallest member in this class, which has one unpaired electron with total spin multiplicity of $2S+1=2$ (Figure 1-15). Extension along three zigzag edges results in the formation of triangulene (**1-62**), which has two unpaired electrons and triplet states. Further extension produces **1-63** with 3 unpaired electrons and much higher spin states. It is important to note that, in all of these systems, the spins are delocalized over the whole conjugation system. However, the largest spin density is localized at the zigzag edges, making them prone to undergo dimerization or oxidation reactions in air.

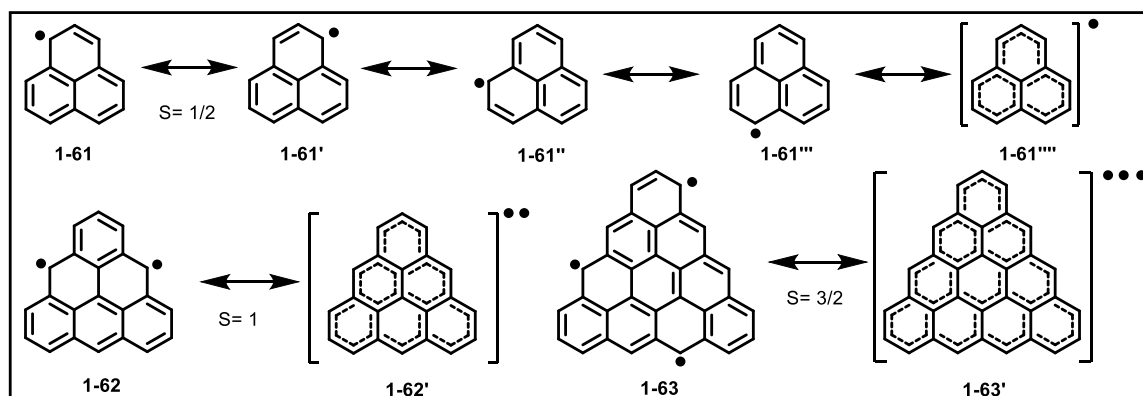


Figure 1-15. non-Kekulé PAHs and GMs with three zigzag edges.

The other category of fully zigzag-edged GMs can be drawn as fully conjugated Kekulé structure. They could be obtained by fusing extra C=C bonds to all bay regions of armchair-edged GMs. As a consequence, compared with fully armchair-edged GMs of similar sizes, they have lower energy gap. Similar to periacenes, the transformation from the fully conjugated closed-shell form to the biradicaloid open-shell form depends on the size of the aromatic core (especially length of zigzag edges).⁷⁴ Since π -electrons are all delocalized through the backbone of the aromatic core, spin localized edge states will also be expected for larger zigzag edged GMs.

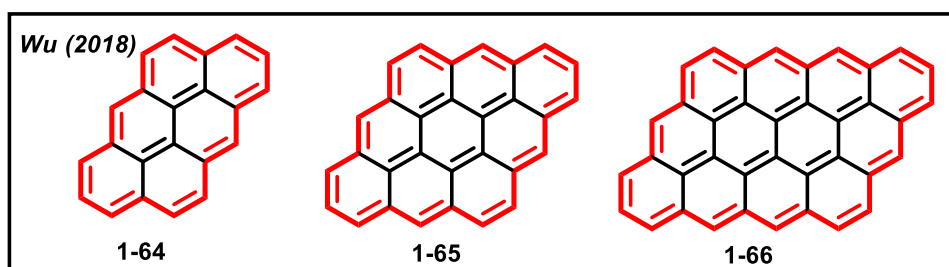


Figure 1-16. GMs with four zigzag edges.

In 2018, Wu's group firstly reported the stepwise syntheses of three fully zigzag-edged GMs (**1-64**–**1-66**) based on anthryl groups with different sizes (Figure 1-16).⁸⁷ These three GMs were all characterized by bearing four zigzag edges in a parallelogram shape and obtained as highly stable compounds under ambient conditions. In their UV-vis absorption spectra, these three GMs showed two intense and well-resolved absorption bands (Figure 1-17a). The bands at longest absorption wavelengths of each sample were red shifted with increasing the molecule sizes, indicating decreased energy gaps. These absorption bands are similar to the characterized ρ -band of many closed-shell PAHs. The biradical characters were calculated to be zero for **1-64** and **1-65**, while a very small biradical character of 18% was obtained for **1-66**. So, they all behave as closed-shell compounds in the ground state.

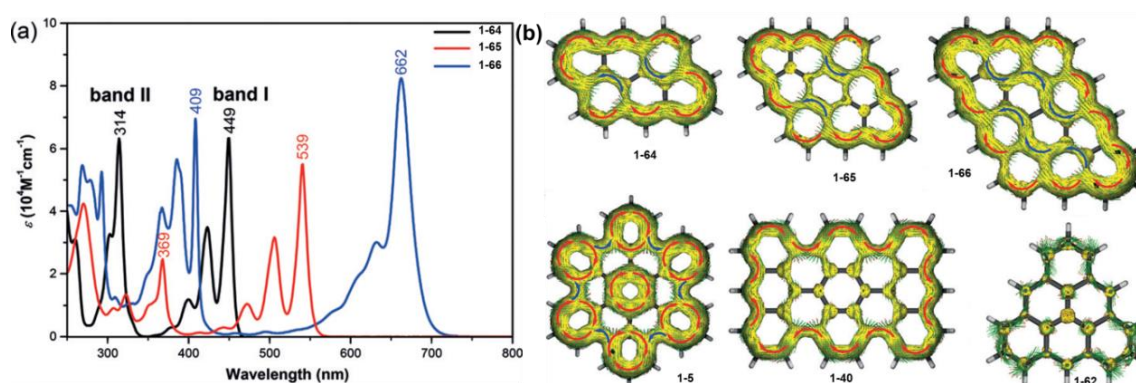


Figure 1-17. a) UV-vis absorption of **1-64**–**1-66**; b) ACID plots calculated for nanographenes with four zigzag edges, full armchair edges, two armchair/zigzag edges and triangulene with three zigzag edges. Ref.⁸⁷ Copyright: 2018 WILEY - VCH Verlag GmbH & Co. KGaA, Weinheim.

Anisotropy of the induced current density (ACID) plot is a useful tool to study the π -conjugation and aromaticity of aromatic macrocycle compounds.⁸⁸ As shown in the calculated ACID plots of these three compounds in Figure 1-17b, the backbone of fully zigzag-edged GMs show clockwise diatropic ring current, which are mainly delocalized through the outer rim, thus indicating that they are all global aromatic, while the other rings with reverse ring current directions are less aromatic. In comparison, the ACID plot of the fully armchair-edged HBC (**1-5**) shows that the ring current is more localized on the seven benzene rings and that there is minor electron conjugation along the periphery. The GM with two zigzag and two armchair edges (**1-40**) exhibits a diatropic ring current also mainly delocalized along the periphery, thus indicating its global aromaticity. However, in contrast, the GM with three zigzag edges, for example tirangulene **1-62**, has no ring current, suggesting that the electrons are localized at the zigzag edge.

Circumarene is a subclass of fully zigzag-edged GMs composed of six zigzag edges (Figure 1-18). They could be obtained by fusing extra C=C bonds to the bay positions of appropriate full armchair/partial zigzag edged GMs. The name circumarene comes from the feature that the central aromatic unit is circularly annulated by benzene rings. Accordingly, they are named circumbenzene (coronene) (**1-67**), circumnaphthalene (ovalene) (**1-68**), circumanthracene (**1-69**), circumpyrene (**1-70**), circumcoronene (**1-22**) and so on, depending on the structure of the core unit. In their full conjugated Kekulé resonance structures, three disjoint aromatic π -sextets could be drawn while four could be depicted for higher circumacenes. However, only two isolated aromatic π -sextets are possible for the Kekulé resonance structures of periacenes (Figure 1-11). So, the circumarenes are expected to have higher HOMO-LUMO energy gaps and higher stability compared with their corresponding periacenes, which may be explained by Clar's rule.

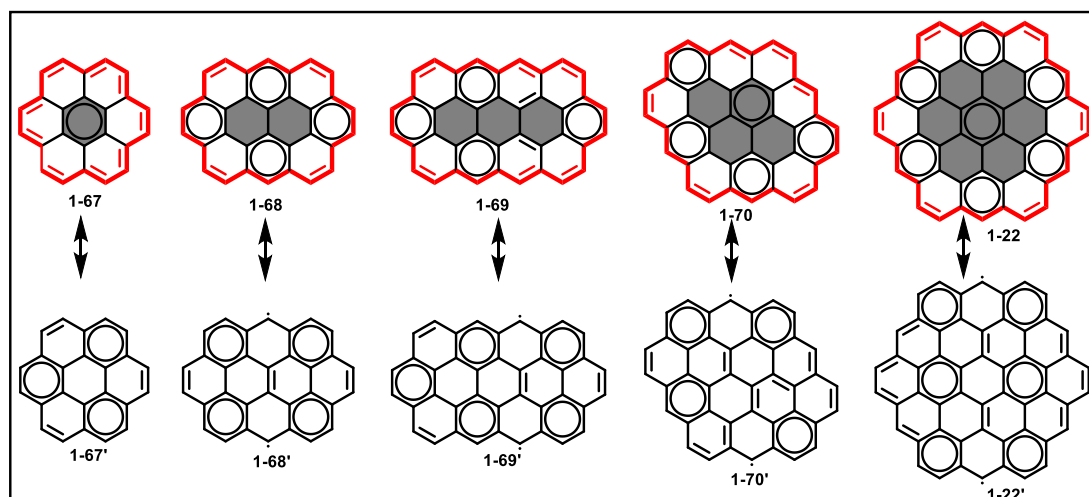


Figure 1-18. Structures of circumarenes as GMs with six zigzag edges, from left to right: Circumbenzene (**1-67**, coronene), Circumnaphthalene (**1-68**, ovalene), Circumanthracene (**1-69**), Circumpyrene (**1-70**), and Circumcoronene (**1-22**).

Coronene **1-67**, also known as circumbenzene, is the smallest member of the fully zigzag-edged GMs family (Figure 1-19). The conjugation of six outer benzene rings resulted in unique electronic structures and high chemical stability. Unsubstituted coronene was synthesized by Clar's group in 1957 through D-A addition of perylene and maleic anhydride in the presence of *p*-chloranil as oxidants, followed by decarboxylation with soda-lime at high temperature to give **1-74**, which further underwent D-A reaction and decarboxylation.⁸⁹ By reacting with highly reactive electron-deficient dienophiles, numerous coronene

derivatives (**1-75–1-77**) were also obtained, exhibiting varied electronic and self-assembly properties.^{85, 90}

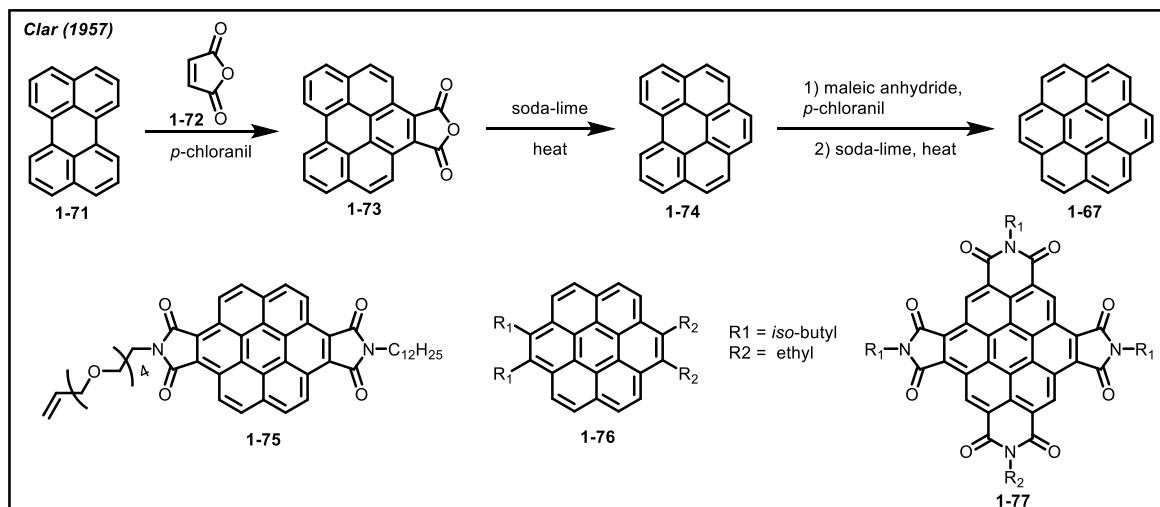


Figure 1-19. Synthesis of coronene by two-fold Diels-Alder reaction and chemical structures of different coronene derivatives.

The second member in the family of circumarene is ovalene, which contains a naphthalene core circularly benzannulated by 8 benzene rings. The synthesis of ovalene was firstly reported by Clar's group in 1948, using a similar strategy as for the synthesis of coronene.⁹¹ Two-fold D-A addition of bisanthene with maleic anhydride in the presence of oxidants, followed by decarboxylation gave unsubstituted ovalene. A series of ovalene derivatives were also obtained by two-fold oxidative D-A addition of bisanthene with electron-deficient dienophiles (**1-79–1-81**), which showed unique self-assembly behavior and good performance in OFETs.^{77, 92-94}

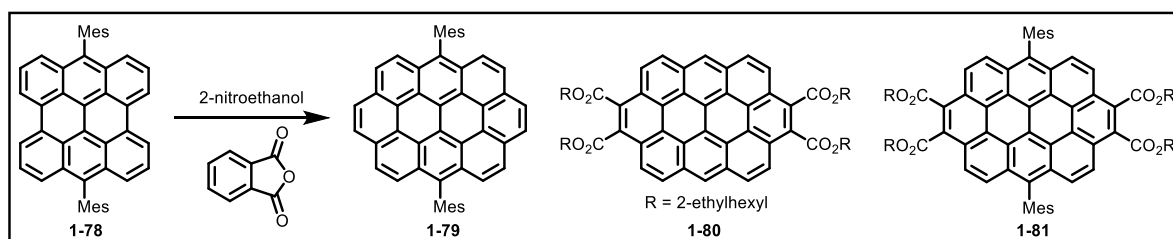


Figure 1-20. Synthesis of *meso*-substituted ovalene by Diels-Alder addition reaction of bisanthene with nitroethene and structures of two substituted ovalene derivatives.

Although Clar's group reported the first synthesis of circumanthracene in 1956 through a controlled graphitization process,⁹⁵ his group published a correction 25 years later based on the correlations between photoelectron spectra and PAH structures and claimed that the

structure published in that early paper was not the desired circumanthracene.⁹⁶ Then in 1991, Diederich et al. reported the first synthesis of unsubstituted circumanthracene **1-84** by a sequence of four-fold photocyclodehydrogenation under UV-light irradiation, followed by direct ring-closure of methyl groups promoted by DDQ in the dark.⁹⁷ The circumanthracene was obtained as insoluble crystalline precipitate. Substituted circumanthracene **1-52a** was reported recently by Feng's group when preparing the peritetracene (**1-51a**), which reacted with DDQ at room temperature slowly to give tetracyano substituted circumanthracene.⁸² This result also indicates the high reactivity of peritetracene towards Diels-Alder addition compared with bisanthenes, which is in good accordance with theoretical predictions.^{82, 93}

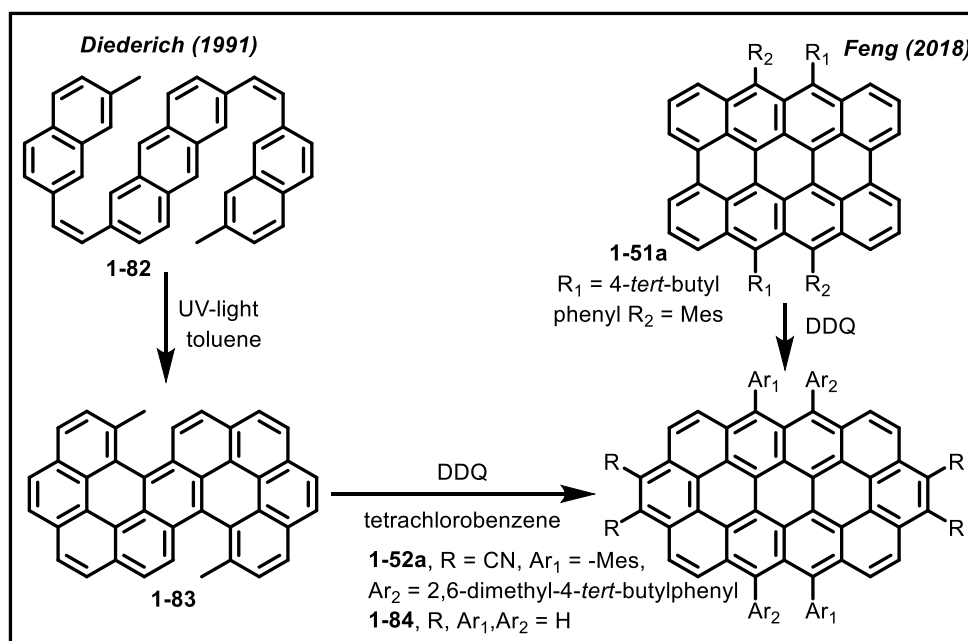


Figure 1-21. Syntheses of circumanthracenes by oxidative cyclodehydrogenation and D-A reaction methods, respectively.

Although some circumarenes have been reported and extensively studied for their intriguing electronic structures and self-assembly behavior, the syntheses of circumarenes with aromatic core units larger than three benzene rings have never been achieved, such as circumpyrene (**1-70**) and circumcoronene (**1-22**) (Figure 1-18). These aromatic compounds have attracted a lot of interests from theoretical chemists for their ability to coordinate with transition metals. For example, circumpyrene is predicted to coordinate with Pd atoms to form sandwich layered structures.⁹⁸ On the other hand, enlarging the sizes of fully zigzag-edged GMs, more Clar's aromatic π -sextets will be obtained in the biradical form than in the Kekulé structure with closed-shell characteristic, making them promising for use in spintronics. However, experimental data on large circumarenes remains elusive because of lacking proper synthetic

methods to introduce long zigzag edges. Enlarged π -conjugation will also contribute to increase their tendency to form ordered self-assembly structures, and increase intermolecular overlap.

1.3 π -System Extended Porphyrins

In addition to altering their shapes, sizes and edge structures, incorporation of heteroatoms is another strategy to tune the electronic and photophysical properties of GMs. In comparison with their all-carbon counterparts, heteroatom-doped GMs are attracting increasing interests in recent years for their important role in catalysis, energy storage, magnetics, and optoelectronics.^{99, 100} However, their controlled syntheses with atomically precise structures are generally very challenging.

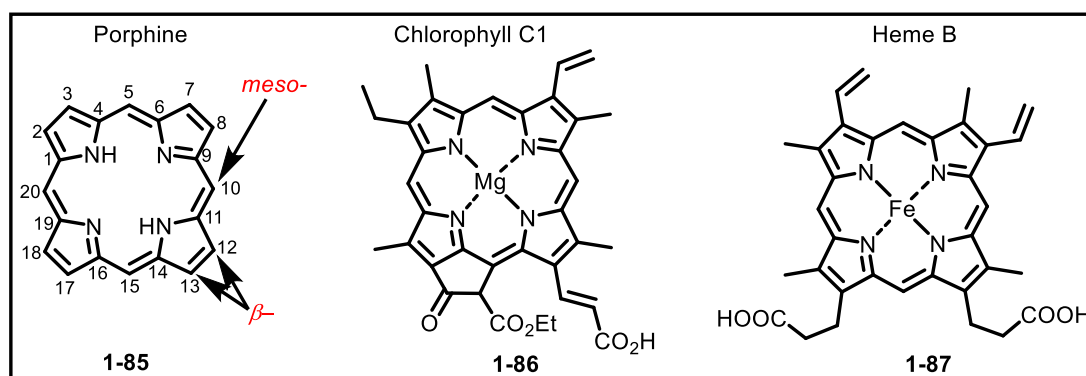


Figure 1-22. Structures of porphine and its natural derivatives.

Nitrogen is one important dopant often used to tune the optical, chemical, and electronic properties of carbon materials. The size of the nitrogen atom is similar to that of carbon, which makes it fit well into the carbon framework, so their atomic orbitals perfectly overlap with each other to form stable covalent bonds. Nitrogen doped carbon materials have shown wide applications in various important process, for example, they can promote the transformation of carbon dioxide to useful gases, like CO or methane, of methanol to formic acid, or the activation of small molecules, such as hydrogen and oxygen.¹⁰¹⁻¹⁰⁴ Most of these materials are synthesized by introducing nitrogen to the prepared graphene during later stage of synthesis, which inevitably introduce defects of unknown nature regarding the positions (edge-located or internal-located) and types of nitrogen (pyridinic, pyrrolic or amine).¹⁰⁵ These uncertain defects and structural differences may affect the performance of such carbon materials and prevent understanding the reaction mechanism of catalytic process and other important process they participated in. This also hinders a deep understanding of the

structure-property relationship at the molecular or atomic level, as well as rationally designing new materials with improved performance.

In addition to the above-mentioned nitrogen-doped GMs, some other nitrogen containing molecules were prepared that show similar functions as N-doped graphene and help to better understand the catalytic processes. Porphine (**1-85**) is a macromolecule composed of four pyrrole units (N-containing) connected by four methine bridges (Figure 1-22). Its versatility makes it one of the most important building blocks used in many artificial and biological systems. For example, iron(III) porphyrin derivatives have been used for catalytic oxidation of C-H groups¹⁰⁶ and other natural porphyrins participate in very essential bioactivities, like that of the light harvesting center in photosynthesis (Chlorophyll C1, **1-86**) and transport of oxygen in blood (Heme B, **1-87**).¹⁰⁷ Recently, porphyrin and other tetrapyrrole derivatives containing different metals have found wide applications in molecular electronics, sensing and medicine.^{108, 109} However, porphyrin has intense Soret band (420 nm) absorption and relatively weak absorption in the Q band (600–800 nm), which limits its application in photovoltaics and NIR absorption materials.

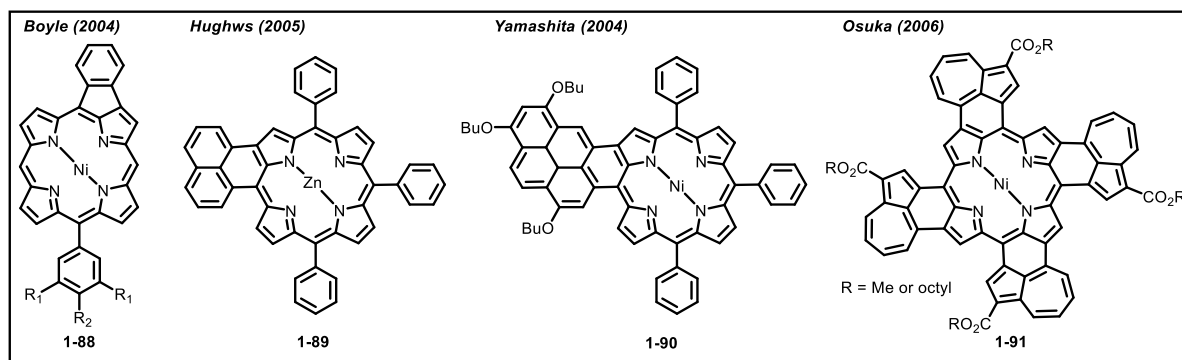


Figure 1-23. Representative examples of π -system extended porphyrins by fusing porphine with small PAHs at *meso*-Ar, β positions.

In recent years, the synthesis of porphyrin derivatives with intense long-wavelength absorption has attracted a lot of interests.¹¹⁰ To achieve this purpose, some small molecule aromatics have been fused to porphyrin core across the *meso*- and β -position, such as benzene,^{111, 112} naphthalene,^{113, 114} pyrene,¹¹⁵ and azulene¹¹⁵ through appropriate cyclodehydrogenation (**1-88–1-91**). Some of these examples are shown in Figure 1-23. In these systems, the conjugation of small molecule aromatics strongly perturbs the electronic properties of the porphyrin framework, which results in large red-shifts of their corresponding absorption bands. In addition to the absorption wavelength, the nonlinear optical properties of

porphyrin were also strongly influenced.¹¹⁶ As a result, these new materials have shown unusual optical and electronic properties suitable for photodynamic therapy,¹¹⁷ two-photo absorption,¹¹⁸ nonlinear absorption,¹¹⁶ organic semiconduction¹¹⁹ and photovoltaics.¹²⁰

In addition to fusion at *meso*-, β - positions, small PAHs could also be fused to the porphyrin core at β -, *meso*-, β - positions. Representative achievements have been made by Anderson's group that reported the syntheses of anthryl fused porphyrins.¹²¹⁻¹²³ As shown in Figure 1-24, the synthesis started from *meso*-substituted A3 type (three *meso*-positions are substituted with the same groups) ¹²¹ and A2 type (two *meso*-positions are substituted with the same groups) porphyrins.¹²² After bromination, borylation, and Suzuki coupling with 1,8-disubstituted 10-bromoanthrene (**1-93**), porphyrin intermediate with one or two anthryl groups could be obtained. The fusion of anthryl groups to the β -positions of the porphyrin core was accomplished through cyclodehydrogenation by using a combination of DDQ as oxidants and Sc(OTf)₃ as Lewis acid. FeCl₃ was also found to be applicable for this kind of cyclodehydrogenation. Later in 2011, tetraanthryl fused porphyrin **1-100** was synthesized through a modified Adler-Longo method, with propanic acid as solvent under reflux condition, followed by FeCl₃ participated Scholl reaction.¹²³ Here, 1,8-di(mesityloxy)anthracen-10-yl substituents were used to overcome the intrinsic solubility problem of the fused planar porphyrin derivative.

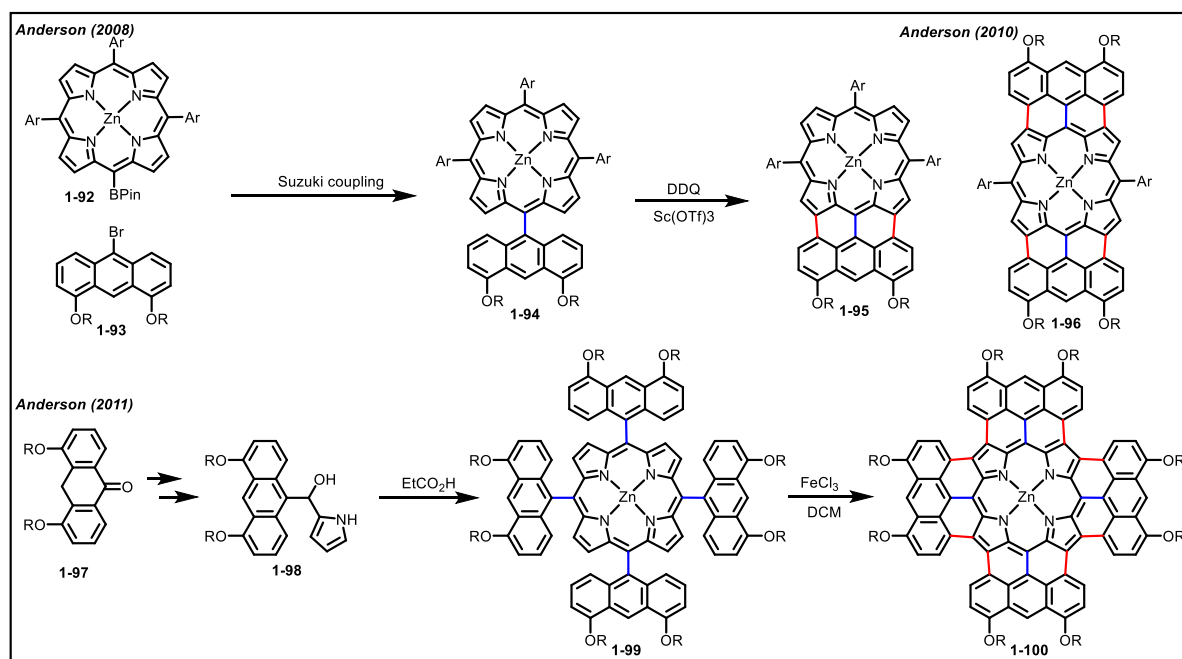


Figure 1-24. Synthetic methods towards anthracene fused porphyrins (β -, *meso*-, β - type).

The UV-vis absorption of **1-95**, **1-96**, **1-100** are shown and compared in Figure 1-25. For one, two and four anthryl fused porphyrins, their absorptions at maximum wavelengths were largely red-shifted to 855, 973 and 1417 nm, respectively, as a result of the expanded π -conjugation systems. The spectrum covers a wide range from UV to visible and NIR region. These results demonstrate that the π -extension is a useful strategy to extend the absorption features of porphyrin. The tetraanthryl fused porphyrin **1-100** has by now the most red-shifted absorption compared with the other small porphyrin derivatives with only one porphyrin core.

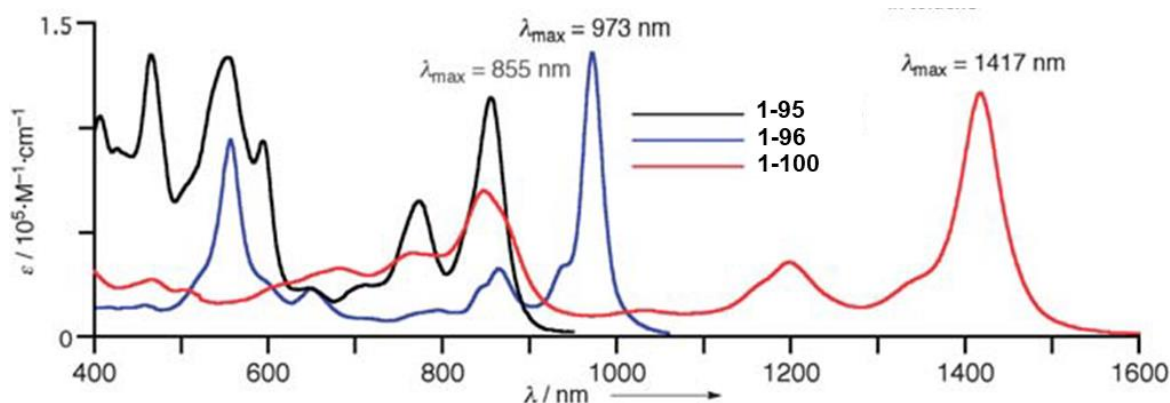


Figure 1-25. Comparison of UV-vis absorption between mono-, bis-, and tetraanthryl fused porphyrins.

In addition to anthracene, other aromatic units could also be fused to porphyrin with a β -, *meso*-, β - fusion type. In 2000, Osuka's group reported the synthesis of triply fused diporphyrin **1-101** by treating *meso-meso* linked diporphyrin with two equivalents of tris(4-bromo-phenyl)aminium hexachloroantimonat (BAHA) in hexafluorobenzene at room temperature.¹²⁴ The very low one-electron oxidation potentials and largely red-shifted intense absorption bands indicated extremely strong electronic interaction between these two porphyrin units, making it a promising component of an electronic wire. By using this strategy, in 2001 they successfully obtained fully conjugated porphyrin tapes with a total number of 12 porphyrin units, which showed largely red-shifted absorptions extending to the IR region and longer porphyrin tapes with 24 units were obtained later.^{125, 126} Boron-dipyrromethene (BODIPY) fused porphyrin **1-102** could also be synthesized by cyclodehydrogenation of a single bond connected non-planar precursor with FeCl_3 .¹²⁷ Bulky functional groups facilitate its dispersion in organic solutions and increase its stability. High stability and NIR absorption were observed, making it useful for photovoltaic devices. Compounds with open-shell character are interesting for their potential applications in spintronic or magnetic equipments. However, their syntheses are very challenging due to their

intrinsic instability. In 2015, Wu's groups synthesized a new type of phenalenyl-fused porphyrin compounds **1-103** with high stability, tunable ground state and photophysical properties.¹²⁷ At room temperature and ambient condition, **1-103** showed prominent triplet biradical character. Another achievement was made by Osuka's group, who successfully synthesized di-*peri*-dinaphthoporphyrins **1-104** by using PtCl₂-mediated cyclization of ethynyl groups, preinstalled to the *meso*-positions of the precursor.¹²⁸ The obtained porphyrin exhibited a characteristic paratropic ring current most probably because of its 24 π antiaromatic circuits.

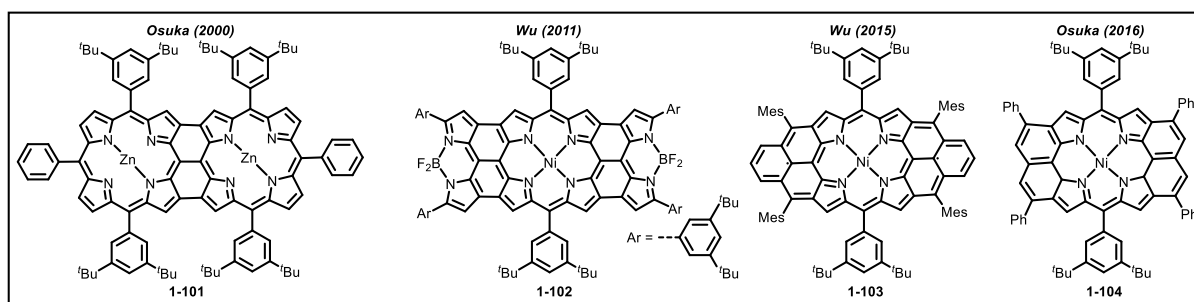


Figure 1-26. Other types of π -conjugation expanded porphyrin derivatives.

The incorporation of porphyrin into (nano)graphene has also been attempted, in order to make functional-multicomponent systems. Indeed, there are many attempts at covalently linking porphyrin to graphene in wet chemistry to make composite materials for use in catalysis, energy conversion and storage.¹²⁹ The bond forming reactions are either through esterification with graphene oxide^{130, 131} or carbene insertion with infinite graphene,^{132, 133} which actually destroyed the graphene's fully conjugated electronic structure. Further, these methods lack specificity and structural precision, complex systems cannot be achieved on this basis.

As shown in Figure 1-27, a covalently connected HBC-porphyrin hybrid **1-108** with a *meso*-linkage between these two chromophoric units was firstly synthesized by Hirsch's group in 2013, using a formylated HPB precursor **1-107**.¹³⁴ Subsequent cyclodehydrogenation of the HPB subunit with FeCl₃ as oxidant worked successfully in the presence of free base porphyrin without necessity to protect the macrocycle with metalation. Electronic communication between HBC and porphyrin was discussed in view of complete quenching of HBC emission. Then in 2014, they further reported the synthesis of free base porphyrin carrying two HBC units at two trans *meso*-positions and its zinc complex **1-110**.¹³⁵ The synthesis proceeds through a Lindsey [2+2] condensation of soluble HBC aldehyde having five *tert*-butyl groups

with diary substituted dipyrromethane using $\text{BF}_3 \cdot \text{OEt}_2$ as catalyst followed by oxidation with DDQ. This molecule has a strong tendency to aggregate into clusters in the gas phase as proven by matrix-assisted laser desorption/ionization (MALDI) (hexamer) and electrospray ionization (ESI) (dimer) mass (MS) spectra, most probably because of the strong intermolecular π - π interaction between each HBC units. Extension of the HBC parts was achieved by Fischer's group in 2017, by introducing two 4-atoms-wide "cove"-type edged GNR (4-CGNR, **1-109**).^{62, 136} The synthesis was based on D-A type copolymerization of a tetraphenylcyclopentadienone with one ethynyl bond and diethynylphenylporphyrin, followed by cyclodehydrogenation with FeCl_3 .

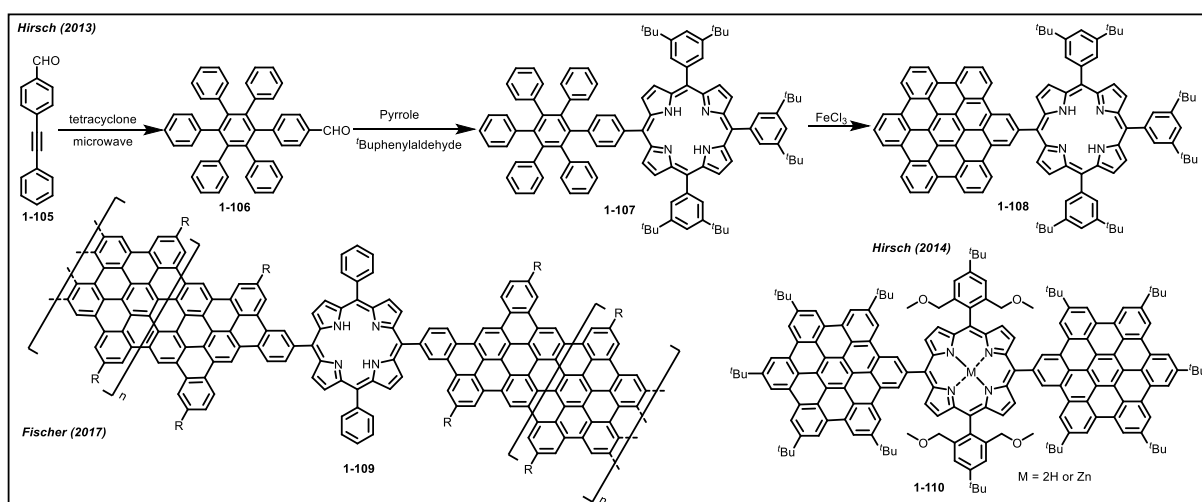


Figure 1-27. Syntheses of porphyrin-HBC and porphyrin-GNR conjugates.

Despite some successful examples of incorporating porphyrin into nanographene materials, most of them are through C-C single bond linkage. Due to strong steric hindrance between hydrogen atoms on porphyrin β -positions with the nanographene, these two subunits tend to adopt a perpendicular conformation. This limits efficient electron conjugation between these two linked chromophores, and as a result they behave like isolated units. Development of novel synthetic strategies is essential in order to enhance the intramolecular electron interaction and produce new materials with unique electronic and photophysical properties.

1.4 Motivation

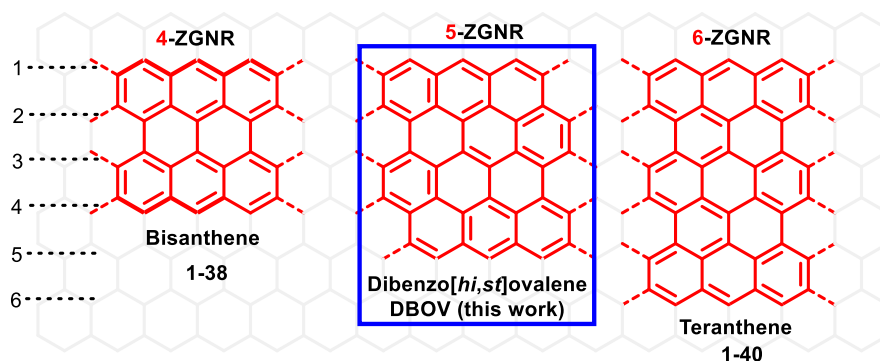


Figure 1-28. Structures of bisanthene, DBOV and teranthene as segments of 4-, 5-, and 6-ZGNR, respectively.

As discussed in the previous sections, “bottom-up” synthesis based on organic reactions has advantages to precisely control the sizes, shapes and edge structures of resulting GMs. These factors will determine their corresponding chemical and optoelectronic properties. By using the “bottom-up” protocol, GMs with sizes up to several nanometers (for example, C_{222}) have been synthesized.⁶⁴ However, most of the GMs prepared using this method have full armchair type peripheral structures and feature large energy gaps. This could on the one hand be beneficial for the syntheses, isolation and characterization of GMs. On the other hand, large energy gaps limit their practical applications. By contrast, GMs with a combination of armchair and zigzag edges are relatively rare, although they have many interesting properties, such as low energy gap, intense absorption in the visible light region and strong fluorescence emission. By now, the most widely studied GMs with both armchair and zigzag edges are periacenes and anthene derivatives, which could be seen as short segments of full zigzag edged GNRs (ZGNR) (Figure 1-28). Studies on these GMs will shed light on the properties of ZGNRs with different width. Segments of 4-ZGNR and 6-ZGNR, such as bisanthene (**1-38**) and teranthene (**1-40**) have been synthesized, whose properties have been discussed in the introduction section (1.2.2). However, the synthesis of 5-ZGNR and its segments has remained elusive. Thereby, in Chapter 2, a new kind of GM with 5-carbon-atoms width between two parallel zigzag edges is designed and synthesized. This GM could also be regarded as derivative of ovalene by fusing two benzene rings to its L-regions and thus named as dibenzo[*hi,st*]ovalene (DBOV). The synthesis is based on the recent achievements on cove edged PAHs.^{137, 138} Filling two cove positions with sp^2 -hybridized carbon atoms may give rise to two parallel zigzag edges. Investigations into the property of DBOV will help to disclose the nature of 5-ZGNR.

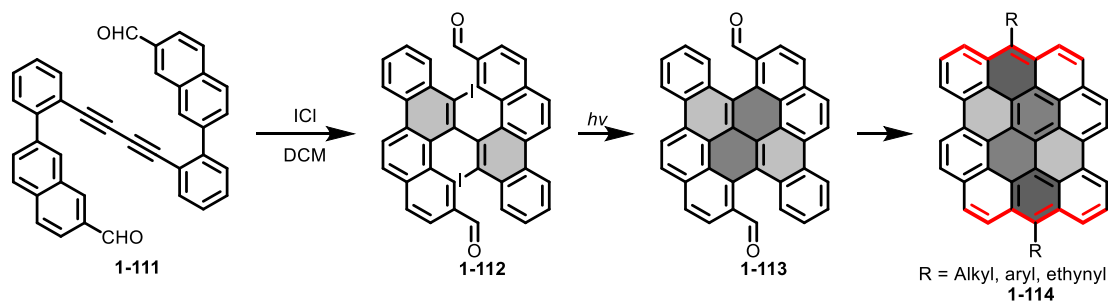


Figure 1-29. Efficient syntheses of DBOV derivatives by a sequence of ICl promoted iodination annulation and photochemical cyclodehydroiodination (PCDHI).

In Chapter 2, DBOV was synthesized in a sequence of totally 12 steps with low overall yield of 2%. It exhibits intense absorption in the red light region (625 nm), very strong fluorescence emission with high fluorescence quantum yields (PLQY) up to 79% and small Stokes shift (12 nm). Furthermore, ultra-fast transient absorption measurement demonstrated its stimulated emission (SE) in both solution and solid film when mixed into polystyrene matrix (1%). This is the first stimulated emission observed in structurally precise nanographene molecules, and it makes DBOV a promising candidate as active layer in organic lasers. The high PLQY is also very attractive for organic light-emitting diodes (OLED). However, from the chemistry point of view, the tedious synthesis and low total yield hinder further investigations of its fundamental chemical and physical property. So, in Chapter 3, I describe an efficient synthesis of DBOV derivatives (Figure 1-29). It relies on a sequence of iodination benzannulation of diene **1-111**, followed by photochemical cyclodehydroiodination (PCDHI). This protocol allows the preparation of DBOV derivatives with different substitutions (alkyl, aryl and ethynyl groups) at the *meso*-positions in large amounts with high yield of up to ca. 40%. As a consequence, we can easily tune the photophysical and electronic properties of DBOV by changing the *meso*-substituents. In addition, I also investigated single molecular spectroscopy of DBOV to further understand its intrinsic photophysical properties at the molecular level.

The supramolecular self-assembly of disc-shaped PAHs into ordered structures such as columns or nanotubes is important to achieve high performance in electronics or photonics. The combination of rigid PAH cores and soft alkyl chains at the periphery can result in phase separation. Columnar self-assembled structures are expected to be formed to show discotic liquid crystalline (LC) properties. The self-assembly of triphenylene, perylene and hexa-*peri*-hexabenzocoronene (HBC) derivatives with different peripheral substituents has been widely studied. However, the self-assembly of PAHs other than these three PAHs are still

underexplored and PAHs which show LC properties are relatively rare. In Chapter 4, I aim at synthesizing DBOV derivative which can self-assemble into ordered structures. To do this, two 3,4,5-tris(dodecyloxy)phenyl (TDOP) groups were attached to the *meso*- positions of DBOV core using the improved synthetic method described in the previous chapter, which can increase the solubility without preventing the π - π interactions between DBOV cores. The self-assembly of this compound (**DBOV-TDOP**) in the solid state and at the solid/liquid interface was comprehensively investigated.

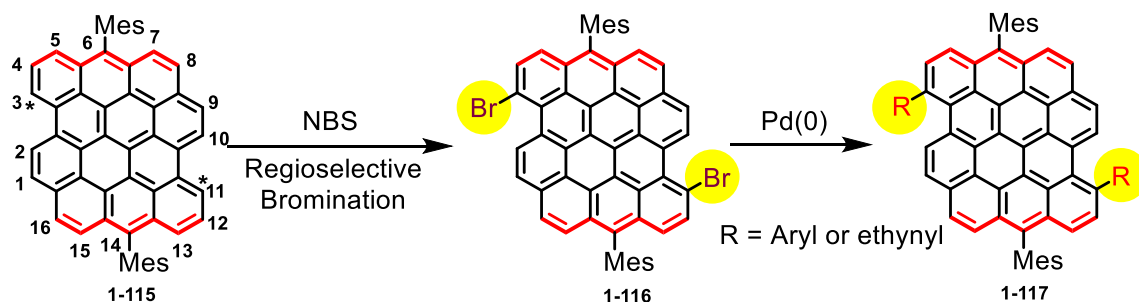


Figure 1-30. Post-synthetic functionalization of DBOV derivatives through regioselective bromination and subsequent transition-metal catalyzed coupling reactions.

In Chapters 2, I elucidated DBOV's interesting properties, such as low energy gap, intense absorption bands in the red light region, high PLQY and stimulated emission. The improved synthetic method disclosed in Chapter 3, however, allows the preparation of DBOV derivatives only by changing functional groups at the two *meso*- positions. As a result of strong intermolecular aggregation, only two functional groups are not sufficient to keep the discs "apart" in solution. On the other hand, the highly reactive Grignard reagent used in the later stage of DBOV synthesis is not compatible with protonic or electrophilic functional groups. So, DBOV with these substituents cannot be obtained by the previous protocols. This limits further application of DBOV in different fields, such as biological imaging, which needs to use GMs with water-solubility and reactive clickable groups. So, in Chapter 5, I mainly focused on the development of post-synthetic functionalization of the DBOV core. After screening several different conditions, I found that the DBOV core could be selectively brominated at its 3,11-positions and the obtained dibromo intermediate could be used for Suzuki or Sonogashira coupling reactions to introduce aryl or ethynyl groups (Figure 1-30). These products have red-shifted UV-vis absorption and fluorescence emission and enhanced fluorescence quantum yield, as a result of their enhanced solubility. Furthermore, I also demonstrated that these molecules could be reversibly oxidized to stable radical cations and

reduced back to their neutral states by chemical methods, which process was proved by electron paramagnetic resonance (EPR) measurements.

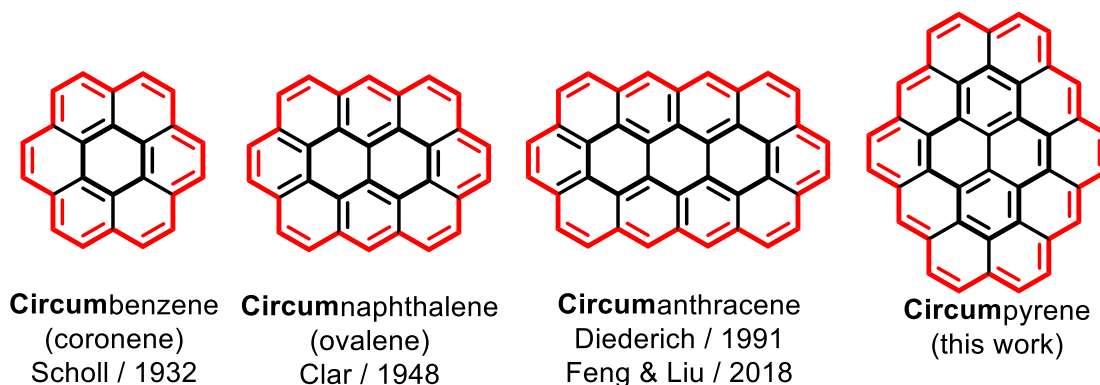


Figure 1-31. Structures of representative circumarenes.

Compared with GMs bearing full armchair edges and both armchair/zigzag edges, full zigzag edged GMs are rare because of lacking proper synthetic methods. This hinders further study of their electronic and optical properties. Circumarene represents one subclass of full zigzag edged GMs (Figure 1-31). Small circumarenes, such as circumbenzene, circumnaphthalene and circumanthracene have been reported and found applications in organic electronic devices and liquid crystal materials.⁹² Enlarging the aromatic core sizes of circumarenes will enhance intermolecular overlap in the solid state, which is expected to increase the charge carrier mobility along the direction perpendicular to the aromatic cores. On the other hand, this will also lower the energy gap and shift the electron absorption spectra to long wavelength region. However, the syntheses of circumarenes with core sizes larger than three fused benzene rings have not been demonstrated. Thus, in Chapter 6, I show the first bottom-up syntheses of circumpyrene derivatives with DBOV as starting material. Its ring-in-ring backbone structure was unambiguously characterized by X-ray diffraction single-crystal analysis. Compared with the DBOV precursor, fusing of two extra C=C bonds significantly increases the energy gap.

As discussed in the previous introduction section, the energy gap is a very important parameter to determine the property and application of GMs, which can be tuned by their edge structures. In addition, incorporation of heteroatoms plays an important role for their use in sensing, catalysis, energy storage and conversion. Porphyrin, as a planar nitrogen-containing aromatic compound, has been widely used as building block to fabricate functional molecules. Hybrids of porphyrin and carbon-based molecules can furnish new properties. Historically, there have been several attempts to synthesize covalently linked porphyrin-nanographene hybrids. Some of them are achieved either through ester groups or carbene

insertion reactions, which destroy the perfect structure of the sp^2 -hybridized carbon materials; or through single C-C bond, which suffer from limited electron conjugation between these two units. Up to now, porphyrin nanographene conjugates with strong electron delocalization all over the π -conjugated system have rarely been reported. Taking a careful look at the zigzag edges of GMs, one recognizes that the zigzag edge geometry fits well with the peripheral structures of porphyrin (Figure 1-32). By connection through three C-C bonds, fully conjugated porphyrin-nanographenes are expected to be obtained. Consequently, in Chapter 6, I disclose the syntheses of porphyrin-nanographene conjugates. To this end, I designed one benzo[*m*]tetraphene unit (**1-118**) as precursor of partial zigzag edged nanographene, which was first connected to *meso*-positions of porphyrin through Suzuki coupling. After cyclodehydrogenation, two porphyrin fused nanographene molecules could be obtained, which show intense and wide absorption bands in the NIR region, with maximum absorption wavelength located at 800 nm and 1200 nm respectively, indicating their significantly decreased energy gaps.

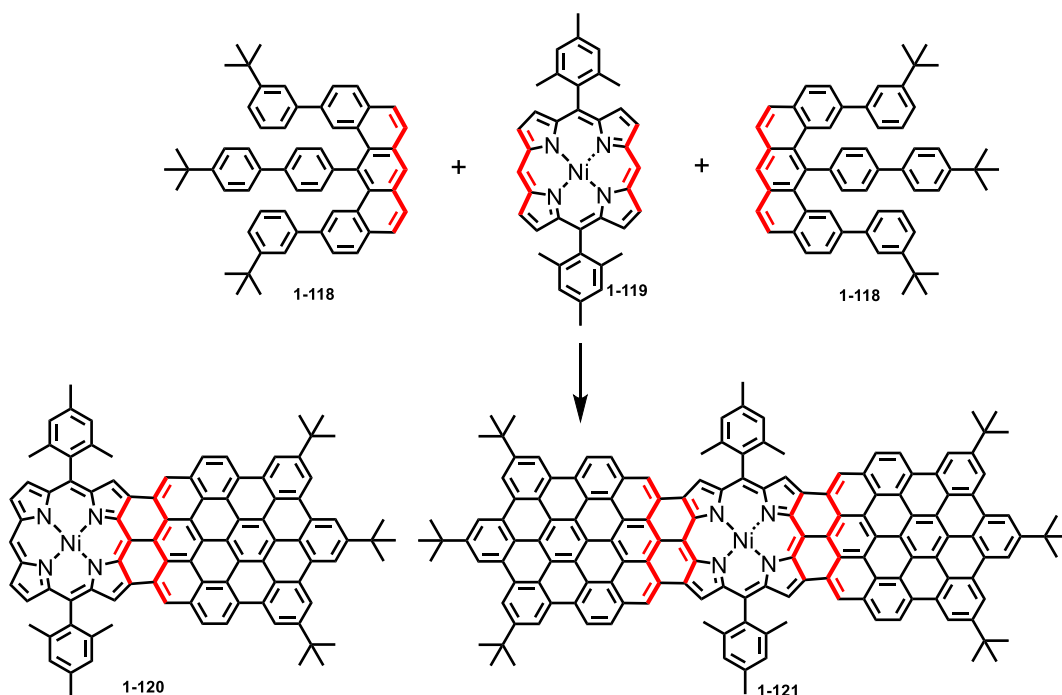


Figure 1-32. Fusion of porphyrin to zigzag-edged GMs for triply fused porphyrin-nanographene conjugates.

References

- (1) Otero, G.; Biddau, G.; Sanchez-Sanchez, C.; Caillard, R.; Lopez, M. F.; Rogero, C.; Palomares, F. J.; Cabello, N.; Basanta, M. A.; Ortega, J.; Mendez, J.; Echavarren, A. M.; Perez, R.; Gomez-Lor, B.; Martin-Gago, J. A. Fullerenes from aromatic precursors by surface-catalysed cyclodehydrogenation. *Nature* **2008**, *454*, 865-868.
- (2) Geim, A. K.; Novoselov, K. S. The rise of graphene. *Nat Mater* **2007**, *6*, 183-191.
- (3) Mermin, N. D.; Wagner, H. Absence of Ferromagnetism or Antiferromagnetism in One- or Two-Dimensional Isotropic Heisenberg Models. *Phys Rev Lett* **1966**, *17*, 1133-1136.
- (4) Mermin, N. D. Crystalline Order in Two Dimensions. *Phys Rev* **1968**, *176*, 250-254.
- (5) Novoselov, K. S.; Geim, A. K.; Morozov, S. V.; Jiang, D.; Zhang, Y.; Dubonos, S. V.; Grigorieva, I. V.; Firsov, A. A. Electric field effect in atomically thin carbon films. *Science* **2004**, *306*, 666-669.
- (6) Novoselov, K. S.; Jiang, Z.; Zhang, Y.; Morozov, S. V.; Stormer, H. L.; Zeitler, U.; Maan, J. C.; Boebinger, G. S.; Kim, P.; Geim, A. K. Room-temperature quantum Hall effect in graphene. *Science* **2007**, *315*, 1379.
- (7) Bolotin, K. I.; Sikes, K. J.; Jiang, Z.; Klima, M.; Fudenberg, G.; Hone, J.; Kim, P.; Stormer, H. L. Ultrahigh electron mobility in suspended graphene. *Solid State Commun* **2008**, *146*, 351-355.
- (8) Nika, D. L.; Pokatilov, E. P.; Askerov, A. S.; Balandin, A. A. Phonon thermal conduction in graphene: Role of Umklapp and edge roughness scattering. *Phys Rev B* **2009**, *79*.
- (9) Nair, R. R.; Blake, P.; Grigorenko, A. N.; Novoselov, K. S.; Booth, T. J.; Stauber, T.; Peres, N. M.; Geim, A. K. Fine structure constant defines visual transparency of graphene. *Science* **2008**, *320*, 1308.
- (10) Geim, A. K. Random walk to graphene (Nobel lecture). *Angew Chem Int Ed Engl* **2011**, *50*, 6966-6985.
- (11) Novoselov, K. S. Graphene: materials in the Flatland (Nobel lecture). *Angew Chem Int Ed Engl* **2011**, *50*, 6986-7002.
- (12) Novoselov, K. S.; Fal'ko, V. I.; Colombo, L.; Gellert, P. R.; Schwab, M. G.; Kim, K. A roadmap for graphene. *Nature* **2012**, *490*, 192-200.
- (13) Zhang, W.; Cui, J.; Tao, C. A.; Wu, Y.; Li, Z.; Ma, L.; Wen, Y.; Li, G. A strategy for producing pure single-layer graphene sheets based on a confined self-assembly approach. *Angew Chem Int Ed Engl* **2009**, *48*, 5864-5868.
- (14) Ren, S.; Rong, P.; Yu, Q. Preparations, properties and applications of graphene in functional devices: A concise review. *Ceram Int* **2018**, *44*, 11940-11955.

- (15) Hernandez, Y.; Nicolosi, V.; Lotya, M.; Blighe, F. M.; Sun, Z.; De, S.; McGovern, I. T.; Holland, B.; Byrne, M.; Gun'Ko, Y. K.; Boland, J. J.; Niraj, P.; Duesberg, G.; Krishnamurthy, S.; Goodhue, R.; Hutchison, J.; Scardaci, V.; Ferrari, A. C.; Coleman, J. N. High-yield production of graphene by liquid-phase exfoliation of graphite. *Nat Nanotechnol* **2008**, *3*, 563-568.
- (16) Su, C. Y.; Lu, A. Y.; Xu, Y.; Chen, F. R.; Khlobystov, A. N.; Li, L. J. High-quality thin graphene films from fast electrochemical exfoliation. *ACS Nano* **2011**, *5*, 2332-2339.
- (17) Wang, J.; Manga, K. K.; Bao, Q.; Loh, K. P. High-yield synthesis of few-layer graphene flakes through electrochemical expansion of graphite in propylene carbonate electrolyte. *J Am Chem Soc* **2011**, *133*, 8888-8891.
- (18) Pu, N.-W.; Wang, C.-A.; Sung, Y.; Liu, Y.-M.; Ger, M.-D. Production of few-layer graphene by supercritical CO₂ exfoliation of graphite. *Mater Lett* **2009**, *63*, 1987-1989.
- (19) Tung, V. C.; Allen, M. J.; Yang, Y.; Kaner, R. B. High-throughput solution processing of large-scale graphene. *Nat Nanotechnol* **2009**, *4*, 25-29.
- (20) Li, X.; Cai, W.; An, J.; Kim, S.; Nah, J.; Yang, D.; Piner, R.; Velamakanni, A.; Jung, I.; Tutuc, E.; Banerjee, S. K.; Colombo, L.; Ruoff, R. S. Large-area synthesis of high-quality and uniform graphene films on copper foils. *Science* **2009**, *324*, 1312-1314.
- (21) Rollings, E.; Gweon, G. H.; Zhou, S. Y.; Mun, B. S.; McChesney, J. L.; Hussain, B. S.; Fedorov, A. V.; First, P. N.; de Heer, W. A.; Lanzara, A. Synthesis and characterization of atomically thin graphite films on a silicon carbide substrate. *J Phys Chem Solids* **2006**, *67*, 2172-2177.
- (22) Randviir, E. P.; Brownson, D. A. C.; Banks, C. E. A decade of graphene research: production, applications and outlook. *Mater Today* **2014**, *17*, 426-432.
- (23) Ponomarenko, L. A.; Schedin, F.; Katsnelson, M. I.; Yang, R.; Hill, E. W.; Novoselov, K. S.; Geim, A. K. Chaotic Dirac billiard in graphene quantum dots. *Science* **2008**, *320*, 356-358.
- (24) Zhu, S.; Song, Y.; Zhao, X.; Shao, J.; Zhang, J.; Yang, B. The photoluminescence mechanism in carbon dots (graphene quantum dots, carbon nanodots, and polymer dots): current state and future perspective. *Nano Res* **2015**, *8*, 355-381.
- (25) Kobayashi, Y.; Fukui, K.-i.; Enoki, T.; Kusakabe, K. Edge state on hydrogen-terminated graphite edges investigated by scanning tunneling microscopy. *Phys Rev B* **2006**, *73*.
- (26) Han, W.; Kawakami, R. K.; Gmitra, M.; Fabian, J. Graphene spintronics. *Nat Nanotechnol* **2014**, *9*, 794-807.
- (27) Cai, J.; Ruffieux, P.; Jaafar, R.; Bieri, M.; Braun, T.; Blankenburg, S.; Muoth, M.; Seitsonen, A. P.; Saleh, M.; Feng, X.; Müllen, K.; Fasel, R. Atomically precise bottom-up fabrication of graphene nanoribbons. *Nature* **2010**, *466*, 470-473.

- (28) Ruffieux, P.; Wang, S.; Yang, B.; Sanchez-Sanchez, C.; Liu, J.; Dienel, T.; Talirz, L.; Shinde, P.; Pignedoli, C. A.; Passerone, D.; Dumslaff, T.; Feng, X.; Müllen, K.; Fasel, R. On-surface synthesis of graphene nanoribbons with zigzag edge topology. *Nature* **2016**, *531*, 489-492.
- (29) Jiang, D.-E.; Chen, Z., *Graphene Chemistry*; 2013.
- (30) Draine, B. T. Interstellar Dust Grains. *Annu Rev Astron Astrophys* **2003**, *41*, 241-289.
- (31) Harvey, R. G. Bridged Polycyclic Aromatic Hydrocarbons. A Review. *Org Prep Proced Int* **1997**, *29*, 243-283.
- (32) Harvey, R. G. Mechanisms Of Carcinogenesis of Polycyclic Aromatic Hydrocarbons. *Polycycl Aromat Comp* **1996**, *9*, 1-23.
- (33) Humans, I. W. G. o. t. E. o. C. R. t. Chemical agents and related occupations. *IARC monographs on the evaluation of carcinogenic risks to humans* **2012**, *100*, 9-562.
- (34) Venedictov, E. A.; Tulikova, E. J. The effect of solvent on tetracene oxidation by singlet molecular oxygen ($^1\Delta_g$): aspects of specific solvation. *Tetrahedron Lett* **2003**, *44*, 3215-3216.
- (35) Figueira-Duarte, T. M.; Müllen, K. Pyrene-based materials for organic electronics. *Chem Rev* **2011**, *111*, 7260-314.
- (36) Ito, H.; Segawa, Y.; Murakami, K.; Itami, K. Polycyclic Arene Synthesis by Annulative pi-Extension. *J Am Chem Soc* **2019**, *141*, 3-10.
- (37) Rieger, R.; Müllen, K. Forever young: polycyclic aromatic hydrocarbons as model cases for structural and optical studies. *J Phys Org Chem* **2010**, n/a-n/a.
- (38) Clar, E., *The Aromatic Sextet*; Wiley-VCH: London, 1972.
- (39) Schleyer, P. v. R.; Manoharan, M.; Jiao, H.; Stahl, F. The Acenes: Is There a Relationship between Aromatic Stabilization and Reactivity? *Org Lett* **2001**, *3*, 3643-3646.
- (40) Feng, J.; Jiang, W.; Wang, Z. Synthesis and Application of Rylene Imide Dyes as Organic Semiconducting Materials. *Chem Asian J* **2018**, *13*, 20-30.
- (41) Kitamura, M.; Arakawa, Y. Pentacene-based organic field-effect transistors. *J Phys Condens Matter* **2008**, *20*.
- (42) Minder, N. A.; Ono, S.; Chen, Z.; Facchetti, A.; Morpurgo, A. F. Band-like electron transport in organic transistors and implication of the molecular structure for performance optimization. *Adv Mater* **2012**, *24*, 503-508.
- (43) Wang, X.-Y.; Narita, A.; Müllen, K. Precision synthesis versus bulk-scale fabrication of graphenes. *Nat Rev Chem* **2017**, *2*.

- (44) Chua, C. K.; Sofer, Z.; Simek, P.; Jankovsky, O.; Klimova, K.; Bakardjieva, S.; Hrdlickova Kuckova, S.; Pumera, M. Synthesis of strongly fluorescent graphene quantum dots by cage-opening buckminsterfullerene. *ACS Nano* **2015**, *9*, 2548-2555.
- (45) Chen, L.; Hernandez, Y.; Feng, X.; Müllen, K. From nanographene and graphene nanoribbons to graphene sheets: chemical synthesis. *Angew Chem Int Ed* **2012**, *51*, 7640-7654.
- (46) Pan, D.; Zhang, J.; Li, Z.; Wu, M. Hydrothermal route for cutting graphene sheets into blue-luminescent graphene quantum dots. *Adv Mater* **2010**, *22*, 734-738.
- (47) Chen, G.; Zhuo, Z.; Ni, K.; Kim, N. Y.; Zhao, Y.; Chen, Z.; Xiang, B.; Yang, L.; Zhang, Q.; Lee, Z.; Wu, X.; Ruoff, R. S.; Zhu, Y. Rupturing C60 Molecules into Graphene-Oxide-like Quantum Dots: Structure, Photoluminescence, and Catalytic Application. *Small* **2015**, *11*, 5296-5304.
- (48) Stabel, A.; Herwig, P.; Müllen, K.; Rabe, J. P. Diodelike Current–Voltage Curves for a Single Molecule–Tunneling Spectroscopy with Submolecular Resolution of an Alkylated,peri-Condensed Hexabenzocoronene. *Angew Chem Int Ed Engl* **1995**, *34*, 1609-1611.
- (49) Treier, M.; Pignedoli, C. A.; Laino, T.; Rieger, R.; Müllen, K.; Passerone, D.; Fasel, R. Surface-assisted cyclodehydrogenation provides a synthetic route towards easily processable and chemically tailored nanographenes. *Nat Chem* **2011**, *3*, 61-67.
- (50) Clar, E.; schmidt, W. Localised vs delocalised molecular orbitals in aromatic hydrocarbons. *Tetrahedron* **1979**, *35*, 2673-2680.
- (51) Clar, E.; Stewart, D. G. Aromatic Hydrocarbons. LXV. Triangulene Derivatives1. *J Am Chem Soc* **1953**, *75*, 2667-2672.
- (52) Clar, E., *Polycyclic Hydrocarbons*; Academic Press: New York, 1964; Vol. I/II.
- (53) Clar, E.; Ironside, C. T. Hexabenzocoronene. *Proc Chem Soc* **1958**, 150.
- (54) Ito, S.; Herwig, P. T.; Böhme, T.; Rabe, J. P.; Rettig, W.; Müllen, K. Bishexa-peri-hexabenzocorononyl: A “Superbiphenyl”. *J Am Chem Soc* **2000**, *122*, 7698-7706.
- (55) Rempala, P.; Kroulik, J.; King, B. T. Investigation of the mechanism of the intramolecular Scholl reaction of contiguous phenylbenzenes. *J Org Chem* **2006**, *71*, 5067-5081.
- (56) King, B. T.; Kroulik, J.; Robertson, C. R.; Rempala, P.; Hilton, C. L.; Korinek, J. D.; Gortari, L. M. Controlling the Scholl reaction. *J Org Chem* **2007**, *72*, 2279-2288.
- (57) Dou, X.; Yang, X.; Bodwell, G. J.; Wagner, M.; Enkelmann, V.; Müllen, K. Unexpected phenyl group rearrangement during an intramolecular Scholl reaction leading to an alkoxy-substituted hexa-peri-hexabenzocoronene. *Org Lett* **2007**, *9*, 2485-2488.

- (58) Zhai, L.; Shukla, R.; Rathore, R. Oxidative C-C bond formation (Scholl reaction) with DDQ as an efficient and easily recyclable oxidant. *Org Lett* **2009**, *11*, 3474-3477.
- (59) Zhai, L.; Shukla, R.; Wadumethrige, S. H.; Rathore, R. Probing the arenium-ion (protontransfer) versus the cation-radical (electron transfer) mechanism of Scholl reaction using DDQ as oxidant. *J Org Chem* **2010**, *75*, 4748-4760.
- (60) Navale, T. S.; Thakur, K.; Rathore, R. Sequential oxidative transformation of tetraarylethylenes to 9,10-diarylphenanthrenes and dibenzo[g,p]chrysenes using DDQ as an oxidant. *Org Lett* **2011**, *13*, 1634-1637.
- (61) Debije, M. G.; Piris, J.; de Haas, M. P.; Warman, J. M.; Tomovic, Z.; Simpson, C. D.; Watson, M. D.; Müllen, K. The optical and charge transport properties of discotic materials with large aromatic hydrocarbon cores. *J Am Chem Soc* **2004**, *126*, 4641-4645.
- (62) Narita, A.; Feng, X.; Hernandez, Y.; Jensen, S. A.; Bonn, M.; Yang, H.; Verzhbitskiy, I. A.; Casiraghi, C.; Hansen, M. R.; Koch, A. H.; Fytas, G.; Ivasenko, O.; Li, B.; Mali, K. S.; Balandina, T.; Mahesh, S.; De Feyter, S.; Müllen, K. Synthesis of structurally well-defined and liquid-phase-processable graphene nanoribbons. *Nat Chem* **2014**, *6*, 126-132.
- (63) Iyer, V. S.; Wehmeier, M.; Brand, J. D.; Keegstra, M. A.; Müllen, K. From Hexa-peri-hexabenzocoronene to "Superacenes". *Angew Chem Int Ed Engl* **1997**, *36*, 1604-1607.
- (64) Simpson, C. D.; Brand, J. D.; Berresheim, A. J.; Przybilla, L.; Räder, H. J.; Müllen, K. Synthesis of a Giant 222 Carbon Graphite Sheet. *Chem Eur J* **2002**, *8*, 1424-1429.
- (65) Kastler, M.; Schmidt, J.; Pisula, W.; Sebastiani, D.; Müllen, K. From armchair to zigzag peripheries in nanographenes. *J Am Chem Soc* **2006**, *128*, 9526-9534.
- (66) Wang, Z.; Tomovic, Z.; Kastler, M.; Pretsch, R.; Negri, F.; Enkelmann, V.; Müllen, K. Graphitic molecules with partial "zig/zag" periphery. *J Am Chem Soc* **2004**, *126*, 7794-7795.
- (67) Dumsclaff, T.; Yang, B.; Maghsoumi, A.; Velpula, G.; Mali, K. S.; Castiglioni, C.; De Feyter, S.; Tommasini, M.; Narita, A.; Feng, X.; Müllen, K. Adding Four Extra K-Regions to Hexa-peri-hexabenzocoronene. *J Am Chem Soc* **2016**, *138*, 4726-4729.
- (68) Yang, B. Bottom-Up Synthesis of Graphene Nanoribbons and Nanographene Molecules with New Types of Periphery. PhD Thesis, Mainz University, Mainz, **2015**.
- (69) Dumsclaff, T. Synthese und Charakterisierung neuartiger Graphennanostreifen und Graphenmoleküle mit Armlehnen- und Zickzack-Kanten. PhD Thesis, Mainz University, Mainz, **2017**.
- (70) Zhan, X.; Facchetti, A.; Barlow, S.; Marks, T. J.; Ratner, M. A.; Wasielewski, M. R.; Marder, S. R. Rylene and related diimides for organic electronics. *Adv Mater* **2011**, *23*, 268-284.

- (71) Würthner, F. Perylene bisimide dyes as versatile building blocks for functional supramolecular architectures. *Chem Commun (Camb)* **2004**, 1564-1579.
- (72) Weil, T.; Vosch, T.; Hofkens, J.; Peneva, K.; Müllen, K. The rylene colorant family--tailored nanoemitters for photonics research and applications. *Angew Chem Int Ed Engl* **2010**, *49*, 9068-9093.
- (73) Jiang, D. E.; Sumpter, B. G.; Dai, S. First principles study of magnetism in nanographenes. *J Chem Phys* **2007**, *127*, 124703.
- (74) Jiang, D.-e.; Dai, S. Circumacenes versus periacenes: HOMO–LUMO gap and transition from nonmagnetic to magnetic ground state with size. *Chem Phys Lett* **2008**, *466*, 72-75.
- (75) Clar, E. Das Kondensationsprinzip, ein einfaches neues Prinzip im Aufbau der aromatischen Kohlenwasserstoffe (Aromatische Kohlenwassertoffe XLII. Mitteilung). *Chemische Berichte* **1948**, *81*, 52-63.
- (76) Arabei, S. M.; Pavich, T. A. Spectral-luminescent properties and photoinduced transformations of bisanthene and bisanthenequinone. *J Appl* **2000**, *67*, 236-244.
- (77) Saidi-Besbes, S.; Grelet, E.; Bock, H. Soluble and liquid-crystalline ovalenes. *Angew Chem Int Ed Engl* **2006**, *45*, 1783-1786.
- (78) Yao, J. H.; Chi, C.; Wu, J.; Loh, K. P. Bisanthracene bis(dicarboxylic imide)s as soluble and stable NIR dyes. *Chem Eur J* **2009**, *15*, 9299-9302.
- (79) Li, J.; Zhang, K.; Zhang, X.; Huang, K. W.; Chi, C.; Wu, J. meso-Substituted bisanthenes as soluble and stable near-infrared dyes. *J Org Chem* **2010**, *75*, 856-863.
- (80) Zhang, K.; Huang, K. W.; Li, J.; Luo, J.; Chi, C.; Wu, J. A soluble and stable quinoidal bisanthene with NIR absorption and amphoteric redox behavior. *Org Lett* **2009**, *11*, 4854-4857.
- (81) Liu, J.; Ravat, P.; Wagner, M.; Baumgarten, M.; Feng, X.; Müllen, K. Tetrabenzo[a,f,j,o]perylene: a polycyclic aromatic hydrocarbon with an open-shell singlet biradical ground state. *Angew Chem Int Ed* **2015**, *54*, 12442-1246.
- (82) Ajayakumar, M. R.; Fu, Y.; Ma, J.; Hennesdorf, F.; Komber, H.; Weigand, J. J.; Alfonso, A.; Popov, A. A.; Berger, R.; Liu, J.; Müllen, K.; Feng, X. Toward Full Zigzag-Edged Nanographenes: peri-Tetracene and Its Corresponding Circumanthracene. *J Am Chem Soc* **2018**, *140*, 6240-6244.
- (83) Ni, Y.; Gopalakrishna, T. Y.; Phan, H.; Heng, T. S.; Wu, S.; Han, Y.; Ding, J.; Wu, J. A Peri-tetracene Diradicaloid: Synthesis and Properties. *Angew Chem Int Ed* **2018**, *57*, 9697-9701.
- (84) Zöphel, L.; Berger, R.; Gao, P.; Enkelmann, V.; Baumgarten, M.; Wagner, M.; Müllen, K. Toward the *peri*-Pentacene Framework. *Chem Eur J* **2013**, *19*, 17821-17826.

- (85) Konishi, A.; Hirao, Y.; Nakano, M.; Shimizu, A.; Botek, E.; Champagne, B.; Shiomi, D.; Sato, K.; Takui, T.; Matsumoto, K.; Kurata, H.; Kubo, T. Synthesis and characterization of teranthene: a singlet biradical polycyclic aromatic hydrocarbon having Kekule structures. *J Am Chem Soc* **2010**, *132*, 11021-11023.
- (86) Konishi, A.; Hirao, Y.; Matsumoto, K.; Kurata, H.; Kishi, R.; Shigeta, Y.; Nakano, M.; Tokunaga, K.; Kamada, K.; Kubo, T. Synthesis and characterization of quarteranthene: elucidating the characteristics of the edge state of graphene nanoribbons at the molecular level. *J. Am. Chem. Soc.* **2013**, *135*, 1430-1437.
- (87) Gu, Y.; Wu, X.; Gopalakrishna, T. Y.; Phan, H.; Wu, J. Graphene-like Molecules with Four Zigzag Edges. *Angew Chem Int Ed Engl* **2018**, *57*, 6541-6545.
- (88) Geuenich, D.; Hess, K.; Kohler, F.; Herges, R. Anisotropy of the induced current density (ACID), a general method to quantify and visualize electronic delocalization. *Chem Rev* **2005**, *105*, 3758-3772.
- (89) Clar, E.; Zander, M. 927. Syntheses of coronene and 1 : 2-7 : 8-dibenzocoronene. *Journal of the Chemical Society (Resumed)* **1957**.
- (90) Alibert-Fouet, S.; Seguy, I.; Bobo, J. F.; Destruel, P.; Bock, H. Liquid-crystalline and electron-deficient coronene oligocarboxylic esters and imides by twofold benzogenic Diels-Alder reactions on perylenes. *Chem Eur J* **2007**, *13*, 1746-1753.
- (91) Clar, E. Synthesis of Ovalene. *Nature* **1948**, *161*, 238-239.
- (92) Li, J.; Chang, J.-J.; Tan, H. S.; Jiang, H.; Chen, X.; Chen, Z.; Zhang, J.; Wu, J. Disc-like 7, 14-dicyano-ovalene-3,4:10,11-bis(dicarboximide) as a solution-processible n-type semiconductor for air stable field-effect transistors. *Chem. Sci.* **2012**, *3*, 846-850.
- (93) Fort, E. H.; Donovan, P. M.; Scott, L. T. Diels-Alder reactivity of polycyclic aromatic hydrocarbon bay regions: implications for metal-free growth of single-chirality carbon nanotubes. *J Am Chem Soc* **2009**, *131*, 16006-16007.
- (94) Fort, E. H.; Scott, L. T. One-step conversion of aromatic hydrocarbon bay regions into unsubstituted benzene rings: a reagent for the low-temperature, metal-free growth of single-chirality carbon nanotubes. *Angew Chem Int Ed Engl* **2010**, *49*, 6626-6628.
- (95) Clar, E.; Kelly, W.; Robertson, J. M.; Rossmann, M. G. 754. Circumanthracene and dinaphtho(7' : 1' -1 : 13)(1'' : 7'' -6 : 8)-peropyrene. *J. Chem. Soc.* **1956**, *0*, 3878-3881.
- (96) Clar, E.; Robertson, J. M.; Schloegl, R.; Schmidt, W. Photoelectron spectra of polynuclear aromatics. 6. Applications to structural elucidation: "circumanthracene". *J Am Chem Soc* **1981**, *103*, 1320-1328.
- (97) Broene, R. D.; Diederich, F. The synthesis of circumanthracene. *Tetrahedron Lett* **1991**, *32*, 5227-5230.

- (98) Philpott, M. R.; Kawazoe, Y. Transition metal sandwich molecules with large (C_n, n ≥ 24) zigzag poly aromatic hydrocarbons. *Chem Phys* **2008**, *348*, 69-82.
- (99) Stepien, M.; Gonka, E.; Zyla, M.; Sprutta, N. Heterocyclic Nanographenes and Other Polycyclic Heteroaromatic Compounds: Synthetic Routes, Properties, and Applications. *Chem Rev* **2017**, *117*, 3479-3716.
- (100) Narita, A.; Wang, X. Y.; Feng, X.; Müllen, K. New advances in nanographene chemistry. *Chem Soc Rev* **2015**, *44*, 6616-6643.
- (101) Wang, X.; Sun, G.; Routh, P.; Kim, D. H.; Huang, W.; Chen, P. Heteroatom-doped graphene materials: syntheses, properties and applications. *Chem Soc Rev* **2014**, *43*, 7067-7098.
- (102) Oh, S.; Gallagher, J. R.; Miller, J. T.; Surendranath, Y. Graphite-Conjugated Rhenium Catalysts for Carbon Dioxide Reduction. *J Am Chem Soc* **2016**, *138*, 1820-1823.
- (103) Sun, X.; Kang, X.; Zhu, Q.; Ma, J.; Yang, G.; Liu, Z.; Han, B. Very highly efficient reduction of CO₂ to CH₄ using metal-free N-doped carbon electrodes. *Chem Sci* **2016**, *7*, 2883-2887.
- (104) Kramm, U. I.; Herrmann-Geppert, I.; Behrends, J.; Lips, K.; Fiechter, S.; Bogdanoff, P. On an Easy Way To Prepare Metal-Nitrogen Doped Carbon with Exclusive Presence of MeN₄-type Sites Active for the ORR. *J Am Chem Soc* **2016**, *138*, 635-640.
- (105) Wang, X.; Li, X.; Zhang, L.; Yoon, Y.; Weber, P. K.; Wang, H.; Dai, H. N-doping of graphene through electrothermal reactions with ammonia. *Science* **2009**, *324*, 768-771.
- (106) Groves, J. T.; Nemo, T. E.; Myers, R. S. Hydroxylation and epoxidation catalyzed by iron-porphine complexes. Oxygen transfer from iodosylbenzene. *J Am Chem Soc* **1979**, *101*, 1032-1033.
- (107) Sheftel, A. D.; Mason, A. B.; Ponka, P. The long history of iron in the Universe and in health and disease. *Biochim Biophys Acta* **2012**, *1820*, 161-187.
- (108) Gottfried, J. M. Surface chemistry of porphyrins and phthalocyanines. *Surface Science Reports* **2015**, *70*, 259-379.
- (109) Auwarter, W.; Seufert, K.; Bischoff, F.; Ecija, D.; Vijayaraghavan, S.; Joshi, S.; Klappenberger, F.; Samudrala, N.; Barth, J. V. A surface-anchored molecular four-level conductance switch based on single proton transfer. *Nat Nanotechnol* **2011**, *7*, 41-46.
- (110) Mori, H.; Tanaka, T.; Osuka, A. Fused porphyrinoids as promising near-infrared absorbing dyes. *J Mater Chem C* **2013**, *1*, 2500-2519.
- (111) Barloy, L.; Dolphin, D.; Dupre, D.; Wijesekera, T. P. Anomalous Double Cyclization Reactions of .beta.-Formylporphyrins. *J Org Chem* **1994**, *59*, 7976-7985.

- (112) Fox, S.; Boyle, R. W. First examples of intramolecular Pd(0) catalysed couplings on ortho-iodinated meso-phenyl porphyrins. *Chem Commun (Camb)* **2004**, 1322-1323.
- (113) Cammidge, A. N.; Scaife, P. J.; Berber, G.; Hughes, D. L. Cofacial porphyrin-ferrocene dyads and a new class of conjugated porphyrin. *Org Lett* **2005**, *7*, 3413-3416.
- (114) Tanaka, M.; Hayashi, S.; Eu, S.; Umeyama, T.; Imahori, H. Novel unsymmetrically π -elongated porphyrin for dye-sensitized TiO₂ cells. *Chem. Commun.* **2007**, 2069-2071.
- (115) Yamane, O.; Sugiura, K.-i.; Miyasaka, H.; Nakamura, K.; Fujimoto, T.; Nakamura, K.; Kaneda, T.; Sakata, Y.; Yamashita, M. Pyrene-Fused Porphyrins: Annulation Reactions of meso-Pyrenylporphyrins. *Chem Lett* **2004**, *33*, 40-41.
- (116) Aratani, N.; Kim, D.; Osuka, A. π -Conjugation enlargement toward the creation of multi-porphyrinic systems with large two-photon absorption properties. *Chem Asian J* **2009**, *4*, 1172-1182.
- (117) Bonnett, R. Photosensitizers of the porphyrin and phthalocyanine series for photodynamic therapy. *Chem Soc Rev* **1995**, *24*, 19-33.
- (118) Pawlicki, M.; Collins, H. A.; Denning, R. G.; Anderson, H. L. Two-photon absorption and the design of two-photon dyes. *Angew Chem Int Ed Engl* **2009**, *48*, 3244-3266.
- (119) Sayyad, M. H.; Saleem, M.; Karimov, K. S.; Yaseen, M.; Ali, M.; Cheong, K. Y.; Mohd Noor, A. F. Synthesis of Zn(II) 5,10,15,20-tetrakis(4'-isopropylphenyl) porphyrin and its use as a thin film sensor. *Applied Physics A* **2009**, *98*, 103-109.
- (120) Mai, C. L.; Huang, W. K.; Lu, H. P.; Lee, C. W.; Chiu, C. L.; Liang, Y. R.; Diao, E. W.; Yeh, C. Y. Synthesis and characterization of diporphyrin sensitizers for dye-sensitized solar cells. *Chem Commun (Camb)* **2010**, *46*, 809-811.
- (121) Davis, N. K.; Pawlicki, M.; Anderson, H. L. Expanding the porphyrin π -system by fusion with anthracene. *Org Lett* **2008**, *10*, 3945-3947.
- (122) Davis, N. K.; Thompson, A. L.; Anderson, H. L. Bis-anthracene fused porphyrins: synthesis, crystal structure, and near-IR absorption. *Org Lett* **2010**, *12*, 2124-2127.
- (123) Davis, N. K.; Thompson, A. L.; Anderson, H. L. A porphyrin fused to four anthracenes. *J Am Chem Soc* **2011**, *133*, 30-31.
- (124) Tsuda, A.; Furuta, H.; Osuka, A. Completely Fused Diporphyrins and Triporphyrin. *Angew Chem Int Ed* **2000**, *39*, 2549-2552.
- (125) Tsuda, A.; Osuka, A. Fully conjugated porphyrin tapes with electronic absorption bands that reach into infrared. *Science* **2001**, *293*, 79-82.
- (126) Ikeda, T.; Aratani, N.; Osuka, A. Synthesis of extremely π -extended porphyrin tapes from hybrid meso-meso linked porphyrin arrays: an approach towards the conjugation length. *Chem Asian J* **2009**, *4*, 1248-1256.

- (127) Jiao, C.; Zhu, L.; Wu, J. BODIPY-fused porphyrins as soluble and stable near-IR dyes. *Chem Eur J* **2011**, *17*, 6610-6614.
- (128) Umetani, M.; Naoda, K.; Tanaka, T.; Lee, S. K.; Oh, J.; Kim, D.; Osuka, A. Synthesis of Di-peri-dinaphthoporphyrins by PtCl₂-Mediated Cyclization of Quinodimethane-type Porphyrins. *Angew Chem Int Ed Engl* **2016**, *55*, 6305-6309.
- (129) Dai, L. Functionalization of graphene for efficient energy conversion and storage. *Acc Chem Res* **2013**, *46*, 31-42.
- (130) Kuila, T.; Bose, S.; Mishra, A. K.; Khanra, P.; Kim, N. H.; Lee, J. H. Chemical functionalization of graphene and its applications. *Prog Mater Sci* **2012**, *57*, 1061-1105.
- (131) Xu, Y.; Liu, Z.; Zhang, X.; Wang, Y.; Tian, J.; Huang, Y.; Ma, Y.; Zhang, X.; Chen, Y. A Graphene Hybrid Material Covalently Functionalized with Porphyrin: Synthesis and Optical Limiting Property. *Adv Mater* **2009**, *21*, 1275-1279.
- (132) Criado, A.; Melchionna, M.; Marchesan, S.; Prato, M. The Covalent Functionalization of Graphene on Substrates. *Angew Chem Int Ed Engl* **2015**, *54*, 10734-10750.
- (133) Dasler, D.; Schafer, R. A.; Minameyer, M. B.; Hitzengerger, J. F.; Hauke, F.; Drewello, T.; Hirsch, A. Direct Covalent Coupling of Porphyrins to Graphene. *J Am Chem Soc* **2017**, *139*, 11760-11765.
- (134) Englert, J. M.; Malig, J.; Zamolo, V. A.; Hirsch, A.; Jux, N. HBC-porphyrin--close contact chromophores. *Chem Commun (Camb)* **2013**, *49*, 4827-4829.
- (135) Lungerich, D.; Hitzengerger, J. F.; Marcia, M.; Hampel, F.; Drewello, T.; Jux, N. Superbenzene-porphyrin conjugates. *Angew Chem Int Ed Engl* **2014**, *53*, 12231-12235.
- (136) Perkins, W.; Fischer, F. R. Inserting Porphyrin Quantum Dots in Bottom-Up Synthesized Graphene Nanoribbons. *Chem Eur J* **2017**, *23*, 17687-17691.
- (137) Liu, J.; Li, B. W.; Tan, Y. Z.; Giannakopoulos, A.; Sanchez-Sanchez, C.; Beljonne, D.; Ruffieux, P.; Fasel, R.; Feng, X.; Müllen, K. Toward cove-edged low band gap graphene nanoribbons. *J Am Chem Soc* **2015**, *137*, 6097-6103.
- (138) Chen, T. A.; Liu, R. S. Synthesis of polyaromatic hydrocarbons from bis(biaryl)diynes: large PAHs with low Clar sextets. *Chem Eur J* **2011**, *17*, 8023-8027.

Chapter 2. Synthesis of Dibenzo[hi,st]ovalene and Its Amplified Spontaneous Emission in a Polystyrene Matrix

This Chapter is based on the following manuscript–

Angew. Chem. Int. Ed., **2017**, 56, 6753–6757

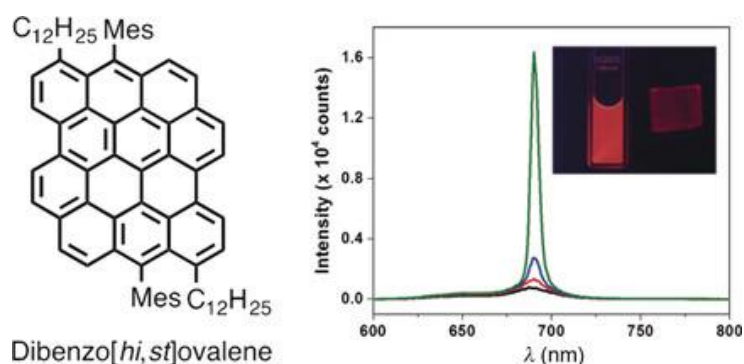
██████████[‡], Qiang Chen[‡], ██████████

and ██████████

Author contributions. Q. C. designed, synthesized and characterized the compound investigated in this research under the supervision of ██████████ and ██████████, ██████████, ██████████ and ██████████ conducted stimulated emission measurements under the supervision of ██████████ ██████████ was responsible for calculation of UV-vis absorption spectra. ██████████, Q. C., ██████████, ██████████, and ██████████ prepared the manuscript. All authors participated in the discussion.

Keywords: graphene molecule • zigzag edges • transient absorption • stimulated emission • amplified spontaneous emission

TOC Figure



Graphene molecules as nanoscale and structurally precise fragments of graphene have recently emerged as promising optoelectronic materials. A novel, highly luminescent, and stable graphene molecule based on dibenzo[hi,st]ovalene features remarkable optical-gain properties, thus holding great potential for applications in laser devices.

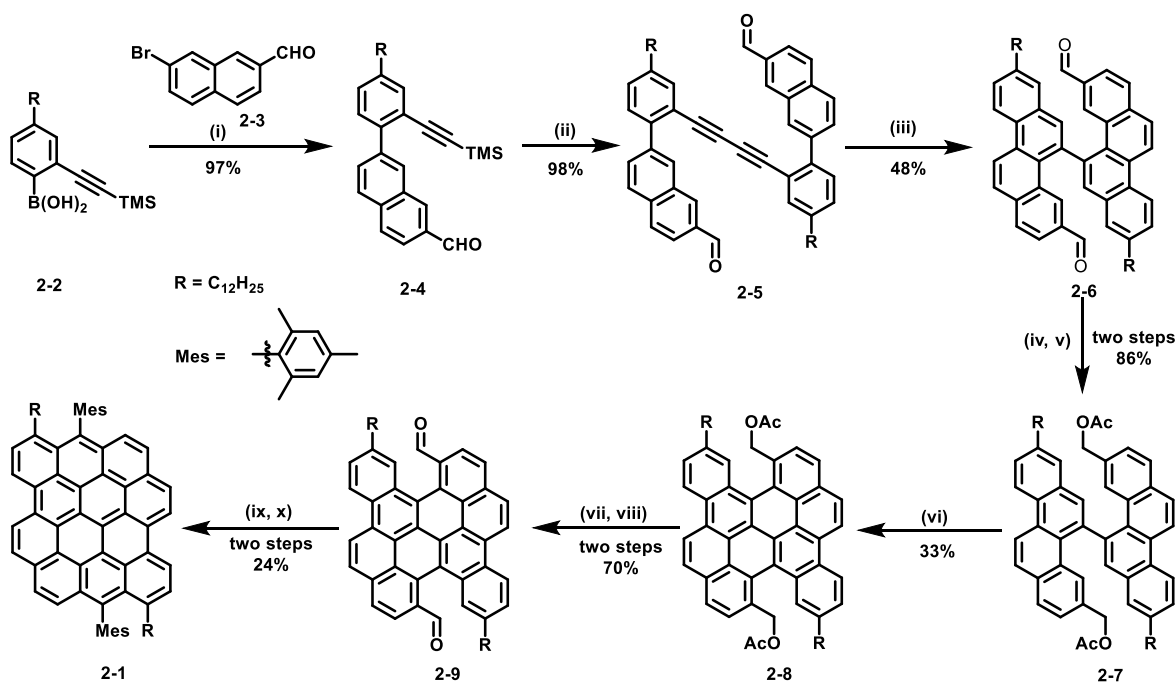
Reprinted with permission from (*Angew. Chem. Int. Ed.*, **2017**, 56, 6753–6757). Copyright © 2017, John Wiley and Sons.

Abstract: A large number of graphene molecules, or large polycyclic aromatic hydrocarbons (PAHs), have been synthesized and display various optoelectronic properties. Nevertheless, their potential for application in photonics has remained largely unexplored. Herein, we describe the synthesis of a highly luminescent and stable graphene molecule, namely a substituted dibenzo[*hi,st*]ovalene (**DBOV**), with zigzag edges and elucidate its promising optical-gain properties by means of ultrafast transient absorption spectroscopy. Upon incorporation of DBOV into an inert polystyrene matrix, amplified stimulated emission can be observed with a relatively low power threshold (ca. $60 \mu\text{J cm}^{-2}$), thus highlighting its high potential for lasing applications.

Along with the development and successful commercialization of organic light-emitting diodes, extensive research has been devoted to the search for stable organic semiconductors (OSCs) that can be employed as optical gain media in laser devices.^[1] The reasons for targeting organic lasers are: 1) the excellent optical features exhibited by organic luminescent materials, 2) the tunability of their optoelectronic properties by means of structural modulation and 3) the high solution processability^[2] that allows for the fabrication of low-cost devices. However, their considerable photodegradation upon intense laser irradiation and intrinsic instability against air and moisture are still major obstacles.^[1b]

Graphene materials have more recently emerged as promising alternative for stable luminescent systems. Although graphene itself has no bandgap, structural patterning into graphene nanostructures, i.e., nanographenes, such as quasi-one-dimensional graphene nanoribbons (GNRs)^[3] and quasi-zero-dimensional graphene quantum dots (GQDs)^[4] allows to open a finite bandgap owing to quantum confinement of the electronic wave function. While top-down fabrication methods cannot precisely control the size and edge structure of the resulting nanographenes, bottom-up chemical synthesis from small molecular building blocks has proven to provide GNRs and GQDs, or graphene molecules, with atomically defined structures.^[5] Such nanographene materials, indeed, exhibit intriguing luminescence features^[6] that depend strongly on the size and edge structures,^[7] making them of great interest for plasmonic^[8] and photonic applications.^[9] There have been a few reports demonstrating or implying stimulated emission (SE) signal from structurally defined GNRs^[10] and graphene molecules^[6a] by transient absorption (TA) measurements in dispersions, which suggests their possible application as optical gain materials. However, to the best of our knowledge, there is hitherto no unambiguous proof for the SE from graphene molecules, and moreover actual amplified spontaneous emission (ASE) of such nanographene materials has

never been observed in films. ASE action would be, in fact, an extremely important effect with the perspective of their role as gain media in laser devices. In this context, a variety of GNRs and graphene molecules featuring armchair-type edge structures have so far been synthesized,^[11] but examples with zigzag edges are still limited, despite their intriguing properties such as lowered energy gaps as well as biradical ground-state characters.^[12] Furthermore, most of the reported zigzag-edged graphene molecules are highly unstable, hindering their in-depth characterisations and applications in devices.^[12b, 13]



Scheme 2-1. Reaction conditions: (i) $Pd(PPh_3)_4$ (0.1 eq.), Na_2CO_3 (6.0 eq.), toluene/EtOH/ H_2O = 4:1:1, 80 °C, 6 h; (ii) $CuCl$ (1.0 eq.), DMF, 80 °C, 12 h, under air; (iii) $PtCl_2$ (0.3 eq.), toluene, 80 °C, 48 h; (iv) $NaBH_4$ (4.0 eq.), THF/MeOH = 2:1, r.t., 2 h; (v) Acetic anhydride, TEA (3.0 eq.), DMAP (0.3 eq.), DCM, r.t., 2 h; (vi) DDQ (4.0 eq.), DCM/ CF_3SO_3H = 20:1, -78 °C, 2 h; (vii) KOH , THF/EtOH/ H_2O , 80 °C, 12 h; (viii) PCC (2.0 eq.), DCM, r.t., 2 h; (ix) $MesMgBr$ (20.0 eq.), THF, r.t. 2 h; (x) $BF_3 \cdot OEt_2$, DCM, r.t., 2 h, under air. DMF: dimethylformamide; THF: tetrahydrofuran; TEA: triethylamine; DMAP: 4-dimethylaminopyridine; DCM: dichloromethane; PCC: pyridinium chlorochromate.

In this work, we have synthesized dibenzo[*hi,st*]ovalene (DBOV) **2-1** (Scheme 2-1) as a novel and stable graphene molecule with both armchair and zigzag edges. DBOV **2-1** exhibits a small optical gap (1.93 eV) based on the UV-*vis* absorption spectrum and an absolute photoluminescence quantum yield (PLQY) of as high as 79%. The investigation of the excited state dynamics, carried out by means of resonant ultrafast TA spectroscopy, clearly reveals the occurrence of SE transitions in solution. Although the prominent optical properties of DBOV **2-1** were largely quenched in the solid state, we were able to recover the SE signal by

blending the molecule with polystyrene (PS), which, interestingly, led to the observation of ASE action from a 1 w% DBOV **2-1** : PS composite film.

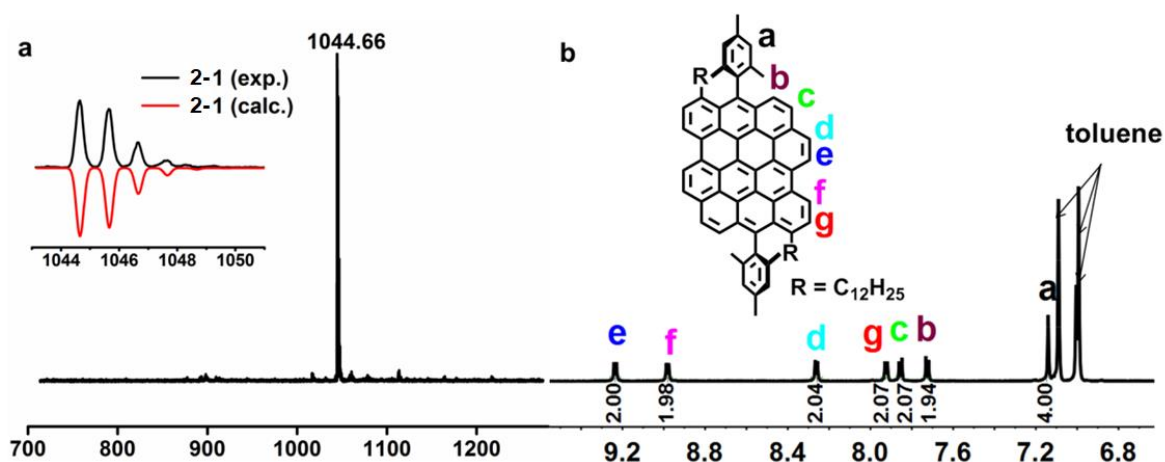


Figure 2-1. a) MALDI-TOF mass spectrum of DBOV **2-1**; Inset shows a comparison between the calculated and experimental isotopic distributions; b) Aromatic region of the ¹H NMR spectrum of DBOV **2-1**, recorded in toluene-*d*₈ at 100 °C (700 MHz).

The synthesis of DBOV **2-1** was carried out as displayed in Scheme 2-1. First, Suzuki coupling of 4-dodecyl-2-(trimethylsilylethynyl)phenylboronic acid (**2-2**) and 7-bromo-2-naphthaldehyde (**2-3**) gave 7-(4-dodecyl-2-(trimethylsilylethynyl)phenyl)-2-naphthaldehyde (**2-4**) in 97% yield. Then CuCl-mediated Glaser coupling of **2-4** provided diaryldiacetylene **2-5** in 98% yield. Subsequently, the key intermediate, bischrysene dialdehyde **2-6** was obtained through a PtCl₂-catalysed cycloaromatization in 48% yield. Direct cyclodehydrogenation of dialdehyde **2-6** to **2-9** under various Scholl conditions failed, most probably because of the strong electron withdrawing properties of the two aldehyde groups. Therefore, compound **2-6** was reduced with NaBH₄ and then protected with acetyl groups to obtain **2-7** in 86% yield over two steps. Notably, the oxidative cyclodehydrogenation of **2-7** succeeded with 2,3-dichloro-5,6-dicyano-1,4-benzoquinone (DDQ)/trifluoromethanesulfonic acid (CF₃SO₃H) at a low temperature (−78 °C), providing cove-edged graphene molecule **2-8** in 33% yield. The low temperature was crucial for this conversion, and no product was obtained when the reaction was carried out at 0 °C. The ester groups of **2-8** were then transformed to dialdehyde groups through a hydrolysis/oxidation sequence in 70% yield. To convert the cove edges of **2-9** into zigzag edges, **2-9** was treated with mesitylmagnesium bromide to give a diol intermediate, which reacted with BF₃•OEt₂ under air to afford the target DBOV **2-1** as a blue solid in 24% yield. The structure of DBOV **2-1** was unambiguously proven by spectroscopic analysis. Figure 2-1a displays the MALDI-TOF MS spectrum of **2-1** with an intense signal at

$m/z = 1044.66$ Da, consistent with the expected molecular mass of 1044.66 Da. The experimental isotopic distribution was in good agreement with the calculated spectrum based on the chemical composition of $C_{80}H_{84}$. A well-resolved 1H NMR spectrum of DBOV **2-1** could be recorded in toluene- d_8 at 100 °C (Figure 2-1b), and all the proton signals could be assigned with the assistance of 2D NMR spectroscopy.

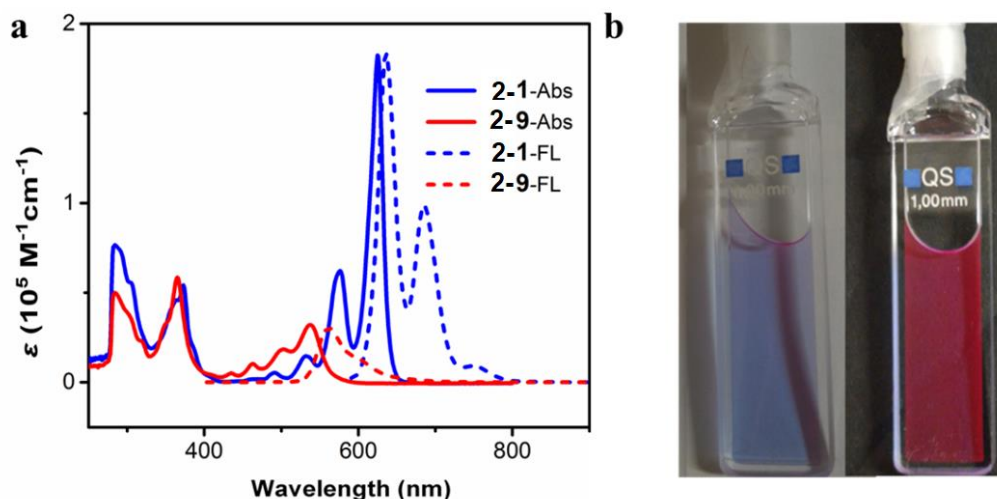


Figure 2-2. a) UV-*vis* absorption and fluorescence spectra of precursor **2-9** and DBOV **2-1** (10^{-5} M in toluene for all measurements). b) Photographs of a toluene solution of DBOV **2-1** with (right) and without (left) a black background, showing the red luminescence under room light.

The UV-*vis* absorption spectrum of DBOV **2-1** in a toluene solution showed a maximum at 625 nm with a large absorption coefficient of $1.83 \times 10^5 \text{ M}^{-1}\text{cm}^{-1}$ (Figure 2-2a). This absorption band could be assigned to HOMO→LUMO transition based on time-dependent density functional theory (TD-DFT) calculations at the B3LYP/6-311G(d,p) level (see Supplementary Figure S2-1 and Supplementary Table S2-1). In comparison to the spectrum of precursor **2-9**, the low-energy absorption band was red-shifted by 88 nm due to the formation of zigzag edges and extension of aromatic core. The optical gap decreased from 2.19 eV to 1.93 eV upon the conversion of **2-9** into **2-1**, according to the onsets of their UV-*vis* absorption spectra. The emission spectra of **2-9** and **2-1** in toluene solutions displayed maxima at 561 and 637 nm, with small Stokes shifts of 23 and 12 nm, respectively, indicating the rigid structures of these two molecules. Interestingly, the emission of **2-1** could be observed already under room light excitation (Figure 2-2b), which is a clear signature of its strong emission properties. The absolute PLQY amounts to 79% (average value = 66.9% with a standard deviation of 6.6% over 35 measurements). To the best of our knowledge, this is one of the highest values reported for graphene molecules.^[14] These promising photophysical

features highlight the important role of the zigzag edges in DBOV **2-1**, significantly lowering the optical gap of **2-9** and realizing highly efficient red light emission.

The electrochemical property of DBOV **2-1** was studied by cyclic voltammetry (CV) in a dichloromethane solution with ferrocene as an external standard (Supplementary Figure S2-2). Two reversible oxidation and reduction waves were observed, indicating the stability of these redox species. The HOMO and LUMO energy levels were estimated to be -4.84 eV and -3.22 eV, based on the onset oxidation and reduction potentials, respectively. The electrochemical HOMO-LUMO gap is 1.62 eV, which is in line with the optical gap of 1.93 eV.

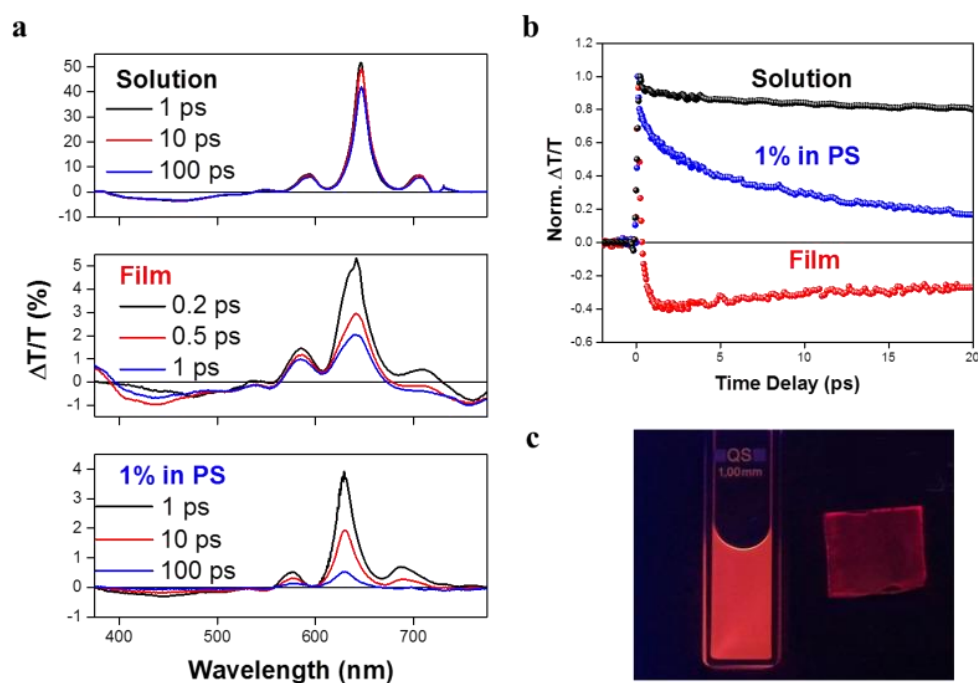


Figure 2-3. a) Ultrafast TA spectra of DBOV **2-1** in solution (0.05 mg/mL in toluene), film and 1 w% blend with PS (deposited on fused silica substrates by drop-casting); b) Normalised time-decay dynamics for the SE emission signal (probe at 695 nm) for solution, film and 1 w% blend with PS. The spectra and time-decay dynamics shown above were taken with a pump fluence of $\approx 50 \mu\text{J cm}^{-2}$; c) Comparison of the luminescence of DBOV **2-1** in solution and 1 w% PS composite film under UV irradiation at 365 nm.

The high PLQY, sharp absorption and emission peaks and small Stokes shift observed for DBOV **2-1** prompted us to gain a deeper insight into its photophysics.^[15] We carried out broadband (375–800 nm) TA measurements by using a pump pulse of 625 nm that is in resonance with the HOMO→LUMO transition. The transient spectrum of DBOV **2-1** (Figure

2-3) displays four features, namely: (i) a negative signal centred at 450 nm that can be interpreted as a photoinduced absorption (PA) from the first excited state S_1 to higher excited states S_i ; (ii) a positive signal at 650 nm that can be assigned to the depletion of the ground state due to the main HOMO→LUMO transition (photobleaching, PB); (iii) another positive PB signal centred at 570 nm, corresponding to its vibronic replica and (iv) a positive signal at 695 nm. The latter is a sign of stimulated emission given that: i) it is not present in the steady state absorption and ii) is red-shifted with respect to the main HOMO→LUMO transition peak^[15a]. Although the origin of the SE signal in such graphene molecule is currently under investigation, we suppose it is related to vibronic relaxation within the higher-lying electronic excited state. Stimulated emission signals are of great interest for acquiring direct information about possible optical gain properties of the material. Thus, we focus the discussion mainly on the SE signal and report the complete transient spectra and time-dynamics (up to 1 ns) data sets in the supplementary information. From the transient spectra of DBOV **2-1** in toluene solution (Figure 2-3a, top graph) the degree of decay is relatively low for all the signals (Supplementary Figure S2-3a-b). This is indicative of stable excited states that can sustain stimulated emission and can also explain the high PLQY.^[16] In addition, the sharp rise of all the transient signals, along with their linear dependence on pump fluence (see Supplementary Fig. S3c-d), suggest that the photoexcitation mechanism is direct and does not involve any non-linear process. For comparison, we have also performed ultrafast TA studies of soluble hexa-*peri*-hexabenzocoronene (HBC) derivative,^[17] which has solely the armchair edge structure, in toluene solution. The preliminary data (Supplementary Figure S2-4) show that all the transient features are incorporated in a large photoinduced absorption signal even at lower concentrations (down to 0.01 mg/mL). Furthermore, we could not observe any clear SE signal in the probed region (from 430 nm to 650 nm) for this HBC derivative, pointing to the uniqueness of the SE observed for DBOV **2-1** and implying an important role of the zigzag edge for achieving the optical gain properties in graphene molecules. We next turn to the characterisation of DBOV **2-1** in thin film, which is essential for device applications (Figure 2-3a, central graph). It appears that the transient peaks are broader than those in solution (e.g., for the PB signal: $\text{FWHM}_{\text{solution}} = 19.4 \pm 0.4 \text{ nm}$; $\text{FWHM}_{\text{film}} = 34.3 \pm 0.9 \text{ nm}$), and all the transient signal intensities decrease considerably in $\approx 200 \text{ fs}$ (Supplementary Figure S2-5a-b). Thereby, the SE peak is overwhelmed by a negative PA feature in a time-frame that is comparable with the instrumental resolution (Figure 2-3b). The broadening of the peaks points toward the aggregation of graphene molecules in films.^[6a] The latter effect can be indicative of ultrafast and non-radiative intermolecular charge transfer processes in the solid

state, which are promoted by the effective supramolecular packing occurring in such planar molecules,^[18] resulting in complete quenching of the PL in films.

To exploit gain properties of the material and possibly employ these features in solid-state devices, we embedded DBOV **2-1** into a polystyrene (PS) matrix by simply mixing their solutions in toluene with 10, 5, 3 and 1 w% ratios. Such dilution approach has been used to inhibit intermolecular charge-transfer processes, and thus enhance SE signals^[18a, 19] and ASE/LASER action in luminescent conjugated polymers.^[20] Notably, this method works effectively also for graphene molecules, as blending allows one to extend the SE signal of DBOV **2-1** for about ≈ 70 ps in the 1 w% **2-1**:PS blend (Figure 2-3b; see Supplementary Figure S2-6a-h for the spectra and dynamics of all the DBOV **2-1**:PS weight ratios). Moreover, the PS blending permits recovery of the emission of DBOV **2-1** in the solid state, and a photoluminescence from the 1 w% DBOV **2-1**:PS composite film can be detected upon UV-light exposure at 365 nm (Figure 2-3c). It is worth noting that by diluting the graphene molecule DBOV **2-1** in the PS matrix, the transient spectral features start resembling those observed in solution, with a progressive narrowing of the PB peaks, and a suppression of the PA signal (Figure 2-3a and Supplementary Figure S2-6). All these spectroscopic findings point toward the occurrence of excitations with charge-transfer character, as it has been reported for luminescent conjugated polymers.^[15a, 18a, 19, 21] In particular, both PA bands at 450 nm and 750 nm seem to stem from the photoinduced excitations of charges possibly originated upon intermolecular transfer, as their intensities decrease in solution and in blends with PS. Remarkably, the 1 w% DBOV **2-1**:PS blend demonstrates amplified stimulated emission (ASE) action triggered above a relatively low laser fluence of $60 \mu\text{J cm}^{-2}$ (Figure 2-4a-b). Although PL line narrowing is observed also in the 3 w% blend (Supplementary Figure S2-7a-b), the laser power needed for FWHM narrowing is higher than the one required for the 1 w% blend ($\approx 150 \mu\text{J cm}^{-2}$). This suggests that the 1 w% blend can minimize the intermolecular cross talking (in terms of charge transfer) that is crucial for avoiding fast non-radiative deactivations, and promote ASE action. Although the 10 w% and 5 w% blends do not show any ASE action, they still allow to observe a PL signal (Supplementary Figure S2-7c-d). To test the stability of DBOV **2-1** against photodegradation, the sample was irradiated under air at a laser fluence 5 times higher than the ASE threshold ($320 \mu\text{J cm}^{-2}$), yielding only a 30% decay after 30 minutes of intense irradiation (2×10^6 pulses). Although DBOV **2-1** : PS blend films were stored under air, the same ASE emission was observed at least for 6 months after the preparation. The remarkable stability of DBOV **2-1** against air, moisture and

photodegradation must be ascribed to, both, the intrinsic robustness of its excited states, and to its incorporation into the inert PS matrix.

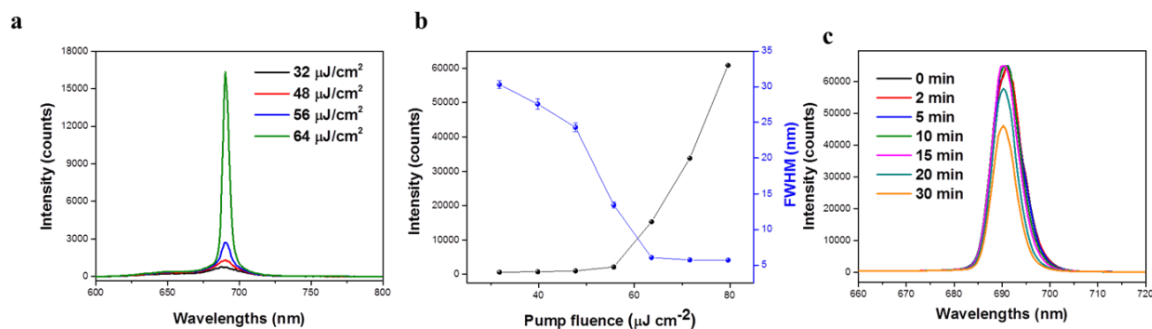


Figure 2-4. a) Photoluminescence spectra taken at laser power fluences below and above the ASE threshold; b) input-output characteristics of ASE action for the 1 w% blend in PS; c) evolution of the ASE signal over time taken at a laser pump fluence 5 times higher than the ASE threshold ($320 \mu\text{J cm}^{-2}$).

In summary, we have synthesized DBOV as a novel graphene molecule with a unique combination of armchair and zigzag edges, demonstrating a low energy gap and strong red emission with remarkable PLQY of 79% as well as promising optical gain properties with low ASE threshold (ca. $60 \mu\text{J cm}^{-2}$) and high photochemical stability. With good solubility and thus enhanced processability, DBOV **2-1** holds great potential for future applications in low-cost organic devices, such as LASERs and OLEDs. Moreover, this study demonstrates the promise of graphene molecules with zigzag edges as stable and highly luminescent materials with optical gain properties. Further variants of such graphene molecules are presently being synthesized in our laboratories and studied in view of their role as optical-gain materials.

Acknowledgements

We thank the financial support from Graphene Flagship (CNECT-ICT-604391), the European Union Project MoQuaS, and the EU Horizon 2020 Research and Innovation Programme under Grant Agreement N. 643238 (SYNCHRONICS) and N. 642196 (iSwitch). X.-Y. W. is grateful for the fellowship from Alexander von Humboldt Foundation.

Reference

- [1] a) I. D. Samuel, G. A. Turnbull, *Chem Rev* **2007**, *107*, 1272-1295; b) A. J. Kuehne, M. C. Gather, *Chem Rev* **2016**, *116*, 12823-12864; c) W. Zhang, J. Yao, Y. S. Zhao, *Acc Chem Res* **2016**, *49*, 1691-1700; d) C. Kallinger, M. Hilmer, A. Haugeneder, M. Perner, W. Spirkel,

- U. Lemmer, J. Feldmann, U. Scherf, K. Müllen, A. Gombert, V. Wittwer, *Adv Mater* **1998**, *10*, 920-923; e) N. Tessler, *Adv Mater* **1999**, *11*, 363-370.
- [2] S. R. Forrest, *Nature* **2004**, *428*, 911-918.
- [3] a) A. Narita, X. Feng, Y. Hernandez, S. A. Jensen, M. Bonn, H. Yang, I. A. Verzhbitskiy, C. Casiraghi, M. R. Hansen, A. H. Koch, G. Fytas, O. Ivasenko, B. Li, K. S. Mali, T. Balandina, S. Mahesh, S. De Feyter, K. Müllen, *Nat Chem* **2014**, *6*, 126-132; b) Y. W. Son, M. L. Cohen, S. G. Louie, *Nature* **2006**, *444*, 347-349.
- [4] a) B. Trauzettel, D. V. Bulaev, D. Loss, G. Burkard, *Nat Phys* **2007**, *3*, 192-196; b) L. Cao, M. J. Meziani, S. Sahu, Y. P. Sun, *Acc Chem Res* **2013**, *46*, 171-180.
- [5] a) A. Narita, X. Y. Wang, X. Feng, K. Müllen, *Chem Soc Rev* **2015**, *44*, 6616-6643; b) L. J. Zhi, K. Müllen, *J Mater Chem* **2008**, *18*, 1472-1484; c) Y. Segawa, H. Ito, K. Itami, *Nat Rev Mater* **2016**, *1*, 15002.
- [6] a) S. Zhu, L. Wang, B. Li, Y. Song, X. Zhao, G. Zhang, S. Zhang, S. Lu, J. Zhang, H. Wang, H. Sun, B. Yang, *Carbon* **2014**, *77*, 462-472; b) S. Zhu, Q. Meng, L. Wang, J. Zhang, Y. Song, H. Jin, K. Zhang, H. Sun, H. Wang, B. Yang, *Angewandte Chemie* **2013**, *52*, 3953-3957.
- [7] K. A. Ritter, J. W. Lyding, *Nat Mater* **2009**, *8*, 235-242.
- [8] J. D. Cox, F. Javier Garcia de Abajo, *Nat Commun* **2014**, *5*, 5725.
- [9] a) V. Gupta, N. Chaudhary, R. Srivastava, G. D. Sharma, R. Bhardwaj, S. Chand, *J Am Chem Soc* **2011**, *133*, 9960-9963; b) S. Osella, A. Narita, M. G. Schwab, Y. Hernandez, X. Feng, K. Müllen, D. Beljonne, *ACS Nano* **2012**, *6*, 5539-5548.
- [10] G. Soavi, S. Dal Conte, C. Manzoni, D. Viola, A. Narita, Y. Hu, X. Feng, U. Hohenester, E. Molinari, D. Prezzi, K. Müllen, G. Cerullo, *Nat Commun* **2016**, *7*, 11010.
- [11] a) X. Yang, X. Dou, A. Rouhanipour, L. Zhi, H. J. Rader, K. Müllen, *J Am Chem Soc* **2008**, *130*, 4216-4217; b) M. G. Schwab, A. Narita, Y. Hernandez, T. Balandina, K. S. Mali, S. De Feyter, X. Feng, K. Müllen, *J Am Chem Soc* **2012**, *134*, 18169-18172; c) M. El Gemayel, A. Narita, L. F. Dossel, R. S. Sundaram, A. Kiersnowski, W. Pisula, M. R. Hansen, A. C. Ferrari, E. Orgiu, X. Feng, K. Müllen, P. Samori, *Nanoscale* **2014**, *6*, 6301-6314.
- [12] a) P. Ruffieux, S. Wang, B. Yang, C. Sanchez-Sanchez, J. Liu, T. Dienel, L. Talirz, P. Shinde, C. A. Pignedoli, D. Passerone, T. Dumslaff, X. Feng, K. Müllen, R. Fasel, *Nature* **2016**, *531*, 489-492; b) A. Konishi, Y. Hirao, K. Matsumoto, H. Kurata, R. Kishi, Y. Shigeta, M. Nakano, K. Tokunaga, K. Kamada, T. Kubo, *J Am Chem Soc* **2013**, *135*, 1430-1437.
- [13] J. Liu, P. Ravat, M. Wagner, M. Baumgarten, X. Feng, K. Müllen, *Angewandte Chemie* **2015**, *54*, 12442-12446.

- [14] a) S. Seifert, K. Shoyama, D. Schmidt, F. Würthner, *Angewandte Chemie* **2016**, *55*, 6390-6395; b) S. Müller, K. Müllen, *Chem Commun* **2005**, 4045-4046.
- [15] a) J. Cabanillas-Gonzalez, G. Grancini, G. Lanzani, *Advanced materials* **2011**, *23*, 5468-5485; b) G. Cerullo, C. Manzoni, L. Luer, D. Polli, *Photochemical & photobiological sciences : Official journal of the European Photochemistry Association and the European Society for Photobiology* **2007**, *6*, 135-144.
- [16] J. R. Lakowicz, *Principles of fluorescence spectroscopy*, Springer Science & Business Media, **2013**.
- [17] M. Kastler, W. Pisula, D. Wasserfallen, T. Pakula, K. Müllen, *J Am Chem Soc* **2005**, *127*, 4286-4296.
- [18] M. Yan, L. J. Rothberg, E. W. Kwock, T. M. Miller, *Phys Rev Lett* **1995**, *75*, 1992-1995; b) N. J. Turro, *Modern molecular photochemistry*, University science books, **1991**.
- [19] T. Virgili, D. Marinotto, C. Manzoni, G. Cerullo, G. Lanzani, *Phys Rev Lett* **2005**, *94*, 117402.
- [20] M. Morales-Vidal, P. G. Boj, J. M. Villalvilla, J. A. Quintana, Q. Yan, N. T. Lin, X. Zhu, N. Ruangsapapichat, J. Casado, H. Tsuji, E. Nakamura, M. A. Diaz-Garcia, *Nat Commun* **2015**, *6*, 8458.
- [21] T. Virgili, D. Marinotto, G. Lanzani, D. D. C. Bradley, *Appl Phys Lett* **2005**, *86*, 91113.

Copyright Wiley-VCH Verlag GmbH & Co. KGaA, Weinheim 2017

Supporting Information

Synthesis of Dibenzo[*hi, st*]ovalene and Its Amplified Spontaneous Emission in a Polystyrene Matrix

1. Supplementary Methods

General methods

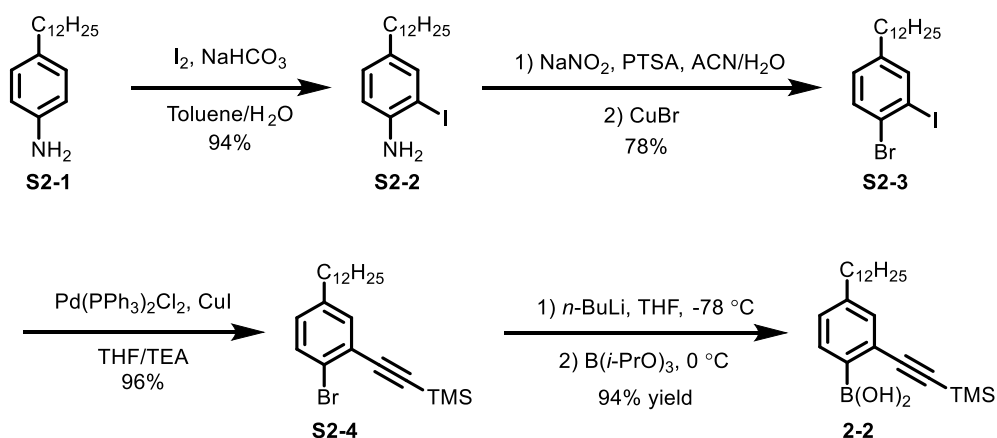
All reactions working with air- or moisture-sensitive compounds were carried out under argon atmosphere using standard Schlenk line techniques. Unless otherwise noted, all starting materials were purchased from commercial sources and used without further purification. All other reagents were used as received. Thin layer chromatography (TLC) was done on silica gel coated aluminum sheets with F254 indicator and preparative chromatographic separation was performed with silica gel (particle size 0.063-0.200 mm). Nuclear Magnetic Resonance (NMR) spectra were recorded using Bruker DPX 250, Bruker DPX 300, and Bruker DRX 700 MHz NMR spectrometers. Chemical shifts (δ) are expressed in ppm relative to the residual of solvent. Coupling constants (J) were recorded in Hertz. Field desorption mass (FD MS) spectra were measured using a VG instruments ZAB 2-SE-FPD using 8 kV accelerating voltage. High-resolution mass spectra (HRMS) were recorded on a Bruker Reflex II-TOF spectrometer by matrix-assisted laser decomposition/ionization (MALDI) using 7,7,8,8-tetracyanoquinodimethane (TCNQ) as matrix. UV-vis absorption spectra were recorded on a Perkin-Elmer Lambda 900 spectrometer at room temperature using a 10 mm quartz cell. Photoluminescence spectra were recorded on a J&MTIDAS spectrofluorometer. Cyclic voltammetry (CV) measurements were performed on a GSTAT-12 in a three-electrode cell in dichloromethane solution of *n*-Bu₄NPF₆ (0.1 M) at a scan rate of 50 mV/s at room temperature. A silver wire, a Pt wire and a glassy carbon electrode were used as the reference electrode, the counter electrode, and the working electrode, respectively.

Synthetic details

Synthesis of 4-dodecyl-2-(trimethylsilylethynyl)phenylboronic acid (**2-2**):

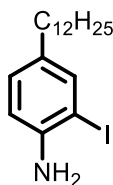
The synthesis of 4-dodecyl-2-(trimethylsilylethynyl)phenylboronic acid (**2-2**) is shown in Supplementary Scheme 2-1. 4-Dodecyl-2-iodoaniline (**S2-2**) was prepared by iodination of 4-dodecylaniline (**S2-1**) with iodine in toluene, followed by Sandmeyer bromination to afford

S2-3 in 78% yield. Subsequently, Sonogashira coupling of **S2-3** with trimethylsilyl acetylene gave **S2-4** in 96% yield, followed by borylation with *n*-BuLi/triisopropyl borate and hydrolysis to give **2-2** in 94% yield.

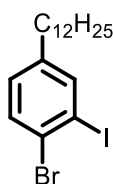


Supplementary Scheme 2-1. Synthetic route to compound **2-2**.

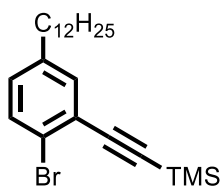
Synthesis of 4-dodecyl-2-iodoaniline (**S2-2**)



To a solution of 4-dodecylaniline (10.00 g, 38.25 mmol) and NaHCO₃ (4.82 g, 57.4 mmol) in toluene (80 mL) and water (9 mL) was added iodine (10.7 g, 42.1 mmol) in portions. The obtained mixture was stirred at room temperature overnight. Saturated Na₂S₂O₃ aqueous solution (50 mL) was added to quench the reaction and stirred for another 0.5 h. The organic phase was separated and the aqueous solution was extracted with ethyl acetate (EA) (50 mL) for 3 times, the combined organic layers were washed with brine (50 mL) and dried over Na₂SO₄. The solvents were evaporated under reduced pressure and the residue was purified by column chromatography over silica gel (eluent: *n*-hexane/EA = 10 : 1) to give compound **S2-2** (14.0 g, 94% yield) as a white solid. TLC R_f = 0.5 (*n*-hexane/EA = 10 : 1); ¹H NMR (250 MHz, CDCl₃, 25 °C, ppm) δ 7.47 (d, J = 1.9 Hz, 1H), 6.96 (dd, J = 8.1, 2.0 Hz, 1H), 6.73 (d, J = 8.1 Hz, 1H), 2.45 (t, J = 7.4 Hz, 2H), 1.61 – 1.43 (m, 2H), 1.37 – 1.01 (m, 18H), 0.88 (t, J = 6.3 Hz, 3H); ¹³C NMR (62.5 MHz, CDCl₃, 25 °C, ppm) δ 144.1, 138.6, 135.4, 129.6, 115.1, 84.8, 34.7, 32.1, 31.8, 29.8, 29.8, 29.7, 29.6, 29.5, 29.3, 22.9, 14.3; FD-MS (8 kV): m/z 388.8; HRMS (ESI): m/z Calcd for C₁₈H₃₀IN: 388.1496 [M + H]⁺, found: 388.1515.

Synthesis of 4-bromo-3-iodododecylbenzene (**S2-3**)

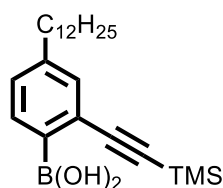
A 500 mL round bottom flask was charged with 4-dodecyl-2-iodoaniline (**S2-2**) (6.00 g, 16.0 mmol), *p*-toluenesulfonic acid monohydrate (8.80 g, 47.0 mmol) and acetonitrile (200 mL). To the suspension was added slowly at 0°C a solution of NaNO₂ (2.10 g, 31.0 mmol) in water (12 mL) over 0.5 h and then the mixture was stirred for another 2 h. Subsequently, CuBr (5.60 g, 39.0 mmol) was added in one portion. After stirring at 0 °C for another 1 h, the mixture was gradually warmed up to r.t. and then heated at 60 °C for 0.5 h. After cooling down to r.t., the mixture was diluted with EA (200 mL), and washed with water (150 mL). The organic phase was separated and washed with brine (100 mL), dried over Na₂SO₄ and concentrated. The obtained residue was purified by column chromatography over silica gel (eluent: *n*-hexane) to give compound **S2-3** (5.50g, 78% yield) as colorless oil. TLC R_f = 0.9 (*n*-hexane); ¹H NMR (250 MHz, CD₂Cl₂, 25 °C, ppm) δ 7.71 (d, *J* = 2.0 Hz, 1H), 7.51 (d, *J* = 8.2 Hz, 1H), 7.04 (dd, *J* = 8.2, 2.1 Hz, 1H), 2.51 (t, *J* = 3.6 Hz, 2H), 1.65 –1.45 (m, 2H), 1.28 (m, 18H), 0.88 (t, *J* = 6.5 Hz, 3H); ¹³C NMR (62.5MHz, CD₂Cl₂, 25 °C, ppm) δ 144.5, 140.6, 132.6, 130.3, 126.5, 101.1, 35.2, 32.3, 31.5, 30.1, 30.1, 30.0, 29.8, 29.7, 29.5, 23.1, 14.3; FD-MS (8 kV): *m/z* 451.4; HRMS (MALDI-TOF): *m/z* Calcd for C₁₈H₂₈BrI: 450.0414 [M]⁺, found: 450.0366.

Synthesis of 4-bromo-3-[(trimethylsilyl)ethynyl]dodecylbenzene (**S2-4**)

To a degassed solution of 4-bromo-3-iodododecylbenzene (**S2-3**) (5.50 g, 12.0 mmol) in THF (34 mL) and triethylamine (34 mL) was added PdCl₂(PPh₃)₂ (170 mg, 0.240 mmol) and CuI (93.0 mg, 0.480 mmol). The resulting mixture was bubbled with Ar for 10 min, then (trimethylsilyl)acetylene (1.30 g, 13.4 mmol) was added via a syringe. After stirring at room temperature overnight, the reaction mixture was diluted with EA (200 mL), washed with water (150 mL) and brine (100 mL) and dried over Na₂SO₄. The solvent was removed under

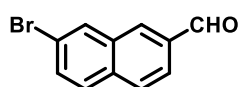
reduced pressure and the residue was purified by column chromatography over silica gel (eluent: *n*-hexane) to give compound **S2-4** (4.90 g, 96% yield) as colorless oil. TLC $R_f = 0.8$ (*n*-hexane/EA = 1:0); $^1\text{H NMR}$ (250 MHz, CD_2Cl_2 , 25 °C, ppm) δ 7.46 (d, $J = 8.2$ Hz, 1H), 7.32 (d, $J = 2.1$ Hz, 2H), 7.01 (dd, $J = 8.3, 2.3$ Hz, 1H), 2.52 (t, $J = 8.0$ Hz, 2H), 1.66 – 1.50 (m, 2H), 1.36 – 1.22 (m, 18H), 0.87 (t, $J = 6.8$ Hz, 3H), 0.27 (s, 9H); $^{13}\text{C NMR}$ (62.5 MHz, CD_2Cl_2 , 25 °C, ppm) δ 142.7, 134.0, 132.5, 130.6, 125.1, 122.6, 103.6, 99.3, 35.4, 32.4, 31.5, 30.1, 30.1, 29.9, 29.8, 29.7, 29.5, 23.1, 14.3, 0.1; FD-MS (8 kV): m/z 126 420.8.

Synthesis of (4-dodecyl-2-((trimethylsilyl)ethynyl)phenyl)boronic acid (**2-2**)



To a solution of 4-bromo-3-[(trimethylsilyl)ethynyl]dodecylbenzene (**S2-4**) (4.90 g, 12.0 mmol) in THF (60 mL) was added dropwise *n*-BuLi (8.7 mL, 1.6 M in hexane) at -78 °C. After stirring at this temperature for 1 h, triisopropyl borate (4.40 g, 23.0 mmol) was added *via* a syringe. The mixture was gradually warmed to room temperature and stirred for 16 h. The reaction was quenched by adding 1 N HCl (36 mL) and stirred at room temperature for 0.5 h. The mixture was extracted with EA (50 mL) for 3 times. The organic layers were combined, washed with brine (100 mL) and dried over Na_2SO_4 . The solvents were evaporated under reduced pressure and the obtained residue was purified by column chromatography over silica gel (*n*-hexane/EA = 10 : 1) to give compound **2** (4.20 g, 94% yield) as a white solid. TLC $R_f = 0.2$ (*n*-hexane/EA = 10 : 1); $^1\text{H NMR}$ (250 MHz, CD_2Cl_2 , 25 °C, ppm) δ 7.84 (d, $J = 7.8$ Hz, 1H), 7.34 (d, $J = 1.7$ Hz, 1H), 7.22 (dd, $J = 7.8, 1.7$ Hz, 2H), 5.79 (s, 2H), 2.60 (t, $J = 7.5$ Hz, 2H), 1.70-1.56 (m, 2H), 1.40 – 1.20 (m, 18H), 0.88 (t, $J = 6.8$ Hz, 3H), 0.29 (s, 9H); $^{13}\text{C NMR}$ (62.5 MHz, CD_2Cl_2 , 25 °C, ppm) δ 146.8, 136.1, 133.2, 129.6, 127.1, 107.3, 98.9, 36.2, 32.5, 31.7, 30.3, 30.3, 30.2, 30.1, 29.9, 29.8, 23.1, 14.3, 0.0; FD-MS (8 kV): m/z 387.0.

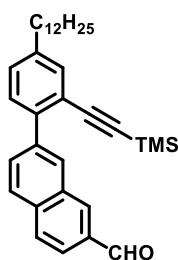
Synthesis of 2-bromo-7-aldehydenaphthalene (**2-3**)



To a THF (28 mL) solution of 2,7-dibromonaphthalene (2.00 g, 7.00 mmol) was added dropwise *n*-BuLi (4.8 mL, 1.6 M in *n*-hexane) at -78 °C. After stirring for 0.5 h, anhydrous

dimethylformamide (DMF) (660 mg, 9.10 mmol) was added via a syringe and the solution was stirred for another 0.5 h at this temperature. Then the mixture was slowly warmed up to room temperature over 1 h. After stirring at room temperature for 1 h, water (20 mL) was added to quench the reaction. THF phase was separated and the aqueous phase was extracted with EA (30 mL) for 3 times. The combined organic layers were washed with brine (50 mL) and dried over Na₂SO₄. The solvent was evaporated under reduced pressure and the residue was purified by column chromatography over silica gel (*n*-hexane/EA = 15 : 1) to give compound **3** (1.30 g, 80% yield) as a white solid. TLC $R_f = 0.3$ (*n*-hexane/EA = 10 : 1); ¹H NMR (250 MHz, CD₂Cl₂, 25 °C, ppm) δ 10.15 (s, 1H), 8.27 (d, $J = 1.1$ Hz, 1H), 8.21 (d, $J = 1.8$ Hz, 1H), 7.95 (d, $J = 1.1$ Hz, 2H), 7.83 (d, $J = 7.5$ Hz, 1H), 7.73 (dd, $J = 8.8, 1.9$ Hz, 1H); ¹³C NMR (62.5 MHz, CD₂Cl₂, 25 °C, ppm) δ 192.1, 135.4, 135.2, 134.2, 133.4, 132.6, 131.8, 130.1, 129.5, 123.6, 121.4; FD-MS (8 kV): m/z 234.5; HRMS (MALDI-TOF): m/z Calcd for C₁₁H₇BrO: 233.9675 [M]⁺, found: 233.9574.

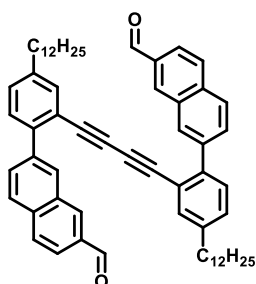
Synthesis of 7-(4-dodecyl-2-(trimethylsilylethynyl)phenyl)-2-naphthaldehyde (**2-4**)



To a two-necked round bottom flask was added compound **2-2** (1.97 g, 5.10 mmol), compound **2-3** (1.21 g, 5.10 mmol) and Na₂CO₃ (3.25 g, 30.6 mmol). The flask was evacuated and backfilled with Ar for 3 times. Then toluene/EtOH/H₂O (128 mL/32mL/32 mL) was added via a syringe. The mixture was degassed by bubbling with Ar for 15 minutes before Pd(PPh₃)₄ (320 mg, 0.300 mmol) was added. The mixture was heated at 80 °C for 6 h under Ar atmosphere. Then the reaction mixture was cooled down to r.t. and extracted with EA (30 mL) for 3 times. The combined organic layers were washed with brine (80 mL) and then dried over anhydrous Na₂SO₄. The solvents were removed under reduced pressure and the residue was purified by column chromatography (*n*-hexane/EA = 20 : 1) to give compound **2-4** (2.45 g, 97% yield) as a white solid. TLC $R_f = 0.5$ (*n*-hexane/EA = 10 : 1); ¹H NMR (250 MHz, CD₂Cl₂, 25 °C, ppm) δ 10.11 (s, 1H), 8.31 (s, 1H), 8.20 (s, 1H), 7.96 – 7.80 (m, 4H), 7.43 – 7.29 (m, 2H), 7.20 (dd, $J = 8.0, 1.9$ Hz, 1H), 2.56 (t, $J = 7.8$ Hz, 2H), 1.66 – 1.49 (m, 2H), 1.34 – 1.12 (m, 18H), 0.79 (t, $J = 6.8$ Hz, 1H), 0.00 (s, 9H); ¹³C NMR (62.5 MHz, CD₂Cl₂, 25 °C, ppm) δ 192.5, 143.2, 139.6, 136.0, 135.2, 135.0, 134.0, 133.0, 131.5, 130.1, 130.0,

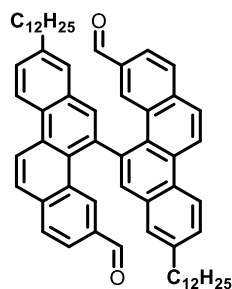
129.8, 129.3, 127.9, 123.2, 105.4, 98.0, 35.9, 32.6, 31.9, 30.3, 30.2, 30.1, 30.0, 29.9, 23.3, 14.6, 0.0; FD-MS (8 kV): m/z 497.0; HRMS (MALDI-TOF): m/z Calcd for $C_{34}H_{44}OSi$: 496.3156 $[M]^+$, found: 496.3100.

Synthesis of 1,4-bis(2-(7-formylnaphthalen-2-yl)-5-dodecylphenyl)buta-1,3-diyne (**2-5**)



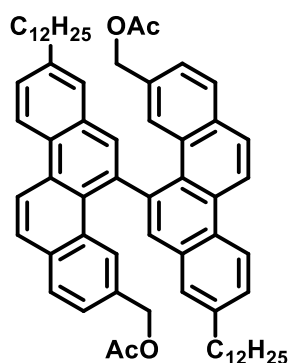
To a solution of compound **2-4** (1.60 g, 3.20 mmol) in DMF (24 mL) was added CuCl (320 mg, 3.20 mmol). The reaction mixture was heated at 80 °C under air. After 12 h, the reaction mixture was diluted with EA (100 mL) and washed with 1 N HCl (50 mL). The aqueous phase was then extracted with EA (30 mL) for 3 times. The combined organic layers were washed with saturated aqueous Na_2CO_3 (60 mL) and brine (60 mL) before drying over Na_2SO_4 . The solvents were removed under reduced pressure and the residue was purified by column chromatography over silica gel (n -hexane/EA = 10 : 1) to give compound **2-5** (1.34 g, 98% yield) as a white solid. TLC R_f = 0.3 (n -hexane/EA = 10 : 1); 1H NMR (250 MHz, CD_2Cl_2 , 25 °C, ppm) δ 10.01 (s, 2H), 8.22 (s, 2H), 8.04 (s, 2H), 7.83 (d, J = 1.4 Hz, 4H), 7.76 (d, J = 1.5 Hz, 4H), 7.40 (d, J = 1.5 Hz, 2H), 7.33 (d, J = 7.9 Hz, 1H), 7.28 – 7.19 (m, 2H), 2.56 (t, J = 7.5 Hz, 4H), 1.70 – 1.45 (m, 4H), 1.40 – 1.15 (m, 20H), 0.84 (t, J = 6.5 Hz, 6H); ^{13}C NMR (62.5 MHz, CD_2Cl_2 , 25 °C, ppm) δ 192.5, 143.3, 141.9, 139.3, 136.0, 135.1, 135.0, 134.7, 133.1, 131.0, 130.7, 130.3, 129.9, 129.2, 128.1, 123.3, 120.3, 82.3, 76.87, 35.8, 32.5, 31.8, 30.3, 30.2, 30.1, 30.0, 29.8, 23.3, 14.5; FD-MS (8 kV): m/z 848.6; HRMS (MALDI-TOF): m/z Calcd for $C_{62}H_{70}O_2$: 846.5370 $[M]^+$, found: 846.5408.

Synthesis of 8,8'-didodecyl-[5,5'-bichrysen]-3,3'-dicarbaldehyde (**2-6**)



A Schlenk flask charged with compound **2-5** (630 mg, 0.744 mmol) and PtCl₂ (59.0 mg, 0.220 mmol) was dried under vacuum for 1 h and then was evacuated and backfilled with Ar for 3 times before anhydrous toluene (50 mL) was added via a syringe. The mixture was degassed by three freeze-pump-thaw cycles and heated at 85 °C for 48 h under Ar atmosphere. After confirming the completion of the reaction by ¹H NMR, the solvent was removed under reduced pressure and the residue was purified by column chromatography over silica gel (eluent: *n*-hexane/EA = 10 : 1) to give compound **2-6** (300 mg, 48% yield) as a white solid. TLC *R_f* = 0.3 (*n*-hexane/EA = 10 : 1); ¹H NMR (250 MHz, CD₂Cl₂, 25 °C, ppm) δ 9.02 (d, *J* = 9.3 Hz, 2H), 8.85 (d, *J* = 8.8 Hz, 2H), 8.69 (s, 2H), 8.20 (s, 2H), 8.00 (d, *J* = 7.7 Hz, 4H), 7.81 (d, *J* = 8.0 Hz, 4H), 7.72 (dd, *J* = 9.1 Hz, 1.4 Hz, 2H), 7.60 (dd, *J* = 8.2, 1.5 Hz, 2H), 2.89 (t, *J* = 7.7 Hz, 4H), 1.90 – 1.70 (m, 4H), 1.49 – 1.15 (m, 36H), 0.94 – 0.73 (m, 6H); ¹³C NMR (62.5 MHz, CD₂Cl₂, 25 °C, ppm) δ 192.0, 143.2, 140.5, 136.7, 134.1, 133.2, 132.8, 131.5, 131.3, 130.5, 129.5, 129.4, 128.7, 128.3, 127.9, 127.6, 125.3, 123.7, 122.4, 36.3, 32.3, 31.7, 30.1, 30.0, 30.0, 29.9, 29.8, 29.7, 23.1, 14.3; FD-MS (8 kV): *m/z* 848.4; HRMS (MALDI-TOF): *m/z* Calcd for C₆₂H₇₀O₂: 869.5268 [M + Na]⁺, found: 869.5292.

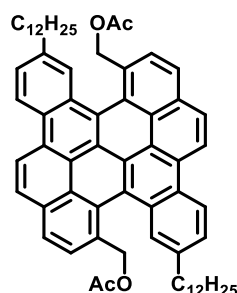
Synthesis of 3,3'-diacetoxymethyl-8,8'-didodecyl-5,5'-bichrysene (**2-7**)



To a solution of compound **2-6** (200 mg, 0.230 mmol) in the mixture of THF (10 mL) and methanol (5 mL) was added NaBH₄ (71.0 mg, 1.90 mmol). The mixture was stirred at room temperature for 1 h. The completion of the reaction by confirmed by TLC analysis (*n*-hexane/EA = 4 : 1), and then acetone (5 mL) was added to quench the reaction. After stirring for another 10 minutes, the solvent was evaporated and the residue was dissolved in EA (50 mL). The organic solution was then washed with water (30 mL) and brine (30 mL), and dried over Na₂SO₄. The solvent was evaporated to give a diol intermediate (195 mg, 95% crude yield) as a white solid. The diol intermediate (150 mg, 177 μmol) was dissolved in anhydrous dichloromethane (DCM) (10 mL), and then triethylamine (54 mg, 0.53 mmol), 4-dimethylaminopyridine (6.5 mg, 53 μmol) and acetic anhydride (54 mg, 0.53 mmol) were

added. The reaction mixture was stirred at room temperature for 2 h, and then TLC analysis (*n*-hexane/EA = 4 : 1) showed the reaction was completed. The solvent was evaporated and the residue was purified by column chromatography over silica gel (*n*-hexane/EA = 5 : 1) to give compound **2-7** (150 mg, 91% yield) as a white solid. TLC R_f = 0.5 (*n*-hexane/EA = 5 : 1); ^1H NMR (250 MHz, CD_2Cl_2 , 25 °C, ppm) δ 8.84 (d, J = 9.2 Hz, 2H), 8.75 (d, J = 9.2 Hz, 2H), 8.05 – 7.95 (m, 4H), 7.80 (d, J = 8.2 Hz, 2H), 7.70 (s, 2H), 7.60 – 7.52 (m, 2H), 7.17 (dd, J = 8.2, 1.5 Hz, 2H), 4.45 – 4.28 (m, 4H), 2.73 (t, J = 7.9 Hz, 4H), 1.73 – 1.58 (m, 4H), 1.40 – 1.10 (m, 38H), 1.13 (s, 6H), 0.85 – 0.72 (m, 6H); ^{13}C NMR (62.5 MHz, CD_2Cl_2 , 25 °C, ppm) δ 170.4, 142.5, 141.2, 133.3, 133.0, 132.5, 131.0, 130.9, 130.5, 128.7, 128.6, 128.3, 127.5, 127.4, 126.8, 125.4, 123.6, 122.2, 66.1, 36.2, 32.3, 31.8, 30.1, 30.0, 29.9, 29.9, 29.8, 29.7, 23.1, 20.0, 14.3; FD-MS (8 kV): m/z 935.7; HRMS (MALDI-TOF): m/z Calcd for $\text{C}_{66}\text{H}_{78}\text{O}_4$: 934.5895 $[\text{M}]^+$, found: 934.5909.

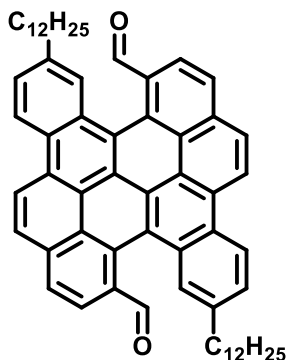
Synthesis of 5,14-diacetoxymethyl-3,12-didodecylbenzo[*a*]dinaphtho[2,1,8-*cde*:1',2',3',4'-*ghi*]perylene (**2-8**)



A solution of compound **2-7** (150 mg, 0.160 mmol) and DDQ (146 mg, 0.640 mmol) in anhydrous DCM (60 mL) was cooled down to -78 °C and stirred at this temperature for 10 min. To this vigorously stirred solution was added slowly trifluoromethanesulfonic acid ($\text{CF}_3\text{SO}_3\text{H}$) (3 mL) and the obtained mixture was stirred at -78 °C for another 2 h. Then the reaction was quenched by pouring into saturated aqueous Na_2CO_3 . DCM phase was separated and the aqueous phase was extracted with DCM (30 mL) for 2 times. The combined organic layers were washed with brine (50 mL), and dried over Na_2SO_4 . The solvents were evaporated and the residue was purified by column chromatography over silica gel (*n*-hexane/EA = 10 : 1) to give compound **2-8** (50 mg, yield 33%) as a yellow solid. TLC R_f = 0.3 (*n*-hexane/EA = 4 : 1); ^1H NMR (250 MHz, CD_2Cl_2 , 25 °C, ppm) δ 8.86 (d, J = 9.1 Hz, 2H), 8.75 (d, J = 9.1 Hz, 2H), 8.10 – 7.89 (m, 2H), 7.80 (d, J = 8.2 Hz, 2H), 7.70 (s, 2H), 7.62 – 7.46 (m, 2H), 7.17 (d, J = 8.2, 2H), 4.49 – 4.18 (m, 4H), 2.74 (t, J = 7.8 Hz, 4H), 1.78 – 1.57 (m, 4H), 1.24 – 1.16 (m, 36H), 1.15 (s, 6H), 0.80 (t, J = 6.6 Hz, 6H); ^{13}C NMR (63 MHz, CD_2Cl_2 , 25 °C, ppm) δ

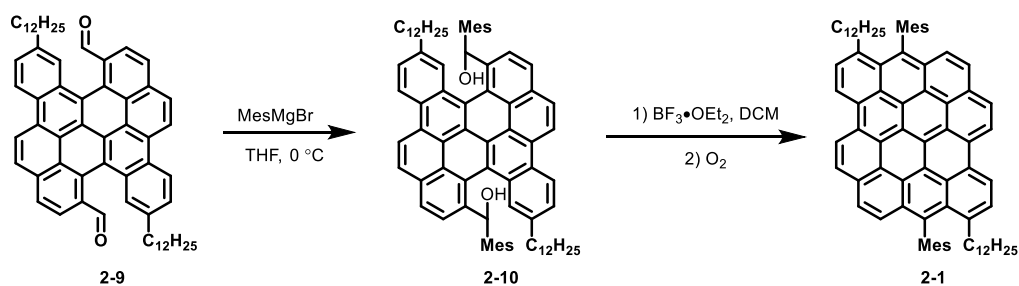
170.8, 142.1, 133.0, 131.2, 130.3, 128.0, 127.9, 127.8, 127.6, 127.4, 127.1, 126.4, 126.2, 125.8, 123.9, 122.3, 122.1, 121.7, 66.6, 36.9, 32.5, 32.2, 30.2, 30.2, 30.2, 30.1, 29.9, 23.3, 21.1, 14.5 FD-MS (8KV): m/z 931.7; HRMS (MALDI-TOF): m/z Calcd for $C_{66}H_{74}O_4$: 930.5582 $[M]^+$, found: 930.5546.

Synthesis of 3,12-didodecyl-5,14-diformylbenzo[*a*]dinaphtho[2,1,8-*cde*:1',2',3',4'-*ghi*]perylene (**2-9**)



To a solution of compound **2-8** (30 mg, 32 μ mol) in THF (9 mL) and ethanol (9 mL) was added 10% aqueous solution of KOH (3 mL). The mixture was stirred at reflux for 12 h. After cooling to r.t., the reaction mixture was diluted with EA (20 mL) and washed with water (10 mL), brine (10 mL) and then dried over Na_2SO_4 . The solvent was evaporated and the obtained residue was dissolved in anhydrous DCM (20 mL). To the obtained solution was added pyridinium chlorochromate (PCC) (15 mg, 69 μ mol) and then the reaction mixture was stirred at room temperature for 2 h. Methanol (1 mL) was added to quench the reaction and the mixture was stirred for another 10 min. The solvent was removed under reduced pressure and the residue was purified by column chromatography over silica gel (*n*-hexane/EA = 4 : 1) to give compound **9** (19 mg, 70% yield) as a red solid. 1H NMR (250 MHz, CD_2Cl_2 , 25 $^\circ C$, ppm) δ 9.59 (s, 2H), 8.94 (d, J = 9.3 Hz, 2H), 8.71 (d, J = 8.8 Hz, 2H), 8.45 (d, J = 8.2 Hz, 2H), 8.36 (s, 2H), 8.31 (d, J = 5.9 Hz, 2H), 8.28 (d, J = 5.0 Hz, 2H), 7.55 – 7.45 (m, 2H), 2.68 (t, J = 7.9 Hz, 2H), 1.65 – 1.55 (m, 2H), 1.23 – 1.55 (s, 36H), 0.75 – 0.95 (m, 6H); ^{13}C NMR (62.5 MHz, CD_2Cl_2 , 25 $^\circ C$, ppm) δ 190.9, 143.6, 134.3, 132.7, 132.5, 131.4, 128.8, 128.6, 128.2, 127.6, 127.4, 125.9, 125.2, 124.9, 124.8, 124.5, 123.6, 121.8, 121.1, 36.9, 32.5, 32.2, 31.8, 30.3, 30.2, 30.1, 30.1, 29.9, 23.3, 23.2, 14.4 FD-MS (8 kV): m/z 843.7; HRMS (MALDI-TOF): m/z Calcd for $C_{66}H_{74}O_4$: 842.5063 $[M]^+$, found: 842.5070.

Synthesis of 5,13-didodecyl-6,14-dimesityldibenzo[*hi,st*]ovalene (**2-1**)

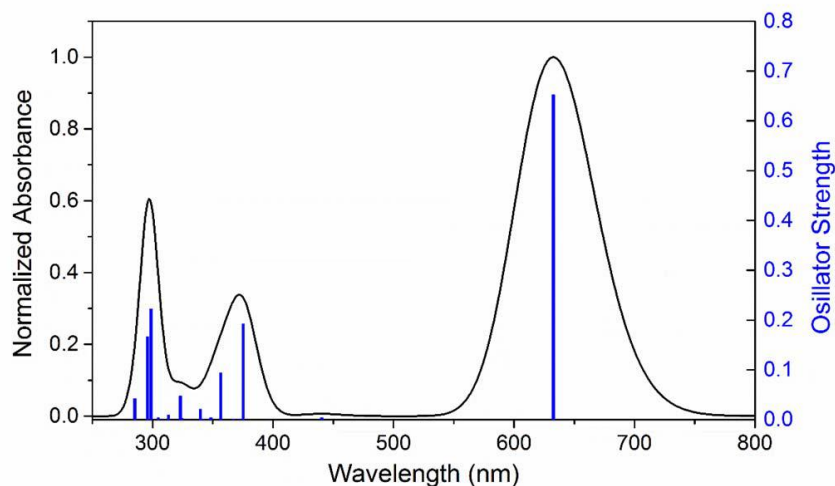


To compound **2-9** (40 mg, 47 μmol) dissolved in anhydrous THF (30 mL) was added mesitylmagnesium bromide (1.0 mL, 1.0 M in diethyl ether, 1.0 mmol) under Ar. The mixture was stirred at room temperature for 2 h, and then the solution was poured into water (20 mL) and extracted with EA (30 mL) for 3 times. The combined organic layers were washed with brine (30 mL) and dried over Na_2SO_4 . After removing the solvents in vacuo the resulting crude product of compound **10** was dissolved in anhydrous DCM (10 mL) and $\text{BF}_3 \cdot \text{OEt}_2$ (1.0 mL) was added. The mixture was stirred at room temperature for 2 h, and then quenched with saturated aqueous NaHCO_3 (10 mL). The organic phase was separated and dried over Na_2SO_4 . The solvents were evaporated under reduced pressure and the residue was purified by column chromatography over silica gel (eluent: *n*-hexane/EA = 10 : 1) to give compound **2-1** (12 mg, 24% yield) as a blue solid. ^1H NMR (700 MHz, toluene- d_8 , 100 $^\circ\text{C}$, ppm) δ 9.23 (d, J = 8.5 Hz, 2H), 8.98 (d, J = 8.5 Hz, 2H), 8.26 (d, J = 7.9 Hz, 2H), 7.92 (d, J = 7.7 Hz, 2H), 7.85 (d, 309 J = 9.4 Hz, 2H), 7.73 (d, J = 9.2 Hz, 2H), 7.14 (s, 4H), 2.88 (t, J = 8.4 Hz, 4H), 2.48 (s, 6H), 2.07 (s, 12H), 1.45 – 1.35 (m, 20H), 1.30 – 1.25 (m, 4H), 0.92 (t, J = 6.9 Hz, 6H). ^{13}C NMR (62.5 MHz, benzene- d_6 , 25 $^\circ\text{C}$, ppm) δ 141.1, 139.9, 137.9, 137.5, 134.9, 131.1, 130.6, 130.5, 130.3, 129.1, 127.1, 127.0, 126.2, 126.0, 125.7, 125.6, 124.8, 124.5, 124.5, 123.9, 123.7, 121.4, 36.4, 33.4, 32.4, 30.8, 30.4, 30.3, 30.3, 30.2, 30.1, 29.9, 23.2, 21.5, 21.0, 14.4; FD-MS (8 kV): m/z 1045.9; HRMS (MALDI-TOF): m/z Calcd for $\text{C}_{80}\text{H}_{84}$: 1044.6573 [M] $^+$, found:1044.6477.

2. DFT Calculations

DFT calculations were performed using the Gaussian 09 software package.¹ The geometry and energies were calculated at the B3LYP/6-311G(d,p) level. Time-dependent DFT (TDDFT) calculations were performed at the same level of theory. Methyl groups were used to replace the long dodecyl chains for computational simplicity.

Supplementary Figure S2-1.



Supplementary Figure S2-1| Simulated absorption spectrum of DBOV **2-1** and the oscillator strengths (blue bars) by TDDFT calculations at the B3LYP/6-311G(d,p) level.

Supplementary Table S2-1| Major electronic transitions of DBOV **2-1** calculated by TDDFT method.

excited state	energy (eV)	wavelength (nm)	oscillator strength	description
1	1.96	633	0.6525	HOMO→LUMO (0.70333) HOMO-2→LUMO (0.46008)
2	3.30	375	0.1921	HOMO-1→LUMO+1 (0.19231) HOMO→LUMO+2 (0.37460) HOMO→LUMO+5 (0.29962) HOMO-9→LUMO (0.15490) HOMO-2→LUMO (-0.19955)
3	3.48	356	0.0939	HOMO→LUMO+2 (-0.16608) HOMO→LUMO+5 (0.60927) HOMO→LUMO+6 (0.13137) HOMO-10→LUMO (0.17297)
4	3.65	340	0.0208	HOMO-9→LUMO (-0.16125) HOMO→LUMO+6 (0.62283) HOMO→LUMO+8 (0.16131) HOMO-10→LUMO (-0.12649) HOMO-3→LUMO+1 (0.43824)
5	4.19	296	0.1668	HOMO-1→LUMO+1 (-0.34967) HOMO-1→LUMO+3 (0.31913) HOMO-1→LUMO+4 (-0.13474)

Table S2-2. Cartesian coordinates of the DFT-optimized **2-1**.

Tag	Symbol	X	Y	Z
1	C	-4.2849776	-3.878662	-0.3125137
2	C	-2.9033849	-4.0084556	-0.2339019
3	C	-2.0848278	-2.8954912	-0.1089299
4	C	-2.6936236	-1.6000378	-0.0825411
5	C	-4.1384394	-1.4626524	-0.122407
6	C	-4.9342381	-2.6582696	-0.2560758
7	C	-1.8522722	-0.4469504	-0.0284391
8	C	-2.4315207	0.8376813	0.0200664
9	C	-3.8600291	0.9764682	0.0490043
10	C	-4.6954394	-0.1457472	-0.0261328
11	C	-1.6001654	1.9984213	0.0479767
12	C	-2.1882838	3.2900516	0.1258445
13	C	-3.6126709	3.4029481	0.189184
14	C	-4.4075029	2.3074597	0.1536298
15	C	-0.6335217	-3.0313979	-0.011688
16	C	0.1814169	-1.8720788	-0.0030873
17	C	-0.4125554	-0.5717634	-0.0258575
18	C	0.4125636	0.5717923	-0.025836
19	C	-0.1814101	1.8721061	-0.0030087
20	C	0.6335281	3.031426	-0.0115714
21	C	0.0132615	4.2892975	0.0798176
22	C	-1.358284	4.4171241	0.1498933
23	C	-0.0132571	-4.2892722	0.0796697
24	C	1.3582888	-4.4171025	0.1497299
25	C	2.18829	-3.2900305	0.125702
26	C	1.6001718	-1.9983967	0.0478847
27	C	2.4315272	-0.8376555	0.0200129
28	C	1.8522812	0.4469797	-0.0284321
29	C	2.6936346	1.6000699	-0.0824828
30	C	2.0848354	2.8955245	-0.1088069
31	C	3.6126781	-3.4029311	0.1890145
32	C	4.4075102	-2.3074416	0.1534897
33	C	3.8600349	-0.9764456	0.0489316
34	C	4.6954494	0.1457697	-0.0261544
35	C	4.1384543	1.4626873	-0.1223545
36	C	4.9342491	2.6583204	-0.2559564
37	C	4.2849825	3.8787131	-0.3123215
38	C	2.9033902	4.0084983	-0.2337058
39	C	-6.173161	0.1258684	0.0238216
40	C	-6.4432334	-2.7205367	-0.3664372
41	C	6.1731658	-0.1258779	0.0237803
42	C	6.4432427	2.7206217	-0.3663245
43	C	6.8752516	-0.4554522	-1.1512573
44	C	8.2362486	-0.7559957	-1.0695056
45	C	8.922118	-0.7506826	0.1458603
46	C	8.2020847	-0.4458177	1.3008265
47	C	6.839761	-0.1382551	1.2629954

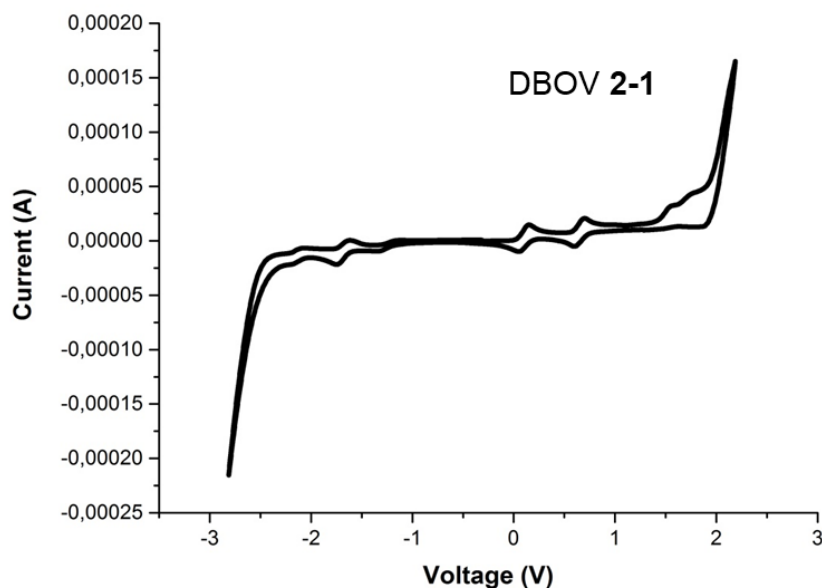
48	C	-6.8752607	0.4554931	-1.1512017
49	C	-8.236259	0.7559931	-1.0694333
50	C	-8.922132	0.7505844	0.145938
51	C	-8.2020971	0.4456542	1.3008772
52	C	-6.8397583	0.1381301	1.2630286
53	C	-10.401619	1.0465204	0.2041211
54	C	10.4016028	-1.0466248	0.2040553
55	H	-4.881453	-4.7774028	-0.4248885
56	H	-2.4812906	-5.001824	-0.2904543
57	H	-4.0490219	4.3935348	0.2650351
58	H	-5.4809781	2.4231607	0.20177
59	H	0.6123406	5.1886414	0.110089
60	H	-1.8070904	5.4019416	0.2250289
61	H	-0.6123388	-5.1886144	0.1099303
62	H	1.8070948	-5.4019221	0.2248377
63	H	4.0490296	-4.393521	0.2648191
64	H	5.4809876	-2.4231433	0.2016047
65	H	4.8814549	4.7774635	-0.4246396
66	H	2.4812951	5.0018704	-0.2901945
67	H	-6.8294313	-2.1441224	-1.2072568
68	H	-6.7427924	-3.7600551	-0.5128143
69	H	-6.9521527	-2.3531478	0.5253575
70	H	6.8294421	2.144293	-1.2072026
71	H	6.7427796	3.7601598	-0.5126106
72	H	6.9521799	2.3531638	0.5254308
73	C	6.1801614	-0.4881554	-2.4927408
74	H	8.7733124	-1.0041891	-1.9805412
75	H	8.7111221	-0.4513825	2.2603256
76	C	6.1060482	0.1740709	2.5467256
77	C	-6.1801691	0.4882945	-2.4926821
78	H	-8.7733286	1.0042301	-1.9804545
79	H	-8.7111383	0.4511332	2.2603738
80	C	-6.1060479	-0.1742682	2.5467426
81	H	-10.6924111	1.7768926	-0.5548705
82	H	-10.991139	0.1401655	0.0268529
83	H	-10.6917257	1.4390197	1.181392
84	H	10.6926581	-1.7758867	-0.5558958
85	H	10.9911231	-0.1399777	0.0282839
86	H	10.6914469	-1.440507	1.180852
87	H	-6.7798312	-0.1139768	3.4033712
88	H	-5.2806526	0.5233772	2.7143594
89	H	-5.6703403	-1.1777032	2.5292686
90	H	-6.8945874	0.6810865	-3.2952086
91	H	-5.6725413	-0.4561355	-2.7090541
92	H	-5.4157462	1.2701164	-2.5267243
93	H	6.7798147	0.1136672	3.4033597
94	H	5.2806096	-0.5235414	2.7142677
95	H	5.6703981	1.1775333	2.5293311

96	H	6.8945802	-0.6808872	-3.2952815
97	H	5.6725311	0.4562899	-2.7090418
98	H	5.4157397	-1.2699771	-2.5268406

Reference:

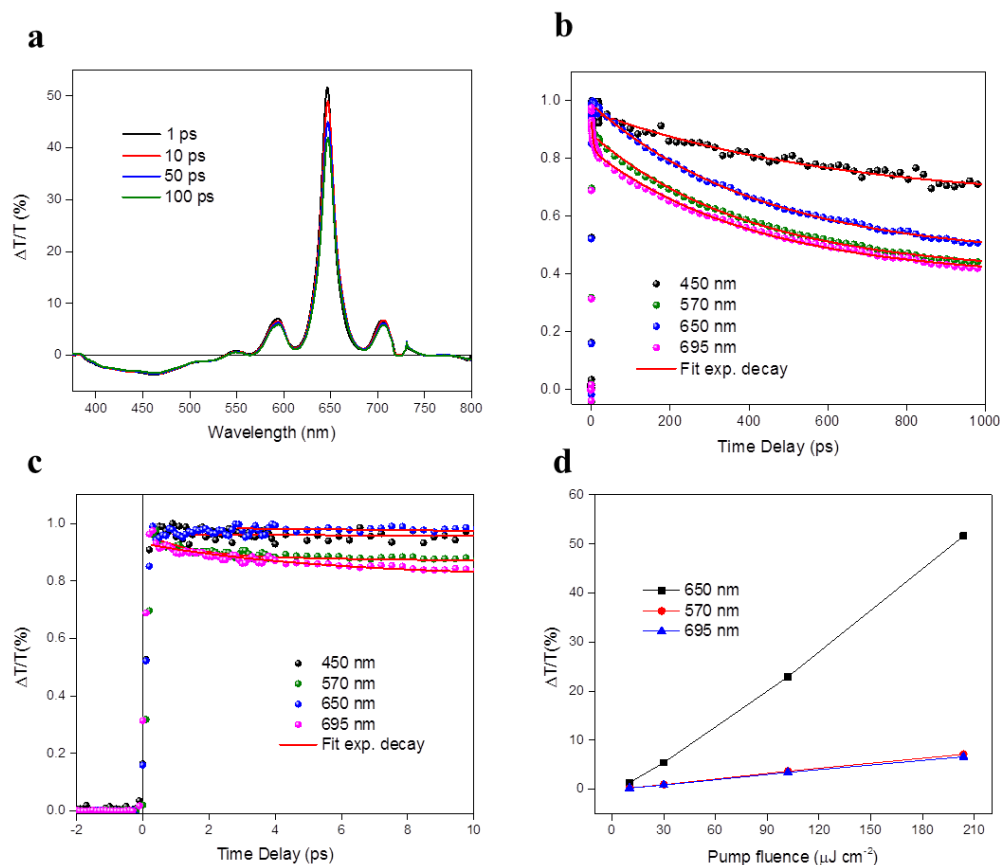
1. Gaussian 09, Revision D.01, Frisch, M. J.; Trucks, G. W.; Schlegel, H. B.; Scuseria, G. E.; Robb, M. A.; Cheeseman, J. R.; Scalmani, G.; Barone, V.; Mennucci, B.; Petersson, G. A.; Nakatsuji, H.; Caricato, M.; Li, X.; Hratchian, H. P.; Izmaylov, A. F.; Bloino, J.; Zheng, G.; Sonnenberg, J. L.; Hada, M.; Ehara, M.; Toyota, K.; Fukuda, R.; Hasegawa, J.; Ishida, M.; Nakajima, T.; Honda, Y.; Kitao, O.; Nakai, H.; Vreven, T.; Montgomery, Jr., J. A.; Peralta, J. E.; Ogliaro, F.; Bearpark, M.; Heyd, J. J.; Brothers, E.; Kudin, K. N.; Staroverov, V. N.; Kobayashi, R.; Normand, J.; Raghavachari, K.; Rendell, A.; Burant, J. C.; Iyengar, S. S.; Tomasi, J.; Cossi, M.; Rega, N.; Millam, N. J.; Klene, M.; Knox, J. E.; Cross, J. B.; Bakken, V.; Adamo, C.; Jaramillo, J.; Gomperts, R.; Stratmann, R. E.; Yazyev, O.; Austin, A. J.; Cammi, R.; Pomelli, C.; Ochterski, J. W.; Martin, R. L.; Morokuma, K.; Zakrzewski, V. G.; Voth, G. A.; Salvador, P.; Dannenberg, J. J.; Dapprich, S.; Daniels, A. D.; Farkas, Ö.; Foresman, J. B.; Ortiz, J. V.; Cioslowski, J.; Fox, D. J. Gaussian, Inc., Wallingford CT, 2013.

3. Supplementary Figures



Supplementary Figure S2-2| Cyclic voltammetry of DBOV **2-1** vs Fc/Fc⁺ (0.1 M *n*-Bu₄NPF₆ in dichloromethane solution), scan rate 50 mVs⁻¹.

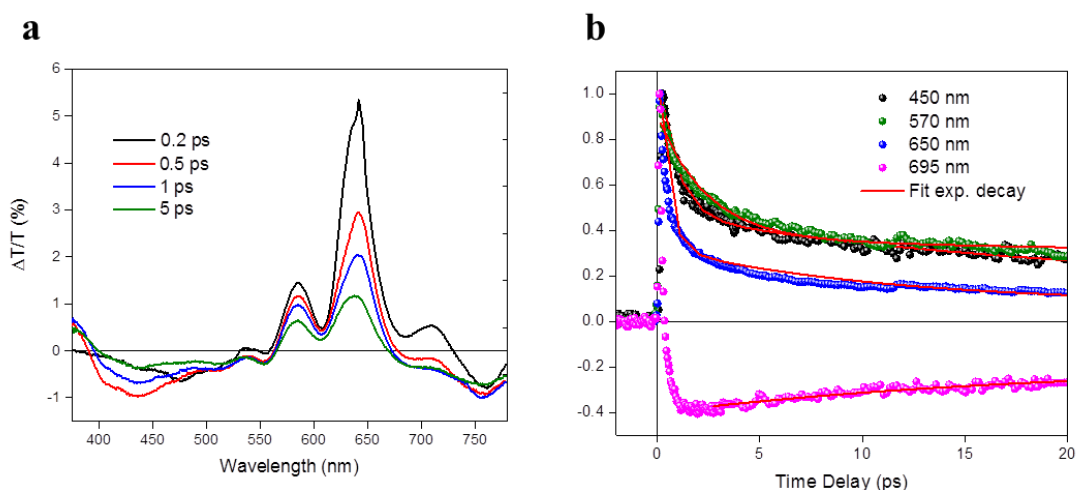
The transient spectra (a) and time-decay dynamics till 1 ns (b) of compound **2-1** in toluene are presented in figure S2-3. We can see that all the signals are relatively long-living (figure S2-3b), with time-constants $\tau_{430 \text{ nm}} = 432 \pm 35 \text{ ps}$, $\tau_{570 \text{ nm}} = 280 \pm 5 \text{ ps}$, $\tau_{650 \text{ nm}} = 302 \pm 5 \text{ ps}$ and $\tau_{695 \text{ nm}} = 292 \pm 7 \text{ ps}$. We can also observe a sharp rise of all the transient signals (c) and a linear dependence on pump fluence (d), which suggest that the photoexcitation mechanism is direct and does not involve any non-linear process.



Supplementary Figure S2-3| Transient spectra/dynamics of DBOV 2-1 in toluene solution. (a) Transient spectra of DBOV 2-1 in solution as a function of pump-probe delay time (0.05 mg/mL in toluene). **(b)** Dynamics at 450 nm, 570 nm, 630 nm and 695 nm probe wavelengths. **(c)** Rise time of the transient signals. **(d)** Signal intensities vs. Pump fluence.

Supplementary figure S2-4.

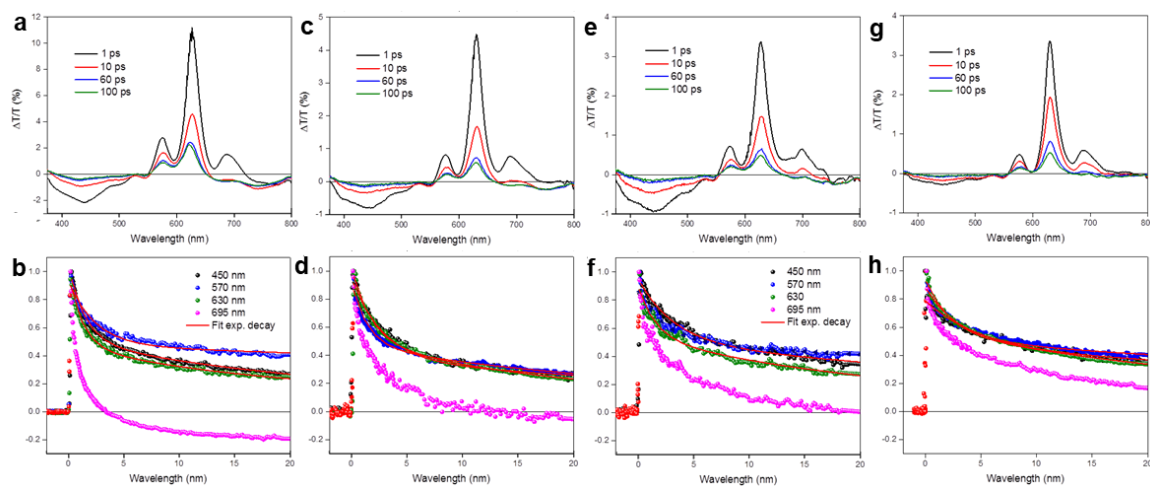
Here we report the transient spectra (a) and dynamics (b) of compound **2-1** in film. We can note a clear broadening of all the transient features and a step decrease of all the transient signal lifetimes. The calculated time-constants are: $\tau_{430 \text{ nm}} = 15.2 \pm 0.7 \text{ ps}$, $\tau_{570 \text{ nm}} = 12 \pm 6 \text{ ps}$, $\tau_{650 \text{ nm}} = 7.9 \pm 0.3 \text{ ps}$. The SE signal at 695 nm is completely overwhelmed in $\approx 200 \text{ fs}$ by a long-living PA signal.



Supplementary Figure S2-4| Transient spectra/dynamics of DBOV 2-1 in film. Transient spectra of DBOV 2-1 in film as a function of pump-probe delay time. **(b)** Dynamics at 450 nm, 570nm, 630 nm and 695 nm probe wavelengths.

Supplementary figure S2-5.

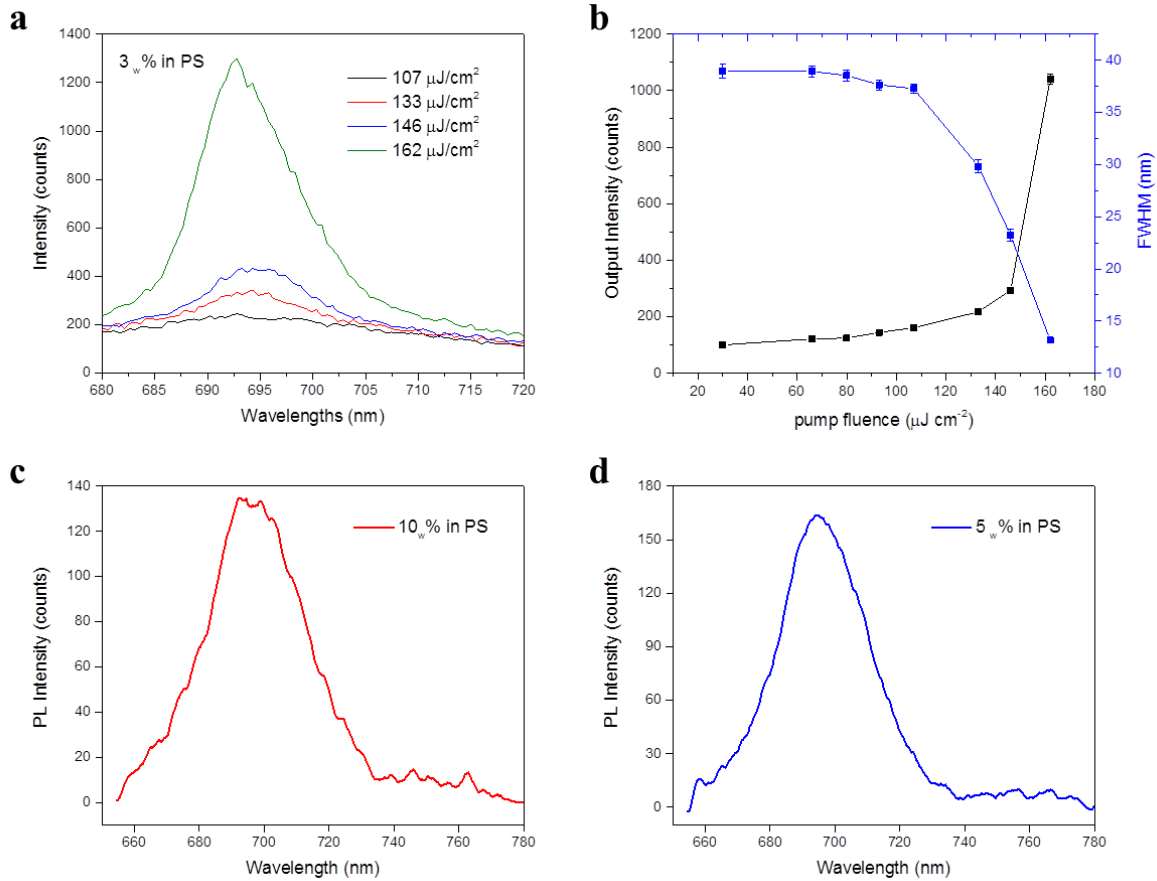
By blending the DBOV 2-1 with PS we note a general increase of life-times and a recover of the SE signal from the large PA. Interestingly, the DBOV 2-1 : PS 1 w% blend shows similar transient features with the ones observed in solution, with a relatively narrow PB peak and a suppressed PA signal.



Supplementary Figure S2-5: Transient spectra for **(a)** DBOV 2-1:PS 10_w%, **(c)** 5_w%, **(e)** 3_w %, **(g)** 1_w % blends. Normalised time-decay dynamics for **(b)** DBOV 2-1:PS 10_w%, **(d)** 5_w%, **(f)** 3_w %, **(h)** 1_w % blends.

Supplementary figure S2-6.

We also observed line narrowing for the DBOV **2-1**:PS 3 w% composite film, with a threshold lying at $\approx 150 \mu\text{W cm}^{-2}$ (figure S2-6a-b). For 5 w% and 10 w% blends, we were able to observe a recovery of the PL, which was completely suppressed in pure DBOV **2-1** films (c-d).



Supplementary Figure S2-6 (a) PL for different pump power from the DBOV **2-1**:PS 3 w% composite film and (b) input-output characteristics of ASE action for the 3 w% blend in PS. (c) PL from the the DBOV **2-1**:PS 10 w% and (d) PL from the DBOV **2-1**:PS 5 w%.

Chapter 3. Dibenzo[*hi,st*]ovalene as Highly Luminescent Nanographene: Efficient Synthesis *via* Photochemical Cyclodehydroiodination, Opto-electronic Properties and Single Molecule Spectroscopy

This Chapter is based on the following manuscript –

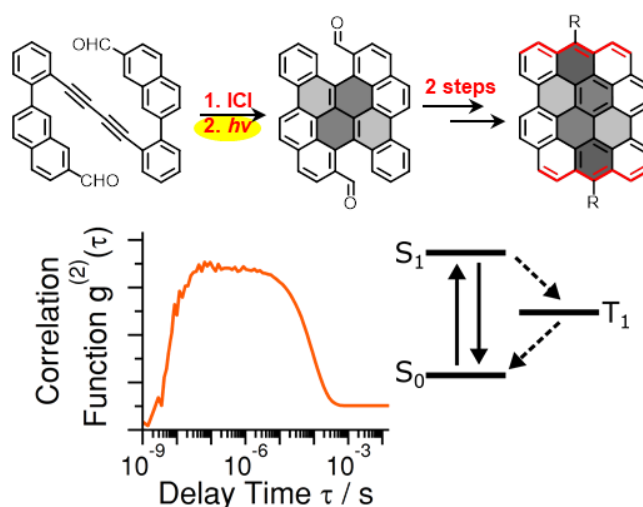
J. Am. Chem. Soc., **2019**, 141, 16439–16449

Qiang Chen[†], [REDACTED]

and [REDACTED]

Author contributions. Q. C. designed, synthesized and characterized the compounds investigated in this research under the supervision of [REDACTED] and [REDACTED]. [REDACTED] and [REDACTED] conducted single molecule spectroscopy measurements under the supervision of [REDACTED]. [REDACTED] was responsible for the single-crystal structure measurement. The manuscript was written through contributions of all authors.

TOC Figure



Dibenzo[*hi,st*]ovalene (DBOV), as a new nanographene, has demonstrated promising optical properties, such as red emission with a high fluorescence quantum yield of 79% and stimulated emission, as well as high thermal stability and photostability, which indicated its promise as a light-emitting and optical gain material. However, the previous synthetic routes required at least 12 steps. This obstructed access to different derivatives, e.g., to obtain crystals suitable for X-ray diffraction analysis and to tune the optoelectronic properties. Here, we report an efficient synthetic pathway to DBOV based on a sequential iodination-

benzannulation of bi(naphthylphenyl)diyne, followed by photochemical cyclodehydroiodination (PCDHI). This protocol included a fused bischrysene as a key intermediate and furnished scalable amounts of *meso*-substituted DBOV derivatives with different substituents. DBOV with 2,6-dimethylphenyl groups could be used for single-crystal X-ray analysis, revealing the precise structure of the DBOV core. The optoelectronic properties of the DBOV derivatives were investigated by UV-*vis* absorption and fluorescence spectroscopy, cyclic voltammetry, and density functional theory calculations. Single-molecule spectroscopy at room and low temperatures provided novel insights into the photophysics of DBOV embedded in a polymer film. As a result of weak coupling of the optical transitions to the matrix, single-molecule emission spectra at 4.5 K showed narrow vibronic lines. The fluorescence autocorrelation function covering 9 orders of magnitude in time displayed high contrast photon antibunching and bunching, from which the fluorescence decay rate and the triplet population and depopulation rates could be retrieved. Remarkably, the intersystem crossing rate into the triplet state decreased by more than an order of magnitude at low temperature, demonstrating that temperature can be a crucial parameter to boost single photon emission of an aromatic hydrocarbon.

Reprinted with permission from (*J. Am. Chem. Soc.*, **2019**, in press, DOI: 10.1021/jacs.9b08320). Copyright © 2019, ACS.

Introduction

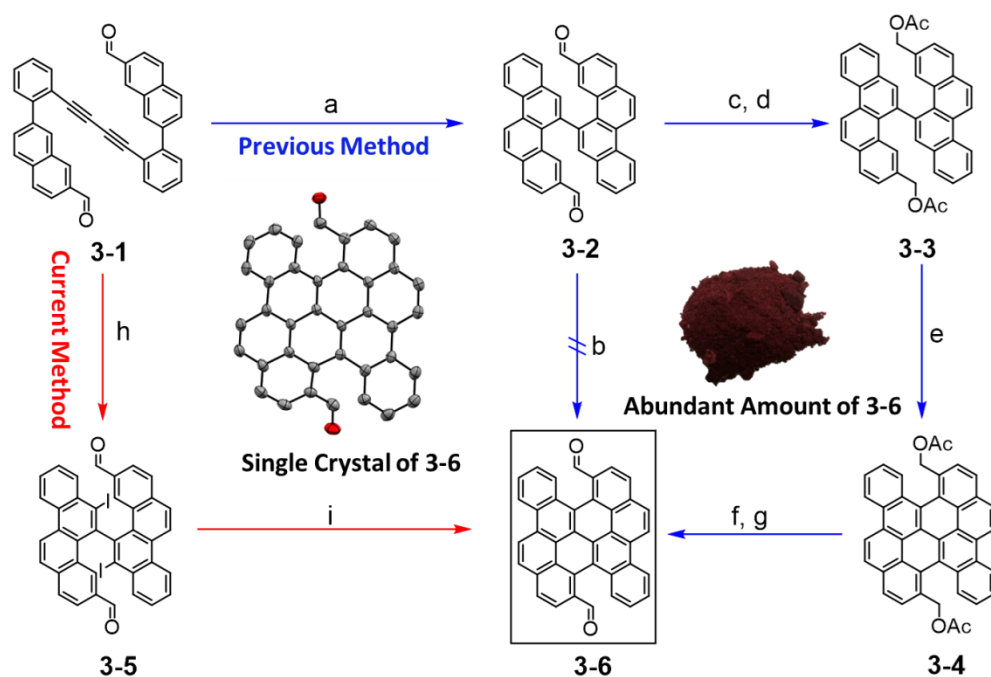
Structural confinement of graphene into nanoscale subunits, namely, nanographenes, such as graphene nanoribbons (GNRs) and graphene quantum dots (GQDs), can furnish discrete electronic energy levels with an open bandgap, thus allowing their applications in optoelectronic and photonic devices.¹⁻⁷ Compared with the top-down strategies, such as “cutting” of graphene⁸⁻¹³ and “unzipping” of carbon nanotubes,^{14, 15} which offer little structural control, sophisticated bottom-up synthesis can produce nanographenes with atomically precise and uniform structures.¹⁶⁻¹⁸ In recent years, numerous nanographenes have been synthesized in this way, among which nanographene molecules with zigzag edges, i.e., large polycyclic aromatic hydrocarbons (PAHs), such as periacenes¹⁹⁻²¹ and anthenes,^{22, 23} have attracted considerable attention for their unique properties, including small energy gaps, unique optical properties, and open-shell biradical character.^{24, 25} While nanographene molecules with zigzag edges are often kinetically unstable and subject to immediate oxidation,^{23, 26, 27} dibenzo[*hi,st*]ovalene (DBOV) has recently been reported as a highly inert nanographene molecule with a combination of both zigzag and armchair edges.²⁸ It exhibited strong red emission with a high absolute fluorescence quantum yield (Φ) of up to 79%. Moreover, stimulated emission and amplified spontaneous emission (ASE) could be demonstrated, highlighting the potential of DBOV for optoelectronic and photonic applications, such as in light-emitting diodes and lasers.²⁹ Nevertheless, the total yield of DBOV was only 2% after a 12-step synthesis.²⁹ This drawback severely hindered further studies into chemical derivatization, crystallization for single-crystal X-ray analysis, and fabrication of optoelectronic devices.

The synthesis of a great majority of nanographene molecules has been performed using the Scholl reaction, namely, intramolecular oxidative cyclodehydrogenation, of predesigned, branched oligoarylene precursors.³⁰⁻³² Whereas numerous nanographene molecules and GNRs could thus be achieved, this method entails significant drawbacks, including the use of excess oxidants, frequently unavoidable peripheral chlorination, rearrangements through aryl migration, low efficiency for electron-deficient systems, and limited scope of functional groups due to the required oxidative conditions.³³⁻³⁷ Alternative synthetic methods have been reported, such as acid-promoted cyclization of ethynyl derivatives^{38, 39} and metal-catalyzed^{40, 41} or photochemical cyclodehydrohalogenation of halogenated precursors.^{42, 43} Nevertheless, syntheses of nanographene molecules without Scholl reactions remain scarce.⁴⁴⁻⁴⁶

Herein, we report an efficient synthesis of DBOV through a sequence of iodination-benzannulation and photochemical cyclodehydroiodination (PCDHI) without using the Scholl reaction. In the previous synthetic route, to promote the Scholl reaction, we had to convert an electron-withdrawing aldehyde group into an electron-donating acetoxymethyl group (see Scheme 3-1) and then convert it back. This complication can be avoided in the new method, achieving the synthesis of different DBOV derivatives with alkyl (**DBOV-C12**), aryl (**DBOV-DMEP**, **DBOV-TMOP**, **DBOV-CF3**), and triisopropylsilyl (TIPS)-ethynyl (**DBOV-TIPS**) groups at the *meso*-positions in 7 steps, with total yields of 23–41% (see Scheme 2). DBOV with 2,6-dimethylphenyl units (**DBOV-DMEP**) provided crystals suitable for single-crystal X-ray analysis. The optical absorption and emission spectra could be fine-tuned by attaching electron-donating or electron-withdrawing aryl substituents, and a redshift of ~40 nm was achieved by introducing TIPS-ethynyl groups. While the absorption and emission spectra of DBOV have been well characterized, little is known about its intrinsic photophysical kinetics. Therefore, we conducted a comprehensive single-molecule study of immobilized **DBOV-DMEP** molecules at room and low temperatures. A crucial incentive for single-molecule spectroscopy relates to the fact that spectroscopic and photophysical properties can be retrieved, which are barely accessible from the ensemble average. Fluorescence spectra recorded at 4.5 K displayed sharp vibronic features dominated by a strong purely electronic zero-phonon line. The fluorescence intensity autocorrelation function covering 9 orders of magnitude in time showed high-contrast photon antibunching at short times and photon bunching due to shelving in the triplet state at long times. Quantitative analysis of the correlation function of single **DBOV-DMEP** molecules provided access to the lifetimes of the singlet (S1) and triplet (T1) states as well as the intersystem crossing rate from S1 to T1. Remarkably, by lowering the temperature, the intersystem crossing (ISC) rate decreased by a factor of ~ 10, while the triplet lifetime remained almost constant.

Results and Discussion

Photochemical cyclodehydroiodination (PCDHI)



Scheme 3-1. Synthesis of fused bischrysenyl **3-6** through a sequence of ICl -promoted iodination-benzannulation and PCDHI (red arrow) vs. the previous route²⁹ via the Scholl reaction (blue arrow). Reagents and conditions: a) PtCl_2 , toluene, $80\text{ }^\circ\text{C}$, 24 h, 45% yield; b) FeCl_3 , DCM, nitromethane, r.t.; or DDQ, triflic acid, DCM, r.t.; or $h\nu$, I_2 , benzene, 2 h; c) NaBH_4 , THF/methanol = 5:1, r.t., 1 h; d) Acetic anhydride, TEA, 4-DMAP, DCM, r.t., 2 h, 87% yield in two steps; e) DDQ, triflic acid, DCM, r.t., 33% yield; f) K_2CO_3 , THF/methanol = 1:1, r.t., overnight; g) PCC, DCM, r.t., 2 h, 59% yield in two steps; h) ICl , DCM, $-78\text{ }^\circ\text{C}$, 2 h, 76% yield; i) TEA, acetone, $h\nu$, 2 h, 86% yield. DCM: dichloromethane; DDQ: 2,3-dichloro-5,6-dicyano-1,4-benzoquinone; THF: tetrahydrofuran; TEA: triethylamine; 4-DMAP: 4-dimethylaminopyridine; PCC: pyridinium chlorochromate.

Bi(naphthylphenyl)diyne **3-1** was prepared by CuCl -catalyzed Glaser self-coupling of (2-ethynylphenyl)naphthalene in air.²⁹ Afterwards, iodination-benzannulation of **3-1** with ICl at $-78\text{ }^\circ\text{C}$ provided iodinated bichrysenyl **3-5** in 76% yield (Scheme 3-1). Transition-metal-catalyzed cyclization of **3-5** to fused product **3-6** was initially attempted by heating with $\text{Pd}(\text{PPh}_3)_2\text{Cl}_2 \cdot \text{CH}_2\text{Cl}_2$ in the presence of NaOAc at $140\text{ }^\circ\text{C}$ for 12 h,⁴⁰ which gave only deiodinated bichrysenyl **3-2**. $\text{Pd}(\text{PPh}_3)_4$ was next used as a catalyst and gave the same result. Further attempts to planarize **3-2** through the Scholl reaction (with FeCl_3 or DDQ/triflic acid) or photocyclodehydrogenation (I_2 , $h\nu$, benzene) also failed, most likely due to the electron-withdrawing nature of the aldehyde groups, consistent with our previous results.²⁸

Interestingly, we noticed that the color of diiodobichrysenyl precursor **3-5** on the thin-layer chromatography (TLC) plate gradually changed to red when the material was exposed to a handheld UV lamp, indicating the formation of a large π -conjugated system. This observation prompted us to explore the photochemical cyclodehydroiodination (PCDHI)⁴³ of **3-5** for the preparation of **3-6**.

Table 3-1. Effects of solvents and base on photocyclization from **3-5** to **3-6**^a

Entry	Solvent	Base	Yield ^b (%)
1	acetone	0.1 M Na ₂ CO ₃	73
2	toluene	0.1 M Na ₂ CO ₃	66
3	DCM	0.1 M Na ₂ CO ₃	60
4	acetone	TEA	86
5	acetone	No base	10

^aReaction conditions: Reactions were carried out in the indicated solvents with a concentration of 10⁻⁴ M under irradiation of UV light (300 nm, 224 W) for 2 h. ^bIsolated yield.

The photoreaction of **3-5** was initially tried with a concentration of 6 × 10⁻⁴ M in acetone and aqueous Na₂CO₃ solution (0.1 M, 1.0 equiv. per PCDHI reaction), which had previously been used as standard conditions for photocyclodehydrohalogenation.⁴² After irradiation with 16 UV lamps (300 nm, 14 W) for 2 h, product **3-6** precipitated from the reaction solution as a red solid in 73% yield. Toluene and dichloromethane were then tested as solvents, resulting in relatively low isolated yields of 66% and 60%, respectively (Table 3-1). Using acetone as the solvent, the effect of the base was next investigated, and triethylamine gave a higher isolated yield of 86%, presumably due to the formation of a homogeneous solution and its well-known electron-donating ability in photocyclization.⁴⁷ The resulting product **3-6** could be easily collected by filtration. When no base was added, product **3-6** further underwent acid-promoted intramolecular Friedel–Crafts cyclization to give a black insoluble diketone as a byproduct (see Figure S3-1). A single crystal of **3-6**, obtained by slow diffusion of acetonitrile into an *o*-dichlorobenzene solution, illustrates its twisted core geometry (see inset of Scheme 3-1, Figure S3-4).⁴⁸ By using the PCDHI reaction, key intermediate **3-6** could be prepared on the gram scale, thus affording larger amounts of DBOV with different substituents.

Syntheses and characterization of DBOV derivatives

upfield, as expected from π - π stacking. Some of the representative zigzag-edged nanographene molecules, such as periacenes and anthenes,^{22, 23} are expected to have smaller energy gaps with the potential to generate open-shell ground states with a contribution from thermally accessible triplet biradicals, which often hamper NMR measurements. However, variable-temperature ^1H NMR experiments of **DBOV-DMEP** in *o*-dichlorobenzene- d_4 showed no obvious signal broadening when increasing the temperature to 423 K (Figure S3-3). DFT calculations conducted at the B3LYP/6-31G(d,p) level of theory indicated that the closed-shell form of DBOV is energetically more stable than its open-shell forms, in agreement with the NMR results, accounting for its high stability under ambient conditions (see Table S3-1).

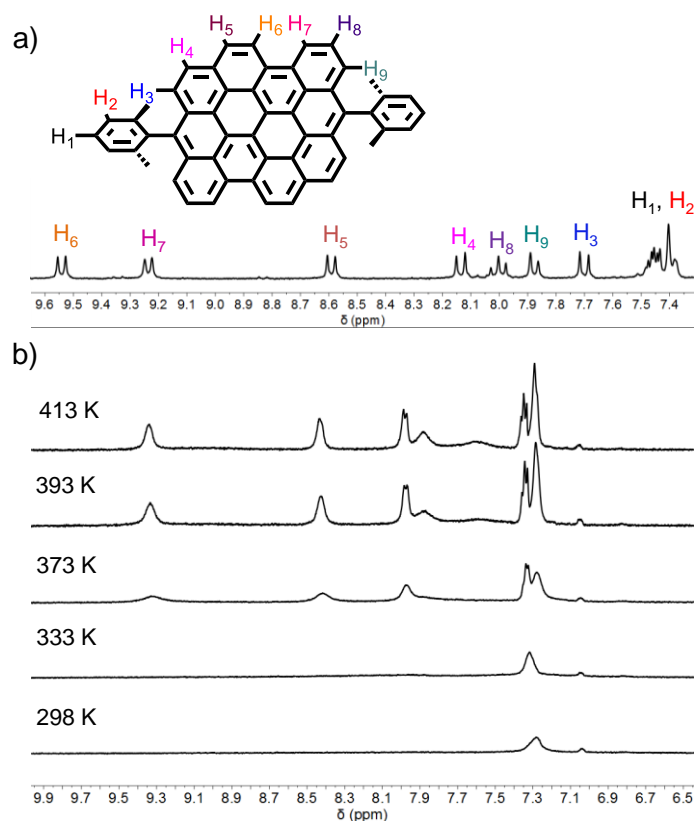


Figure 3-1. a) ^1H NMR spectrum of **DBOV-DMEP** in tetrahydrofuran- d_8 measured at room temperature (300 MHz); b) variable-temperature ^1H NMR spectra (500 MHz) of **DBOV-DMEP** measured in 1,1,2,2-tetrachloroethane- d_2 (4.4×10^{-3} M).

The structure of **DBOV-DMEP** was further characterized by X-ray diffraction analysis of crystals obtained by slow diffusion of methanol vapor into a tetrahydrofuran solution of **DBOV-DMEP** and measured at 193 K (Figure 3-2a). The **DBOV-DMEP** molecule adopts C_{2h} symmetry with a rigid, almost planar core with the two 2,6-dimethylphenyl groups nearly

perpendicular (dihedral angle $\sim 85^\circ$) as a result of the steric effect of the two methyl groups. The bond lengths are essentially uniform in rings A, D and F, while obvious alternations within a range of 0.05–0.30 Å occur in rings B, C and E (Figure 3-2b). In addition, the **DBOV-DMEP** molecules are staggered and exhibit a herringbone π -stacking motif in a layered structure. In the crystal, the face-to-face distance between two DBOV cores is 3.13 Å, which is shorter than the interlayer distance of graphite (3.35 Å). Close CH- π contact with a distance of 3.25 Å is also observed (see Figure S3-5). Such close packing and strong intermolecular π - π interactions are key features of high-performance, acene-based organic field-effect transistors (OFETs),^{49, 50} which suggests the potential of **DBOV-DMEP** for applications in electronic devices.

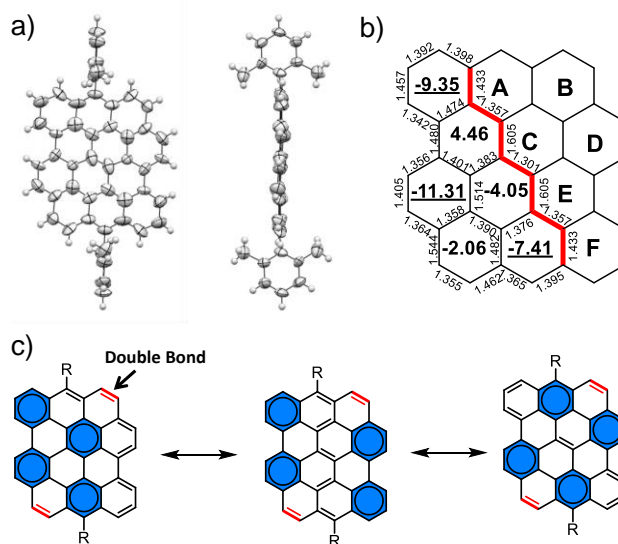


Figure 3-2. a) X-ray crystallographic structure of **DBOV-DMEP** (measured at 193 K): front view (left) and side view (right); b) bond lengths from single-crystal analysis and NICS (0) values of each ring calculated at the GIAO-B3LYP/6-31G(d,p) level of theory using the Gaussian 09 simulation package and c) three resonance structures of the DBOV core with four Clar's aromatic sextet benzene rings indicated with circles and blue background.

The local aromaticity of individual rings was evaluated by means of nucleus-independent chemical shift (NICS) values calculated at the GIAO-B3LYP/6-31G(d,p) level of theory using the Gaussian 09 simulation package (see supporting information for details).⁵¹ Rings A, D, and F showed negative NICS values of -7.41 , -11.31 and -9.35 , respectively, accounting for the experimentally observed chemical shifts of up to 9.6 ppm for protons on these three rings. On the other hand, rings B, C, and E exhibited larger values of -2.06 , -4.05 , and 4.46 , reflecting decreased aromaticity and antiaromaticity. Clar formulae could be drawn having

benzene rings localized on these rings with negative NICS values (Figure 3-2b). Three of the Clar structures containing four benzene sextets are shown in Figure 3-2c. All structures possess two isolated double bonds in ring B, which cannot be integrated into any benzene rings, explaining the observed upfield shifts of their proton signals (H₃ and H₄) (Figure 3-2a).

Photophysical and electrochemical properties

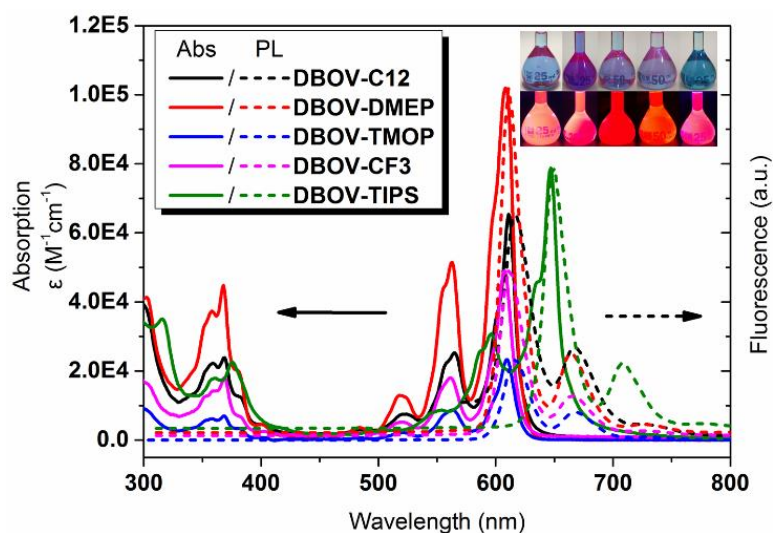


Figure 3-3. UV-*vis* absorption and fluorescence spectra of the DBOV derivatives measured in toluene solution at room temperature with a concentration of 10^{-5} M (inset shows photographs of these solutions (top row) and fluorescence under UV light (bottom row); from left to right: **DBOV-C12**, **DBOV-DMEP**, **DBOV-TMOP**, **DBOV-CF3** and **DBOV-TIPS**).

To understand the relationship between the peripheral substituents and the electronic structure of the DBOV core, their photophysical properties in solution were first investigated. Figure 3-3 illustrates the UV-*vis* absorption and fluorescence spectra of DBOV derivatives measured in toluene. These solutions showed well-resolved absorption bands between 450 and 700 nm with maximum absorption peaks at 611 nm (**DBOV-C12**, molar extinction coefficient $\epsilon = 6.54 \times 10^4 \text{ M}^{-1} \text{ cm}^{-1}$), 608 nm (**DBOV-DMEP**, $\epsilon = 1.02 \times 10^5 \text{ M}^{-1} \text{ cm}^{-1}$), 609 nm (**DBOV-TMOP**, $\epsilon = 2.33 \times 10^4 \text{ M}^{-1} \text{ cm}^{-1}$), 607 nm (**DBOV-TMOP**, $\epsilon = 4.90 \times 10^4 \text{ M}^{-1} \text{ cm}^{-1}$), and 647 nm (**DBOV-TIPS**, $\epsilon = 7.88 \times 10^4 \text{ M}^{-1} \text{ cm}^{-1}$), which can be attributed mainly to the HOMO-LUMO transitions based on time-dependent density functional theory (TD-DFT) calculations (see Figure S3-7 and Table S3-2). At shorter wavelengths, vibronic replica involving C-C-stretching vibrations appear.²⁸ The aryl substituents have a negligible influence on the UV-*vis* absorption of the DBOV core due to the large dihedral angles and thus limited π -conjugation. In contrast, the maximum absorption peak of **DBOV-TIPS** is redshifted by approximately 40

nm, indicating efficient π -conjugation between the DBOV core and ethynyl groups. The absorption spectra showed no change after storing the solutions under air for 1 month, indicating the high stability of the DBOV core, which is an essential requirement for the applications of these materials in electronic and optical devices.

All derivatives showed strong fluorescence with maximum emission peaks located at 617 nm (**DBOV-C12**), 611 nm (**DBOV-DMEP**), 617 nm (**DBOV-TTMOP**), 611 nm (**DBOV-CF3**), and 650 nm (**DBOV-TIPS**). The small Stokes shifts of only 3–8 nm indicate a rigid structure of the core and small structural changes between the ground states and excited states. The fluorescence quantum yields (see Table 3-2) were determined against a Nile blue A perchlorate standard by measuring dilute solutions ($A < 0.05$) with decreasing concentrations. DBOV with alkyl or aryl groups exhibit high fluorescence quantum yields of 0.79–0.89, while the comparatively low value of 0.67 observed for **DBOV-TIPS** is most likely due to the presence of the silylethynyl groups. The latter increase the vibronic coupling and enhance intersystem crossing.⁵² The optical gap of each derivative was estimated from the wavelength at which its absorption and fluorescence spectra cross each other, as listed in Table 3-2.

DFT calculations were performed to understand the effects of the substituents on the orbital energies. As shown in Table 3-2 and Figure S3-6, **DBOV-CF3** possesses HOMO and LUMO levels at -4.72 and -2.62 eV, respectively, which are lower than those of **DBOV-C12**, **DBOV-DMEP**, and **DBOV-TMOP**, which are at approximately -4.5 and -2.4 eV, respectively. **DBOV-TIPS** was calculated to have the lowest LUMO among the five DBOV derivatives, with an energy of -2.68 eV, leading to a smaller HOMO-LUMO gap of 1.90 eV compared to the gaps of approximately 2.1 eV of the other cases. This trend observed for the calculated HOMO-LUMO gaps agrees well with that of the experimental optical gaps. The electrochemical properties of these DBOV derivatives were investigated by cyclic voltammetry (CV) in dry dichloromethane solutions at room temperature. In the test window of the CV, reversible oxidation waves were observed (Figure S3-8). The HOMO energy levels were calculated from the onset potential of the first oxidation wave using the following equation: $\text{HOMO} = -(4.8 + E_{\text{ox}}^{\text{onset}})$, where the potentials were calibrated with Fc/Fc^+ . The electrochemical HOMO levels approximately agreed with the calculated values (Table 3-2).

Table 3-2. Optical and electrochemical properties of DBOV derivatives

Compound	λ_{\max} (nm)	λ_{em} (nm)	λ_{edge} (nm)	Φ	$E_g(\text{opt})$ (eV) ^a	$E_g(\text{cal})$ (eV) ^b	HOMO(c al) (eV) ^b	LUMO(ca l) (eV) ^b	HOMO(C V) (eV) ^c
DBOV-C12	611	617	621	0.79	2.02	2.10	-4.46	-2.37	-4.72
DBOV-DMEP	608	611	621	0.85	2.03	2.09	-4.52	-2.43	-4.80
DBOV-TMOP	609	617	623	0.86	2.02	2.10	-4.47	-2.37	-4.57
DBOV-CF3	607	611	622	0.89	2.03	2.10	-4.72	-2.62	-4.73
DBOV-TIPS	647	650	661	0.67	1.91	1.90	-4.58	-2.68	-4.71

^aOptical gaps were estimated based on the wavelength at which the normalized absorption and fluorescence spectra cross each other. ^bDFT calculations were performed at the B3LYP/6-31G (d,p) level of theory with the Gaussian 09 calculation package. ^cThe HOMO energy levels were calculated by using the onset of the first oxidation potential of CV calibrated with Fc/Fc⁺.

Single-molecule spectroscopy of DBOV-DMEP

Single-molecule spectroscopy at room and low temperatures (4.5 K) was conducted with **DBOV-DMEP** embedded at very low concentrations in thin Zeonex polymer films. Although aggregation is unlikely under these conditions ($c \sim 10^{-10}$ M in solution), we chose this derivative because the 2,6-dimethylphenyl groups would hinder the aggregation of the molecules. Benefiting from the large absorption cross-section and high fluorescence quantum yield of **DBOV-DMEP**, the single-molecule experiments provided deep insight into its photophysics, revealing many parameters previously unknown for DBOV.

Figure 3-4a displays the fluorescence emission spectra of two single **DBOV-DMEP** molecules (in Zeonex) measured at 296 K and 4.5 K. While the room-temperature spectrum closely resembles the bulk solution spectrum in toluene (see Figure 3-3), the spectrum at 4.5 K is characterized by a series of narrow vibronic transitions indicating weak linear electron-phonon coupling in the Zeonex host. The low-temperature spectrum clearly reveals that the broad bands observed at room temperature are composed of many vibronic transitions that are not resolved as a result of thermal broadening. The frequencies and relative intensities of the strongest vibrational transitions to the S_0 ground state determined from the low-temperature emission spectrum (Figure 3-4a, inset) are given in Table S3-3. As expected for a rigid planar PAH, the purely electronic zero-phonon line (ZPL) has by far the highest intensity reflected in the large Franck-Condon factor of 0.36. Since a normal mode analysis is not currently

available, we cannot assign the nature of the different vibrational modes. Qualitatively, literature data of other PAHs^{53, 54} suggest that frequencies in the range of 100 cm^{-1} to 650 cm^{-1} belong to totally symmetric modes involving movements of larger parts of the aromatic skeleton. In particular, we tentatively assume that the modes at $\sim 150\text{ cm}^{-1}$ are related to a long-axis breathing vibration of the whole molecule.

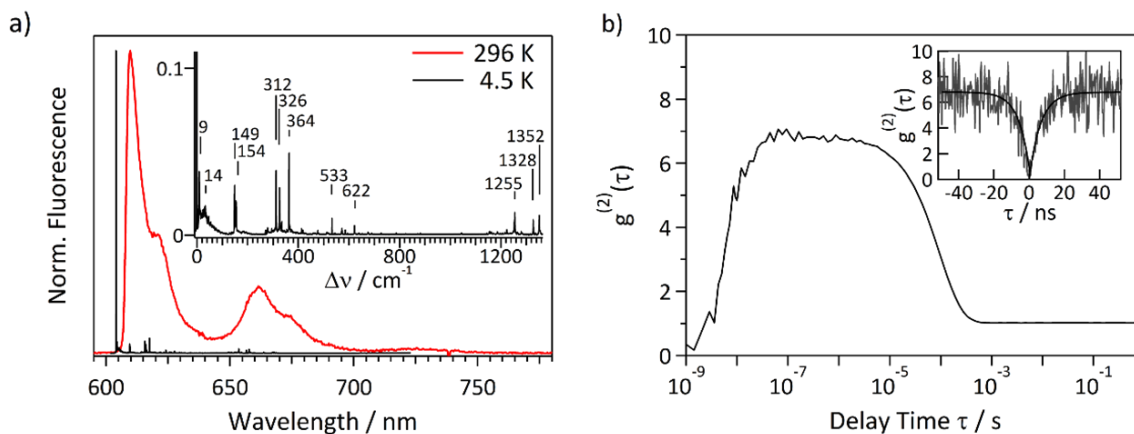


Figure 3-4. a) Fluorescence spectra of two single **DBOV-DMEP** molecules embedded in a Zeonex film at 296 K (red; $\lambda_{\text{exc}} = 561\text{ nm}$) and 4.5 K (black; $\lambda_{\text{exc}} = 565\text{ nm}$). The inset shows a magnified version of the high-resolution spectrum at 4.5 K with the vibronic transitions on an energy scale relative to the [0,0]-transition. b) Fluorescence intensity autocorrelation function $g^{(2)}(\tau)$ of a single **DBOV-DMEP** molecule over 9 orders of magnitude in time ($I_{\text{exc}} = 4\text{ kW/cm}^2$). The photon antibunching at short times is displayed in the inset on a linear time axis (also for negative delay times) together with a mono-exponential fit to the data ($T = 296\text{ K}$; $\lambda_{\text{exc}} = 561\text{ nm}$).

Since the temporal sequence of photons emitted by a single molecule constitutes a hallmark of its internal photophysical transitions, fluorescence correlation spectroscopy is an ideal tool to measure the rates of these transitions for immobilized single molecules.⁵⁵⁻⁵⁷ The fluorescence intensity autocorrelation function $g^{(2)}(\tau)$ of a single **DBOV-DMEP** molecule at room temperature covering 9 orders of magnitude in time is portrayed in Figure 3-4b. $g^{(2)}(\tau)$ displays the typical features expected in the photon statistics of a single organic dye molecule. At short times, the correlation function approaches zero, indicating single photon emission or photon antibunching,⁵⁸ while at longer times, the decay of the correlation function reveals photon bunching⁵⁵ caused by the sequence of bright and dark periods as a result of transitions between the singlet and triplet manifolds.

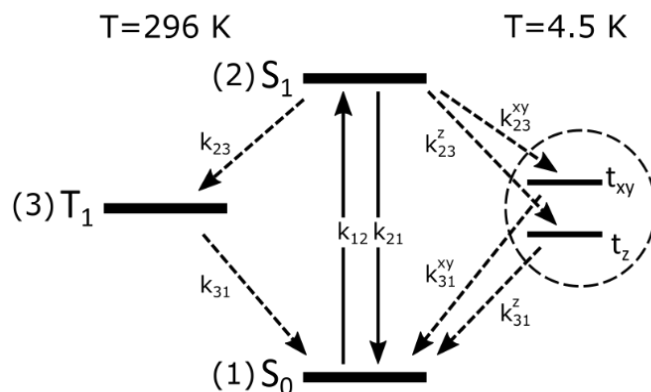


Figure 3-5. Simplified energy level scheme to highlight the relevant photophysical transitions in **DBOV-DMEP**. At 4.5 K, the zero-field splitting of the triplet is taken into account. The $t_{xy}-t_z$ - splitting is not to scale.

To analyze the room-temperature correlation data, we treat the **DBOV-DMEP** molecule as an effective three-level system (Figure 3-5) and follow the pertinent procedures described in the literature.^{55, 57, 59} Since we excite the molecule nonresonantly into a higher energy vibronic level of S_1 at elevated temperature, we need not consider any coherences but can describe the transitions between levels by a system of rate equations. First, we want to focus on the behavior of the correlation function at short times. In the inset of Figure 3-4b, this part is displayed on an enlarged scale also for negative delay times. Without taking into account background contributions,⁵⁵ which diminish the antibunching contrast, for the given intensity, $g^{(2)}(\tau)$ still approaches zero, i.e., $g^{(2)}(\tau=0) \approx 0$. This fact clearly demonstrates that even at room temperature, single **DBOV-DMEP** molecules appear to be high-contrast single photon emitters. When increasing the excitation intensity, the contrast grows, and the rise of the correlation function becomes steeper, as clearly seen in Figure S3-9, where $g^{(2)}(\tau)$ is given for different intensities. The rise of $g^{(2)}(\tau)$ at short times has been approximated by the following expression (see SI):

$$g^{(2)}(\tau) = A(1 - e^{-\lambda_a |\tau|}) + B \quad (\text{Equation 1})$$

$\lambda_a \approx k_{21} + k_{12}$ and k_{21} and k_{12} denote the fluorescence decay and excitation rates, respectively. From the intensity dependence of λ_a ($\lambda_a(I_{\text{exc}} \rightarrow 0) \approx k_{21}$), the fluorescence decay rate can be obtained.⁵⁷ The average k_{21} value of four **DBOV-DMEP** molecules is given in Table 3.

In the next step, the photon bunching part (μs – ms) of the room-temperature correlation data was analyzed to determine the ISC rate k_{23} and the triplet decay rate k_{31} . $g^{(2)}(\tau)$ data at long times were fitted for different excitation intensities by the following expression:

$$g^{(2)}(\tau) \cong C e^{-\lambda_b \tau} + 1 \quad (\text{Equation 2})$$

where C is the contrast and λ_b is the decay parameter of the correlation function. From the intensity dependence of C and λ_b , the rates k_{23} and k_{31} were determined by globally fitting the appropriate equations to the data (see SI). The average values of both rates for the same four molecules for which the fluorescence decay rate k_{21} was determined are given in Table 3-3.

Table 3-3. Transition rates of single **DBOV-DMEP** and terrylene molecules.

T / K	k_{21}/s^{-1}	k_{23}/s^{-1}	$k_{23}^{\text{xy}}/\text{s}^{-1}$ $k_{23}^{\text{z}}/\text{s}^{-1}$	k_{31}/s^{-1}	$k_{31}^{\text{xy}}/\text{s}^{-1}$ $k_{31}^{\text{z}}/\text{s}^{-1}$
<u>DBOV-DMEP in Zeonex</u>					
296	$1.5 \cdot 10^8$	$2.2 \cdot 10^5$	—	$2.2 \cdot 10^3$	—
4.5	—	—	$2.0 \cdot 10^4$ $1.6 \cdot 10^3$	—	$2.0 \cdot 10^3$ $4.4 \cdot 10^2$
<u>Terrylene in <i>p</i>-Terphenyl</u>					
300 ⁵⁶	—	$9.5 \cdot 10^5$	—	$6.9 \cdot 10^3$	—
1.4 ⁵⁹	—	—	$2.0 \cdot 10^3$ $4.0 \cdot 10^2$	—	$1.9 \cdot 10^3$ $8.0 \cdot 10^1$

k_{21} : fluorescence decay rate; k_{23} : intersystem crossing rate; k_{31} : triplet decay rate. **DBOV-DMEP**: 296 K (average of 4 molecules); 4.5 K (average of 13 molecules).

The experiments described above were conducted under an argon atmosphere. Preliminary experiments under air have indicated that both k_{23} and k_{31} increase, indicating a quenching of S_1 and T_1 by oxygen.⁶¹ Moreover, photobleaching becomes much more efficient, most likely caused by a reaction of the electron-rich PAH with singlet oxygen, which is formed via quenching of the triplet state T_1 .⁶²

$g^{(2)}(\tau)$ at long times was also measured for single **DBOV-DMEP** molecules at low temperature (4.5 K). Under these conditions, the correlation function could be well approximated by a biexponential decay (Figure 3-6a), as has been found in single-molecule studies of other PAHs, such as terrylene⁶³ and perylene⁶⁴. At low temperatures, the distributed kinetics of the triplet sublevels originating from the zero-field splitting of the triplet state emerge because spin-lattice relaxation is largely suppressed. Given the low symmetry of the molecule (C_{2h}), the splitting should result in three sublevels. As shown here by X-ray analysis of **DBOV-DMEP** crystals, the molecules adopt a nearly planar core. For planar PAHs – with the molecular plane as the sufficient symmetry element – it typically has been found that the out-of-plane sublevel (t_z) is characterized by smaller rates in and out of the triplet state compared to the two in-plane levels.⁶³⁻⁶⁸ The kinetics of the latter two are often similar and difficult to distinguish in the correlation decay. In the remainder of the text, we will treat the two in-plane levels as a single level t_{xy} , keeping in mind that the actual relation between the molecular x and y axes and the magnetic axes is not known for **DBOV-DMEP**. Accordingly, the biexponential decay of the correlation function reflects the population and depopulation kinetics of the triplet sublevels t_{xy} and t_z . The pertinent rates again have been determined from the intensity dependence of the corresponding contrasts C_i and decay parameters λ_i of the correlation function, following a procedure from the literature.⁶⁴ This analysis is different from the treatment of the room-temperature data as outlined in the SI. Moreover, to fit the intensity dependences of C_i and λ_i adequately, we had to introduce an additional intensity dependence of the triplet decay rates leading to apparent rates $K_{i31} = k_{i31} + \alpha_i I_{exc}$. We assume that the additional term results from triplet-triplet absorption, as has been proposed in other studies.^{57, 69} This process shows up in the low-temperature experiments because we had to use high laser intensities due to the very weak absorption of **DBOV-DMEP** at the excitation wavelength.

In Table 3-3, the average values of the various population and depopulation rates (k_{23}^{xy} , k_{23}^z , k_{31}^{xy} , k_{31}^z) at 4.5 K are listed. The ISC rates k_{23}^{xy} and k_{23}^z differ by a factor of 13, and the triplet decay rates k_{31}^{xy} and k_{31}^z differ by a factor of 5, supporting the distinction in terms of in-plane and out-of-plane sublevels.

To compare the room and low temperature rates, we refer to the values of the t_{xy} level for the latter, since those will dominate the kinetics at elevated temperatures. While k_{31} basically did not change between room and low temperature, k_{23} decreased on average by more than an

order of magnitude at 4.5 K. (At both temperatures, the molecules were studied under noble gas atmospheres.) This remarkable change in the ISC rate is nicely visualized in Figure 3-6b, where the fluorescence intensity as a function of time is displayed for two **DBOV-DMEP** molecules at the two temperatures. For these particular molecules, which were studied at comparable excitation rates to minimize the effects caused by the intensity dependence of k_{23} , the ISC rates differed by a factor of 30. At room temperature, only very short bright intervals are visible because the molecule quickly crosses from the singlet state S_1 into the triplet state T_1 , and no emission occurs. In contrast, much longer bright periods are observed at low temperature, where the probability for ISC is substantially reduced. In other words, the number of single photons emitted before the molecule crosses into the triplet state is significantly enhanced. Obviously, for an ideal single photon emitter, ISC should be absent. We note that the rates k_{31} can be directly extracted from such traces, since the lengths of the dark intervals are directly related to the T_1 lifetime.⁶⁰

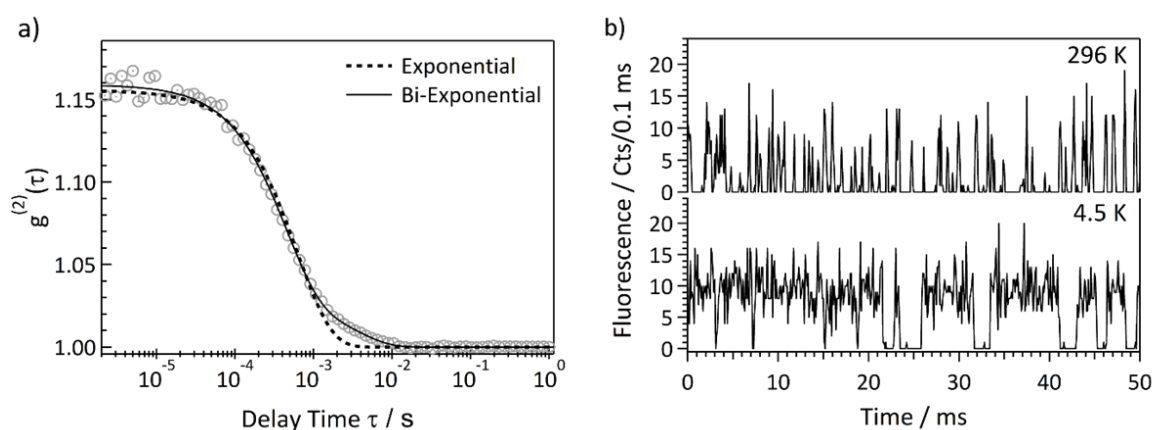


Figure 3-6. (a) Fluorescence intensity autocorrelation function $g^{(2)}(\tau)$ of a single **DBOV-DMEP** molecule at long times ($I_{\text{exc}} = 42 \text{ kW/cm}^2$, $T = 4.5 \text{ K}$). Mono-exponential (dashed line) and biexponential (drawn line) fits to the data are also shown. b) Fluorescence counts as a function of time for two **DBOV-DMEP** molecules at the given temperatures. The different appearances of the two traces reflect the temperature dependence of the ISC rate k_{23} .

The temperature dependence of S_1 - T_1 ISC has been studied for several PAHs, particularly linear polyacenes such as naphthalene and anthracene.^{66, 70-72} In general, ISC will be temperature dependent if higher vibrational levels v of S_1 ($S_{1,v}$) have a different mechanism for the nonradiative transition to T_1 than the vibrationally relaxed $S_{1,0}$ level. In most cases, the temperature dependence of the ISC rate has been expressed as a thermally activated process, by which a higher triplet state T_n ($n > 1$) is populated at elevated temperatures. Typically, such studies have been based on the measurement of the changes in the fluorescence quantum

yield or intensity with temperature. We note that such an approach is feasible only when the ISC rate can compete with the radiative decay rate of S_1 , which is obviously not the case for **DBOV-DMEP**. For anthracene crystals, it was found that in the range of 140–430 K, the temperature dependence of ISC follows a thermally activated process with an activation energy of 800 cm^{-1} .⁷⁰ Studies of brominated anthracenes in 3-methylpentane over a comparable temperature range gave similar activation energies.⁷² For pentacene/*p*-terphenyl mixed crystals, the temperature dependence of the pentacene ISC rate between 4.2 K and 140 K was attributed to a vibronically induced process due to a low-frequency ($\sim 30\text{ cm}^{-1}$) out-of-plane vibrational mode of pentacene.⁷¹ Although the details of the coupling mechanism between S_1 and T_1 can be quite involved and diverse,⁶⁶ owing to the varying contributions of, e.g., direct and vibronically induced spin-orbit coupling for different species, the common conclusion for the few systems studied appears to be that the thermal population of higher vibrational levels of S_1 lowers the energy gap to higher triplet states T_n ($n > 1$), thereby increasing the ISC rate.

To date, most of the single-molecule studies in which the ISC and triplet decay rates have been determined for a particular dye molecule were performed either at low temperature or at room temperature by employing the correlation method.^{55, 73-75} (A compilation of mainly low-temperature data can be found in the literature.⁶⁴) To our knowledge, only the mixed crystalline system terrylene/*p*-terphenyl has been investigated at room temperature and at 1.4 K, but these experiments have been performed in different laboratories.^{57, 63} The k_{23} and k_{31} values for single terrylene molecules at different temperatures are given in Table 3-3. In this case, the k_{23} value decreases by more than two orders of magnitude at low temperature, while the triplet lifetime changes only slightly. Unfortunately, for this system, a comparison is also complicated by the fact that the *p*-terphenyl crystal undergoes an order/disorder phase-transition at $\sim 190\text{ K}$ and the relation between molecules from the four low-temperature sites⁶³ and the molecules in the crystal under ambient conditions is not clear. Nevertheless, the same trend as observed for the ovalene is noticed for terrylene.

Since the measurements of **DBOV-DMEP** were performed at only two temperatures, the functional form of the temperature dependence of k_{23} could not be established. As discussed above, the increased ISC rate at room temperature could be caused by the thermal population of vibrational modes of S_1 . In addition to an activated process, a static distortion of the molecule could lead to increased ISC rates because in a nonplanar geometry of the ovalene core, spin-orbit coupling might be enhanced due to σ - π interactions.^{74, 76, 77} However, **DBOV-**

DMEP is a relatively rigid structure and was observed to be planar in the crystal. In addition, it is not obvious why a change in temperature should affect the degree of static distortion in the rigid Zeonex host. Although we cannot completely rule out a distortion of the molecules as the origin of the increased ISC rate at room temperature, we feel that the description by an activated process, which has been reported for several PAHs, is more appealing. To shed more light on this issue, it would be most helpful to measure the ISC rate over the whole temperature range from 4.5 K to 296 K for a given single molecule. Such an experiment, however, is challenging due to the enhanced photobleaching probability at elevated temperatures.

Conclusion and Outlook

In summary, we have achieved efficient syntheses of a series of DBOV derivatives with different *meso*-substituents by using a photochemical cyclodehydroiodination reaction (PCDHI) as the key step. The number of synthesis steps could be reduced from 12 to 7, and the total yield was improved from approximately 2% up to approximately 40%, which enabled scalable syntheses of different DBOV derivatives. 2,6-Dimethylphenyl groups as the substituents allowed for the unambiguous single-crystal X-ray analysis, revealing the planar structure of the DBOV core. Relatively uniform bond lengths observed in rings A, D, and F indicated the localization of aromatic sextets in these benzene rings, in accordance with the results derived from ^1H NMR experiments and NICS calculations. UV-*vis* absorption measurements showed that the aliphatic and aromatic substituents had minor effects on the electronic properties of the DBOV core, while a redshift of the optical absorption by approximately 40 nm could be achieved through the introduction of the TIPS-ethynyl group. Strong red fluorescence was observed for all DBOVs in toluene solutions, with a high relative fluorescence quantum yield of up to 0.89, showing the promise of these molecules in applications as light-emitting materials.

Our comprehensive single-molecule spectroscopy study of **DBOV-DMEP** at room and low temperatures has provided novel insights into the photophysics of this ovalene derivative. By analyzing the fluorescence correlation function at long times, the triplet kinetics could be assessed. While the triplet decay rate basically did not change between room and low temperature, the ISC rate decreased by more than an order of magnitude at low temperature. Based on a comparison to literature data, we concluded that the increase in the ISC rate at room temperature results from the thermal population of higher vibrational levels of S_1 , which decreases the energy gap to higher-lying triplet states T_n ($n > 1$) and accelerates the ISC. The

observation of high-contrast photon antibunching combined with a high fluorescence yield and photostability as well as the presence of intense ZPLs at low temperature qualify **DBOV-DMEP** as a promising single quantum emitter, which is ideally suited for high-resolution, frequency-resolved single-molecule spectroscopy. While lowering the temperature typically is considered advantageous mainly because of the appearance of sharp ZPLs and the increased photostability of single molecules, our results imply that low temperatures can also improve the intrinsic dynamics of a single photon emitter.

The current results thus provide not only a reliable synthetic route to obtain large amounts of various DBOV derivatives but also deeper insights into its structural, optoelectronic, and photophysical properties. These findings lay the foundation for the further development of DBOV as a promising luminescent nanographene material. Studies on further derivatizations of DBOV and the reactivity of its peripheral positions as well as applications in optoelectronic devices are ongoing. With respect to the photophysics of nanographenes, it would be most valuable to disclose how the actual rate constants depend on the chemical structure and energy level scheme of a particular compound. Along these lines, it will be interesting to study photophysical changes occurring from bisanthene to the parent ovalene, whereby a structure with armchair edges develops into a structure with zigzag edges only.

Experimental

Lightly doped polymer films for the single molecule measurements were prepared by spin-coating a toluene solution of **DBOV-DMEP** and the polymer (Nippon Zeon K.K., Zeonex ® 330R, 20 g/L) at 4000 rpm onto glass substrates. The concentration of the dye in the solution was $\sim 10^{-10}$ M. For the room temperature measurements borosilicate glass substrates were used, while at 4.5 K fused silica was employed. All substrates were cleaned following standard procedures.

Single molecule measurements at room temperature were done using a home-built confocal setup. Briefly, the output of a fiber coupled cw solid state laser (Toptica iChrome CLE, 561 nm) was collimated and focused onto the sample plane by an oil-immersion objective (Zeiss, Plan-Apochromat 100x/1.41), after having passed a 565 nm band-pass filter and being reflected off a beam splitter (80T:20R). Residual excitation light in the detection path was blocked by a 594 nm long-pass filter before the fluorescence light was divided by a beam splitter (50T:50R). One-half was split again (50T:50R) and detected by two APDs in a Hanbury-Brown Twiss configuration to circumvent detector dead times. The other half was

dispersed by a spectrograph (Acton Spectra Pro 300i, resolution: $\sim 25 \text{ cm}^{-1}$) and detected with a CCD camera (Andor, Newton EM-CCD).

Measurements at 4.5 K were performed with a customized variable temperature confocal microscope (attocube, CFM1). The excitation light from a cw solid-state laser (Coherent Sapphire, 568 nm) first was guided through a single-mode fiber for spatial filtering. After collimation, the beam passed a 565 nm band-pass filter and was reflected by a beam splitter (80T:20R) into the back aperture of a low-temperature objective (attocube, LT-APO/VISIR, NA = 0.82), mounted in the cryostat. The fluorescence, collected by the same objective, was cleaned up by a 594 nm long-pass filter after passing the exit window of the cryostat and guided through a multimode fiber (NA: 0.1). The fluorescence light emerging from the fiber was collimated and directed to a beam splitter (50T:50R). The transmitted light was focused onto an APD, while the reflected light was focused onto the entrance slit of a spectrograph (Andor, Spectra Pro HRS-750-B1-R, resolution: $\sim 1 \text{ cm}^{-1}$ in high-resolution mode) equipped with a CCD camera (Andor, Newton EM-CCD).

In both setups the photon counts of the APDs were fed into a TCSPC module (PicoQuant, PicoHarp 300, Time-Tagged Time-Resolved (TTTR) mode). Fluorescence intensity autocorrelation functions were calculated from the time delays between the photon arrival times

ASSOCIATED CONTENT

Supporting Information

Further experimental details, single-crystal data for **3-6** and **DBOV-DMEP**, NMR, MS, IR, UV-*vis* absorption and fluorescence spectra, cyclic voltammetry, calculation details, single molecule data and analysis.

This material is available free of charge via the Internet at <http://pubs.acs.org>.

AUTHOR INFORMATION

Corresponding Author

*thomas.basche@uni-mainz.de

*muellen@mpip-mainz.mpg.de

*narita@mpip-mainz.mpg.de

Author Contributions

#Q. C. and S. T. contributed equally to this work. The manuscript was written through contributions of all authors.

Notes

Qiang Chen, Klaus Müllen, and Akimitsu Narita are listed as inventors on patent applications (application no. 18199451.8 - EPO and application no. 18199447.6 - EPO) related to the work presented in this manuscript. All other authors have nothing to disclose.

ACKNOWLEDGMENT

This work was financially supported by Max Planck Society and the European Union's Horizon 2020 research and innovation programme under Marie-Curie ITN project "iSwitch" (GA No.642196).

REFERENCES

- (1) Son, Y. W.; Cohen, M. L.; Louie, S. G. Half-metallic graphene nanoribbons. *Nature* **2006**, *444* (7117), 347-349.
- (2) Trauzettel, B.; Bulaev, D. V.; Loss, D.; Burkard, G. Spin qubits in graphene quantum dots. *Nat Phys.* **2007**, *3* (3), 192-196.
- (3) Nakada, K.; Fujita, M.; Dresselhaus, G.; Dresselhaus, M. S. Edge state in graphene ribbons: Nanometer size effect and edge shape dependence. *Phys. Rev. B* **1996**, *54* (24), 17954-17961.
- (4) Son, Y. W.; Cohen, M. L.; Louie, S. G. Energy gaps in graphene nanoribbons. *Phys. Rev. Lett.* **2006**, *97* (21), 216803.
- (5) Hod, O.; Barone, V.; Scuseria, G. E. Half-metallic graphene nanodots: A comprehensive first-principles theoretical study. *Phys. Rev. B* **2008**, *77* (3), 035411.
- (6) Barone, V.; Hod, O.; Scuseria, G. E. Electronic structure and stability of semiconducting graphene nanoribbons. *Nano Lett.* **2006**, *6* (12), 2748-2754.
- (7) Döhnert, D.; Koutecky, J. Occupation numbers of natural orbitals as a criterion for biradical character. Different kinds of biradicals. *J. Am. Chem. Soc.* **1980**, *102* (6), 1789-1796.
- (8) Li, X.; Wang, X.; Zhang, L.; Lee, S.; Dai, H. Chemically derived, ultrasmooth graphene nanoribbon semiconductors. *Science* **2008**, *319* (5867), 1229-1232.

- (9) Jeon, S.-C.; Kim, Y.-S.; Lee, D.-K. Fabrication of a Graphene Nanoribbon with Electron Beam Lithography Using a XR-1541/PMMA Lift-Off Process. *Trans. Electr. Electron. Mater.* **2010**, *11* (4), 190-193.
- (10) Lemme, M. C.; Bell, D. C.; Williams, J. R.; Stern, L. A.; Baugher, B. W.; Jarillo-Herrero, P.; Marcus, C. M. Etching of graphene devices with a helium ion beam. *ACS Nano* **2009**, *3* (9), 2674-2676.
- (11) Ruffieux, P.; Cai, J.; Plumb, N. C.; Patthey, L.; Prezzi, D.; Ferretti, A.; Molinari, E.; Feng, X.; Müllen, K.; Pignedoli, C. A.; Fasel, R. Electronic structure of atomically precise graphene nanoribbons. *ACS Nano* **2012**, *6* (8), 6930-6935.
- (12) Tapaszto, L.; Dobrik, G.; Lambin, P.; Biro, L. P. Tailoring the atomic structure of graphene nanoribbons by scanning tunnelling microscope lithography. *Nat. Nanotechnol.* **2008**, *3* (7), 397-401.
- (13) Bai, J.; Duan, X.; Huang, Y. Rational fabrication of graphene nanoribbons using a nanowire etch mask. *Nano Lett.* **2009**, *9* (5), 2083-2087.
- (14) Kosynkin, D. V.; Higginbotham, A. L.; Sinitskii, A.; Lomeda, J. R.; Dimiev, A.; Price, B. K.; Tour, J. M. Longitudinal unzipping of carbon nanotubes to form graphene nanoribbons. *Nature* **2009**, *458* (7240), 872-876.
- (15) Jiao, L.; Zhang, L.; Wang, X.; Diankov, G.; Dai, H. Narrow graphene nanoribbons from carbon nanotubes. *Nature* **2009**, *458* (7240), 877-880.
- (16) Narita, A.; Wang, X. Y.; Feng, X.; Müllen, K. New advances in nanographene chemistry. *Chem. Soc. Rev.* **2015**, *44* (18), 6616-6643.
- (17) Chen, L.; Hernandez, Y.; Feng, X.; Müllen, K. From nanographene and graphene nanoribbons to graphene sheets: chemical synthesis. *Angew. Chem. Int. Ed.* **2012**, *51* (31), 7640-7654.
- (18) Wang, X.-Y.; Narita, A.; Müllen, K. Precision synthesis versus bulk-scale fabrication of graphenes. *Nat. Rev. Chem.* **2017**, *2* (1), 0100.
- (19) Li, J.; Zhang, K.; Zhang, X.; Huang, K. W.; Chi, C.; Wu, J. meso-Substituted bisanthenes as soluble and stable near-infrared dyes. *J. Org. Chem.* **2010**, *75* (3), 856-863.
- (20) Ni, Y.; Gopalakrishna, T. Y.; Phan, H.; Herng, T. S.; Wu, S.; Han, Y.; Ding, J.; Wu, J. A Peri-tetracene Diradicaloid: Synthesis and Properties. *Angew. Chem. Int. Ed.* **2018**, *57* (31), 9697-9701.
- (21) Ajayakumar, M. R.; Fu, Y.; Ma, J.; Hennersdorf, F.; Komber, H.; Weigand, J. J.; Alfonsov, A.; Popov, A. A.; Berger, R.; Liu, J.; Müllen, K.; Feng, X. Toward Full Zigzag-

Edged Nanographenes: peri-Tetracene and Its Corresponding Circumanthracene. *J. Am. Chem. Soc.* **2018**, *140* (20), 6240-6244.

(22) Konishi, A.; Hirao, Y.; Nakano, M.; Shimizu, A.; Botek, E.; Champagne, B.; Shiomi, D.; Sato, K.; Takui, T.; Matsumoto, K.; Kurata, H.; Kubo, T. Synthesis and characterization of teranthene: a singlet biradical polycyclic aromatic hydrocarbon having Kekule structures. *J. Am. Chem. Soc.* **2010**, *132* (32), 11021-11023.

(23) Konishi, A.; Hirao, Y.; Matsumoto, K.; Kurata, H.; Kishi, R.; Shigeta, Y.; Nakano, M.; Tokunaga, K.; Kamada, K.; Kubo, T. Synthesis and characterization of quarteranthene: elucidating the characteristics of the edge state of graphene nanoribbons at the molecular level. *J. Am. Chem. Soc.* **2013**, *135* (4), 1430-1437.

(24) Sun, Z.; Zeng, Z.; Wu, J. Benzenoid polycyclic hydrocarbons with an open-shell biradical ground state. *Chem. Asian J.* **2013**, *8* (12), 2894-2904.

(25) Sun, Z.; Ye, Q.; Chi, C.; Wu, J. Low band gap polycyclic hydrocarbons: from closed-shell near infrared dyes and semiconductors to open-shell radicals. *Chem. Soc. Rev.* **2012**, *41* (23), 7857-7889.

(26) Liu, J.; Ravat, P.; Wagner, M.; Baumgarten, M.; Feng, X.; Müllen, K. Tetrabenz[a,f,j,o]perylene: a polycyclic aromatic hydrocarbon with an open-shell singlet biradical ground state. *Angew. Chem. Int. Ed.* **2015**, *54* (42), 12442-12446.

(27) Arabei, S. M.; Pavich, T. A. Spectral-luminescent properties and photoinduced transformations of bisanthene and bisanthenequinone. *J. Appl. Spectrosc.* **2000**, *67* (2), 236-244.

(28) Paterno, G. M.; Chen, Q.; Wang, X. Y.; Liu, J.; Motti, S. G.; Petrozza, A.; Feng, X.; Lanzani, G.; Müllen, K.; Narita, A.; Scotognella, F. Synthesis of Dibenzo[hi,st]ovalene and Its Amplified Spontaneous Emission in a Polystyrene Matrix. *Angew. Chem. Int. Ed.* **2017**, *56* (24), 6753-6757.

(29) Coles, D. M.; Chen, Q.; Flatten, L. C.; Smith, J. M.; Müllen, K.; Narita, A.; Lidzey, D. G. Strong Exciton-Photon Coupling in a Nanographene Filled Microcavity. *Nano Lett.* **2017**, *17* (9), 5521-5525.

(30) Stabel, A.; Herwig, P.; Müllen, K.; Rabe, J. P. Diodelike Current–Voltage Curves for a Single Molecule–Tunneling Spectroscopy with Submolecular Resolution of an Alkylated,peri-Condensed Hexabenzocoronene. *Angew. Chem. Int. Ed.* **1995**, *34* (15), 1609-1611.

(31) Iyer, V. S.; Wehmeier, M.; Brand, J. D.; Keegstra, M. A.; Müllen, K. From Hexa-peri-hexabenzocoronene to “Superacenes”. *Angew. Chem. Int. Ed.* **1997**, *36* (15), 1604-1607.

- (32) Watson, M. D.; Fechtenkötter, A.; Müllen, K. Big Is Beautiful—“Aromaticity” Revisited from the Viewpoint of Macromolecular and Supramolecular Benzene Chemistry. *Chem. Rev.* **2001**, *101* (5), 1267-1300.
- (33) King, B. T.; Kroulik, J.; Robertson, C. R.; Rempala, P.; Hilton, C. L.; Korinek, J. D.; Gortari, L. M. Controlling the Scholl reaction. *J. Org. Chem.* **2007**, *72* (7), 2279-2288.
- (34) Liu, J.; Narita, A.; Osella, S.; Zhang, W.; Schollmeyer, D.; Beljonne, D.; Feng, X.; Müllen, K. Unexpected Scholl Reaction of 6,7,13,14-Tetraarylbenzo[k]tetraphene: Selective Formation of Five-Membered Rings in Polycyclic Aromatic Hydrocarbons. *J. Am. Chem. Soc.* **2016**, *138* (8), 2602-2608.
- (35) Wadumethrige, S. H.; Rathore, R. A facile synthesis of elusive alkoxy-substituted hexa-peri-hexabenzocoronene. *Org. Lett.* **2008**, *10* (22), 5139-5142.
- (36) Ormsby, J. L.; Black, T. D.; Hilton, C. L.; Bharat; King, B. T. Rearrangements in the Scholl oxidation: implications for molecular architectures. *Tetrahedron* **2008**, *64* (50), 11370-11378.
- (37) Graczyk, A.; Murphy, F. A.; Nolan, D.; Fernandez-Moreira, V.; Lundin, N. J.; Fitchett, C. M.; Draper, S. M. Terpyridine-fused polyaromatic hydrocarbons generated via cyclodehydrogenation and used as ligands in Ru(II) complexes. *Dalton. Trans.* **2012**, *41* (25), 7746-7754.
- (38) Yang, W.; Lucotti, A.; Tommasini, M.; Chalifoux, W. A. Bottom-Up Synthesis of Soluble and Narrow Graphene Nanoribbons Using Alkyne Benzannulations. *J. Am. Chem. Soc.* **2016**, *138* (29), 9137-9144.
- (39) Yang, W.; Longhi, G.; Abbate, S.; Lucotti, A.; Tommasini, M.; Villani, C.; Catalano, V. J.; Lykhin, A. O.; Varganov, S. A.; Chalifoux, W. A. Chiral Peropyrene: Synthesis, Structure, and Properties. *J. Am. Chem. Soc.* **2017**, *139* (37), 13102-13109.
- (40) Li, C. W.; Wang, C. I.; Liao, H. Y.; Chaudhuri, R.; Liu, R. S. Synthesis of dibenzo[g,p]chrysenes from bis(biaryl)acetylenes via sequential ICl-induced cyclization and Mizoroki-Heck coupling. *J. Org. Chem.* **2007**, *72* (24), 9203-9207.
- (41) Zhu, C.; Wang, D.; Wang, D.; Zhao, Y.; Sun, W. Y.; Shi, Z. Bottom-up Construction of pi-Extended Arenes by a Palladium-Catalyzed Annulative Dimerization of o-Iodobiaryl Compounds. *Angew. Chem. Int. Ed.* **2018**, *57* (29), 8848-8853.
- (42) Daigle, M.; Picard-Lafond, A.; Soligo, E.; Morin, J. F. Regioselective Synthesis of Nanographenes by Photochemical Cyclodehydrochlorination. *Angew. Chem. Int. Ed.* **2016**, *55* (6), 2042-2047.

- (43) Mohamed, R. K.; Mondal, S.; Guerrero, J. V.; Eaton, T. M.; Albrecht-Schmitt, T. E.; Shatruck, M.; Alabugin, I. V. Alkynes as Linchpins for the Additive Annulation of Biphenyls: Convergent Construction of Functionalized Fused Helicenes. *Angew. Chem. Int. Ed.* **2016**, *55* (39), 12054-12058.
- (44) Pun, S. H.; Chan, C. K.; Luo, J.; Liu, Z.; Miao, Q. A Dipleadiene-Embedded Aromatic Saddle Consisting of 86 Carbon Atoms. *Angew. Chem. Int. Ed.* **2018**, *57* (6), 1581-1586.
- (45) Cheung, K. Y.; Chan, C. K.; Liu, Z.; Miao, Q. A Twisted Nanographene Consisting of 96 Carbon Atoms. *Angew. Chem. Int. Ed.* **2017**, *56* (31), 9003-9007.
- (46) Kawasumi, K.; Zhang, Q.; Segawa, Y.; Scott, L. T.; Itami, K. A grossly warped nanographene and the consequences of multiple odd-membered-ring defects. *Nat. Chem.* **2013**, *5* (9), 739-944.
- (47) Fukuyama, T.; Fujita, Y.; Miyoshi, H.; Ryu, I.; Kao, S. C.; Wu, Y. K. Electron transfer-induced reduction of organic halides with amines. *Chem Commun (Camb)* **2018**, *54* (44), 5582-5585.
- (48) Liu, J.; Li, B. W.; Tan, Y. Z.; Giannakopoulos, A.; Sanchez-Sanchez, C.; Beljonne, D.; Ruffieux, P.; Fasel, R.; Feng, X.; Müllen, K. Toward cove-edged low band gap graphene nanoribbons. *J. Am. Chem. Soc.* **2015**, *137* (18), 6097-6103.
- (49) Mattheus, C. C.; Dros, A. B.; Baas, J.; Meetsma, A.; Boer, J. L. d.; Palstra, T. T. M. Polymorphism in pentacene. *Acta Crystallogr. C* **2001**, *57* (8), 939-941.
- (50) Watanabe, M.; Chang, Y. J.; Liu, S. W.; Chao, T. H.; Goto, K.; Islam, M. M.; Yuan, C. H.; Tao, Y. T.; Shinmyozu, T.; Chow, T. J. The synthesis, crystal structure and charge-transport properties of hexacene. *Nat. Chem.* **2012**, *4* (7), 574-578.
- (51) Schleyer, P. V. R.; Maerker, C.; Dransfeld, A.; Jiao, H.; van Eikema Hommes, N. J. R. Nucleus-Independent Chemical Shifts: A Simple and Efficient Aromaticity Probe. *J. Am. Chem. Soc.* **1996**, *118* (26), 6317-6318.
- (52) Yamaji, M.; Maeda, H.; Nanai, Y.; Mizuno, K. Substitution effects of CC triple bonds on the fluorescent properties of perylenes studied by emission and transient absorption measurements. *Chem. Phys. Lett.* **2012**, *536*, 72-76.
- (53) Kummer, S.; Kulzer, F.; Kettner, R.; Basché, T.; Tietz, C.; Glowatz, C.; Kryschi, C. Absorption, excitation, and emission spectroscopy of terrylene in p-terphenyl: Bulk measurements and single molecule studies. *J. Chem. Phys.* **1997**, *107* (19), 7673-7684.
- (54) D'Yachenko, G. G.; Petukhov, V. A.; Arabei, S. M.; Pavich, T. A. Analysis of the Electronic Vibrational Spectra of Bisanthene by Calculating Normal Modes. *J. Appl. Spectrosc.* **2003**, *70* (2), 208-215.

- (55) Bernard, J.; Fleury, L.; Talon, H.; Orrit, M. Photon bunching in the fluorescence from single molecules: A probe for intersystem crossing. *J. Chem. Phys.* **1993**, *98* (2), 850-859.
- (56) Weston, K. D.; Carson, P. J.; DeAro, J. A.; Buratto, S. K. Single-molecule detection fluorescence of surface-bound species in vacuum. *Chem. Phys. Lett.* **1999**, *308* (1-2), 58-64.
- (57) Fleury, L.; Segura, J.; Zumofen, G.; Hecht, B.; Wild, U. P. Nonclassical photon statistics in single-molecule fluorescence at room temperature. *Phys. Rev. Lett.* **2000**, *84* (6), 1148-1151.
- (58) Basché, T.; Moerner, W. E.; Orrit, M.; Talon, H. Photon antibunching in the fluorescence of a single dye molecule trapped in a solid. *Phys. Rev. Lett.* **1992**, *69* (10), 1516-1519.
- (59) Novotny, L.; Hecht, B., *Principles of Nano-Optics*; Cambridge University Press: Cambridge, 2012.
- (60) Basché, T.; Kummer, S.; Bräuchle, C. Direct spectroscopic observation of quantum jumps of a single molecule. *Nature* **1995**, *373* (6510), 132-134.
- (61) Turro, N. J.; Ramamurthy, V.; Scaiano, J. C., *Modern Molecular Photochemistry of Organic Molecules*; University Science Books: Sausalito, 2010.
- (62) Christ, T.; Kulzer, F.; Bordat, P.; Basché, T. Watching the Photo-Oxidation of a Single Aromatic Hydrocarbon Molecule. *Angew. Chem. Int. Ed.* **2001**, *40* (22), 4192-4195.
- (63) Kummer, S.; Basché, T.; Bräuchle, C. Terrylene in p-terphenyl: a novel single crystalline system for single molecule spectroscopy at low temperatures. *Chem. Phys. Lett.* **1994**, *229* (3), 309-316.
- (64) Verhart, N. R.; Navarro, P.; Faez, S.; Orrit, M. Intersystem crossing rates of single perylene molecules in ortho-dichlorobenzene. *Phys. Chem. Chem. Phys.* **2016**, *18* (26), 17655-17659.
- (65) Henry, B. R.; Siebrand, W. Spin-Orbit Coupling in Aromatic Hydrocarbons. Analysis of Nonradiative Transitions between Singlet and Triplet States in Benzene and Naphthalene. *J. Chem. Phys.* **1971**, *54* (3), 1072-1085.
- (66) Lawetz, V.; Orlandi, G.; Siebrand, W. Theory of Intersystem Crossing in Aromatic Hydrocarbons. *J. Chem. Phys.* **1972**, *56* (8), 4058-4072.
- (67) Metz, F.; Friedrich, S.; Hohlneicher, G. What is the leading mechanism for the nonradiative decay of the lowest triplet state of aromatic hydrocarbons? *Chem. Phys. Lett.* **1972**, *16* (2), 353-358.
- (68) Bräuchle, C. Symmetry distortions and pseudo-Jahn-Teller effect of peri- and cata-hexabenzocoronene in their triplet states as observed by ODMR techniques. *Chem. Phys.* **1982**, *67* (1), 97-109.

- (69) Banasiewicz, M.; Morawski, O.; Wiącek, D.; Kozankiewicz, B. Triplet population and depopulation rates of single terrylene molecules in p-terphenyl crystal. *Chem. Phys. Lett.* **2005**, *414* (4-6), 374-377.
- (70) Adolph, J.; Williams, D. F. Temperature Dependence of Singlet—Triplet Intersystem Crossing in Anthracene Crystals. *J. Chem. Phys.* **1967**, *46* (11), 4248-4251.
- (71) Kryschi, C.; Wagner, B.; Gorgas, W.; Schmid, D. Vibronically induced intersystem crossing in pentacene in p-terphenyl and benzoic acid crystals. *J. Lumin.* **1992**, *53* (1-6), 468-472.
- (72) Hamanoue, K.; Nakayama, T.; Ikenaga, K.; Ibuki, K. Temperature effect on the formation of the lowest excited triplet states of 9-bromoanthracene and 9,10-dibromoanthracene. *J. Photochem. Photobiol. A: Chemistry* **1993**, *74* (2-3), 147-152.
- (73) Boiron, A. M.; Lounis, B.; Orrit, M. Single molecules of dibenzanthanthrene in n-hexadecane. *J. Chem. Phys.* **1996**, *105* (10), 3969-3974.
- (74) Lang, E.; Hildner, R.; Engelke, H.; Osswald, P.; Wurthner, F.; Kohler, J. Comparison of the photophysical parameters for three perylene bisimide derivatives by single-molecule spectroscopy. *Chemphyschem* **2007**, *8* (10), 1487-1496.
- (75) Blom, H.; Chmyrov, A.; Hassler, K.; Davis, L. M.; Widengren, J. Triplet-state investigations of fluorescent dyes at dielectric interfaces using total internal reflection fluorescence correlation spectroscopy. *J. Phys. Chem. A* **2009**, *113* (19), 5554-5566.
- (76) Clarke, R. H.; Frank, H. A. Triplet state radiationless transitions in polycyclic hydrocarbons. *J. Chem. Phys.* **1976**, *65* (1), 39-47.
- (77) Wu, Y.; Zhen, Y.; Ma, Y.; Zheng, R.; Wang, Z.; Fu, H. Exceptional Intersystem Crossing in Di(peryene bisimide)s: A Structural Platform toward Photosensitizers for Singlet Oxygen Generation. *J. Phys. Chem. Lett.* **2010**, *1* (17), 2499-2502.

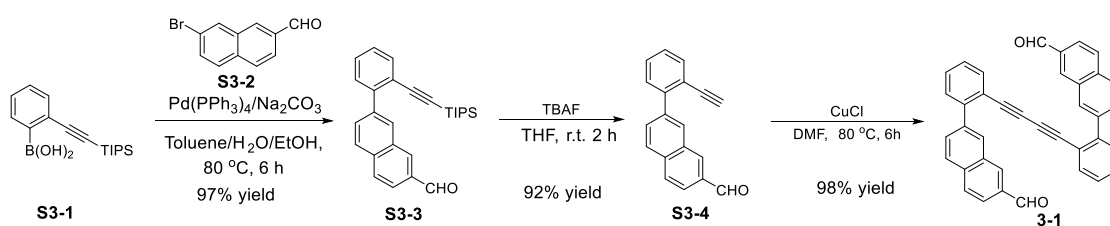
Supplementary Information

Dibenzo[*hi,st*]ovalene as Highly Luminescent Nanographene: Efficient Synthesis via Photochemical Cyclodehydroiodination, Optoelectronic Properties and Single Molecule Spectroscopy**General Methods**

All reactions working with air- or moisture- sensitive compounds were carried out under argon atmosphere using standard Schlenk line techniques. Unless otherwise noted, all starting materials were purchased from commercial sources and used without further purification. All other reagents were used as received. Thin layer chromatography (TLC) was done on silica gel coated aluminum sheets with F254 indicator and column chromatography separation was performed with silica gel (particle size 0.063–0.200 mm). Melting points were determined on a Büchi hot stage apparatus and were uncorrected. Nuclear Magnetic Resonance (NMR) spectra were recorded using Bruker DPX 300, and Bruker DRX 500 MHz NMR spectrometers. Chemical shifts (δ) were expressed in ppm relative to the residual of solvents (CD_2Cl_2 , ^1H : 5.32 ppm, ^{13}C : 53.84 ppm; $\text{C}_2\text{D}_2\text{Cl}_4$, ^1H : 6.00 ppm, ^{13}C : 73.78 ppm; $\text{THF-}d_8$, ^1H : 3.58 ppm, ^{13}C : 67.57 ppm; *o*-DCB- d_4 , ^1H : 7.20 ppm, ^{13}C : 132.35 ppm). Coupling constants (J) were recorded in Hertz. Field desorption mass (FD MS) measurements were carried out on a VG instruments ZAB 2-SE-FPD. High resolution mass spectra (HR MS) were recorded on a Bruker Reflex II-TOF spectrometer by matrix-assisted laser decomposition/ionization (MALDI) using 7,7,8,8-tetracyanoquinodimethane (TCNQ) as matrix calibrated with poly(ethylene glycol). UV-*vis* absorption spectra were recorded on a Perkin-Elmer Lambda 900 spectrometer at room temperature using a 10 mm quartz cell. Photoluminescence spectra were recorded on a J&MTIDAS spectrofluorometer. The fluorescence quantum yield (Φ) was measured using Nile blue A perchlorate (in ethanol under air, $\Phi = 0.27$) as a reference.¹ Infrared spectroscopy was recorded on a Bruker TENSOR II FTIR spectrometer. Each sample was measured with a scan number of 128 and the background was subtracted. Cyclic voltammetry (CV) measurements were performed on a GSTAT-12 in a three-electrode cell in dichloromethane solution of *n*-Bu₄NPF₆ (0.1 M) at a scan rate of 50 mV/s at room temperature. A silver wire, a Pt wire and a glassy carbon electrode were used as the reference electrode, the counter electrode, and the working electrode, respectively. Density functional theory calculations were conducted at the B3LYP/6-31G(d,p) level using Gaussian 09 software package.²

For single molecule studies, thin polymer films (≈ 100 nm) were prepared by spin-coating a highly dilute toluene solution of **DBOV-DMEP** containing a suitable amount of Zeonex® onto glass cover slips. These samples were either mounted into a room-temperature home-built confocal fluorescence microscope or into a variable temperature confocal fluorescence microscope (atto CFM1, attocube) operated at 4.5 K. For the room-temperature measurements a Zeiss Plan-Apochromat 100x objective (NA = 1.4) was used while at low temperature an attocube LT-APO objective (NA = 0.82) was employed. Single molecules were excited at 568 nm (Coherent Sapphire 568) to measure fluorescence spectra and correlation functions. To record emission spectra, the fluorescence transmitted by a 594 nm long pass filter was dispersed either by a 300 mm (Acton; room temperature) or a 750 mm (Andor; low temperature) focal length spectrograph. Both spectrographs were equipped with a sensitive CCD camera (Newton, Andor). The fluorescence intensity autocorrelation function was computed from the stream of photons detected by an avalanche photodiode whose output was fed into a PicoHarp300 board (PicoQuant) operated in time-tagged mode.

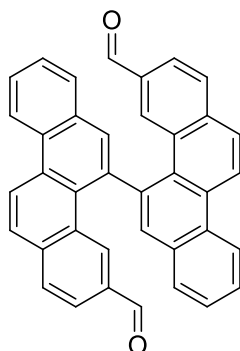
Synthetic Details



Scheme S3-1. Synthetic scheme towards diyne **3-1**.³

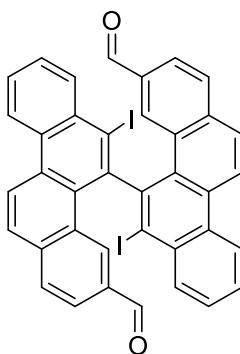
The starting material **3-1** was prepared using previously reported method in three steps with a total yield of 87%.³ First, Suzuki coupling of (2-((triisopropylsilyl)ethynyl)phenyl)boronic acid (**S3-1**) and 7-bromo-2-naphthaldehyde (**S3-2**) gave 7-(2-((triisopropylsilyl)ethynyl)phenyl)-2-naphthaldehyde (**S3-3**) in an excellent yield of 97%. After deprotection with tetra-*n*-butylammonium fluoride (TBAF) in tetrahydrofuran at room temperature, 7-(2-ethynylphenyl)-2-naphthaldehyde (**S3-4**) was obtained in 92% yield, which was then subjected to CuCl-promoted Glaser coupling in N,N-dimethylformide to afford compound **3-1** in 98% yield.

Synthesis of [5,5'-bichrysene]-3,3'-dicarbaldehyde (**3-2**):



To an oven-dried Schlenk tube was added diyne **3-1** (120 mg, 0.235 mmol) and PtCl_2 (19 mg, 0.071 mmol). The reaction tube was dried under vacuum for 2 h before dry toluene (12 mL) was added. After degassing the solution by three times freeze-pump-thaw cycles, the mixture was heated at 80 °C for 24 h. After completion of the reaction, the mixture was cooled down to room temperature and the solvent was evaporated under reduced pressure. The obtained residue was purified by column chromatography (*n*-hexane:ethyl acetate = 4:1) to give title compound (54 mg, 45%) as light yellow solid. ^1H NMR (300 MHz, Methylene Chloride- d_2) δ 9.06 (d, $J = 9.2$ Hz, 2H), 8.96 (d, $J = 8.5$ Hz, 2H), 8.78 – 8.67 (m, 2H), 8.29 (s, 2H), 8.12 – 7.97 (m, 6H), 7.94 – 7.72 (m, 6H), 7.67 – 7.57 (m, 2H); ^{13}C NMR (75 MHz, Methylene Chloride- d_2) δ 191.9, 140.5, 136.9, 134.0, 133.3, 132.7, 131.7, 131.4, 130.6, 130.4, 129.6, 129.0, 128.5, 128.1, 128.1, 125.2, 123.89, 122.7; HR MS (MALDI-TOF, positive): m/z Calcd for $\text{C}_{38}\text{H}_{22}\text{O}_2$: 510.1620 $[\text{M}]^+$, found: 510.1596.

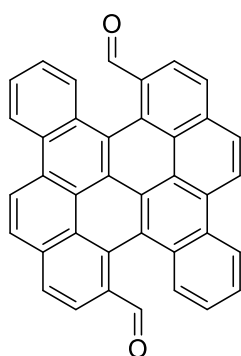
Synthesis of 6,6'-diiodo-[5,5'-bichrysen]-3,3'-dicarbaldehyde (**3-5**):



To a solution of compound **3-1** (2.0 g, 3.9 mmol) dissolved in anhydrous dichloromethane (240 mL) was added ICl (8.6 mL, 1.0 M in dichloromethane) at -78 °C. After stirring at room temperature for 2 h, excess ICl was quenched by adding a saturated aqueous solution of $\text{Na}_2\text{S}_2\text{O}_3$ (50 mL). The organic phase was separated, washed with brine (50 mL), dried over Na_2SO_4 , and evaporated. The residual solid was recrystallized with dichloromethane and

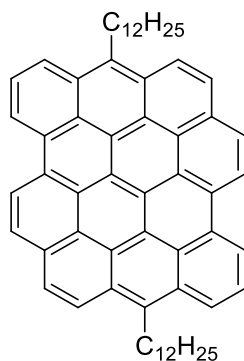
methanol to give the title compound (2.2 g, 76%) as white solid. ^1H NMR (300 MHz, Methylene Chloride- d_2) δ 9.18 (d, $J = 9.2$ Hz, 2H), 9.00 (d, $J = 8.5$ Hz, 2H), 8.72 (s, 2H), 8.53 – 8.42 (m, 4H), 8.28 (d, $J = 9.1$ Hz, 2H), 8.04 (d, $J = 8.3$ Hz, 2H), 7.98 – 7.88 (m, 2H), 7.86 – 7.74 (m, 4H); ^{13}C NMR (75 MHz, Methylene Chloride- d_2) δ 191.8, 150.1, 137.4, 135.3, 134.6, 134.5, 133.7, 132.1, 130.9, 130.5, 130.4, 130.2, 129.7, 129.5, 129.3, 125.7, 124.4, 123.7, 114.1; HR MS (MALDI-TOF, positive): m/z Calcd for $\text{C}_{38}\text{H}_{20}\text{I}_2\text{O}_2$: 761.9553 $[\text{M}]^+$, found: 761.9553.

Synthesis of 5,14-diformylbenzo[*a*]dinaphtho[2,1,8-*cde*:1',2',3',4'-*ghi*]perylene (**3-6**):



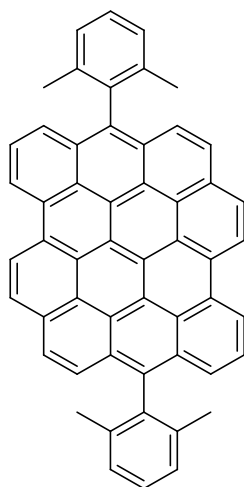
To a 3-L cylindrical quartz reactor containing 6,6'-diiodo-[5,5'-bichryseno]-3,3'-dicarbaldehyde (**3-5**) (300 mg, 0.394 mmol) was added a solution of acetone (600 mL) and triethylamine (6 mL). Then the mixture was degassed by bubbling with argon for 20 minutes, and stirred at room temperature in a photoreactor for 2 h under irradiation by sixteen UV lamps (300 nm, 14 W) with strong stirring. After cooling down to a room temperature, the solvents were evaporated and the residue was purified by column chromatography (eluent: *n*-hexane:ethyl acetate = 4:1) to give the title compound (170 mg, 86% yield) as a red solid. ^1H NMR (300 MHz, 1,1,2,2-tetrachloroethane- d_2) δ 9.66 (s, 2H), 9.21 (d, $J = 9.0$ Hz, 2H), 9.09 (d, $J = 8.3$ Hz, 2H), 8.67 (d, $J = 8.5$ Hz, 2H), 8.62 (d, $J = 8.2$ Hz, 2H), 8.52 (d, $J = 8.9$ Hz, 2H), 8.46 (d, $J = 8.2$ Hz, 2H), 7.89 (t, $J = 7.5$ Hz, 2H), 7.84 – 7.71 (m, 2H); ^{13}C NMR (75 MHz, 1,1,2,2-tetrachloroethane- d_2) δ 191.0, 134.0, 131.9, 131.8, 130.9, 128.7, 128.4, 128.1, 127.8, 127.3, 127.2, 126.1, 125.2, 124.6, 124.2, 123.3, 121.5, 120.8; HR MS (MALDI-TOF, positive): m/z Calcd for $\text{C}_{38}\text{H}_{18}\text{O}_2$: 506.1307 $[\text{M}]^+$, found: 506.1288.

Synthesis of 6,14-didodecyldibenzo[*hi*,*st*]ovalene (**DBOV-C12**):

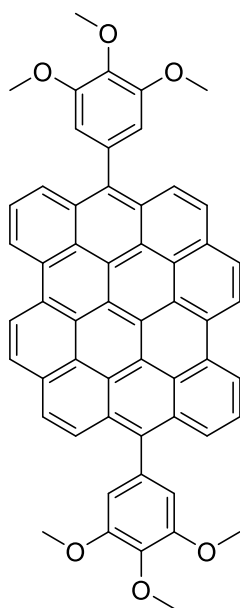


To a 50-mL round-bottom flask were added 5,14-diformylbenzo[*a*]dinaphtho[2,1,8-*cde*:1',2',3',4'-*ghi*]perylene (**3-6**) (10.1 mg, 0.0199 mmol) and dry tetrahydrofuran (10 mL) under argon. To the mixture was added dropwise a solution of *n*-C₁₂H₂₅MgBr (0.30 mL, 1.0 M in ether) via syringe. After stirring at a room temperature for 5 h, the reaction was quenched by adding a saturated aqueous solution of NH₄Cl (10 mL). The organic phase was separated and the aqueous phase was extracted with ethyl acetate (15 mL) for three times. Combined organic layers were washed with brine (30 mL), dried over Na₂SO₄, and evaporated. After purification by column chromatography with silica gel (eluent: *n*-hexane:ethyl acetate = 3:1), the resulting diol intermediate was dissolved in dry dichloromethane (10 mL). Then methanesulfonic acid (0.1 mL) was added and the mixture was stirred overnight at a room temperature. After quenching with methanol (1 mL), *p*-chloranil (10 mg, 0.041 mmol) was added into the mixture and stirred for another 2 hours. The crude product was precipitated by addition of methanol (30 mL), which was further purified by column chromatography (eluent: *n*-hexane:tetrahydrofuran = 4:1 to 0:1) to give the title compound (6.5 mg, 41% yield) as a blue solid. FTIR (powder) 3067, 3034, 2950, 2919, 2847, 1603, 1554, 1461, 1072, 823, 758, 714 cm⁻¹; ¹H NMR (500 MHz, 413 K, *o*-dichlorobenzene-*d*₄) δ 8.98 – 8.79 (br, 2H), 8.77 – 8.48 (br, 2H), 8.48 – 8.22 (br, 2H), 8.21 – 8.07 (m, 2H), 8.06 – 7.90 (m, 2H), 7.84 – 7.49 (m, 4H), 1.82 (p, *J* = 6.8 Hz, 4H), 1.49 (p, *J* = 7.4 Hz, 4H), 1.28 (p, *J* = 7.2 Hz, 4H), 1.20 – 0.92 (m, 29H), 0.58 (t, *J* = 6.7 Hz, 6H); HRMS (MALDI-TOF, positive): *m/z* Calcd for C₆₂H₆₄: 808.5008 [M]⁺, found: 808.4978.

Synthesis of 6,14-bis(2,6-dimethylphenyl)dibenzo[*hi,st*]ovalene (**DBOV-DMEP**):

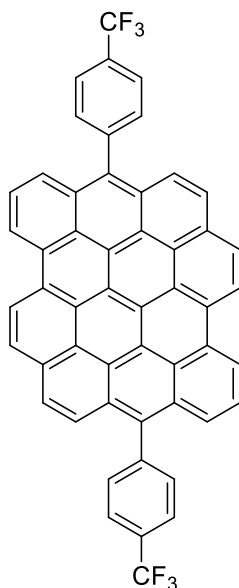


To a mixture of 5,14-diformylbenzo[*a*]dinaphtho[2,1,8-*cde*:1',2',3',4'-*ghi*]perylene (**3-6**) (63 mg, 0.12 mmol) dissolved in dry THF (63 mL) was added dropwise 2,6-dimethylphenylmagnesium bromide (1.8 mL, 1.0 M in THF). After stirring for 3 h at a room temperature, the reaction was quenched with a saturated aqueous solution of NH₄Cl (45 mL). The organic phase was separated and the aqueous phase was extracted with ethyl acetate (50 mL) for three times. The combined organic layers were washed with brine (30 mL), dried over Na₂SO₄, and evaporated to give crude diol intermediate. After drying under vacuum for 2 h, the diol intermediate was dissolved in anhydrous dichloromethane (60 mL) and degassed by bubbling with dichloromethane vapor saturated argon flow. BF₃·OEt₂ (0.6 mL) was added to the solution and the mixture was allowed to stir overnight. After quenching the reaction with methanol (2 mL), *p*-chloranil (30 mg, 0.12 mmol) was added and stirred for 2 h at room temperature. The solvent was evaporated and the residue was purified by column chromatography (eluent: *n*-hexane:dichloromethane = 3:1) to give the title compound (59 mg, 72% yield) as blue solid. FTIR (powder) 3060, 3037, 2945, 2914, 2849, 1601, 1573, 834, 765, 719 cm⁻¹; ¹H NMR (300 MHz, THF-*d*₈) δ 9.54 (d, *J* = 8.3 Hz, 2H), 9.23 (d, *J* = 7.7 Hz, 2H), 8.59 (d, *J* = 8.2 Hz, 2H), 8.13 (d, *J* = 9.2 Hz, 2H), 8.00 (t, *J* = 7.9 Hz, 2H), 7.87 (d, *J* = 8.1 Hz, 2H), 7.70 (d, *J* = 9.1 Hz, 2H), 7.45 (dd, *J* = 6.1, 2.7 Hz, 4H), 7.40 (s, 3H), 2.00 (s, 12H); ¹³C NMR (75 MHz, THF-*d*₈) δ 138.8, 138.7, 135.9, 133.2, 131.8, 131.5, 130.6, 129.9, 129.9, 129.1, 128.9, 128.8, 128.1, 127.0, 126.9, 126.1, 125.5, 125.4, 124.1, 124.1, 122.5, 121.9, 20.9; HRMS (MALDI-TOF, positive): *m/z* Calcd for C₅₄H₃₂: 680.2504 [M]⁺, found: 680.2487.

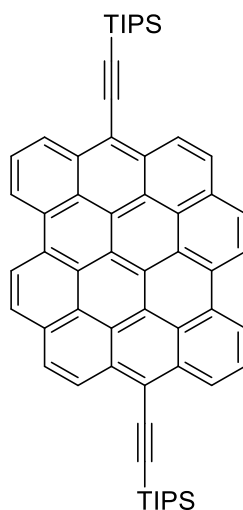
Synthesis of 6,14-bis(3,4,5-tris(methoxy)phenyl)dibenzo[*hi,st*]ovalene (**DBOV-TMOP**):

To a solution of 5-bromo-1,2,3-trimethoxybenzene (146 mg, 0.591 mmol) dissolved in anhydrous THF (5 mL) was added dropwise *n*-BuLi (0.41 mL, 1.6 M in *n*-hexane) at -78 °C. After addition, the mixture was stirred at this temperature for 1 h to generate (3,4,5-trimethoxyphenyl)lithium. The organolithium reagent was transferred to a solution of 5,14-diformylbenzo[*a*]dinaphtho[2,1,8-*cde*:1',2',3',4'-*ghi*]perylene (**3-6**) (30 mg, 0.059 mmol) in dry THF (30 mL) at 0 °C. After stirring at room temperature for 0.5 h, the reaction was quenched by addition of a saturated aqueous solution of NH_4Cl (15 mL). The organic phase was separated and aqueous layer was extracted with ethyl acetate (50 mL) for three times. The combined organic phases were washed with brine, dried with Na_2SO_4 , and evaporated. The residue was dried under vacuum for 2 h and purified by column chromatography (eluent: *n*-hexane:ethyl acetate = 1:2) to give a diol intermediate as yellow solid. Then the yellow solid was dissolved in anhydrous dichloromethane (30 mL). After bubbling with dichloromethane vapor saturated argon flow for 15 mins, $\text{BF}_3\cdot\text{OEt}_2$ (0.1 mL) was added and the stirring was continued overnight. After quenching with methanol (2 mL), *p*-chloranil (12 mg, 0.049 mmol) was added and the mixture was stirred for 2 h at room temperature. The product was precipitated by addition of methanol (30 mL) and filtered to give the title product (16 mg, 33% yield) as blue solid. FTIR (powder) 3063, 2999, 2931, 2828, 1574, 1503, 1401, 1333, 1228, 1124, 1004, 835, 766, 718 cm^{-1} ; HRMS (MALDI-TOF, positive): m/z Calcd for $\text{C}_{56}\text{H}_{36}\text{O}_6$: 804.2506 $[\text{M}]^+$, found: 804.2677.

Synthesis of 6,14-bis(4-trifluoromethylphenyl)dibenzo[hi,st]ovalene (**DBOV-CF3**):



n-BuLi (0.41 mL, 1.6 M in *n*-hexane) was added dropwise to a solution of 1-bromo-4-(trifluoromethyl)benzene (132 mg, 0.587 mmol) in dry tetrahydrofuran (5 mL) at $-78\text{ }^{\circ}\text{C}$ and stirred at this temperature for 1 h to generate (4-(trifluoromethyl)phenyl)lithium. The lithium reagent was transferred to a solution of 5,14-diformylbenzo[*a*]dinaphtho[2,1,8-*cde*:1',2',3',4'-*ghi*]perylene (**3-6**) (30 mg, 0.059 mmol) dissolved in dry THF (30 mL) at $0\text{ }^{\circ}\text{C}$. After stirring at room temperature for 0.5 h, the reaction was quenched by addition of saturated NH_4Cl solution (15 mL). The organic phase was separated and the aqueous solution was extracted with ethyl acetate (50 mL) for three times. The combined organic phases were washed with brine, dried with Na_2SO_4 and evaporated. The residue was purified by column chromatography (*n*-hexane:ethyl acetate = 2:1) to give diol intermediate as yellow solid. Then the yellow solid was dissolved in anhydrous dichloromethane (30 mL). After bubbling with dichloromethane vapor saturated argon flow for 15 mins, $\text{BF}_3\cdot\text{OEt}_2$ (0.1 mL) was added and stirred continuously overnight. The reaction was quenched with methanol (2 mL) and *p*-chloranil (12 mg, 0.049 mmol) was added. After evaporation of solvent, the residue was purified by recrystallization from tetrahydrofuran and methanol to give title compound (21 mg, 47% yield) as blue solid. FTIR (powder) 3050, 1614, 1325, 1158, 1099, 1077, 1017, 834, 768 cm^{-1} ; ^1H NMR (500 MHz, 393K, *o*-dichlorobenzene-*d*₄) δ 9.31 (d, $J = 8.0$ Hz, 2H), 9.02 (d, $J = 7.2$ Hz, 2H), 8.42 (d, $J = 8.8$ Hz, 2H), 8.01 – 7.92 (m, 6H), 7.92 – 7.86 (m, 2H), 7.79 (t, $J = 8.7$ Hz, 4H), 7.08 (d, $J = 7.7$ Hz, 2H), 6.99 (d, $J = 7.7$ Hz, 2H); HRMS (MALDI-TOF): m/z Calcd for $\text{C}_{52}\text{H}_{22}\text{F}_6$: 760.1620 $[\text{M}]^+$, found: 760.1501.

Synthesis of 6,14-bis((triisopropylsilyl)ethynyl)dibenzo[*hi,st*]ovalene (**DBOV-TIPS**):

The lithium reagent was prepared using a literature reported method.⁴ To an oven dried 25 mL Schlenk tube was added tetrahydrofuran (1.4 mL) and (triisopropylsilyl)acetylene (182 mg, 0.998 mmol). The solution was cooled down to 0 °C followed by dropwise addition of *n*-BuLi (0.6 mL, 1.6 M in *n*-hexane). The resulting solution was stirred at room temperature for 30 mins and transferred to a solution of 5,14-diformylbenzo[*a*]dinaphtho[2,1,8-*cde*:1',2',3',4'-*ghi*]perylene (**3-6**) (25 mg, 0.049 mmol) in dry THF (25 mL). After stirring for 24 h, the reaction was quenched by addition of saturated aqueous solution of NH₄Cl (20 mL) and extracted with ethyl acetate (20 mL) for three times. The combined organic phase was washed with brine (20 mL), dried over Na₂SO₄ and evaporated. After purification by column chromatography (*n*-hexane:ethyl acetate = 4:1), the diol intermediate was dissolved in anhydrous dichloromethane (25 mL) and degassed with dichloromethane vapor saturated argon flow. After addition of BF₃·OEt₂ (0.025 mL), the resulting solution was stirred at room temperature for 6 h. The reaction was quenched by addition of methanol (1 mL) and *p*-chloranil (12 mg, 0.049 mmol) was added. After addition of methanol (50 mL), the solid was collected by filtration and purified by recrystallization from dichloromethane and methanol to give title product (10 mg, 50% yield) as blue solid. FTIR (powder) 3059, 3033, 2939, 2861, **2126** (C≡C), 1735, 1602, 1460, 1231, 992, 879, 827, 754 cm⁻¹; ¹H NMR (500 MHz, 393K, *o*-dichlorobenzene-*d*₄) δ 8.80 (s, 2H), 8.55 – 8.05 (m, 6H), 7.91 (s, 2H), 7.70 (s, 4H), 1.56 (s, 42H); HRMS (MALDI-TOF, positive): *m/z*. Calcd for C₆₀H₅₆Si₂: 832.3921 [M]⁺, found: 832.3859.

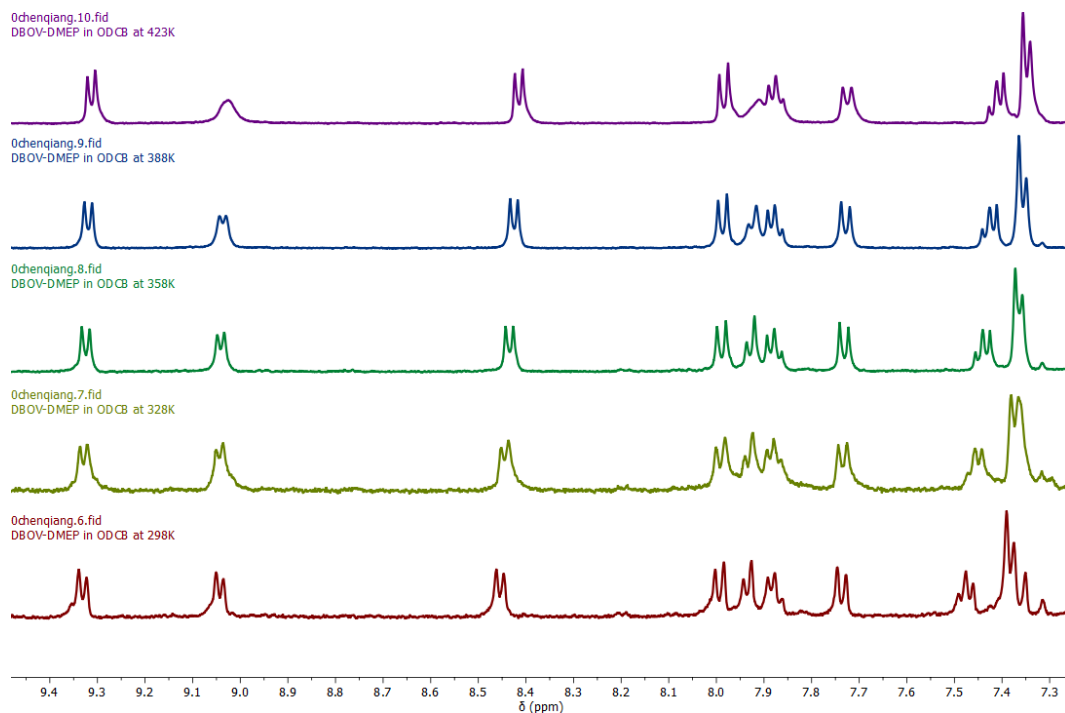


Figure S3-3. Variable temperature ^1H NMR spectra of **DBOV-DMEP** measured in *o*-DCB- d_4 from 298 K to 423 K, indicating no peak broadening (500 MHz).

Table S3-1. The energy level of **DBOV** from theoretical calculations (DFT/B3LYP/6-31G(d,p)).

compound	closed-shell, E (eV)	E singlet open-shell, E (eV)	S^2	triplet open-shell, E (eV)	S^2
DBOV-C12	-41811.021353364	-41811.021352275	0	-41810.074121809	2.0474
DBOV-DMEP	-56527.207303882	-56527.207303066	0	-56526.268089321	2.0482
DBOV-TMOP	-70943.761038523	-70943.761038523	0	-70943.761038523	2.0460
DBOV-CF3	-70588.611110193	-70588.61109104	0	-70587.66450078	2.0479
DBOV-TIPS	-78895.646549477	-78895.646549477	0	-78894.822923801	2.0460

Single Crystal X-ray Diffraction Analysis

Single crystals of compound **3-6** suitable for X-ray diffraction crystallography were grown by slow evaporation of acetonitrile vapor into its solution in *o*-dichlorobenzene at a room temperature. Single crystals of **DBOV-DMEP** were obtained by slow evaporation of methanol vapor into its solution in tetrahydrofuran at a room temperature. The X-ray diffraction data were collected at 193 K on a STOE IPDS 2T diffractometer by using graphite monochromated Mo-K α radiation. The structures were solved with the SIR-2004 program and refined by the SHELXT-2014 and SHELXT-2017, respectively. H-atoms at calculated positions are refined with isotropic displacement parameters and all non H-atoms are refined anisotropically. The data have been deposited at the Cambridge Crystallographic Data Centre (CCDC) with the deposition number of CCDC1852850 and CCDC1852851 can be obtained free of charge from CCDC via www.ccdc.cam.ac.uk/structures/.

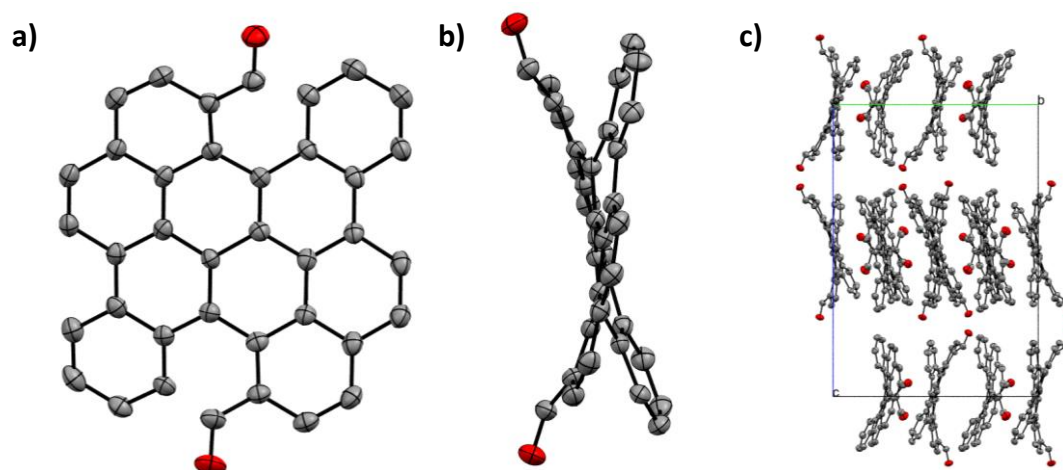


Figure S3-4. Single crystal structure of compound **3-6**. a) front view; b) side view; c) packing pattern along *a*-axis. Hydrogen atoms and solvent molecules were omitted for a better overview.

Crystal data for compound **3-6** (CCDC1852850)

formula	C ₃₈ H ₁₈ O ₂ , C ₂ H ₃ N		
molecular weight	547.58 gmol ⁻¹		
absorption	$\mu = 0.088 \text{ mm}^{-1}$		
crystal size	0.09 x 0.14 x 0.56 mm ³ brown needle		
space group	P b c a (orthorhombic)		
lattice parameters	a = 24.2958(5) Å		
(calculate from	b = 17.0876(2) Å		
77793 reflections with	c = 24.3610(3) Å		
1.68° < θ < 28.34°)	V = 10113.6(3) Å ³ z = 16 F(000) = 4544		
temperature	-80°C		
density	$d_{\text{xray}} = 1.438 \text{ gcm}^{-3}$		

data collection

diffractometer	STOE IPDS 2T
radiation	Mo-K α Graphitmonochromator
Scan – type	ω scans
Scan – width	1°
scan range	$2^\circ \leq \theta < 28^\circ$ $-32 \leq h \leq 32$ $-22 \leq k \leq 21$ $-32 \leq l \leq 32$
number of reflections:	
measured	94219
unique	13022 ($R_{\text{int}} = 0.0532$)
observed	10483 ($ F /\sigma(F) > 4.0$)

data correction, structure solution and refinement

corrections	Lorentz and polarisation correction.
Structure solution	Program: SIR-2004 (Direct methods)
refinement	Program: SHELXL-2014 (full matrix). 778 refined parameters, weighting scheme: $w=1/[\sigma^2(F_o^2) + (0.0185*P)^2+31.53*P]$ with $(\text{Max}(F_o^2,0)+2*F_c^2)/3$. H-atoms at calculated positions and refined with isotropic displacement parameters, non H- atoms refined anisotropically.
R-values	wR2 = 0.1999 (R1 = 0.0878 for observed reflections, 0.1134 for all reflections)
goodness of fit	S = 1.153
maximum deviation of parameters	0.001 * e.s.d
maximum peak height in diff. Fourier synthesis	0.32, -0.32 e \AA^{-3}
remark	structure contains two independent molecules and two molecules CH ₃ CN. Crystallize as twin a \leftrightarrow c BASF =0.1699(12)

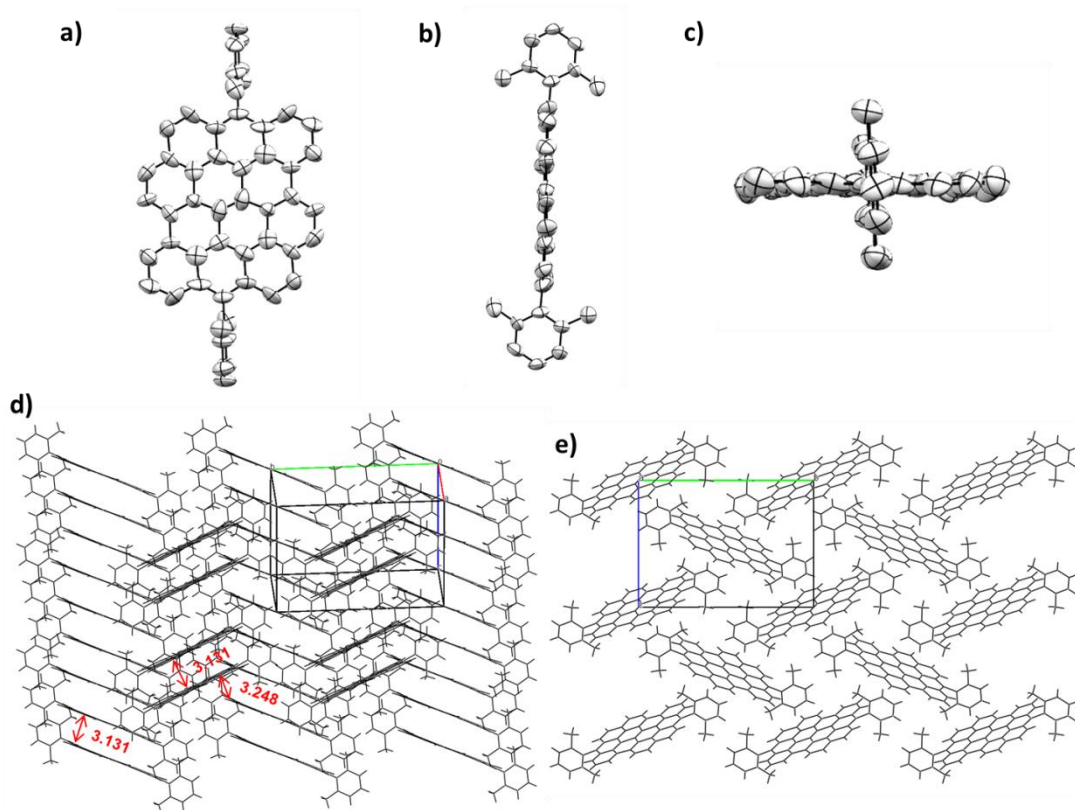


Figure S3-5. Single crystal structure of **DBOV-DMEP**. a) front view; b) side view; c) Top view (H-atoms were omitted for clarity); d) three-dimensional layer like packing; e) packing pattern along *a*-axis.

Crystal data for **DBOV-DMEP** (CCDC1852851)

formula	$C_{54}H_{32}$
molecular weight	680.79 gmol^{-1}
absorption	$\mu = 0.06 \text{ mm}^{-1}$
crystal size	$0.06 \times 0.06 \times 0.25 \text{ mm}^3$ brown needle
space group	$P 2_1/n$ (monoclinic)
lattice parameters	$a = 8.9726(19) \text{ \AA}$
(calculate from	$b = 17.601(3) \text{ \AA}$ $\beta = 93.916(19)^\circ$
3846 reflections with	$c = 12.768(3) \text{ \AA}$
$2^\circ < \theta < 28^\circ$)	$V = 2011.7(7) \text{ \AA}^3$ $z = 2$ $F(000) = 712$
temperature	-80°C
density	$d_{\text{xray}} = 1.124 \text{ gcm}^{-3}$

data collection

diffractometer	STOE IPDS 2T
radiation	Mo- K_α Graphitmonochromator

Scan – type	ω scans
Scan – width	1°

scan range	$2^{\circ} \leq \theta < 28^{\circ}$ $-11 \leq h \leq 11 \quad -23 \leq k \leq 20 \quad -16 \leq l \leq 16$
number of reflections:	
measured	9414
unique	4813 ($R_{\text{int}} = 0.1181$)
observed	1616 ($(F/\sigma(F)) > 4.0$)

data correction, structure solution and refinement

corrections	Lorentz and polarisation correction.
Structure solution	Program: SIR-2004 (Direct methods)
refinement	Program: SHELXL-2017 (full matrix). 246 refined parameters, weighting scheme: $w=1/[\sigma^2(F_o^2) + (0.2*P)^2]$ with $(\text{Max}(F_o^2, 0)+2*F_c^2)/3$. H-atoms at calculated positions and refined with isotropic displacement parameters, non H- atoms refined anisotropically.
R-values	$wR2 = 0.6393$ ($R1 = 0.2540$ for observed reflections, 0.4114 for all reflections)
goodness of fit	$S = 1.597$
maximum deviation of parameters	0.001 * e.s.d
maximum peak height in diff. Fourier synthesis	0.76, -0.36 eÅ ⁻³
remark	molecule has Ci symmetry, crystal contains solvent which could not be located, SQUEEZE was used.

Computational Details

Geometry optimization for all DBOV derivatives were performed at the B3LYP level of theory with 6-31G(d,p) basis set, using Gaussian 09 software and energy levels were calculated at the same level of theory.² Calculation of NICS (0) values were carried out using the gauge invariant atomic orbital (GIAO) method at GIAO-B3LYP/6-31G(d,p) level at the central position of each hexagonal rings.^{5, 6} UV-*vis* absorption spectra were calculated by TD-DFT method with the same basis set. Dodecyl chains for **DBOV-C12** were replaced by methyl groups for saving resource.

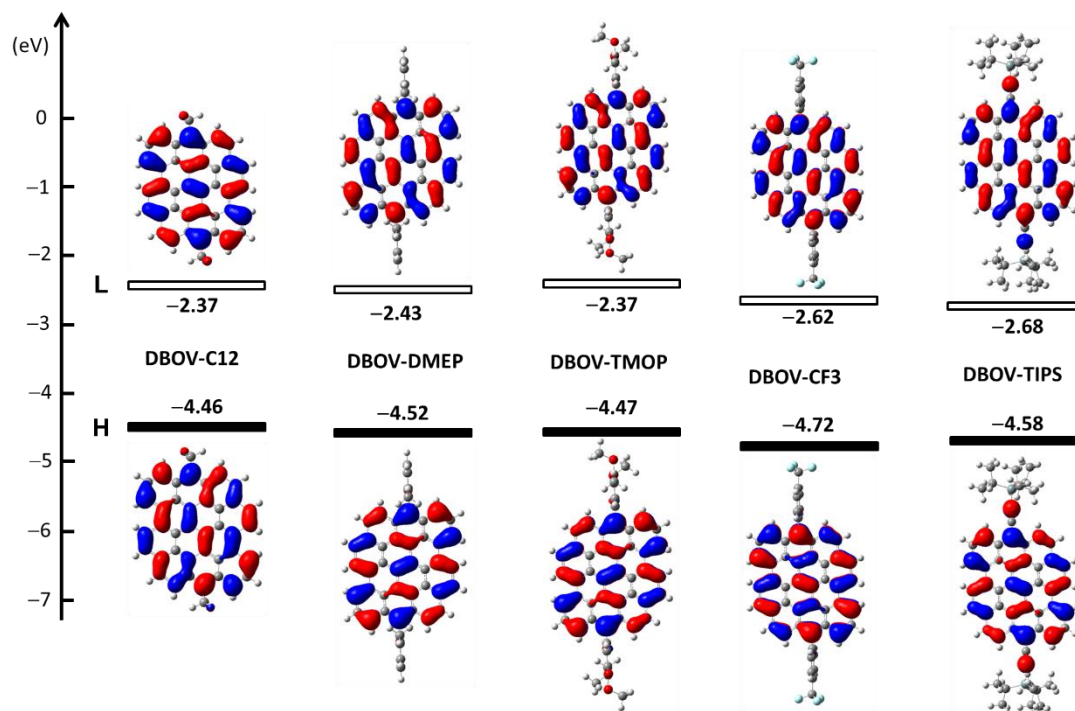


Figure S3-6. Optimized structure and frontier molecular orbital distribution of DBOV derivatives at the B3LYP/6-31G(d,p) level.

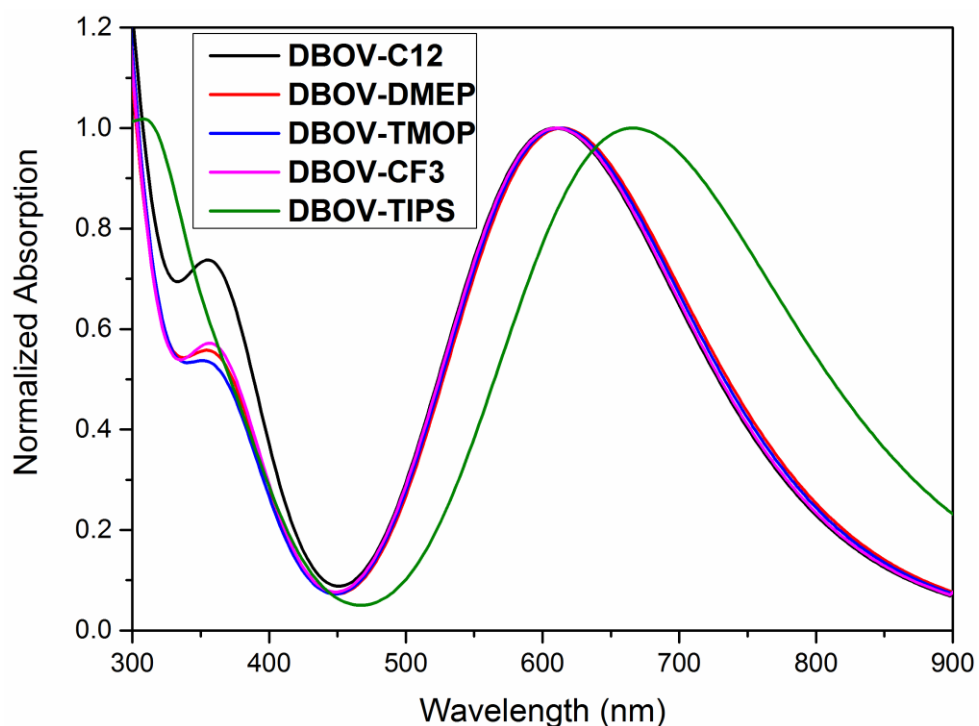


Figure S3-7. UV-*vis* spectra of DBOV derivatives by TD-DFT method.

Table S3-2. Characteristic electron transitions for DBOV derivatives calculated by TDDFT at the B3LYP/6-31G(d,p) level by Gaussian 09.

Compound	Excited states	Transition energy (eV)	Wavelength (nm)	Oscillator strength	Description
	1	2.03	609	0.4714	HOMO→LUMO (0.70326)
	4	2.85	434	0.0004	HOMO-2→LUMO (0.49879) HOMO→LUMO+2 (0.49599)
DBOV-C12	7	3.29	377	0.2638	HOMO-2→LUMO (-0.43374) HOMO-1→LUMO+1 (-0.20505) HOMO→LUMO+2 (0.44119) HOMO→LUMO+4 (0.24045)
	1	2.02	614	0.5963	HOMO→LUMO (0.70335)
	4	2.85	434	0.0007	HOMO-2→LUMO (0.50056) HOMO→LUMO+2 (0.49419) HOMO-2→LUMO (-0.43540)
DBOV-DMEP	7	3.38	367	0.2561	HOMO-1→LUMO+1 (-0.20804) HOMO→LUMO+2 (0.44606) HOMO→LUMO+5 (0.21897)
	1	2.04	612	0.6382	HOMO→LUMO (0.70306)
	4	2.86	434	0.0007	HOMO-4→LUMO (0.24834) HOMO-2→LUMO (-0.43362) HOMO→LUMO+2 (0.49464)
DBOV-TMOP	6	3.12	397	0.0035	HOMO-4→LUMO (0.56267) HOMO-2→LUMO (0.41272)
	1	2.03	610	0.6023	HOMO→LUMO (0.70309)
DBOV-CF3	4	2.86	434	0.0014	HOMO-2→LUMO (0.51285) HOMO→LUMO+2 (0.48085)
	1	1.86	666	0.8660	HOMO→LUMO (0.70637) LUMO→HOMO (-0.10433)
	4	2.79	444	0.0089	HOMO-2→LUMO (0.54575) HOMO→LUMO+2 (-0.44256)
DBOV-TIPS	7	3.29	376	0.1984	HOMO-2→LUMO (0.36837) HOMO-1→LUMO+1 (-0.22776) HOMO→LUMO+2 (0.47345) HOMO→LUMO+6 (-0.12644)

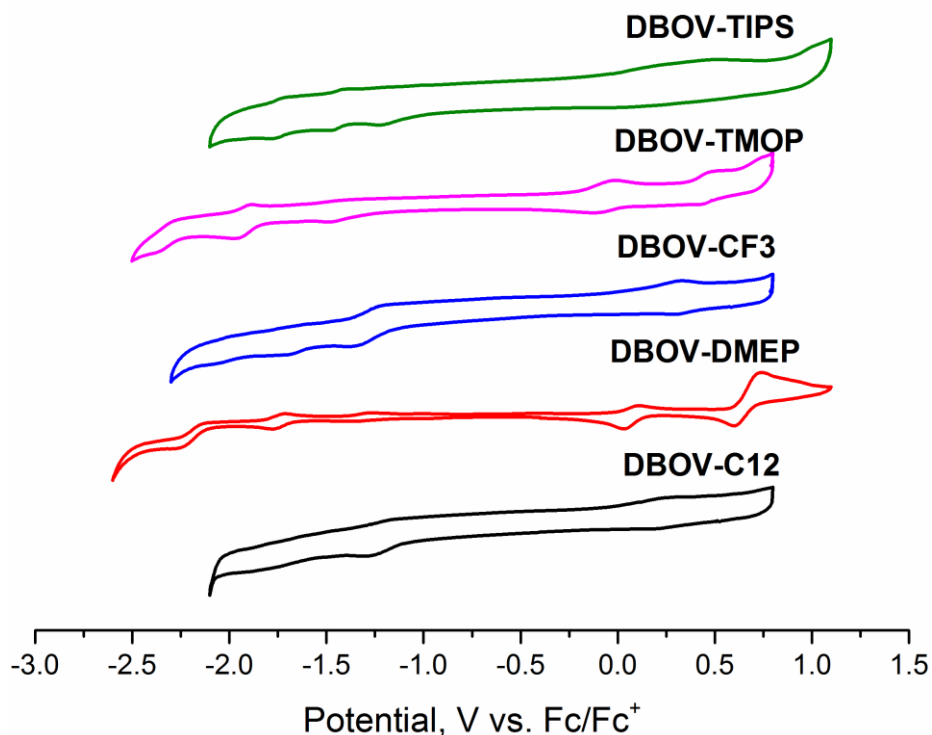


Figure S3-8. Cyclic voltammetry of **DBOV** vs Fc/Fc^+ (0.1 M $n\text{-Bu}_4\text{NPF}_6$ in dichloromethane at room temperature, scan rate 50 mV/s)

Single Molecule Spectroscopy

Emission spectroscopy

Table S3-3: Ground state vibrational frequencies and relative intensities of $S_1 \rightarrow S_0$ vibronic transitions of a single **DBOV-DMEP** molecule at 4.5 K (see Figure 3-4a). The absolute spectral position for $\Delta\nu = 0$ corresponds to 16555.5 cm^{-1} . Intensities are not corrected for the detection efficiency of the setup.

$\Delta\nu / \text{cm}^{-1}$	0	9	14	149	154	312	326	364	533	622	1255	1328	1352
Rel. Int.	100	3.8	1.4	3	2	3.8	2.8	4.9	1	0.5	1.3	0.9	1.1

Fluorescence intensity autocorrelation function $g^{(2)}(\tau)$

Room temperature

i) Intensity dependence of $g^{(2)}(\tau)$ at short times (photon antibunching)

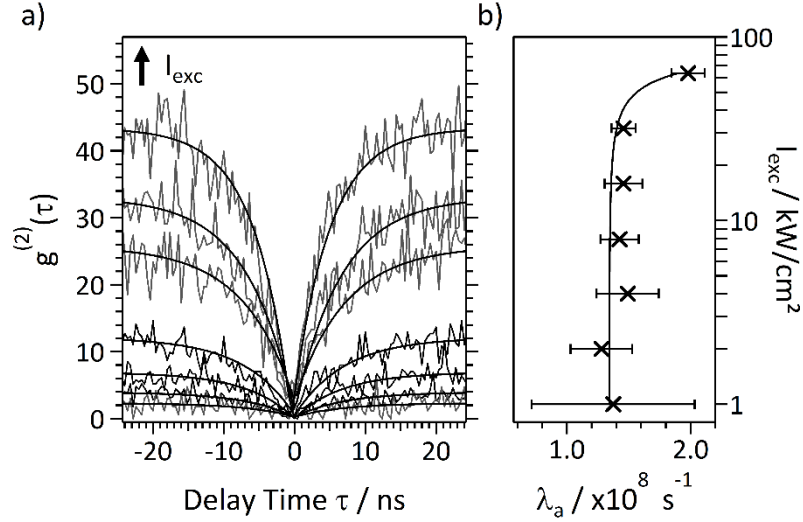


Figure S3-9. a) $g^{(2)}(\tau)$ at short times for a single **DBOV-DMEP** molecule at different excitation intensities. Even at the highest intensity, strong antibunching contrast prevails. The drawn lines are fits of equation S1 (equation 1 in the main text) to the data. b) Intensity dependence of λ_a for the molecule shown in Fig. S9a. At low intensities, λ_a is dominated by the fluorescence decay rate k_{21} ⁹.

To extract the rise time λ_a of the antibunching signal (see Fig. S3-9a), $g^{(2)}(\tau)$ at short times was approximated by

$$g^{(2)}(\tau) = A(1 - e^{-\lambda_a|\tau|}) + B. \quad (\text{S1})$$

For long delay times within the time range depicted in Figure S9a, the contrast is given by $g^{(2)}(\tau \rightarrow \infty) = A+B$ and B represents the value of $g^{(2)}(\tau = 0)$. However, both values were of no further interest here.

ii) Extraction of k_{23} and k_{31} from $g^{(2)}(\tau)$ at long times (photon bunching)

Following previous work from the literature, we used equation S2 (equation 2 in the main text) to describe the room temperature decay of $g^{(2)}(\tau)$ at long delay times⁷⁻⁹:

$$g^{(2)}(\tau) \cong C e^{-\lambda_b \tau} + 1. \quad (\text{S2})$$

This expression relates to a three-level system (see Figure 5), which is an appropriate approximation for **DBOV-DMEP** at room temperature. For slow intersystem crossing, e.g.

k_{31} and k_{23} are much smaller than the fluorescence decay rate k_{21} , the contrast C and decay parameter λ_b can be expressed as follows⁷:

$$\lambda_b \cong - \left(k_{31} + k_{31} \frac{\frac{I_{exc}}{I_S}}{1 + \frac{k_{31} I_{exc}}{k_{23} I_S}} \right) \quad (S3)$$

$$C \cong \frac{\lambda_b - k_{31}}{k_{31}} \quad (S4)$$

I_{exc} and I_S are the excitation and saturation intensity, respectively. Since we consider nonresonant excitation, equation S3 differs by a factor of 2 from the original expression⁷ derived for resonant excitation. The parameters λ_b and C were determined for different excitations intensities and fitted globally.

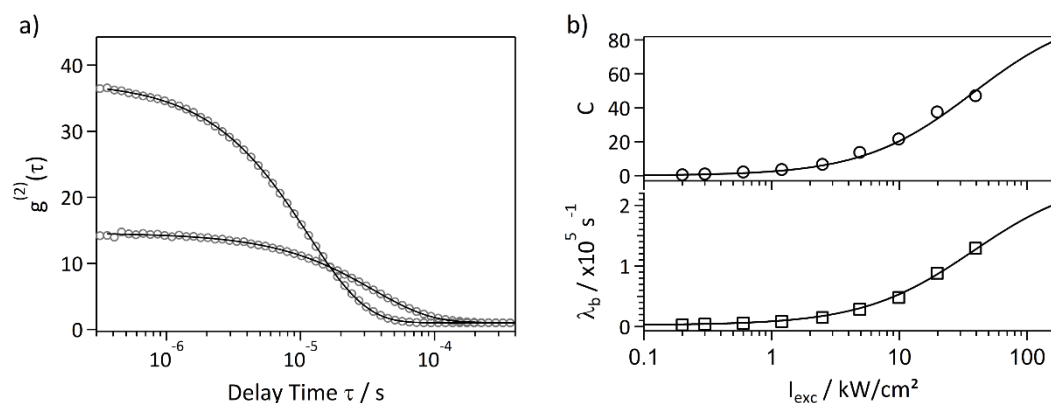


Figure S3-10. a) Fluorescence intensity autocorrelation function $g^{(2)}(\tau)$ for a single **DBOV-DMEP** molecule at room temperature for two values of the excitation intensity. The drawn lines are fits of equation S2 to the data. b) Intensity dependence of the contrast C (o) and decay parameter λ_b (\square) of the correlation function for the same single molecule. The drawn lines are fits of equations S3 (λ_b) and S4 (C), respectively, to the data. At room temperature, the range of excitation intensities was mainly limited by photobleaching.

Low temperature

At low temperatures ($T = 4.5$ K) the three level description is no longer appropriate, since we have to consider the zero-field splitting of the triplet state (see Figure 5 and discussion in the main text). As pointed out in the main text, t_x and t_y are treated as a single level t_{xy} and the bunching regime of the correlation function $g^{(2)}(\tau)$ now shows two decaying components

(see Figure 6a) instead of only one at room temperature. Following Verhart et al.¹⁰, the data were fitted with the following expressions:

$$g^{(2)}(\tau) = C_+ e^{-\Lambda_+ \tau} + C_- e^{-\Lambda_- \tau} + 1 \quad (\text{S5})$$

$$\Lambda_{\pm} = \frac{1}{2}(\Sigma \pm D) \quad (\text{S6})$$

$$C_{\pm} = \frac{\Lambda_{\mp}(K_{31}^{XY} - \Lambda_{\pm})(K_{31}^Z - \Lambda_{\pm})}{K_{31}^{XY} K_{31}^Z (\Lambda_{\pm} - \Lambda_{\mp})} \quad (\text{S7})$$

$$\Sigma = K_{23}^{XY} + K_{23}^Z + K_{31}^{XY} + K_{31}^Z \quad (\text{S8})$$

$$D = \sqrt{\Sigma^2 - 4(K_{23}^{XY} K_{31}^Z + K_{23}^Z K_{31}^{XY} + K_{31}^{XY} K_{31}^Z)} \quad (\text{S9})$$

Moreover, the following relations hold:

$$K_{23}^{XY} = k_{23}^{XY} p_2^*, \quad K_{23}^Z = k_{23}^Z p_2^* \quad \text{and}$$

$$p_2^* = \frac{I_{exc}/I_S^*}{1 + I_{exc}/I_S^*} \quad (\text{S10})$$

Equation S10 represents a steady-state excited-state population with the molecule being in the singlet manifold (S_1). Note, I_S^* is different from I_S in equation S3. Although the model turned out to be fine for low excitation intensities ($I_{exc} \lesssim 10 \text{ kW/cm}^2$), we noticed a discrepancy for higher excitation intensities and the model could not describe the intensity dependence of the four determined parameters Λ_{\pm} & C_{\pm} adequately. The determined rates Λ_{\pm} (contrasts C_{\pm}) were higher (lower) than the presented model predicts. Therefore, we assume an additional process for the depopulation of the dark states, e.g. triplet-triplet-absorption, the rate of which depends on the excitation intensity. In a first approximation, we introduced apparent triplet decay rates $K_{31}^{XY} = k_{31}^{XY} + \alpha^{xy} I_{exc}$ and $K_{31}^Z = k_{31}^Z + \alpha^Z I_{exc}$, which fit the data well. Such linear dependencies have been applied in previous studies to reproduce the experimental data.^{9, 11}

To fit the autocorrelations with equation S5, an additional variable offset was used, although this offset was always close to zero. Subsequently, Λ_{\pm} and C_{\pm} were fitted globally for different excitation intensities with equations S6 and S7, respectively.

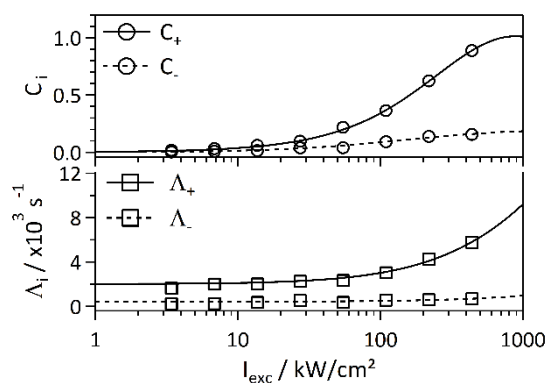


Figure S3-11. Intensity dependence of the contrasts C_i (o) and decay parameters λ_i (\square) of the low temperature correlation function for a single **DBOV-DMEP** molecule. The drawn lines are fits of equations S6 and S7 to the data.

All contrasts C were corrected with the background (B) to signal (S) ratio using the following relation⁷:

$$C = \left(1 + \frac{B}{S}\right)^2 C_{exp} \quad (\text{S11})$$

References

- (1) Sens, R.; Drexhage, K. H. Fluorescence quantum yield of oxazine and carbazine laser dyes. *J. Lumin.* **1981**, 24-25, 709-712.
- (2) Gaussian 09, R. D., M. J. Frisch, G. W. Trucks, H. B. Schlegel, G. E. Scuseria, M. A. Robb, J. R. Cheeseman, G. Scalmani, V. Barone, B. Mennucci, G. A. Petersson, H. Nakatsuji, M. Caricato, X. Li, H. P. Hratchian, A. F. Izmaylov, J. Bloino, G. Zheng, J. L. Sonnenberg, M. Hada, M. Ehara, K. Toyota, R. Fukuda, J. Hasegawa, M. Ishida, T. Nakajima, Y. Honda, O. Kitao, H. Nakai, T. Vreven, J. A. Montgomery, Jr., J. E. Peralta, F. Ogliaro, M. Bearpark, J. J. Heyd, E. Brothers, K. N. Kudin, V. N. Staroverov, T. Keith, R. Kobayashi, J. Normand, K. Raghavachari, A. Rendell, J. C. Burant, S. S. Iyengar, J. Tomasi, M. Cossi, N. Rega, J. M. Millam, M. Klene, J. E. Knox, J. B. Cross, V. Bakken, C. Adamo, J. Jaramillo, R. Gomperts, R. E. Stratmann, O. Yazyev, A. J. Austin, R. Cammi, C. Pomelli, J. W. Ochterski, R. L.

Martin, K. Morokuma, V. G. Zakrzewski, G. A. Voth, P. Salvador, J. J. Dannenberg, S. Dapprich, A. D. Daniels, O. Farkas, J. B. Foresman, J. V. Ortiz, J. Cioslowski, and D. J. Fox, Gaussian, Inc., Wallingford CT, 2013.

(3) Coles, D. M.; Chen, Q.; Flatten, L. C.; Smith, J. M.; Müllen, K.; Narita, A.; Lidzey, D. G. Strong Exciton-Photon Coupling in a Nanographene Filled Microcavity. *Nano Lett.* **2017**, *17* (9), 5521-5525.

(4) Frederickson, C. K.; Zakharov, L. N.; Haley, M. M. Modulating Paratropicity Strength in Diareno-Fused Antiaromatics. *J. Am. Chem. Soc.* **2016**, *138* (51), 16827-16838.

(5) Schleyer, P. V. R.; Maerker, C.; Dransfeld, A.; Jiao, H.; van Eikema Hommes, N. J. R. Nucleus-Independent Chemical Shifts: A Simple and Efficient Aromaticity Probe. *J. Am. Chem. Soc.* **1996**, *118* (26), 6317-6318.

(6) Chen, Z.; Wannere, C. S.; Corminboeuf, C.; Puchta, R.; Schleyer, P. Nucleus-independent chemical shifts (NICS) as an aromaticity criterion. *Chem. Rev.* **2005**, *105* (10), 3842-3888.

(7) Bernard, J.; Fleury, L.; Talon, H.; Orrit, M. Photon bunching in the fluorescence from single molecules: A probe for intersystem crossing. *J. Chem. Phys.* **1993**, *98* (2), 850-859.

(8) Novotny, L.; Hecht, B., *Principles of Nano-Optics*; Cambridge University Press: Cambridge, 2012.

(9) Fleury, L.; Segura, J.; Zumofen, G.; Hecht, B.; Wild, U. P. Nonclassical photon statistics in single-molecule fluorescence at room temperature. *Phys. Rev. Lett.* **2000**, *84* (6), 1148-1151.

(10) Verhart, N. R.; Navarro, P.; Faez, S.; Orrit, M. Intersystem crossing rates of single perylene molecules in ortho-dichlorobenzene. *Phys. Chem. Chem. Phys.* **2016**, *18* (26), 17655-17659.

(11) Banasiewicz, M.; Morawski, O.; Wiącek, D.; Kozankiewicz, B. Triplet population and depopulation rates of single terrylene molecules in p-terphenyl crystal. *Chem. Phys. Lett.* **2005**, *414* (4-6), 374-377.

Chapter 4. Synthesis and Helical Supramolecular Organization of Discotic Liquid Crystalline Dibenzo[*hi,st*]ovalene

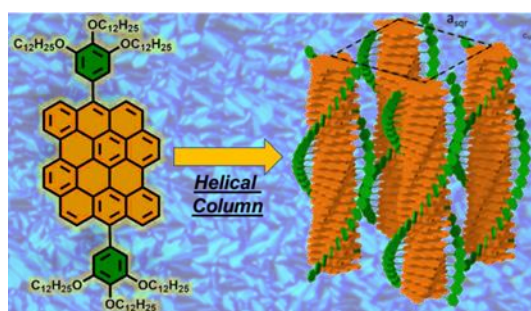
This Chapter is based on the following manuscript–

J. Mater. Chem. C, 2019, 7, 12898–12906

Qiang Chen,[#]

Author contributions. Q. C. designed, synthesized and characterized the compound investigated in this research under the supervision of [REDACTED] and [REDACTED]. [REDACTED] conducted the POM and 2D-WAX and –SAXS measurements under the supervision of [REDACTED]. [REDACTED] measured the STM under supervision of [REDACTED]. The manuscript was written through contributions of all authors.

TOC Figure



Novel dibenzo[*hi,st*]ovalene derivative (DBOV-TDOP) was synthesized to show an ordered helical hexagonal columnar assembly at room temperature.

Reprinted with permission from (*J. Mater. Chem. C*, 2019, in press, DOI: 10.1039/C9TC03350E). Copyright © 2019, RSC.

Abstract: Dibenzo[*hi, st*]ovalene (DBOV) has emerged as a new polycyclic aromatic hydrocarbon (PAH) with intriguing optical properties with strong red emission. Nevertheless, DBOV derivatives thus far synthesized either had mesityl groups that hinder the π - π stacking of the aromatic cores or showed low solubility, and the self-assembly of DBOVs has not been investigated. In this work, two 3,4,5-tris(dodecyloxy)phenyl (TDOP) groups are introduced at the *meso*-positions of DBOV in order to enhance its solubility without compromising the intermolecular interactions. The obtained **DBOV-TDOP** forms at elevated temperatures a discotic liquid crystalline phase. Due to π - π -stacking interactions as well as local phase separation between the aromatic cores and the flexible alkoxy side chains, the **DBOV-TDOP** molecules self-assemble into columnar stacks. In the low temperature phase, the space demanding TDOP substituents induce a rotation of the discs towards each other leading to an exceptionally long helical pitch within the columnar structures. Moreover, scanning tunnelling microscopy (STM) elucidates intriguing self-assembly of **DBOV-TDOP** at the interface of highly oriented pyrolytic graphite (HOPG) and 1-phenyloctane (PO). Individual molecules are visualized by STM, revealing that the alkyl chains protrude from the surface into the solution and suggesting that self-assembled bilayer film structure is predominantly formed.

Introduction

Polycyclic aromatic hydrocarbons (PAHs) are attractive molecules not only because of their intriguing (opto)electronic and photophysical properties, but also for their unique self-assembly behaviour induced by the large aromatic core structures. A wide range of applications has thus been proposed for PAHs, not only as semiconductor materials in organic field-effect transistors and light-emitting devices, but also as fluorescent dyes in bioimaging.¹⁻
¹⁴ The supramolecular organization of the disc-shaped PAH molecules is of particular interest, leading to various self-assembled structures such as columns, nanotubes, and micelles.¹⁵⁻²³ The combination of the rigid PAH cores with flexible aliphatic chains at the peripheral positions can induce a phase separation between these two components at the molecular level, resulting in the formation of columnar structures due to the strong intermolecular π - π interactions, and discotic liquid crystalline (LC) properties.²⁴⁻³⁵ Triphenylene, perylene and hexa-*peri*-hexabenzocoronene (HBC) derivatives are representative examples, which have been extensively studied with a variety of peripheral substituents, demonstrating controllable self-assembly behaviour and high charge-carrier mobility along the column direction.^{21, 36-38}

Their intermolecular packing can be tuned by attaching soft chains to provide supramolecular structures with specific organization, such as columnar self-assemblies with controlled rotation angle as well as intra- and intercolumnar distances.^{21, 32} PAHs larger than HBC, as well as non-planar bowl-shaped PAHs, such as corannulene and sumanene were demonstrated to be also applicable as discotic LC materials.^{23, 39-42} Nevertheless, the LC behaviours of PAHs other than triphenylenes, HBCs and perylenes are still underexplored and there is so far only a limited number of PAHs that are known to show LC properties. In particular, LC PAHs with smaller HOMO-LUMO gaps are seldom reported, despite the interest in their longer-wavelength absorption and emission as well as potential to achieve higher charge-carrier mobilities.⁴³

Further, two-dimensional (2D) self-assembly of PAHs has been studied at the liquid-solid interface between an organic solvent and highly-oriented pyrolytic graphite (HOPG). For studies at the liquid-solid interface PAHs are often substituted with long or bulky aliphatic groups at the periphery to increase their solubility. For example, alkoxy-substituted extended triphenylenes were found to form ordered monolayers at the 1,2,4-trichlorobenzene (TCB)/HOPG interface with a hexagonal structure.⁴⁴ A representative result with a larger PAH was reported in 1995, demonstrating that HBC substituted with six alkyl chains can form 2D self-assembled structures at the liquid-solid interface.⁴⁵ The HBC core extended with four additional K-regions has been shown to form a highly ordered monolayer at the TCB/HOPG interface, extending defect-free area over several hundred square nanometers, but with occasional molecular stacking on top of the first layer.⁴⁶ In contrast thereto, unsubstituted HBC has been shown to form complete bilayers at the TCB/HOPG interface.⁴⁷ Under ultra-high vacuum (UHV) conditions and at low temperatures, perchlorinated HBC has been studied on the Au(111) surface, revealing formation of islands of highly ordered supramolecular networks even at coverages lower than a full monolayer.⁴⁸ More recently, we have observed preferential bilayer formation of triply-fused nanographene-porphyrin-nanographene conjugates at the TCB/HOPG interface.⁴⁹ However, reported self-assemblies of PAHs at liquid-solid interfaces are predominantly monolayers, and formation of such self-assembled bilayers, where intermolecular interactions are stronger than the molecule-surface interactions, still remains rare.⁵⁰

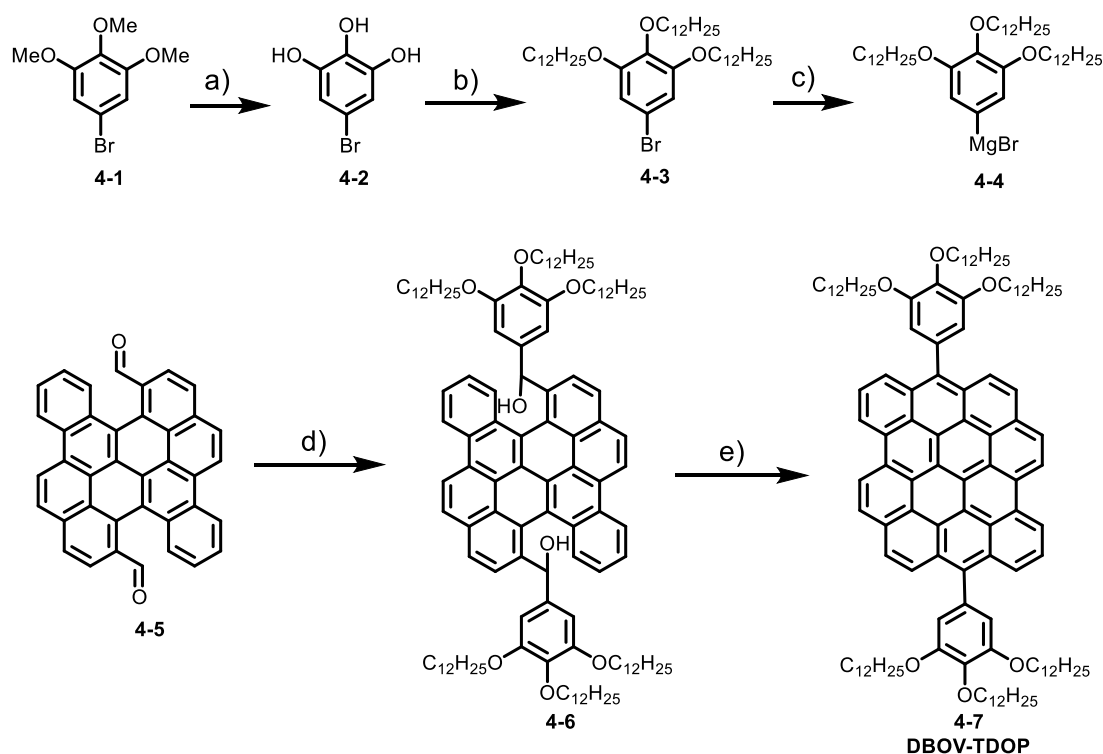
We recently reported the synthesis of a new type of nanographene, namely dibenzo[*hi, st*]ovalene (DBOV) with both zigzag and armchair edge structures, showing intensive absorption and emission in the visible light region.^{51, 52} The molecules also revealed

stimulated emission in a polystyrene matrix, which is crucial for potential applications in organic lasers or optical amplifiers.⁵³ Moreover, this molecule has high chemical stability under ambient conditions, allowing easy processing and potentially long-term device application. However, derivatives of DBOV that have so far been synthesized were substituted with mesityl groups, which prevent the π - π stacking of the aromatic cores, or had low solubility.^{51, 52, 54, 55} Packing mode in the solid state and self-assembly behaviour at solid/liquid interface of substituted DBOV derivatives with a new type of aromatic core remained so far unknown, although such information will be essential for further implementation of them in (opto)electronic devices.

Herein, we report a synthesis of a DBOV derivative functionalized with two 3,4,5-tris(dodecyloxy)phenyl substituents (**DBOV-TDOP**, Scheme 4-1). TDOP groups were selected in order to enhance the solubility without significantly affecting the π - π interactions between the DBOV cores, in comparison to the mesityl group with two *ortho*-methyl groups. The structure of **DBOV-TDOP** was unambiguously characterized by a combination of nuclear magnetic resonance (NMR) spectroscopy, high resolution matrix-assisted laser desorption/ionization time of flight mass spectroscopy (MALDI-TOF MS), and the optoelectronic properties were studied by UV-vis absorption and fluorescence spectroscopy. The large rigid aromatic core has strong tendency to aggregate with the long *n*-dodecyl chains stretched to the periphery, enabling the formation of columnar self-assembly structures. The phase formation and self-assembly in the solid state was investigated by differential scanning calorimetry (DSC), polarized optical microscopy (POM), and two-dimensional wide- and small-angle X-ray scattering (2D-WAXS and -SAXS), which clearly indicated its packing into helical stacks with an exceptionally long pitch. It has been proven that the helical packing can be well controlled by attaching side alkyl chains with a suitable steric demand, while a tight packing and good intracolumnar order were maintained. In addition, this molecule tends to form bilayer structures at the interface of HOPG and 1-phenyloctane (PO) due to strong intermolecular interactions.

Results and Discussion

Synthesis and characterization of DBOV-TDOP



Scheme 4-1. Synthetic route towards 6,14-bis{3,4,5-tris(dodecyloxy)phenyl}dibenzo-[*hi,st*]ovalene (**DBOV-TDOP**). Reaction conditions: a) BBr_3 , $-78\text{ }^\circ\text{C}$ to r.t., overnight, 98% yield; b) $\text{C}_{12}\text{H}_{25}\text{Br}$, K_2CO_3 , *N,N*-dimethylformimide, $80\text{ }^\circ\text{C}$, 20 h, 63% yield; c) Mg, I_2 , tetrahydrofuran, reflux, overnight; d) **4-4**, tetrahydrofuran, 4 h, room temperature; e) $\text{BF}_3\cdot\text{OEt}_2$, dichloromethane, room temperature, overnight, then *p*-chloranil, 2 h, 85% yield in three steps.

DBOV-TDOP was synthesized as shown in Scheme 4-1. First, 5-bromo-1,2,3-tris(dodecyloxy)benzene (**4-3**) was synthesized from 5-bromo-1,2,3-trimethoxybenzene (**4-1**) through a sequence of demethylation with BBr_3 and three-fold nucleophilic substitution with 1-dodecanol. Then Grignard reagent **4-4** was prepared by refluxing **4-3** and magnesium turning in tetrahydrofuran with I_2 as initiator. 5,14-diformylbenzo[*a*]dinaphtho[2,1,8-*cde*:1',2',3',4'-*ghi*]perylene (**4-5**)^{52, 56} was subsequently treated with Grignard reagent **4-4** at room temperature followed by quenching with NH_4Cl to give diol intermediate **4-6**, which was subjected to $\text{BF}_3\cdot\text{OEt}_2$ promoted Friedel-Crafts reaction and oxidation by *p*-chloranil to afford **DBOV-TDOP** with a high yield of 85% in three steps. This compound showed high solubility in dichloromethane, tetrahydrofuran or toluene, which allowed unambiguous characterization of its structure in solution.

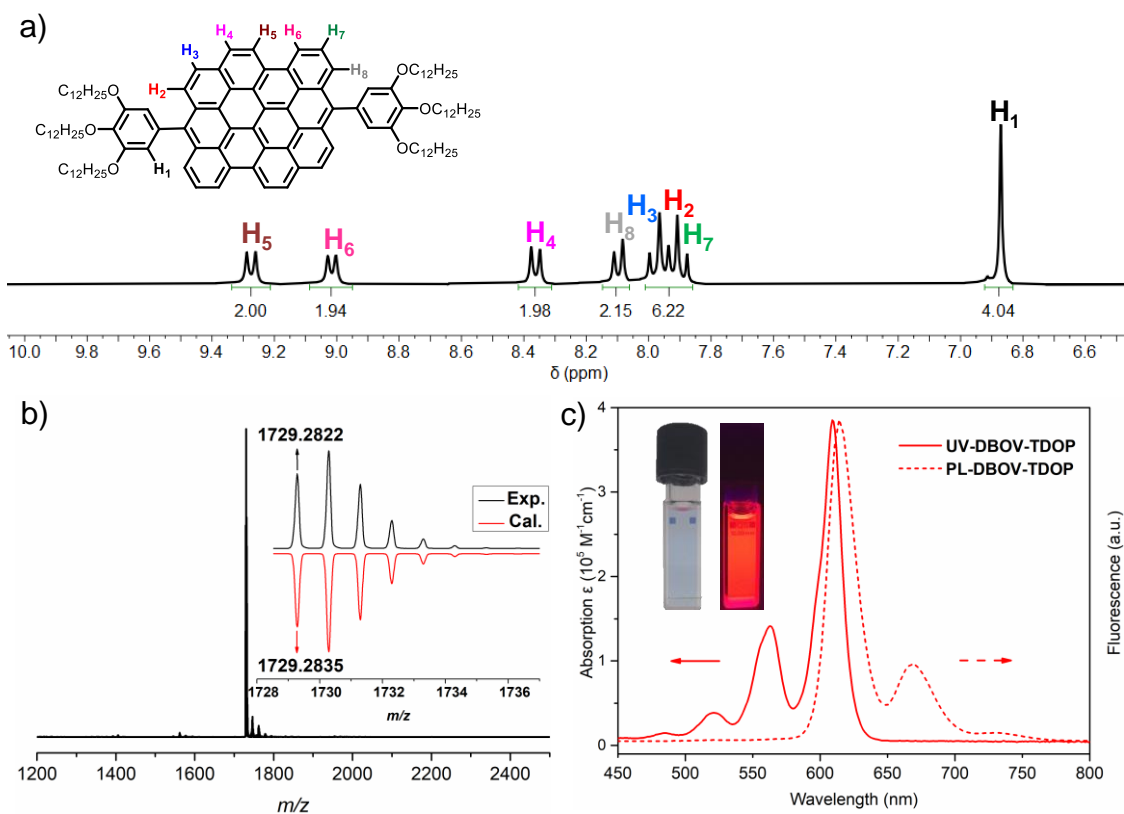


Figure 4-1. a) ^1H NMR spectra of **DBOV-TDOP** in $[\text{D}_8]\text{THF}:\text{CS}_2 = 2:1$; b) HR MALDI-TOF MS spectrum of **DBOV-TDOP**, inset: magnified spectrum showing isotopic distribution pattern in comparison with theoretical calculation; c) UV-vis absorption and fluorescence spectra of **DBOV-TDOP** measured in toluene solution with concentration of 10^{-6} M, inset shows pictures of toluene solution under room light (left) and UV light (right).

As shown in Figure 4-1a, well-resolved sharp peaks are observed in its ^1H NMR spectrum, which could be assigned with two-dimensional NMR techniques (see Figure S4-1–S4-2). High-resolution (HR) MALDI-TOF MS spectra (Figure 4-1b) exhibited one intense peak with m/z of 1729.2822, in very good agreement with the calculated value of 1729.2835. The UV-vis absorption was measured in toluene at a concentration of 10^{-6} M (Figure 4-1c). Similar to other DBOV derivatives,^{51, 52, 54, 55} the maximum absorption wavelength (λ_{max}) is located at 609 nm with very high extinction coefficient of $3.85 \times 10^5 \text{ M}^{-1}\text{cm}^{-1}$. Three characteristic shoulder peaks are observed at shorter wavelength, arising from the vibronic coupling involving C=C stretch. The solution showed very strong red fluorescence with maximum emission peak wavelength at 615 nm. Small Stokes shift of only 6 nm indicates its rigid core structure and minor energy loss in the excited state. Moreover, high relative fluorescence

quantum yield (Φ) of 0.89 was measured with Nile blue A perchlorate as standard,⁵⁷ indicating the potential of **DBOV-TDOP** for optoelectronic applications.

Solid-state self-assembly into helical columns

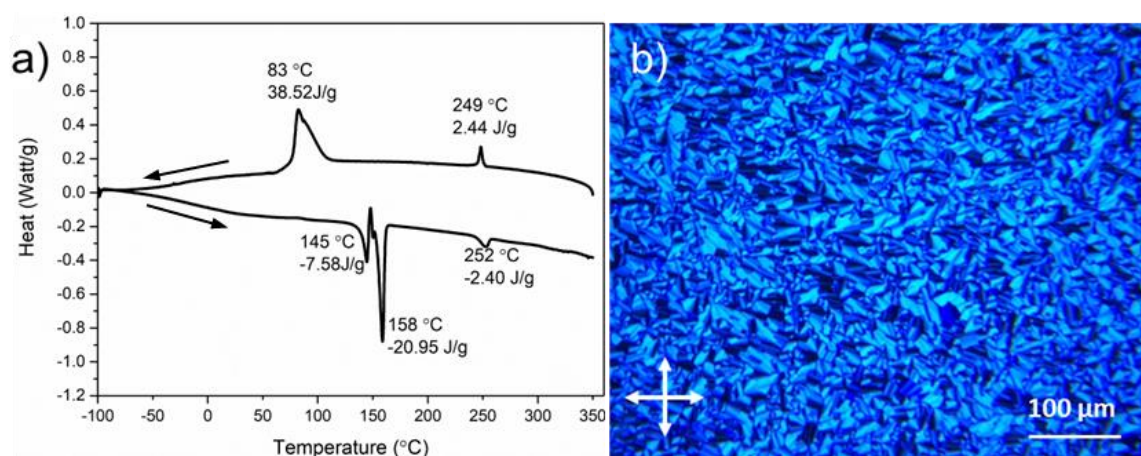


Figure 4-2. a) Differential scanning calorimetry (DSC) scans (1st cooling and 2nd heating at 10 °C/min) and b) polarized optical microscopy (POM) photograph at 150 °C of **DBOV-TDOP**.

The thermal stability of **DBOV-TDOP** was investigated by thermogravimetric analysis (TGA), which showed a high decomposition temperature of up to 365 °C (5% weight loss, Figure S4-3). The attachment of the six dodecyloxy chains induced distinct thermotropic properties which were studied by DSC and POM. The 2nd DSC heating scan showed two prominent peaks (Figure 4-2a). The first peak at 145 °C was attributed to the reorganization of the side chains, while the second at 158 °C was related to the melting into the liquid crystalline phase. The clearing temperature for the compound was found at 252 °C and was confirmed by POM. Cooling the compound between two glass slides under cross-polarized microscopy from its isotropic into the liquid crystalline phase resulted in a characteristic birefringent fan-shaped focal conic texture (Figure 4-2b). A typical supramolecular liquid crystalline organization was also found in the liquid crystalline phase by 2D-WAXS and -SAXS on extruded fibers. The hexagonal liquid crystalline phase typically leads to π -stacking reflections in the wide-angle range on the meridional plane of the 2DWAXS pattern and to equatorial reflections in the small angle region that are related to the hexagonal intercolumnar arrangement.⁵⁸ As derived from the positions at the ratio of $1:\sqrt{3}:2$ of the equatorial scattering intensities (Figure 4-3a,c), the **DBOV-TDOP** self-assembled into columnar stacks arranged in a hexagonal lattice. The equatorial reflections were indexed according to a hexagonal lattice parameter of $a_{\text{hex}} = 3.07$ nm (Figure 4-3e). The meridional reflections were assigned to the intracolumnar π -stacking distance of 0.36 nm. In the liquid crystalline phase, the molecular

dynamics are high and the aromatic discs can perform an axial motion around the column axes. As the thermal energy decreases at lower temperature, this molecular motion is reduced leading to higher intracolumnar order and the formation of a more complex organization.⁵⁹

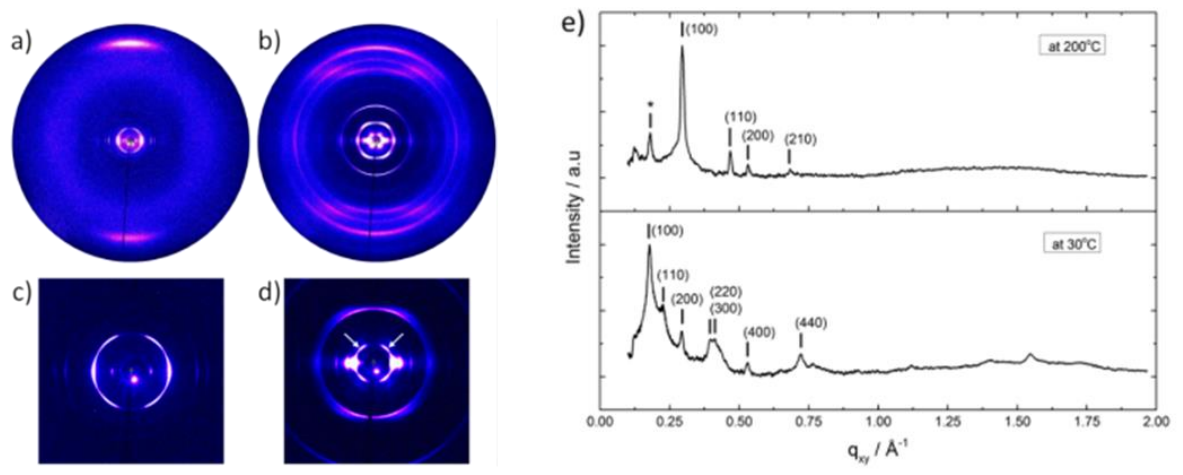


Figure 4-3. 2D-WAXS and -SAXS patterns of **DBOV-TDOP** obtained at a), c) 200 °C and b), d) 30 °C (* indicates remaining reflection from the crystalline phase; white arrows assign reflections of the first scattering line) and e) equatorial integration for both measurements (reflections are indexed by Miller indices).

Cooling the sample to the crystalline phase at 30 °C changed the supramolecular organization of **DBOV-TDOP** as indicated by the complex pattern in Figure 4-3b. The large number of new scattering intensities confirmed the higher long-range order in the crystalline phase. The π -stacking distance slightly increased to 0.37 nm, while the intercolumnar arrangement turned into a square lattice with $a_{\text{sqr}} = 5.35$ nm. The reflections with mixed indices out of the equator and of the meridian located on scattering lines was characteristic for helical packing within the stacks.⁶⁰⁻⁶² Additional off-meridional reflections in the small-angle region implied a helical intracolumnar packing of the molecules. The helical pitch of 5.55 nm was determined from the first scattering line (Figure 4-3d) and corresponded to 15 molecules per helical pitch including a 180° rotation (Figure 4-4). This exceptionally long helical pitch, in comparison to the typical pitch of around 1 nm for other PAHs, was related to good intracolumnar packing of the molecules.⁶³ A rotation of 12° between adjacent molecules in the stack was induced to overcome the steric hindrance of the out-of-plane arranged TDOP group in the periphery of the aromatic DBOV core. The strategy to control the helical organization in supramolecular columns of disc-shaped molecules by employing sterically demanding substituents has been also realized for other nanographenes,^{35, 38, 64} but for the first time for a dibenzo[*hi,st*]ovalene

of this aromatic shape. Interestingly, this concept could be applied for a DBOV core by attaching only two bulky substituents as proven in this work. Comparison to other core extended discotic PAHs, we confirmed the exceptionally long helical pitch of the DBOV molecules.⁶³ Since the corresponding reflections of mixed indices are distinct and well defined, the molecular ordering in the stacks is pronounced and the helical twist between neighboring discs is well defined. Fluctuations in the twist angle would lead to poor or none reflections related to the helical packing. The high intracolumnar order of the helical structure with such long pitch is attributed to good intermolecular π -interactions.

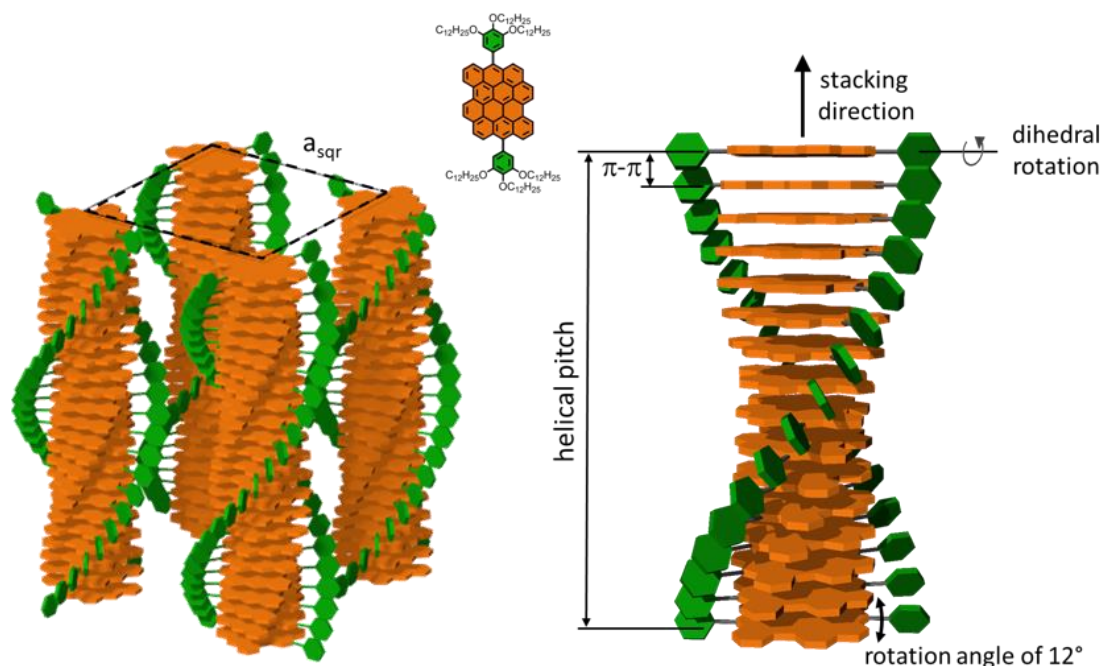


Figure 4-4. Schematic illustration of the helical organization of **DBOV-TDOP** at 30 °C. Due to π -stacking interactions, the molecules self-assemble in columnar structures that are arranged in a hexagonal fashion. In the stacks, the molecules are rotated by 12° with respect to each other and form a helix. Alkoxy side chains are omitted for clarity.

STM characterization of DBOV-TDOP

Scanning tunnelling microscopy (STM) was used to study the 2D self-assembly behaviour of **DBOV-TDOP** at the interface between PO and HOPG. A solution of **DBOV-TDOP** in PO was drop-casted on freshly-cleaved HOPG and subsequently imaged by STM at room temperature, at the liquid-solid interface. Already at a concentration of $c = 6 \times 10^{-5}$ mol/L the HOPG surface was found to be covered by a molecular layer, appearing as a row-like structure, with only a few single-molecule defects and small non-covered areas (Figure 4-5a). The apparent height of the layer was found to be approximately 0.7 nm (see inset in Figure 4-

5a). The unit cell ($a = 2.32 \pm 0.05$ nm, $b = 1.49 \pm 0.04$ nm, $\alpha = 74.8 \pm 2.0^\circ$) was determined with several drift-corrected high-resolution STM images, *i.e.* by imaging first the molecular layer and subsequently the HOPG surface underneath by changing the tunnelling parameters (Figure S4-4). A tentative model of the monolayer structure, based on high-resolution STM images and unit cell dimensions, is shown in Figure 4-5d. The molecules assemble with the DBOV cores aligned in a row-like fashion with the long molecular axes oriented perpendicular to the row direction. Adjacent rows are shifted half a molecular width, so that interdigitation of the peripheral phenyl groups allows close-packing. Single-molecule defects thereby help to identify the position in the assembly (Figure 4-5d and S4-5). The unit cell parameters indicate that the space between adjacent aromatic cores is not sufficient for the adsorption of the alkyl-chains. Thus, they are most likely desorbed from the surface and back-folded in the supernatant solution. More dilute solutions ($c = 6 \times 10^{-6}$ mol/L) lead to the formation of similar molecular assemblies, albeit with much lower surface coverage, while maintaining the same apparent height (~ 0.7 nm) (Figure 4-5b and Figure S4-6).

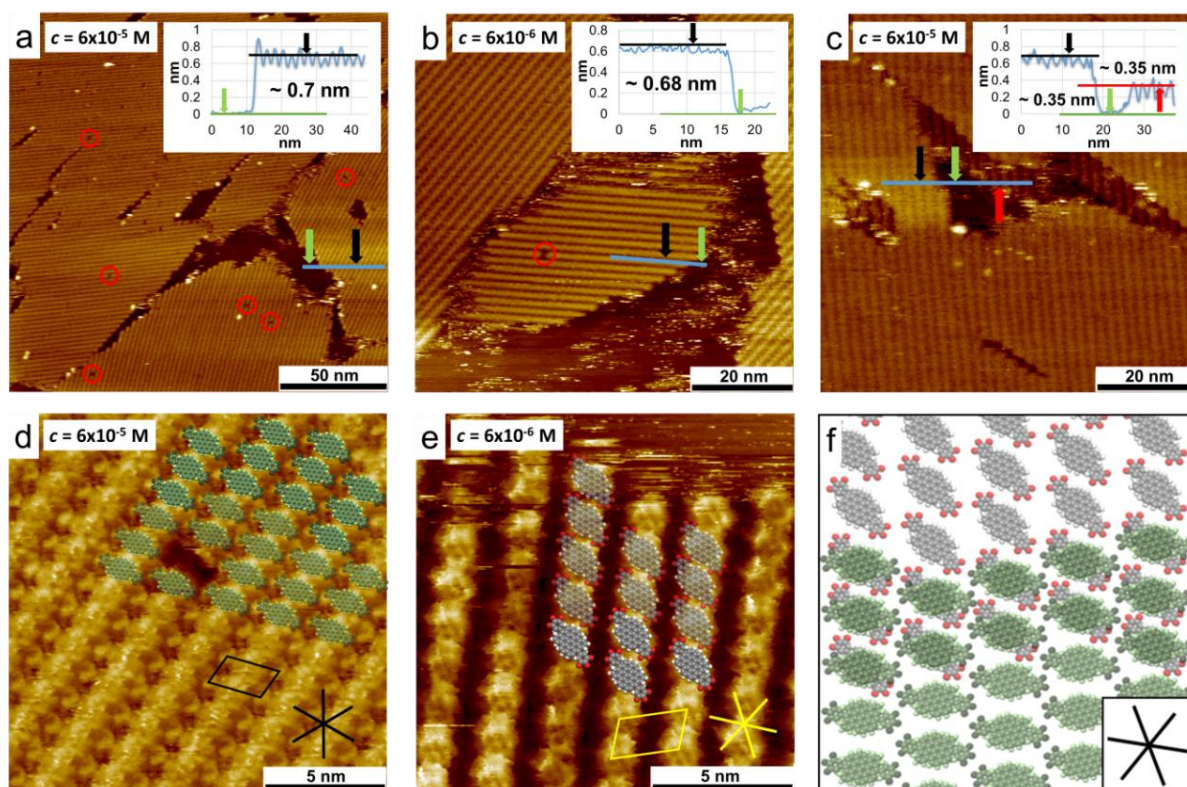


Figure 4-5. STM characterization of **DBOV-TDOP** at the PO/HOPG interface. a) Large-scale STM image showing the long-range order with few single-molecule defects (red circles) and non-covered areas ($c = 6 \times 10^{-5}$ mol/L). The line profile across a non-covered area reveals an apparent layer height of approximately 0.7 nm (see inset). b) Large-scale STM image at lower concentration ($c = 6 \times 10^{-6}$ mol/L)

showing an increase of disordered areas and the same layer height (see inset). c) STM image revealing double layer formation with an apparent height of about 0.35 nm for each layer. d) High-resolution STM images superimposed with a tentative model of the molecular assembly. e) High-resolution STM image and tentative model of the molecular assembly in the lower layer. The alkyl chains are presumably desorbed from the surface and omitted in the model for clarity. f) Superposition of the tentative molecular models for the first and second layer. Imaging parameters: a) $V_{\text{bias}} = -1.1$ V, $I_{\text{set}} = 80$ pA, b) $V_{\text{bias}} = -1.2$ V, $I_{\text{set}} = 60$ pA, c) $V_{\text{bias}} = -1.1$ V, $I_{\text{set}} = 60$ pA, d) $V_{\text{bias}} = -1.1$ V, $I_{\text{set}} = 230$ pA, e) $V_{\text{bias}} = -0.9$ V, $I_{\text{set}} = 50$ pA.

Closer inspection of the molecular layers adjacent to the uncovered areas revealed that the molecules assemble in a bilayer instead of a monolayer as evidenced by the STM image provided in Figure 4-5c, which clearly shows a lower molecular layer that extends beneath the second layer. Furthermore, high-resolution images of this lower layer show a different molecular orientation, *i.e.* the long axes of the DBOV cores are not perpendicular, but instead rotated by approximately 40° with respect to the row propagation (Figure 4-5e). A superposition of the tentative molecular assembly of the first and second layer is shown in Figure 4-5f. The DBOV cores of the molecules in the first and second layer are proposed to be at the same positions, while the long molecular axes are rotated in a way that the peripheral aryl moieties, which are assumed to be out-of-plane compared to the DBOV core, are not on top of each other, allowing a closer distance between the cores and thus increased π - π interactions. The observed preferential double layer formation even at low concentrations indicates that the π - π interactions between the DBOV cores are stronger than the DBOV-HOPG interactions. Note that additional layers above the double layer may form, which, however, could be removed by the STM tip during the imaging process.⁶⁵ Additional layers would decrease the tunnelling current and thus the STM tip would have to move closer to the surface to maintain the current setpoint, thereby removing the additional layers again while scanning. In the liquid crystalline phase, these strong π - π interactions lead to the observed columnar structures. The apparent layer height of about 0.35 nm is also comparable with the π -stacking distance of 0.36 nm found in the columnar stacks as is the relative orientation of the molecules in the first and second layer.

Conclusion

In conclusion, we reported the synthesis of the discotic dibenzo[*hi,st*]ovalene molecule functionalized with two 3,4,5-tris(dodecyloxy)phenyl groups at the *meso*-positions. The self-assembly behavior of this molecule was extensively investigated. The attachment of 1,2,3-

tris(dodecyloxy)phenyl substituents induced thermotropic properties and self-assembly into columnar structures of **DBOV-TDOP**. Due to the distinct steric demand of the side groups, the molecules arranged in a helical fashion in the stacks. Interestingly, an especially long helical pitch is found indicating a tight molecular packing and high intracolumnar order despite the pronounced steric hindrance of the substituents. A well-defined rotation of the aromatic cores together with long-range ordering in the columnar stacks are prerequisites for an unhindered intrinsic charge carrier transport in discotic liquid crystals. Additionally, at the liquid-solid interface, large-area bilayer film formation was observed even at low concentrations as a result of the strong intermolecular π - π interactions. The tendency to form self-organized and well-defined supramolecular structures, both columns and film, makes **DBOV-TDOP** a promising candidate for fabricating electronic devices.

Experimental Methods

General

All reactions working with air- or moisture- sensitive compounds were carried out under argon atmosphere using standard Schlenk line techniques. Thin layer chromatography (TLC) was done on silica gel coated aluminum sheets with F254 indicator and column chromatography separation was performed with silica gel (particle size 0.063–0.200 mm). Nuclear Magnetic Resonance (NMR) spectra were recorded using Bruker DPX 300 MHz NMR spectrometers. Chemical shifts (δ) were expressed in ppm relative to the residual of solvents (CD_2Cl_2 , ^1H : 5.32 ppm, ^{13}C : 53.84 ppm; $\text{THF-}d_8$, ^1H : 3.58 ppm, ^{13}C : 67.57 ppm). Coupling constants (J) were recorded in Hertz. High resolution mass spectra (HR MS) were recorded on a Bruker Reflex II-TOF spectrometer by matrix-assisted laser decomposition/ionization (MALDI) using 7,7,8,8-tetracyanoquinodimethane (TCNQ) as matrix and calibrated against poly(ethylene glycol). Thermogravimetric analysis (TGA) was measured on a Mettler Toledo TGA-851 system with a heating speed of 10 K/min under nitrogen atmosphere. Differential scanning calorimetry (DSC) was recorded on a Mettler DSC 30 instrument with a heating speed of 10 K/min under nitrogen atmosphere. UV-*vis* absorption spectra were recorded on a Perkin-Elmer Lambda 900 spectrometer at room temperature using a 10 mm quartz cell. Photoluminescence spectra were recorded on a J&MTIDAS spectrofluorometer. The fluorescence quantum yield (Φ) was measured using Nile blue A perchlorate (in ethanol under air, $\Phi = 0.27$) as a reference.⁵⁷

Materials

Unless otherwise noted, all starting materials and reagents were purchased from commercial sources and used without further purification. The synthesis of 5,14-diformylbenzo[*a*]dinaphtho[2,1,8-cde:1',2',3',4'-ghi]perylene (**4-5**) is described in our previously report,⁵² and we also used an improved synthetic route, which we have more recently developed.⁵⁶

Synthesis of 5-bromo-1,2,3-tris(dodecyloxy)benzene (**4-3**)

5-Bromo-1,2,3-trimethoxybenzene (**4-1**) (2.5 g, 10 mmol) was dissolved in dry dichloromethane (30 mL), and the solution was cooled down to $-78\text{ }^{\circ}\text{C}$. BBr_3 (8.26 g, 33.0 mmol) was added dropwise to the solution then the reaction mixture was gradually warmed up to room temperature and stirred overnight. After completion of reaction, the mixture was poured into 100 mL of ice water and extracted with ethyl acetate (100 mL) for three times. The organic layers were combined, washed with brine (100 mL) and dried over Na_2SO_4 . After evaporation of the solvent and drying under reduced pressure, a crude product of 5-bromobenzene-1,2,3-triol (**4-2**) (2.0 g, 98%) was obtained as white solid, which was used directly for the next step without further purification. To a 100-mL Schlenk flask was added the crude product of 5-bromobenzene-1,2,3-triol (**4-2**) (2.0 g, 9.8 mmol), 1-bromododecyl (9.92 g, 40.0 mmol) and K_2CO_3 (5.52 g, 40.0 mmol). The flask was evacuated and backfilled with argon for three times before *N,N*-dimethylformamide (50 mL) was added. After stirring at $80\text{ }^{\circ}\text{C}$ for 20 h, the mixture was cooled down to room temperature and diluted with ethyl acetate (200 mL), washed with water (50 mL) and brine (50 mL), dried over Na_2SO_4 and evaporated. The obtained residue was purified by silica gel column chromatography (eluent: *n*-hexane) and recrystallized with ethanol to give 5-bromo-1,2,3-tris(dodecyloxy)benzene (**4-3**) (4.5 g, 63% yield over two steps) as white solid. ^1H NMR (300 MHz, Methylene Chloride-*d*₂) δ 6.68 (s, 2H), 3.97 – 3.83 (m, 6H), 1.85 – 1.72 (m, 4H), 1.72 – 1.62 (m, 2H), 1.51 – 1.39 (m, 6H), 1.39 – 1.22 (m, 48H), 0.94 – 0.82 (m, 9H); ^{13}C NMR (75 MHz, Methylene Chloride-*d*₂) δ 154.3, 137.8, 115.8, 110.3, 73.8, 69.7, 32.4, 30.7, 30.2, 30.2, 30.1, 30.1, 30.1, 30.0, 29.8, 29.8, 29.7, 26.5, 26.5, 23.1, 14.3; HRMS (MALDI-TOF): m/z Calcd for $\text{C}_{42}\text{H}_{77}\text{BrO}_3$: 708.5056 $[\text{M}]^+$, found: 708.5005.

Synthesis of DBOV-TDOP (**4-7**)

To a 25-mL Schlenk tube was added magnesium turnings (27 mg, 1.1 mmol), I_2 (3 mg, 0.01 mmol) and tetrahydrofuran (1 mL). The mixture was gently heated while approximately 1 mL

of 5-bromo-1,2,3-tris(dodecyloxy)benzene (**4-3**) (568 mg, 0.800 mmol) dissolved in tetrahydrofuran (THF) (3 mL) was added. As soon as the solution became colorless, the remaining solution was added dropwise under mild reflux and stirring was continued overnight. The obtained solution of Grignard reagent (4 mL) was transferred to a solution of 5,14-diformylbenzo[*a*]dinaphtho[2,1,8-*cde*:1',2',3',4'-*ghi*]perylene (**4-5**) (25 mg, 0.049 mmol) in dry THF (30 mL). After stirring at room temperature for 4 h, the reaction was quenched by addition of saturated NH₄Cl solution (15 mL). After stirring for 15 min, the solution was extracted with ethyl acetate (50 mL) for three times. The combined organic layers were washed with brine, dried with Na₂SO₄ and evaporated. The residue was dried under vacuum for 2 h and dissolved in anhydrous dichloromethane (30 mL). After bubbling with argon saturated with dichloromethane vapour for 15 min, BF₃·OEt₂ (0.1 mL) was added and the stirring was continued overnight. After quenching with methanol (2 mL), *p*-chloranil (12 mg, 0.049 mmol) was added and the mixture was stirred for 2 h at room temperature. The solvent was evaporated and the residue was purified by silica gel column chromatography (eluent: *n*-hexane:dichloromethane = 3:1 to 0:1) to give the title compound (72 mg, 85% yield) as blue solid. ¹H NMR (300 MHz, THF-*d*₈) δ 9.27 (d, *J* = 8.5 Hz, 2H), 9.02 (d, *J* = 7.7 Hz, 2H), 8.36 (d, *J* = 8.4 Hz, 2H), 8.10 (d, *J* = 8.3 Hz, 2H), 7.97 (t, *J* = 9.1 Hz, 4H), 7.89 (d, *J* = 9.3 Hz, 2H), 6.87 (s, 4H), 4.16 (t, *J* = 6.2 Hz, 4H), 4.05 (t, *J* = 6.2 Hz, 8H), 1.97 – 1.79 (m, 15H), 1.69 – 1.61 (m, 4H), 1.61 – 1.15 (m, 119H), 0.97 – 0.80 (m, 18H); ¹³C NMR (75 MHz, THF-*d*₈) δ 139.1, 137.5, 134.9, 132.7, 132.5, 131.3, 130.3, 130.1, 128.9, 127.9, 127.5, 127.3, 126.5, 125.5, 125.1, 124.7, 124.3, 123.6, 123.4, 122.1, 121.4, 111.0, 74.0, 70.0, 33.2, 33.1, 31.9, 31.1, 31.1, 31.1, 31.0, 30.9, 30.9, 30.8, 30.7, 30.7, 30.6, 27.6, 27.4, 23.9, 23.9, 14.9, 14.9; HRMS (MALDI-TOF): *m/z* Calcd for C₁₂₂H₁₆₈O₆: 1729.2841 [M]⁺, found: 1729.2822.

POM

The optical textures of the compound were investigated using a Zeiss microscope with polarizing filters equipped with a Hitachi KP-D50 colour digital CCD camera. The samples were sandwiched between two glass slides and thermally treated on a Linkam hot stage regulated with a Linkam TMS 91 temperature controller.

2DWAXS and -SAXS

2DWAXS and -SAXS measurements were performed using a setup consisting of copper solid-anode X-ray tube (Bruker AXS Krystalloflex 760, operated at 35 kV and 30 mA),

Osmic confocal MaxFlux optics and a three pin-hole collimation system. The fiber samples for the measurements were prepared by extrusion at 25 °C and were positioned perpendicular to the incident X-ray beam and vertical to the 2D detector. The scattering intensity was detected on a 2-D image plate (MAR-345) with a pixel size of 100 μm (2345 \times 2345 pixels). Scattering data are expressed as a function of the scattering vector: $q=4\pi/\lambda \sin(\Theta)$, where Θ is a half the scattering angle and $\lambda=0.154 \text{ \AA}$ is the wavelength of the incident radiation. All X-ray scattering measurements were performed under vacuum (~ 20 mbar) to reduce air scattering and beam damage to the sample. All 2DWAXS data processing and analysis was performed by using the software package Datasqueeze (<http://www.datasqueezesoftware.com>).

STM

STM measurements were performed with a Molecular Imaging or Agilent PicoLE system in constant-current mode (PicoSPM) at the 1-phenyloctane/highly-oriented pyrolytic graphite (PO/HOPG) interface at room temperature (20–22 °C). The imaging parameters I_{set} (tunneling current) and V_{bias} (substrate bias) are indicated in the figure captions. STM tips were obtained by mechanical cutting of a Pt/Ir wire (80%/20%, diameter 0.25 mm). Immediately before use, the HOPG substrate (grade ZYB, Advanced Ceramics) was freshly cleaved using adhesive tape. The solvent, 1-phenyloctane (Sigma-Aldrich, 98%), was used without further purification. Scanning Probe Imaging Processor (SPIP 6.5.1) software from Image Metrology ApS was used for STM image processing.

Conflicts of interest

There are no conflicts to declare.

Acknowledgements

We are grateful for the financial support from the Max Planck Society and the Fund of Scientific Research Flanders (FWO) under EOS 30489208. J. S. acknowledges financial support through a Marie Skłodowska-Curie Individual Fellowship (EU project 789865 - EnSurf). Open Access funding provided by the Max Planck Society.

References

- (1) Watson, M. D.; Fechtenkötter, A.; Müllen, K. Big Is Beautiful—"Aromaticity" Revisited from the Viewpoint of Macromolecular and Supramolecular Benzene Chemistry. *Chem Rev* **2001**, *101*, 1267-1300.
- (2) Narita, A.; Wang, X. Y.; Feng, X.; Müllen, K. New advances in nanographene chemistry. *Chem Soc Rev* **2015**, *44*, 6616-6643.
- (3) Pisula, W.; Feng, X.; Müllen, K. Charge-Carrier Transporting Graphene-Type Molecules. *Chem Mater* **2011**, *23*, 554-567.
- (4) Ye, Q.; Chi, C. Recent Highlights and Perspectives on Acene Based Molecules and Materials. *Chem Mater* **2014**, *26*, 4046-4056.
- (5) Li, J.; Zhang, Q. Linearly Fused Azaacenes: Novel Approaches and New Applications Beyond Field-Effect Transistors (FETs). *ACS Appl Mater Interf* **2015**, *7*, 28049-28062.
- (6) Zhang, L.; Cao, Y.; Colella, N. S.; Liang, Y.; Bredas, J. L.; Houk, K. N.; Briseno, A. L. Unconventional, chemically stable, and soluble two-dimensional angular polycyclic aromatic hydrocarbons: from molecular design to device applications. *Acc Chem Res* **2015**, *48*, 500-509.
- (7) Ball, M.; Zhong, Y.; Wu, Y.; Schenck, C.; Ng, F.; Steigerwald, M.; Xiao, S.; Nuckolls, C. Contorted polycyclic aromatics. *Acc Chem Res* **2015**, *48*, 267-276.
- (8) Gupta, R. K.; Sudhakar, A. A. Perylene-Based Liquid Crystals as Materials for Organic Electronics Applications. *Langmuir* **2019**, *35*, 2455-2479.
- (9) Meng, D.; Liu, G.; Xiao, C.; Shi, Y.; Zhang, L.; Jiang, L.; Baldrige, K. K.; Li, Y.; Siegel, J. S.; Wang, Z. Corannulylene Pentapetalae. *J Am Chem Soc* **2019**, *141*, 5402-5408.
- (10) Liu, X.; Chen, M.; Xiao, C.; Xue, N.; Zhang, L. Soluble Twisted Diarenoperylene: Synthesis, Characterization, and Device Performance. *Org Lett* **2018**, *20*, 4512-4515.
- (11) Cui, X.; Xiao, C.; Winands, T.; Koch, T.; Li, Y.; Zhang, L.; Doltsinis, N. L.; Wang, Z. Hexacene Diimides. *J Am Chem Soc* **2018**, *140*, 12175-12180.
- (12) Li, J.; Zhou, K.; Liu, J.; Zhen, Y.; Liu, L.; Zhang, J.; Dong, H.; Zhang, X.; Jiang, L.; Hu, W. Aromatic Extension at 2,6-Positions of Anthracene toward an Elegant Strategy for Organic Semiconductors with Efficient Charge Transport and Strong Solid State Emission. *J Am Chem Soc* **2017**, *139*, 17261-17264.
- (13) Ruiz, C.; Pandey, U. K.; Termine, R.; Garcia-Frutos, E. M.; Lopez-Espejo, G.; Ortiz, R. P.; Huang, W.; Marks, T. J.; Facchetti, A.; Ruiz Delgado, M. C.; Golemme, A.; Gomez-Lor,

- B. Mobility versus Alignment of a Semiconducting pi-Extended Discotic Liquid-Crystalline Triindole. *ACS Appl Mater Interf* **2016**, *8*, 26964-26971.
- (14) Lin, H. A.; Sato, Y.; Segawa, Y.; Nishihara, T.; Sugimoto, N.; Scott, L. T.; Higashiyama, T.; Itami, K. A Water-Soluble Warped Nanographene: Synthesis and Applications for Photoinduced Cell Death. *Angew Chem Int Ed* **2018**, *57*, 2874-2878.
- (15) Kaafarani, B. R. Discotic Liquid Crystals for Opto-Electronic Applications. *Chem Mater* **2011**, *23*, 378-396.
- (16) Xiao, S.; Myers, M.; Miao, Q.; Sanaur, S.; Pang, K.; Steigerwald, M. L.; Nuckolls, C. Molecular wires from contorted aromatic compounds. *Angew Chem Int Ed* **2005**, *44*, 7390-7394.
- (17) Hill, J. P.; Jin, W.; Kosaka, A.; Fukushima, T.; Ichihara, H.; Shimomura, T.; Ito, K.; Hashizume, T.; Ishii, N.; Aida, T. Self-assembled hexa-peri-hexabenzocoronene graphitic nanotube. *Science* **2004**, *304*, 1481-1483.
- (18) Xiao, S.; Tang, J.; Beetz, T.; Guo, X.; Tremblay, N.; Siegrist, T.; Zhu, Y.; Steigerwald, M.; Nuckolls, C. Transferring self-assembled, nanoscale cables into electrical devices. *J Am Chem Soc* **2006**, *128*, 10700-10701.
- (19) Chen, Z.; Lohr, A.; Saha-Moller, C. R.; Wurthner, F. Self-assembled pi-stacks of functional dyes in solution: structural and thermodynamic features. *Chem Soc Rev* **2009**, *38*, 564-584.
- (20) Moulin, E.; Cid, J. J.; Giuseppone, N. Advances in supramolecular electronics - from randomly self-assembled nanostructures to addressable self-organized interconnects. *Adv Mater* **2013**, *25*, 477-487.
- (21) Jin, W.; Yamamoto, Y.; Fukushima, T.; Ishii, N.; Kim, J.; Kato, K.; Takata, M.; Aida, T. Systematic studies on structural parameters for nanotubular assembly of hexa-peri-hexabenzocoronenes. *J Am Chem Soc* **2008**, *130*, 9434-40.
- (22) Chen, L.; Puniredd, S. R.; Tan, Y. Z.; Baumgarten, M.; Zschieschang, U.; Enkelmann, V.; Pisula, W.; Feng, X.; Klauk, H.; Müllen, K. Hexathienocoronenes: synthesis and self-organization. *J Am Chem Soc* **2012**, *134*, 17869-17872.
- (23) Yuan, W.; Ren, X. K.; Li, M.; Guo, H.; Han, Y.; Wu, M.; Wang, Q.; Li, M.; Chen, Y. From S,N-Heteroacene to Large Discotic Polycyclic Aromatic Hydrocarbons (PAHs): Liquid Crystal versus Plastic Crystalline Materials with Tunable Mechanochromic Fluorescence. *Angew Chem Int Ed* **2018**, *57*, 6161-6165.

- (24) Laschat, S.; Baro, A.; Steinke, N.; Giesselmann, F.; Hagele, C.; Scalia, G.; Judele, R.; Kapatsina, E.; Sauer, S.; Schreivogel, A.; Tosoni, M. Discotic liquid crystals: from tailor-made synthesis to plastic electronics. *Angew Chem Int Ed* **2007**, *46*, 4832-4887.
- (25) Pal, S. K.; Setia, S.; Avinash, B. S.; Kumar, S. Triphenylene-based discotic liquid crystals: recent advances. *Liquid Crystals* **2013**, *40*, 1769-1816.
- (26) Sergeyev, S.; Pisula, W.; Geerts, Y. H. Discotic liquid crystals: a new generation of organic semiconductors. *Chem Soc Rev* **2007**, *36*, 1902-1929.
- (27) Boden, N.; Bushby, R. J.; Clements, J.; Movaghar, B. Device applications of charge transport in discotic liquid crystals. *J Mater Chem* **1999**, *9*, 2081-2086.
- (28) Kumar, S. Self-organization of disc-like molecules: chemical aspects. *Chem Soc Rev* **2006**, *35*, 83-109.
- (29) Wohrle, T.; Wurzbach, I.; Kirres, J.; Kostidou, A.; Kapernaum, N.; Litterscheidt, J.; Haenle, J. C.; Staffeld, P.; Baro, A.; Giesselmann, F.; Laschat, S. Discotic Liquid Crystals. *Chem Rev* **2016**, *116*, 1139-1241.
- (30) Pisula, W.; Zorn, M.; Chang, J. Y.; Müllen, K.; Zentel, R. Liquid crystalline ordering and charge transport in semiconducting materials. *Macromol Rapid Commun* **2009**, *30*, 1179-1202.
- (31) Warman, J. M.; Piris, J.; Pisula, W.; Kastler, M.; Wasserfallen, D.; Müllen, K. Charge recombination via intercolumnar electron tunneling through the lipid-like mantle of discotic hexa-alkyl-hexa-peri-hexabenzocoronenes. *J Am Chem Soc* **2005**, *127*, 14257-14262.
- (32) Adam, D.; Schuhmacher, P.; Simmerer, J.; Häussling, L.; Siemensmeyer, K.; Etzbach, K. H.; Ringsdorf, H.; Haarer, D. Fast photoconduction in the highly ordered columnar phase of a discotic liquid crystal. *Nature* **1994**, *371*, 141-143.
- (33) Bushby, R. J.; Lozman, O. R. Discotic liquid crystals 25 years on. *Curr Opin Colloid Interface Sci* **2002**, *7*, 343-354.
- (34) Kastler, M.; Pisula, W.; Laquai, F.; Kumar, A.; Davies, R. J.; Balushev, S.; Garcia-Gutiérrez, M. C.; Wasserfallen, D.; Butt, H. J.; Riekel, C.; Wegner, G.; Müllen, K. Organization of Charge-Carrier Pathways for Organic Electronics. *Adv Mater* **2006**, *18*, 2255-2259.
- (35) Chen, L.; Mali, K. S.; Puniredd, S. R.; Baumgarten, M.; Parvez, K.; Pisula, W.; De Feyter, S.; Müllen, K. Assembly and fiber formation of a gemini-type hexathienocoronene amphiphile for electrical conduction. *J Am Chem Soc* **2013**, *135*, 13531-13537.

- (36) Craats, A. M. v. d.; Warman, J. M.; Fechtenkötter, A.; Brand, J. D.; Harbison, M. A.; Müllen, K. Record Charge Carrier Mobility in a Room-Temperature Discotic Liquid-Crystalline Derivative of Hexabenzocoronene. *Adv Mater* **1999**, *11*, 1469-1472.
- (37) Feng, X.; Pisula, W.; Kudernac, T.; Wu, D.; Zhi, L.; De Feyter, S.; Müllen, K. Controlled self-assembly of C₃-symmetric hexa-peri-hexabenzocoronenes with alternating hydrophilic and hydrophobic substituents in solution, in the bulk, and on a surface. *J Am Chem Soc* **2009**, *131*, 4439-4448.
- (38) Pisula, W.; Tomovic, Z.; Watson, M. D.; Müllen, K.; Kussmann, J.; Ochsenfeld, C.; Metzroth, T.; Gauss, J. Helical packing of discotic hexaphenyl hexa-peri-hexabenzocoronenes: theory and experiment. *J Phy Chem B* **2007**, *111*, 7481-7487.
- (39) Nagano, T.; Nakamura, K.; Tokimaru, Y.; Ito, S.; Miyajima, D.; Aida, T.; Nozaki, K. Functionalization of Azapentabenzocorannulenes by Fivefold C-H Borylation and Cross-Coupling Arylation: Application to Columnar Liquid-Crystalline Materials. *Chem Eur J* **2018**, *24*, 14075-14078.
- (40) Shoji, Y.; Kajitani, T.; Ishiwari, F.; Ding, Q.; Sato, H.; Anetai, H.; Akutagawa, T.; Sakurai, H.; Fukushima, T. Hexathioalkyl sumanenes: an electron-donating bucky bowl as a building block for supramolecular materials. *Chem Sci* **2017**, *8*, 8405-8410.
- (41) Miyajima, D.; Tashiro, K.; Araoka, F.; Takezoe, H.; Kim, J.; Kato, K.; Takata, M.; Aida, T. Liquid crystalline corannulene responsive to electric field. *J Am Chem Soc* **2009**, *131*, 44-45.
- (42) Idelson, A.; Sterzenbach, C.; Jester, S. S.; Tschierske, C.; Baumeister, U.; Hoyer, S. A Liquid-Crystalline Phenylene-Based Shape-Persistent Molecular Spoked Wheel. *J Am Chem Soc* **2017**, *139*, 4429-4434.
- (43) Aumaitre, C.; Morin, J. F. Polycyclic Aromatic Hydrocarbons as Potential Building Blocks for Organic Solar Cells. *Chem Rec* **2019**, *19*, 1142-1154.
- (44) Yatabe, T.; Harbison, M. A.; Brand, J. D.; Wagner, M.; Müllen, K.; Samorí, P.; Rabe, J. P. Extended triphenylenes: synthesis, mesomorphic properties and molecularly resolved scanning tunneling microscopy images of hexakis(dialkoxyphenyl)triphenylenes and dodeca(alkoxy)tris(triphenylene)s. *J Mater Chem* **2000**, *10*, 1519-1525.
- (45) Stabel, A.; Herwig, P.; Müllen, K.; Rabe, J. P. Diodelike Current–Voltage Curves for a Single Molecule–Tunneling Spectroscopy with Submolecular Resolution of an Alkylated,peri-Condensed Hexabenzocoronene. *Angew Chem Int Ed* **1995**, *34*, 1609-1611.

- (46) Dumslaff, T.; Yang, B.; Maghsoumi, A.; Velpula, G.; Mali, K. S.; Castiglioni, C.; De Feyter, S.; Tommasini, M.; Narita, A.; Feng, X.; Müllen, K. Adding Four Extra K-Regions to Hexa-peri-hexabenzocoronene. *J Am Chem Soc* **2016**, *138*, 4726-4729.
- (47) Samorí, P.; Severin, N.; Simpson, C. D.; Müllen, K.; Rabe, J. P. Epitaxial Composite Layers of Electron Donors and Acceptors from Very Large Polycyclic Aromatic Hydrocarbons. *J Am Chem Soc* **2002**, *124*, 9454-9457.
- (48) Zhang, Y.; Zhang, Y.; Li, G.; Lu, J.; Lin, X.; Tan, Y.; Feng, X.; Du, S.; Müllen, K.; Gao, H. J. Construction of single-crystalline supramolecular networks of perchlorinated hexa-peri-hexabenzocoronene on Au(111). *J Chem Phys* **2015**, *142*, 101911.
- (49) Chen, Q.; Brambilla, L.; Daukiya, L.; Mali, K. S.; De Feyter, S.; Tommasini, M.; Müllen, K.; Narita, A. Synthesis of Triply Fused Porphyrin-Nanographene Conjugates. *Angew Chem Int Ed* **2018**, *57*, 11233-11237.
- (50) Samorí, P.; Fechtenkötter, A.; Jäckel, F.; Böhme, T.; Müllen, K.; Rabe, J. P. Supramolecular Staircase via Self-Assembly of Disklike Molecules at the Solid-Liquid Interface. *J Am Chem Soc* **2001**, *123*, 11462-11467.
- (51) Paterno, G. M.; Chen, Q.; Wang, X. Y.; Liu, J.; Motti, S. G.; Petrozza, A.; Feng, X.; Lanzani, G.; Müllen, K.; Narita, A.; Scotognella, F. Synthesis of Dibenzo[hi,st]ovalene and Its Amplified Spontaneous Emission in a Polystyrene Matrix. *Angew Chem Int Ed* **2017**, *56*, 6753-6757.
- (52) Coles, D. M.; Chen, Q.; Flatten, L. C.; Smith, J. M.; Müllen, K.; Narita, A.; Lidzey, D. G. Strong Exciton-Photon Coupling in a Nanographene Filled Microcavity. *Nano Lett* **2017**, *17*, 5521-5525.
- (53) Kuehne, A. J.; Gather, M. C. Organic Lasers: Recent Developments on Materials, Device Geometries, and Fabrication Techniques. *Chem Rev* **2016**, *116*, 12823-12864.
- (54) Chen, Q.; Wang, D.; Baumgarten, M.; Schollmeyer, D.; Müllen, K.; Narita, A. Regioselective Bromination and Functionalization of Dibenzo[hi,st]ovalene as Highly Luminescent Nanographene with Zigzag Edges. *Chem Asian J* **2019**, *14*, 1703-1707.
- (55) Paternò, G. M.; Nicoli, L.; Chen, Q.; Müllen, K.; Narita, A.; Lanzani, G.; Scotognella, F. Modulation of the Nonlinear Optical Properties of Dibenzo[hi,st]ovalene by Peripheral Substituents. *J Phys Chem C* **2018**, *122*, 25007-25013.
- (56) Chen, Q.; Thoms, S.; Stöttinger, S.; Schollmeyer, D.; Müllen, K.; Narita, A.; Basché, T. Dibenzo[hi,st]ovalene as Highly Luminescent Nanographene: Efficient Synthesis *via*

Photochemical Cyclodehydroiodination, Opto-electronic Properties and Single Molecule Spectroscopy, *J Am Chem Soc*, **2019**, 141, 16439-16449.

(57) Sens, R.; Drexhage, K. H. Fluorescence quantum yield of oxazine and carbazine laser dyes. *J Lumin* **1981**, 24-25, 709-712.

(58) Ban, K.; Nishizawa, K.; Ohta, K.; van de Craats, A. M.; Warman, J. M.; Yamamoto, I.; Shirai, H. Discotic liquid crystals of transition metal complexes 29: mesomorphism and charge transport properties of alkylthio-substituted phthalocyanine rare-earth metal sandwich complexes. *J Mater Chem* **2001**, 11, 321-331.

(59) Fischbach, I.; Pakula, T.; Minkin, P.; Fechtenkötter, A.; Müllen, K.; Spiess, H. W.; Saalwächter, K. Structure and Dynamics in Columnar Discotic Materials: A Combined X-ray and Solid-State NMR Study of Hexabenzocoronene Derivatives. *J Phys Chem B* **2002**, 106, 6408-6418.

(60) Martín-Rapún, R.; Byelov, D.; Palmans, A. R. A.; de Jeu, W. H.; Meijer, E. W. Lyomesophases of C₃-Symmetrical Bipyridine-Based Discs in Alkanes: An X-ray Diffraction Study. *Langmuir* **2009**, 25, 8794-8801.

(61) Beltran, E.; Cavero, E.; Barbera, J.; Serrano, J. L.; Elduque, A.; Gimenez, R. Self-assembly in helical columnar mesophases and luminescence of chiral 1H-pyrazoles. *Chem Eur J* **2009**, 15, 9017-9023.

(62) Peterca, M.; Imam, M. R.; Ahn, C. H.; Balagurusamy, V. S.; Wilson, D. A.; Rosen, B. M.; Percec, V. Transfer, amplification, and inversion of helical chirality mediated by concerted interactions of C₃-supramolecular dendrimers. *J Am Chem Soc* **2011**, 133, 2311-2328.

(63) Pisula, W.; Feng, X.; Müllen, K. Tuning the columnar organization of discotic polycyclic aromatic hydrocarbons. *Adv Mater* **2010**, 22, 3634-3649.

(64) Feng, X.; Pisula, W.; Müllen, K. From helical to staggered stacking of zigzag nanographenes. *J Am Chem Soc* **2007**, 129, 14116-14117.

(65) Azzam, W. Adlayer structures of anthracethiol on Au(111) after removal of covering multilayers with probe scan. *Appl Surf Sci* **2016**, 371, 562-570.

Supporting Information

Synthesis and Helical Supramolecular Organization of Discotic Liquid Crystalline
Dibenzo[*hi,st*]ovalene

Supplementary Figures and Tables

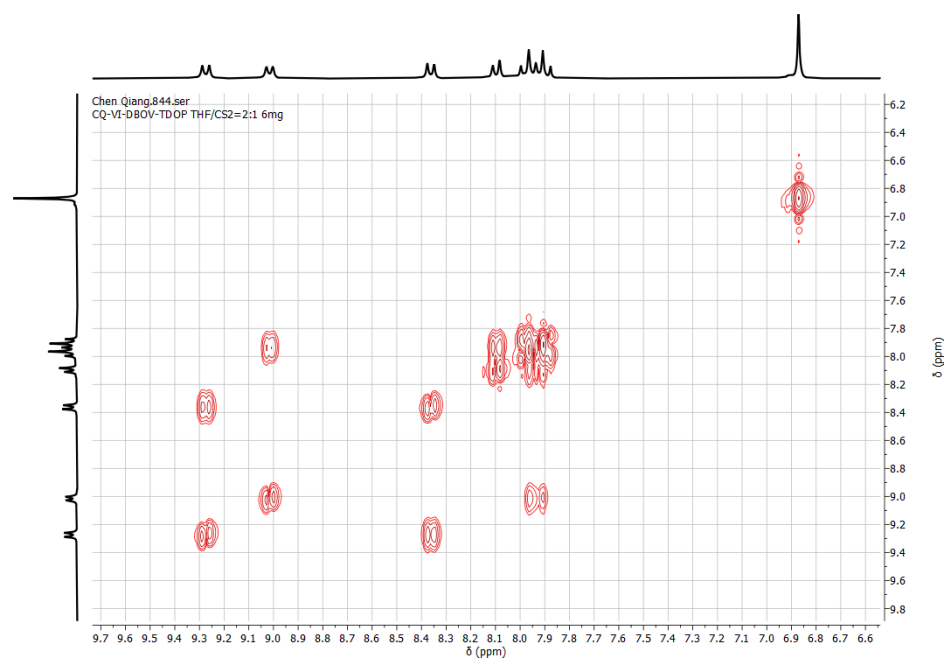


Figure S4-1. ^1H , ^1H -COSY spectra of **DBOV-TDOP** in $[\text{D}_8]\text{THF}:\text{CS}_2 = 2:1$ (300 MHz, 298K).

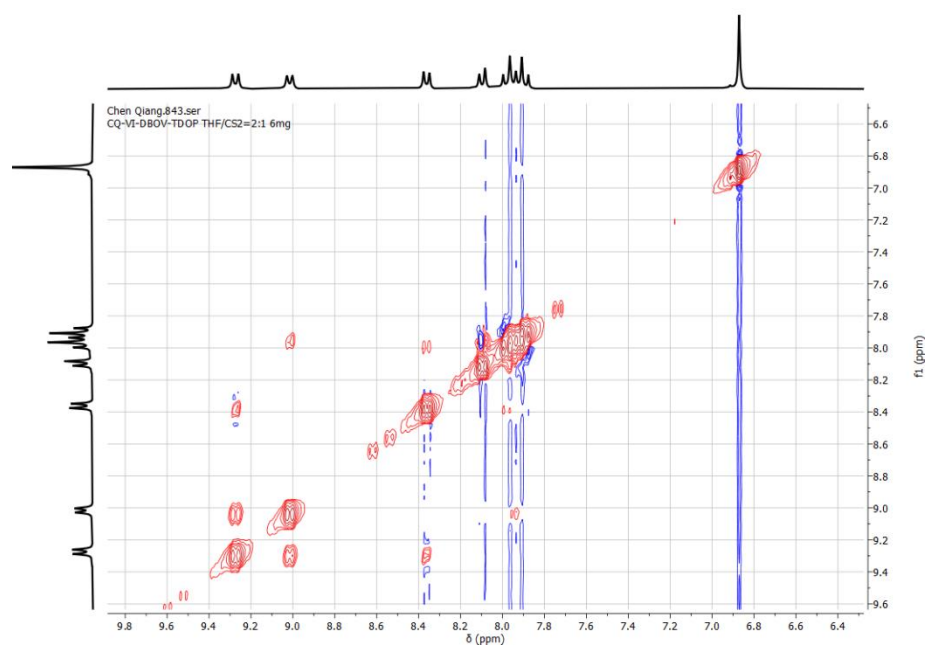


Figure S4-2. ^1H , ^1H -NOESY spectrum of **DBOV-TDOP** in $[\text{D}_8]\text{THF}:\text{CS}_2 = 2:1$ (300 MHz, 298K).

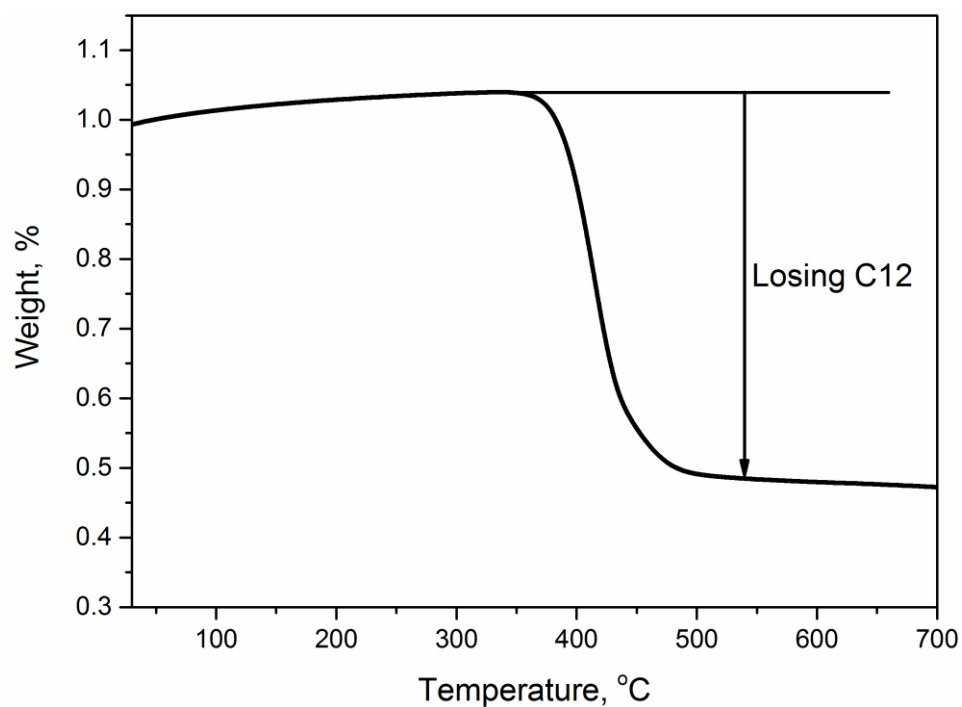


Figure S4-3. Thermogravimetric analysis (TGA) spectrum of **DBOV-TDOP**.

Additional STM Images

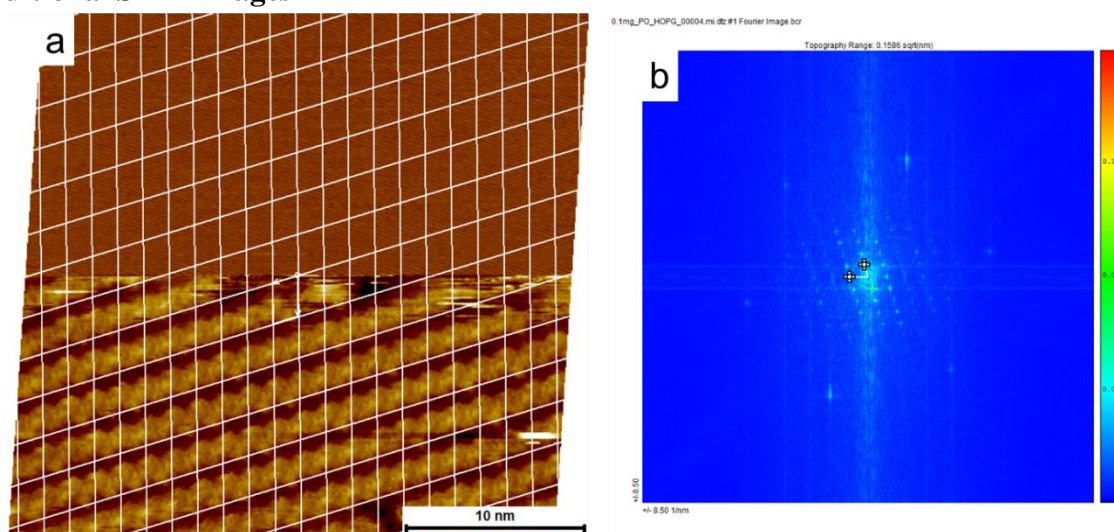


Figure S4-4. Example for the drift correction and unit cell determination. In the top half of a the HOPG surface lattice is imaged ($V_{\text{bias}} = -0.001$ V, $I_{\text{set}} = 1.0$ nA) and in the bottom part the molecular layer ($V_{\text{bias}} = -1.1$ V, $I_{\text{set}} = 70$ pA). The HOPG is used to correct for drift and the Fast-Fourier Transform (b) to determine the unit cell in the corrected image.

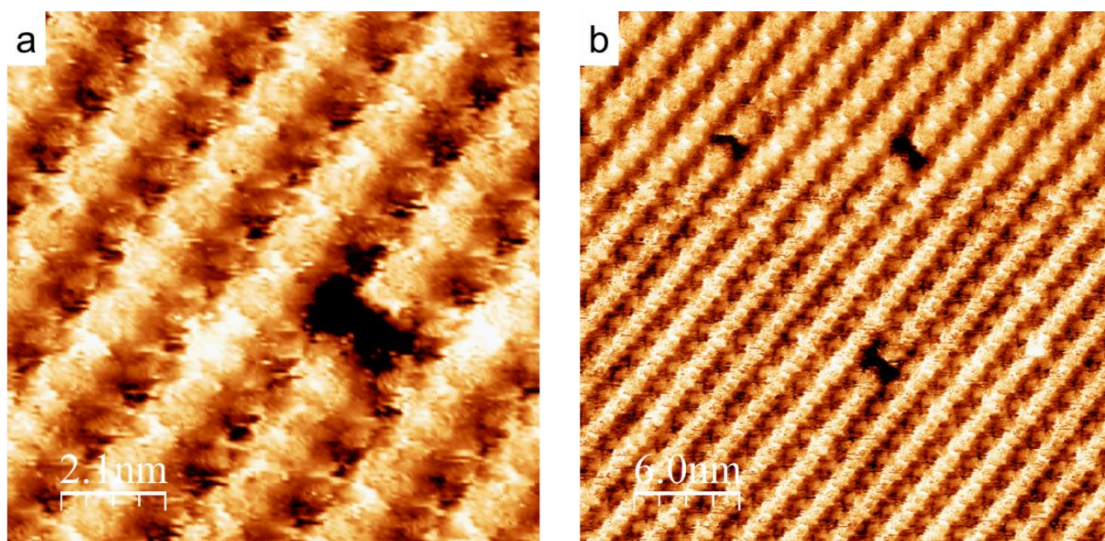


Figure S4-5. Additional STM images illustrating the molecular assembly in the second layer structure through single-molecules defects. Imaging parameters: a) $V_{\text{bias}} = -1.1$ V, $I_{\text{set}} = 80$ pA, b) $V_{\text{bias}} = -1.1$ V, $I_{\text{set}} = 80$ pA.

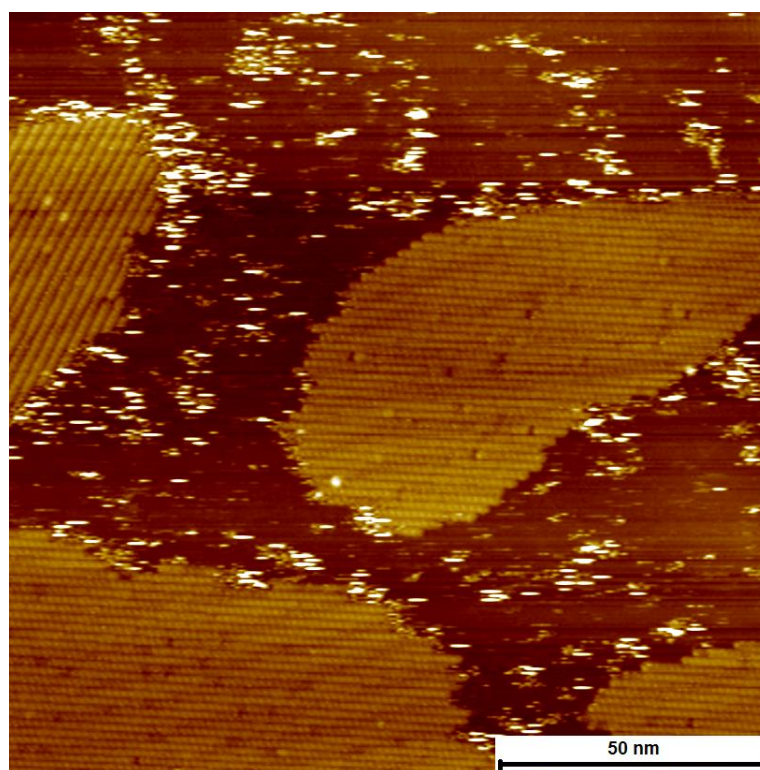


Figure S4-6. Additional STM image showing the increase in non-covered areas at lower concentrations ($c = 6 \times 10^{-6}$ mol/L). Imaging parameters: $V_{\text{bias}} = -1.1$ V, $I_{\text{set}} = 80$ pA.

Chapter 5. Regioselective Bromination and Functionalization of Dibenzo[hi,st]ovalene as Highly Luminescent Nanographene with Zigzag Edges

This Chapter is based on the following manuscript–

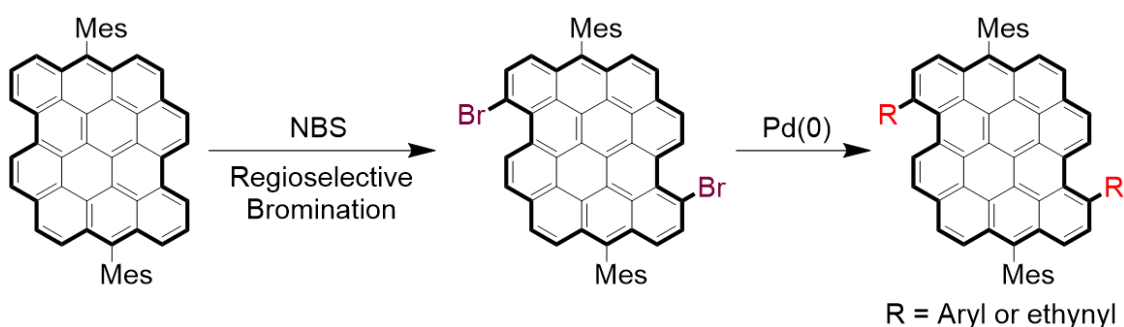
Chem. Asian J. **2019**, 14, 1703–1707

Qiang Chen, [REDACTED] and [REDACTED]

[REDACTED]

Author contributions. Q. C. designed, synthesized and characterized the compounds investigated in this research under the supervision of [REDACTED] and [REDACTED] performed the EPR measurements under the supervision of [REDACTED] was responsible for the single-crystal structure determination. The manuscript was written through contributions of all authors.

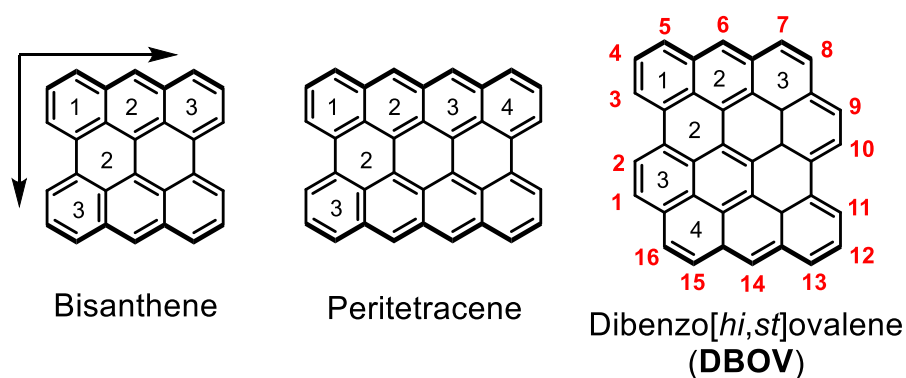
TOC Figure



Fluorescent material: An efficient post-synthetic functionalization of dibenzo[hi,st]ovalene (DBOV) has been developed by a combination of regioselective bromination and transition-metal-catalyzed cross-coupling reactions, enabling introduction of aryl and ethynyl substituents to its 3,11-position and demonstrating enhanced red fluorescence.

Reprinted with permission from (*Chem. Asian J.* **2019**, 14, 1703–1707). Copyright © 2019, John Wiley and Sons.

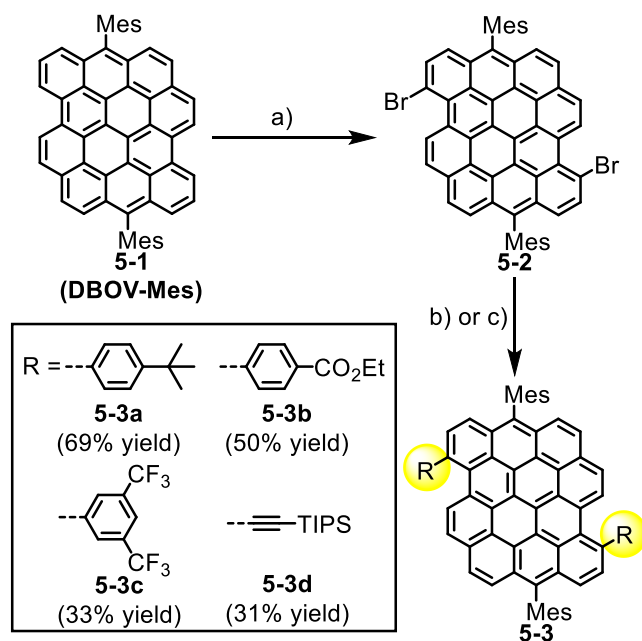
Abstract: Dibenzo[*hi,st*]ovalene (DBOV) is a nanographene with a combination of zigzag and armchair edges, consisting of 38 sp^2 carbons. Excellent optical properties with strong red emission have been demonstrated. Here we report the regioselective bromination of DBOV bearing two mesityl groups (**DBOV-Mes**) by treatment with *N*-bromosuccinimide (NBS) under a mild condition. The dibrominated DBOV was further subjected to transition-metal-catalyzed cross-coupling reactions, i.e. Suzuki and Sonogashira coupling, demonstrating the edge-decoration of DBOV with different functional groups. Notably, DBOVs arylated at the bay regions showed intense red emission and enhanced fluorescence quantum yields of up to 0.97. Amphoteric reduction and oxidation behavior was observed by cyclic voltammetry (CV) measurements. Chemical oxidation to stable radical cation species was also demonstrated, followed by reduction back to their neutral species.



Scheme 5-1. Structures of representative zigzag edged nanographene molecules with different lengths and widths (from left to right: bisanthene, peritetracene and dibenzo[*hi,st*]ovalene (DBOV)).

Nanographenes, namely extended polycyclic aromatic hydrocarbons,^[1] have attracted a growing interest not only because of their outstanding electronic and optical properties, but also for their wide range of potential applications in (opto-)electronic devices, such as light-emitting diodes (OLEDs) and field-effect transistors (OFETs).^[2] Numerous nanographenes with armchair edge structures have been synthesized and reported, showing tunable energy gaps between the highest occupied molecular orbital (HOMO) and the lowest unoccupied molecular orbital (LUMO), mainly dependent on the shapes and sizes of their aromatic cores.^[3] Edge functionalization of nanographenes has been widely studied, imparting them with intriguing properties,^[4] such as n-type semiconductor characteristics,^[5] intramolecular charge-transfer,^[6] and/or liquid-crystalline nature,^[7] distinct from their pristine, non-substituted counterparts. However, such functionalization predominantly relies on the modification of starting materials and/or precursor structures involving multiple synthetic

steps, while post-synthetic direct substitution of nanographene edges has been starkly underexplored. In particular, while there are several versatile methods, such as direct borylation^[8] or perchlorination of the nanographene edges,^[9] selective edge-halogenation has rarely been reported,^[10] despite the fact that halogen groups can be converted into various other functional groups through transition-metal-catalyzed coupling reactions.^[4b, c, 5]



Scheme 5-2. Selective bromination of **DBOV-Mes** at the peripheral positions and transition-metal-catalyzed cross-coupling reactions. Conditions: a) NBS, tetrahydrofuran, r.t., 12 h, 79% yield; for **5-3a–5-3c**, b) Pd(PPh₃)₄, K₂CO₃, toluene/ethanol/water = 4:1:1, 80 °C, 12 h, 33–69% yield; for **5-3d**: c) Pd(PPh₃)₄, CuI, tetrahydrofuran/triethylamine = 1:1, 70 °C, 6 h, 31% yield.

Nanographenes having zigzag edges (such as anthenes and periacenes; see Scheme 5-1) are attracting more and more attention for their intriguing optical properties, low HOMO-LUMO gaps, and potential open-shell character.^[11] However, examples of zigzag-edge nanographenes are still rather limited and the majority of them suffer from low stability, hindering further characterizations. To this end, we have recently described a synthesis of a new nanographene having zigzag edges, that is dibenzo[*hi, st*]ovalene (DBOV) (Scheme 5-1). DBOV showed sharp absorption and emission peaks in the red light region ($\lambda_{\text{max}} = 610\text{--}625$ nm) with high photoluminescence quantum yield (PLQY, Φ) up to 0.79,^[12] as well as high stability under ambient conditions.^[13] DBOV also exhibited amplified spontaneous emission (ASE) in a polystyrene (PS) matrix, with a low threshold of 60 $\mu\text{J cm}^{-2}$. These characteristics make DBOV promising for light-emitting devices and bioimaging.^[14] We have more recently developed an efficient synthetic route to obtain scalable amounts of DBOV derivatives using

photochemical cyclization instead of the Scholl reaction.^[15] However, the peripheral substitution of the DBOV core was possible only at the 6,14-positions (see Scheme 5-1) and at 5,13-positions through the modification of starting materials and/or reagents during the synthesis.^[12-13]

In this study, we have explored the post-synthetic, direct edge-functionalization of DBOV and achieved a regioselective electrophilic bromination at 3,11-positions. The brominated DBOV could be used for transition-metal-catalyzed coupling reactions to introduce aryl groups with electron-withdrawing substituents and triisopropylsilyl (TIPS)-protected ethynyl group. Photophysical properties and electronic structures of DBOV could be modulated by such edge-functionalization and interestingly, the obtained 3,11-aryl-substituted DBOVs demonstrated enhanced PLQY of up to 0.97.

DBOV with two mesityl groups at the 6,14-positions (**DBOV-Mes**, **5-1**) was used to investigate the selective functionalization, considering its easy accessibility and good solubility in common solvents, such as tetrahydrofuran and toluene.^[13] Mulliken charge distributions calculated using density functional theory (DFT) at the B3LYP/6-31G(d,p) level showed that the 3- and 11- positions of DBOV have higher electron density at ground state (Figure S5-1), which were expected to be prone to electrophilic substitution reactions. We have attempted the bromination initially by adding 2.0 equivalent of Br₂ into a solution of **DBOV-Mes** in dichloromethane, which induced a drastic change of the color from magenta to green, suggesting the oxidation of **DBOV-Mes** to cationic species. Addition of zinc powder changed the color back to magenta. Non-oxidative *N*-bromosuccinimide (NBS) was next used as bromination reagents in a mixture of chloroform and *N,N*-dimethylformamide, but there was no reaction even after heating at 50 °C overnight. Nevertheless, when the solvent was changed to tetrahydrofuran (THF), the bromination worked smoothly to give dibrominated product **5-2** (Figure S5-2).

The solubility of **5-2** was low in common organic solvents, but was sufficient for characterizations by NMR in a mixture of THF and carbon disulfide (CS₂). The ¹H NMR analyses revealed the disappearance of the doublet peak of **DBOV-Mes** at 9.21 ppm and exhibited 6 doublet signals after the bromination (Figure 5-1), indicating the selective substitution of -H³ and -H¹¹. All protons could be assigned with the help of two-dimensional NMR techniques (Figure S5-12–5-15). High-resolution matrix-assisted laser desorption-ionization time-of-flight mass spectrometry (HR-MALDI-TOF MS) showed one intense peak

located at $m/z = 864.1015$ with the isotopic distribution pattern in agreement with the calculated spectrum for $C_{56}H_{34}Br_2$ (Figure S5-16). Single crystals suitable for X-ray diffraction analysis were obtained by slow diffusion of acetonitrile vapor into a solution of **5-2** in THF/ CS_2 . The structure of **5-2** with two bromo groups at 3,11-positions (Figure 5-1c–d) could be unambiguously confirmed, which is in accordance with the theoretical prediction. The DBOV core appeared to be slightly distorted compared with **DBOV-Mes**. This is a result of steric repulsion between the bromo and the neighboring proton at the bay region.

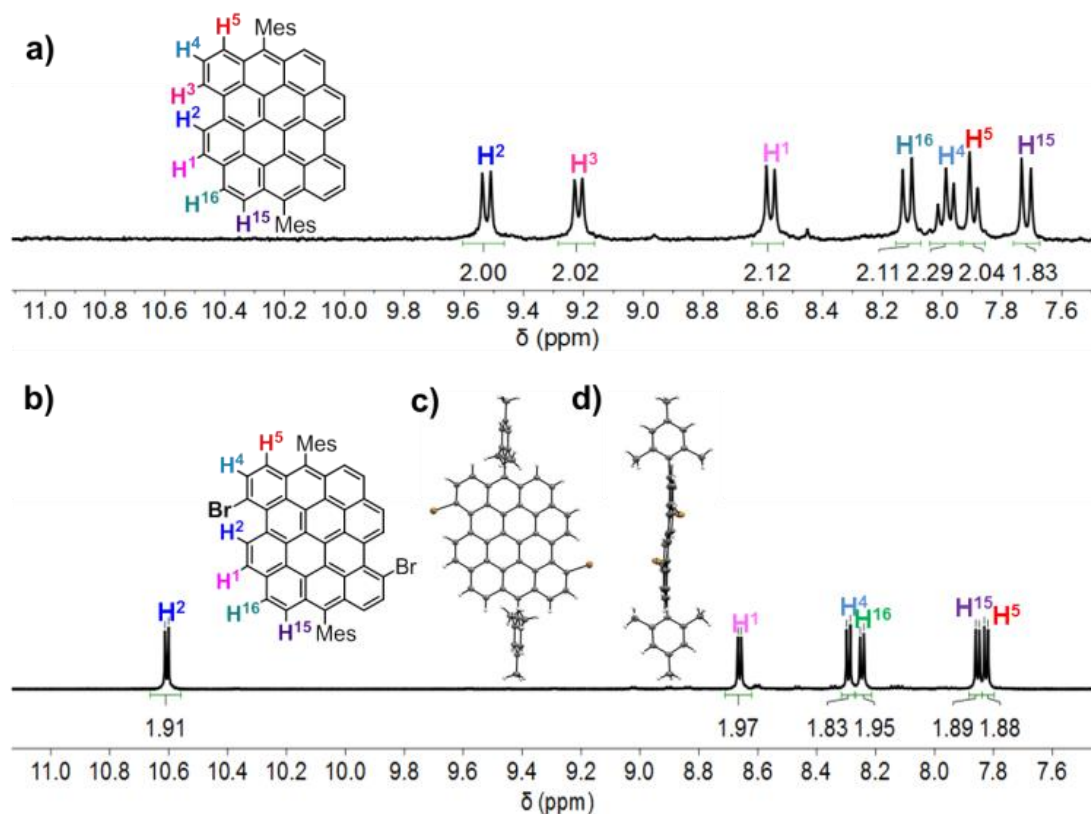


Figure 5-1. a) ¹H NMR spectra of **DBOV-Mes** in tetrahydrofuran-*d*₈:CS₂ = 1:1 (300 MHz, 298 K); and b) ¹H NMR spectra of 3,11-dibromo-6,14-dimesityldibenzo[hi,st]ovalene (**5-2**) in tetrahydrofuran-*d*₈:CS₂ = 1:1 (700 MHz, 298 K), showing the loss of –H³, –H¹¹; c, d) X-ray single crystallographic structure of **5-2** (measured at 120 K): c) front view and d) side view. Hydrogens are omitted for clarity. Ellipsoids are drawn at 50% probability level.

With brominated DBOV **5-2** in hand, we have next investigated the possibility of further functionalization through transition-metal-catalyzed cross-coupling reactions. Suzuki coupling of **5-2** was carried out with substituted phenylboronic acid bearing *tert*-butyl, ethyl ester, or trifluoromethyl groups under the presence of Pd(PPh₃)₄ as catalyst and K₂CO₃ as base, which proceeded smoothly to provide products **5-3a–5-3c** with isolated yields ranging from 33% to 69% (Scheme 5-2). Sonogashira coupling of **5-2** was also conducted with

(triisopropylsilyl)acetylene under standard conditions using Pd(PPh₃)₄ and CuI as catalysts and trimethylamine as base, which gave 3,11-bis(triisopropylsilyl)ethynyl-substituted DBOV **5-3d** with isolated yield of 31%. The structures of products **5-3a–5-3d** were unambiguously characterized by a combination of NMR and HR-MALDI-TOF MS analyses (see the Supporting Information).

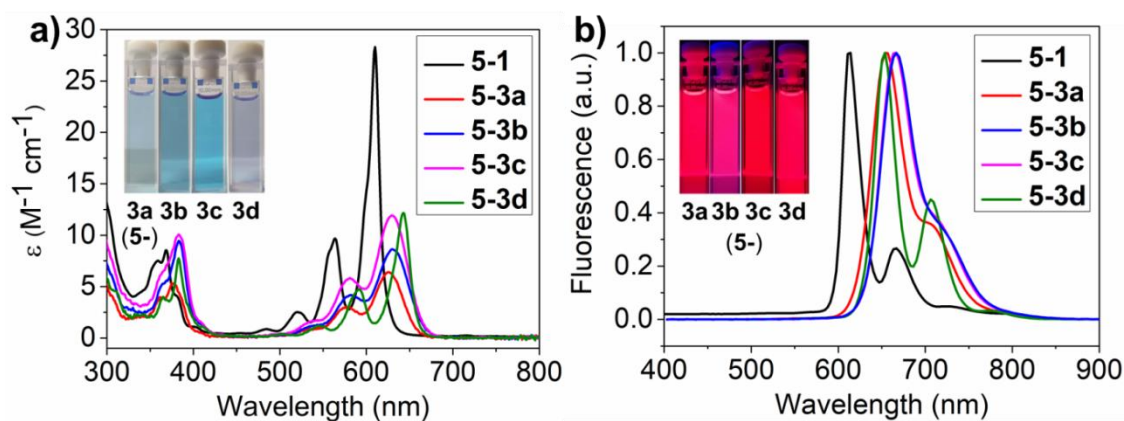


Figure 5-2. (a) UV-*vis*-NIR absorption and (b) fluorescence spectra of compound **5-1**, **5-3a–5-3d** in toluene with concentration of 10⁻⁶ M (molar absorption coefficients: **5-1** ($2.8 \times 10^5 \text{ M}^{-1}\text{cm}^{-1}$), **5-3a** ($6.4 \times 10^4 \text{ M}^{-1}\text{cm}^{-1}$), **5-3b** ($8.5 \times 10^4 \text{ M}^{-1}\text{cm}^{-1}$), **5-3c** ($1.2 \times 10^5 \text{ M}^{-1}\text{cm}^{-1}$), **5-3d** ($1.2 \times 10^5 \text{ M}^{-1}\text{cm}^{-1}$). Each compound was excited at their maximum absorption wavelength.

The photophysical properties of DBOV derivatives **5-3a–5-3d** were next investigated in comparison with **DBOV-Mes (5-1)** as displayed in Figure 5-2. The UV-*vis*-NIR absorption and fluorescence spectra were measured in toluene solutions with a concentration of 10⁻⁶ M. The blue solutions of **5-3a–5-3d** showed intense absorption in the range of 500–670 nm. The absorption maxima were located at 625, 633, 630, and 646 nm, respectively, which were red-shifted by 10–35 nm in comparison with that of **DBOV-Mes**. These results indicated that the substitution of the DBOV core with the aryl and triisopropylsilylethynyl groups slightly extended the π -conjugation. The UV-*vis*-NIR absorption of these toluene solutions did not show any changes under ambient conditions for at least 4 weeks, indicating their high stability to air and light.

DFT (B3LYP/6-31G(d,p)) calculations were conducted to obtain better insight into the structures and electronic distributions of **5-3a–5-3c**. In their optimized structures, the phenyl groups are twisted by 55–57 degrees from the DBOV core (Figure S5-3). The relatively small dihedral angles facilitate electron conjugation between the aryl rings and the DBOV core,

leading to the above-mentioned red-shifts of the absorption peaks. On the other hand, in the optimized structure of **5-3d**, there is obvious electron delocalization between DBOV core and the triple bonds, thus accounting for its larger red-shift of 35 nm. Additionally, time-dependent density functional theory (TDDFT) calculations at the B3LYP/6-31G(d,p) level indicated the maximum absorption wavelengths for **5-3a–5-3d** to be located at 649, 658, 650, and 668 nm (Table S5-1), respectively, which was in good agreement with the trend observed in the experimental spectra.

Table 5-1. Summary of photophysical and electrochemical data of all compounds **5-3a–5-3d**.

compound	λ_{abs} (nm)	Φ	$E_{\text{opt}}^{\text{[a]}}$ (eV)	E_{ox}^1 (V)	E_{red}^1 (V)	HOMO (eV) ^[b]	LUMO (eV) ^[b]
5-3a	625	0.97	1.94	0.02	-1.63	-4.82	-3.17
5-3b	633	0.94	1.91	0.14	-1.55	-4.94	-3.25
5-3c	630	0.91	1.91	0.05	-1.60	-4.85	-3.20
5-3d	646	0.69	1.92	0.14	-1.46	-4.94	-3.34

[a] Optical energy gap (E_{opt}) was calculated according to the crossing wavelength (λ_{cross}) of the UV-vis-NIR absorption and fluorescence spectra by using the following equation: $E_{\text{opt}} = 1240/\lambda_{\text{cross}}$. [b] HOMO and LUMO were calculated from the onset of their corresponding first oxidation waves and first reduction waves by using the following equation: HOMO = $-(4.8 + E_{\text{ox}}^{\text{onset}})$ eV, LUMO = $-(4.8 + E_{\text{red}}^{\text{onset}})$ eV, where E is calibrated with Fc/Fc⁺.

DBOV derivatives **5-3a–5-3d** showed strong fluorescence in the toluene solution with maximum emission wavelengths at 654, 667, 667, and 654 nm, respectively. The Stokes shifts are larger than that of **DBOV-Mes** because of the flexible molecule structures of **5-3**, where the rotation of substituted functional groups can promote the intersystem crossing. The PLQYs (Φ) of **5-3a–5-3d** were measured with Nile blue A perchlorate as standard by a dilution method to be 0.97, 0.94, 0.91, and 0.69, respectively.^[16] It is notable that the PLQYs of aryl-substituted **5-3a–5-3c** were enhanced compared with **DBOV-Mes**, which might be due to the suppression of intermolecular interactions by the additional bulky substituents.

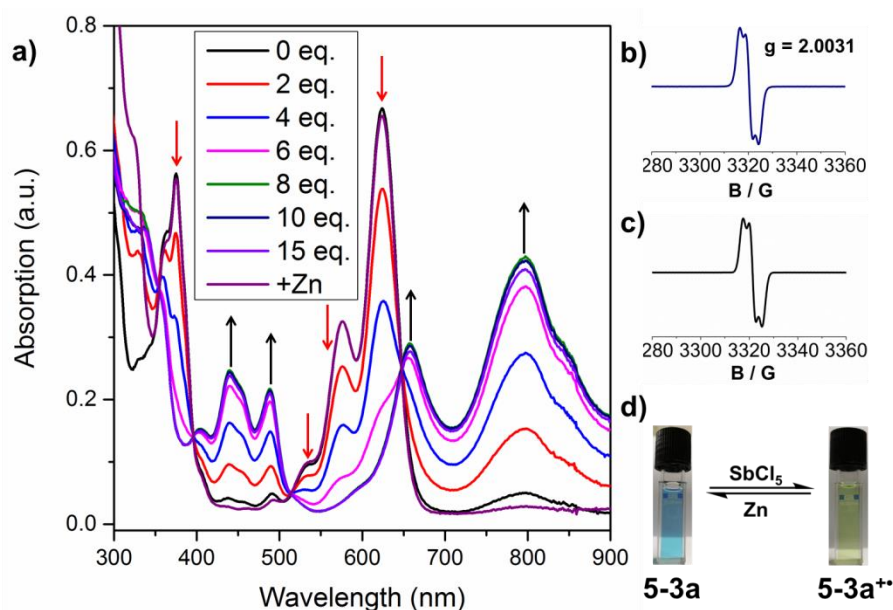


Figure 5-3. (a) Changes in the UV-*vis*-NIR absorption spectra during titration of **5-3a** with SbCl_5 . The arrows show the changes of each peak. (b) Experimental EPR spectra after addition of 10 equivalents of SbCl_5 to a solution of **5-3a** in dry dichloromethane. (c) Simulated EPR spectra of **5-3a⁺**. (d) Color change of the dichloromethane solution of **5-3a** after oxidation with 10 equivalents of SbCl_5 and reduction with Zn powder.

The redox properties of DBOVs **5-3a–5-3d** were studied by cyclic voltammetry (CV) in dichloromethane solution using a three electrodes method with 0.1 mol/L *n*- Bu_4NPF_6 as a supporting electrolyte (Figure S5-4), and the electrochemical data are summarized in Table 1. The first oxidation potential of **5-3b** and **5-3c** were higher than that of **5-3a** as a result of the electron withdrawing groups attached to them. **5-3d** with triisopropylsilylethynyl groups showed the highest first oxidation potential due to more electronegative sp hybridized ethynyl carbons, which was also observed for pentacene.^[17] All of these DBOVs **5-3a–5-3d** could be oxidized or reduced to charged species, revealing their amphoteric redox behavior.^[11a, 18] The HOMO and LUMO energy levels were calculated according to the onset of the first oxidation ($E_{\text{ox}}^{\text{onset}}$) and reduction ($E_{\text{red}}^{\text{onset}}$) waves using the following equations: $\text{HOMO} = -(4.8 + E_{\text{ox}}^{\text{onset}})$ and $\text{LUMO} = -(4.8 + E_{\text{red}}^{\text{onset}})$ (see Table 1), in which the potentials were calibrated with Fc/Fc^+ .

The amphoteric redox properties of DBOV derivatives and the observation of its apparent oxidation by Br_2 prompted us to study their oxidation to radical cations. We first conducted a UV-*vis*-NIR titration of **5-3a–5-3d** in anhydrous dichloromethane with one electron oxidation

reagent antimony chloride (SbCl_5). For **5-3a**, addition of an excess of SbCl_5 resulted in a continuous and gradual change of the blue solution into green with new UV-vis-NIR peaks appearing at 800, 650, 480, and 440 nm (Figure 5-3a). Further addition of more than 10 equivalents of SbCl_5 had no effect on the UV-vis-NIR absorption spectra, indicating the DBOV core can only be oxidized to this state with SbCl_5 . This phenomenon was also observed for **5-3b–5-3d** (Figure S5-7). Electron paramagnetic resonance (EPR) measurement displayed intensive signals with g factors of 2.00312 (**5-3a**), 2.00311 (**5-3b**), 2.00311 (**5-3c**), and 2.00330 (**5-3d**), indicating the formation of radical cation species (Figure S5-6). Interestingly, the dichloromethane solution of compound **5-3a** without SbCl_5 already contained around 12% of radical cations estimated from the UV-vis-NIR absorption spectra (Figure 5-3a), probably due to its high HOMO level, making it susceptible to oxidation by air under presence of a trace amount of acid in the solvent (Table 5-1). It is noted that such a peak was not observed in the toluene solution of **5-3a** (Figure 5-2a). All of the oxidized species could be cleanly reduced back to the neutral state with Zn powder, indicating high stability of DBOV radical cations.

In summary, we have achieved the edge-functionalization of **DBOV-Mes** at the 3,11-positions through regioselective bromination and Suzuki or Sonogashira cross-coupling reaction. The functionalized DBOVs with aryl groups at the bay regions showed red-shifted UV-vis absorption/emission with enhanced fluorescence quantum yield and amphoteric redox properties. These results pave the way towards the synthesis of novel nanographene structures by π -extension of DBOV as well as introduction of different functional groups for further applications. For example, synthesis of water-soluble DBOV for bioimaging applications is ongoing in our laboratory.

Acknowledgements

We are grateful for the financial support from the Max Planck Society and the European Union's Horizon 2020 research and innovation programme under Marie-Curie ITN project “iSwitch” (GA No. 642196).

Keywords: Nanographene • Bromination • Post-Functionalization • Fluorescent material • Chemical oxidation

References:

- [1] a) K. Müllen and J. P. Rabe, *Acc. Chem. Res.* **2008**, *41*, 511-520; b) J. Wu, W. Pisula and K. Müllen, *Chem. Rev.* **2007**, *107*, 718-747; c) J. Wu, A. C. Grimsdale and K. Müllen, *J. Mater. Chem.* **2005**, *15*, 41-52.
- [2] a) F. Schwierz, *Nat. Nanotechnol.* **2010**, *5*, 487-496; b) K. S. Novoselov, V. I. Fal'ko, L. Colombo, P. R. Gellert, M. G. Schwab and K. Kim, *Nature* **2012**, *490*, 192-200; c) A. Narita, X. Y. Wang, X. Feng and K. Müllen, *Chem. Soc. Rev.* **2015**, *44*, 6616-6643.
- [3] a) A. Stabel, P. Herwig, K. Müllen and J. P. Rabe, *Angew. Chem. Int. Ed.* **1995**, *34*, 1609-1611; b) V. S. Iyer, M. Wehmeier, J. D. Brand, M. A. Keegstra and K. Müllen, *Angew. Chem. Int. Ed.* **1997**, *36*, 1604-1607; c) V. S. Iyer, K. Yoshimura, V. Enkelmann, R. Epsch, J. P. Rabe and K. Müllen, *Angew. Chem. Int. Ed.* **1998**, *37*, 2696-2699; d) C. D. Simpson, J. D. Brand, A. J. Berresheim, L. Przybilla, H. J. Räder and K. Müllen, *Chem. Eur. J.* **2002**, *8*, 1424-1429.
- [4] a) J. Holzwarth, K. Y. Amsharov, D. I. Sharapa, D. Reger, K. Roshchyna, D. Lungerich, N. Jux, F. Hauke, T. Clark and A. Hirsch, *Angew. Chem. Int. Ed.* **2017**, *56*, 12184-12190; b) D. Joshi, M. Hauser, G. Veber, A. Berl, K. Xu and F. R. Fischer, *J. Am. Chem. Soc.* **2018**, *140*, 9574-9580; c) Y. M. Liu, H. Hou, Y. Z. Zhou, X. J. Zhao, C. Tang, Y. Z. Tan and K. Müllen, *Nat. Commun.* **2018**, *9*, 1901.
- [5] A. Keerthi, B. Radha, D. Rizzo, H. Lu, V. Diez Cabanes, I. C. Hou, D. Beljonne, J. Cornil, C. Casiraghi, M. Baumgarten, K. Müllen and A. Narita, *J. Am. Chem. Soc.* **2017**, *139*, 16454-16457.
- [6] A. Keerthi, I. C. Hou, T. Marszalek, W. Pisula, M. Baumgarten and A. Narita, *Chem. Asian J.* **2016**, *11*, 2710-2714.
- [7] a) Y. Hu, L. F. Dössel, X.-Y. Wang, S. Mahesh, W. Pisula, S. De Feyter, X. Feng, K. Müllen and A. Narita, *ChemPlusChem* **2017**, *82*, 1030-1033; b) J. Wu, A. Fechtenkötter, J. Gauss, M. D. Watson, M. Kastler, C. Fechtenkötter, M. Wagner and K. Müllen, *J. Am. Chem. Soc.* **2004**, *126*, 11311-11321; c) J. Wu, M. D. Watson and K. Müllen, *Angew. Chem. Int. Ed.* **2003**, *115*, 5487-5491.
- [8] a) H. A. Lin, Y. Sato, Y. Segawa, T. Nishihara, N. Sugimoto, L. T. Scott, T. Higashiyama and K. Itami, *Angew. Chem. Int. Ed.* **2018**, *57*, 2874-2878; b) M. N. Eliseeva and L. T. Scott, *J. Am. Chem. Soc.* **2012**, *134*, 15169-15172.
- [9] Y. Z. Tan, B. Yang, K. Parvez, A. Narita, S. Osella, D. Beljonne, X. Feng and K. Müllen, *Nat. Commun.* **2013**, *4*, 2646.

- [10] a) G. Li, H. Phan, T. S. Heng, T. Y. Gopalakrishna, C. Liu, W. Zeng, J. Ding and J. Wu, *Angew. Chem. Int. Ed.* **2017**, *56*, 5012-5016; b) R. Yamaguchi, S. Hiroto and H. Shinokubo, *Chem. Lett.* **2014**, *43*, 1637-1639.
- [11] a) J. Li, K. Zhang, X. Zhang, K. W. Huang, C. Chi and J. Wu, *J. Org. Chem.* **2010**, *75*, 856-863; b) M. R. Ajayakumar, Y. Fu, J. Ma, F. Hennesdorf, H. Komber, J. J. Weigand, A. Alfonsov, A. A. Popov, R. Berger, J. Liu, K. Müllen and X. Feng, *J. Am. Chem. Soc.* **2018**, *140*, 6240-6244; c) Y. Ni, T. Y. Gopalakrishna, H. Phan, T. S. Heng, S. Wu, Y. Han, J. Ding and J. Wu, *Angew. Chem. Int. Ed.* **2018**, *57*, 9697-9701; d) Y. W. Son, M. L. Cohen and S. G. Louie, *Nature* **2006**, *444*, 347-349; e) G. Z. Magda, X. Jin, I. Hagymasi, P. Vancso, Z. Osvath, P. Nemes-Incze, C. Hwang, L. P. Biro and L. Tapasztó, *Nature* **2014**, *514*, 608-611; f) P. Ruffieux, S. Wang, B. Yang, C. Sanchez-Sanchez, J. Liu, T. Dienel, L. Talirz, P. Shinde, C. A. Pignedoli, D. Passerone, T. Dumslaff, X. Feng, K. Müllen and R. Fasel, *Nature* **2016**, *531*, 489-492.
- [12] G. M. Paterno, Q. Chen, X. Y. Wang, J. Liu, S. G. Motti, A. Petrozza, X. Feng, G. Lanzani, K. Müllen, A. Narita and F. Scotognella, *Angew. Chem. Int. Ed.* **2017**, *56*, 6753-6757.
- [13] D. M. Coles, Q. Chen, L. C. Flatten, J. M. Smith, K. Müllen, A. Narita and D. G. Lidzey, *Nano Lett.* **2017**, *17*, 5521-5525.
- [14] a) W. Chen, S. Xu, J. J. Day, D. Wang and M. Xian, *Angew. Chem. Int. Ed.* **2017**, *56*, 16611-16615; b) L. Yuan, W. Lin, K. Zheng, L. He and W. Huang, *Chem. Soc. Rev.* **2013**, *42*, 622-661; c) C.-T. Chen, *Chem. Mater.* **2004**, *16*, 4389-4400; d) X. H. Zhang, B. J. Chen, X. Q. Lin, O. Y. Wong, C. S. Lee, H. L. Kwong, S. T. Lee and S. K. Wu, *Chem. Mater.* **2001**, *13*, 1565-1569; e) X. H. Zhu, J. Peng, Y. Cao and J. Roncali, *Chem. Soc. Rev.* **2011**, *40*, 3509-3524; f) T. Khanasa, N. Prachumrak, R. Rattanawan, S. Jungsuttiwong, T. Keawin, T. Sudyoasuk, T. Tuntulani and V. Promarak, *Chem. Commun.* **2013**, *49*, 3401-3403.
- [15] Q. Chen, W. Zajaczkowski, J. Seibel, S. Stöttinger, S. Thoms, T. Basché, S. Feyter, W. Pisula, K. Müllen and A. Narita, *J. Mater. Chem. C*, **2019**, *7*, 12898-12906.
- [16] R. Sens and K. H. Drexhage, *J. Lumin.* **1981**, *24-25*, 709-712.
- [17] a) A. Maliakal, K. Raghavachari, H. Katz, E. Chandross and T. Siegrist, *Chem. Mater.* **2004**, *16*, 4980-4986; b) I. Kaur, W. Jia, R. P. Kopreski, S. Selvarasah, M. R. Dokmeci, C. Pramanik, N. E. McGruer and G. P. Miller, *J. Am. Chem. Soc.* **2008**, *130*, 16274-16286.
- [18] a) T. Kubo, M. Sakamoto, M. Akabane, Y. Fujiwara, K. Yamamoto, M. Akita, K. Inoue, T. Takui and K. Nakasuji, *Angew. Chem. Int. Ed.* **2004**, *43*, 6474-6479; b) J. Li, C. Jiao, K. W. Huang and J. Wu, *Chemistry* **2011**, *17*, 14672-14680; c) Z. Zeng, Y. M. Sung, N. Bao, D. Tan,

R. Lee, J. L. Zafra, B. S. Lee, M. Ishida, J. Ding, J. T. Lopez Navarrete, Y. Li, W. Zeng, D. Kim, K. W. Huang, R. D. Webster, J. Casado and J. Wu, *J. Am. Chem. Soc.* **2012**, *134*, 14513-14525.

Copyright Wiley-VCH Verlag GmbH & Co. KGaA, Weinheim 2019

Supporting Information

Regioselective Bromination and Functionalization of Dibenzo[*hi,st*]ovalene as Highly Luminescent Nanographene with Zigzag Edges

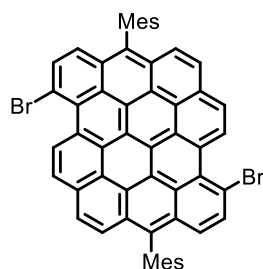
1. Supplementary Methods

General

All reactions dealing with air- or moisture-sensitive compounds were carried out in a dry reaction vessel under argon. Analytical thin layer chromatography (TLC) was performed on silica gel coated substrates “60 F₂₅₄” from Merck. Preparative column chromatography was performed on silica gel from Merck with a grain size of 0.063–0.200 mm or 0.040–0.063 mm. High-resolution mass spectra (HRMS) were recorded by matrix-assisted laser decomposition/ionization (MALDI) using 7,7,8,8-tetracyanoquinodimethane (TCNQ) as matrix on a Bruker Reflex II-TOF spectrometer and calibrated with polystyrene (PS) as internal standard. Nuclear Magnetic Resonance (NMR) spectra were recorded using Bruker DPX 500, and Bruker DRX 700 MHz NMR spectrometers. Chemical shifts (δ) were expressed in ppm relative to the residual of solvents (CD₂Cl₂, ¹H: 5.32 ppm, ¹³C: 53.84 ppm; C₂D₂Cl₄, ¹H: 6.00 ppm, ¹³C: 73.78 ppm; THF-*d*₈, ¹H: 3.58 ppm, ¹³C: 67.57 ppm). Coupling constants (*J*) were recorded in Hertz. UV-*vis* absorption spectra were recorded on a Perkin-Elmer Lambda 900 spectrometer at room temperature using a 10 mm quartz cell. Photoluminescence spectra were recorded on a J&MTIDAS spectrofluorometer. The fluorescence quantum yield (Φ) was measured using Nile blue A perchlorate (in ethanol under air, $\Phi = 0.27$) as a reference.^[1] Cyclic voltammetry (CV) measurements were performed on a GSTAT-12 in a three-electrode cell in dichloromethane solution of *n*-Bu₄NPF₆ (0.1 M) at a scan rate of 50 mV/s at room temperature. A silver wire, a Pt wire and a glassy carbon electrode were used as the reference electrode, the counter electrode, and the working electrode, respectively. Geometry optimizations and energy calculations were performed using the Gaussian 09 quantum chemical package with density functional (DFT) method at the B3LYP level with the 6-31G (d,p) basis set.^[2] Time-dependent DFT (TDDFT) calculations were performed at the same level of theory.

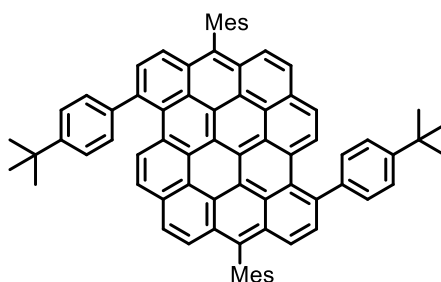
Experimental Details

Synthesis of 3,11-dibromo-6,14-dimesityldibenzo[*hi,st*]ovalene (**5-2**):



To a solution of 6,14-dimesityldibenzo[*hi,st*]ovalene (**5-1**) (90 mg, 0.13 mmol) dissolved in anhydrous tetrahydrofuran (100 mL) was added *N*-bromosuccinimide (100 mg, 0.562 mmol). The resulting solution was stirred at room temperature overnight. After quenching with acetone (5 mL), the solvents were evaporated and the residue was purified by silica gel column chromatography (eluent: *n*-hexane:tetrahydrofuran = 5:1) to give the title compound (87 mg, 79% yield) as blue solid. ^1H NMR (700 MHz, THF-*d*₈:CS₂ = 1:1) δ 10.61 (d, *J* = 8.2 Hz, 2H), 8.66 (d, *J* = 8.3 Hz, 2H), 8.29 (d, *J* = 8.8 Hz, 2H), 8.25 (d, *J* = 9.1 Hz, 2H), 7.85 (d, *J* = 9.0 Hz, 2H), 7.82 (d, *J* = 8.8 Hz, 2H), 7.24 (s, 4H), 2.55 (s, 6H), 1.94 (s, 12H); ^{13}C NMR (176 MHz, THF-*d*₈:CS₂ = 1:1) δ 138.6, 138.5, 136.3, 136.0, 135.3, 132.2, 131.2, 130.4, 129.9, 129.8, 129.8, 128.7, 128.0, 127.5, 127.4, 126.5, 126.2, 125.5, 124.3, 123.6, 123.3, 123.2, 119.3, 22.1, 20.9; HR MS (MALDI-TOF): *m/z* Calcd. for C₅₆H₃₄Br₂: 864.1027 [M]⁺, found: 864.1015 (error = -1.4 ppm).

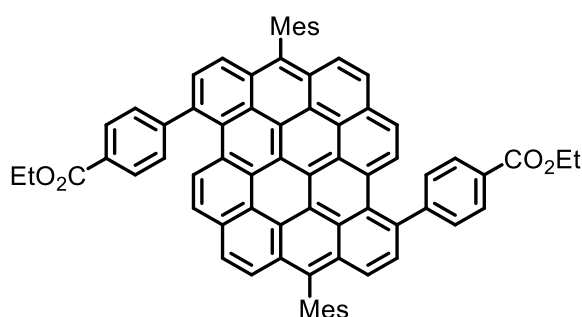
Synthesis of 3,11-bis(4-*tert*-butylphenyl)-6,14-dimesityldibenzo[*hi,st*]ovalene (**5-3a**):



A degassed suspension of 3,11-dibromo-6,14-dimesityldibenzo[*hi,st*]ovalene (17.9 mg, 20.7 μmol), 4-*tert*-butylphenylboronic acid (42.0 mg, 236 μmol), Pd(PPh₃)₄ (5.4 mg, 4.7 μmol) and K₂CO₃ (57.5 mg, 416 μmol) in a mixture of toluene/ethanol/water = 20 mL/5 mL/5 mL was heated at 90 °C for 24 h. After cooling down to room temperature, water (20 mL) was added, and the aqueous layer was extracted with ethyl acetate (20 mL) for three times. The separated organic phases were combined, washed with brine, dried over MgSO₄ and evaporated. The blue residue was purified by silica gel column chromatography (eluent: *n*-hexane:tetrahydrofuran = 10:1) and then recrystallized from dichloromethane and methanol to

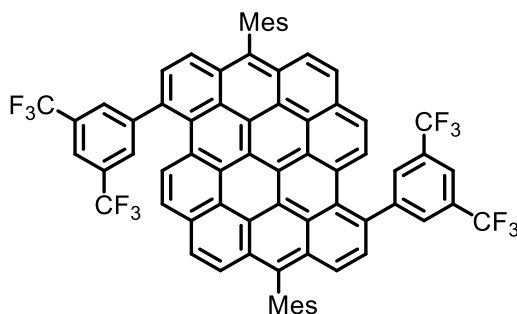
give the title compound (13.9 mg, 69% yield) as blue solid. ^1H NMR (700 MHz, $\text{THF-}d_8\text{:CS}_2 = 1:1$) δ 8.78 (d, $J = 8.3$ Hz, 2H), 8.01 (d, $J = 5.2$ Hz, 2H), 7.99 (d, $J = 6.0$ Hz, 2H), 7.93 (d, $J = 8.4$ Hz, 2H), 7.86 (d, $J = 8.3$ Hz, 2H), 7.71 (d, $J = 9.0$ Hz, 2H), 7.63 (d, $J = 8.1$ Hz, 4H), 7.58 (d, $J = 8.2$ Hz, 4H), 7.22 (s, 4H), 2.53 (s, 6H), 1.96 (s, 12H), 1.48 (s, 19H); ^{13}C NMR (176 MHz, $\text{THF-}d_8\text{:CS}_2 = 1:1$) δ 151.1, 143.8, 139.2, 138.6, 138.3, 135.9, 135.8, 132.9, 131.1, 130.7, 130.5, 130.0, 130.0, 129.7, 129.6, 129.4, 127.9, 127.5, 127.0, 126.6, 125.6, 124.9, 124.8, 124.4, 123.9, 123.7, 32.2, 22.0, 20.9; HR MS (MALDI-TOF): m/z Calcd. for $\text{C}_{76}\text{H}_{60}$: 972.4695 $[\text{M}]^+$, found: 972.470 (error = 0.5 ppm).

Synthesis of 3,11-bis(4-ethoxycarbonylphenyl)-6,14-dimesityldibenzo[*hi,st*]ovalene (**5-3b**):



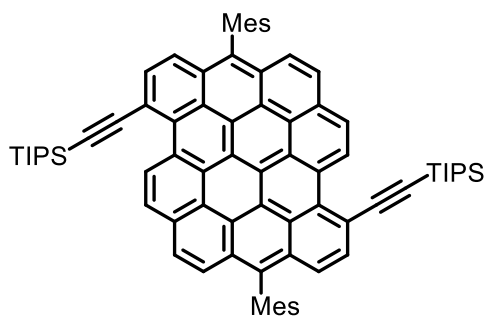
A degassed suspension of 3,11-dibromo-6,14-dimesityldibenzo[*hi,st*]ovalene (18.6 mg, 21.5 μmol), 4-ethoxycarbonylphenylboronic acid (41.7 mg, 215 μmol), $\text{Pd}(\text{PPh}_3)_4$ (5.6 mg, 4.8 μmol) and K_2CO_3 (63.6 mg, 460 μmol) in a mixture of toluene/ethanol/water = 20 mL/5 mL/5 mL was heated at 90 $^\circ\text{C}$ for 24 h. After cooling down to room temperature, water (20 mL) was added, and the aqueous layer was extracted with ethyl acetate (20 mL) for three times. The separated organic phases were combined, washed with brine, dried over MgSO_4 and evaporated. The blue residue was purified by silica gel column chromatography (eluent: *n*-hexane:tetrahydrofuran = 10:1) and then recrystallized from dichloromethane and methanol to give the title compound (10.8 mg, 50% yield) as blue solid. ^1H NMR (700 MHz, $\text{THF-}d_8\text{:CS}_2 = 1:1$) δ 8.71, 8.70, 8.18, 8.17, 8.06, 8.05, 8.02, 8.01, 7.98, 7.97, 7.88, 7.87, 7.80, 7.79, 7.76, 7.75, 7.21, 4.42, 4.41, 4.40, 4.39, 2.53, 1.96, 1.46, 1.45, 1.44; ^{13}C NMR (176 MHz, $\text{THF-}d_8\text{:CS}_2 = 1:1$) δ 163.3, 148.47, 135.8, 135.7, 135.2, 133.3, 132.9, 129.6, 129.4, 128.6, 128.3, 127.9, 127.8, 127.7, 127.5, 127.2, 127.0, 126.9, 126.6, 124.6, 124.5, 123.8, 123.1, 122.4, 122.1, 121.6, 121.1, 120.9, 58.8, 19.4, 18.2; HR MS (MALDI-TOF): m/z Calcd. for $\text{C}_{74}\text{H}_{52}\text{O}_4$: 1004.3866 $[\text{M}]^+$, found: 1004.3857 (error = -0.9 ppm).

Synthesis of 3,11-bis{3,5-bis(trifluoromethyl)phenyl}-6,14-dimesityldibenzo[*hi,st*]ovalene (**5-3c**):



A degassed suspension of 3,11-dibromo-6,14-dimesityldibenzo[*hi,st*]ovalene (17.9 mg, 20.7 μmol), 3,5-bis(trifluoromethyl)phenylboronic acid (55.2 mg, 214 μmol), $\text{Pd}(\text{PPh}_3)_4$ (5.1 mg, 4.4 μmol) and K_2CO_3 (65.6 mg, 475 μmol) in a mixture of toluene/ethanol/water = 20 mL/5 mL/5 mL was heated at 90 $^\circ\text{C}$ for 24 h. After cooling down to room temperature, water (20 mL) was added, and the aqueous layer was extracted with ethyl acetate (20 mL) for three times. The separated organic phases were combined, washed with brine, dried over MgSO_4 and evaporated. The blue residue was purified by silica gel column chromatography (eluent: *n*-hexane:tetrahydrofuran = 10:1) and then recrystallized from dichloromethane and methanol to give the title compound (7.7 mg, 33% yield) as blue solid. ^1H NMR (700 MHz, $\text{THF}-d_8:\text{CS}_2 = 1:1$) δ 8.60 (d, $J = 8.2$ Hz, 2H), 8.33 (s, 4H), 8.16 (d, $J = 8.2$ Hz, 2H), 8.09 (d, $J = 8.3$ Hz, 4H), 8.06 (d, $J = 8.4$ Hz, 2H), 7.92 (d, $J = 8.4$ Hz, 2H), 7.81 (d, $J = 9.0$ Hz, 2H), 7.24 (s, 4H), 2.55 (s, 6H), 1.96 (s, 12H); ^{13}C NMR (176 MHz, $\text{THF}:\text{CS}_2 = 1:1$) δ 149.1, 138.7, 138.5, 136.5, 135.6, 135.4, 134.3, 134.1, 132.5, 131.8, 131.4, 131.3, 130.8, 130.3, 130.1, 130.0, 129.8, 128.7, 127.6, 127.2, 126.6, 126.4, 125.3, 124.9, 124.3, 123.9, 123.8, 121.9, 22.0, 20.9; ^{19}F NMR (471 MHz, $\text{THF}-d_8:\text{CS}_2 = 1:1$) δ -65.02; HR MS (MALDI-TOF): m/z Calcd for $\text{C}_{72}\text{H}_{40}\text{F}_{12}$: 1132.2938 $[\text{M}]^+$, found: 1132.2893 (error = -4.0 ppm).

Synthesis of 3,11-bis(triisopropylsilylethynyl)-6,14-dimesityldibenzo[*hi,st*]ovalene (**5-3d**):



A degassed suspension of 3,11-dibromo-6,14-dimesityldibenzo[*hi,st*]ovalene (22.0 mg, 25.4 μmol), triisopropylsilylacetylene (23.5 mg, 129 μmol), $\text{Pd}(\text{PPh}_3)_4$ (6.8 mg, 5.9 μmol), CuI

(4.5 mg, 2.4 μmol) was heated at 80 $^{\circ}\text{C}$ for 24 h. After completion of the reaction, the solvents were evaporated under reduced pressure. The residue was purified by silica gel column chromatography (eluent: *n*-hexane:tetrahydrofuran = 5:1) and then recrystallized from dichloromethane and methanol to give the title compound (8.5 mg, 31% yield) as blue solid. ^1H NMR (700 MHz, $\text{THF-}d_8\text{:CS}_2 = 1\text{:}1$) δ 11.43 (d, $J = 8.2$ Hz, 2H), 8.61 (d, $J = 8.3$ Hz, 2H), 8.25 (d, $J = 9.0$ Hz, 2H), 8.17 (d, $J = 8.5$ Hz, 2H), 7.91 (d, $J = 8.5$ Hz, 2H), 7.86 (d, $J = 8.9$ Hz, 2H), 2.55 (s, 6H), 1.94 (s, 12H), 1.36 (s, 42H); ^{13}C NMR (176 MHz, $\text{THF:CS}_2 = 1\text{:}1$) δ 193.5, 138.6, 136.4, 135.7, 133.6, 132.4, 131.3, 130.3, 130.2, 126.4, 125.7, 124.6, 124.2, 124.0, 123.9, 117.6, 113.2, 100.2, 67.8, 67.7, 67.6, 67.4, 25.8, 25.7, 22.0, 20.8, 19.8, 12.9; HR MS (MALDI-TOF): m/z Calcd for $\text{C}_{78}\text{H}_{76}\text{Si}_2$: 1068.5487 $[\text{M}]^+$, found: 1068.5484 (error = -0.3 ppm).

Supplementary Figures

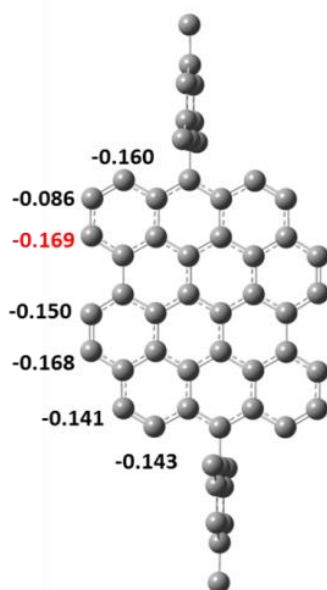


Figure S5-1. Mulliken charge distribution on peripheral carbon atoms on DBOV core of **DBOV-Mes** (negative values indicate these atoms can give electrons for reaction).

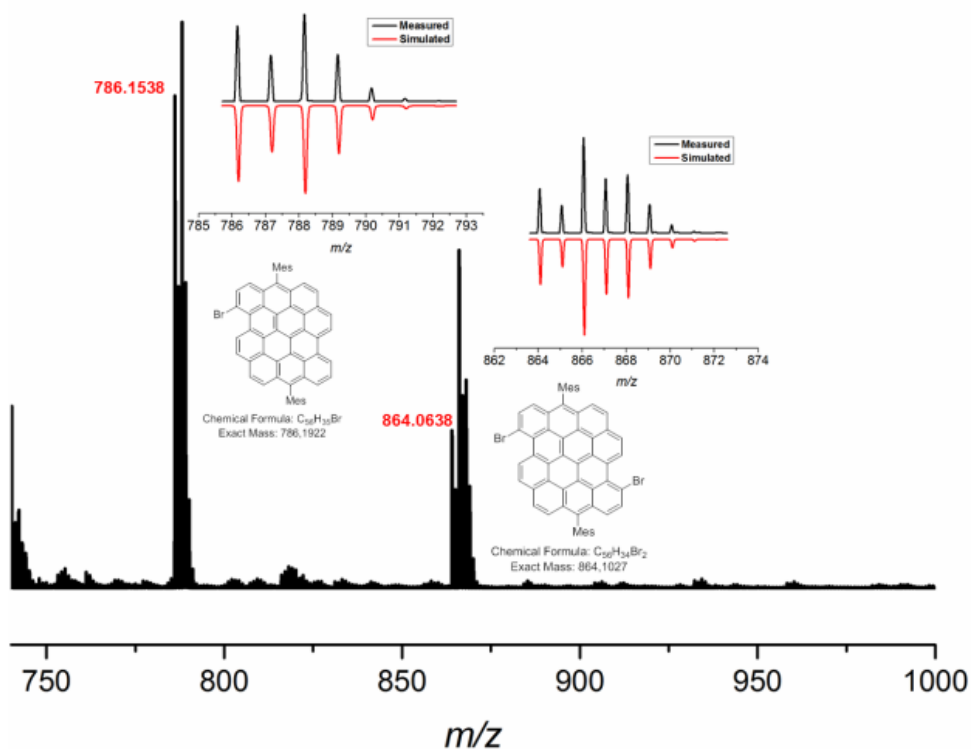


Figure S5-2. MALDI-TOF mass analysis of a crude product mixture after bromination of **DBOV-Mes** by treatment with NBS (2.5 eq.) in tetrahydrofuran at room temperature for 12 h.

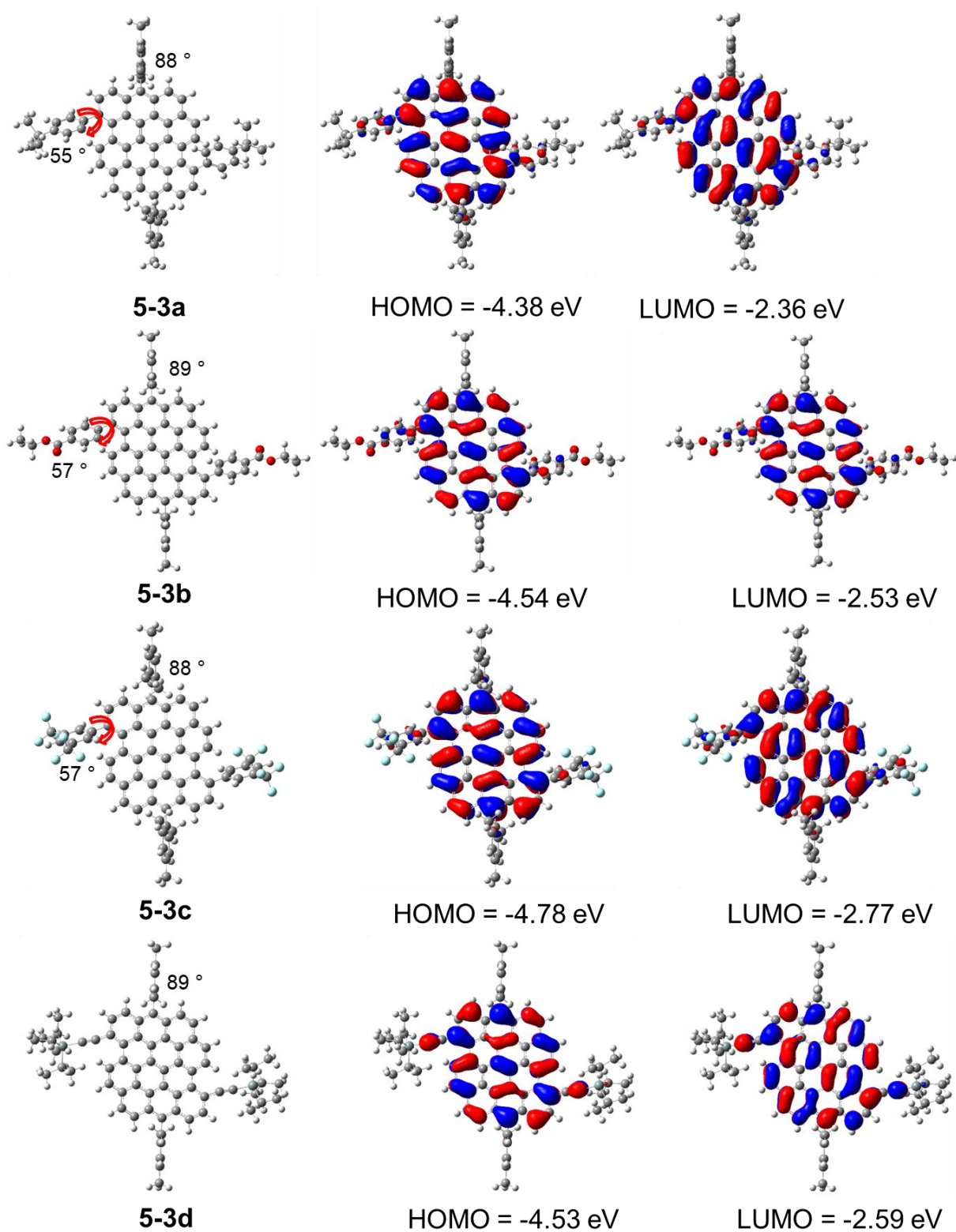


Figure S5-3. Optimized structures of **5-3a–5-3d** and frontier molecular orbitals based on DFT (B3LYP/6-31G(d,p)) calculations.

Table S5-1. Characteristic electron transitions for **5-3a–5-3d** calculated by TDDFT at the B3LYP/6-31G(d,p) level by Gaussian 09.^[2]

Compound	Excited states	Transition energy (eV)	Wavelength (nm)	Oscillator strength	Description
5-3a	1	1.91	649	0.6367	HOMO→LUMO (0.70377)
	8	3.29	377	0.5548	HOMO-2→LUMO (0.44237)
					HOMO-1→LUMO+1 (0.17298)
					HOMO→LUMO+2 (0.47760)
					HOMO→LUMO+5 (-0.14180)
5-3b	1	1.89	658	0.6573	HOMO→LUMO (0.70368)
	6	2.00	413	0.2801	HOMO-2→LUMO (0.26472)
					HOMO→LUMO+3 (0.55455)
5-3c					HOMO→LUMO+4 (0.33286)
	1	1.91	650	0.6278	HOMO→LUMO (0.70370)
	7	3.05	407	0.1059	HOMO-2→LUMO (0.25970)
					HOMO→LUMO+3 (0.48022)
5-3d					HOMO→LUMO+5 (0.43155)
	1	1.86	668	0.7478	HOMO→LUMO (0.70512)
	3	2.71	458	0.0553	HOMO-2→LUMO (0.58596)
				HOMO→LUMO+3 (-0.38607)	

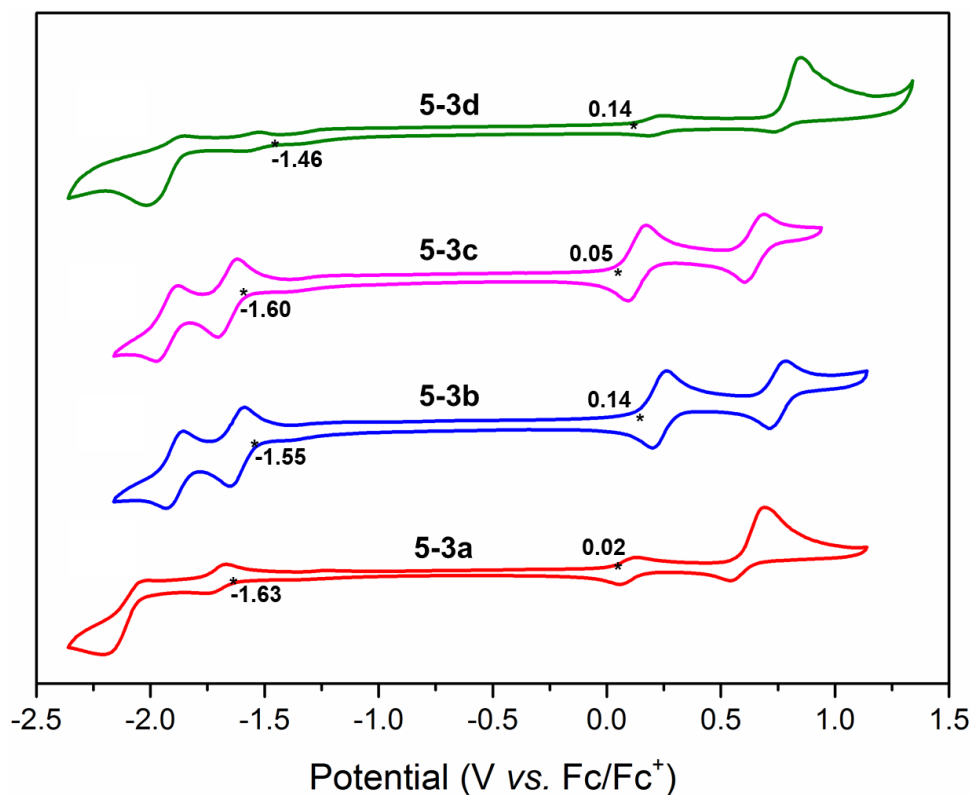


Figure S5-4. Cyclic voltammety spectra of **5-3a–5-3d** in dichloromethane with 0.1 mol/L *n*-Bu₄NPF₆ as supporting electrolyte, 25 °C, scan rate 50 mV/s (ferrocene was used as standard).

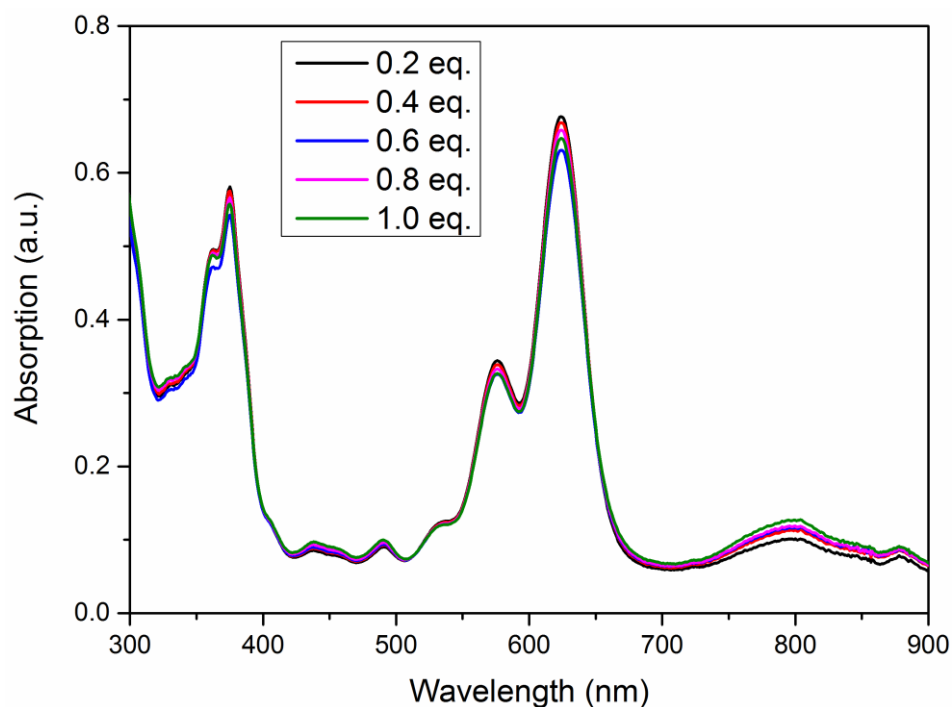


Figure S5-5. UV-*vis*-NIR spectra change of **5-3a** in dichloromethane while addition of 0.1–1.0 equivalent of SbCl₅.

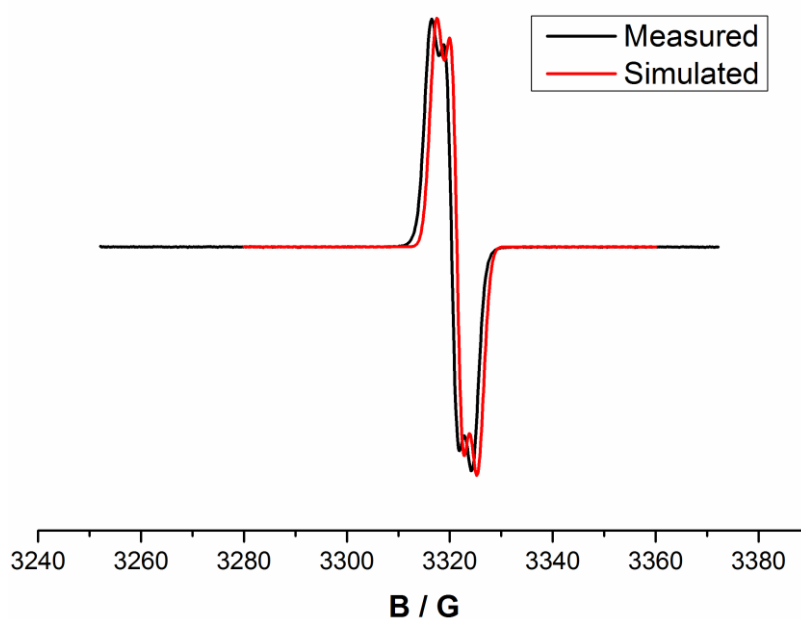


Figure S5-6. Experimental and simulated EPR spectra of **5-3a⁺**

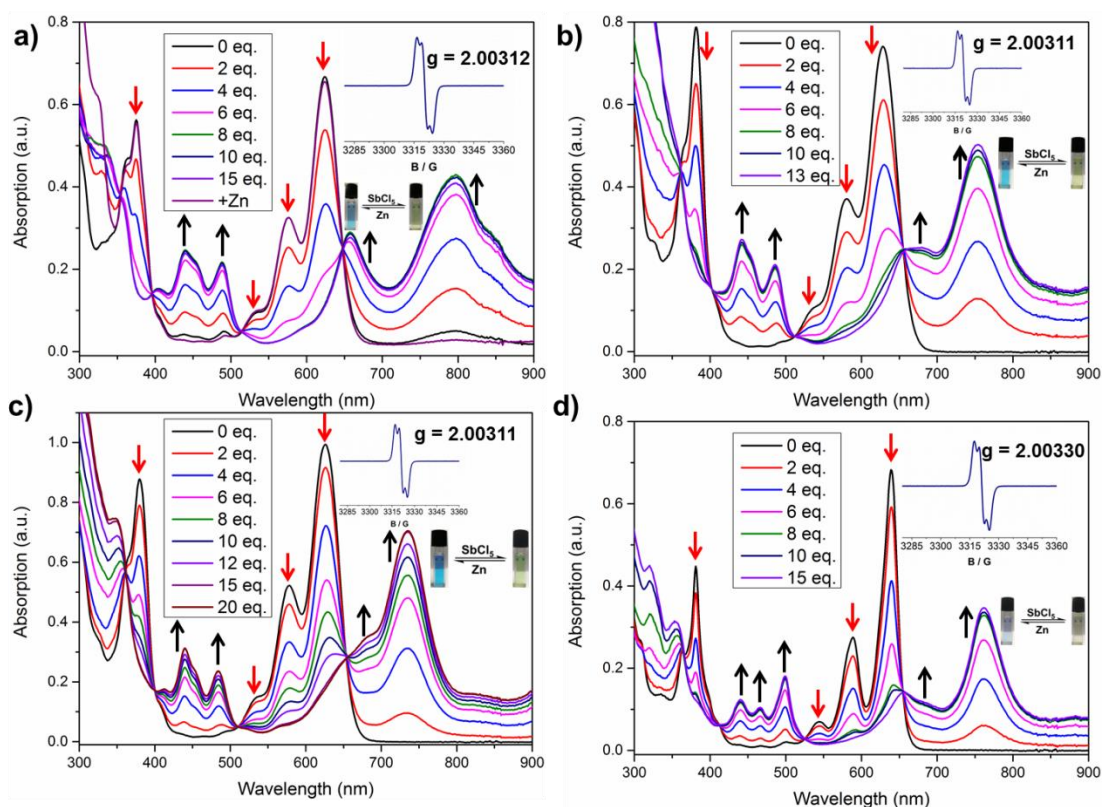


Figure S5-7. UV-*vis*-NIR absorption spectra during titration of DBOV derivatives (Figure a–d show compound **5-3a–5-3d**) with SbCl_5 and EPR spectra after addition of 10 equivalents of SbCl_5 (displayed in the inset) in dry dichloromethane. The arrows show the changes of each peak during the titration. The pictures show the solution color change before and after oxidation.

X-ray single crystal structure

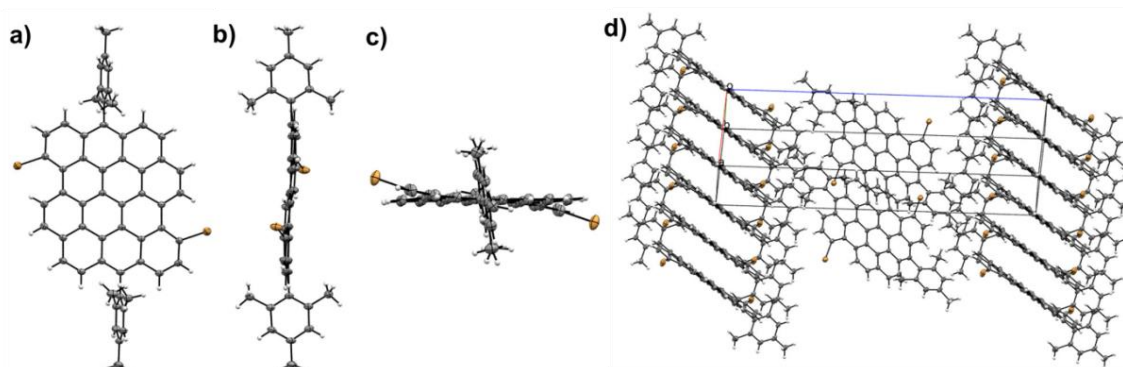


Figure S5-8. X-ray single-crystal structure of 3,11-dibromo-6,14-dimesityldibenzo[*hi,st*]ovalene (**5-2**) measured at 120 K. a) front view; b) side view; c) top view; d) stacking pattern in the crystal structure.

Crystal data for compound **5-2** (CCDC1880682)

formula	$C_{56}H_{34}Br_2$
molecular weight	866.6 gmol^{-1}
absorption	$\mu = 2.25 \text{ mm}^{-1}$ correction with 6 crystal faces
transmission	$T_{\min} = 0.6521, T_{\max} = 0.8399$
crystal size	$0.08 \times 0.15 \times 0.22 \text{ mm}^3$ brown block
space group	$P 2_1/n$ (monoclinic)
lattice parameters	$a = 8.3746(2) \text{ \AA}$
(calculate from	$b = 7.2923(3) \text{ \AA} \quad \beta = 94.549(2)^\circ$
21607 reflections with	$c = 30.1856(9) \text{ \AA}$
$2.5^\circ < \theta < 28.3^\circ$)	$V = 1837.61(11) \text{ \AA}^3 \quad z = 2 \quad F(000) = 880$
temperature	120K
density	$d_{\text{xray}} = 1.566 \text{ gcm}^{-3}$

data collection

diffractometer	STOE IPDS 2T
radiation	Mo- K_α
Scan – type	ω scans
Scan – width	1°
scan range	$2^\circ \leq \theta < 27.8^\circ$ $-11 \leq h \leq 11 \quad -9 \leq k \leq 9 \quad -39 \leq l \leq 37$
number of reflections:	
measured	17645
unique	4357 ($R_{\text{int}} = 0.0284$)
observed	3614 ($ F /\sigma(F) > 4.0$)

data correction, structure solution and refinement

corrections	Lorentz and polarisation correction.
Structure solution	Program: SIR-2004 (Direct methods)

refinement	Program: SHELXL-2018 (full matrix). 265 refined parameters, weighting scheme: $w=1/[\sigma^2(F_o^2) + (0.092*P)^2+2.81*P]$ with $(\text{Max}(F_o^2,0)+2*F_c^2)/3$. H-atoms at calculated positions and refined with isotropic displacement parameters, non H- atoms refined anisotropically.
R-values	wR2 = 0.1513 (R1 = 0.0493 for observed reflections, 0.0617 for all reflections)
goodness of fit	S = 1.042
maximum deviation of parameters	0.001 * e.s.d
maximum peak height in diff. Fourier synthesis	0.88, -0.84 eÅ ⁻³
remark	molecule has C _i - symmetry

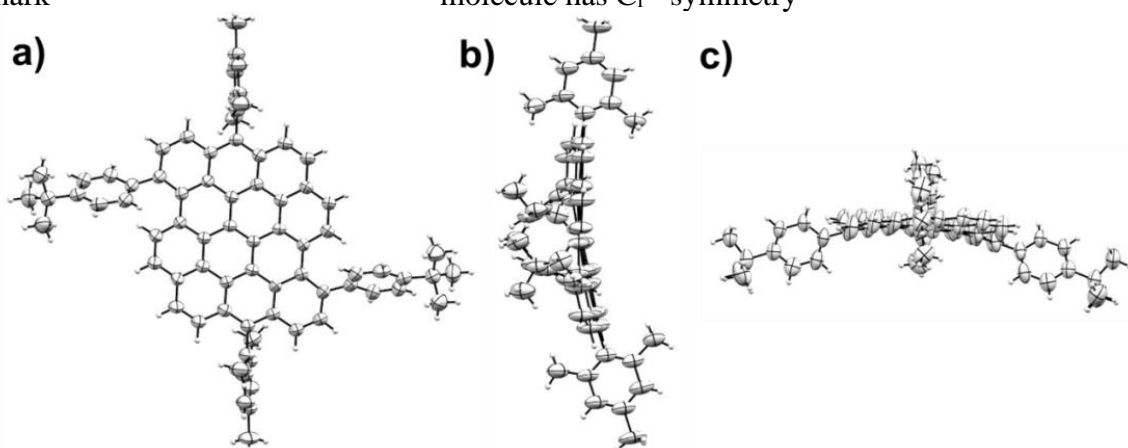


Figure S5-9. X-ray single-crystal structure of 3,11-bis(4-*tert*-butylphenyl)-6,14-dimesityldibenzo[*hi,st*]ovalene (**5-3a**) measured at 120 K. a) front view; b) side view; c) top view.

Crystal data for **5-3a** (CCDC 1893173)

formula	C ₇₆ H ₆₀
molecular weight	973.29 gmol ⁻¹
absorption	$\mu = 0.57 \text{ mm}^{-1}$
crystal size	0.04 x 0.07 x 0.09 mm ³ blue block
space group	C 2/c (monoclinic)
lattice parameters	a = 26.064(3)Å
(calculate from	b = 9.7058(8)Å $\beta = 94.212(8)^\circ$
5769 reflections with	c = 19.2173(19)Å
3.4° < θ < 60.5°)	V = 4848.3(8)Å ³ z = 4 F(000) = 2064
temperature	120K
density	$d_{\text{xray}} = 1.333 \text{ gcm}^{-3}$

data collection

diffractometer	STOE IPDS 2T
radiation	Cu-K α I μ S mirror system
Scan – type	ω scans

Scan – width	1°
scan range	$2^\circ \leq \theta < 67.5^\circ$ $-30 \leq h \leq 31 \quad -11 \leq k \leq 11 \quad -23 \leq l \leq 22$
number of reflections:	
measured	14183
unique	4328 ($R_{\text{int}} = 0.0523$)
observed	1664 ($ F /\sigma(F) > 4.0$)

data correction, structure solution and refinement

corrections	Lorentz and polarisation correction.
Structure solution	Program: SIR-2004 (Direct methods)
refinement	Program: SHELXL-2018 (full matrix). 350 refined parameters, weighting scheme: $w=1/[\sigma^2(F_o^2) + (0.1313*P)^2+11.28*P]$ with $(\text{Max}(F_o^2,0)+2*F_c^2)/3$. H-atoms at calculated positions and refined with isotropic displacement parameters, non H- atoms refined anisotropically.
R-values	wR2 = 0.3346 (R1 = 0.0964 for observed reflections, 0.2199 for all reflections)
goodness of fit	S = 1.045
maximum deviation of parameters	0.001 * e.s.d
maximum peak height in diff. Fourier synthesis	0.27, -0.24 eÅ ⁻³
remark	molecule has C ₂ symmetry

References

- [1] R. Sens and K. H. Drexhage, *J. Lumin.* **1981**, 24-25, 709-712.
- [2] Gaussian 09, Revision D.01, M. J. Frisch, G. W. Trucks, H. B. Schlegel, G. E. Scuseria, M. A. Robb, J. R. Cheeseman, G. Scalmani, V. Barone, B. Mennucci, G. A. Petersson, H. Nakatsuji, M. Caricato, X. Li, H. P. Hratchian, A. F. Izmaylov, J. Bloino, G. Zheng, J. L. Sonnenberg, M. Hada, M. Ehara, K. Toyota, R. Fukuda, J. Hasegawa, M. Ishida, T. Nakajima, Y. Honda, O. Kitao, H. Nakai, T. Vreven, J. A. Montgomery, Jr., J. E. Peralta, F. Ogliaro, M. Bearpark, J. J. Heyd, E. Brothers, K. N. Kudin, V. N. Staroverov, T. Keith, R. Kobayashi, J. Normand, K. Raghavachari, A. Rendell, J. C. Burant, S. S. Iyengar, J. Tomasi, M. Cossi, N. Rega, J. M. Millam, M. Klene, J. E. Knox, J. B. Cross, V. Bakken, C. Adamo, J. Jaramillo, R. Gomperts, R. E. Stratmann, O. Yazyev, A. J. Austin, R. Cammi, C. Pomelli, J. W. Ochterski, R. L. Martin, K. Morokuma, V. G. Zakrzewski, G. A. Voth, P. Salvador, J. J. Dannenberg, S. Dapprich, A. D. Daniels, O. Farkas, J. B. Foresman, J. V. Ortiz, J. Cioslowski, and D. J. Fox, Gaussian, Inc., Wallingford CT, 2013.

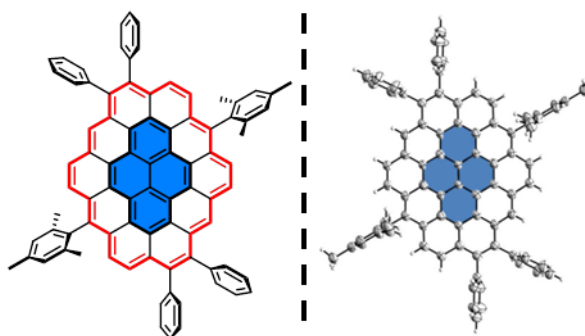
Chapter 6. Synthesis of Circumpyrene: Nanographene with a Full Zigzag Periphery

This Chapter is based on the following manuscript–

Qiang Chen, [REDACTED]

Author contributions. Q. C. designed, synthesized and characterized the compound investigated in this research under the supervision of [REDACTED] was responsible for the single-crystal structure analysis. The manuscript was written through contributions of all authors.

TOC Figure



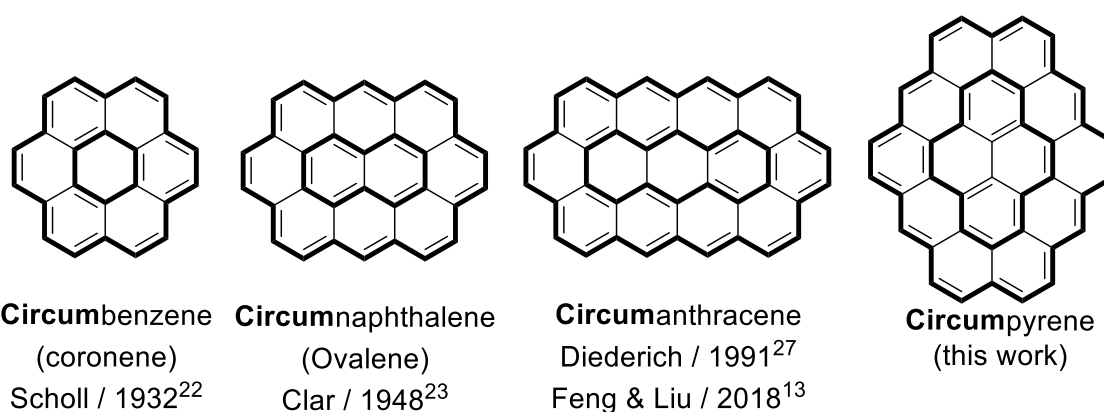
ABSTRACT: A transition-metal catalyzed benzannulation allowed an unprecedented synthesis of circumpyrene, starting from 3,11-dibromo-6,14-dimesityldibenzo[*hi,st*]ovalene (DBOV). The circumpyrene was characterized by a combination of NMR, mass spectrometry, and single-crystal X-ray diffraction analysis, revealing its fully zigzag-edged structure. Two extra C=C bonds in circumpyrene perturbed the electronic structures of DBOV, as evidenced by increased optical and electrochemical energy gaps. This is in good agreement with a decreased number of electrons in the conjugation pathway of circumpyrene, according to anisotropy of the induced current density (ACID) calculations. The present approach opens up a new avenue to fully zigzag-edged nanographenes and provides insights into their (opto)electronic properties.

Submitted to:

Journal of the American Chemical Society

Nanographenes, extended, nanosized, polycyclic aromatic hydrocarbons (PAHs), exhibit unique and structure-dependent electronic, optical, and magnetic properties,¹⁻³ highlighting their potential as next-generation carbon materials for photonics, (opto)electronics, and spintronics.⁴⁻¹⁰ Nanographenes with partial zigzag edges, e.g. periacenes, anthenes, and zethrenes, have attracted particular attention because of their low energy gaps and/or open-shell character.¹¹⁻¹⁹ Fully zigzag-edged nanographenes have also been frequent targets of theoretical studies, but there are still a limited number of synthesized examples, precluding detailed experimental investigations.¹¹ Circumarenes are a subclass of fully zigzag-edged nanographenes that have a central aromatic core surrounded by one outer layer of annulene (Scheme 6-1). The smallest circumarenes, namely circumbenzene (coronene)²⁰⁻²⁴ and circumnaphthalene (ovalene),²⁵ were synthesized by Scholl and Clar, respectively, and their soluble derivatives were later employed in supramolecular self-assembly and (opto)electronic device studies.²⁶⁻²⁸ Larger circumanthracene was first synthesized by Diederich and his colleagues²⁹ and its tetracyano derivative was more recently reported by Feng et al.¹³ Circumpyrene and circumcoronene, as the next members of the circumarene family, have been targets of theoretical studies.³⁰⁻³⁵ However, to the best of our knowledge, synthesis of circumarenes comprising a central aromatic unit larger than three benzene rings has never been achieved.

Scheme 6-1. Structures of representative circumarenes.

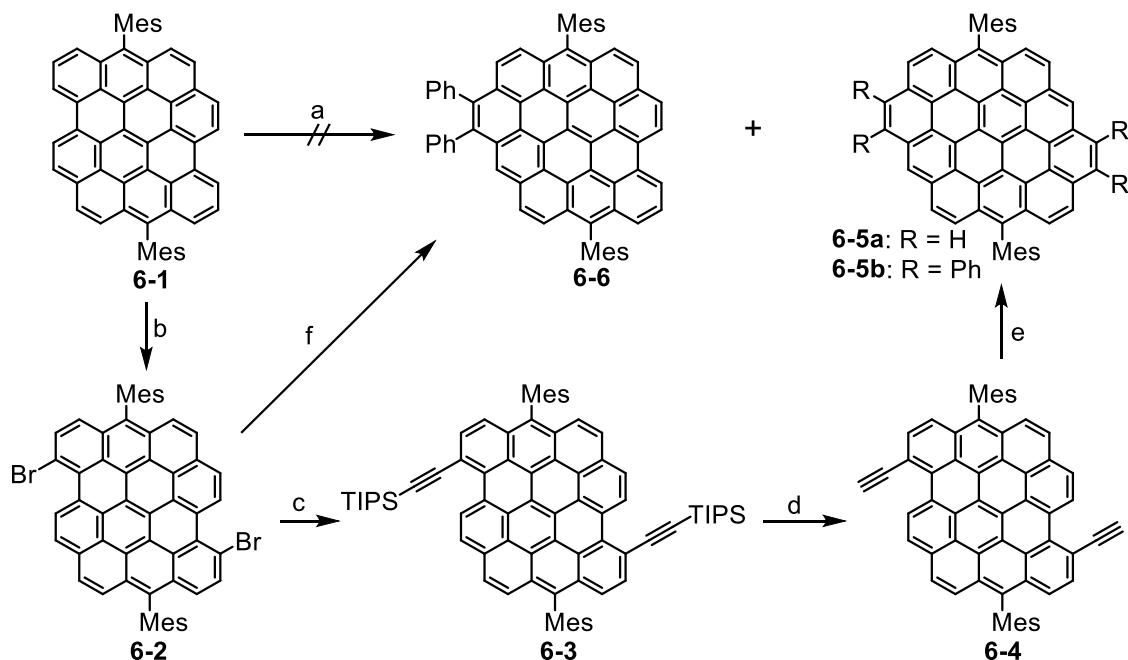


The challenge is that fully zigzag-edged nanographenes cannot be readily obtained by the cyclodehydrogenation of pre-formed polyphenylene precursors, which has been well established and has yielded numerous PAHs in recent decades.³⁶ Reactions occurring at bay regions of PAHs, such as intramolecular Friedel-Crafts alkylation,³⁷⁻³⁹ Diels-Alder cycloaddition^{20, 25} and cyclization of pre-installed ethynyl bonds,²⁶ permit this obstacle to be surmounted and are capable of building up extended aromatic cores. In addition, Pd-catalyzed

direct annulation of substituted acetylenes and halogenated PAHs has been used to form new fused ring systems appended with extra five-, six- or eight-membered rings.⁴⁰⁻⁴³ Recently, we reported syntheses of dibenzo[*hi, st*]ovalene (DBOV) derivatives, including **6-1** (Scheme 6-2), as new nanographenes with both zigzag and armchair edges.^{39, 44-46} Anticipating that introduction of two additional double bonds to the bay regions of DBOV would lead to the long-awaited circumpylene, we explored possible synthetic strategies.

Herein, we describe a concise synthesis of two circumpylene derivatives **6-5a** and **6-5b** using platinum- and palladium-catalyzed cyclization and benzannulation reactions, respectively, as the key steps, starting from DBOV derivatives. Although possessing full zigzag peripheries, these molecules exhibit remarkably high stability under ambient conditions. Spectroscopic and electrochemical characterizations reveal significant electronic effects of the fused C=C bonds when going from DBOV to circumpylene.

Scheme 6-2. Synthesis of circumpyrenes via transition-metal-catalyzed benzannulation.^a



^aReagents and conditions: a) diphenylacetylene, *o*-dichlorobenzene, 180 °C, 24 h, no reaction; b) NBS, THF, r.t., 79% yield; c) Pd(PPh₃)₂Cl₂•CH₂Cl₂, CuI, TEA, THF, 80 °C, overnight, 31% yield; d) TBAF, THF, r.t., 32% yield; e) PtCl₂, toluene, 80 °C, 24 h, 46% yield; f) Pd(OAc)₂, NaOAc, LiCl, DMF, 130 °C, 12 h, for **6-6**: 40% yield; for **6-5b**: 15% yield. THF: tetrahydrofuran; DMF: *N,N*-dimethylformamide; TEA: triethylamine.

Toward the synthesis of circumpylene **6-5**, we initially attempted direct Diels-Alder cycloaddition of **6-1** with diphenyl acetylene (Scheme 6-2). However, no reaction occurred

even when heated at 180 °C in *o*-dichlorobenzene for 24 h, most probably because of the weakly pronounced diene character of **6-1**.⁴⁷ In an alternative approach, 3,11-dibromo-6,14-dimesityldibenzo[*hi,st*]ovalene (**6-2**) was considered as a precursor that could be obtained by regioselective bromination of **6-1** with *N*-bromosuccinimide (NBS).⁴⁵ We previously reported a Sonogashira coupling of **6-2** with triisopropylsilyl (TIPS) acetylene to obtain **6-3** in 31% yield. Deprotection of **6-3** with tetra-*n*-butylammonium fluoride (TBAF) proceeded at room temperature to give **6-4** in 32% yield. Subsequently, PtCl₂ catalyzed cyclization of the ethynyl groups yielded circumpyrene **6-5a** in 46% yield. **6-5a** could be characterized by ¹H NMR and high-resolution mass spectrometry (see SI), but its low solubility hampered further characterizations, for example, by ¹³C NMR and cyclic voltammetry. In order to increase the solubility of the circumpyrene and also to simplify its synthesis, we considered direct benzannulation of **6-2** with diarylacetylenes.⁴⁰ To our delight, reaction of **6-2** and diphenylacetylene in toluene at 130 °C using Pd(PPh₃)₄ as catalyst provided a mixture of **6-6** and **6-5b** as one- and two-fold benzannulated products (Figure S6-1). After optimizing reaction conditions, the combination of Pd(OAc)₂/NaOAc/LiCl achieved the best result, affording **6-6** and **6-5b** in 40% and 15% yield, respectively.

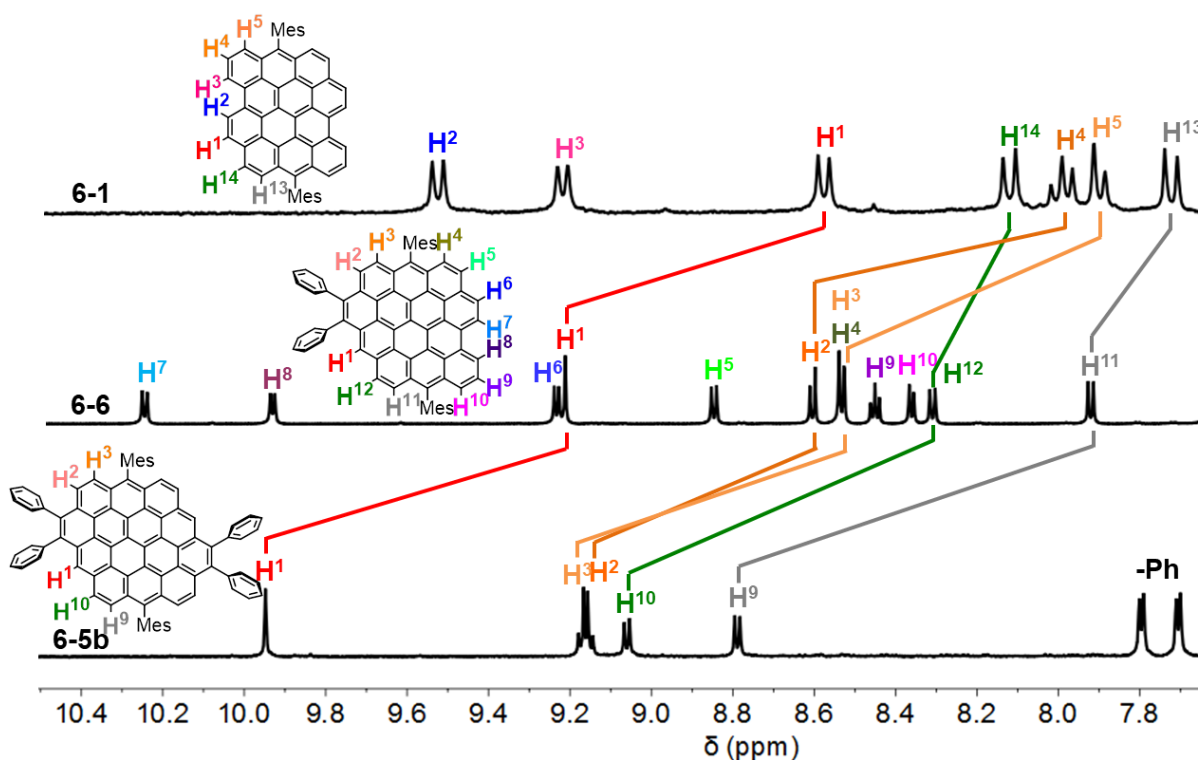


Figure 6-1. Comparison of ¹H NMR spectra of **6-1** (300 MHz, 298 K), **6-6**, and **6-5b** in tetrahydrofuran-*d*₈:CS₂ (1:1) (700 MHz, 298 K).

^1H NMR spectra of **6-1**, **6-6**, and **6-5b** displayed well-resolved peaks (Figure 6-1), which could be fully assigned by two-dimensional (2D) NMR techniques (Figure S6-11–6-12 and S6-16–6-17). After fusing one C=C bond to **6-1**, the ^1H NMR spectrum of **6-6** became more complex and twelve sets of peaks could be observed. In contrast, circumpyrene **6-5b** exhibited only one singlet peak and four sets of doublet peaks, in accordance with its C_{2h} symmetry. Compared with **6-1**, the signals of protons on the core of **6-5b** are shifted downfield as a result of the extended size of its aromatic core and thus more significant deshielding effect. For example, the doublet peak of **6-1** (H^1) at 8.61 ppm was moved to 9.27 ppm in the spectrum of **6-6** and 9.95 ppm in that of circumpyrene **6-5b**. The other peaks also displayed similar low-field shifts. The potential open-shell character of circumpyrene is excluded by these sharp ^1H NMR peaks observed at room temperature and high chemical stability under air. To obtain further insights into the aromaticity of the whole circumpyrene skeleton, we conducted nucleus independent chemical shift (NICS) analysis (Figure 6-2a–6-2c).^{48, 49} It is obvious to see that from **6-1** to **6-6** and **6-5b**, the NICS(1) values of all the benzene rings are decreased. The newly formed benzene rings have the second highest aromaticity. Moreover, the antiaromatic rings B/B' in **6-1** (Figure 6-2a) become aromatic in **6-5b**. These results are in accordance with the experimentally observed low-field chemical shifts of H^1 , H^2 , and H^3 compared with H^9 and H^{10} for **6-5b**.

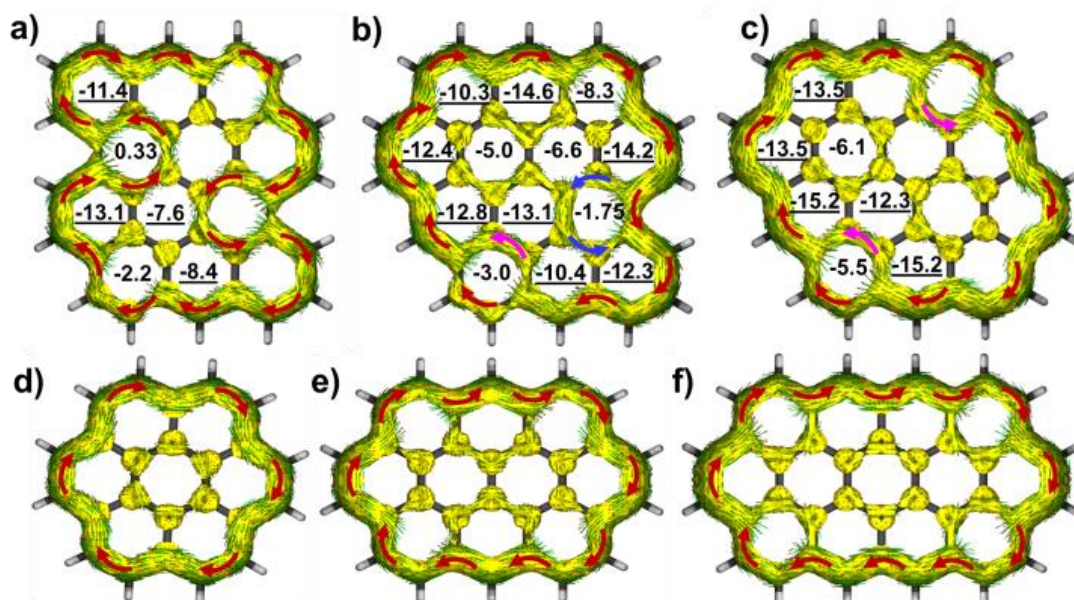


Figure 6-2. Calculated ACID (B3LYP/6-31G(d,p)) plots of a) **6-1**, b) **6-6**, c) **6-5b**, d) coronene, e) ovalene, and f) circumanthracene (isovalue = 0.05; Only contributions from π -electrons of the aromatic cores are considered; The magnetic field vector is perpendicular to the ring plane and points

outward; Red arrows indicate direction of induced ring current.). For a–c), the numbers inside the six-membered rings indicate NICS (1) values calculated at the same level (the substituents were replaced by H for all calculations).

The anisotropy of the induced current density (ACID)⁵⁰ plot of DBOV calculated at B3LYP/6-31G(d,p) (Figure 6-2a) indicates that at the isosurface value of 0.05, there is clockwise (diatropic) ring current delocalized over a pathway constituted by 34 carbon atoms. After fusing with one C=C bond, the carbon atoms involved in the conjugation pathway decreased to 30 (Figure 6-2b). In circumpyrene, only 26 carbon atoms in the outer rim participate in the diatropic ring current, and the 2 benzene rings in the center have almost no induced ring current (Figure 6-2c). These results are in very good agreement with the low aromaticity of the B/B' and E/E' rings in the circumpyrene core, and also similar to characteristics of the ACID calculated for smaller circumarenes (Figure 6-2d–6-2f).

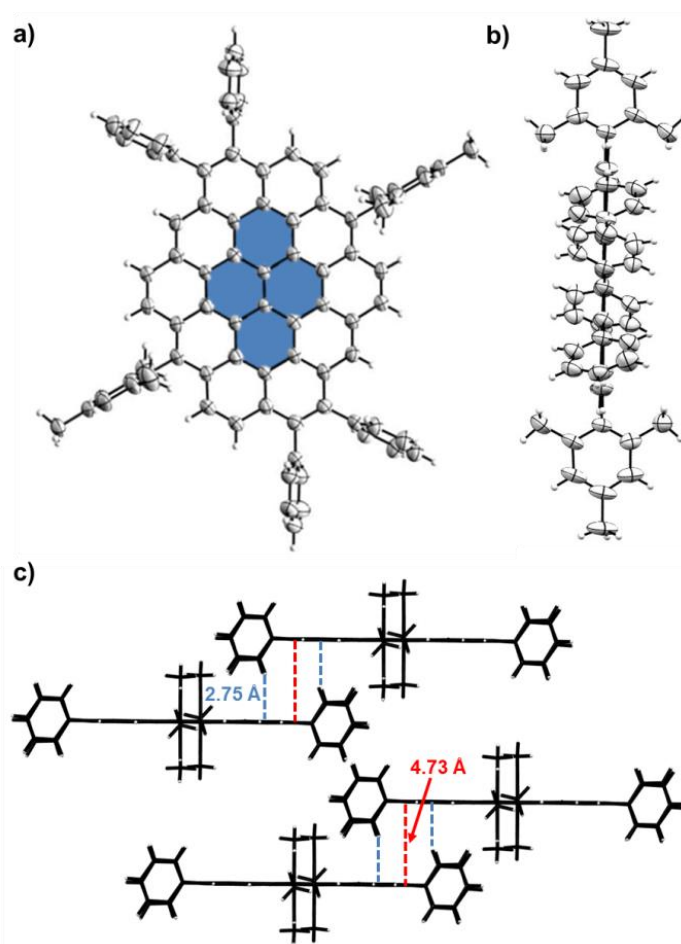


Figure 6-3. X-ray single-crystal structure of circumpyrene **6-5b**, a) front view, b) side view (H, C atoms are shown as ellipsoids set at 50% probability); c) The packing arrangement pattern of **6-5b** in the crystal (the solvents are omitted for clarity).

Single-crystal structure of **6-5b** clearly revealed the central pyrene and zigzag-shaped periphery shaping the outer rim (Figure 6-3a-b). The main skeleton of **6-5b** adopts a planar configuration, with all the peripheral substituents being nearly perpendicular to the core (dihedral angles 85–90°). Two circumpyrene molecules are stacked almost parallel to each other to form a dimer with a plane to plane distance of 4.73 Å, and such dimers are staggered with each other in the whole crystal (Figure 6-3c and Figure S6-2). As a result, there is no significant π - π interaction between circumpyrene molecules. Additionally, the distance between the CH bonds of the phenyl rings and the core of the neighboring circumpyrene molecules is as short as 2.75 Å (less than the sum of the van der Waals radius), indicating the existence of CH- π interactions,⁵¹ which is responsible for the close intermolecular packing in the single crystal structure.

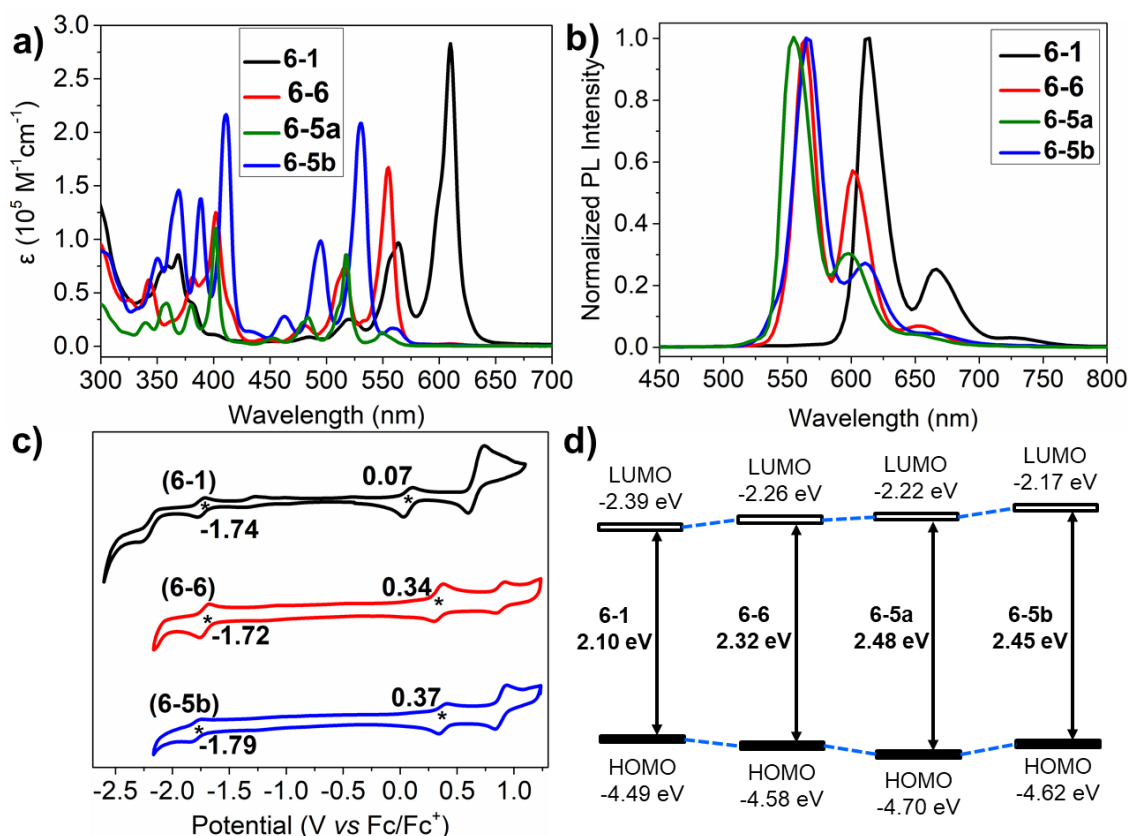


Figure 6-4. a) UV-vis absorption and b) fluorescence spectra of **6-1**, **6-6** and **6-5a/6-5b** in toluene with concentration of 10^{-6} M; c) Cyclic voltammograms of **6-1**, **6-6**, and **6-5b** measured in 0.1 M tetra-*n*-butylammonium hexafluorophosphate in dichloromethane (* indicates the onset potential of these oxidation/reduction peaks); d) HOMO, LUMO, and energy gaps of **6-1–6-5b** calculated by DFT at the B3LYP/6-31G(d,p) level.

The UV-vis absorption and fluorescence spectra of **6-1**, **6-6**, **6-5a**, and **6-5b** were measured in toluene to elucidate the effect of benzannulation on their optoelectronic properties (Figure 6-4a). All the absorption spectra exhibited intense and well-resolved absorption bands in two separated regions (300–450 nm and 450–650 nm). Fusion of one double bond to the bay region of **6-1** induced significant blue shifts of the longest absorption wavelength (λ_{max}) from 611 nm (**6-1**) to 555 nm (**6-6**), while there was no obvious effect on the shape of the absorption peaks. In contrast, the longest-wavelength absorption bands of **6-5a** and **6-5b** located at 549 and 558 nm, respectively, were apparently a forbidden transition, while the second-longest-wavelength bands at 519 nm and 531 nm, respectively, appeared as the absorption maxima. The intensity ratios of these peaks were independent of the concentration of **6-5** (10^{-5} – 10^{-8} M), which excluded a possibility of aggregation-induced effects (Figure S6-4). Notably, these observations agreed very well with a recent report by Lischka and co-workers, who theoretically predicted forbidden HOMO–1 (H-1)→LUMO (L) and H→L+1 transitions as the longest-wavelength absorption of circumpyrene, based on density functional theory/multireference configuration interaction (DFT/MRCI) calculations.³⁴ On the other hand, the second-longest-wavelength band of **6-5** was mainly assigned to H→L transitions,³⁴ which are split into several small shoulder peaks due to vibronic coupling. The latter corresponded to the longest-wavelength bands of **6-1** and **6-6**. The absorption wavelength of **6-5a** was slightly blue shifted relative to **6-5b** due to decreased conjugation by removal of four substituted phenyl groups. There was no detectable change in the absorption spectra of **6-5b** after storage of the solution under ambient conditions for more than 8 months, marking its extremely high stability. In fluorescence spectra, the maximum emission wavelengths of **6-1**, **6-6**, **6-5a**, and **6-5b** were located at 614, 563, 555, and 566 nm, respectively, and their absolute fluorescence quantum yields (Φ) decreased dramatically after fusing extra double bond from 0.79 to 0.42, 0.11, and 0.17. The Stokes shifts were less than 10 nm, indicating rigid structures of these molecules.

Cyclic voltammetry (CV) analysis of **6-1** revealed two sets of reversible reduction and oxidation potentials with the half-wave potential of the first oxidation and reduction potential to be –0.01 and –1.67 V relative to Fc/Fc⁺. Fusion with one double bond to form **6-6** had a negligible effect on the reduction potential of **6-1**, but greatly improved its first oxidation potential to 0.26 V. **6-5b** exhibited the first oxidation potential at 0.31 V and slightly lowered first reduction potential at –1.71 V. The electrochemical energy gaps were estimated from the onsets of the first oxidation and reduction potential to be 1.81, 2.06, and 2.16 eV, for **6-1**, **6-6**,

and **6-5b**, respectively. This trend agreed with the HOMO-LUMO gaps based on the DFT calculations (Figure 6-4d and S6-5) and could be reasonably explained by decreased number of electrons in the conjugation pathway after fusing with C=C bonds according to the ACID plots (Figure 6-2).

In conclusion, we have achieved the synthesis of circumpyrenes as novel fully zigzag-edged nanographenes, based on 1) transition-metal-catalyzed cyclization of ethynyl-substituted DBOV and 2) direct benzannulation of dibrominated DBOV with diphenylacetylene. Stepwise fusion of extra benzene rings to the bay region of DBOV enlarged their energy gaps, which was demonstrated by UV-vis absorption spectroscopy, CV measurements, and supported with theoretical calculations. Circumpyrene represents the largest circumarene molecule ever synthesized and can now provide further insights into this intriguing class of PAHs, not only the optoelectronic and electrochemical properties as studied here, but also more detailed photophysics, self-assembly behavior, and potential applications in electronic devices as the next steps. Moreover, the current synthetic approach for circumpyrenes offers opportunity to obtain a further variety of unprecedented nanographenes having full zigzag edges.

ASSOCIATED CONTENT

Supporting Information

The Supporting Information is available free of charge on the ACS Publications website.

Experimental details, synthesis, X-ray crystallography details, HR mass spectra, NMR spectra and computational studies (PDF)

Data for **6-5b** (CIF)

AUTHOR INFORMATION

Corresponding Author

*narita@mpip-mainz.mpg.de

*muellen@mpip-mainz.mpg.de

Notes

The authors declare no competing financial interests.

ACKNOWLEDGMENT

This work was financially supported by the Max Planck Society.

REFERENCES

- (1) Narita, A.; Wang, X. Y.; Feng, X.; Müllen, K. New advances in nanographene chemistry. *Chem. Soc. Rev.* **2015**, *44*, 6616-6643.
- (2) Ponomarenko, L. A.; Schedin, F.; Katsnelson, M. I.; Yang, R.; Hill, E. W.; Novoselov, K. S.; Geim, A. K. Chaotic Dirac billiard in graphene quantum dots. *Science* **2008**, *320*, 356-358.
- (3) Zhao, S.; Lavie, J.; Rondin, L.; Orcin-Chaix, L.; Diederichs, C.; Roussignol, P.; Chassagneux, Y.; Voisin, C.; Müllen, K.; Narita, A.; Campidelli, S.; Lauret, J. S. Single photon emission from graphene quantum dots at room temperature. *Nat. Commun* **2018**, *9*, 3470.
- (4) Kim, S.; Kim, B.; Lee, J.; Shin, H.; Park, Y.-I.; Park, J. Design of fluorescent blue light-emitting materials based on analyses of chemical structures and their effects. *Mater. Sci. Eng. R Rep* **2016**, *99*, 1-22.
- (5) Laschat, S.; Baro, A.; Steinke, N.; Giesselmann, F.; Hagele, C.; Scalia, G.; Judele, R.; Kapatsina, E.; Sauer, S.; Schreivogel, A.; Tosoni, M. Discotic liquid crystals: from tailor-made synthesis to plastic electronics. *Angew. Chem. Int. Ed. Engl.* **2007**, *46*, 4832-4887.
- (6) Mei, J.; Diao, Y.; Appleton, A. L.; Fang, L.; Bao, Z. Integrated materials design of organic semiconductors for field-effect transistors. *J. Am. Chem. Soc.* **2013**, *135*, 6724-6746.
- (7) Pisula, W.; Feng, X.; Müllen, K. Tuning the columnar organization of discotic polycyclic aromatic hydrocarbons. *Adv. Mater.* **2010**, *22*, 3634-3649.
- (8) Sergeyev, S.; Pisula, W.; Geerts, Y. H. Discotic liquid crystals: a new generation of organic semiconductors. *Chem. Soc. Rev.* **2007**, *36*, 1902-29.
- (9) Wohrle, T.; Wurzbach, I.; Kirres, J.; Kostidou, A.; Kapernaum, N.; Litterscheidt, J.; Haenle, J. C.; Staffeld, P.; Baro, A.; Giesselmann, F.; Laschat, S. Discotic Liquid Crystals. *Chem. Rev.* **2016**, *116*, 1139-1241.
- (10) Wu, J.; Pisula, W.; Müllen, K. Graphenes as potential material for electronics. *Chem. Rev.* **2007**, *107*, 718-747.
- (11) Gu, Y.; Wu, X.; Gopalakrishna, T. Y.; Phan, H.; Wu, J. Graphene-like Molecules with Four Zigzag Edges. *Angew. Chem. Int. Ed. Engl.* **2018**, *57*, 6541-6545.
- (12) Inoue, J.; Fukui, K.; Kubo, T.; Nakazawa, S.; Sato, K.; Shiomi, D.; Morita, Y.; Yamamoto, K.; Takui, T.; Nakasuji, K. The First Detection of a Clar's Hydrocarbon, 2,6,10-Tri-tert-Butyltriangulene: A Ground-State Triplet of Non-Kekulé Polynuclear Benzenoid Hydrocarbon. *J. Am. Chem. Soc.* **2001**, *123*, 12702-12703.
- (13) Ajayakumar, M. R.; Fu, Y.; Ma, J.; Hennersdorf, F.; Komber, H.; Weigand, J. J.; Alfonsov, A.; Popov, A. A.; Berger, R.; Liu, J.; Müllen, K.; Feng, X. Toward Full Zigzag-

Edged Nanographenes: peri-Tetracene and Its Corresponding Circumanthracene. *J. Am. Chem. Soc.* **2018**, *140*, 6240-6244.

(14) Ni, Y.; Gopalakrishna, T. Y.; Phan, H.; Heng, T. S.; Wu, S.; Han, Y.; Ding, J.; Wu, J. A Peri-tetracene Diradicaloid: Synthesis and Properties. *Angew. Chem. Int. Ed. Engl.* **2018**, *57*, 9697-9701.

(15) Liu, J.; Ravat, P.; Wagner, M.; Baumgarten, M.; Feng, X.; Müllen, K. Tetrabenz[a,f,j,o]perylene: a polycyclic aromatic hydrocarbon with an open-shell singlet biradical ground state. *Angew. Chem. Int. Ed. Engl.* **2015**, *54*, 12442-12446.

(16) Konishi, A.; Hirao, Y.; Nakano, M.; Shimizu, A.; Botek, E.; Champagne, B.; Shiomi, D.; Sato, K.; Takui, T.; Matsumoto, K.; Kurata, H.; Kubo, T. Synthesis and characterization of teranthene: a singlet biradical polycyclic aromatic hydrocarbon having Kekule structures. *J. Am. Chem. Soc.* **2010**, *132*, 11021-11023.

(17) Konishi, A.; Hirao, Y.; Matsumoto, K.; Kurata, H.; Kishi, R.; Shigeta, Y.; Nakano, M.; Tokunaga, K.; Kamada, K.; Kubo, T. Synthesis and characterization of quarteranthene: elucidating the characteristics of the edge state of graphene nanoribbons at the molecular level. *J. Am. Chem. Soc.* **2013**, *135*, 1430-1437.

(18) Sun, Z.; Zeng, Z.; Wu, J. Zethrenes, extended p-quinodimethanes, and periacenes with a singlet biradical ground state. *Acc. Chem. Res.* **2014**, *47*, 2582-2591.

(19) Umeda, R.; Hibi, D.; Miki, K.; Tobe, Y. Tetradehydrodinaphtho[10]annulene: A Hitherto Unknown Dehydroannulene and a Viable Precursor to Stable Zethrene Derivatives. *Org. Lett.* **2009**, *11*, 4104-4106.

(20) Newman, M. S. A New Synthesis of Coronene. *J. Am. Chem. Soc.* **1940**, *62*, 1683-1687.

(21) Craig, J. T.; Halton, B.; Lo, S. A new coronene synthesis. *Aust. J. Chem.* **1975**, *28*, 913.

(22) Shen, H. C.; Tang, J. M.; Chang, H. K.; Yang, C. W.; Liu, R. S. Short and efficient synthesis of coronene derivatives via ruthenium-catalyzed benzannulation protocol. *J. Org. Chem.* **2005**, *70*, 10113-101136.

(23) van Dijk, J. T. M.; Hartwijk, A.; Bleeker, A. C.; Lugtenburg, J.; Cornelisse, J. Gram Scale Synthesis of Benzo[ghi]perylene and Coronene†. *J. Org. Chem.* **1996**, *61*, 1136-1139.

(24) Scholl, R.; Meyer, K. Synthese desanti-diperi-Dibenz-coronens und dessen Abbau zum Coronen (Hexabenzobenzol). (Mitbearbeitet von Horst v. Hoeßle und Solon Brissimdj). *Berichte der deutschen chemischen Gesellschaft (A and B Series)* **1932**, *65*, 902-915.

(25) Clar, E. Synthesis of Ovalene. *Nature* **1948**, *161*, 238-239.

- (26) Rohr, U.; Schlichting, P.; Böhm, A.; Gross, M.; Meerholz, K.; Bräuchle, C.; Müllen, K. Liquid Crystalline Coronene Derivatives with Extraordinary Fluorescence Properties. *Angew. Chem. Int. Ed.* **1998**, *37*, 1434-1437.
- (27) Saidi-Besbes, S.; Grelet, E.; Bock, H. Soluble and liquid-crystalline ovalenes. *Angew. Chem. Int. Ed. Engl.* **2006**, *45*, 1783-1786.
- (28) Li, J.; Chang, J.-J.; Tan, H. S.; Jiang, H.; Chen, X.; Chen, Z.; Zhang, J.; Wu, J. Disc-like 7, 14-dicyano-ovalene-3,4:10,11-bis(dicarboximide) as a solution-processible n-type semiconductor for air stable field-effect transistors. *Chem. Sci.* **2012**, *3*, 846-850.
- (29) Broene, R. D.; Diederich, F. The synthesis of circumanthracene. *Tetrahedron Lett.* **1991**, *32*, 5227-5230.
- (30) Weisman, J. L.; Lee, T. J.; Salama, F.; Head-Gordon, M. Time-dependent Density Functional Theory Calculations of Large Compact Polycyclic Aromatic Hydrocarbon Cations: Implications for the Diffuse Interstellar Bands. *Astrophys. J.* **2003**, *587*, 256-261.
- (31) Philpott, M. R.; Kawazoe, Y. Transition metal sandwich molecules with large (C_n, n ≥ 24) zigzag poly aromatic hydrocarbons. *Chem. Phys.* **2008**, *348*, 69-82.
- (32) Philpott, M. R.; Kawazoe, Y. Metal Sandwich Molecules: Planar Metal Atom Arrays between Aromatic Hydrocarbons. *Mater. Trans.* **2007**, *48*, 693-699.
- (33) Soncini, A.; Steiner, E.; Fowler, P. W.; Havenith, R. W. A.; Jennekens, L. W. Perimeter Effects on Ring Currents in Polycyclic Aromatic Hydrocarbons: Circumcoronene and Two Hexabenzocoronenes. *Chem.: Eur. J* **2003**, *9*, 2974-2981.
- (34) Shi, B.; Nachtigallova, D.; Aquino, A. J. A.; Machado, F. B. C.; Lischka, H. High-level theoretical benchmark investigations of the UV-vis absorption spectra of paradigmatic polycyclic aromatic hydrocarbons as models for graphene quantum dots. *J. Chem. Phys.* **2019**, *150*, 124302.
- (35) Menon, A.; Dreyer, J. A. H.; Martin, J. W.; Akroyd, J.; Robertson, J.; Kraft, M. Optical band gap of cross-linked, curved, and radical polyaromatic hydrocarbons. *Phys. Chem. Chem. Phys.* **2019**, *21*, 16240-16251.
- (36) Dumslaff, T.; Yang, B.; Maghsoumi, A.; Velpula, G.; Mali, K. S.; Castiglioni, C.; De Feyter, S.; Tommasini, M.; Narita, A.; Feng, X.; Müllen, K. Adding Four Extra K-Regions to Hexa-peri-hexabenzocoronene. *J. Am. Chem. Soc.* **2016**, *138*, 4726-4729.
- (37) Harvey, R. G.; Pataki, J.; Cortez, C.; Di Raddo, P.; Yang, C. X. A new general synthesis of polycyclic aromatic compounds based on enamine chemistry. *J. Org. Chem.* **1991**, *56*, 1210-1217.

- (38) Lungerich, D.; Papaianina, O.; Feofanov, M.; Liu, J.; Devarajulu, M.; Troyanov, S. I.; Maier, S.; Amsharov, K. Dehydrative pi-extension to nanographenes with zig-zag edges. *Nat. Commun* **2018**, *9*, 4756.
- (39) Paterno, G. M.; Chen, Q.; Wang, X. Y.; Liu, J.; Motti, S. G.; Petrozza, A.; Feng, X.; Lanzani, G.; Müllen, K.; Narita, A.; Scotognella, F. Synthesis of Dibenzo[hi,st]ovalene and Its Amplified Spontaneous Emission in a Polystyrene Matrix. *Angew. Chem. Int. Ed. Engl.* **2017**, *56*, 6753-6757.
- (40) Lutke Eversloh, C.; Avlasevich, Y.; Li, C.; Müllen, K. Palladium-catalyzed pentannulation of polycyclic aromatic hydrocarbons. *Chem.: Eur. J* **2011**, *17*, 12756-12762.
- (41) Mandal, A. B.; Lee, G.-H.; Liu, Y.-H.; Peng, S.-M.; Leung, M.-k. Formation of 4-Methylphenanthrenes in Palladium-Catalyzed Annulation of Diethyl 2,2'-Diiodo-4,4'-biphenyldicarboxylate with Internal Alkynes, Using Methyl Nitrobenzoates as the Methylating Agent. *J. Org. Chem.* **2000**, *65*, 332-336.
- (42) Campo, M. A.; Huang, Q.; Yao, T.; Tian, Q.; Larock, R. C. 1,4-palladium migration via C-H activation, followed by arylation: synthesis of fused polycycles. *J. Am. Chem. Soc.* **2003**, *125*, 11506-11507.
- (43) Ozaki, K.; Murai, K.; Matsuoka, W.; Kawasumi, K.; Ito, H.; Itami, K. One-Step Annulative pi-Extension of Alkynes with Dibenzosiloles or Dibenzogermoles by Palladium/o-chloranil Catalysis. *Angew. Chem. Int. Ed. Engl.* **2017**, *56*, 1361-1364.
- (44) Coles, D. M.; Chen, Q.; Flatten, L. C.; Smith, J. M.; Müllen, K.; Narita, A.; Lidzey, D. G. Strong Exciton-Photon Coupling in a Nanographene Filled Microcavity. *Nano Lett.* **2017**, *17*, 5521-5525.
- (45) Chen, Q.; Wang, D.; Baumgarten, M.; Schollmeyer, D.; Müllen, K.; Narita, A. Regioselective Bromination and Functionalization of Dibenzo[hi,st]ovalene as Highly Luminescent Nanographene with Zigzag Edges. *Chem. Asian J* **2019**.
- (46) Chen, Q.; Thoms, S.; Thoms, S.; Stöttinger, S.; Schollmeyer, D.; Müllen, K.; Narita, A.; Basché, T. Dibenzo[hi,st]ovalene as Highly Luminescent Nanographene: Efficient Synthesis via Photochemical Cyclodehydroiodination, Opto-electronic Properties and Single-Molecule Spectroscopy. *J. Am. Chem. Soc.* **2019**, *141*, 16439-16449.
- (47) Fort, E. H.; Donovan, P. M.; Scott, L. T. Diels-Alder reactivity of polycyclic aromatic hydrocarbon bay regions: implications for metal-free growth of single-chirality carbon nanotubes. *J. Am. Chem. Soc.* **2009**, *131*, 16006-16007.

- (48) Chen, Z.; Wannere, C. S.; Corminboeuf, C.; Puchta, R.; Schleyer, P. Nucleus-independent chemical shifts (NICS) as an aromaticity criterion. *Chem. Rev.* **2005**, *105*, 3842-3888.
- (49) Schleyer, P. V. R.; Maerker, C.; Dransfeld, A.; Jiao, H.; van Eikema Hommes, N. J. R. Nucleus-Independent Chemical Shifts: A Simple and Efficient Aromaticity Probe. *J. Am. Chem. Soc.* **1996**, *118*, 6317-6318.
- (50) Geuenich, D.; Hess, K.; Kohler, F.; Herges, R. Anisotropy of the induced current density (ACID), a general method to quantify and visualize electronic delocalization. *Chem. Rev.* **2005**, *105*, 3758-3772.
- (51) Umezawa, Y.; Tsuboyama, S.; Takahashi, H.; Uzawa, J.; Nishio, M. interaction in the conformation of organic compounds. A database study. *Tetrahedron* **1999**, *55*, 10047-10056.

Supporting Information

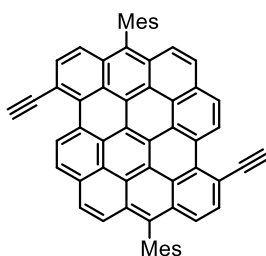
Synthesis of Circumpyrene: Nanographene with Full a Zigzag Periphery**1. Supplementary Methods****General methods**

All reactions working with air- or moisture- sensitive compounds were carried out under argon atmosphere using standard Schlenk line techniques. Unless otherwise noted, all starting materials were purchased from commercial sources and used without further purification. All other reagents were used as received. Thin layer chromatography (TLC) was done on silica gel coated aluminum sheets with F254 indicator and column chromatography separation was performed with silica gel (particle size 0.063–0.200 mm). Nuclear Magnetic Resonance (NMR) spectra were recorded using Bruker DPX 300, Bruker DPX 500, and Bruker DRX 700 MHz NMR spectrometers. Chemical shifts (δ) were expressed in ppm relative to the residual of solvents (*o*-dichlorobenzene-*d*₄, ¹H: 7.20 ppm, ¹³C: 132.35 ppm; THF-*d*₈, ¹H: 3.58 ppm, ¹³C: 67.57 ppm). Coupling constants (*J*) were recorded in Hertz. High resolution mass spectra (HR MS) were recorded on a Bruker Reflex II-TOF spectrometer by matrix-assisted laser decomposition/ionization (MALDI) using 7,7,8,8-tetracyanoquinodimethane (TCNQ) as matrix calibrated with poly(ethylene glycol). UV-*vis* absorption spectra were recorded on a Perkin-Elmer Lambda 900 spectrometer at room temperature using a 10 mm quartz cell. Photoluminescence spectra were recorded on a J&MTIDAS spectrofluorometer. The fluorescence quantum yield (Φ) of **DBOV-Mes** was measured using Nile blue A perchlorate (in ethanol under air, $\Phi = 0.27$) as a reference.¹ Absolute fluorescence quantum yields were measured using an integrating sphere. Cyclic voltammetry (CV) measurements were performed on a GSTAT-12 in a three-electrode cell in dichloromethane solution of *n*-Bu₄NPF₆ (0.1 M) at a scan rate of 50 mV/s at room temperature. A silver wire, a Pt wire and a glassy carbon electrode were used as the reference electrode, the counter electrode, and the working electrode, respectively.

Synthetic Details

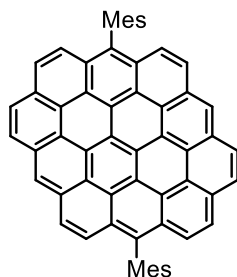
DBOV intermediates **6-1**, **6-2**, **6-3** were prepared according to the methods reported by our group recently. The characterization data were the same as that reported in these references.^{2,3}

3,11-diethynyl-6,14-dimesityldibenzo[*hi,st*]ovalene (**6-4**)



To a solution of 3,11-bis{(triisopropylsilyl)ethynyl}-6,14-dimesityldibenzo[*hi,st*]ovalene (**6-3**) (21.9 mg, 0.0205 mmol) in dry tetrahydrofuran (50 mL) was added tetra-*n*-butylammonium fluoride (0.037 mL, 1.0 M in tetrahydrofuran). The resulting mixture was stirred at room temperature for 2 h. After completion of the reaction, methanol (2 mL) was added and the solvents were evaporated. The obtained residue was purified by silica gel column chromatography (*n*-hexane:tetrahydrofuran = 10:1) followed by recrystallization from dichloromethane/methanol to give the title compound (4.5 mg, 32% yield) as blue solid. ¹H NMR (500 MHz, *o*-dichlorobenzene-*d*₄, 403 K) δ 11.22 (d, *J* = 8.3 Hz, 2H), 8.57 (d, *J* = 8.4 Hz, 2H), 8.16 (d, *J* = 8.5 Hz, 2H), 8.11 (d, *J* = 9.1 Hz, 2H), 7.97 (d, *J* = 8.7 Hz, 2H), 7.89 (d, *J* = 9.1 Hz, 2H), 3.85 (s, 2H), 2.48 (s, 6H), 1.98 (s, 12H); HRMS (MALDI-TOF): *m/z* Calcd for C₆₀H₃₆: 756.2812 [M]⁺, found: 756.2787. The ¹³C NMR cannot be obtained due to low solubility and instability of target compound at high temperature.

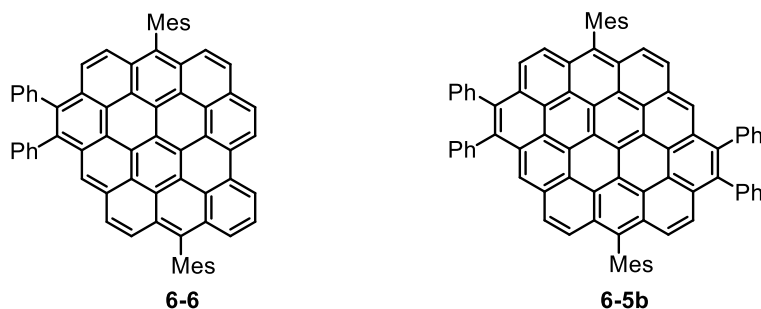
5,13-dimesitylcircumpyrene (**6-5a**)



To a 25 mL Schlenk tube was added 3,11-diethynyl-6,14-dimesityldibenzo[*hi,st*]ovalene (**6-4**) (3.66 mg, 0.00484 mmol) and PtCl₂ (0.72 mg, 0.0025 mmol). The tube was evacuated and backfilled with argon for three times then dried under vacuum for 2 h. Dry toluene (5 mL) was added and the solution was degassed by three times freeze-pump-thaw cycles. The mixture was heated at 90 °C for 24 h. After cooling down to room temperature, the solvent was removed under reduced pressure and the residue was purified by column chromatography (*n*-hexane:tetrahydrofuran = 10:1) to give title compound (1.7 mg, 46%) as red solid. ¹H NMR (300 MHz, *o*-dichlorobenzene-*d*₄) δ 10.17 (s, 2H), 9.72 (d, *J* = 8.5 Hz, 2H), 9.54 (d, *J* = 8.5 Hz, 2H), 9.45 (d, *J* = 8.8 Hz, 2H), 9.38 (d, 2H), 9.20 (d, *J* = 9.3 Hz, 2H), 8.97 (d, *J* = 9.3

Hz, 2H), 7.43 (s, 4H), 2.79 (s, 6H), 2.10 (s, 12H); HRMS (MALDI-TOF): m/z Calcd for $C_{60}H_{36}$: 756.2812 $[M]^+$, found: 756.2846. The ^{13}C NMR cannot be obtained due to low solubility of target compound.

Compound **6-6** and circumpyrene **6-5b**



3,11-dibromo-6,14-dimesityldibenzo[*hi, st*]ovalene (27 mg, 0.031 mmol), diphenylacetylene (21 mg, 0.12 mmol), LiCl (7.5 mg, 0.18 mmol), NaOAc (9.9 mg, 0.12 mmol), and Pd(OAc)₂ (1.5 mg, 0.0067 mmol) were dissolved in dry N,N-dimethylformamide (9 mL). After degassing by three times freeze-pump-thaw cycles, the resulting solution was heated at 110 °C for 12 h. The mixture was cooled down to room temperature, diluted with ethyl acetate (50 mL), washed with water, brine, dried over anhydrous MgSO₄ and evaporated. The obtained residue was first passed through short silica gel column, then further separated by preparative gel permeation column chromatography (Bio-Beads S-X1 support, Bio-Rad Laboratories, eluent: toluene) to give the title compound **6-6** (11 mg, 40% yield) and **6-5b** (5 mg, 15 yield) as orange solids. **6-6**: 1H NMR (700 MHz, THF-*d*₈) δ 10.24 (d, $J = 8.1$ Hz, 1H), 9.93 (d, $J = 7.5$ Hz, 1H), 9.23 (d, $J = 8.1$ Hz, 1H), 9.21 (s, 1H), 8.84 (d, $J = 8.8$ Hz, 1H), 8.60 (d, $J = 9.0$ Hz, 1H), 8.53 (d, $J = 10.2$ Hz, 2H), 8.45 (t, $J = 7.6$ Hz, 1H), 8.36 (d, $J = 7.8$ Hz, 1H), 8.31 (d, $J = 9.1$ Hz, 1H), 7.92 (d, $J = 9.1$ Hz, 1H), 7.62 (d, $J = 6.9$ Hz, 2H), 7.56 (d, $J = 6.9$ Hz, 2H), 7.47 (t, $J = 7.6$ Hz, 2H), 7.40 (t, $J = 7.6$ Hz, 3H), 7.35 – 7.32 (m, 3H), 7.30 (s, 2H), 2.59 (s, 3H), 2.58 (s, 3H), 2.03 (s, 6H), 1.94 (s, 6H); ^{13}C NMR (176 MHz, THF-*d*₈) δ 141.45, 141.37, 139.03, 138.89, 138.73, 138.63, 138.53, 136.36, 136.30, 136.08, 135.69, 132.97, 132.74, 132.38, 132.04, 131.91, 131.35, 131.25, 130.34, 130.03, 129.83, 129.77, 129.47, 129.45, 129.15, 128.84, 128.80, 128.67, 128.63, 128.05, 127.93, 127.79, 127.72, 127.24, 126.90, 126.21, 125.87, 125.44, 125.15, 124.79, 124.04, 123.01, 122.83, 122.76, 122.68, 122.59, 122.54, 122.34, 122.27, 122.09, 121.66, 21.88, 20.97, 20.86; HRMS (MALDI-TOF): m/z Calcd for $C_{70}H_{44}$: 884.3438 $[M]^+$, found: 884.3624. **6-5b**: 1H NMR (700 MHz, THF-*d*₈) δ 9.95 (s, 2H), 9.17 (d, $J = 8.7$ Hz, 2H), 9.15 (d, $J = 8.7$ Hz, 2H), 9.06 (d, $J =$

9.0 Hz, 2H), 8.79 (d, $J = 8.9$ Hz, 2H), 7.80 (d, $J = 7.2$ Hz, 4H), 7.71 (d, $J = 7.2$ Hz, 4H), 7.56 (t, $J = 7.6$ Hz, 4H), 7.51 – 7.46 (m, 6H), 7.40 (t, $J = 7.9$ Hz, 3H), 7.38 (s, 4H), 2.65 (s, 6H), 2.00 (s, 12H); ^{13}C NMR (176 MHz, THF) δ 141.73, 139.01, 136.62, 135.60, 133.48, 133.12, 132.86, 131.95, 131.02, 129.87, 129.51, 128.94, 127.97, 127.77, 127.48, 127.46, 125.73, 125.72, 125.33, 122.95, 122.43, 121.43, 121.39, 121.21, 121.13, 120.95, 120.84, 120.66, 30.52, 21.40; HRMS (MALDI-TOF): m/z Calcd for $\text{C}_{84}\text{H}_{52}$: 1060.4064 $[\text{M}]^+$, found: 1060.4006.

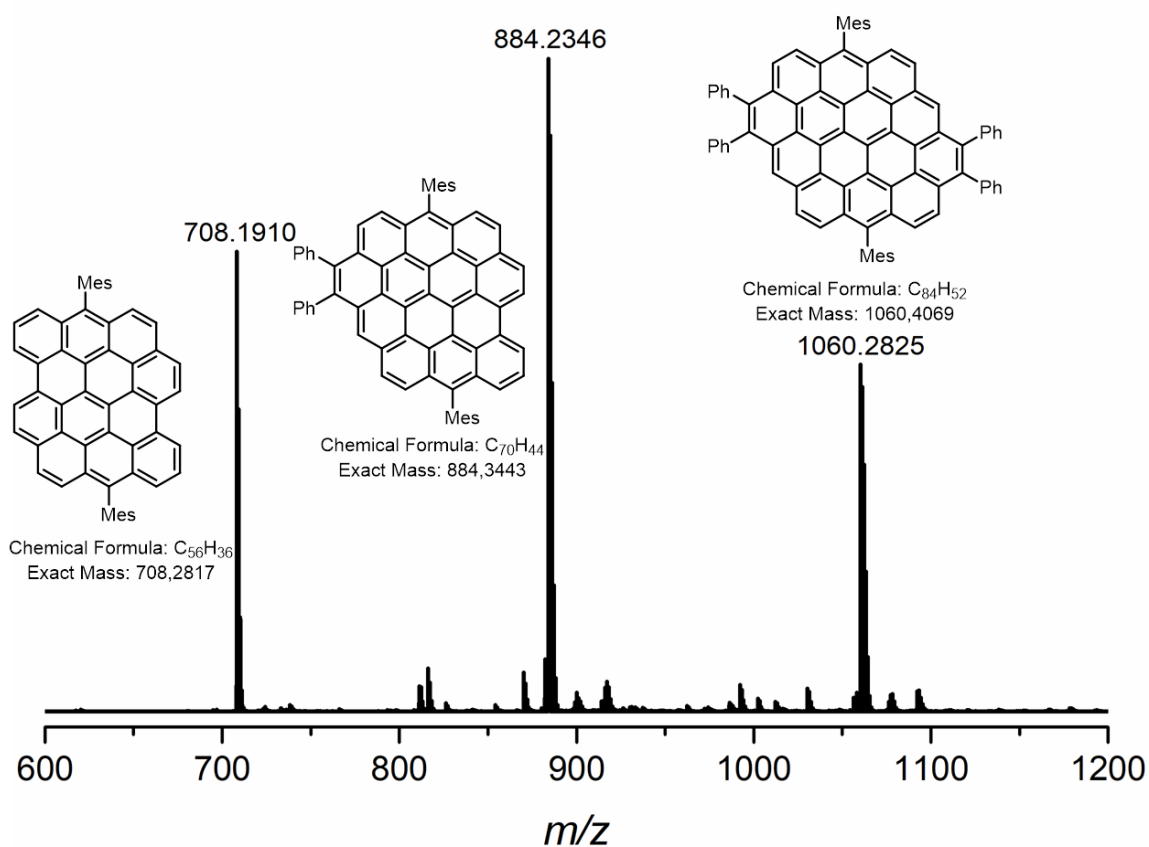


Figure S6-1. MALDI-TOF MS spectra of benzannulation of **6-2** and diphenylacetylene in toluene at 130 °C for 24 h with $\text{Pd}(\text{PPh}_3)_4$ as catalyst, showing one-fold and two-fold adducts along with the remaining starting material.

Single-crystal X-ray analysis

Brown needle-like single crystals of compound **6-5b** suitable for single-crystal analysis were grown by slow diffusion of acetonitrile vapor into its THF/ CS_2 solution over several days. The X-ray crystallographic analysis of **6-5b** performed at 120 K disclosed a triclinic P-1 space

group with a Z value of 2. The data were deposited at Cambridge Crystallographic Data Centre (CCDC number: 1946099).

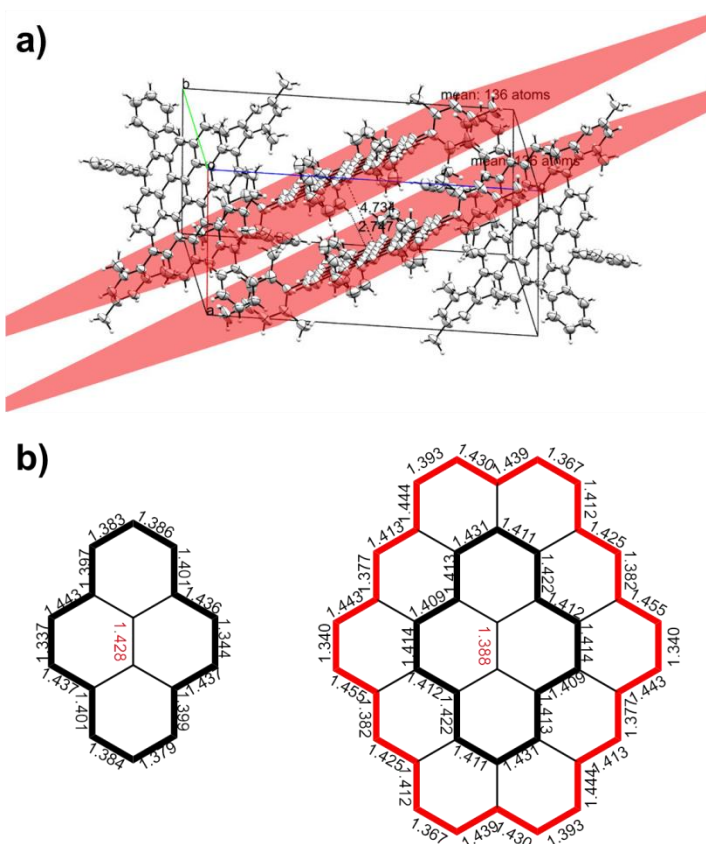


Figure S6-2. a) Single-crystal structure of **6-5b** showing CH- π interaction (solvents were omitted for clarity); b) Comparison of bond lengths between pyrene (CCDC 118728) and circumpyrene (**6-5b**). The outer rim C-C bonds of pyrene display pronounced bond length alternation between 1.34 Å and 1.44 Å (Figure S6-2b, left), with a relatively long C-C bond (1.43 Å) in the center, indicating its single bond character. However, as demonstrated in Figure S6-2b (right), the outer rim of the central pyrene unit exhibits bond length homogenous (average is 1.42 Å) and the central C-C bond length was shortened to 1.39 Å, indicating its enhanced double bond character (C=C bond length is 1.33 Å). Obvious bond length alternation could be observed for the outer rim of circumpyrene **6-5b**. This indicates significant effect of the peripheral double bonds on the structure of the center pyrene core.

Crystal data for 6-5b (CCDC 1946099)

formula	C ₈₄ H ₅₂ , 3(CS ₂)	
molecular weight	1289.64 gmol ⁻¹	
absorption	μ = 0.27 mm ⁻¹	
crystal size	0.05 x 0.07 x 0.22 mm ³ brown needle	
space group	P -1 (triclinic)	
lattice parameters	a = 12.0637(11)Å	α = 80.650(8)°
(calculate from	b = 12.2837(11)Å	β = 74.979(7)°
9099 reflections with	c = 22.965(2)Å	γ = 77.213(7)°
2.5° < θ < 28.3°)	V = 3185.3(5)Å ³	z = 2 F(000) = 1340
temperature	120K	
density	d _{xray} = 1.345 gcm ⁻³	

data collection

diffractometer	STOE IPDS 2T
radiation	Mo-K _α Graphitmonochromator
Scan – type	ω scans
Scan – width	1°
scan range	2° ≤ θ < 28° -15 ≤ h ≤ 15 -16 ≤ k ≤ 16 -27 ≤ l ≤ 30
number of reflections:	
measured	21011
unique	10929 (R _{int} = 0.1574)
observed	3258 (F /σ(F) > 4.0)

data correction, structure solution and refinement

corrections	Lorentz and polarisation correction.
Structure solution	Program: SHELXT-2014
refinement	Program: SHELXL-2018 (full matrix). 847 refined parameters, weighting scheme: w=1/[σ ² (F _o ²) + (0.1483*P) ² +1.91*P] with (Max(F _o ² ,0)+2*F _c ²)/3. H-atoms at calculated positions and refined with isotropic displacement parameters, non H- atoms refined anisotropically.
R-values	wR2 = 0.392 (R1 = 0.1204 for observed reflections, 0.3011 for all reflections)
goodness of fit	S = 1.016
maximum deviation of parameters	0.001 * e.s.d
maximum peak height in diff. Fourier synthesis	0.62, -0.27 eÅ ⁻³
remark	structure contains two independent molecules (A & B), both with Ci symmetry and 3 molecules C ₂ S, probably not full occupied

DFT calculations

Theoretical calculations were performed using Gaussian 09 software package.⁴ Geometry optimizations of all compounds were performed at the B3LYP level of theory using 6-31G(d,p) basis set. UV-vis absorption spectra for all compounds were calculated using TD-DFT method at the same level of theory. Nucleus independent chemical shifts (NICS) were calculated using the gauge invariant atomic orbital (GIAO) approach at the GIAO-B3LYP/6-31G(d,p) level.^{5, 6} The anisotropy of the induced current density (ACID) plots were calculated using the AICD-2.0.0 software provided by Prof. Rainer Herges based on the optimized geometries.⁷

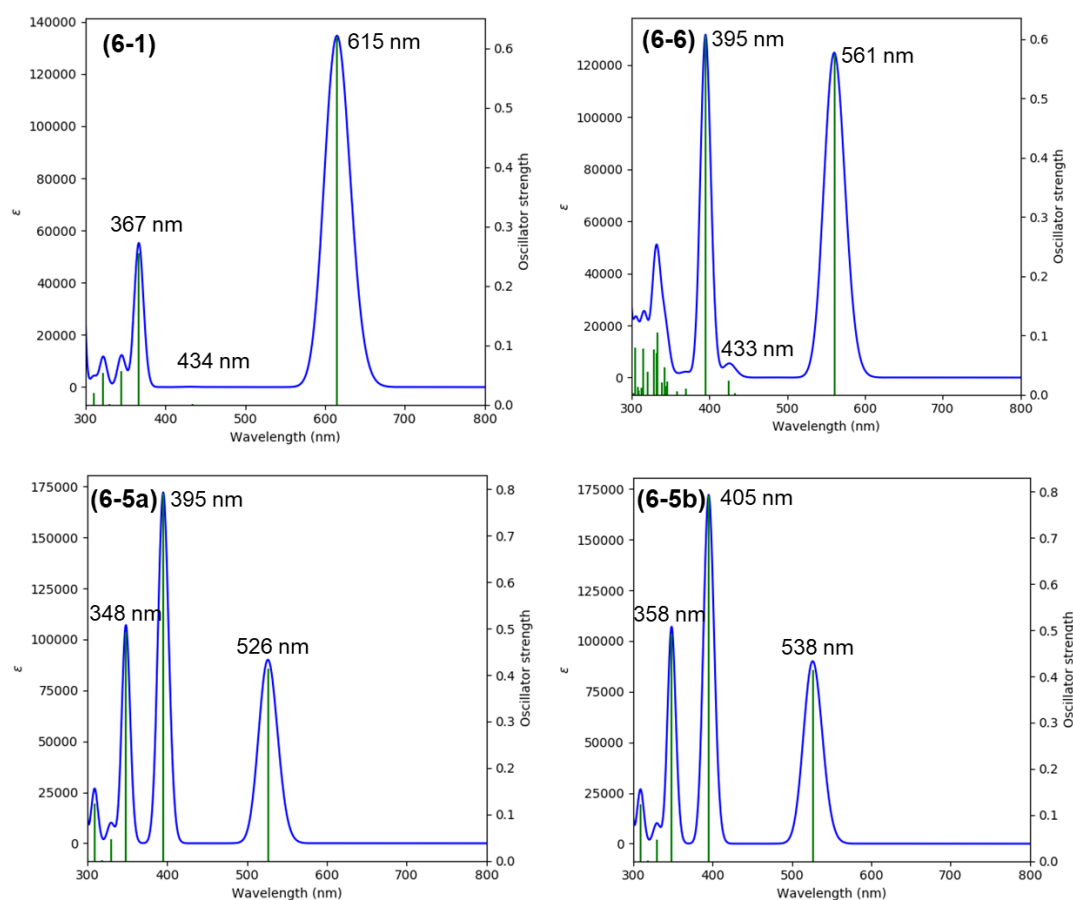


Figure S6-3. Simulated UV-vis absorption spectra of **6-1**, **6-6**, **6-5a**, and **6-5b**, the green lines are in proportional to oscillator strengths at corresponding wavelengths. For **6-1** and **6-6**, the calculated UV-vis spectra agree well with experimental data. For **6-5a** and **6-5b**, TD-DFT precisely reproduces the bright states mainly corresponding to HOMO \rightarrow LUMO transitions, while gives wrong order for forbidden transition corresponding to HOMO-1 \rightarrow LUMO and HOMO \rightarrow LUMO+1 (Table S1), which should have the longest absorption wavelength. The mismatching of this transition state between TD-DFT calculation and experimental data are discussed in the paper by Lischka et al. recently.⁸

Table S6-1. Characteristic electron transitions for **6-1**, **6-6**, **6-5a**, and **6-5b** calculated using TD-DFT at the B3LYP/6-31G(d,p) level by Gaussian 09.³

Compound	Excited states	Transition energy (eV)	Wavelength (nm)	Oscillator strength	Description
6-1	1	2.02	615	0.6199	HOMO→LUMO (0.70332)
	4	2.85	434	0.0007	HOMO-2→LUMO (0.49794) HOMO→LUMO+2 (-0.49683)
6-6	1	2.21	561	0.5742	HOMO-1→LUMO+1 (0.10623) HOMO→LUMO (0.69446)
	2	2.57	483	0.0002	HOMO-1→LUMO (-0.49311) HOMO→LUMO+1 (0.50199)
	3	2.86	433	0.0027	HOMO-2→LUMO (-0.37121) HOMO→LUMO+2 (0.58320)
6-5a	1	2.36	526	0.4143	HOMO-1→LUMO+1 (0.17660) HOMO→LUMO (0.68075)
	2	2.51	495	0.0002	HOMO-1→LUMO (-0.49388) HOMO→LUMO+1 (0.50291)
	5	3.14	395	0.7916	HOMO-1→LUMO (0.49244) HOMO→LUMO+1 (0.48352) HOMO-2→LUMO+2 (-0.23423)
	8	3.56	348	0.4925	HOMO-1→LUMO+1 (0.63790) HOMO→LUMO (-0.13914)
6-5b	1	2.30	538	0.5736	HOMO-1→LUMO+1 (0.16262) HOMO→LUMO (0.68434)
	2	2.46	503	0.0001	HOMO-1→LUMO (-0.49779) HOMO→LUMO+1 (0.49857)
	5	3.06	405	0.8469	HOMO-1→LUMO (0.48960) HOMO→LUMO+1 (0.48960) HOMO-2→LUMO+2 (-0.17994)
	8	3.47	358	0.9236	HOMO-1→LUMO+1 (0.66064) HOMO→LUMO (-0.13730)

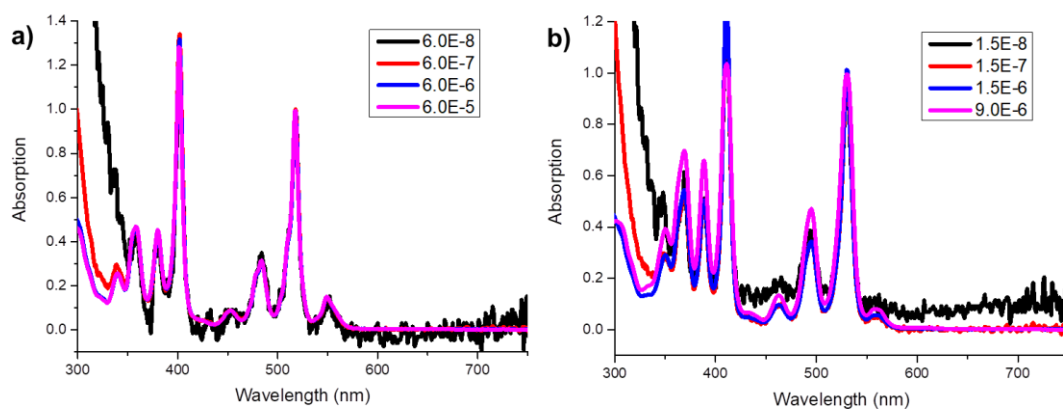


Figure S6-4. Normalized UV-vis absorption of **6-5a** (a) and **6-5b** (b) measured at different concentrations in the range of 10^{-5} – 10^{-8} M, showing no difference in characteristic absorption band.

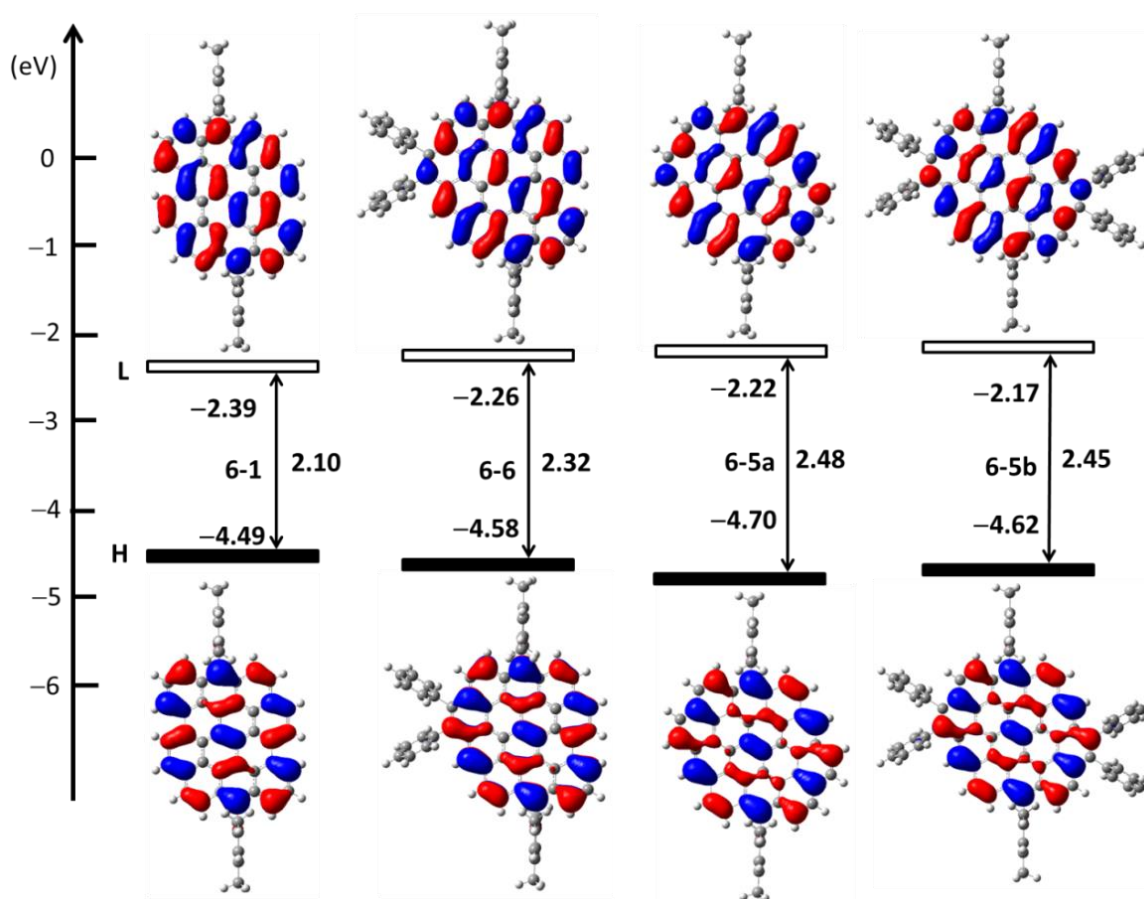


Figure S6-5. Calculated frontier molecular orbitals and energy gaps of **6-1**, **6-6**, **6-5a**, and **6-5b**.

Appendix

Cartesian coordinates of the optimized structure of **6-1** (xyz format; number of atoms: 92)

C	-2.11561000	2.89626800	-0.00037500	C	-8.27764200	-0.25995900	1.19864000
C	-0.65790700	3.04231200	-0.00130400	C	-8.99422900	-0.33116400	0.00105200
C	0.16685700	1.88220200	-0.00122200	C	-8.27831600	-0.25887500	-1.19688100
C	-0.41394100	0.57114600	-0.00071900	C	-6.88734400	-0.11254500	-1.22042300
C	-1.84671700	0.43016800	-0.00052400	C	-6.16005600	-0.04373000	-2.54406700
C	-2.68535800	1.58174300	-0.00027200	C	-6.15862500	-0.04602200	2.54483300
C	0.41386600	-0.57035200	-0.00051900	C	-10.49952700	-0.45651600	0.00143100
C	1.84664000	-0.42937800	-0.00056800	C	6.16249600	0.02659200	-2.54408100
C	2.68527900	-1.58095900	0.00019400	C	6.15822600	0.04311600	2.54489800
C	2.11552000	-2.89548000	0.00071700	C	10.49539900	0.49688700	0.00189000
C	0.65782700	-3.04152000	-0.00002600	H	-6.00808300	2.46356000	0.00129000
C	-0.16693100	-1.88140900	-0.00033100	H	-5.00208800	4.71959700	0.00170600
C	-4.11341500	1.42193600	0.00021800	H	-2.57360400	5.00339100	0.00070900
C	-4.93075900	2.58151100	0.00087700	H	-0.63984700	5.20503600	-0.00274100
C	-4.36592900	3.83931100	0.00107000	H	1.78481500	5.43168900	-0.00385400
C	-2.97408500	3.99701300	0.00044200	H	4.03560700	4.43772800	-0.00423200
C	-0.03731500	4.30493600	-0.00234000	H	5.48667500	2.45594100	-0.00324300
C	1.33900800	4.44070600	-0.00302700	H	6.00800600	-2.46293200	0.00285100
C	2.17639800	3.31626300	-0.00265700	H	5.00198600	-4.71881500	0.00395800
C	1.58916900	2.01814900	-0.00174200	H	2.57348800	-5.00260800	0.00267400
C	3.60537400	3.43971700	-0.00327700	H	0.63978100	-5.20424500	-0.00051800
C	4.40833400	2.34522800	-0.00269900	H	-1.78488800	-5.43090200	-0.00107200
C	3.86118200	1.01112300	-0.00140600	H	-4.03566300	-4.43694100	-0.00107200
C	2.42723500	0.86019800	-0.00127300	H	-5.48672900	-2.45534300	-0.00071100
C	4.68981700	-0.11529500	-0.00023800	H	8.81539900	0.30172500	2.14390000
C	4.11331900	-1.42115800	0.00068000	H	8.81891700	0.28762200	-2.14054200
C	4.93066400	-2.58074800	0.00214900	H	-8.81362100	-0.32125400	2.14339800
C	4.36581500	-3.83854200	0.00279700	H	-8.81483600	-0.31932100	-2.14138800
C	2.97397800	-3.99623500	0.00203700	H	-6.86423800	-0.09156700	-3.37882100
C	0.03724500	-4.30415000	-0.00041500	H	-5.58524200	0.88367000	-2.63843400
C	-1.33907300	-4.43992300	-0.00077500	H	-5.44834800	-0.86903800	-2.65479600
C	-2.17645400	-3.31547600	-0.00071900	H	-5.58404900	0.88146600	2.63984600
C	-1.58923400	-2.01736100	-0.00054100	H	-6.86232000	-0.09494600	3.37993500
C	-3.60541800	-3.43893800	-0.00086300	H	-5.44659600	-0.87121500	2.65429100
C	-4.40840200	-2.34446300	-0.00067000	H	-10.85666900	-0.99095400	0.88687500
C	-3.86124300	-1.01034100	-0.00040000	H	-10.98031600	0.52987500	0.00200100
C	-2.42731000	-0.85941400	-0.00050300	H	-10.85719700	-0.99017600	-0.88427000
C	-4.68988600	0.11608800	0.00003900	H	6.86696000	0.07427600	-3.37860800
C	6.18295700	0.03961400	0.00047500	H	5.59186500	-0.90376600	-2.63515500
C	-6.18301800	-0.03881700	0.00039200	H	5.44720000	0.84825000	-2.65840300
C	6.88632300	0.11227400	1.22171400	H	5.58305700	-0.88410600	2.63901700
C	8.27841800	0.24942800	1.19919400	H	6.86191000	0.09089500	3.38007700
C	8.99536600	0.31838900	0.00196900	H	5.44673600	0.86865700	2.65512300
C	8.28034200	0.24157600	-1.19635900	H	10.94759800	0.08472500	0.90884700
C	6.88862600	0.10442700	-1.22031200	H	10.95711800	0.00622500	-0.86038600
C	-6.88665000	-0.11365900	1.22153000	H	10.76950200	1.55844300	-0.04450200

Cartesian coordinates of the optimized structure of **6-6** (xyz format; number of atoms:

114)

C	-4.36675200	1.42592000	-0.01093500	C	-2.26084500	-0.44921100	-0.00882500
C	-3.02092000	1.90715800	0.00815500	C	-3.61957700	-0.89957300	-0.01258300
C	-1.96814000	0.95360500	-0.00418300	C	-4.65271900	0.09066000	-0.01945500

C	-0.61225400	1.39567900	-0.01248400	C	-4.19256000	5.02065800	-1.11762000
C	0.45088800	0.44366000	-0.00964100	C	-5.24741800	5.93323200	-1.09522900
C	0.16294400	-0.95479100	-0.00885000	C	-5.97599700	6.13614300	0.07755500
C	-1.20292300	-1.39531000	-0.01105800	C	-5.64492600	5.41802300	1.22759700
C	-0.32148900	2.79350700	-0.02178800	C	-4.59119900	4.50402700	1.20343500
C	1.03334600	3.20067600	-0.00500300	C	-0.59514900	5.82261100	-1.19963600
C	2.07798800	2.29033700	0.00125900	C	-0.28952700	7.18374500	-1.21593200
C	1.80124600	0.88220800	-0.00491600	C	-0.45469800	7.95303200	-0.06316100
C	3.45369800	2.71794800	0.01533200	C	-0.92649900	7.35202200	1.10456200
C	4.47301600	1.82484500	0.01779100	C	-1.23382800	5.99141200	1.11924200
C	4.23487000	0.39758500	0.00936400	H	-5.17708900	2.14476000	-0.02341400
C	2.86536600	-0.06018200	-0.00045200	H	-5.68532500	-0.23969100	-0.03548500
C	1.21779600	-1.89511200	-0.00776900	H	1.26525000	4.25938900	0.00767900
C	2.57780200	-1.44844100	-0.00331500	H	3.65789000	3.78528800	0.02239800
C	3.64635500	-2.39364200	-0.00074500	H	5.50082900	2.16966100	0.02662400
C	3.37094400	-3.79832200	-0.00447200	H	7.07676900	-2.53279700	0.01285900
C	1.98102800	-4.25479800	-0.00915000	H	6.58356700	-4.95378600	0.00393800
C	0.92833800	-3.29999200	-0.01000700	H	4.27565400	-5.75891200	-0.00608900
C	5.00406700	-1.92748500	0.00618400	H	2.42254200	-6.37537900	-0.01149200
C	6.04975300	-2.87938300	0.00774300	H	0.10258600	-7.11159700	-0.01704300
C	5.77023300	-4.23399100	0.00289000	H	-2.31571600	-6.60992100	-0.01979600
C	4.44992400	-4.68988000	-0.00293500	H	-4.14960200	-4.97760000	-0.01955100
C	1.64176300	-5.62449300	-0.01199800	H	9.23420400	0.79851800	-2.09544700
C	0.32817900	-6.04859300	-0.01511200	H	9.20227700	0.78020000	2.18940100
C	-0.73313300	-5.12586500	-0.01553300	H	-7.84871800	-3.60517000	2.12158400
C	-0.43366900	-3.73449700	-0.01321800	H	-7.84742600	-3.59222100	-2.16326000
C	-2.10201100	-5.54430600	-0.01797100	H	-5.98940500	-2.94902100	-3.39784500
C	-3.11928600	-4.64027600	-0.01781900	H	-4.96449600	-1.71006700	-2.65640200
C	-2.86424800	-3.22457900	-0.01543900	H	-4.43616200	-3.38669800	-2.66973400
C	-1.49916700	-2.78124800	-0.01331900	H	-4.43933500	-3.40105100	2.63231800
C	-3.91428100	-2.28484100	-0.01530600	H	-4.96672900	-1.72415700	2.62628500
C	5.28301800	-0.51973400	0.01251600	H	-5.99298100	-2.96604500	3.36122400
C	-5.34150700	-2.75061900	-0.01782200	H	-9.66136000	-4.80114600	0.79968200
C	6.70749600	-0.04600600	0.02465800	H	-10.14543900	-3.25622900	0.10181300
C	7.38834700	0.18235900	-1.19021100	H	-9.72445700	-4.60250000	-0.95894000
C	8.71425900	0.62673800	-1.15537200	H	5.83854100	0.61667100	-2.64139400
C	9.38651100	0.85418200	0.04842000	H	7.39147800	0.14590400	-3.34872600
C	8.69644500	0.61657500	1.24021800	H	6.33467300	-1.06963100	-2.61238000
C	7.37030700	0.17199200	1.25151500	H	7.34113000	0.11748500	3.40947300
C	-6.01343200	-2.97954500	1.20257500	H	5.79886700	0.59393100	2.68292400
C	-7.33812000	-3.42628900	1.17765200	H	6.29586500	-1.09201400	2.64727000
C	-8.02046100	-3.65069100	-0.02166300	H	11.35873100	1.04194600	-0.82602900
C	-7.33745200	-3.41939900	-1.21803700	H	10.83349600	2.46374500	0.07627400
C	-6.01151800	-2.97279900	-1.23928300	H	11.35093100	1.01848900	0.94488300
C	-2.71814800	3.31058300	0.01103300	H	-3.62800600	4.86665500	-2.03200000
C	-1.40000800	3.74547200	-0.01962300	H	-5.50007700	6.48549600	-1.99583900
C	-5.31587200	-2.74299500	-2.56184800	H	-6.79649200	6.84754300	0.09492500
C	-5.31865700	-2.75643000	2.52673900	H	-6.20626800	5.56888300	2.14532600
C	-9.46113100	-4.10510600	-0.02098000	H	-4.33722300	3.94525700	2.09987300
C	6.70451100	-0.04308400	-2.51963800	H	-0.46391200	5.22658100	-2.09842600
C	6.66673000	-0.06466300	2.56863700	H	0.07659500	7.64263900	-2.12999200
C	10.80737700	1.36681200	0.06144200	H	-0.21685200	9.01270800	-0.07483200
C	-3.84709700	4.29650600	0.03198200	H	-1.05559000	7.94233100	2.00721700
C	-1.07665200	5.20840700	-0.03315300	H	-1.60085000	5.52867200	2.03009500

Cartesian coordinates of the optimized structure of **6-5a** (xyz format; number of atoms: 96)

C	-2.18191000	2.80629200	-0.00046600	C	-0.76711100	3.00031000	-0.00075200
---	-------------	------------	-------------	---	-------------	------------	-------------

C	0.10671300	1.87900700	-0.00080200	C	-6.86758000	-0.32209100	1.22140400
C	-0.43414400	0.55704700	-0.00056500	C	-10.47112500	-0.75106300	0.00152900
C	-1.85111000	0.36323500	-0.00046500	C	10.46580000	0.79336500	0.00083700
C	-2.72513400	1.48382500	-0.00035000	C	-6.14291900	-0.23450000	-2.54440300
C	0.43408500	-0.55655900	-0.00047100	C	-6.14159400	-0.23562900	2.54477500
C	1.85104800	-0.36274900	-0.00040900	C	6.14132500	0.23506500	2.54496200
C	2.72507200	-1.48334600	0.00002700	C	6.14578900	0.21451500	-2.54429200
C	2.18184100	-2.80581200	0.00024500	C	2.48255200	-5.24015700	0.00076700
C	0.76704800	-2.99982600	-0.00004700	C	1.12622800	-5.42980500	0.00038000
C	-0.10677200	-1.87852100	-0.00029500	C	-2.48261900	5.24063200	-0.00045100
C	-4.14132800	1.28803700	-0.00010800	C	-1.12629300	5.43028200	-0.00081100
C	-4.97926100	2.44667500	0.00015900	H	-6.05456400	2.30770000	0.00043500
C	-4.45289200	3.71195900	0.00007200	H	-5.11460600	4.57427300	0.00027600
C	-3.04759600	3.93236800	-0.00028100	H	1.58131000	5.49881900	-0.00156900
C	-0.22606100	4.32250900	-0.00097400	H	3.87709600	4.57554100	-0.00229400
C	1.17332900	4.49081900	-0.00133400	H	5.38584900	2.64611400	-0.00201400
C	2.04408300	3.40559100	-0.00136400	H	6.05451800	-2.30734300	0.00191300
C	1.51408500	2.07170100	-0.00099800	H	5.11454100	-4.57378100	0.00193200
C	3.47416100	3.56617900	-0.00177700	H	-1.58137200	-5.49833400	-0.00016800
C	4.31190200	2.49641300	-0.00158800	H	-3.87714800	-4.57505300	-0.00053800
C	3.81545700	1.14017100	-0.00082300	H	-5.38589600	-2.64578400	-0.00050800
C	2.39049300	0.94966300	-0.00078600	H	8.79474100	0.54210500	-2.14103500
C	4.67785600	0.03244800	-0.00011000	H	8.79106100	0.55999100	2.14344300
C	4.14125000	-1.28756000	0.00038900	H	-8.79003300	-0.57505000	-2.14160000
C	4.97919600	-2.44620100	0.00127200	H	-8.78887600	-0.57601300	2.14327200
C	4.45281100	-3.71148300	0.00134300	H	-10.81790300	-1.27956400	-0.89149400
C	3.04752000	-3.93188900	0.00075600	H	-10.81414800	-1.30679700	0.87945400
C	0.22600100	-4.32202700	0.00002800	H	-10.97460800	0.22381000	0.01786500
C	-1.17338500	-4.49033700	-0.00019000	H	10.71449600	1.86044000	-0.05946600
C	-2.04413100	-3.40510500	-0.00034700	H	10.92640300	0.40403600	0.91359600
C	-1.51413600	-2.07121700	-0.00037700	H	10.94035500	0.30256700	-0.85441300
C	-3.47420000	-3.56569900	-0.00045300	H	-5.59662500	0.70971900	-2.64184200
C	-4.31196200	-2.49594500	-0.00042900	H	-5.40610600	-1.03782800	-2.65248100
C	-3.81550200	-1.13969100	-0.00031200	H	-6.84509700	-0.30640000	-3.37908400
C	-2.39055300	-0.94918300	-0.00038900	H	-5.59557800	0.70873700	2.64242200
C	-4.67791100	-0.03195800	-0.00011100	H	-6.84323700	-0.30826700	3.37984000
C	6.16610600	0.23035800	0.00043300	H	-5.40441600	-1.03873900	2.65191900
C	-6.16616500	-0.22977100	0.00015900	H	6.84307800	0.30717900	3.37998200
C	6.86967200	0.31214700	-1.22055800	H	5.40472600	1.03866300	2.65234100
C	8.25750200	0.48374900	-1.19678200	H	5.59467900	-0.70895500	2.64250300
C	8.97048000	0.57900000	0.00152400	H	5.60369300	-0.73261900	-2.63722000
C	8.25552500	0.49371200	1.19882100	H	5.40555100	1.01401000	-2.65692800
C	6.86720600	0.32198800	1.22156200	H	6.84820100	0.28518400	-3.37888200
C	-6.86812800	-0.32149500	-1.22064000	H	3.15392800	-6.09479600	0.00110400
C	-8.25520800	-0.50161500	-1.19708100	H	0.71290700	-6.43476900	0.00039500
C	-8.96919900	-0.59055800	0.00080300	H	-3.15399000	6.09527700	-0.00030400
C	-8.25453200	-0.50215700	1.19849400	H	-0.71297900	6.43524900	-0.00095800

Cartesian coordinates of the optimized structure of **6-5b** (xyz format; number of atoms: 136)

C	-3.56102400	0.07669900	-0.00869600	C	2.87118900	1.17817200	-0.01461900
C	-2.82026100	1.29625500	-0.02065400	C	3.56102500	-0.07670000	-0.00867600
C	-1.39595600	1.26554200	-0.02236300	C	2.82026100	-1.29625600	-0.02062500
C	-0.70682200	0.01419400	-0.02094200	C	1.39595600	-1.26554300	-0.02234200
C	-1.45014000	-1.20625400	-0.01996500	C	-3.60457900	-2.40454500	-0.01545900
C	-2.87118900	-1.17817200	-0.01462000	C	-5.02914100	-2.32797000	-0.01991500
C	0.70682200	-0.01419500	-0.02093800	C	-5.68523500	-1.12576600	-0.00933800
C	1.45014100	1.20625300	-0.01997100	C	-4.98155600	0.11371900	0.00889200

C	-3.50805700	2.54884200	-0.02800300	C	6.34860200	-5.91093900	-1.17927900
C	-2.74557700	3.73671000	-0.01778800	C	5.69679600	-4.67743500	-1.17739000
C	-1.35530900	3.72503600	-0.01744700	C	7.16432400	-1.39250800	0.04917800
C	-0.65401300	2.47603300	-0.02233300	C	7.90705300	-1.74522700	-1.08630900
C	-0.58368200	4.93940800	-0.01037700	C	9.30158500	-1.75182300	-1.05249500
C	0.77450900	4.91905600	-0.01166100	C	9.97761200	-1.40445700	0.11785000
C	1.51543400	3.67967900	-0.01685800	C	9.24979500	-1.04706300	1.25389900
C	0.76921500	2.45104100	-0.02065100	C	7.85525300	-1.03845900	1.21818500
C	2.91803800	3.65232800	-0.01611300	H	-5.59821000	-3.25085900	-0.03462300
C	3.60458100	2.40454500	-0.01546800	H	-6.76846100	-1.11151100	-0.01853700
C	5.02914300	2.32796900	-0.01991200	H	-3.25744800	4.69214700	-0.00625100
C	5.68523700	1.12576500	-0.00931500	H	-1.11721400	5.88616300	-0.00492500
C	4.98155600	-0.11371900	0.00892100	H	1.33356000	5.84813800	-0.00751200
C	3.50805700	-2.54884300	-0.02795600	H	5.59821100	3.25085800	-0.03462600
C	2.74557800	-3.73671200	-0.01773600	H	6.76846300	1.11150800	-0.01850300
C	1.35530900	-3.72503700	-0.01740200	H	3.25744900	-4.69214800	-0.00619000
C	0.65401300	-2.47603400	-0.02230300	H	1.11721400	-5.88616400	-0.00486000
C	0.58368100	-4.93940800	-0.01032300	H	-1.33356000	-5.84813800	-0.00745600
C	-0.77450900	-4.91905600	-0.01161200	H	5.05507100	7.20892300	-2.15462800
C	-1.51543300	-3.67967900	-0.01682400	H	5.07075200	7.19498200	2.13007900
C	-0.76921500	-2.45104200	-0.02062700	H	4.06936400	5.50571400	3.36520600
C	-2.91803700	-3.65232800	-0.01608500	H	2.60792000	4.81979900	2.63867300
C	-4.95011200	2.56692500	-0.01656200	H	4.10426300	3.89724800	2.62637300
C	5.66583600	-1.38020000	0.01717200	H	2.58760200	4.84402900	-2.66334700
C	-5.66583600	1.38019900	0.01712300	H	4.04978600	5.52457600	-3.39335700
C	4.95011200	-2.56692600	-0.01650500	H	4.07827700	3.91222100	-2.66286800
C	3.70079300	4.93332600	-0.01467900	H	5.75827100	9.23741400	-0.89571500
C	4.06167800	5.54341800	-1.23498400	H	5.75872000	9.23540800	0.87542600
C	4.78342400	6.74150500	-1.21054200	H	7.04591100	8.41810900	-0.01136300
C	5.16167600	7.35260500	-0.01217000	H	-5.05507300	-7.20894600	-2.15455700
C	4.79234500	6.73359800	1.18498400	H	-5.07075000	-7.19495700	2.13014900
C	4.07098100	5.53530500	1.20689800	H	-4.06936800	-5.50567100	3.36525600
C	3.69422500	4.90833400	2.53008900	H	-2.60791500	-4.81977900	2.63871900
C	3.67497500	4.92527800	-2.55947600	H	-4.10424900	-3.89721400	2.62640100
C	5.96911100	8.62930000	-0.01090100	H	-2.58760800	-4.84403100	-2.66329500
C	-3.70079200	-4.93332500	-0.01463500	H	-4.04976800	-5.52462900	-3.39330700
C	-4.06168000	-5.54343200	-1.23493300	H	-4.07830700	-3.91226100	-2.66284700
C	-4.78342500	-6.74151800	-1.21047700	H	-5.75806300	-9.23755200	-0.89548800
C	-5.16167600	-7.35260400	-0.01209600	H	-5.75892900	-9.23526800	0.87565300
C	-4.79234300	-6.73358400	1.18504900	H	-7.04591200	-8.41810800	-0.01157200
C	-4.07097800	-5.53528900	1.20694700	H	-7.38540700	2.01694300	-1.99876900
C	-3.69422100	-4.90830500	2.53013200	H	-9.85978600	2.02848700	-1.94242500
C	-3.67497900	-4.92530600	-2.55943300	H	-11.06337000	1.41118300	0.14418100
C	-5.96911100	-8.62929900	-0.01081800	H	-9.76692000	0.77528800	2.16967800
C	-7.16432300	1.39250800	0.04911000	H	-7.29184100	0.75756000	2.10350300
C	-7.90703500	1.74524600	-1.08638200	H	-6.24673700	3.77488400	2.04890500
C	-9.30156700	1.75184400	-1.05259100	H	-7.39867800	5.96593300	2.05271300
C	-9.97761400	1.40446000	0.11773800	H	-7.47154100	7.34055000	-0.01847300
C	-9.24981500	1.04704900	1.25379200	H	-6.37541200	6.50458300	-2.08876200
C	-7.85527300	1.03844300	1.21810100	H	-5.21650800	4.31638400	-2.08260800
C	-5.65530200	3.88895700	-0.01720900	H	6.24667400	-3.77490000	2.04899700
C	-6.27483200	4.37314400	1.14353900	H	7.39861300	-5.96595000	2.05282400
C	-6.92418700	5.60773900	1.14361000	H	7.47153900	-7.34055200	-0.01836900
C	-6.96449800	6.38005800	-0.01802700	H	6.37547400	-6.50456900	-2.08868600
C	-6.34856700	5.91094500	-1.17935800	H	5.21657000	-4.31637000	-2.08255200
C	-5.69676100	4.67744300	-1.17745700	H	7.38544000	-2.01691000	-1.99870800
C	5.65530300	-3.88895800	-0.01713700	H	9.85981900	-2.02845200	-1.94232400
C	6.27479700	-4.37315400	1.14362700	H	11.06336800	-1.41117900	0.14431000
C	6.92415100	-5.60774900	1.14370900	H	9.76688600	-0.77531500	2.16979600
C	6.96449600	-6.38006000	-0.01793300	H	7.29180700	-0.75759000	2.10358200

NMR and MS spectra

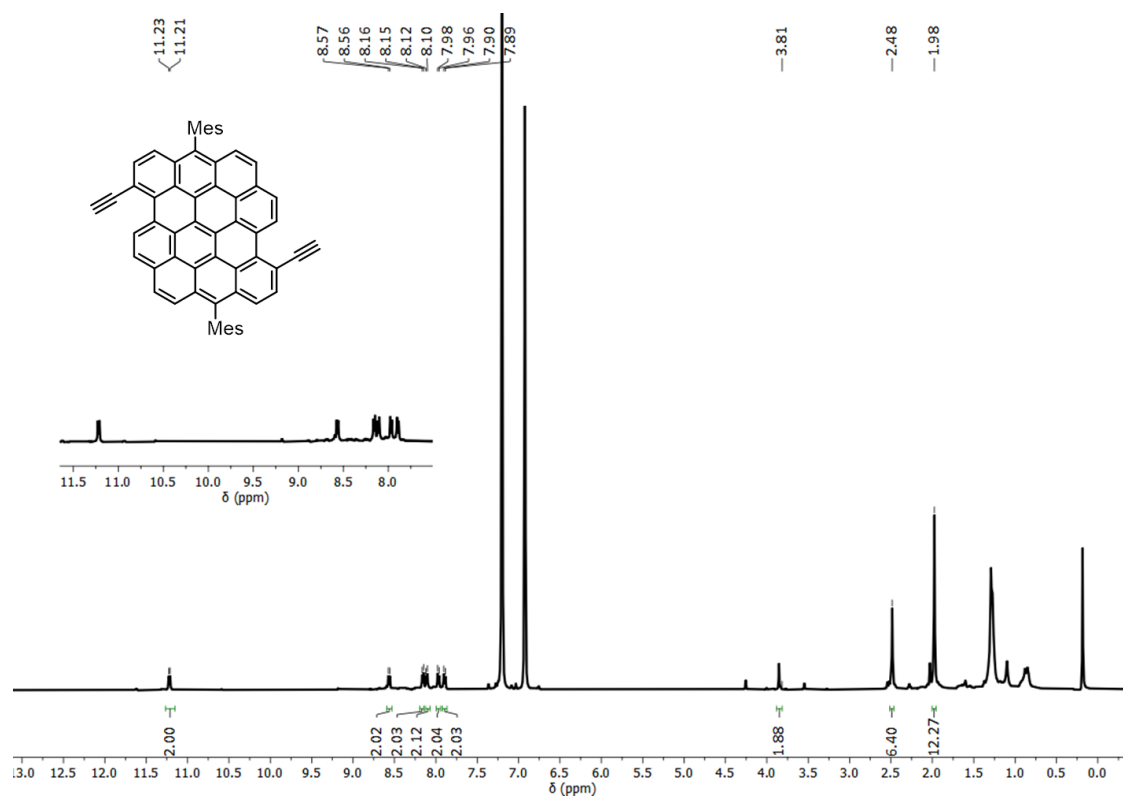


Figure S6-6. ^1H NMR spectra of compound **6-4** measured in *o*-DCB (d_4) (500 MHz, 403 K).

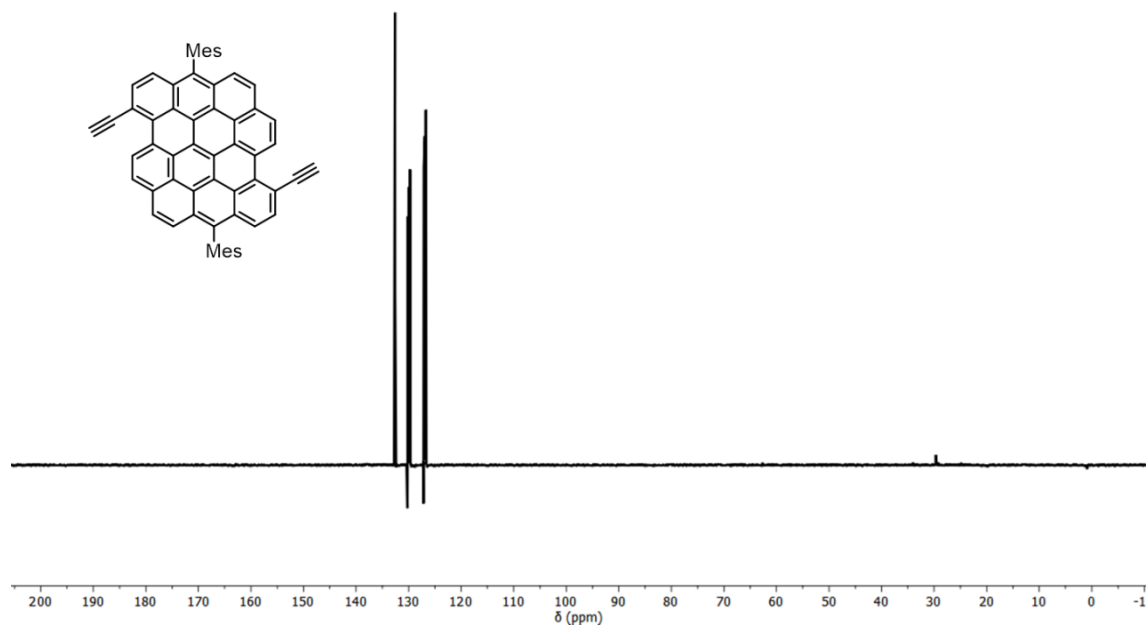


Figure S6-7. ^{13}C NMR spectra of compound **6-4** measured in *o*-DCB (d_4) (500 MHz, 403 K).

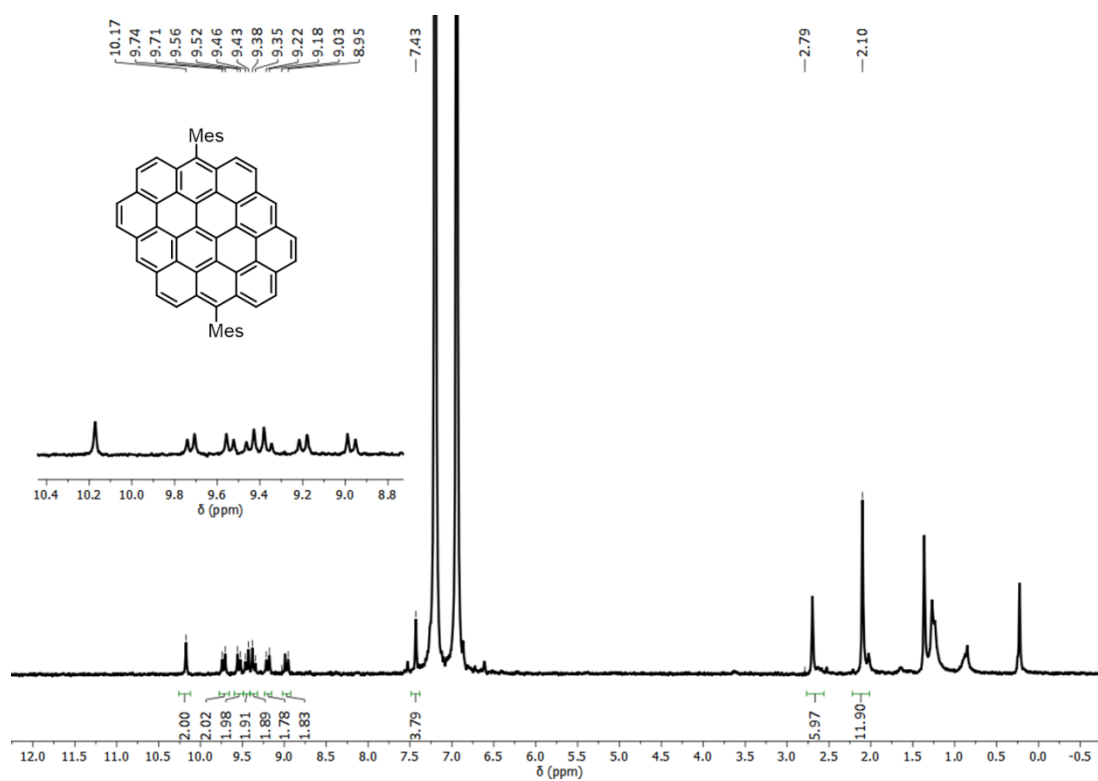


Figure S6-8. ^1H NMR spectra of compound **6-5a** measured in o -DCB (d_4) (300 MHz, 298 K).

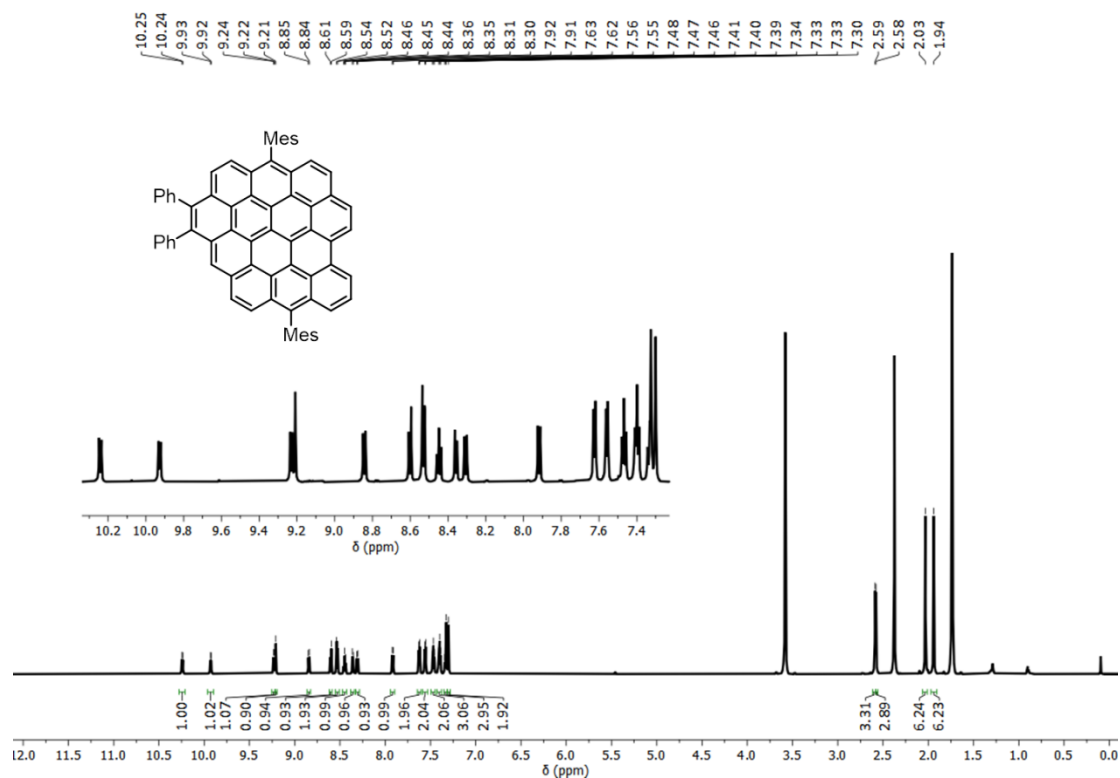


Figure S6-9. ^1H NMR spectra of compound **6-6** measured in THF/ CS_2 (d_8) (700 MHz, 298 K).

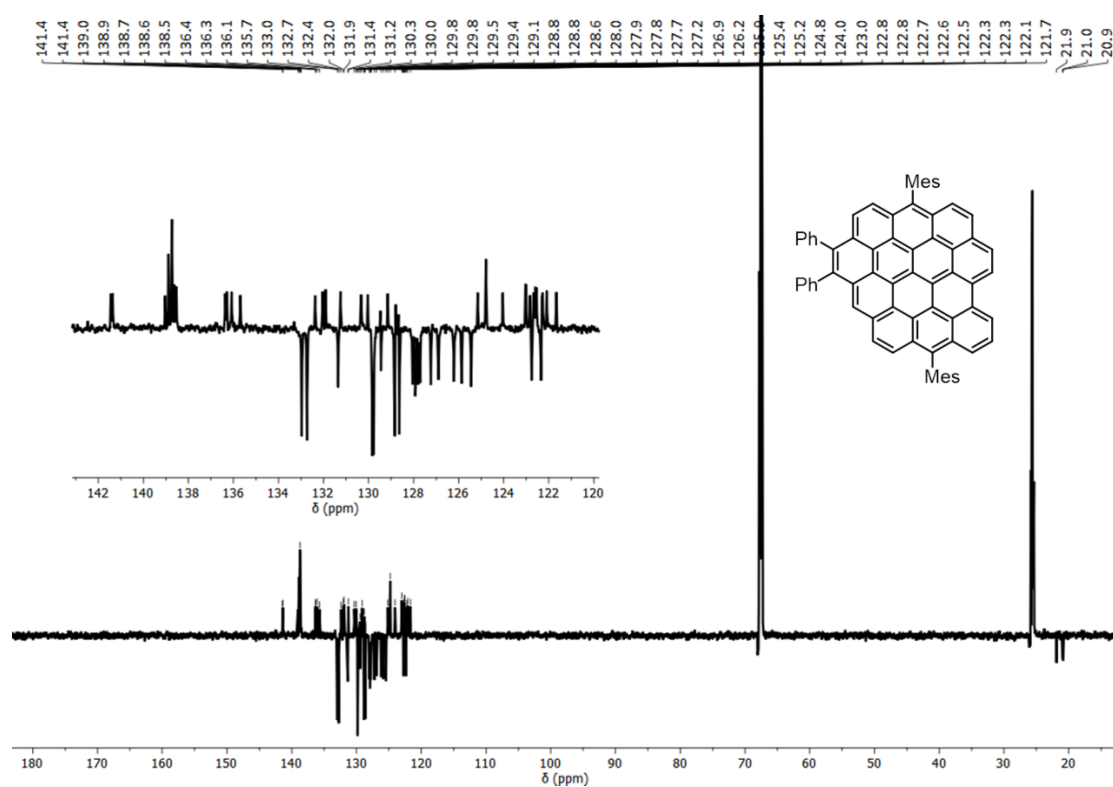


Figure S6-10. ^{13}C NMR spectra of compound **6-6** measured in THF/ CS_2 (d_8) (175 MHz, 298 K).

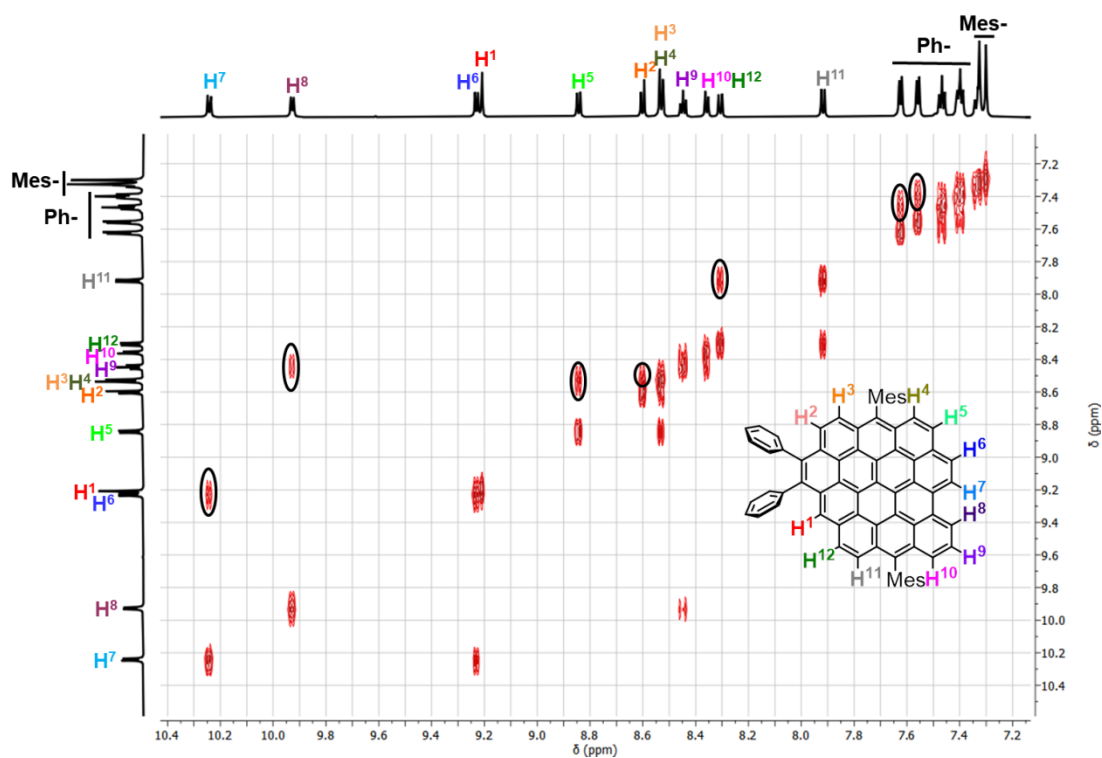


Figure S6-11. Aromatic region of ^1H , ^1H -COSY spectrum of **6-6** (700 MHz, THF- d_8) at 298 K.

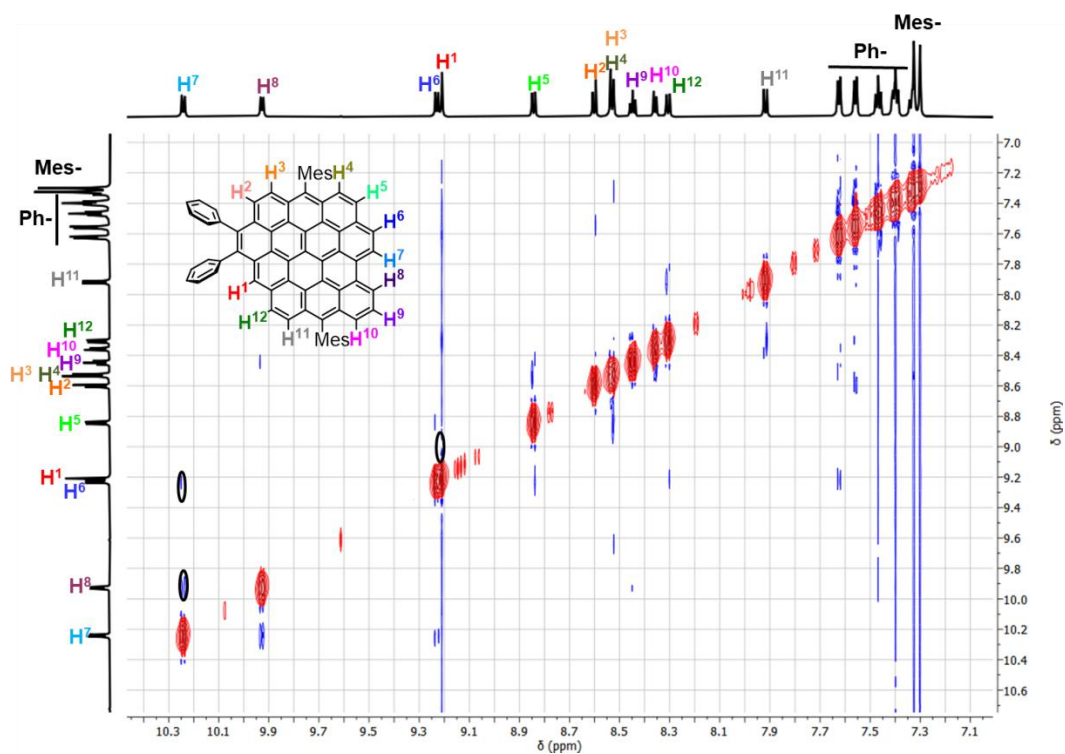


Figure S6-12. Aromatic region of $^1\text{H}, ^1\text{H}$ -NOESY spectrum of **6-6** (700 MHz, $\text{THF-}d_8$) at 298 K.

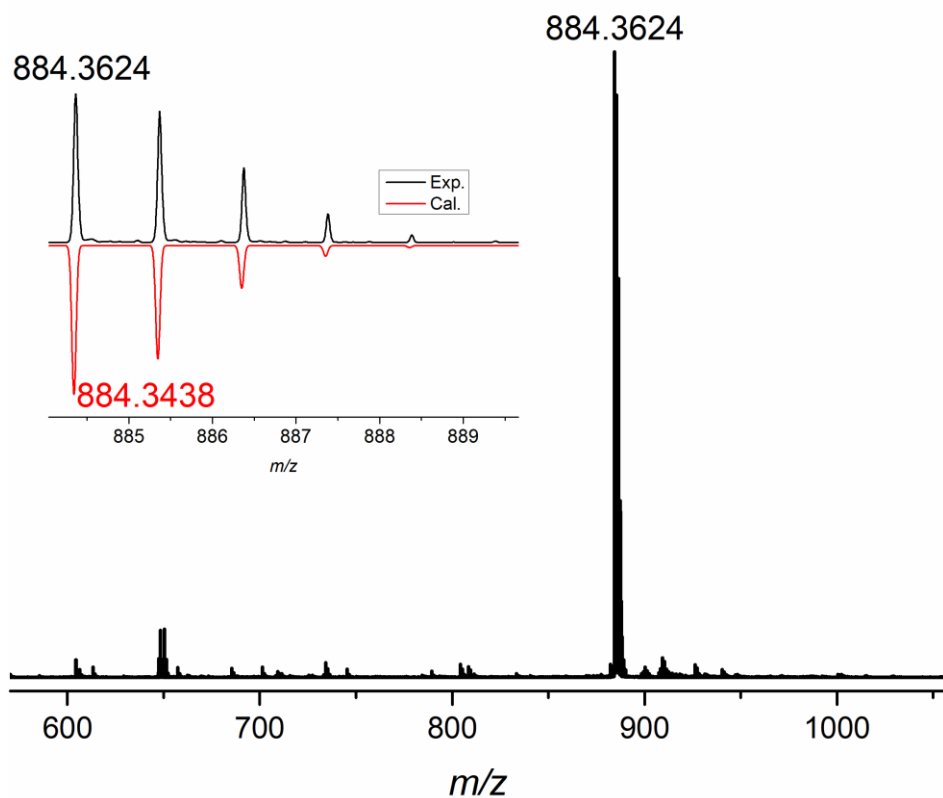


Figure S6-13. High-resolution MALDI-TOF MS spectra of **6-6** and isotopic distribution pattern in comparison with calculation.

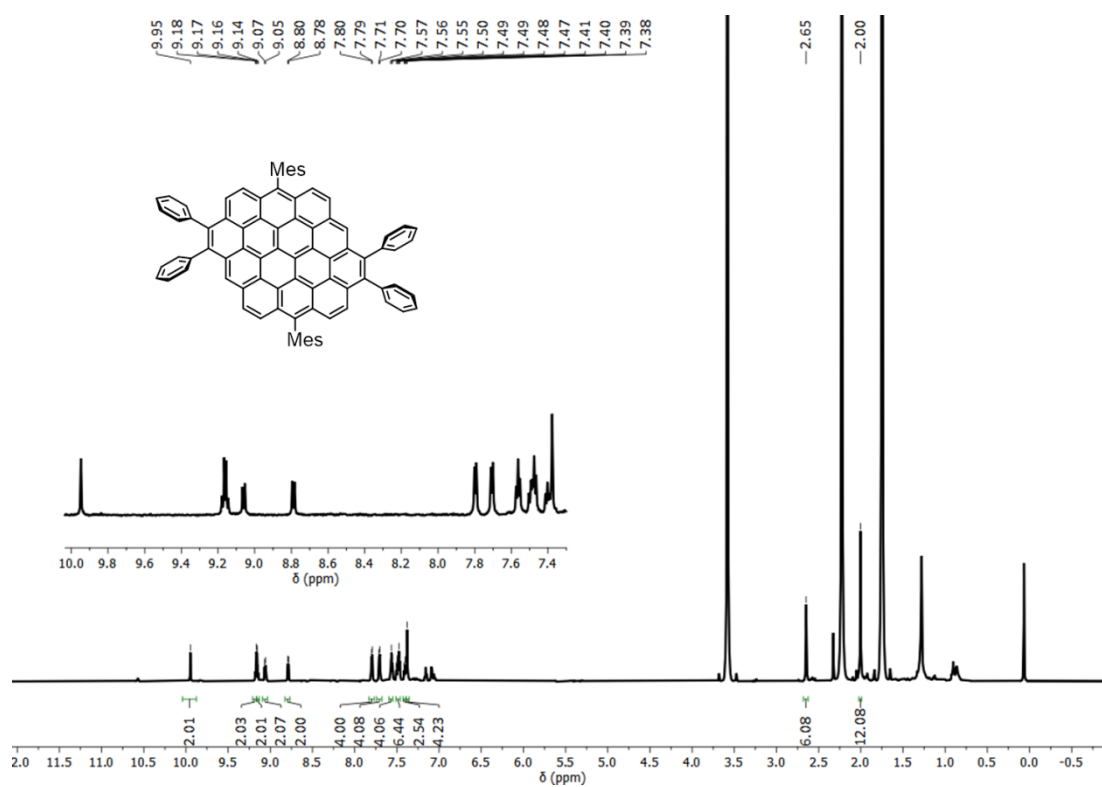


Figure S6-14. ^1H NMR spectra of compound **6-5b** measured in $\text{THF}/\text{CS}_2 (d_8)$ (700 MHz, 298 K).

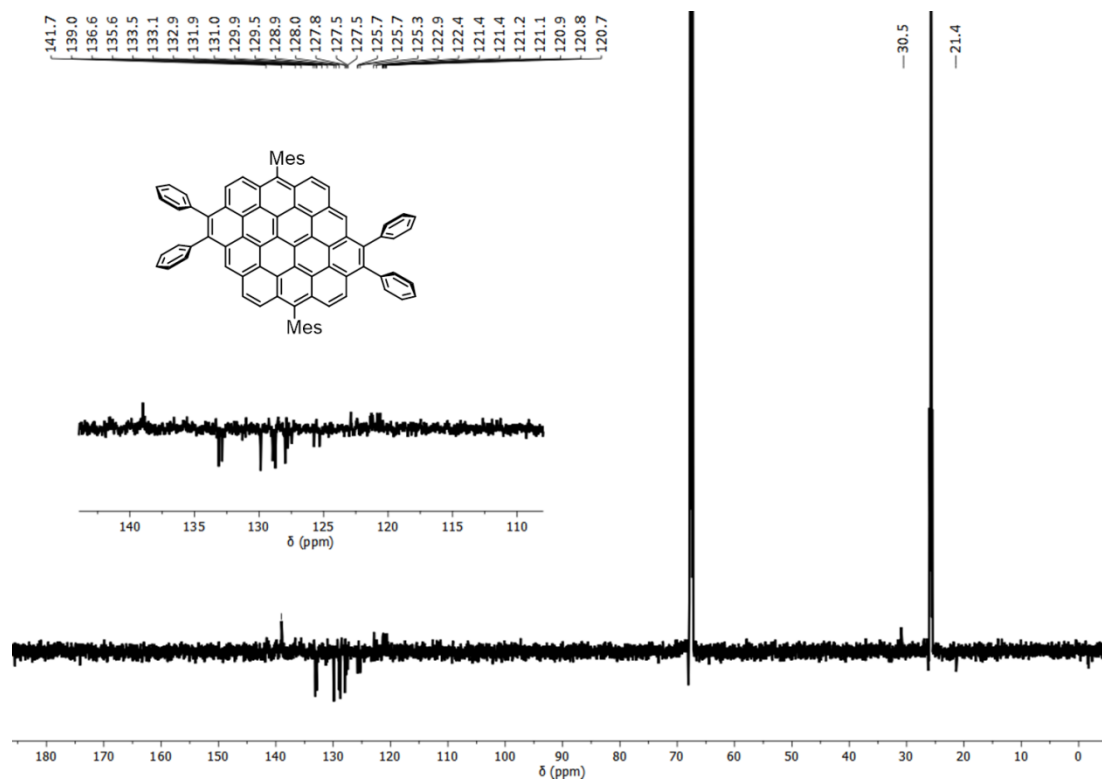


Figure S6-15. ^{13}C NMR spectra of compound **6-5b** measured in $\text{THF}/\text{CS}_2 (d_8)$ (175 MHz, 298 K).

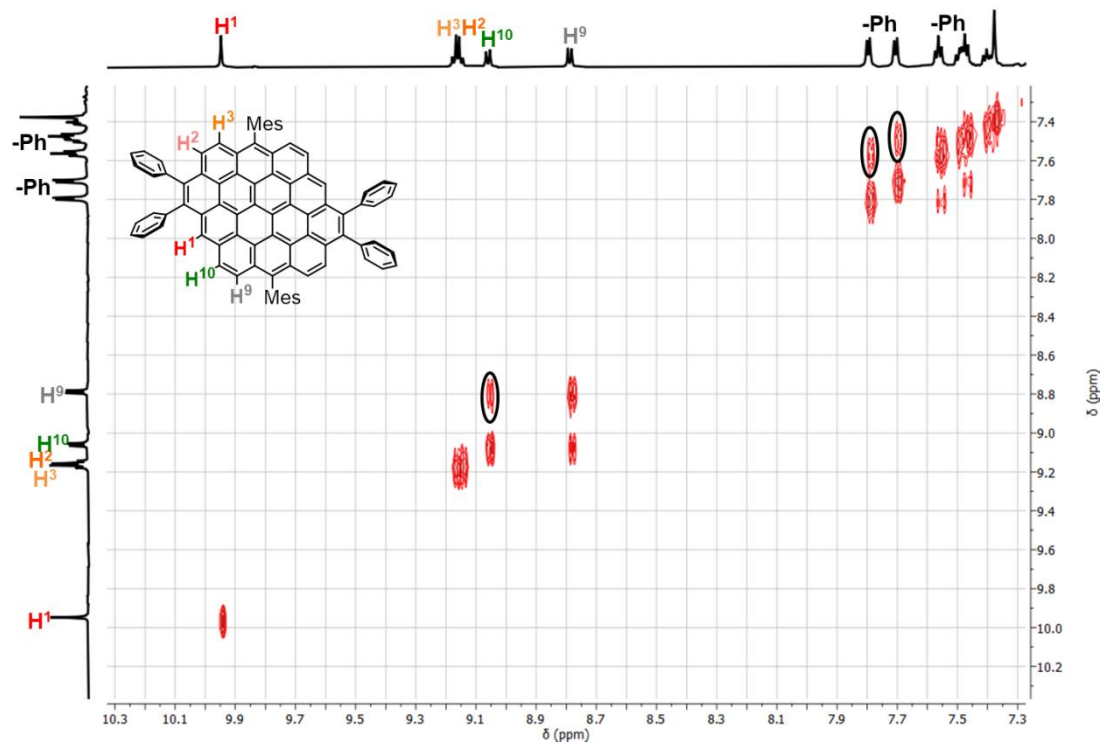


Figure S6-16. Aromatic region of $^1\text{H}, ^1\text{H}$ -COSY spectrum of **6-5b** (700 MHz, $\text{THF-}d_8$) at 298 K.

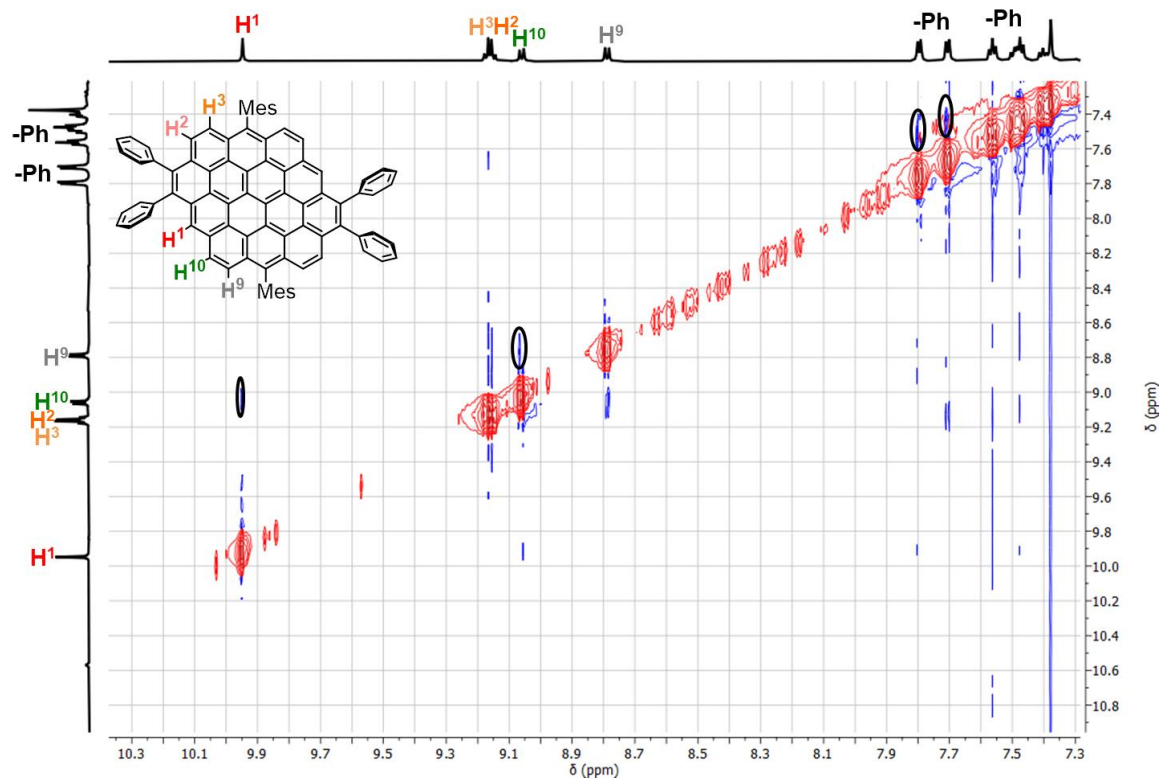


Figure S6-17. Aromatic region of $^1\text{H}, ^1\text{H}$ -NOESY spectrum of **6-5b** (700 MHz, $\text{THF-}d_8$) at 298 K.

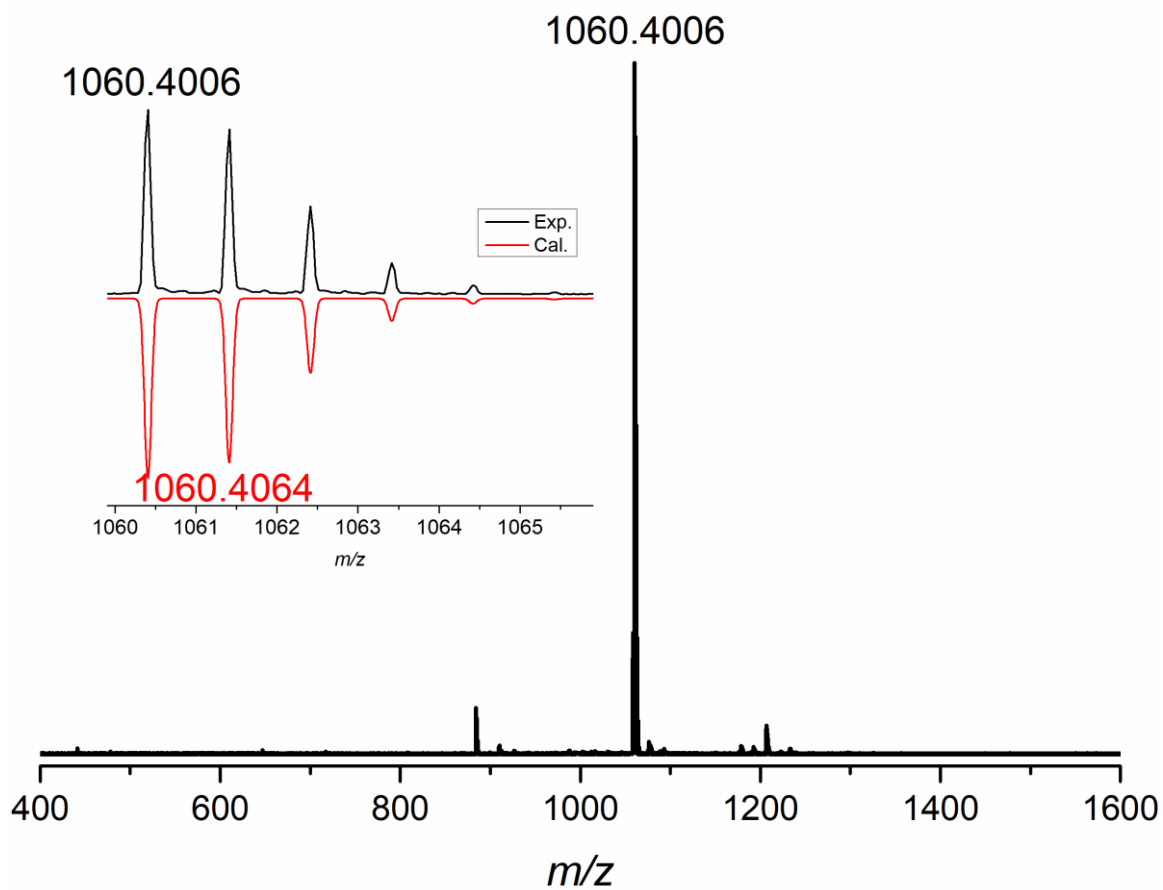


Figure S6-18. High-resolution MALDI-TOF MS spectra of **6-5b** and isotopic distribution pattern in comparison with calculation.

Reference

- (1) Sens, R.; Drexhage, K. H. Fluorescence quantum yield of oxazine and carbazine laser dyes. *J. Lumin.* **1981**, *24-25*, 709-712.
- (2) Chen, Q.; Thoms, S.; Thoms, S.; Stöttinger, S.; Schollmeyer, D.; Müllen, K.; Narita, A.; Basché, T. Dibenzo[*hi,st*]ovalene as Highly Luminescent Nanographene: Efficient Synthesis via Photochemical Cyclodehydroiodination, Opto-electronic Properties and Single-Molecule Spectroscopy. *J Am Chem Soc* **2019**, *141*, 16439-16449.
- (3) Chen, Q.; Wang, D.; Baumgarten, M.; Schollmeyer, D.; Müllen, K.; Narita, A. Regioselective Bromination and Functionalization of Dibenzo[*hi,st*]ovalene as Highly Luminescent Nanographene with Zigzag Edges. *Chem. Asian J* **2019**, *14*, 1703-1707.
- (4) Gaussian 09, R. D., M. J. Frisch, G. W. Trucks, H. B. Schlegel, G. E. Scuseria, M. A. Robb, J. R. Cheeseman, G. Scalmani, V. Barone, B. Mennucci, G. A. Petersson, H. Nakatsuji, M. Caricato, X. Li, H. P. Hratchian, A. F. Izmaylov, J. Bloino, G. Zheng, J. L. Sonnenberg, M. Hada, M. Ehara, K. Toyota, R. Fukuda, J. Hasegawa, M. Ishida, T. Nakajima, Y. Honda, O. Kitao, H. Nakai, T. Vreven, J. A. Montgomery, Jr., J. E. Peralta, F. Ogliaro, M. Bearpark, J. J. Heyd, E. Brothers, K. N. Kudin, V. N. Staroverov, T. Keith, R. Kobayashi, J. Normand, K. Raghavachari, A. Rendell, J. C. Burant, S. S. Iyengar, J. Tomasi, M. Cossi, N. Rega, J. M. Millam, M. Klene, J. E. Knox, J. B. Cross, V. Bakken, C. Adamo, J. Jaramillo, R. Gomperts, R. E. Stratmann, O. Yazyev, A. J. Austin, R. Cammi, C. Pomelli, J. W. Ochterski, R. L. Martin, K. Morokuma, V. G. Zakrzewski, G. A. Voth, P. Salvador, J. J. Dannenberg, S. Dapprich, A. D. Daniels, O. Farkas, J. B. Foresman, J. V. Ortiz, J. Cioslowski, and D. J. Fox, Gaussian, Inc., Wallingford CT, 2013.
- (5) Chen, Z.; Wannere, C. S.; Corminboeuf, C.; Puchta, R.; Schleyer, P. Nucleus-independent chemical shifts (NICS) as an aromaticity criterion. *Chem. Rev.* **2005**, *105*, 3842-3888.
- (6) Schleyer, P. V. R.; Maerker, C.; Dransfeld, A.; Jiao, H.; van Eikema Hommes, N. J. R. Nucleus-Independent Chemical Shifts: A Simple and Efficient Aromaticity Probe. *J. Am. Chem. Soc.* **1996**, *118*, 6317-6318.
- (7) Geuenich, D.; Hess, K.; Kohler, F.; Herges, R. Anisotropy of the induced current density (ACID), a general method to quantify and visualize electronic delocalization. *Chem. Rev.* **2005**, *105*, 3758-3772.

(8) Shi, B.; Nachtigallova, D.; Aquino, A. J. A.; Machado, F. B. C.; Lischka, H. High-level theoretical benchmark investigations of the UV-vis absorption spectra of paradigmatic polycyclic aromatic hydrocarbons as models for graphene quantum dots. *J Chem Phys* **2019**, *150*, 124302.

Chapter 7. Synthesis of Triply Fused Porphyrin-Nanographene Conjugates

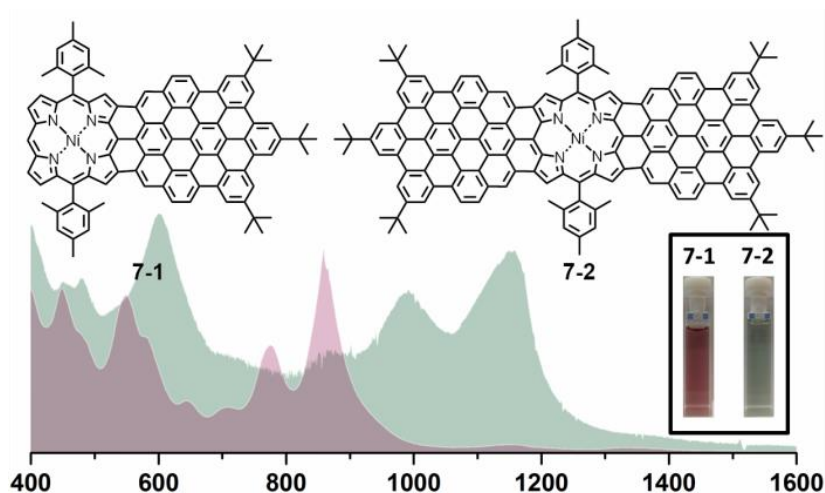
This Chapter is based on the following manuscript–

Angew. Chem. Int. Ed., **2018**, 57, 11233–11237

Author contributions. Q. C. designed, synthesized and characterized the compound investigated in this research under the supervision of [REDACTED] and [REDACTED] measured the FT-IR and Raman spectra under the supervision of [REDACTED] [REDACTED] was responsible for STM measurement under the supervision of [REDACTED] and [REDACTED].

Keywords: nanographene • porphyrin • Scholl reaction • π -extension • near-infrared absorption

TOC Figure

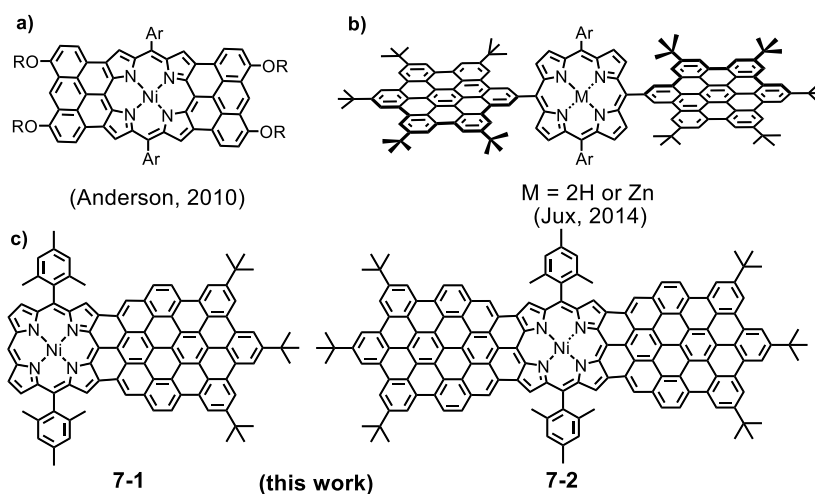


Triple whammy: Triply fused porphyrin-nanographene conjugates (**7-1** and **7-2**) have been synthesized by the Scholl reaction using tailor-made porphyrin based precursors. The conjugates show broad and intense near-infrared absorption. The self-assembled bilayer of **7-2** was observed at the trichlorobenzene/highly oriented pyrolytic graphite (HOPG) interface.

Reprinted with permission from (*Angew. Chem. Int. Ed.*, **2018**, 57, 1123–11237). Copyright © 2018, John Wiley and Sons.

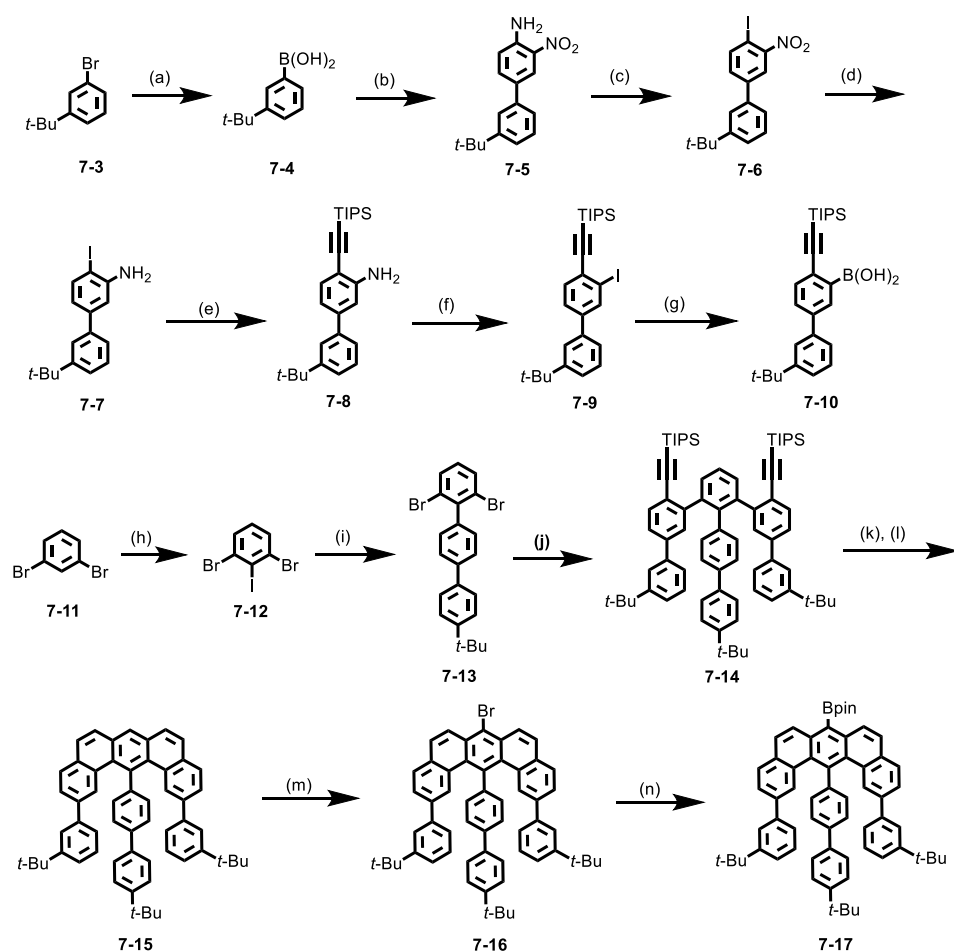
Abstract: Two unprecedented porphyrin fused nanographene molecules **7-1** and **7-2** have been synthesized by Scholl reaction of tailor-made precursors based on benzo[*m*]tetraphene-substituted porphyrins. The chemical structures were validated by a combination of high-resolution matrix-assisted laser desorption/ionization time-of-flight mass spectrometry (HR MALDI-TOF MS), IR and Raman spectroscopy, and scanning tunnelling microscopy (STM). The UV-vis-near infrared absorption spectroscopy of **7-1** and **7-2** demonstrated broad and largely red-shifted absorption spectra extending up to 1000 and 1400 nm, respectively, marking the significant extension of the π -conjugated systems.

In the past decades, synthesis of π -extended porphyrins has attracted immense interests for their unique optical and electronic properties,^[1] which render them highly valuable for a variety of applications, e.g., as near-infrared (NIR) dyes,^[2] organic semiconductors,^[3] and nonlinear optical materials.^[4] Various aromatic hydrocarbons, including benzene,^[5] naphthalene,^[1c, 6] pyrene,^[7] azulene,^[8] corannulene^[9] and coronene,^[10] have thus been fused to the *meso*- and β -positions of porphyrin. More recently, Anderson and his colleagues have explored the π -extension of porphyrin with anthracene subunits, which have the geometry that fully matches the periphery of porphyrin and can form three C-C bonds (Scheme 7-1a).^[11] Mono-, bis-, and tetrakis-anthracene-fused porphyrins have thus been reported, demonstrating markedly red-shifted UV-vis-near infrared (NIR) absorption spectra and reduced highest occupied molecular orbital–lowest unoccupied molecular orbital (HOMO-LUMO) gaps. However, further π -extension of porphyrin cores by fusion with larger polycyclic aromatic hydrocarbons (PAHs) has remained challenging.



Scheme 7-1. Structures of (a) bis-anthracene fused porphyrin; (b) covalently connected HBC-porphyrin conjugates, and (c) triply fused porphyrin-nanographene conjugates **7-1** and **7-2**.

Large PAHs, which can be regarded as nanographenes,^[12] are known to exhibit attractive (opto)electronic properties and self-assembly behavior,^[13] which can be further fine-tuned by precise control over their size, shape, and edge structure.^[14] Hexa-*peri*-hexabenzocoronene (HBC) with 42 sp^2 -hybridized carbons has been extensively investigated as an archetypal nanographene.^[15] Recently, we have achieved a synthesis of π -extended HBC with four extra K-regions, namely “isolated” double bonds that do not belong to the Clar sextets, employing a precursor having benzo[*m*]tetraphene units.^[16] The K-regions shaped zigzag edges at the HBC periphery, which significantly lowered the HOMO–LUMO gap.



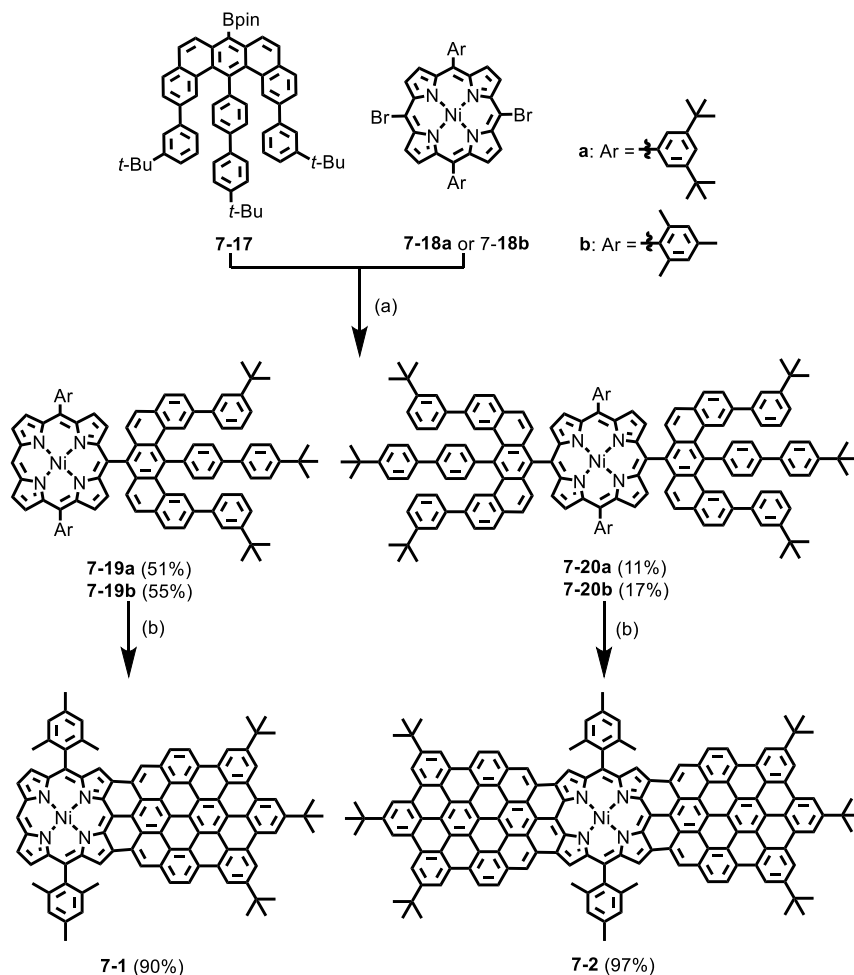
Scheme 7-2. Synthesis of boronate ester **7-17**. Reagents and conditions: a) (1) n -BuLi, -78 °C, 3 h, (2) $B(i\text{-PrO})_3$, -78 °C to r.t., 17 h, (3) 1 N HCl, r.t., 0.5 h, 66%; b) 4-bromo-2-nitroaniline, $\text{Pd}(\text{PPh}_3)_4$, Na_2CO_3 , toluene/EtOH/ H_2O = 3:1:1, 100 °C, 24 h, 88%; c) (1) PTSA· H_2O , NaNO_2 , acetonitrile/ H_2O = 10:1, 0 °C, 2 h, (2) KI, 0 °C to r.t., overnight, 85%; d) Fe powder, AcOH/EtOH = 1:1, reflux, 1 h, 98%; e) TIPS-acetylene, $\text{Pd}(\text{PPh}_3)_2\text{Cl}_2\cdot\text{CH}_2\text{Cl}_2$, CuI, THF:TEA = 2:1, r.t., 5 h, 99%; f) (1) PTSA· H_2O , NaNO_2 , KI, acetonitrile/ H_2O = 10:1, 0 °C to r.t., 21 h, 88%; g) (1) n -BuLi, THF, -78 °C, 0.5 h, (2) $B(i\text{-PrO})_3$, -78 °C for 0.5 h then r.t. for 1 h, (3) 1 N HCl, r.t., 0.5 h, 86%; h) LDA, -78 °C, 2 h, then I_2 , -78 °C, 2 h, 76%; i) (4'-*tert*-butyl)-[1,1'-biphenyl]-4-yl)boronic acid, $\text{Pd}(\text{PPh}_3)_4$, Na_2CO_3 ,

toluene/EtOH/H₂O = 3:1:1, 100 °C, 48 h, 70%; j) **7-10**, Pd(PPh₃)₄, K₂CO₃, 1,4-dioxane/H₂O = 3:1, 100 °C, 14 h, 86%; k) TBAF, THF, r.t., 2 h, 100%; l) PtCl₂, toluene, 80 °C, 24 h, 65%; m) Br₂, CH₂Cl₂, r.t., 1 h, 91%; n) AcOK, Pd(dppf)Cl₂·CH₂Cl₂, DMF, 80°C, 24 h, 83%. PTSA – *p*-toluenesulfonic acid, TIPS – triisopropylsilyl, THF – tetrahydrofuran, TEA – trimethylamine, LDA – lithium diisopropylamide, TBAF – tetrabutylammonium fluoride, DMF – dimethylformamide.

In recent years, numerous efforts have been made to introduce nanographenes as substituents to the periphery of porphyrin for making hybrid structures with tunable photophysical characteristics. For example, covalently bonded HBC-porphyrin conjugates have been synthesized, showing efficient energy transfer from HBC substituents to the porphyrin unit (Scheme 7-1b).^[17] More recently, porphyrin was successfully bonded to two graphene nanoribbons.^[18] However, the nanographene substituents can rotate with respect to the porphyrin core in such systems, which limits intramolecular conjugation. Moreover, the previous structural designs do not allow planarization of the porphyrin and nanographene units through formation of additional sextet rings. Here, we report a synthesis of β -,*meso*-, β -triply fused porphyrin-nanographene conjugates **7-1** and **7-2** by fusing porphyrin with π -extended HBCs with two extra K-regions. The zigzag edge of an anthracene substructure shaped at the periphery of HBC can geometrically fit *meso*- and β -positions of porphyrin (Scheme 1c). The fully conjugated planar structures facilitate electron delocalization over the porphyrin and HBC units, which induced narrowing of the HOMO-LUMO gap and large red-shifts in the UV-vis-NIR absorption spectra. STM measurements also validated the planar structure of **7-2** while showing its bilayer assembly behavior at the interface of 1,2,4-trichlorobenzene (TCB) and highly oriented pyrolytic graphite (HOPG).

As shown in Scheme 7-3, the synthesis of targeted porphyrin-nanographene conjugates **7-1** and **7-2** was carried out through cyclodehydrogenation of corresponding precursors **7-19** and **7-20**, respectively, which were based on benzo[*m*]tetraphene-substituted porphyrins. Precursors **7-19** and **7-20** were obtained by Suzuki coupling of boronate ester **7-17** and dibromoporphyrin (Ni) **7-18**. The key intermediate **7-17** was synthesized as displayed in Scheme 7-2. First, triisopropylsilyl (TIPS)-ethynylbiphenylboronic acid **7-10** was prepared from 1-bromo-3-*tert*-butylbenzene (**7-3**). Lithium halogen exchange of **7-3** using *n*-BuLi at –78 °C followed by quenching with triisopropylborate and hydrolysis gave (3-*tert*-butylphenyl)boronic acid (**7-4**) in 66% yield. Suzuki coupling of **7-4** with 4-bromo-2-nitroaniline provided 3-nitro-4-aminobiphenyl **7-5** in 88% yield, which was subjected to Sandmeyer iodination to afford 4-iodo-3-nitrobiphenyl **7-6** in 85% yield. Reduction of **7-6**

produced 3-amino-4-iodobiphenyl **7-7** in 98% yield, which was subjected to Sonogashira coupling with TIPS-acetylene to provide 3-amino-4-TIPS-ethynylbiphenyl **7-8** in 99% yield. Finally, Sandmeyer iodination gave 3-iodo-4-TIPS-ethynylbiphenyl **7-9** in 88% yield, which was treated with *n*-BuLi and quenched with triisopropylborate ester followed by hydrolysis to obtain desired boronic acid **7-10** in 86% yield.



Scheme 7-3. Syntheses of triply fused porphyrin-nanographene conjugates **7-1** and **7-2**. Reagents and conditions: a) (1) Pd(PPh₃)₄, K₂CO₃, toluene/DMF = 1:1, 110 °C, 36 h, then (2) Pd(PPh₃)₄, triethylamine, formic acid, toluene, 100 °C, 2 h; b) DDQ, CH₂Cl₂/triflic acid = 100:1, r.t., 10 h, Ar = mesityl.

On the other hand, for the preparation of 2,6-dibromoterphenyl **7-13**, 1,3-dibromobenzene (**7-11**) was first subjected to selective lithiation by lithium diisopropylamide (LDA) and subsequently treated with I₂ to give 1,3-dibromo-2-iodobenzene (**7-12**) in 76% yield. Selective Suzuki coupling of **7-12** with (4'-(*tert*-butyl)-[1,1'-biphenyl]-4-yl)boronic acid provided **7-13** in 70% yield. Then, Suzuki coupling of **7-13** and 2.0 equivalents of **7-10** afforded bis(TIPS-ethynyl)quinquephenyl **7-14** in 86% yield. After deprotection and Pt-

catalyzed cycloaromatization, benzo[*m*]tetraphene **7-15** was obtained in 65% yield. The *meso*-position of **7-15** could be selectively brominated to provide 7-bromo-benzo[*m*]tetraphene **7-16** in 91% yield, which was converted to boronate ester **7-17** by Miyaura borylation in 83% yield. The structure of **7-17** was characterized by using ^1H NMR, ^{13}C NMR, and high-resolution mass spectrometry (see Figures S7-45 and S7-46).

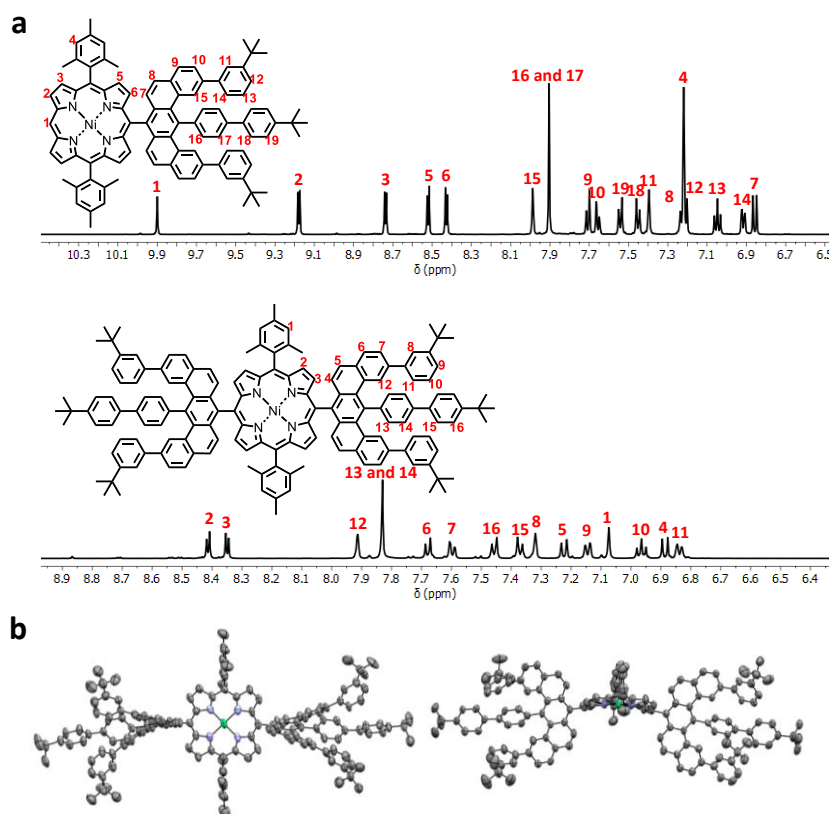


Figure 7-1. a) Aromatic region of the ^1H NMR spectra of **7-19b** (top) and **7-20b** (bottom) measured in CD_2Cl_2 at 298 K (500 MHz); b) X-ray crystallographic structure of **7-20b** (measured at 193 K): top view (left) and front view (right). Atom colors: C-gray; N-blue; Ni-green. Hydrogen atoms and solvents have been omitted for clarity.

For the synthesis of precursors **7-19** and **7-20**, two dibromo-substituted porphyrin (Ni) derivatives **7-18a**^[19] and **7-18b**^[20] with bulky substituents were selected to increase the solubility of the final products in common organic solvents,^[19, 21] and prepared following reported methods (see synthetic details in Supporting Information). The nickel (II) ion was inserted into the porphyrin core considering the high stability of nickel (II)-porphyrin under strong oxidation conditions required for the final Scholl reaction.^[11c] The Suzuki coupling of boronate ester **7-17** and dibromoporphyrin **7-18a/b** provided corresponding one- and two-fold coupling products **7-19a**, **7-20a**, **7-19b**, and **7-20b** in 51%, 11%, 55%, and 17% yield,

respectively. The structures of these coupling products were unambiguously characterized by ^1H NMR, ^{13}C NMR, and high-resolution matrix-assisted laser desorption/ionization time-of-flight mass spectrometry (HR MALDI-TOF MS). All the proton signals could be assigned with the help of $^1\text{H},^1\text{H}$ -correlation spectroscopy (COSY), $^1\text{H},^1\text{H}$ -nuclear overhauser enhancement spectroscopy (NOESY), and $^1\text{H},^1\text{H}$ -total correlation spectroscopy (TOCSY) spectra (see Figures 7-1a and S7-1). Although growing single crystals of **7-19** suitable for X-ray diffraction analysis failed under various conditions, we successfully obtained a single crystal of **7-20b** by slow evaporation of its dichloromethane solution at room temperature, allowing the unambiguous structural confirmation by single-crystal X-ray analysis (Figure 7-1b).

The Scholl reaction of **7-19a** was first attempted with FeCl_3 , which is widely used for cyclodehydrogenation of polyphenylenes and also employed in previous syntheses of π -extended porphyrin derivatives.^[11b, 11c] However, MALDI-TOF MS analysis of the reaction mixture indicated the presence of partially fused species even after the reaction overnight in addition to significant chlorination (see Figure S7-2). On the other hand, use of 2,3-dichloro-5,6-dicyano-1,4-benzoquinone (DDQ) with catalytic amount of triflic acid turned out to be effective, providing completely dehydrogenated product (formation of 8 carbon-carbon bonds) together with over-dehydrogenated byproducts (formation of 10 carbon-carbon bonds). We assumed that the over-dehydrogenation was caused by the formation of five-membered rings between the 3,5-di-*tert*-butylphenyl groups and the porphyrin core (see Figure S7-3), similar to observations in a previous report on electron deficient porphyrin (Ni) systems.^[22] To avoid this undesired side reaction, we next employed precursors **7-19b** and **7-20b** with mesityl groups. To our delight, the oxidative cyclodehydrogenation of **7-19b** and **7-20b** with DDQ and a catalytic amount (100:1, v/v) of triflic acid successfully provided triply fused porphyrin-nanographene conjugates **1** and **2**, respectively, in 90% and 97% yields.

The strong intermolecular interactions of both **7-1** and **7-2** prevented their characterization by NMR spectroscopy. High temperature ^1H NMR measurement at 140 °C in *o*-dichlorobenzene- d_4 and addition of CS_2 in an attempt to prevent the aggregation failed to give highly resolved spectra. The possibility of the presence of remaining radical cation species was excluded by addition of hydrazine as quencher. Nevertheless, characterizations by high-resolution MALDI-TOF MS, IR and Raman spectroscopy, and STM clearly verified the formation of the desired structures. MALDI-TOF MS analysis demonstrated the removal of 16 and 32 protons for **7-19b** and **7-20b**, respectively, after cyclodehydrogenation reaction (see Figure S7-4),

corroborating the complete dehydrogenation. High-resolution mass spectra of **7-1** and **7-2** display intense signals at $m/z = 1334.4831$ and 2066.7644 , which are in good agreement with calculated molecular mass of 1334.4797 and 2066.7614 , respectively. Furthermore, the observed isotopic distribution patterns are fully consistent with the calculated spectra (Figure 7-2a).

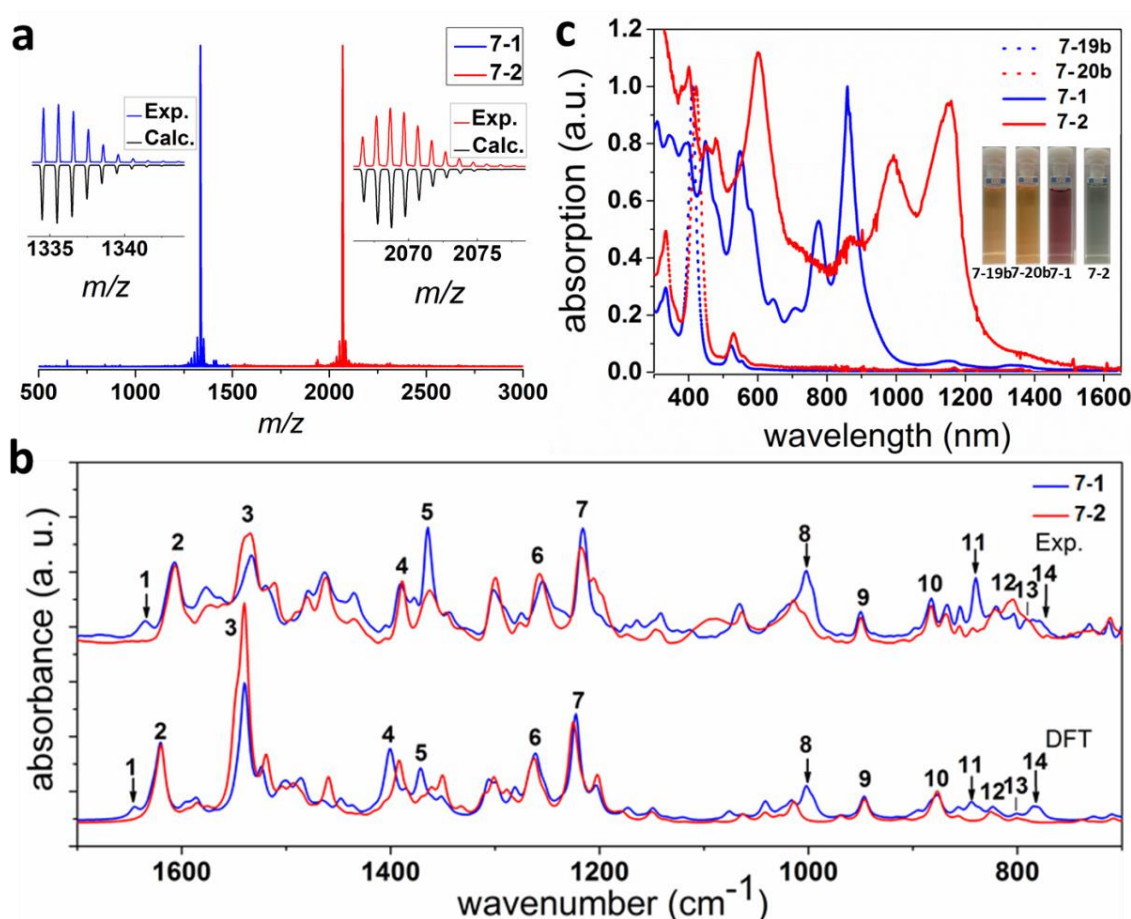


Figure 7-2. a) MALDI-TOF MS spectra of porphyrin-nanographene conjugates **7-1** and **7-2**, inset: experimental and theoretical isotopic distribution patterns; b) Experimental FT-IR spectra of **7-1** and **7-2** compared with simulated spectra obtained from DFT calculations (computed wavenumbers have been scaled by 0.98). Characteristic features of **7-1** are marked with arrows (see Table S7-1 and Figure S7-5 for details); c) UV-vis-NIR absorption spectra of **7-1** and **7-2** in comparison with corresponding precursors **7-19b** and **7-20b** measured in tetrahydrofuran at room temperature. The inset photographs show the tetrahydrofuran solutions of **7-19b**, **7-20b**, **7-1**, and **7-2**.

Figure 7-2b shows the experimental FT-IR spectra of **7-1** and **7-2** compared with the simulated spectra obtained from density functional theory (DFT) calculations. The overall agreement between the experimentally measured and simulated spectra provides strong

support for the successful synthesis of both compounds. Moreover, the observed differences between the IR spectra can be traced back to the distinct features in their chemical structures. For instance, both **7-1** and **7-2** display IR bands at 1606/1605, 1532/1534, 819/820, and 803 cm^{-1} , which can be attributed to vibration modes of chemical features common to both structures (Figure S7-5). In contrast, the IR bands located at 1634, 1001, 838, and 790 cm^{-1} are only observed for **7-1** (see arrows in Figure 7-2b), and indeed characteristic for the bare periphery of the porphyrin unit (see Table S7-1 and Figure S7-5 for the details about the assignment of the IR bands mentioned above). The FT-Raman spectra of **7-1** and **7-2** showed a fluorescence background, which hindered a precise analysis of the Raman features. However, good overall agreement between the experimentally obtained characteristic peaks and DFT results further corroborated the desired structures. (see Figure S7-6 – S7-8).

The optical properties of **7-1** and **7-2** were studied by UV-vis-NIR absorption spectrometry in tetrahydrofuran in comparison with corresponding precursors **7-19b** and **7-20b**, respectively (Figure 7-2c). Both precursors exhibited intense absorption peaks at 420 and 560 nm, which could be assigned to the Soret and Q band of the nickel (II) porphyrin core, respectively.^[11b] After expansion of the π -systems by cyclodehydrogenation, the maximum absorption peak of **7-1** is red-shifted to 866 nm with the tail extended to around 1000 nm. Fusion of another nanographene unit to the porphyrin core red-shifted the maximum absorption peak of **7-2** to 1176 nm with the tail extending to approximately 1400 nm. The observed absorption bands were in good agreement with the simulation by time-dependent DFT (TDDFT) calculations (see Figure S7-11). The HOMO/LUMO energy levels of **7-1** and **7-2** were calculated by DFT to be $-4.53 \text{ eV}/-2.75 \text{ eV}$ and $-4.23 \text{ eV}/-2.88 \text{ eV}$, respectively, corresponding to low HOMO-LUMO gaps of 1.78 eV and 1.35 eV. Fluorescence measurements on these molecules were not successful because of the heavy atom effect of the central Ni^{2+} ion, which quenched the luminescence.^[23]

STM analysis of **7-2** at the TCB/HOPG interface revealed a self-assembled network consisting of an ordered array of C_2 -symmetric dumbbell-shaped features. The size and shape of these features agrees well with the expected shape and size of **7-2** (Figure 7-3a). At each end of these features, three lobes could be discerned, representing the peripheral *tert*-butyl groups (Figure 7-3b). The molecules were close-packed along one of the unit cell vectors (vector a), but well-separated from each other along the other (vector b) unit cell vector. Such packing is rather unusual, since a close-packed structure is expected considering the lack of specific functional groups on the periphery of this molecule. We ascribe this packing to

formation of a bilayer film with a continuous first layer adsorbed on HOPG and a discontinuous second layer, presumably due to steric repulsion, as displayed in a proposed molecular model (Figure 7-3b, inset). Only the molecules in the second layer (in yellow color in Figure 7-3b, inset) were observed in STM images, as confirmed by investigating the edge of molecular domains (see more detailed discussion in the Supporting Information).

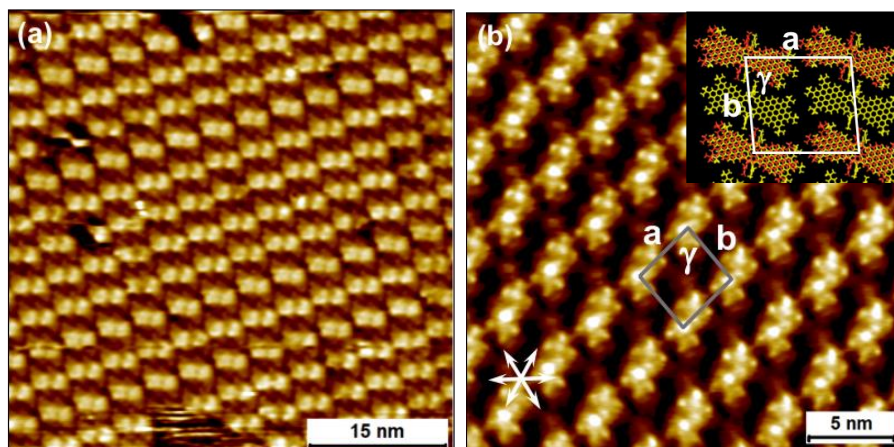


Figure 7-3. STM characterization of **7-2** at the TCB/HOPG interface. (a) Large-scale STM image showing long-range ordered assembly of **7-2**; (b) High-resolution STM image of the self-assembled network. Unit cell parameters: $a = 3.7 \pm 0.1$ nm, $b = 4.0 \pm 0.1$ nm and $\gamma = 86 \pm 2^\circ$. The graphite symmetry axes are shown in the lower left corner. The inset displays proposed molecular model for the bilayer self-assembly. The molecules in yellow form a continuous, densely packed lower layer whereas those in red occupy the second layer. Imaging parameters (a) $V_{bias} = -1.1$ V, $I_{set} = 50$ pA (b) $V_{bias} = -900$ mV, $I_{set} = 85$ pA.

In conclusion, we have synthesized two triply fused porphyrin-nanographene conjugates **7-1** and **7-2** through the cyclodehydrogenation of carefully designed precursors featuring benzo[*m*]tetraphene-substituted porphyrins. The significantly π -extended porphyrins have small HOMO-LUMO gaps of 1.78 eV and 1.35 eV based on DFT calculations. The optical absorption spectra of **7-1** and **7-2** were considerably red-shifted to the NIR region, making them of high potential as NIR dyes for optoelectronic applications such as infrared sensing. This strategy for fusion of porphyrin cores into nanographene planes can potentially be applied to synthesize a large variety of hybrid structures, for example porphyrin-fused graphene nanoribbons (GNRs). Further synthetic studies on these extended structures are ongoing in our group.

Acknowledgements

We are grateful for the financial support from the Max Planck Society and EC through the Graphene Flagship and Marie-Curie ITN project “iSwitch” (GA No. 642196). This work was supported in part by FWO under EOS 30489208, and internal funds – KU Leuven.

Reference

- [1] a) M. Stepien, E. Gonka, M. Zyla, N. Sprutta, *Chem. Rev.* **2017**, *117*, 3479-3716; b) T. D. Lash, T. M. Werner, M. L. Thompson, J. M. Manley, *J. Org. Chem.* **2001**, *66*, 3152-3159; c) H. S. Gill, M. Harmjan, J. Santamaria, I. Finger, M. J. Scott, *Angew. Chem. Int. Ed.* **2004**, *43*, 485-490; d) Y. Nakamura, N. Aratani, H. Shinokubo, A. Takagi, T. Kawai, T. Matsumoto, Z. S. Yoon, D. Y. Kim, T. K. Ahn, D. Kim, A. Muranaka, N. Kobayashi, A. Osuka, *J. Am. Chem. Soc.* **2006**, *128*, 4119-4127; e) S. Hiroto, Y. Miyake, H. Shinokubo, *Chem. Rev.* **2017**, *117*, 2910-3043; f) T. Tanaka, A. Osuka, *Chem. Soc. Rev.* **2015**, *44*, 943-969; g) H. Mori, T. Tanaka, A. Osuka, *J. Mater. Chem. C* **2013**, *1*, 2500.
- [2] C. Jiao, N. Zu, K. W. Huang, P. Wang, J. Wu, *Org. Lett.* **2011**, *13*, 3652-3655.
- [3] M. H. Sayyad, M. Saleem, K. S. Karimov, M. Yaseen, M. Ali, K. Y. Cheong, A. F. Mohd Noor, *Appl. Phys. A* **2009**, *98*, 103-109.
- [4] N. Aratani, D. Kim, A. Osuka, *Chem. Asian J.* **2009**, *4*, 1172-1182.
- [5] a) L. Barloy, D. Dolphin, D. Dupre, T. P. Wijesekera, *J. Org. Chem.* **1994**, *59*, 7976-7985; b) S. Richeter, C. Jeandon, J.-P. Gisselbrecht, R. Ruppert, H. J. Callot, *J. Am. Chem. Soc.* **2002**, *124*, 6168-6179; c) S. Fox, R. W. Boyle, *Chem. Commun.* **2004**, 1322-1323; d) D. M. Shen, C. Liu, Q. Y. Chen, *Chem Commun (Camb)* **2005**, 4982-4984; e) D. M. Shen, C. Liu, Q. Y. Chen, *J. Org. Chem.* **2006**, *71*, 6508-6511.
- [6] a) A. N. Cammidge, P. J. Scaife, G. Berber, D. L. Hughes, *Org. Lett.* **2005**, *7*, 3413-3416; b) M. Tanaka, S. Hayashi, S. Eu, T. Umeyama, Y. Matano, H. Imahori, *Chem. Commun.* **2007**, 2069-2071.
- [7] a) O. Yamane, K.-i. Sugiura, H. Miyasaka, K. Nakamura, T. Fujimoto, K. Nakamura, T. Kaneda, Y. Sakata, M. Yamashita, *Chem. Lett.* **2004**, *33*, 40-41; b) V. V. Diev, K. Hanson, J. D. Zimmerman, S. R. Forrest, M. E. Thompson, *Angew. Chem. Int. Ed.* **2010**, *49*, 5523-5526.
- [8] K. Kurotobi, K. S. Kim, S. B. Noh, D. Kim, A. Osuka, *Angew. Chem. Int. Ed.* **2006**, *45*, 3944-3947.
- [9] K. Ota, T. Tanaka, A. Osuka, *Org. Lett.* **2014**, *16*, 2974-2977.
- [10] V. V. Diev, C. W. Schlenker, K. Hanson, Q. Zhong, J. D. Zimmerman, S. R. Forrest, M. E. Thompson, *J. Org. Chem.* **2012**, *77*, 143-159.

- [11] a) N. K. Davis, M. Pawlicki, H. L. Anderson, *Org. Lett.* **2008**, *10*, 3945-3947; b) N. K. Davis, A. L. Thompson, H. L. Anderson, *Org. Lett.* **2010**, *12*, 2124-2127; c) N. K. Davis, A. L. Thompson, H. L. Anderson, *J. Am. Chem. Soc.* **2011**, *133*, 30-31.
- [12] L. Chen, Y. Hernandez, X. Feng, K. Müllen, *Angew. Chem. Int. Ed.* **2012**, *51*, 7640-7654.
- [13] a) J. Wu, A. Fechtenkotter, J. Gauss, M. D. Watson, M. Kastler, C. Fechtenkotter, M. Wagner, K. Müllen, *J. Am. Chem. Soc.* **2004**, *126*, 11311-11321; b) L. F. Dossel, V. Kamm, I. A. Howard, F. Laquai, W. Pisula, X. Feng, C. Li, M. Takase, T. Kudernac, S. De Feyter, K. Müllen, *J. Am. Chem. Soc.* **2012**, *134*, 5876-5886; c) X. Feng, W. Pisula, T. Kudernac, D. Wu, L. Zhi, S. De Feyter, K. Müllen, *J. Am. Chem. Soc.* **2009**, *131*, 4439-4448; d) Y. Yamamoto, T. Fukushima, Y. Suna, N. Ishii, A. Saeki, S. Seki, S. Tagawa, M. Taniguchi, T. Kawai, T. Aida, *Science* **2006**, *314*, 1761-1764.
- [14] S. Fujii, T. Enoki, *Accounts. Chem. Res.* **2012**, *46*, 2202-2210.
- [15] J. Holzwarth, K. Y. Amsharov, D. I. Sharapa, D. Reger, K. Roshchyna, D. Lungerich, N. Jux, F. Hauke, T. Clark, A. Hirsch, *Angew. Chem. Int. Ed.* **2017**, *56*, 12184-12190.
- [16] T. Dumsloff, B. Yang, A. Maghsoumi, G. Velpula, K. S. Mali, C. Castiglioni, S. De Feyter, M. Tommasini, A. Narita, X. Feng, K. Müllen, *J. Am. Chem. Soc.* **2016**, *138*, 4726-4729.
- [17] a) J. M. Englert, J. Malig, V. A. Zamolo, A. Hirsch, N. Jux, *Chem. Commun.* **2013**, *49*, 4827-4829; b) D. Lungerich, J. F. Hitzemberger, M. Marcia, F. Hampel, T. Drewello, N. Jux, *Angew. Chem. Int. Ed.* **2014**, *53*, 12231-12235.
- [18] W. Perkins, F. R. Fischer, *Chem. Eur. J.* **2017**, *23*, 17687-17691.
- [19] O. B. Locos, D. P. Arnold, *Org. Biomol. Chem.* **2006**, *4*, 902-916.
- [20] L. Yu, K. Muthukumar, I. V. Sazanovich, C. Kirmaier, E. Hindin, J. R. Diers, P. D. Boyle, D. F. Bocian, D. Holten, J. S. Lindsey, *Inorg. Chem.* **2003**, *42*, 6629-6647.
- [21] K. Jyothish, Q. Wang, W. Zhang, *Adv. Synth. Catal.* **2012**, *354*, 2073-2078.
- [22] N. Fukui, S.-K. Lee, K. Kato, D. Shimizu, T. Tanaka, S. Lee, H. Yorimitsu, D. Kim, A. Osuka, *Chem. Sci.* **2016**, *7*, 4059-4066.
- [23] A. Harriman, *J. Chem. Soc., Faraday Trans. 1* **1980**, *76*, 1978.

Copyright Wiley-VCH Verlag GmbH & Co. KGaA, Weinheim 2018

Supporting Information

Synthesis of Triply Fused Porphyrin-Nanographene Conjugates

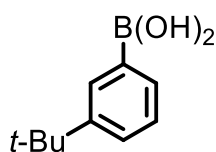
General methods

All reactions working with air- or moisture- sensitive compounds were carried out under argon atmosphere using standard Schlenk line techniques. Unless otherwise noted, all starting materials were purchased from commercial sources (Alfa Aesar, Sigma-Aldrich or TCI) and used without further purification. All other reagents were used as received. Thin layer chromatography (TLC) was done on silica gel coated aluminum sheets with F254 indicator and column chromatography separation was performed with silica gel (particle size 0.063-0.200 mm). Melting points were measured on a Büchi hot stage apparatus and were uncorrected. Nuclear Magnetic Resonance (NMR) spectra were recorded in deuterated solvents using Bruker AVANCE III 300, Bruker AVANCE III 500 and Bruker AVANCE III 700 MHz NMR spectrometers. Chemical shifts (δ) were expressed in ppm relative to the residual of solvent (CD_2Cl_2 @ 5.32 ppm ^1H NMR, 54.00 ppm ^{13}C NMR, $\text{C}_2\text{D}_2\text{Cl}_4$ @ 6.00 ppm ^1H NMR, 73.78 ppm ^{13}C NMR). Coupling constants (J) were recorded in Hertz with multiplicities explained by the following abbreviations: s = singlet, d = doublet, t = triplet, q = quartet, dd = double of doublets, dt = doublet of triplets, m = multiplet. The assignment of proton signals were accomplished by $^1\text{H}, ^1\text{H}$ COSY (correlated spectroscopy), $^1\text{H}, ^1\text{H}$ TOCSY (total correlated spectroscopy), $^1\text{H}, ^{13}\text{C}$ HSQC (heteronuclear single-quantum coherence) and $^1\text{H}, ^1\text{H}$ NOESY (nuclear overhauser enhancement spectroscopy) experiments. UV-vis-NIR absorption spectra were measured on a Perkin-Elmer Lambda 900 spectrophotometer at room temperature. High-resolution mass spectra (HRMS) were recorded by electrospray ionization (ESI) and Atmospheric Pressure Photoionization (APPI) on a Q-ToF Ultima 3 (micromass/Waters) and by matrix-assisted laser decomposition/ionization (MALDI) using 7,7,8,8-tetracyanoquinodimethane (TCNQ) as matrix on a Bruker Reflex II-TOF spectrometer. The micro-FT-IR spectra were recorded through a diamond anvil cell (transmission mode) with a Nicolet Nexus FT-IR spectrometer coupled with a Thermo Electron Continuum IR microscope. The micro-FT-Raman spectra were recorded with a Nicolet NXR9650 FT-Raman spectrometer (1064 nm excitation wavelength). Density functional theory (DFT) calculations were carried out with the B3LYP functional using the Gaussian 09 code (revision D.01).¹ For describing the Ni atom of **7-1** and **7-2**, we selected the Stuttgart effective core potential

ECP10MDF and basis set (8s7p6d2f1g)/[6s5p3d2f1g].^{2, 3} The 6-31G(d,p) basis set was chosen for the remaining atoms. The calculation of the Raman intensities was carried out in off-resonance conditions. Time-dependent DFT (TDDFT) calculations were carried out with the functional and basis set described above, on the same optimized geometries which were used for the calculation of IR and Raman spectra. For both **7-1** and **7-2** we computed the lowest 150 excited states.

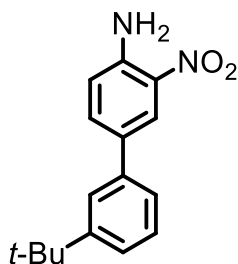
Synthetic details

(3-*tert*-butylphenyl)boronic acid (**7-4**):



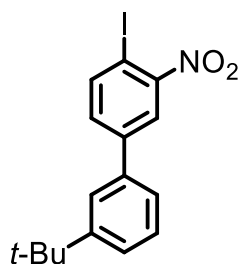
To a solution of 1-bromo-3-*tert*-butylbenzene (**7-3**) (27.20 g, 127.6 mmol) in dry THF (257 mL) was added dropwise *n*-BuLi (1.6 M in *n*-hexane, 88 mL, 0.14 mol) at $-78\text{ }^{\circ}\text{C}$ over 20 min. After stirring for 2 h at this temperature, trimethyl borate (33.41 g, 321.5 mmol) was added and the resulting mixture was allowed to gradually warm up to room temperature overnight. The reaction was quenched by addition of 1 N HCl (160 mmol, 160 mL). After stirring for 30 min at room temperature, the resulting biphasic solution was extracted for three times with ethyl acetate (250 mL), washed with brine (250 mL), dried over Na_2SO_4 , and evaporated. Purification by silica gel column chromatography (*n*-hexane:ethyl acetate = 10:1 to 2:1) gave the title compound (15 g, 66% yield) as white solid. Mp: $154.9 - 156.5\text{ }^{\circ}\text{C}$; ^1H NMR (300 MHz, Methylene Chloride- d_2) δ 8.34 (s, 1H), 8.13 – 8.03 (m, 1H), 7.71 – 7.63 (m, 1H), 7.48 (t, $J = 7.6\text{ Hz}$, 1H), 1.44 (s, 9H); ^{13}C NMR (75 MHz, Methylene Chloride- d_2) δ 151.0, 133.1, 132.7, 130.3, 128.2, 35.0, 31.5; HRMS (ESI+) m/z : calcd. for $\text{C}_{10}\text{H}_{15}\text{BO}_2^+$ (M) $^+$:178.1160; found: 178.0674.

3'-*tert*-butyl-3-nitro-[1,1'-biphenyl]-4-amine (**7-5**)



To a 250-mL Schlenk flask was added 4-bromo-2-nitroaniline (11.0 g, 50.7 mmol), (3-*tert*-butylphenyl)boronic acid (**7-4**) (9.5 g, 53 mmol), Pd(PPh₃)₄ (1.5 g, 1.3 mmol) and Na₂CO₃ (20.1 g, 189 mmol). The flask was evacuated and backfilled with Ar for three times before addition of degassed mixture of toluene/ethanol/water (100 mL/25 mL/25 mL). After heating at 100 °C for 8 h, the mixture was cooled down to room temperature and extracted with ethyl acetate (100 mL) for three times. The organic phases were combined, washed with brine, dried over Na₂SO₄, and evaporated. The residue was purified by silica gel column chromatography (*n*-hexane:ethyl acetate = 3:1) to give the title compound (12.1 g, 88% yield) as red solid. Mp: 139.8 – 141.3 °C; ¹H NMR (300 MHz, Methylene Chloride-*d*₂) δ 8.35 (d, *J* = 2.3 Hz, 1H), 7.68 (dd, *J* = 8.7, 2.2 Hz, 1H), 7.62 – 7.56 (m, 1H), 7.45 – 7.33 (m, 3H), 6.94 (d, *J* = 8.7 Hz, 1H), 6.16 (s, 2H), 1.38 (s, 9H); ¹³C NMR (75 MHz, Methylene Chloride-*d*₂) δ 152.4, 144.3, 139.0, 135.1, 132.8, 131.2, 129.0, 124.8, 124.1, 123.9, 123.8, 119.7, 35.1, 31.5; HRMS (ESI+) *m/z*: calcd. for C₁₆H₁₉N₂O₂⁺ (M+H)⁺:271.1441; found: 271.1446.

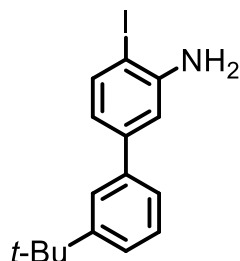
3'-*tert*-butyl-4-iodo-3-nitro-1,1'-biphenyl (**7-6**)



To a suspension of 3'-*tert*-butyl-3-nitro-[1,1'-biphenyl]-4-amine (**7-5**) (12.0 g, 44.4 mmol) and *p*-toluenesulfonic acid monohydrate (25.0 g, 133 mmol) in acetonitrile (600 mL) was added dropwise a solution of KI (18.4 g, 111 mmol) and NaNO₂ (9.2 g, 0.13 mol) dissolved in water (100 mL) at 0 °C. The mixture was gradually warmed up to room temperature and stirred for another 24 h. After completion of the reaction, the dark solution was extracted with ethyl acetate (200 mL) for 3 times. The organic phases were combined, washed with brine (200 mL), dried over Na₂SO₄, and evaporated. The residue was purified by silica gel column chromatography (*n*-hexane:ethyl acetate = 50:1) to give the title compound (14.47 g, 85% yield) as yellow solid. Mp: 85.5 – 87.3 °C; ¹H NMR (300 MHz, Methylene Chloride-*d*₂) δ 8.10 (d, *J* = 8.3 Hz, 1H), 8.06 (d, *J* = 2.2 Hz, 1H), 7.62 – 7.58 (m, 1H), 7.53 (dd, *J* = 8.2, 2.2 Hz, 1H), 7.50 – 7.44 (m, 1H), 7.44 – 7.38 (m, 2H), 1.37 (s, 9H); ¹³C NMR (75 MHz, Methylene Chloride-*d*₂) δ 154.0, 152.8, 143.8, 142.5, 137.8, 132.3, 129.4, 126.4, 124.5, 124.4,

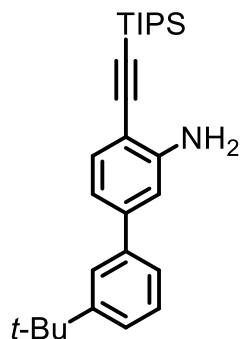
124.2, 84.3, 35.2, 31.5; HRMS (ESI+) m/z : calcd. for $C_{16}H_{16}INO_2^+$ (M)⁺: 381.0220; found: 381.0226.

3'-*tert*-butyl-4-iodo-[1,1'-biphenyl]-3-amine (**7-7**)



Iron powder (8.47 g, 152 mmol) was added to a refluxing solution of 3'-*tert*-butyl-4-iodo-3-nitro-1,1'-biphenyl (**7-6**) (13.8 g, 36.2 mmol) in acetic acid (120 mL) and ethanol (120 mL). After refluxing for another 2 h, the suspension was cooled down to room temperature. The insoluble solid was filtered off and washed with ethyl acetate (200 mL) for three times. The combined organic solutions were washed with water (150 mL), brine (150 mL), dried over Na_2SO_4 , and evaporated. The residue was purified by silica gel column chromatography (*n*-hexane:ethyl acetate = 10:1) to give the title compound (12.5 g, 98% yield) as yellow solid. Mp: 60.7 – 61.6 °C; 1H NMR (300 MHz, Methylene Chloride- d_2) δ 7.69 (d, J = 8.2 Hz, 1H), 7.61 – 7.55 (m, 1H), 7.46 – 7.32 (m, 3H), 6.99 (d, J = 2.2 Hz, 1H), 6.73 (dd, J = 8.2, 2.2 Hz, 1H), 4.22 (s, 2H), 1.37 (s, 9H); ^{13}C NMR (75 MHz, Methylene Chloride- d_2) δ 152.2, 147.7, 143.6, 140.4, 139.6, 128.9, 125.1, 124.4, 124.4, 119.3, 113.6, 82.8; HRMS (ESI+) m/z : calcd. for $C_{16}H_{19}IN^+$ (M+H)⁺: 352.0557; found: 352.0581.

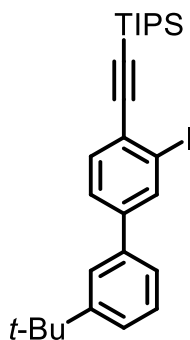
3'-*tert*-butyl-4-(triisopropylsilylethynyl)-[1,1'-biphenyl]-3-amine (**7-8**)



To a 250-mL Schlenk flask was added 3'-*tert*-butyl-4-iodo-[1,1'-biphenyl]-3-amine (**7-7**) (12.3 g, 35.0 mmol), $Pd(PPh_3)_2Cl_2$ (1.2 g, 1.7 mmol), and CuI (665 mg, 3.49 mmol). The flask was evacuated and backfilled with Ar for three times before a mixture of tetrahydrofuran (150

mL) and triethyl amine (40 mL) was added. After bubbling with Ar flow for 15 min, (triisopropylsilyl)acetylene (7.03 g, 38.5 mmol) was added via a syringe. The mixture was stirred at room temperature for 6 h. After completion of the reaction, saturated aqueous ammonium chloride solution (100 mL) and ethyl acetate (100 mL) was added. The organic phase was separated and the aqueous layer was extracted twice with ethyl acetate (100 mL). The combined organic layers were washed with brine (150 mL), dried over Na₂SO₄, and evaporated. The residue was purified by silica gel column chromatography (*n*-hexane:ethyl acetate = 10:1) to give the title (13.9 g, 99% yield) as colorless oil. ¹H NMR (300 MHz, Methylene Chloride-*d*₂) δ 7.60 (s, 1H), 7.45 – 7.31 (m, 4H), 7.00 – 6.87 (m, 2H), 4.39 (s, 2H), 1.38 (s, 9H), 1.18 (s, 21H); ¹³C NMR (75 MHz, Methylene Chloride-*d*₂) δ 152.2, 149.3, 143.7, 140.9, 133.0, 128.9, 125.1, 124.5, 124.5, 117.1, 113.0, 107.4, 104.2, 96.9, 35.2, 31.6, 19.0, 11.8; HRMS (ESI+) *m/z*: calcd. for C₂₇H₄₀NSi⁺ (M+H)⁺: 406.2925; found: 406.2926.

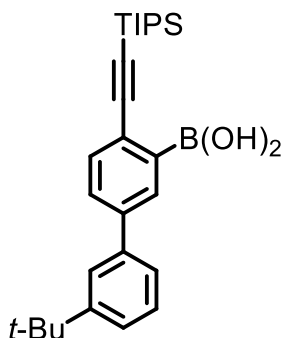
{(3-iodo-3'-*tert*-butyl-[1,1'-biphenyl]-4-yl)ethynyl}triisopropylsilane (**7-9**)



To a solution of 3'-*tert*-butyl-4-(triisopropylsilylethynyl)-[1,1'-biphenyl]-3-amine (**7-8**) (16.92 g, 41.17 mmol) in acetonitrile (600 mL) was added *p*-toluenesulfonic acid monohydrate (24.30 g, 127.7 mmol) at 0 °C. Then a solution of NaNO₂ (7.163g, 103.8 mmol) and KI (20.83 g, 125.5 mmol) in water (40 mL) was added dropwise. After stirring for 2 h at 0 °C, the reaction mixture was gradually warmed up to room temperature and stirred for another 18 h. After completion of the reaction, water (200 mL) and ethyl acetate (300 mL) were added. The organic phase was separated and the aqueous phase was extracted twice with ethyl acetate (200 mL). The combined organic layers were washed with brine (300 mL), dried over Na₂SO₄, and evaporated. The residue was purified by silica gel column chromatography (*n*-hexane:ethyl acetate = 10:1) to give the title compound (18.9 g, 88% yield) as colorless oil. ¹H NMR (300 MHz, Methylene Chloride-*d*₂) δ 8.11 (s, 1H), 7.60 – 7.53 (m, 3H), 7.46 – 7.34 (m, 3H), 1.38 (s, 9H), 1.20 (s, 21H); ¹³C NMR (75 MHz, Methylene Chloride-*d*₂) δ 152.5, 143.5, 139.0, 137.6, 133.6, 132.7, 129.1, 127.1, 125.7, 124.6, 124.5, 108.5, 101.5, 96.3, 35.2,

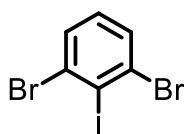
31.6, 19.0, 11.9; HRMS (ESI+) m/z : calcd. for $C_{18}H_{18}I^+$ (M+H-TIPS)⁺: 361.0448; found: 361.0507.

{3'-*tert*-butyl-4-(triisopropylsilylethynyl)-[1,1'-biphenyl]-3-yl}boronic acid (**7-10**)



To a solution of {(3-iodo-3'-*tert*-butyl-[1,1'-biphenyl]-4-yl)ethynyl}triisopropylsilane (**7-9**) (18.3 g, 35.4 mmol) in dry tetrahydrofuran (300 mL) was added *n*-BuLi (1.6 M in *n*-hexane, 26.6 mL, 43 mmol) dropwise at -78 °C. The mixture was stirred at this temperature for 30 min, and then triisopropyl borate (13.3 g, 70.8 mmol) was added in one portion. After stirring for 30 min the reaction mixture was warmed up to room temperature and stirred for another 1 h. The resulting mixture was hydrolyzed by addition of 2 N HCl (100 mL, 200 mmol) and stirred for 30 min. The crude product was extracted with ethyl acetate (200 mL) for three times. The combined organic layers were washed with brine (300 mL), dried over Na_2SO_4 , and evaporated. The residue was purified by silica gel column chromatography (*n*-hexane:ethyl acetate = 30:1 to 10:1) to give the title compound (13.2 g, 86% yield) as colorless oil. 1H NMR (300 MHz, Methylene Chloride- d_2) δ 8.26 – 8.18 (m, 1H), 7.73 – 7.59 (m, 3H), 7.48 – 7.35 (m, 3H), 6.02 (s, 2H), 1.38 (s, 9H), 1.22 – 1.14 (m, 21H); ^{13}C NMR (75 MHz, Methylene Chloride- d_2) δ 152.3, 142.0, 140.3, 134.5, 134.0, 129.8, 129.0, 126.0, 125.3, 124.7, 124.6, 108.8, 96.8, 35.2, 31.6, 18.8, 11.8; HRMS (ESI+) m/z : calcd. for $C_{27}H_{40}BO_2Si^+$ (M+H)⁺: 435.2885; found: 435.2867.

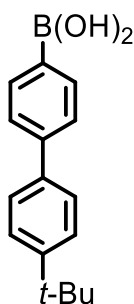
1,3-dibromo-2-iodobenzene (**7-12**)⁴



To a solution of diisopropyl amine (4.29 g, 42.4 mmol) in THF (50 mL) was added *n*-BuLi (1.6 N in *n*-hexane, 26.8 mL, 42 mmol) at -78 °C. After stirring for 15 min, to the resulting

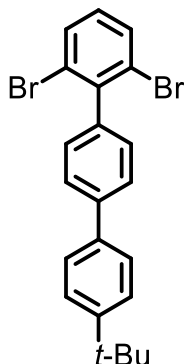
solution of LDA was added 1,3-dibromobenzene (10 g, 42 mmol) dropwise using a syringe. After stirring the mixture for another 2 h at $-78\text{ }^{\circ}\text{C}$, the reaction was quenched by slowly adding a solution of iodine (10.76 g, 42.39 mmol) in THF (20 mL). Excess iodine was quenched by addition of 10% aqueous solution of thiosulfate (100 mL) and the resulting mixture was extracted with diethyl ether (100 mL) for three times. The combined organic layers were washed with brine (100 mL), dried over Na_2SO_4 , and evaporated. The residue was recrystallized from ethanol/ H_2O = 10:1 to give the title compound (11.5 g, 76% yield) as colorless crystals. All analytical data was in agreement with the literature.⁴ Mp: $93.5 - 95.1\text{ }^{\circ}\text{C}$; ^1H NMR (300 MHz, Methylene Chloride- d_2) δ 7.58 (d, $J = 8.0$ Hz, 2H), 7.10 (t, $J = 8.0$ Hz, 1H); ^{13}C NMR (75 MHz, Methylene Chloride- d_2) δ 131.6, 130.9, 109.5.

(4'-*tert*-butyl-[1,1'-biphenyl]-4-yl)boronic acid (**S7-1**)



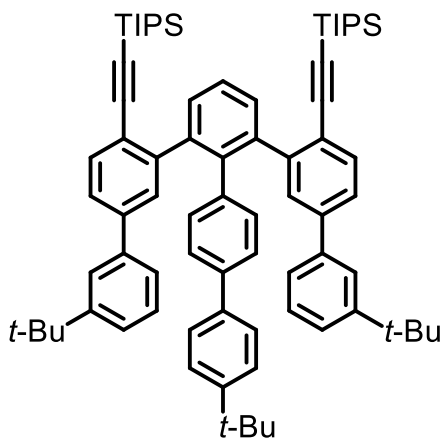
To a solution of 4-bromo-4'-*tert*-butyl-1,1'-biphenyl (12.0 g, 41.5 mmol) in THF (360 mL) was added *n*-BuLi (1.6 N in *n*-hexane, 28.5 mL, 46 mmol) at $-78\text{ }^{\circ}\text{C}$. The mixture was stirred for 2 h at this temperature, and then triisopropyl borate (10.8 g, 57.4 mmol) was added. After stirring for another 30 min, the mixture was gradually warmed up to room temperature over 3 h. The reaction was quenched by addition of 1 N HCl (120 mL, 120 mmol). After stirring for 30 min, the crude product was extracted with ethyl acetate (300 mL) for three times, and combined organic layers were washed with brine (300 mL), dried over Na_2SO_4 , and evaporated. The obtained residue was washed with *n*-hexane and filtered to give the title compound (10.1 g, 97% yield) as white solid. Mp: $271.7 - 272.0\text{ }^{\circ}\text{C}$; ^1H NMR (300 MHz, Methylene Chloride- d_2) δ 7.88 – 7.50 (m, 6H), 7.46 (d, $J = 7.8$ Hz, 2H), 1.34 (s, 9H); ^{13}C NMR (75 MHz, Methylene Chloride- d_2) δ 151.1, 143.1, 138.4, 134.6, 127.0, 126.5, 126.2, 118.7, 34.8, 31.4; HRMS (ESI+) m/z : calcd. for $\text{C}_{16}\text{H}_{19}\text{BO}_2^+$ (M)⁺: 254.1473; found: 254.1475.

2,6-dibromo-4''-*tert*-butyl-1,1':4',1''-terphenyl (**7-13**)



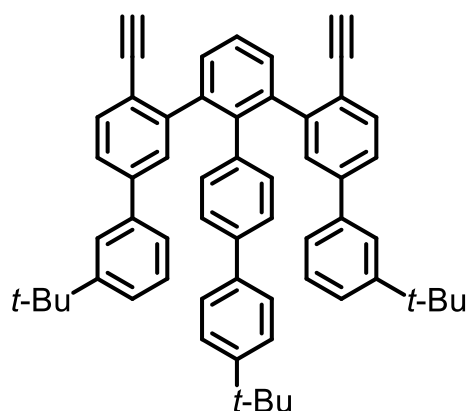
To a 250-mL Schelenk flask was added 1,3-dibromo-2-iodobenzene (**7-12**) (7.8 g, 22 mmol), (4'-*tert*-butyl-[1,1'-biphenyl]-4-yl)boronic acid (**S7-1**) (5.8 g, 23 mmol), Pd(PPh₃)₄ (1.25 g, 1.08 mmol), and Na₂CO₃ (9.16 g, 86.4 mmol). The flask was evacuated and backfilled with Ar for three times before a mixture of toluene/EtOH/H₂O (80 mL/20 mL/20 mL) was added. After bubbling with Ar flow for 20 min, the mixture was heated at 100 °C for 36 h. The reaction mixture was cooled down to room temperature and extracted twice with ethyl acetate (80 mL). The combined organic phases were washed with brine (150 mL), dried over Na₂SO₄, and evaporated. The residue was purified by silica gel column chromatography (*n*-hexane:ethyl acetate = 100:1) to give the title compound (6.75 g, 70% yield) as white solid. Mp: 162.3 – 163.9 °C; ¹H NMR (300 MHz, Methylene Chloride-*d*₂) δ 7.74 – 7.60 (m, 6H), 7.55 – 7.47 (m, 2H), 7.29 (d, *J* = 8.4 Hz, 2H), 7.12 (t, *J* = 8.0 Hz, 1H), 1.38 (s, 9H); ¹³C NMR (75 MHz, Methylene Chloride-*d*₂) δ 151.1, 143.1, 141.0, 140.3, 137.9, 132.4, 130.4, 130.1, 127.1, 127.0, 126.2, 124.9, 34.9, 31.5; HRMS (APPI+) *m/z*: calcd. for C₂₂H₂₀Br₂⁺ (M)⁺: 441.9926; found: 441.9928.

[{3,3''-di-*tert*-butyl-2''-(4'-*tert*-butyl-[1,1'-biphenyl]-4-yl)-[1,1':3',1'':3''',1''':3''',1''''-quinquephenyl]-4',6''-diyl}bis(ethyne-2,1-diyl)]bis(triisopropylsilane) (**7-14**)



To a 500-mL Schlenk flask was added 2,6-dibromo-4''-*tert*-butyl-1,1':4',1''-terphenyl (**7-13**) (6.268 g, 14.11 mmol), {3'-*tert*-butyl-4-(triisopropylsilylethynyl)-[1,1'-biphenyl]-3-yl}boronic acid (**7-10**) (13.42 g, 30.89 mmol), Pd(PPh₃)₄ (1.613 g, 1.396 mmol), and K₂CO₃ (11.58 g, 83.76 mmol). The flask was evacuated and backfilled with Ar for three times before addition of degassed 1,4-dioxane (300 mL) and water (75 mL). After heating at 100 °C for 24 h, the mixture was cooled down to room temperature and ethyl acetate was added (100 mL). The organic phase was separated and the aqueous solution was extracted twice with ethyl acetate (100 mL). The combined organic layers were washed with brine (150 mL), dried over Na₂SO₄, and evaporated. The residue was purified by silica gel column chromatography (*n*-hexane:ethyl acetate = 50:1) to give the title compound (12.79 g, 86% yield) as white solid. Mp: 109.2 – 110.4 °C; ¹H NMR (300 MHz, Methylene Chloride-*d*₂) δ 7.58 (d, *J* = 8.1 Hz, 2H), 7.51 – 7.46 (m, 2H), 7.38 (s, 1H), 7.37 – 7.16 (m, 16H), 7.09 (dt, *J* = 7.2, 1.5 Hz, 2H), 7.04 (d, *J* = 1.7 Hz, 2H), 1.27 – 1.22 (m, 27H), 1.03 (s, 42H); ¹³C NMR (75 MHz, Methylene Chloride-*d*₂) δ 152.1, 150.5, 146.1, 141.0, 140.3, 139.8, 139.4, 138.6, 137.8, 132.8, 131.3, 130.8, 129.9, 128.7, 126.8, 126.5, 125.9, 125.8, 125.4, 124.9, 124.4, 124.3, 122.6, 107.0, 95.2, 35.0, 34.7, 31.5, 31.4, 18.9, 11.7; HRMS (MALDI⁺) *m/z*: calcd. for C₇₆H₉₄Si₂⁺ (M)⁺: 1062.6889; found: 1062.6884.

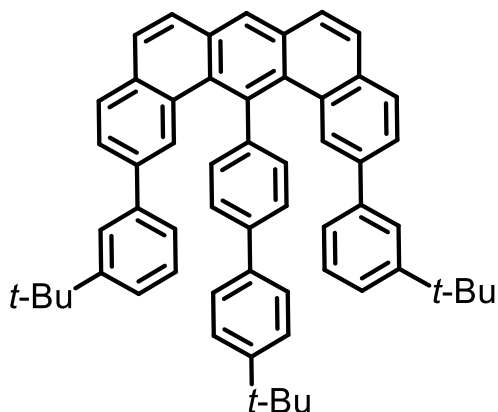
4'-ethynyl-3''-(4-ethynyl-3'-*tert*-butyl-[1,1'-biphenyl]-3-yl)-3-*tert*-butyl-4''''-*tert*-butyl-1,1':3',1'':2'',1''':4''',1''''-quinquephenyl (**S7-2**)



To a solution of [[3,3''''-di-*tert*-butyl-2''-(4'-*tert*-butyl-[1,1'-biphenyl]-4-yl)-[1,1':3',1'':3'',1''':3''',1''''-quinquephenyl]-4',6'''-diyl]bis(ethyne-2,1-diyl)]bis(triisopropylsilane) (**7-14**) (12.79 g, 12.02 mmol) in dry THF (300 mL) was added tetra-*n*-butylammonium fluoride (1 N in dry THF, 16 mL, 16 mmol) at room temperature. After stirring for 2 h, methanol (50 mL) was added to quench the reaction. The suspension was concentrated to ca. 50 mL and the precipitates were collected by filtration and washed with methanol to give the

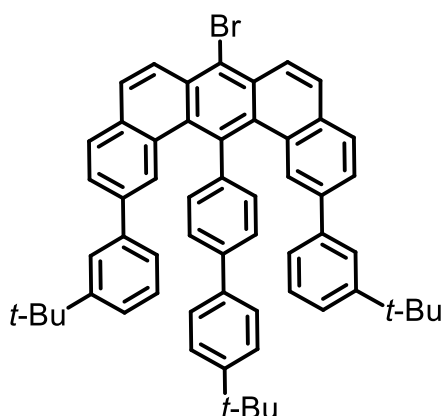
title compound (9.010 g, 100% yield) as white solid. Mp: 251.2 – 251.9 °C; ^1H NMR (300 MHz, Methylene Chloride- d_2) δ 7.78 – 6.87 (m, 25H), 3.19 (s, 2H), 1.27 (s, 27H); ^{13}C NMR (75 MHz, Methylene Chloride- d_2) δ 152.2, 150.6, 141.7, 140.8, 140.2, 138.8, 138.6, 137.7, 133.5, 132.1, 128.8, 126.6, 125.9, 125.8, 125.1, 124.6, 124.4, 121.0, 118.6, 83.6, 81.2, 35.0, 34.7, 31.5, 31.4; MS (MALDI+) m/z : calcd. for $\text{C}_{58}\text{H}_{54}^+$ (M) $^+$: 750.42; found: 750.40.

14-(4'-*tert*-butyl-[1,1'-biphenyl]-4-yl)-2,12-bis(3-*tert*-butylphenyl)benzo[*m*]tetraphene (**7-15**)



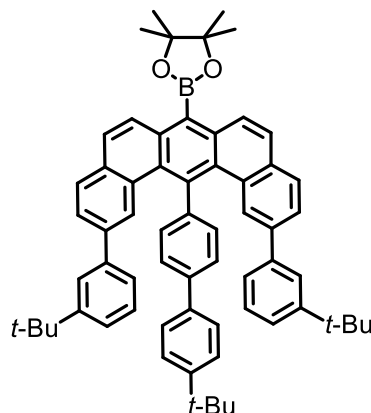
To a 500-mL Schlenk flask was added 4'-ethynyl-3''-(4-ethynyl-3'-*tert*-butyl-[1,1'-biphenyl]-3-yl)-3-*tert*-butyl-4''''-*tert*-butyl-1,1':3',1'':2'',1''':4''',1''''-quinquephenyl (**S7-2**) (8.0 g, 11 mmol) and PtCl_2 (567 mg, 2.13 mmol). The flask was dried under vacuum for 2 h at room temperature before toluene (400 mL) was added. After heating at 80 °C for 24 h, the mixture was cooled down to room temperature and the solvent was evaporated. The residue was purified by silica gel column chromatography (*n*-hexane:ethyl acetate = 50:1) to give the title compound (5.2 g, 65% yield) as yellow solid. Mp: 304.1 – 305.6 °C; ^1H NMR (300 MHz, Methylene Chloride- d_2) δ 8.44 (s, 1H), 7.95 (s, 1H), 7.92 (d, $J = 3.7$ Hz, 2H), 7.87 (d, $J = 5.6$ Hz, 2H), 7.85 – 7.78 (m, 3H), 7.77 (s, 2H), 7.72 (dd, $J = 8.1, 1.6$ Hz, 2H), 7.67 (d, $J = 8.2$ Hz, 2H), 7.57 – 7.50 (m, 2H), 7.45 – 7.36 (m, 4H), 7.21 (dt, $J = 7.8, 1.0$ Hz, 2H), 6.99 (t, $J = 7.7$ Hz, 2H), 6.86 (dt, $J = 7.6, 1.2$ Hz, 2H), 1.48 (s, 10H), 1.25 (s, 19H); ^{13}C NMR (75 MHz, Methylene Chloride- d_2) δ 151.7, 151.1, 144.5, 142.3, 141.3, 138.9, 138.2, 138.0, 133.8, 132.3, 132.2, 131.8, 130.1, 129.1, 128.9, 128.7, 128.7, 128.3, 128.2, 127.5, 127.3, 126.0, 125.9, 125.0, 124.8, 124.5, 35.0, 34.9, 31.6, 31.4; MS (MALDI+) m/z : calcd. for $\text{C}_{58}\text{H}_{54}^+$ (M) $^+$: 750.42; found: 750.40.

7-bromo-14-(4'-*tert*-butyl-[1,1'-biphenyl]-4-yl)-2,12-bis(3-*tert*-butylphenyl)benzo[*m*]tetraphene (**7-16**)

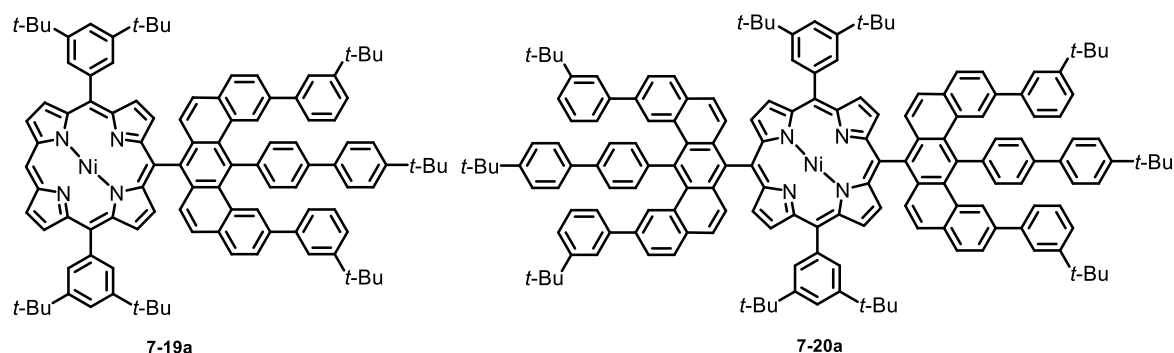


To a solution of 14-(4'-*tert*-butyl-[1,1'-biphenyl]-4-yl)-2,12-bis(3-*tert*-butylphenyl)benzo[*m*]tetraphene (**7-15**) (4.0 g, 5.3 mmol) in dry dichloromethane (150 mL) was added bromine (1.024 g, 6.408 mmol) at room temperature. After stirring for 1 h, saturated aqueous solution of Na₂S₂O₃ (50 mL) was added to quench the excess bromine. The organic phase was separated and the aqueous phase was extracted with dichloromethane (50 mL) for three times. The combined organic phases were washed with brine (100 mL), dried over Na₂SO₄, and evaporated. The residue was purified by silica gel column chromatography (*n*-hexane:ethyl acetate = 4:1) to give the title compound (4.0 g, 91% yield) as yellow solid. Mp: 306.2 – 307.0 °C; ¹H NMR (300 MHz, Methylene Chloride-*d*₂) δ 8.40 (d, *J* = 9.0 Hz, 2H), 7.90 (d, *J* = 7.9 Hz, 2H), 7.83 (d, *J* = 9.2 Hz, 2H), 7.77 – 7.64 (m, 6H), 7.54 (d, *J* = 7.8 Hz, 2H), 7.49 (d, *J* = 7.9 Hz, 2H), 7.40 – 7.29 (m, 4H), 7.19 (d, *J* = 7.7 Hz, 2H), 6.98 (t, *J* = 7.7 Hz, 2H), 6.77 (d, *J* = 7.5 Hz, 2H), 1.43 (s, 9H), 1.21 (s, 18H); ¹³C NMR (75 MHz, Methylene Chloride-*d*₂) δ 151.8, 151.1, 143.9, 142.3, 141.1, 138.2, 138.1, 138.0, 133.3, 132.7, 131.3, 129.9, 129.8, 129.6, 129.4, 128.8, 128.7, 127.4, 126.3, 126.3, 126.0, 125.0, 124.7, 124.6, 123.8, 34.9, 34.9, 31.6, 31.4; HRMS (MALDI+) *m/z*: calcd. for C₅₈H₅₃Br⁺ (M)⁺: 828.3325; found: 828.3311.

2-{14-(4'-*tert*-butyl-[1,1'-biphenyl]-4-yl)-2,12-bis(3-*tert*-butylphenyl)benzo[*m*]tetraphen-7-yl}-4,4,5,5-tetramethyl-1,3,2-dioxaborolane (**7-17**)



To a 250-mL Schlenk flask was added 7-bromo-14-(4'-*tert*-butyl-[1,1'-biphenyl]-4-yl)-2,12-bis(3-*tert*-butylphenyl)benzo[*m*]tetraphene (**7-16**) (3.3 g, 4.0 mmol), bis(pinacolato)diboron (2.02 g, 7.95 mmol), Pd(dppf)Cl₂·CH₂Cl₂ (291 mg, 0.398 mmol), and KOAc (2.34 g, 23.9 mmol). The flask was evacuated and backfilled with Ar for three times before degassed *N,N*-dimethylformamide (150 mL) was added. The mixture was heated at 80 °C for 24 h and cooled down to room temperature after confirming the completion of the reaction. Ethyl acetate (100 mL) and water (100 mL) were added and the organic phase was separated. The aqueous phase was extracted twice with ethyl acetate. The combined organic layers were washed with brine (150 mL), dried over Na₂SO₄, and evaporated. The residue was purified by silica gel column chromatography (*n*-hexane:ethyl acetate = 4:1 to 2:1) to give the title compound (2.9 g, 83% yield) as yellow solid. Mp: 275.8 – 277.4 °C; ¹H NMR (250 MHz, Methylene Chloride-*d*₂) δ 8.08 (d, *J* = 9.0 Hz, 2H), 7.88 (d, *J* = 8.1 Hz, 2H), 7.76 (dd, *J* = 8.6, 3.6 Hz, 4H), 7.67 (dd, *J* = 10.9, 2.9 Hz, 4H), 7.58 (d, *J* = 8.2 Hz, 2H), 7.50 (d, *J* = 8.4 Hz, 2H), 7.39 (d, *J* = 8.4 Hz, 2H), 7.35 (s, 2H), 7.18 (d, *J* = 7.9 Hz, 2H), 6.97 (t, *J* = 7.7 Hz, 2H), 6.78 (d, *J* = 7.7 Hz, 2H), 1.61 (s, 12H), 1.43 (s, 9H), 1.21 (s, 18H); ¹³C NMR (63 MHz, Methylene Chloride-*d*₂) δ 151.6, 151.0, 144.6, 142.0, 141.2, 139.7, 138.1, 137.6, 135.5, 133.3, 132.6, 131.8, 129.8, 129.3, 128.7, 128.5, 128.0, 127.9, 127.4, 126.9, 126.0, 125.7, 125.0, 124.7, 124.4, 85.2, 34.9, 34.9, 31.6, 31.4, 25.4; HRMS (MALDI⁺) *m/z*: calcd. for C₆₄H₆₅BO₂⁺ (M)⁺: 876.5072; found: 876.5054.

(3,5-di-*tert*-butylphenyl)porphyrin-benzo[*m*]tetraphene conjugates **7-19a** and **7-20a**

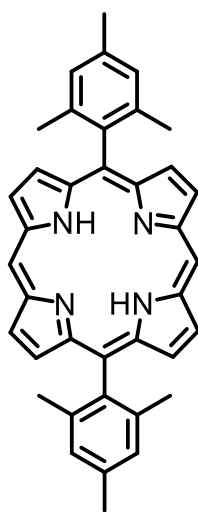
To a 50-mL Schlenk tube was added 5,15-dibromo-10,20-di(3,5-di-*tert*-butylphenyl)porphyrin (Ni)⁵ (**7-18a**) (113 mg, 0.125 mmol), 2-{14-(4'-*tert*-butyl-[1,1'-biphenyl]-4-yl)-2,12-bis(3-*tert*-butylphenyl)benzo[*m*]tetraphen-7-yl}-4,4,5,5-tetramethyl-1,3,2-dioxaborolane (**7-17**) (279 mg, 0.318 mmol), Pd(PPh₃)₄ (64 mg, 0.055 mmol), and K₂CO₃ (276mg, 0.239 mmol). A mixture of toluene/ *N,N*-dimethylformamide (10 mL/10 mL) was added after three cycles of evacuation and backfilling with Ar. The resulting mixture was heated at 110 °C for 24 h, and then cooled down to room temperature and diluted with ethyl acetate (50 mL). The red solution was washed with brine (30 mL), dried over Na₂SO₄, and evaporated. The residue was recrystallized from methanol and transferred into a 25-mL Schlenk tube. To the tube was added Pd(PPh₃)₄ (34 mg, 0.029 mmol), trimethylamine (100 μL), formic acid (100 μL), and toluene (10 mL). The mixture was heated at 100 °C for 2 h under Ar atmosphere, and then cooled down to room temperature. The residue was purified by silica gel column chromatography (*n*-hexane:dichloromethane = 5:1 to 4:1) and then preparative gel permeation column chromatography (Bio-Beads S-X1 support, Bio-Rad Laboratories, eluent: toluene) to give **7-19a** (95 mg, 51% yield) and **7-20a** (31 mg, 11% yield) both as red solid.

7-19a: Mp: >400 °C (decomposition); ¹H NMR (700 MHz, Methylene Chloride-*d*₂) δ 10.03 (s, 1H), 9.28 (d, *J* = 3.6 Hz, 2H), 9.03 (d, *J* = 4.6 Hz, 2H), 8.81 (d, *J* = 4.6 Hz, 2H), 8.54 (d, *J* = 4.6 Hz, 2H), 8.04 (s, 2H), 8.00 (s, 4H), 7.96 (s, 4H), 7.82 (s, 2H), 7.77 (d, *J* = 7.8 Hz, 2H), 7.71 (d, *J* = 7.7 Hz, 2H), 7.59 (d, *J* = 7.9 Hz, 2H), 7.50 (d, *J* = 7.9 Hz, 2H), 7.44 (s, 2H), 7.27 (d, *J* = 8.9 Hz, 4H), 7.09 (t, *J* = 7.6 Hz, 2H), 6.96 (d, *J* = 7.1 Hz, 2H), 6.86 (d, *J* = 9.3 Hz, 2H), 1.52 (s, 36H), 1.29 (s, 18H); ¹³C NMR (176 MHz, CD₂Cl₂) δ 151.3, 150.7, 149.1, 144.3, 143.9, 143.5, 143.3, 143.0, 141.9, 140.92, 139.9, 138.9, 137.8, 135.2, 134.5, 133.0, 132.8, 132.7, 132.5, 132.1, 131.9, 131.2, 129.7, 129.3, 128.9, 128.4, 127.7, 127.4, 127.1, 126.4,

125.7, 124.7, 124.4, 124.1, 121.4, 120.4, 115.4, 105.2, 31.4, 31.2, 31.0; HRMS (MALDI+) m/z : calcd. for $C_{106}H_{104}N_4Ni^+$ (M)⁺: 1490.7609; found: 1490.7657.

7-20a: Mp: >400 °C (decomposition); ¹H NMR (700 MHz, 1,1,2,2-Tetrachloroethane-*d*₂) δ 8.80 (d, $J = 4.7$ Hz, 4H), 8.51 (d, $J = 4.7$ Hz, 4H), 8.03 (s, 4H), 7.97 (s, 8H), 7.91 (s, 4H), 7.80 (d, $J = 7.4$ Hz, 4H), 7.73 (d, $J = 6.6$ Hz, 4H), 7.65 (s, 2H), 7.54 (d, $J = 5.6$ Hz, 8H), 7.43 (s, 4H), 7.34 (d, $J = 8.7$ Hz, 4H), 7.25 (d, $J = 6.8$ Hz, 4H), 7.13 – 7.06 (m, 4H), 7.01 (d, $J = 8.7$ Hz, 4H), 6.94 (d, $J = 6.0$ Hz, 4H), 1.49 (s, 18H), 1.43 (s, 36H), 1.27 (s, 36H); ¹³C NMR (176 MHz, Tetrachloroethane-*d*₂) δ 151.1, 150.5, 148.9, 144.0, 143.8, 142.9, 141.6, 140.6, 139.1, 138.7, 137.3, 137.2, 134.8, 134.3, 133.4, 132.4, 132.4, 131.1, 129.5, 129.2, 128.8, 128.4, 127.5, 127.4, 126.9, 126.6, 125.6, 125.5, 124.6, 124.4, 124.1, 121.1, 120.6, 119.9, 115.2, 34.7, 34.5, 34.4, 31.5, 31.4, 31.2; HRMS (MALDI+) m/z : calcd. for $C_{164}H_{156}N_4Ni^+$ (M)⁺: 2239.1678; found: 2239.1594.

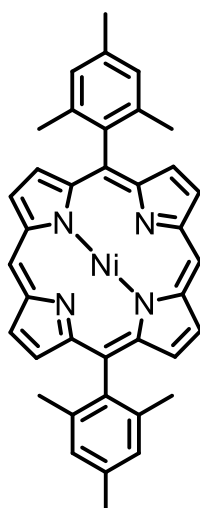
5,15-dimesitylporphyrin (**S7-3**)⁶



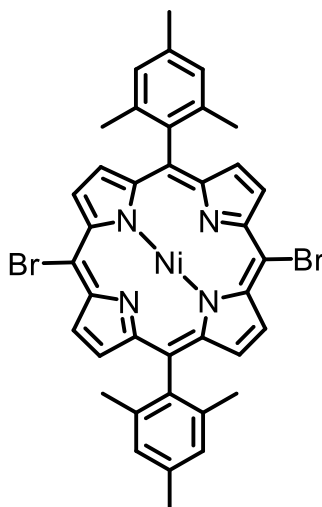
A solution of dipyrromethane (890 mg, 6.09 mmol) and mesitylaldehyde (889 mg, 6.00 mmol) in trichloromethane (600 mL) containing ethanol (4.5 mL) was degassed by bubbling with Ar for 10 min before $BF_3 \cdot OEt_2$ (0.5 mL) was added. The flask was shielded from light using aluminum foil and the solution was stirred under Ar atmosphere for 3 h. 2,3-Dichloro-5,6-dicyano-1,4-benzoquinone (2.04 g, 8.99 mmol) was then added and the mixture was stirred at room temperature for 30 min. The mixture was subsequently neutralized with triethyl amine (8 mL) and passed through a pad of silica gel (eluent: dichloromethane). The solution was concentrated in vacuo and the residue was purified by silica gel column chromatography (*n*-hexane:dichloromethane = 1:1) to give the title compound (410.7 mg, 25% yield) as purple

solid. All analytical data was in agreement with the literature.⁶ ^1H NMR (300 MHz, Methylene Chloride- d_2) δ 10.26 (s, 2H), 9.37 (d, $J = 4.6$ Hz, 4H), 8.87 (d, $J = 4.6$ Hz, 4H), 7.35 (s, 4H), 2.66 (s, 7H), 1.84 (s, 13H), -3.13 (s, 2H); ^{13}C NMR (75 MHz, Methylene Chloride- d_2) δ 147.3, 145.8, 139.8, 138.4, 137.9, 132.3, 130.4, 128.2, 117.8, 104.9, 21.8, 21.6.

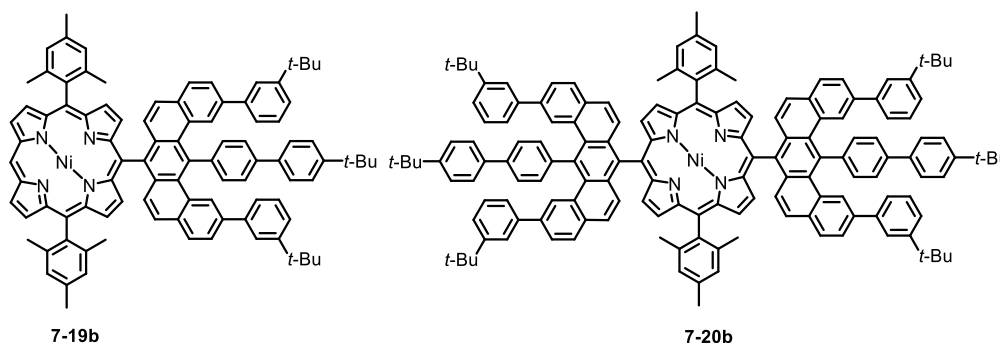
5,15-dimesitylporphyrin (Ni) (**S7-4**)⁷



A solution of 5,15-dimesitylporphyrin (**S7-3**) (200 mg, 0.366 mmol) and $\text{Ni}(\text{OAc})_2 \cdot 4\text{H}_2\text{O}$ (273.1 mg, 1.098 mmol) in dry *N,N*-dimethylformamide (20 mL) was heated at 140 °C for 2 h. After completion of the reaction, the mixture was cooled down to room temperature. Methanol (50 mL) was added and the suspension was stirred overnight. The precipitates were filtered and washed with methanol (20 mL) to give the title compound (206.7 mg, 94% yield) as purple solid. All analytical data was in agreement with literature.⁷ Mp: 375.0 – 375.8 °C; ^1H NMR (300 MHz, Methylene Chloride- d_2) δ 9.93 (s, 2H), 9.18 (d, $J = 4.7$ Hz, 4H), 8.77 (d, $J = 4.7$ Hz, 4H), 7.29 (s, 4H), 2.62 (s, 6H), 1.79 (s, 12H); ^{13}C NMR (75 MHz, Methylene Chloride- d_2) δ 143.2, 139.4, 138.4, 137.6, 132.8, 131.6, 128.2, 117.2, 105.1, 21.6, 21.5.

5,15-dibromo-10,20-dimesitylporphyrin (Ni) (**7-18b**)

To a solution of 5,15-dimesitylporphyrin (Ni) (**S7-4**) (101.9 mg, 0.1689 mmol) in dichloromethane (50 mL) and methanol (10 mL) was added *N*-bromosuccinimide (NBS) (68.0 mg, 0.382 mmol). After stirring for 20 min at room temperature, acetone (5 mL) was added to quench the reaction, and then the solvents were evaporated. The residue was dissolved in dichloromethane (100 mL) and passed through a pad of silica gel (eluent: dichloromethane). After concentration in vacuo, the residue was recrystallized from dichloromethane and methanol to give the title compound (123.7 mg, 96% yield) as purple solid. Mp: >400 °C (decomposition); ^1H NMR (300 MHz, 1,1,2,2-Tetrachloroethane- d_2) δ 9.45 (dd, $J = 5.0, 1.1$ Hz, 4H), 8.62 (dd, $J = 5.0, 1.1$ Hz, 4H), 7.24 (s, 4H), 2.60 (s, 6H), 1.80 (s, 12H); ^{13}C NMR (75 MHz, 1,1,2,2-tetrachloroethane- d_2) δ 143.1, 142.7, 138.7, 138.0, 136.1, 133.7, 132.8, 127.8, 118.7, 102.4, 21.4, 21.3; HRMS (MALDI+) m/z : calcd. for $\text{C}_{38}\text{H}_{30}\text{Br}_2\text{N}_4\text{Ni}^+$ (M) $^+$: 758.0185; found: 758.0179.

5,15-dimesitylporphyrin-benzo[*m*]tetraphene conjugates **7-19b** and **7-20b**

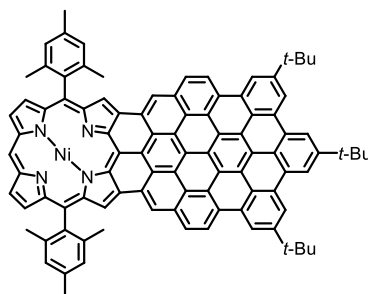
To a 50-mL Schlenk tube was added 5,15-dibromo-10,20-dimesitylporphyrin (Ni) (**7-18b**) (50 mg, 0.074 mmol), 2-{14-(4'-*tert*-butyl-[1,1'-biphenyl]-4-yl)-2,12-bis(3-*tert*-butylphenyl)benzo[*m*]tetraphen-7-yl}-4,4,5,5-tetramethyl-1,3,2-dioxaborolane (**7-17**) (194 mg, 0.221 mmol), Pd(PPh₃)₄ (17 mg, 0.015 mmol), and K₂CO₃ (51 mg, 0.37 mmol). The reaction tube was evacuated and backfilled with Ar for three times before toluene/*N,N*-dimethylformamide (10 mL/10 mL) was added. The suspension was heated at 110 °C for 12 h, and then another portion of Pd(PPh₃)₄ (17 mg, 0.015 mmol) was added. After stirring at 110 °C for another 24 h, the mixture was cooled down to room temperature and diluted with ethyl acetate (50 mL). The organic phase was washed with brine (30 mL), dried over Na₂SO₄, and evaporated. The residue was recrystallized from methanol and added into a 25 mL Schlenk tube. To the tube was added Pd(PPh₃)₄ (17 mg, 0.015 mmol), trimethylamine (50 μL), formic acid (50 μL), and toluene (10 mL). The mixture was heated at 100 °C for 2 h under Ar atmosphere, and then cooled down to room temperature. The residue was purified by silica gel column chromatography (*n*-hexane/dichloromethane = 5:1 to 4:1) to give **7-19b** (53 mg, 55% yield) and **7-20b** (26 mg, 17% yield) both as red solid.

7-19b: Mp: 281.0 – 282.7 °C; ¹H NMR (500 MHz, Methylene Chloride-*d*₂) δ 9.90 (s, 1H), 9.18 (d, *J* = 4.7 Hz, 2H), 8.74 (d, *J* = 4.7 Hz, 2H), 8.52 (d, *J* = 4.9 Hz, 2H), 8.43 (d, *J* = 4.9 Hz, 2H), 7.99 (s, 2H), 7.90 (s, 4H), 7.71 (d, *J* = 8.0 Hz, 2H), 7.65 (d, *J* = 8.0 Hz, 2H), 7.54 (d, *J* = 8.2 Hz, 2H), 7.45 (d, *J* = 8.2 Hz, 2H), 7.40 (s, 2H), 7.25 – 7.17 (m, 8H), 7.05 (t, *J* = 7.7 Hz, 2H), 6.92 (d, *J* = 7.6 Hz, 2H), 6.86 (d, *J* = 9.2 Hz, 2H), 2.55 (s, 6H), 1.82 (s, 12H), 1.47 (s, 9H), 1.25 (s, 18H); ¹³C NMR (126 MHz, Methylene Chloride-*d*₂) δ 151.7, 151.1, 144.8, 144.4, 143.4, 143.3, 143.1, 142.3, 141.3, 139.3, 138.3, 138.2, 138.1, 137.4, 135.6, 135.0, 133.1, 133.0, 132.9, 132.0, 131.8, 131.6, 130.1, 129.7, 128.8, 128.2, 128.0, 127.7, 127.5, 126.9, 126.1, 125.1, 124.8, 124.5, 117.7, 115.5, 105.2, 35.0, 31.6, 31.5, 30.1, 21.5; MS (MALDI+) *m/z*: calcd. for C₉₆H₈₄N₄Ni⁺ (M)⁺: 1350.60; found: 1350.56; UV-*vis*-NIR (THF): λ_{max} (ε) = 412 nm (2.65 × 10⁵ M⁻¹cm⁻¹), 522 nm (2.65 × 10⁴ M⁻¹cm⁻¹).

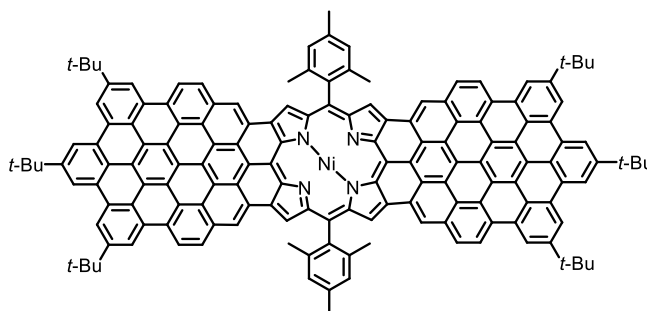
7-20b: Mp: 329.5 – 330.6 °C; ¹H NMR (500 MHz, Methylene Chloride-*d*₂) δ 8.51 (d, *J* = 4.9 Hz, 4H), 8.44 (d, *J* = 4.9 Hz, 4H), 8.01 (s, 4H), 7.92 (s, 8H), 7.77 (d, *J* = 8.0 Hz, 4H), 7.69 (dd, *J* = 8.0, 1.4 Hz, 4H), 7.55 (d, *J* = 8.2 Hz, 4H), 7.46 (d, *J* = 8.1 Hz, 4H), 7.41 (s, 4H), 7.32 (d, *J* = 9.2 Hz, 4H), 7.24 (d, *J* = 7.9 Hz, 4H), 7.17 (s, 4H), 7.06 (t, *J* = 5.8 Hz, 4H), 6.98 (d, *J* = 9.2 Hz, 4H), 6.93 (d, *J* = 7.7 Hz, 4H), 2.49 (s, 6H), 1.87 (s, 12H), 1.48 (s, 18H), 1.26 (s, 36H); ¹³C NMR (126 MHz, Methylene Chloride-*d*₂) δ 151.8, 151.1, 144.8, 144.7, 143.3, 142.3, 141.3, 139.2, 138.3, 138.2, 138.2, 137.2, 135.3, 134.9, 133.1, 132.9, 132.2, 131.6, 130.1, 129.7,

128.8, 128.1, 128.1, 127.8, 127.5, 126.1, 125.1, 124.8, 124.6, 118.3, 115.6, 35.0, 31.6, 31.5, 21.6, 21.5; MS (MALDI+) m/z : calcd. for $C_{154}H_{136}N_4Ni^+$ (M)⁺: 2099.01; found: 2098.90 UV-*vis*-NIR (THF): λ_{max} (\mathcal{E}) = 422 nm ($3.01 \times 10^5 M^{-1}cm^{-1}$), 530 nm ($2.65 \times 10^4 M^{-1}cm^{-1}$).

triply fused porphyrin-nanographene conjugates **7-1** and **7-2**



To a solution of **7-19b** (6.0 mg, 4.6 μ mol) and DDQ (12.6 mg, 55.7 μ mol) in dry degassed dichloromethane (20 mL) was added triflic acid (0.3 mL). After stirring at room temperature for 9 h, triethylamine (0.4 mL) was added via a syringe to quench the reaction. Methanol (30 mL) was added and the precipitates were filtered and washed with a mixture of dichloromethane/methanol (1:1) to give the title compound (5.4 mg, 90% yield) as purple solid. HRMS (MALDI+) m/z : calcd. for $C_{96}H_{68}N_4Ni^+$ (M)⁺: 1334.4792; found: 1334.4831 (error = 3 ppm); UV-*vis*-NIR (THF): λ_{max} (\mathcal{E}) = 866 nm ($9.30 \times 10^4 M^{-1}cm^{-1}$), 776 nm ($5.80 \times 10^4 M^{-1}cm^{-1}$).



To a solution of **7-20b** (3.0 mg, 1.5 μ mol) and DDQ (8.2 mg, 3.6 μ mol) in dry degassed dichloromethane (10 mL) was added triflic acid (0.1 mL). The mixture was stirred at room temperature for 9 h. Triethylamine (0.4 mL) was added via a syringe to quench the reaction. After addition of methanol (20 mL), the title compound (2.9 mg, 97% yield) was obtained as green solid by filtration and washed subsequently with dichloromethane and tetrahydrofuran. HRMS (MALDI+) m/z : calcd. for $C_{154}H_{104}N_4Ni^+$ (M)⁺: 2066.7609; found: 2066.7614 (error = 2 ppm); UV-*vis*-NIR (THF): λ_{max} (\mathcal{E}) = 1176 nm ($9.50 \times 10^4 M^{-1}cm^{-1}$), 997 nm ($3.11 \times 10^4 M^{-1}cm^{-1}$).

NMR and MS spectra

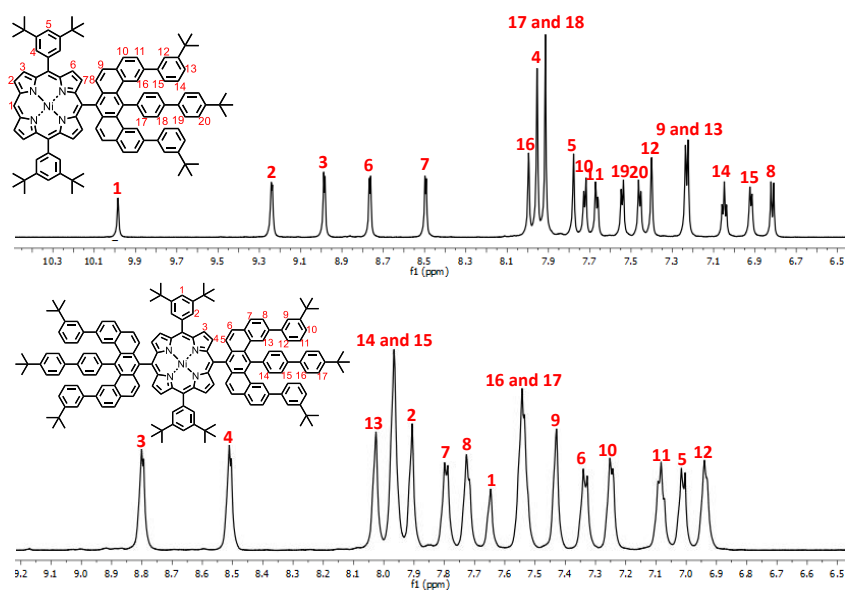


Figure S7-1. Magnified aromatic regions of the ¹H NMR spectra of **7-19a** recorded in CD₂Cl₂ and **7-20a** in C₂D₂Cl₄ at room temperature (700 MHz).

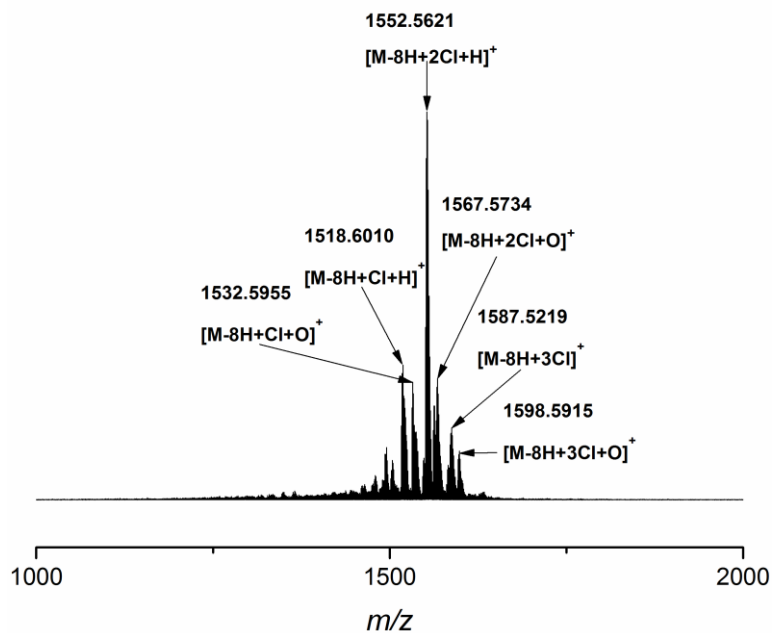


Figure S7-2. MALDI-TOF mass spectrum of a crude mixture after the Scholl reaction of **7-19a** using FeCl₃ at 0 °C for 2 h, showing serious chlorination of the product.

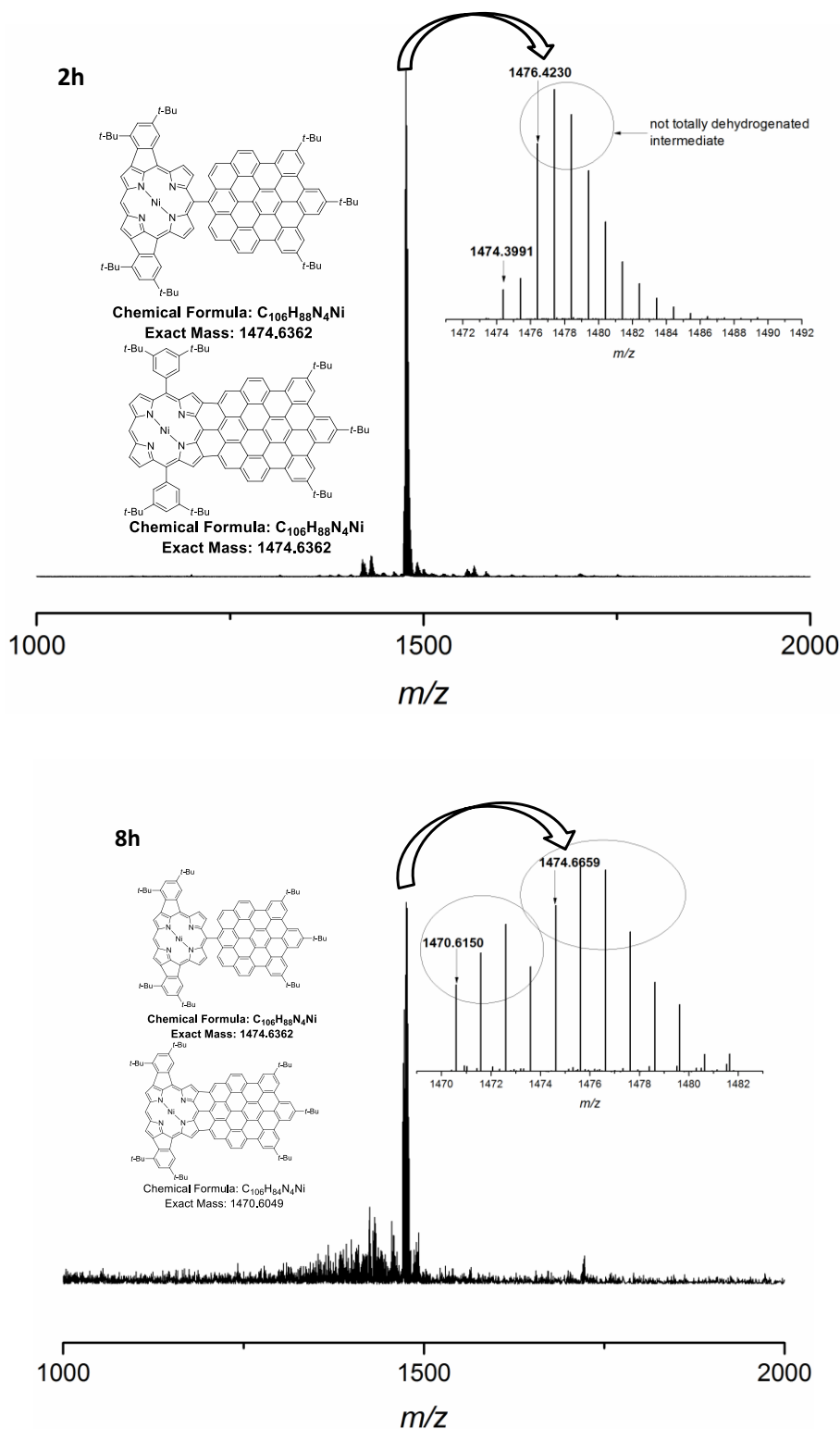


Figure S7-3. MALDI-TOF mass spectra of a crude mixture after the Scholl reaction of **7-19a** using 2,3-dichloro-5,6-dicyano-1,4-benzoquinone with catalytic amount (1%, v/v) of triflic acid (top: reaction time = 2 h; bottom: reaction time = 8 h).

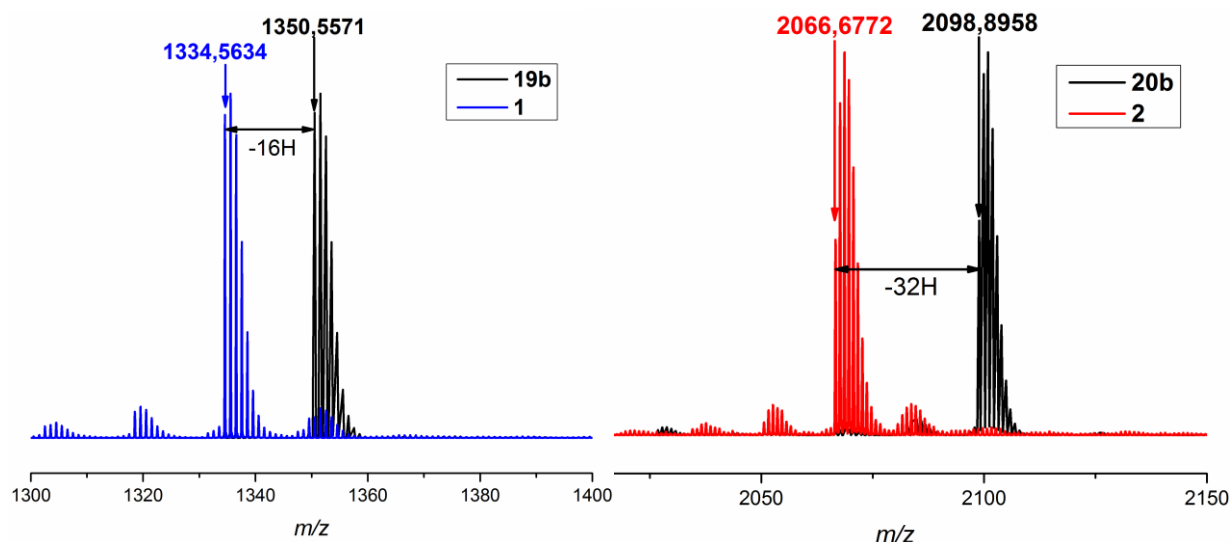


Figure S7-4. MALDI-TOF mass spectra of a crude mixture after the Scholl reaction of **7-19b** and **7-20b** using DDQ with catalytic amount of triflic acid (1%, v/v), which formed 8 and 16 C-C bonds by losing 16H and 32H, respectively.

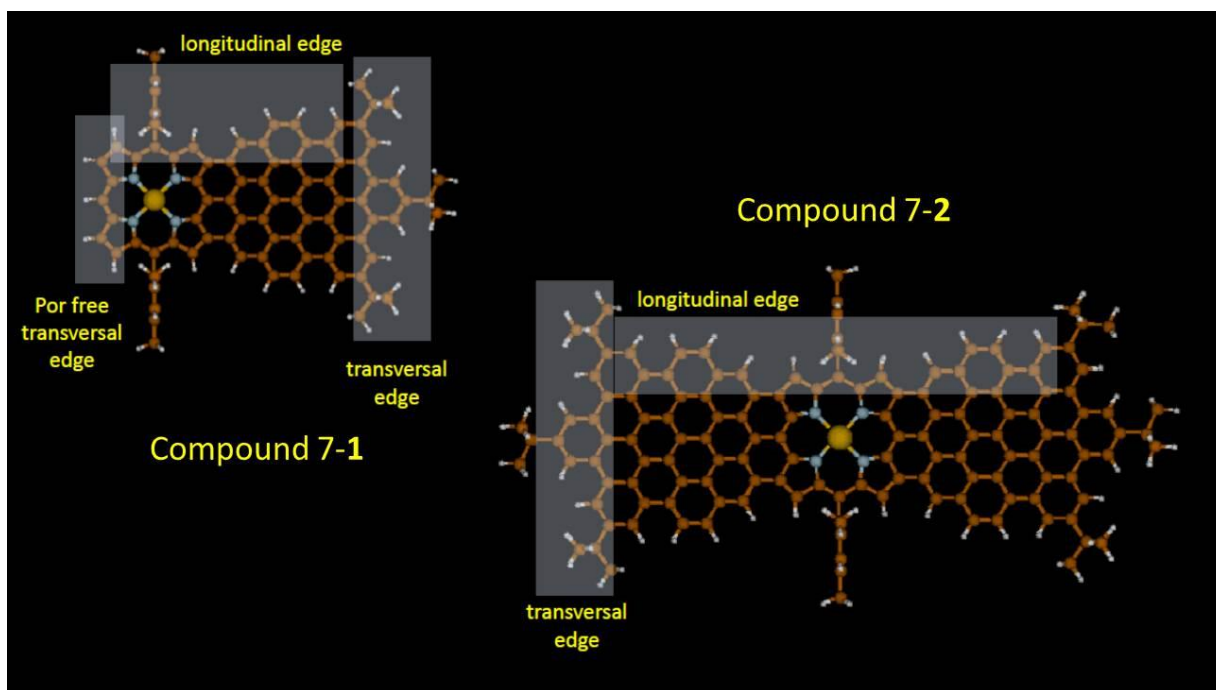
IR and Raman spectroscopy

The micro-FT-IR spectra of powder samples of **7-1** and **7-2** were recorded in transmission mode through a diamond anvil cell. The micro-FT-Raman spectra were recorded on the same samples used for FT-IR characterization. In Figure 7-2b of the main text, we compare the experimental IR spectra of **7-1** and **7-2** vs. the simulated spectra obtained from DFT calculations; the band assignments are reported in Table S1 and Figure S5 below.

Table S7-1. List of the position of the main IR bands (cm^{-1}) observed in the FT-IR spectra of solid samples of **7-1** and **7-2**. Band assignments are based on DFT calculations (see Figure S7-5 below).

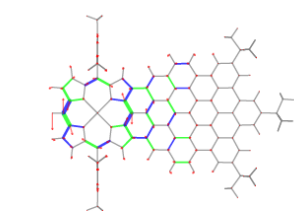
7-1	7-2	assignment	label
1634	-	antisymmetric CC stretching at porphyrin free transversal edge	1
1606	1605	collective ring stretching at the HBC transversal edge	2
1532	1534	collective CC stretching over HBC and Porphyrin	3
1389	1388	collective CC stretching over HBC and porphyrin;	4

		ring deformation	
1363	1363	collective CC stretching over HBC and porphyrin; ring deformation	5
1253	1256	aromatic CH in-plane bending; CC stretching at the <i>t</i> -Bu-HBC linkage; -CH ₃ bending; collective conjugated CC stretching	6
1215	1217	CN stretching at porphyrin; collective CC stretching at Porphyrin and HBC; in-plane CH bending	7
1001	-	pyrrole deformation at porphyrin free transversal edge; Ni-N stretching	8
949	949	CC stretching at the <i>t</i> -Bu-HBC linkage; <i>t</i> -Bu bending; collective CC stretching in HBC; Ni-N stretching	9
854	855	CH opla at HBC transversal edge; collective ring deformation over HBC and porphyrin	10
838	-	CH opla at porphyrin free transversal edge	11
819	820	CH opla at longitudinal porphyrin edge	12
803	803	CH opla HBC (DUO)	13
790	-	two contributions: (a) ring deformation at porphyrin free transversal edge; (b) CH opla at porphyrin free transversal edge (out-of-phase combination of SOLO and DUO)	14



1678 cm^{-1} ; 24 km/mol ; 1203 A^4/amu

antisymmetric CC stretching at Por free transversal edge



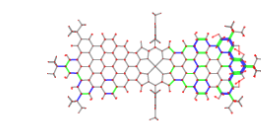
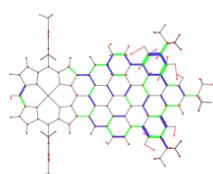
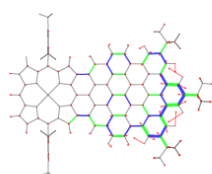
Peak 1

1652 cm^{-1} ; 226 km/mol ; 2386 A^4/amu

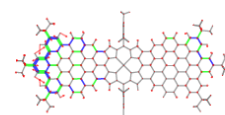
1652 cm^{-1} ; 124 km/mol ; 2371 A^4/amu

Peak 2

1652 cm^{-1} ; 117 km/mol ; 1711 A^4/amu 1653 cm^{-1} ; 58 km/mol ; 25 A^4/amu



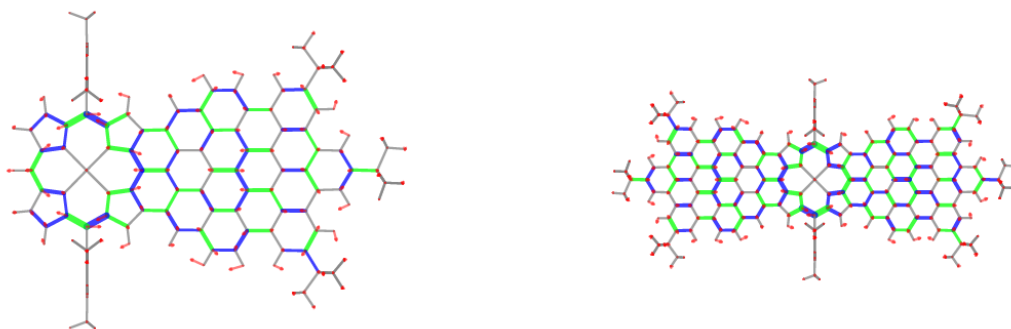
1652 cm^{-1} ; 95 km/mol ; 42 A^4/amu



collective ring stretching at the HBC transversal edge

Peak 3

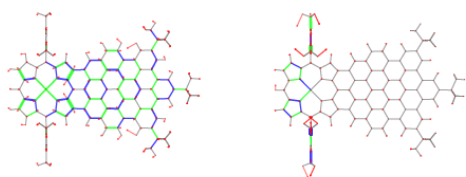
1570 cm^{-1} ; 324 km/mol ; 6277 A^4/amu 1571 cm^{-1} ; 1251 km/mol ; 129 A^4/amu



collective CC stretching over HBC and Por

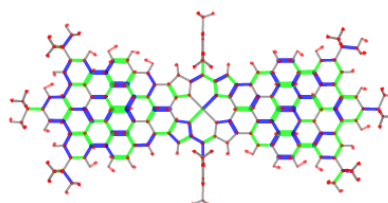
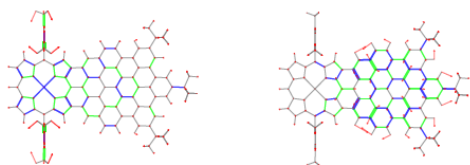
Peak 4

1428 cm^{-1} ; 68 km/mol ; 3975 A^4/amu 1430 cm^{-1} ; 20 km/mol ; 0 A^4/amu



1420 cm^{-1} ; 311 km/mol ; 184 A^4/amu

1430 cm^{-1} ; 43 km/mol ; 865 A^4/amu 1434 cm^{-1} ; 25 km/mol ; 600 A^4/amu

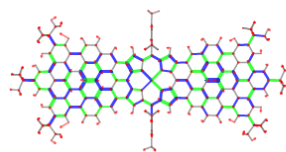
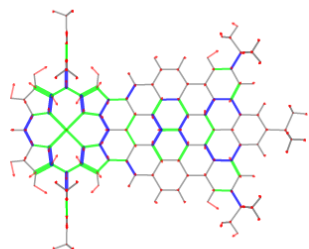


collective CC stretching over HBC and Por; ring deformation

Peak 5

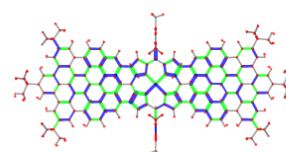
1397 cm^{-1} ; 55 km/mol ; 10360 A^4/amu

1399 cm^{-1} ; 109 km/mol ; 10946 A^4/amu



1399 cm^{-1} ; 25 km/mol ; 327 A^4/amu

collective CC stretching over HBC and Por; ring deformation

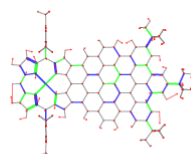
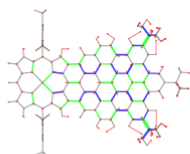


Peak 6

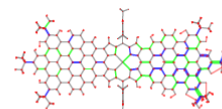
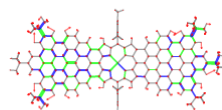
1286 cm^{-1} ; 94 km/mol ; 5371 A^4/amu 1288 cm^{-1} ; 23 km/mol ; 126 A^4/amu

1286 cm^{-1} ; 86 km/mol ; 11591 A^4/amu

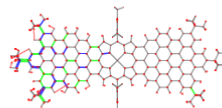
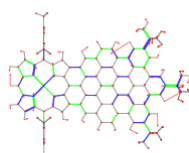
1288 cm^{-1} ; 187 km/mol ; 6750 A^4/amu



1289 cm^{-1} ; 22 km/mol ; 703 A^4/amu



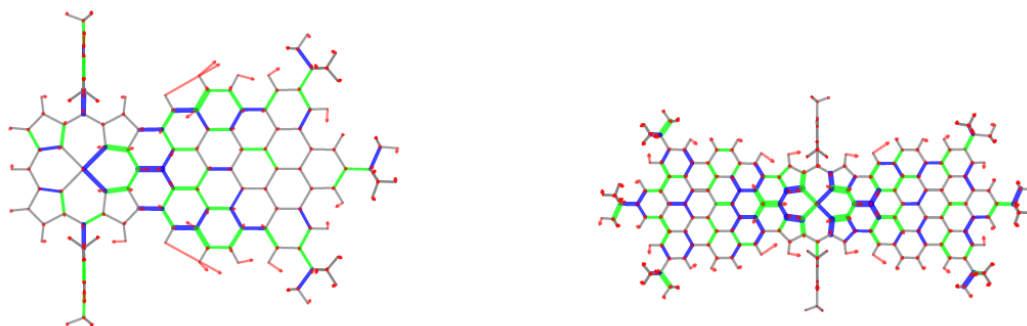
1289 cm^{-1} ; 29 km/mol ; 613 A^4/amu



aromatic CH in-plane bending; CC stretching at the t-Bu – HBC linkage; -CH₃ bending; collective conjugated CC stretching

Peak 7

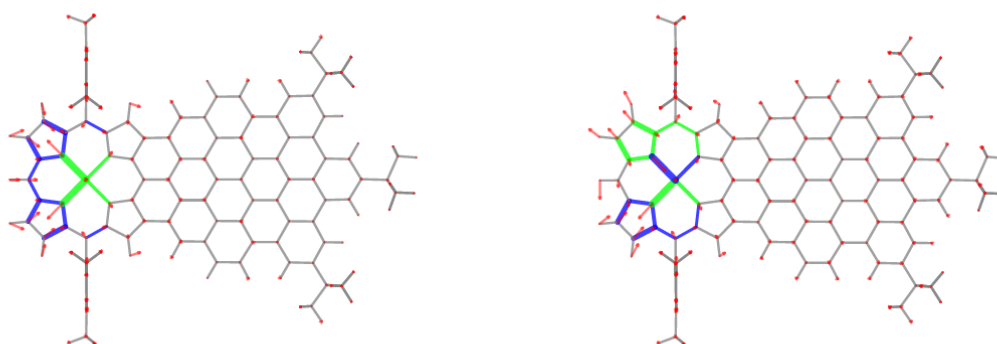
1247 cm^{-1} ; 240 km/mol ; 17608 A^4/amu 1251 cm^{-1} ; 436 km/mol ; 394 A^4/amu



CN stretching at Por; collective CC stretching at Por and HBC; in-plane CH bending

Peak 8

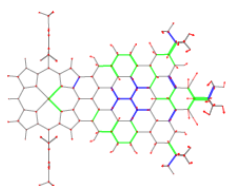
1016 cm^{-1} ; 34 km/mol ; 29 A^4/amu 1023 cm^{-1} ; 73 km/mol ; 104 A^4/amu



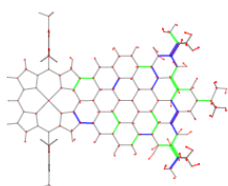
pyrrole deformation at Por free transversal edge; Ni-N stretching

Peak 9

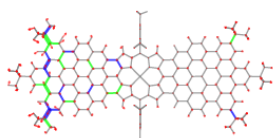
965 cm^{-1} ; 34 km/mol ; 349 A^4/amu



966 cm^{-1} ; 27 km/mol ; 7 A^4/amu

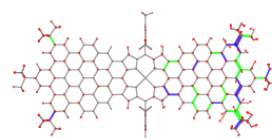


966 cm^{-1} ; 35 km/mol ; 29 A^4/amu



965 cm^{-1} ; 92 km/mol ; 254 A^4/amu

966 cm^{-1} ; 20 km/mol ; 51 A^4/amu

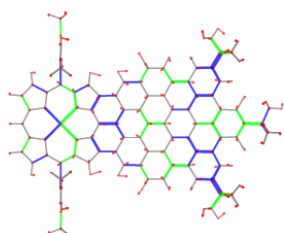


CC stretching at the t-Bu – HBC linkage; t-Bu bending; collective CC stretching in HBC; Ni-N stretching

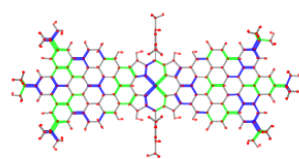
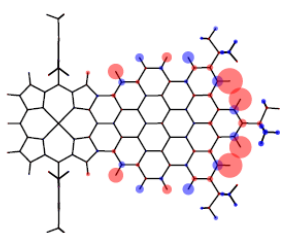
892 cm^{-1} ; 27 km/mol ; 192 A^4/amu

894 cm^{-1} ; 109 km/mol ; 40 A^4/amu

collective ring deformation over HBC and Por

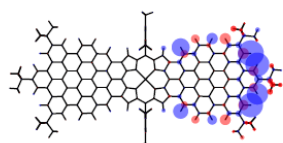


895 cm^{-1} ; 30 km/mol ; 1 A^4/amu



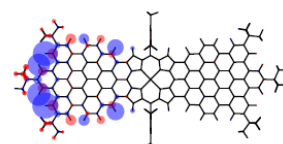
894 cm^{-1} ; 33 km/mol ; 2 A^4/amu

CH opla at HBC transversal edge



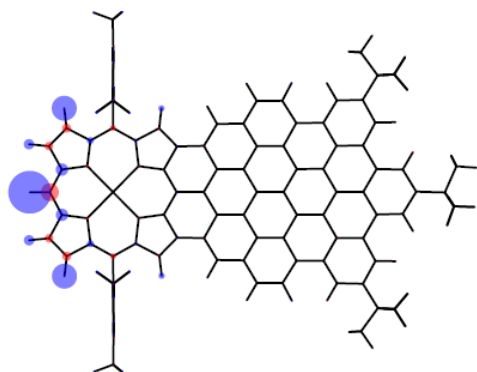
Peak 10

894 cm^{-1} ; 35 km/mol ; 4 A^4/amu



Peak 11

861 cm^{-1} ; 38 km/mol ; 0 A^4/amu

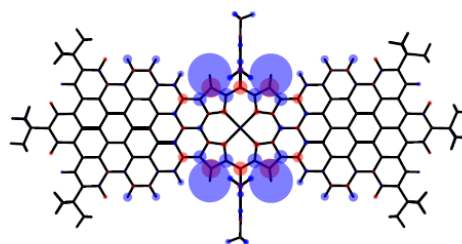
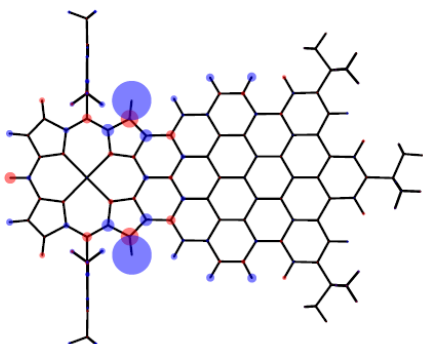


CH opla at Por free transversal edge

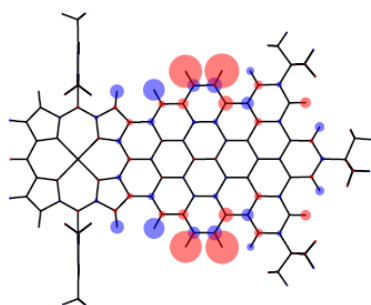
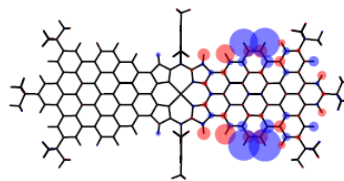
Peak 12

840 cm^{-1} ; 23 km/mol ; 13 A^4/amu

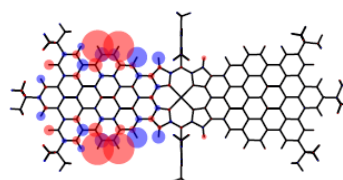
842 cm^{-1} ; 47 km/mol ; 0 A^4/amu



CH opla at longitudinal Por edge

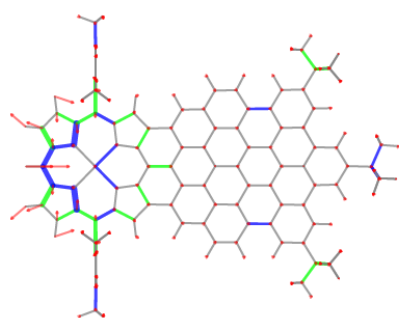
817 cm^{-1} ; 12 km/mol ; 4 A^4/amu 816 cm^{-1} ; 12 km/mol ; 11 A^4/amu 817 cm^{-1} ; 13 km/mol ; 11 A^4/amu **Peak 13**

CH opla HBC (DUO)

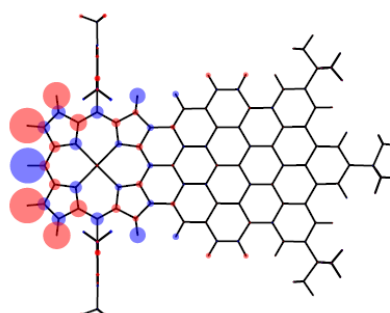
**Peak 14**

two contributions:

- (a) ring deformation at Por free transversal edge;
- (b) CH opla at Por free transversal edge (out-of-phase combination of SOLO and DUO)

801 cm^{-1} ; 25 km/mol ; 59 A^4/amu 

(a)

794 cm^{-1} ; 20 km/mol ; 4 A^4/amu 

(b)

Figure S7-5. Assignment of the IR modes of compounds **7-1** and **7-2** based on the results of DFT calculations. Red arrows (or sticks) represent displacement vectors; the bonds are represented as green (blue) lines of different thickness according to their relative stretching (shrinking). The sizes of blue/red circles are proportional to the nuclear displacements along the out-of-plane direction.

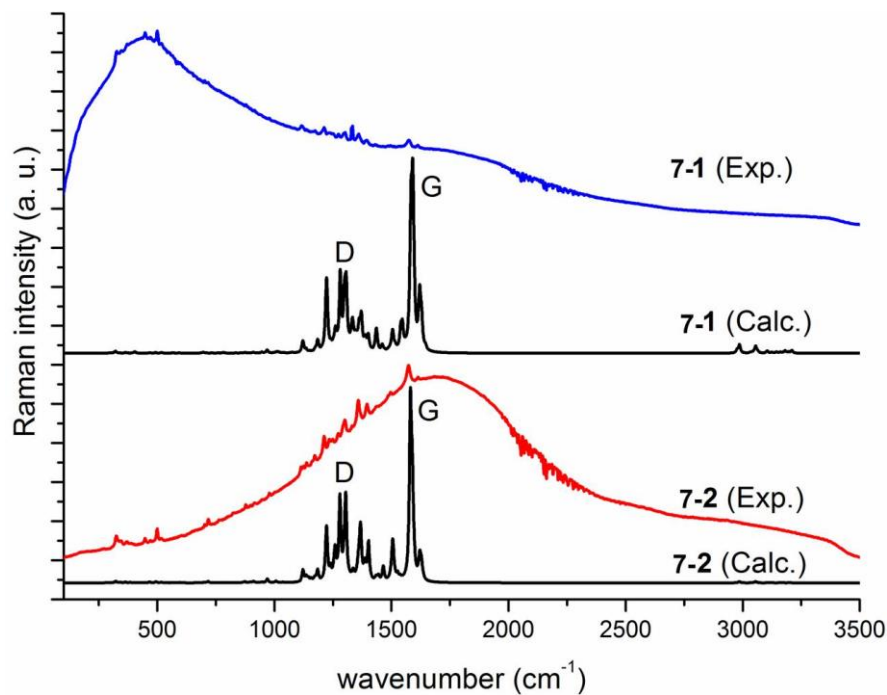


Figure S7-6. Experimental FT-Raman spectra of compound **7-1** and **7-2** compared with simulated spectra obtained from DFT calculations (computed wavenumbers have been scaled by 0.98). See below for details on mode assignments.

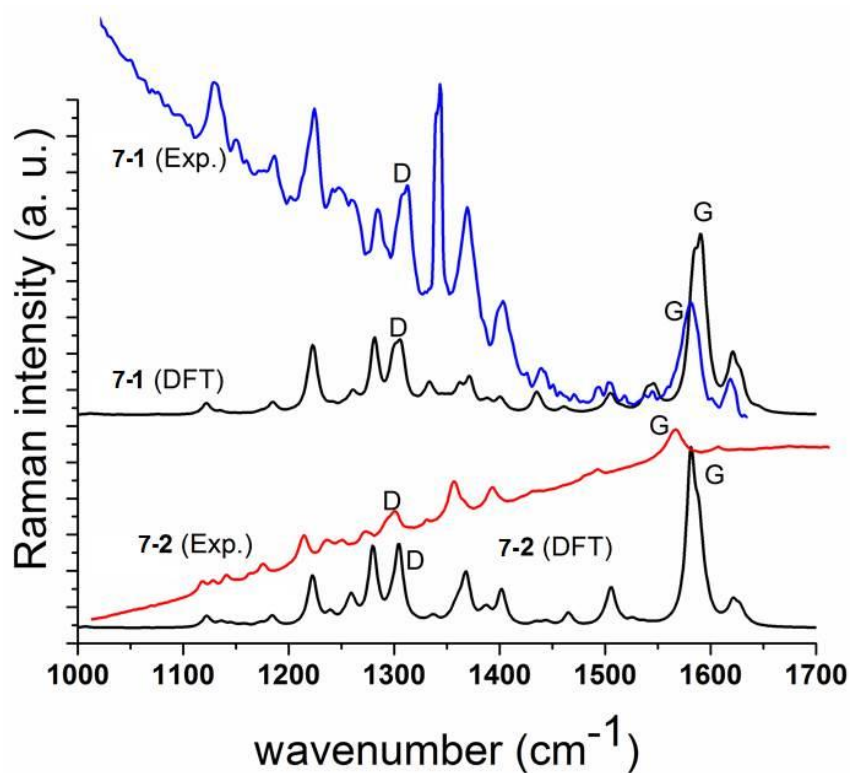
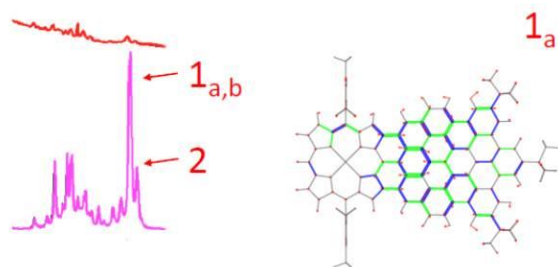


Figure S7-7. Expansion of G and D peak regions of experimental FT-Raman spectra of compound **7-1** and **7-2** in comparison with simulated spectra obtained from DFT calculations.

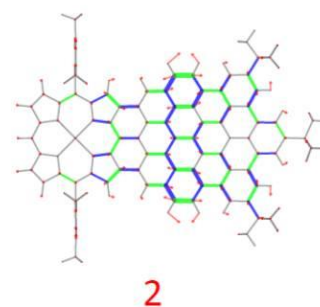
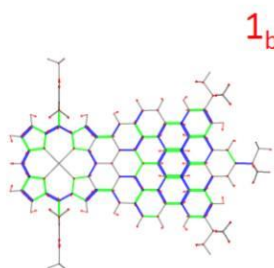
1616 cm^{-1} ; 3 km/mol ; 35391 A^4/amu



1653 cm^{-1} ; 0 km/mol ; 15686 A^4/amu

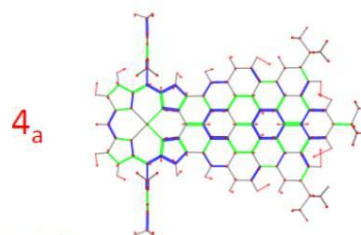
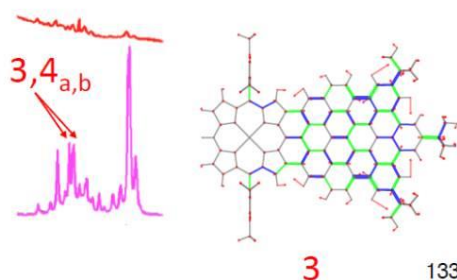
1623 cm^{-1} ; 11 km/mol ; 48714 A^4/amu

Compound 7-1
G modes



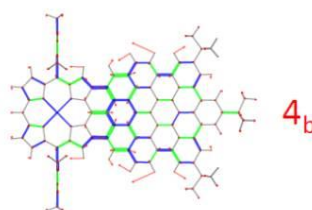
1307 cm^{-1} ; 62 km/mol ; 26325 A^4/amu

1326 cm^{-1} ; 20 km/mol ; 11258 A^4/amu



1333 cm^{-1} ; 67 km/mol ; 11036 A^4/amu

Compound 7-1
D modes



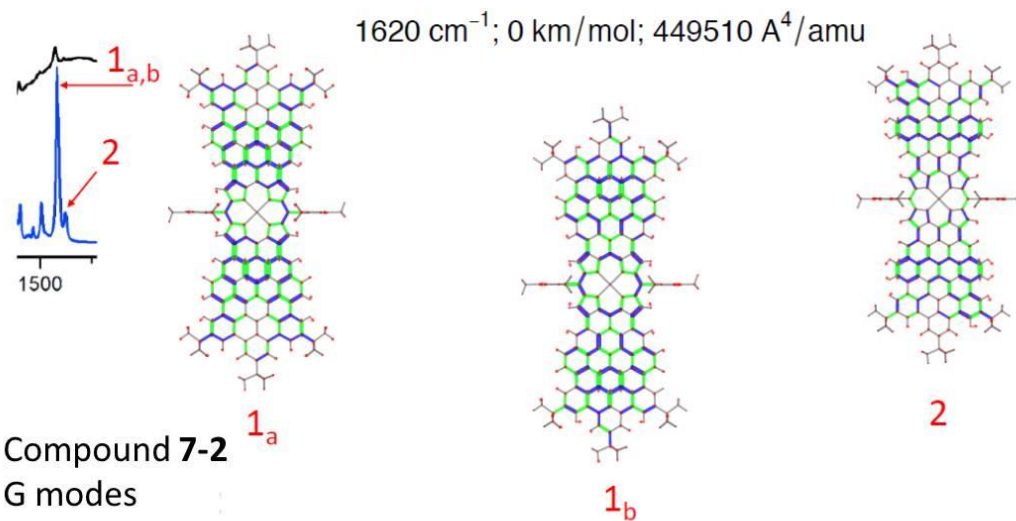
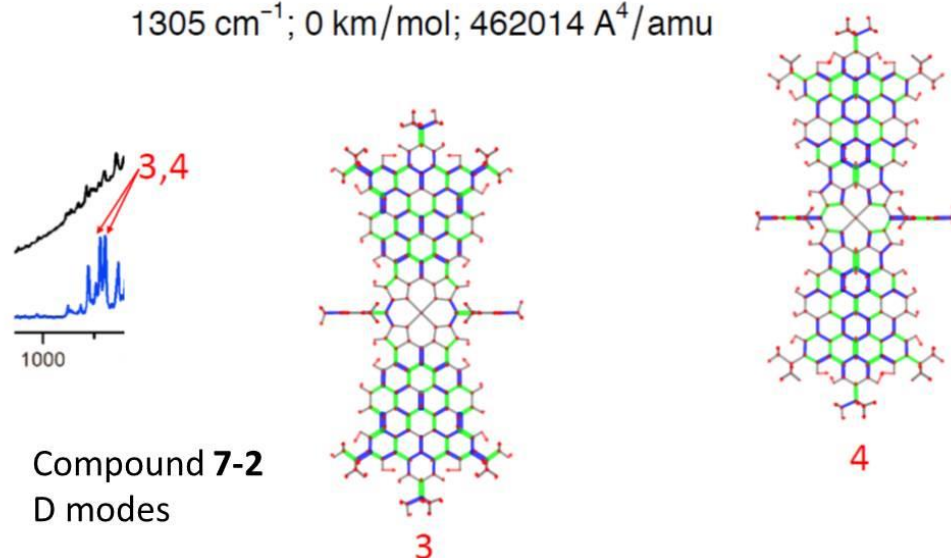
$1613\text{ cm}^{-1}; 0\text{ km/mol}; 958217\text{ A}^4/\text{amu}$
 $1653\text{ cm}^{-1}; 0\text{ km/mol}; 96785\text{ A}^4/\text{amu}$

 $1331\text{ cm}^{-1}; 0\text{ km/mol}; 460316\text{ A}^4/\text{amu}$
 $1305\text{ cm}^{-1}; 0\text{ km/mol}; 462014\text{ A}^4/\text{amu}$


Figure S7-8. Assignment of the Raman G and D modes of 7-1 and 7-2 based on the results of DFT calculations. Red arrows (or sticks) represent displacement vectors; the bonds are represented as green (blue) lines of different thickness according to their relative stretching (shrinking).

DFT calculations

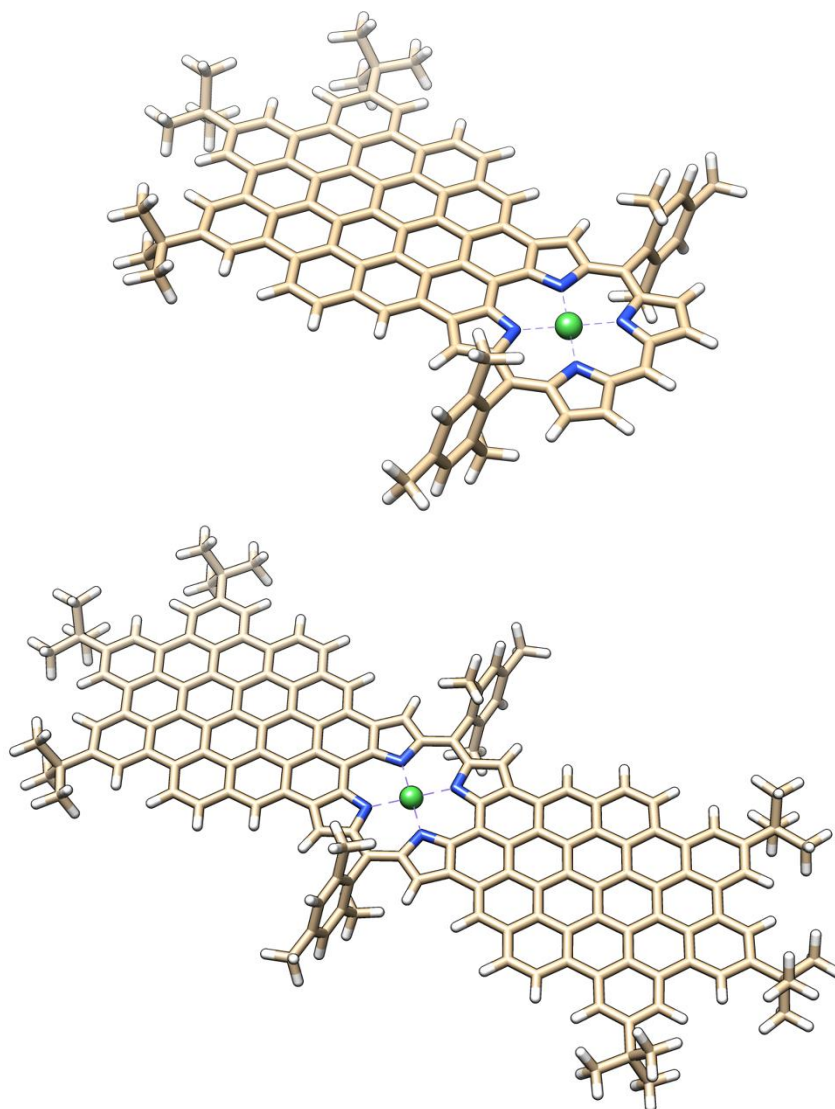


Figure S7-9. Optimized geometries of fused porphyrin nanographene conjugates **7-1** (top) and **7-2** (bottom) obtained by DFT methods (see general method section for details).

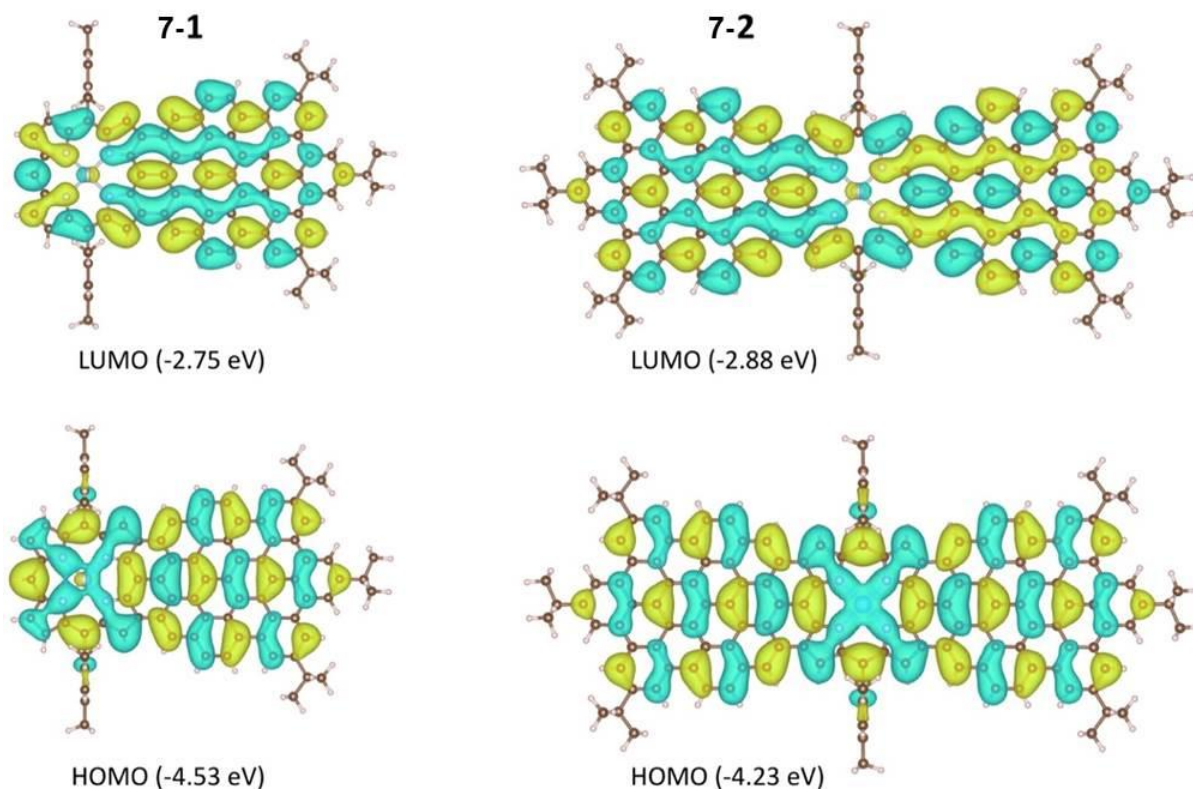


Figure S7-10. Frontier molecular orbitals of fused porphyrin nanographene conjugates **7-1** and **7-2**. The isosurfaces (at 0.0087 atomic units) show that the Ni atom participates to the delocalized π orbitals.

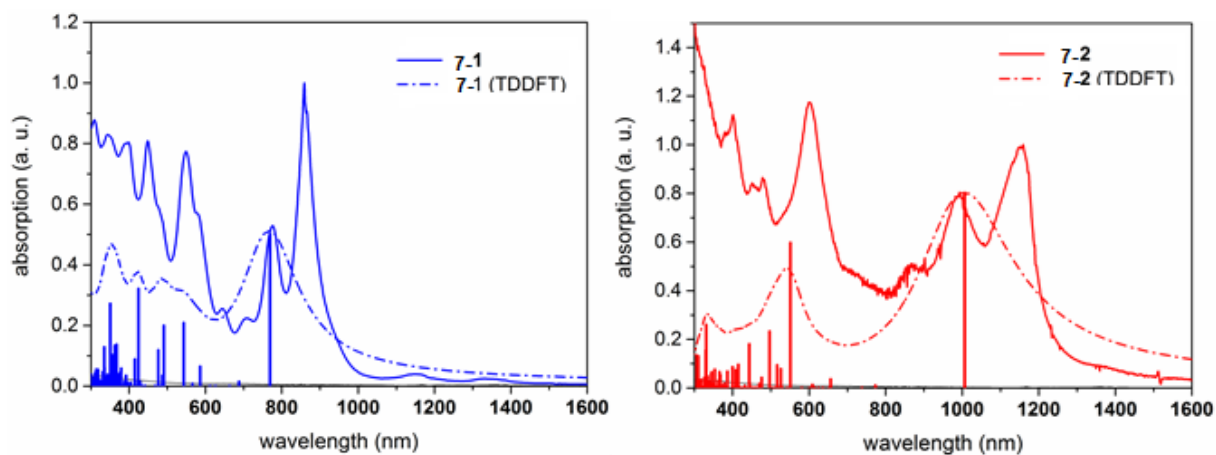


Figure S7-11. Experimental UV-vis-NIR absorption spectra of compound **7-1** (left) and **7-2** (right) and comparison with simulated spectra by TD-DFT methods (line broadening was set at 0.38 eV). The droplines show the position of individual transitions, and their length is proportional to the oscillator strengths. Both **7-1** and **7-2** show clear vibronic progressions in the lowest energy electronic transition (not accounted for by present TDDFT calculations at the Franck-Condon point).

The Cartesian coordinates of the optimized structures of **7-1** and **7-2** are reported below.

Cartesian coordinates of the optimized structure of 7-1 (xyz format; number of atoms: 169)

C -0.782604 -3.661058 -0.000408	N -5.014249 -1.398763 0.000131
C 0.634021 -3.682310 -0.000527	C -6.391808 -3.460656 0.000174
C 1.356302 -2.456234 -0.000470	C -7.607173 -2.787014 0.000384
C 2.783970 -2.467902 -0.000538	C -8.884917 -3.458454 0.000545
C 3.503811 -1.223074 -0.000373	C -9.836949 -2.490876 0.000736
C 2.788737 0.006838 -0.000346	C -9.144552 -1.229872 0.000685
C 3.500136 1.238373 -0.000372	N -7.780238 -1.413387 0.000475
C 2.777311 2.481320 -0.000490	C -9.793776 -0.009836 0.000796
C 1.349727 2.465991 -0.000350	C -9.147790 1.211920 0.000706
C 0.624293 3.690230 -0.000294	C -9.843530 2.471082 0.000782
C -0.792293 3.665256 -0.000138	C -8.894069 3.441182 0.000658
C -1.503173 2.485185 -0.000072	C -7.614548 2.773136 0.000513
C -1.496589 -2.482861 -0.000260	N -7.783968 1.399053 0.000538
C -0.791911 -1.223088 -0.000241	C -6.400976 3.450000 0.000390
C -1.509581 0.001154 -0.000127	C -5.178433 2.772129 0.000267
C -0.795202 1.227227 -0.000155	C -3.912823 3.434296 0.000169
C 0.632703 1.230042 -0.000267	C -2.950163 2.452606 0.000064
C 1.351631 0.004896 -0.000345	C -3.661735 1.208174 0.000098
C 0.635954 -1.222157 -0.000335	N -5.017948 1.391771 0.000224
H -1.311337 -4.610418 -0.000436	C -2.968958 -0.000781 -0.000002
C 1.353848 -4.898439 -0.000672	H -3.777120 -4.510890 -0.000172
C 3.480459 -3.704541 -0.000815	C -6.385513 -4.962968 0.000076
C 4.925133 -1.221420 -0.000157	H -9.009938 -4.531354 0.000512
C 4.921841 1.240530 -0.000183	H -10.913609 -2.598432 0.000895
C 3.470772 3.719729 -0.000766	H -10.878438 -0.011274 0.000946
C 1.341044 4.908113 -0.000353	H -10.920472 2.575780 0.000909
H -1.323528 4.613219 -0.000081	H -9.021936 4.513747 0.000662
C -3.658529 -1.211567 0.000010	C -6.398666 4.952323 0.000404
C -2.943661 -2.454105 -0.000130	H -3.789084 4.507171 0.000185
C -3.903707 -3.438348 -0.000101	C -6.393873 5.658416 -1.221472
C -5.171072 -2.779543 0.000064	C -6.386787 7.057475 -1.197897

C -6.386518 7.777027 0.000434	H -5.892481 -9.706495 0.886138
C -6.386681 7.057444 1.198760	C 5.634473 0.010637 0.000002
C -6.393765 5.658396 1.222305	C 5.635478 2.490836 -0.000438
C -6.378897 -5.668956 -1.221868	C 7.077319 0.013194 0.000723
C -6.368111 -7.067981 -1.198407	C 5.642074 -2.470475 -0.000333
C -6.365895 -7.787631 -0.000122	C 4.937012 -3.708000 -0.001010
C -6.367909 -7.068152 1.198251	C 5.665628 -4.912046 -0.001898
C -6.378691 -5.669117 1.221909	C 7.056422 -4.943699 -0.002144
C -6.412413 9.287751 0.000480	C 7.730250 -3.716127 -0.001164
H -6.379960 7.597309 2.143413	C 7.066848 -2.485350 -0.000034
H -6.380156 7.597360 -2.142537	C 7.796328 1.239926 0.001238
C -6.393046 4.927996 -2.545495	C 9.199926 1.209412 0.003282
C -6.392843 4.927940 2.546307	C 9.924356 0.019131 0.004514
C -6.380081 -4.938422 -2.545827	C 9.199239 -1.176183 0.003379
H -6.360074 -7.607771 -2.143092	C 7.800683 -1.214419 0.001344
C -6.387785 -9.298419 -0.000258	C 4.927408 3.726818 -0.001144
H -6.359714 -7.608074 2.142858	C 5.653100 4.932298 -0.002255
C -6.379675 -4.938777 2.545975	C 7.044135 4.967097 -0.002620
H -6.379717 5.633646 3.381244	C 7.721002 3.741562 -0.001529
H -5.520536 4.272510 2.641822	C 7.060506 2.508553 -0.000228
H -7.278212 4.292041 2.653879	C 2.714972 4.918810 -0.000591
H -5.520575 4.272811 -2.641220	C 2.727713 -4.905639 -0.000824
H -6.380293 5.633728 -3.380415	C 7.847163 6.281733 -0.004194
H -7.278259 4.291854 -2.652889	C 6.938508 7.525863 -0.005195
H -5.918084 9.697089 -0.885879	C 8.739331 6.337960 -1.267429
H -5.915926 9.697075 0.885648	C 8.740073 6.340540 1.258400
H -7.442179 9.667199 0.001760	C 11.464374 -0.021270 0.007111
H -7.267156 -4.304878 -2.653248	C 12.090156 1.386584 0.008017
H -6.365182 -5.644041 -3.380807	C 11.961557 -0.766339 -1.254872
H -5.509536 -4.280665 -2.641414	C 11.957303 -0.766084 1.270911
H -6.364347 -5.644514 3.380848	C 7.862708 -6.256261 -0.003476
H -7.266891 -4.305488 2.653753	C 6.957128 -7.502624 -0.004332
H -5.509280 -4.280800 2.641403	C 8.755656 -6.312688 1.259199
H -5.890109 -9.706376 -0.885389	C 8.755028 -6.310489 -1.266691
H -7.416542 -9.680593 -0.001688	H 8.131847 6.304878 -2.177734

H 9.444947 5.502839 -1.307490	H 13.056531 -0.808734 -1.265324
H 9.322009 7.265943 -1.280745	H 11.805992 1.960486 -0.880292
H 8.133126 6.309312 2.169129	H 13.181698 1.303482 0.009773
H 9.322758 7.268546 1.269482	H 11.803152 1.960608 0.895332
H 9.445713 5.505501 1.299744	H 6.298328 7.563429 -0.892840
H 8.147486 -6.279231 -2.177010	H 7.554574 8.430756 -0.006256
H 9.340181 -7.236912 -1.279763	H 6.298790 7.565194 0.882706
H 9.458449 -5.473512 -1.307120	H 8.802790 3.759817 -0.002000
H 8.148569 -6.283009 2.169875	H 9.742780 2.142672 0.004307
H 9.459100 -5.475785 1.300727	H 9.751963 -2.106384 0.004484
H 9.340812 -7.239132 1.270371	H 8.812161 -3.731401 -0.001554
H 6.317474 -7.543361 0.883547	H 5.126567 -5.847503 -0.002609
H 7.575402 -8.406008 -0.005232	H 3.233807 -5.862692 -0.000852
H 6.317084 -7.541860 -0.891996	H 0.803604 -5.835498 -0.000649
H 11.624994 -0.255874 2.180877	H 3.218633 5.877156 -0.000504
H 13.052237 -0.808475 1.285061	H 5.111953 5.866561 -0.003091
H 11.585085 -1.794057 1.311023	H 0.788463 5.843797 -0.000189
H 11.632317 -0.256317 -2.166060	Ni -6.401880 -0.005335 0.000342
H 11.589479 -1.794321 -1.296026	

**Cartesian coordinates of the optimized structure of 7-2 (xyz format; number of atoms:
263)**

C 7.025980 3.690069 -0.000969	C 7.750623 2.464907 -0.000287
C 5.609638 3.666482 -0.001146	C 7.032677 1.229391 0.000130
C 4.897936 2.486647 -0.000726	C 7.751007 0.003524 0.000784
C 4.901434 -2.483170 0.001178	C 7.034339 -1.223366 0.001155
C 5.614762 -3.662252 0.001881	C 5.606616 -1.223894 0.000852
C 7.030867 -3.683959 0.002239	C 4.888935 0.001752 0.000255
C 7.753893 -2.458130 0.001843	C 5.604834 1.228036 -0.000107
C 9.181652 -2.470823 0.002158	H 5.079175 4.614863 -0.001619
C 9.902389 -1.226438 0.001756	H 5.085466 -4.611285 0.002186
C 9.187923 0.004598 0.001072	C -5.608273 3.658791 0.000149
C 9.900507 1.235286 0.000680	C -7.024428 3.680344 0.000213
C 9.178267 2.479305 -0.000033	C -7.747322 2.454345 -0.000184

C -9.175113 2.466777 -0.000168	C 0.005771 -3.453261 -0.000448
C -9.895565 1.222330 -0.000616	C -1.214988 -2.778754 -0.000843
C -9.180933 -0.008123 -0.000997	C -2.481710 -3.440614 -0.001229
C -9.893432 -1.239304 -0.001421	C -3.444183 -2.459052 -0.001207
C -9.171556 -2.482773 -0.001746	C -2.732048 -1.213841 -0.000879
C -7.743827 -2.468469 -0.001624	N -1.378135 -1.396350 -0.000660
C -7.019313 -3.693540 -0.001892	C -3.425696 -0.004117 -0.000712
C -5.603174 -3.670027 -0.001752	H -2.612356 4.506435 -0.000528
C -4.891304 -2.490063 -0.001394	C -0.000053 4.951928 -0.001306
C -4.894790 2.479800 -0.000254	H 2.612558 4.510076 -0.001564
C -5.599853 1.220415 -0.000554	H 2.619009 -4.509755 0.000801
C -4.882207 -0.005131 -0.000813	C 0.006748 -4.955281 -0.000488
C -5.598093 -1.231611 -0.001145	H -2.605897 -4.513483 -0.001382
C -7.025899 -1.232995 -0.001243	C 0.010384 -5.660943 -1.222698
C -7.744196 -0.007080 -0.000933	C 0.015337 -7.059971 -1.199026
C -7.027619 1.219840 -0.000566	C 0.014261 -7.779573 -0.000633
H -5.079102 4.607895 0.000446	C 0.014260 -7.060136 1.197737
H -5.072678 -4.618394 -0.001928	C 0.009282 -5.661008 1.221562
C -2.733740 1.206603 -0.000530	C -0.002812 5.657856 1.220717
C -3.447629 2.450798 -0.000382	C -0.003442 5.657384 -1.223546
C -2.486566 3.433741 -0.000533	C -0.008368 7.056491 -1.200046
C -1.218906 2.773666 -0.000720	C -0.007510 7.776218 -0.001816
N -1.380102 1.391019 -0.000673	C -0.007759 7.056908 1.196719
C 0.000889 3.449907 -0.001029	H 0.021747 -7.599749 -2.143742
C 1.221617 2.775373 -0.001045	C -0.013003 -9.290317 -0.000978
C 2.488352 3.437208 -0.001252	H 0.019800 -7.600014 2.142387
C 3.450789 2.455623 -0.000850	C 0.010957 -4.930392 2.545426
C 2.738670 1.210447 -0.000479	C 0.013253 -4.930118 -2.546442
N 1.384766 1.392960 -0.000601	C -0.006081 4.926445 -2.547228
C 3.432353 0.000731 0.000027	H -0.014569 7.596148 -2.144821
C 2.740387 -1.209928 0.000244	C 0.019792 9.286962 -0.001981
C 3.454269 -2.454135 0.000746	H -0.013499 7.596906 2.141309
C 2.493225 -3.437061 0.000573	C -0.004757 4.927357 2.544644
C 1.225534 -2.776984 0.000013	C 7.750246 -4.900835 0.002993
N 1.386725 -1.394351 -0.000147	C 9.123752 -4.908750 0.003312

C 9.877359 -3.707887 0.002886	C 13.783013 7.114101 -1.264429
C 9.871919 3.717126 -0.000506	C 13.782875 7.115334 1.261277
C 9.117613 4.916492 -0.001278	H 7.199284 -5.837477 0.003330
C 7.743594 4.907371 -0.001480	H 9.629432 -5.866049 0.003932
C 11.333555 -3.712501 0.003210	H 9.622572 5.874249 -0.001762
C 11.323215 -1.226079 0.002071	H 7.191799 5.843513 -0.002051
C 11.322405 1.236058 0.000980	H 11.521976 -5.852226 0.004165
C 11.329537 3.724029 -0.000196	H 15.208875 -3.738131 0.004408
C 12.038343 2.485319 0.000540	H 15.207529 3.747126 0.000033
C 12.033907 0.005838 0.001681	H 11.521878 5.862953 -0.001028
C 12.039449 -2.475406 0.002817	H 16.149545 -2.113484 0.003690
C 12.061620 -4.917106 0.003933	H 16.143474 2.135537 0.002461
C 13.452260 -4.949445 0.004368	H 14.543797 -6.288414 -2.168116
C 14.126965 -3.722217 0.004022	H 15.735538 -7.245642 -1.269054
C 13.476067 0.007593 0.002061	H 15.854695 -5.482284 -1.298567
C 14.198959 -1.220546 0.002822	H 12.712009 -7.548348 -0.882417
C 13.464330 -2.491128 0.003218	H 12.711520 -7.547555 0.893073
C 13.460515 2.502348 0.000796	H 13.969486 -8.412091 0.006051
C 14.127983 3.737094 0.000120	H 15.853939 -5.481151 1.309223
C 13.452891 4.958255 -0.000536	H 15.734810 -7.244521 1.281129
C 12.057307 4.922715 -0.000610	H 14.542528 -6.286550 2.178685
C 15.597246 -1.183009 0.003211	H 18.028081 -0.265061 -2.169575
C 16.323100 0.012215 0.003074	H 17.984958 -1.802891 -1.299288
C 15.599800 1.202817 0.002393	H 19.453005 -0.818648 -1.270624
C 14.195618 1.234471 0.001746	H 18.205379 1.951813 -0.884502
C 14.257857 -6.262450 0.005189	H 19.581692 1.293651 0.003960
C 15.150860 -6.318874 -1.257446	H 18.204665 1.952410 0.890848
C 13.351672 -7.508373 0.005488	H 17.983956 -1.802079 1.307848
C 15.150126 -6.317773 1.268400	H 18.026368 -0.263718 2.177229
C 17.863102 -0.029467 0.003692	H 19.452016 -0.817828 1.279757
C 18.358060 -0.775252 -1.258743	H 16.072707 5.625205 -0.888439
C 18.490199 1.377789 0.003479	H 16.072589 5.626041 0.886998
C 18.357080 -0.774461 1.266973	H 16.186126 7.147324 -0.001438
C 14.183443 6.314973 -0.001164	H 14.060938 6.572913 -2.174755
C 15.716179 6.158608 -0.000994	H 14.290672 8.085196 -1.277487

H 12.706077 7.302242 -1.304908	C -14.251680 6.258070 0.001862
H 14.060741 6.575057 2.172161	C -13.345431 7.503949 0.002465
H 12.705932 7.303493 1.301482	C -15.144236 6.313339 1.264870
H 14.290504 8.086457 1.273411	C -15.144384 6.314626 -1.260977
C -11.315157 -1.240490 -0.001527	C -14.243998 -6.279761 -0.003750
C -12.027096 -0.010139 -0.001154	C -13.336243 -7.524550 -0.003904
C -11.316909 1.221484 -0.000670	C -15.136270 -6.336326 -1.266894
C -7.737363 -4.910996 -0.002298	C -15.136940 -6.337159 1.258891
C -9.111077 -4.920446 -0.002445	H -7.185494 -5.847110 -0.002498
C -9.866002 -3.720673 -0.002173	H -9.615613 -5.878359 -0.002785
C -7.744013 4.896953 0.000660	H -7.193302 5.833744 0.000969
C -9.117657 4.904623 0.000712	H -9.623417 5.861880 0.001072
C -9.871033 3.703780 0.000304	H -16.136710 -2.139628 -0.002101
C -13.469849 -0.011797 -0.001253	H -11.508536 -5.866467 -0.002957
C -14.189742 -1.238053 -0.001786	H -15.197994 -3.757177 -0.003198
C -15.593329 -1.206664 -0.001831	H -16.143251 2.109465 -0.000759
C -12.029692 -2.490325 -0.002021	H -15.202669 3.733744 0.000667
C -11.322417 -3.726815 -0.002333	H -11.515803 5.847751 0.001432
C -12.049073 -4.931854 -0.002811	H -18.198395 -1.955866 -0.890122
C -13.440064 -4.965652 -0.003118	H -19.575261 -1.298231 -0.002219
C -14.116192 -3.739685 -0.002860	H -18.198555 -1.956490 0.885451
C -13.454786 -2.507157 -0.002238	H -18.020990 0.261045 -2.174980
C -14.192563 1.216248 -0.000808	H -17.978683 1.798810 -1.304550
C -15.591150 1.178879 -0.001004	H -19.446511 0.814214 -1.276707
C -16.317035 -0.015956 -0.001492	H -18.021374 0.259600 2.171869
C -12.033180 2.470965 -0.000173	H -19.446745 0.813352 1.273721
C -11.327360 3.708112 0.000372	H -17.978923 1.797938 1.302460
C -13.457999 2.486742 -0.000148	H -12.705492 7.543046 0.890207
C -14.120766 3.717869 0.000543	H -13.963204 8.407694 0.002943
C -13.446140 4.945025 0.001130	H -12.705556 7.543965 -0.885285
C -12.055430 4.912623 0.000999	H -14.536858 6.282007 2.175297
C -17.857032 0.025421 -0.001618	H -15.848109 5.476754 1.305458
C -18.483752 -1.382023 -0.002160	H -15.728871 7.240118 1.277539
C -18.351564 0.771085 -1.264282	H -14.537117 6.284189 -2.171511
C -18.351796 0.770240 1.261452	H -15.729008 7.241425 -1.272662

H -15.848258 5.478078 -1.302310
H -12.696045 -7.563092 -0.891493
H -13.952948 -8.429026 -0.004365
H -12.696527 -7.563652 0.884006
H -14.528768 -6.304199 -2.177226
H -15.841280 -5.500723 -1.307481
H -15.719580 -7.263944 -1.279622
H -14.529916 -6.305652 2.169561
H -15.720264 -7.264781 1.270681
H -15.841972 -5.501584 1.299666
Ni 0.003311 -0.001685 -0.000553
H 0.492198 -9.700038 -0.881048
H -1.042955 -9.669174 -0.012970
H 0.471957 -9.700041 0.890324
H 0.011785 -5.635970 3.380552
H -0.868007 -4.284899 2.647386
H 0.890056 -4.284790 2.645633
H -0.865498 -4.284429 -2.648992
H 0.014607 -5.635564 -3.381678
H 0.892562 -4.284675 -2.645843
H 0.872672 4.280726 -2.649568
H -0.007264 5.631819 -3.382526
H -0.885388 4.281016 -2.646738
H -0.471118 9.696517 -0.890118
H 1.049811 9.665797 0.002909
H -0.479487 9.696876 0.881350
H -0.883802 4.281653 2.644662
H -0.005893 5.633007 3.379708
H 0.874257 4.281976 2.646894

STM measurements

Experimental Details

Commercially available 1,2,4-trichlorobenzene (Sigma-Aldrich $\geq 99\%$) was used as a solvent. A saturated solution of **7-2** was prepared by dissolving the solid in TCB. All STM experiments were performed at room temperature (21–23 °C) using a PicoLE (Keysight) machine operating in constant-current mode with the tip immersed in the supernatant liquid. STM tips were prepared by mechanically cutting a Pt/Ir wire (80%/20%, diameter 0.2 mm). Prior to imaging, a drop of solution was placed onto a freshly cleaved surface of highly oriented pyrolytic graphite (HOPG, grade ZYB, Advanced Ceramics Inc., Cleveland, USA). The experiments were repeated in 2-3 sessions using different tips to check for reproducibility and to avoid experimental artefacts, if any. For analysis purposes, recording of a monolayer image was followed by imaging the graphite substrate underneath it under the same experimental conditions, except for increasing the current and the lowering the bias. Raw STM images of the molecular monolayers were calibrated by using the STM images of the HOPG lattice obtained immediately after recording of the monolayer image as a reference. This exercise removes the distortions in the STM images that arise due to thermal drift. The lattice parameters of bimolecular monolayer were then obtained from these calibrated images. Scanning Probe Image Processor (SPIP) software (Image Metrology ApS) was used for image calibration. The unit cell parameters were determined by examining at least 4 images and only the average values are reported. The images are Gaussian filtered. The imaging parameters are indicated in the figure caption: tunneling current (I_{set}), and sample bias (V_{bias}). After the determination of the unit cell from drift-corrected STM images, a molecular model of the observed monolayer was constructed using HyperChemTM Professional 7.5 program. First, a molecular model for each single molecule was built, and then this model was geometry optimized in vacuum using molecular mechanics optimization (Fletcher-Reeves algorithm with RMS gradient of 0.1 kcal/Å mol). Following this, a 2D crystal based on unit cell parameters obtained from calibrated STM images was built by duplicating, translating and rotating the molecules at the lattice sites.

Additional discussion on the STM data:

STM was used to study the self-assembly of nanographene **7-2** at the solution-solid interface. This molecule was dissolved in 1,2,4-trichlorobenzene (TCB). The solubility is poor ($\ll 1\text{mg/mL}$) given the strong aggregation tendency due to its extended π -surface. The self-

assembly behavior was studied at the TCB/highly oriented pyrolytic graphite (HOPG) interface. The samples were prepared by drop casting a saturated solution of **7-2** on freshly cleaved HOPG. The self-assembled layers were characterized using STM under ambient conditions.

Figure S7-12a shows a large scale STM image of the self-assembled network formed by **7-2** at the TCB/HOPG interface. The physisorbed layer consists of an ordered array of dumbbell-shaped features. We assign each dumbbell-shaped feature to a single molecule of nanographene **7-2**. The adlayer often shows missing molecule defects (Figure S7-12b). Furthermore, the physisorbed molecular layer was found to be rather fragile and desorption of molecules was observed upon STM scanning at relatively higher values of tunneling currents. High-resolution STM images clearly reveal that each molecule consists of two star-shaped features fused together to yield a dumbbell-shaped feature. At each end of the dumbbell-shaped feature, three lobes can be discerned which represent the peripheral *tert*-butyl groups. The central porphyrin sub-unit as well as the two mesitylene groups are not resolved in STM images. The molecules are close-packed along one of the unit cell vectors (vector *a*) however they are well-separated from each other along the other (vector *b*) unit cell vector. Such packing is rather unusual since a close-packed structure is expected considering the lack of specific functional groups on the periphery of this molecule. This packing can be explained by formation of bilayer at the TCB/HOPG interface. Inset in Figure 7-3b (in the main text) displays a proposed molecular model for a bilayer network which consists of a continuous first layer adsorbed on the basal plane of HOPG. Only the second layer is observed in STM images and consists of a continuous row of molecules adsorbed on top of the first layer along unit cell vector *a* whereas a discontinuous row along unit cell vector *b*. A comparison of the model with the STM image in Figure 7-3b (main text) indicates that molecules represented in yellow color in the model (lower layer) are not visualized by STM. Each molecule in the second layer is stacked on top of another molecule present in the first layer and is shifted slightly to maximize π - π interactions and to avoid steric repulsion between the *tert*-butyl and mesitylene groups of molecules in the top and the bottom layers. The lack of continuous second layer on top of the first layer could be a consequence of steric repulsion. STM images obtained at the edge of molecular domains confirm the formation of bilayer network. Figure S12 clearly reveals a lower layer underneath the top layer. The domain edges are fairly dynamic and are easily disturbed by the scanning STM tip. The high aggregation tendency of the molecule is evident from the fact that despite the formation of a bilayer, the surface

coverage is not complete, indicating dominance of intermolecular π - π stacking interactions over molecule-substrate interactions.

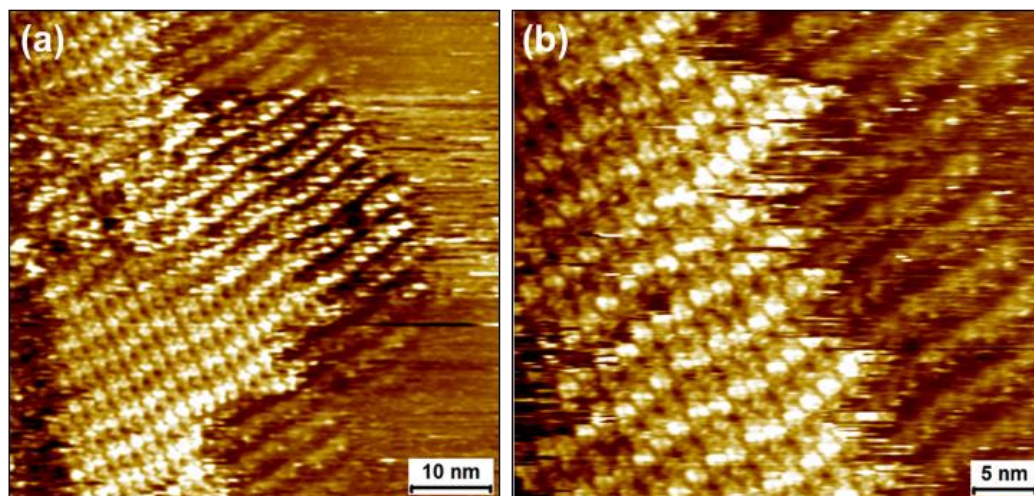


Figure S7-12. (a, b) STM images obtained at the edge of a domain clearly shows the bilayer structure. The lower layer can be seen on the right side of these STM images. Imaging parameters: $V_{bias} = 900$ mV, $I_{set} = 85$ pA.

We also considered an alternative model for the packing which is provided in the Figure S7-13b. It consists of molecules in the top layer oriented at approximately 40° with respect to a continuous, densely packed lower layer. However, such configuration is expected to significantly reduce the π -stacking interactions between molecules due to steric hindrance between the *tert*-butyl and mesitylene groups of molecules in the top and the bottom layers. A schematic comparison between the two packing patterns is represented in Figure S7-13.

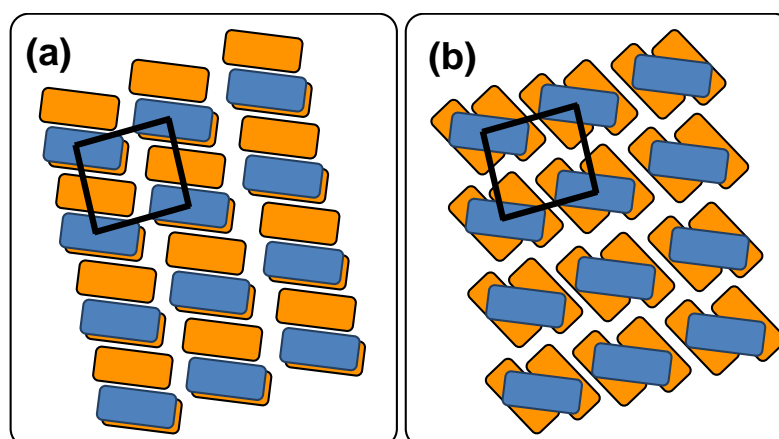


Figure S7-13. Schematic models for proposed packing of molecules in the bilayer. (Lower layer: orange, upper layer: blue) (a) Model similar to that proposed in Figure 7-3b. (b) An alternative model considering the oblique arrangement of molecules in the top and bottom layers.

Additional STM data

Large scale STM images:

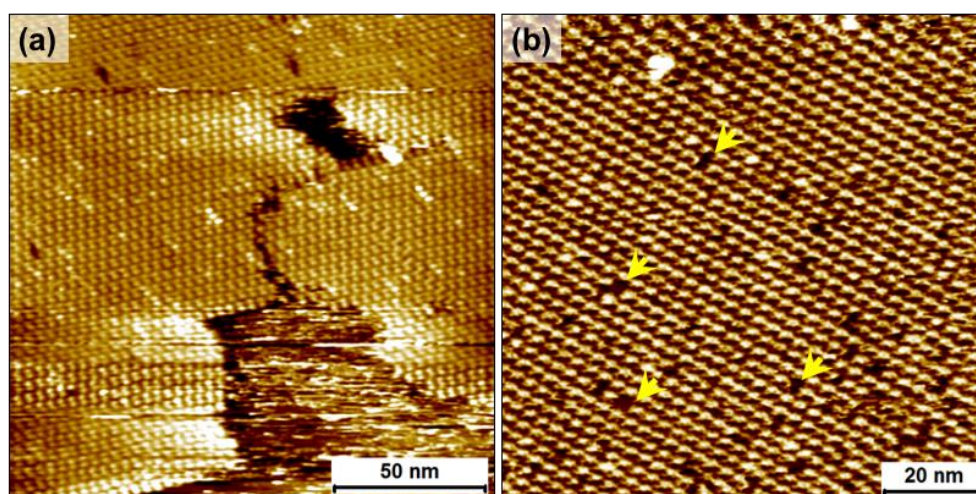


Figure S7-14. Large-scale STM images of the nanographene **7-2** self-assembled network formed at the TCB/HOPG interface. (a) STM image shows that despite formation of a bilayer, the surface coverage is not complete. Imaging parameters: $V_{bias} = -1.2\text{V}$, $I_{set} = 50\text{ pA}$. (b) STM image showing a number of missing molecule defects (few are marked by yellow arrows) in the bilayer. $V_{bias} = -900\text{mV}$, $I_{set} = 70\text{ pA}$. Typically, these defects are present in the second (upper) layer.

Small-scale STM images:

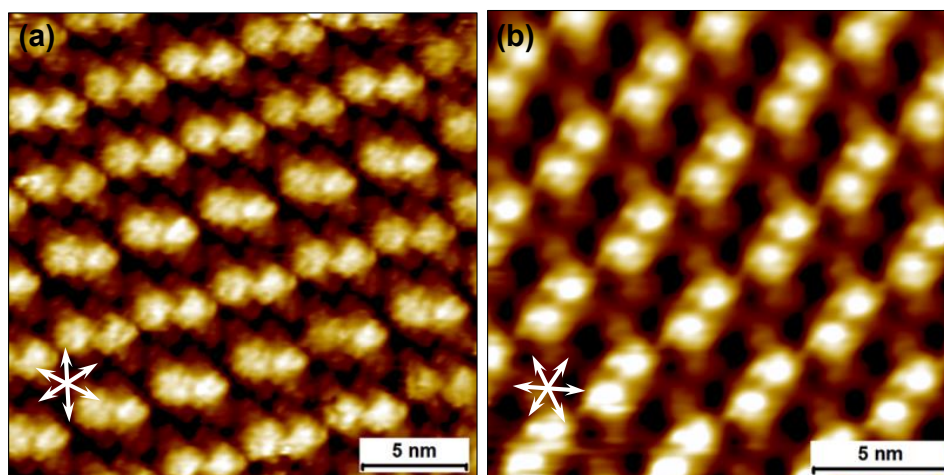


Figure S7-15. Additional small-scale STM images. The STM image in (a) was used as a basis for the alternative packing arrangement presented in Figure S7-13(b). Imaging parameters: $V_{bias} = -950\text{mV}$, $I_{set} = 125\text{ pA}$.

Single crystal X-ray diffraction analysis

Single crystal of **7-20b** suitable for X-ray diffraction crystallography was grown by slowly evaporating its dichloromethane solution. Single crystals of other porphyrin derivatives were not obtained although we tried various conditions. The X-ray diffraction data for **7-20b** were collected at 193 K on a STOE IPDS 2T diffractometer by using graphite monochromated Mo-K α radiation. The structure was solved with the SHELXT-2014 program and refined by the SHELXT-2018. The data has been deposited at the Cambridge Crystallographic Data Centre (CCDC) with the deposition number of CCDC 1835706 and can be obtained free of charge from CCDC *via* www.ccdc.cam.ac.uk/structures/.

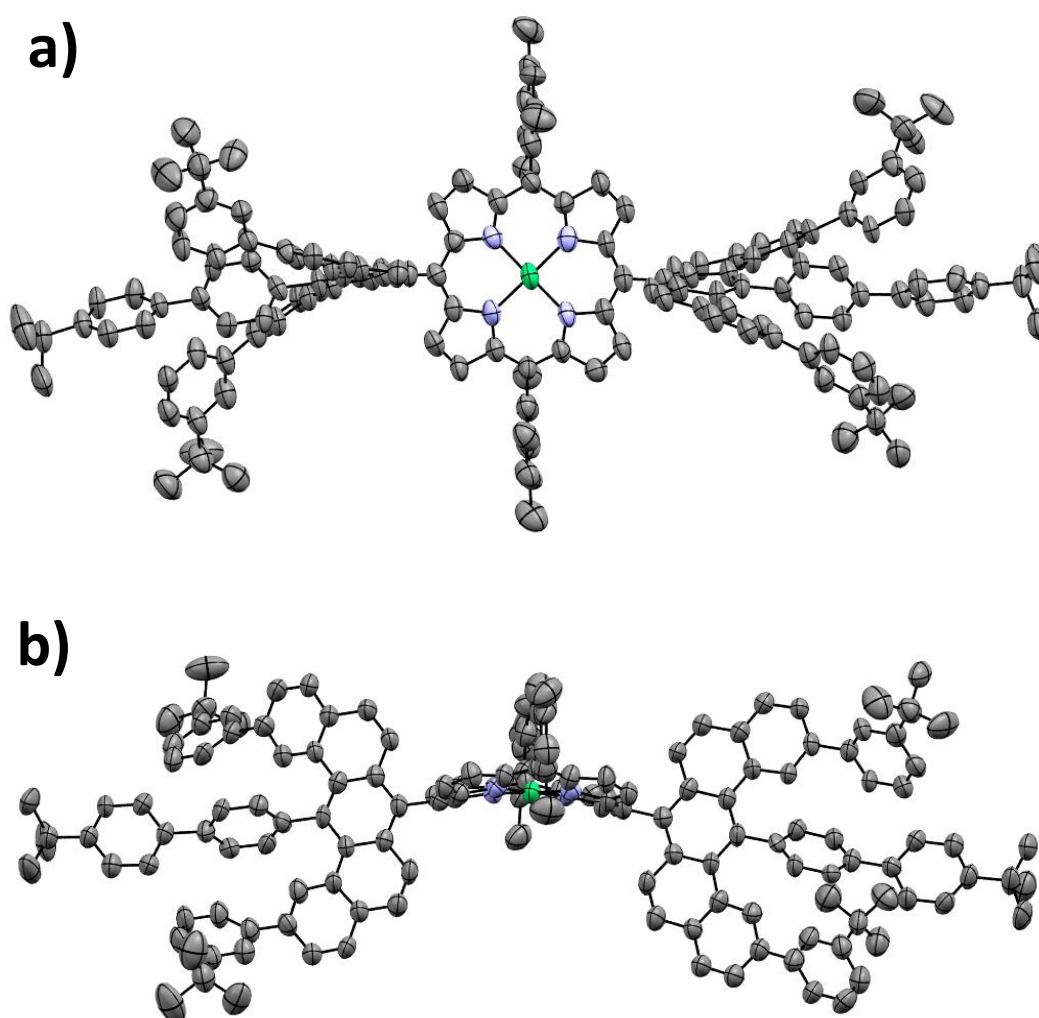


Figure S7-16. Single crystal structure of compound **7-20b**. a) top view; b) front view.

	<u>Crystal data for 7-20b (CCDC 1835706)</u>
formula	$C_{154}H_{136}N_4Ni+3CH_2Cl_2$
molecular weight	$2356.15 \text{ gmol}^{-1}$
absorption	$\mu = 0.32 \text{ mm}^{-1}$

crystal size	0.03 x 0.17 x 0.24 mm ³ brown plate		
space group	P -1 (triclinic)		
lattice parameters	a = 16.8583(12)Å	$\alpha = 87.032(7)^\circ$	
(calculate from	b = 20.6592(17)Å	$\beta = 77.233(6)^\circ$	
23339 reflections with	c = 20.9527(19)Å	$\gamma = 68.853(6)^\circ$	
1.8° < θ < 28.6°)	V = 6634.6(9)Å ³	z = 2	F(000) = 2484.0
temperature	-80°C		
density	$d_{\text{Xray}} = 1.179 \text{ gcm}^{-3}$		

data collection

diffractometer	STOE IPDS 2T
radiation	Mo-K α Graphitmonochromator
Scan – type	ω scans
Scan – width	1°
scan range	$2^\circ \leq \theta < 28^\circ$ $-22 \leq h \leq 21 \quad -27 \leq k \leq 27 \quad -28 \leq l \leq 28$
number of reflections:	
measured	61373
unique	32842 ($R_{\text{int}} = 0.1651$)
observed	10351 ($ F /\sigma(F) > 4.0$)

data correction, structure solution and refinement

corrections	Lorentz and polarisation correction.
Structure solution	Program: SHELXT-2014
refinement	Program: SHELXL-2018 (full matrix). 1564 refined parameters, weighting scheme: $w = 1/[\sigma^2(F_o^2) + (0.1315 * P)^2 + 39.76 * P]$ with $(\text{Max}(F_o^2, 0) + 2 * F_c^2) / 3$. H-atoms at calculated positions and refined with isotropic displacement parameters, non H- atoms refined anisotropically.
R-values	$wR2 = 0.5045$ ($R1 = 0.1876$ for observed reflections, 0.3722 for all reflections)
goodness of fit	S = 1.048
maximum deviation of parameters	0.001 * e.s.d
maximum peak height in diff. Fourier synthesis	0.73, -0.65 eÅ ⁻³

References

1. G. W. T. [M. J. Frisch, H. B. Schlegel, G. E. Scuseria, M. A. Robb, J. R. Cheeseman, G. Scalmani, V. Barone, B. Mennucci, G. A. Petersson, H. Nakatsuji, M. Caricato, X. Li, H. P. Hratchian, A. F. Izmaylov, J. Bloino, G. Zheng, J. L. Sonnenberg, M. Hada, M. Ehara, K. Toyota, R. Fukuda, J. Hasegawa, M. Ishida, T. Nakajima, Y. Honda, O. Kitao, H. Nakai, T.

- Vreven, J. A. Montgomery, Jr., J. E. Peralta, F. Ogliaro, M. Bearpark, J. J. Heyd, E. Brothers, K. N. Kudin, V. N. Staroverov, T. Keith, R. Kobayashi, J. Normand, K. Raghavachari, A. Rendell, J. C. Burant, S. S. Iyengar, J. Tomasi, M. Cossi, N. Rega, J. M. Millam, M. Klene, J. E. Knox, J. B. Cross, V. Bakken, C. Adamo, J. Jaramillo, R. Gomperts, R. E. Stratmann, O. Yazyev, A. J. Austin, R. Cammi, C. Pomelli, J. W. Ochterski, R. L. Martin, K. Morokuma, V. G. Zakrzewski, G. A. Voth, and J. J. D. P. Salvador, S. Dapprich, A. D. Daniels, O. Farkas, J. B. Foresman, J. V. Ortiz, J. Cioslowski, and D. J. Fox, Gaussian, Inc., Wallingford CT, 2013.]
2. M. Dolg, U. Wedig, H. Stoll and H. Preuss, *J. Chem. Phys.*, 1987, **86**, 866-872.
 3. J. M. L. Martin and A. Sundermann, *J. Chem. Phys.*, 2001, **114**, 3408-3420.
 4. T. Dumslaff, B. Yang, A. Maghsoumi, G. Velpula, K. S. Mali, C. Castiglioni, S. De Feyter, M. Tommasini, A. Narita, X. Feng and K. Müllen, *J. Am. Chem. Soc.*, 2016, **138**, 4726-4729.
 5. O. B. Locos and D. P. Arnold, *Org. Biomol. Chem.*, 2006, **4**, 902-916.
 6. L. Yu, K. Muthukumar, I. V. Sazanovich, C. Kirmaier, E. Hindin, J. R. Diers, P. D. Boyle, D. F. Bocian, D. Holten and J. S. Lindsey, *Inorg. Chem.*, 2003, **42**, 6629-6647.
 7. Y. Matano, T. Shibano, H. Nakano and H. Imahori, *Chem. Eur. J.*, 2012, **18**, 6208-6216.

Chapter 8. Summary and Outlook

GMs have numerous exciting properties derived from their delocalized electronic structures, which qualify them as components in optoelectronics. In recent years, bottom-up synthetic methods have been a useful tool to provide atomically precise GMs and facilitate the understanding of their structure-property relationships. Up to now, attentions have been mainly focused on the fully armchair-edged and all benzenoid GMs. Generally, this type of GMs could be synthesized in a two-step manner: the first step is construction of polyphenylene precursors using various coupling methods and the second step is planarization in the presence of Lewis acids and oxidants. By increasing core sizes, their energy gaps could be decreased while their solubility will be inevitably lowered due to enhanced intermolecular π - π aggregation. This drawback further hinders their solution processing as well as practical applications. By now, the largest GM ever synthesized by bottom-up method has a total number of 222 carbons on its aromatic core with a low optical energy gap of 1.6 eV.

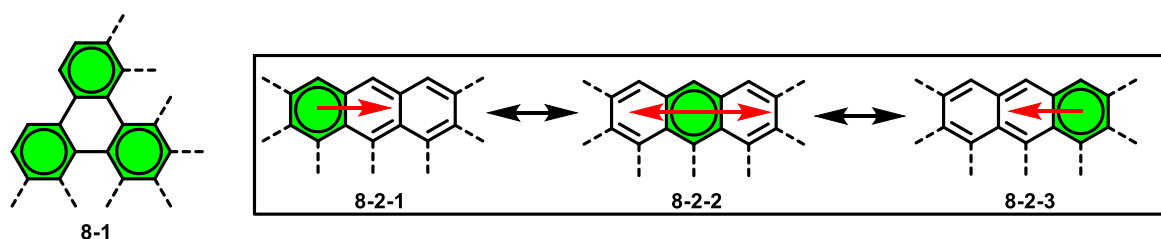


Figure 8-1. Kekulé resonance structures of armchair and zigzag edged GMs, with their Clar's aromatic π -sextets indicated with a circle and green color.

In full armchair edged benzenoid GMs (**8-1**), the π electrons are partially localized (Figure 8-1), only one stable resonance structure could be drawn. By comparison, more resonance structures are possible for zigzag-edged GMs (**8-2**), indicating higher delocalization of their π electrons over the whole aromatic skeleton. This difference results in lower energy gaps for zigzag edged GMs compared with fully armchair-edged ones. However, the synthesis and property elucidation of zigzag-edged GMs remain unexplored. What's more, the application of zigzag-edged GMs as building blocks to fabricate novel π -systems have not been attempted. For this reason, in this thesis I mainly investigated the synthesis of both partial zigzag-edged and fully zigzag-edged GMs, as well as studied their optical, physical, and chemical properties. Finally, I used a partially zigzag-edged GM precursor as building block to synthesize porphyrin doped nanographene conjugates, which proved the concept to fuse

porphyrin into a pure carbon framework of nanographene by solution synthesis method. Detailed results are summarized below:

In Chapter 2, I developed one synthetic method toward a partially zigzag-edged GM, namely 5,13-didodecyl-6,14-dimesityldibenzo[*hi, st*]ovalene (DBOV), for the first time. The DBOV core could be regarded as short segment of 5-ZGNR, whose syntheses and properties have never been investigated experimentally. Scholl reaction of bischrysene **2-6** is the key step, which could not tolerate electron withdrawing functional groups, such as aldehyde and nitro functionalities. After protecting the aldehyde by transforming to more electron-rich methylenes, the cyclodehydrogenation finally worked albeit in relatively low yield. The final product DBOV was obtained after treating the dialdehyde with mesitylmagnesium bromide, followed by Friedel-Crafts reaction and oxidation with air. DBOV shows intense absorption ($\varepsilon = 1.83 \times 10^5 \text{ M}^{-1}\text{cm}^{-1}$) in the red light region (625 nm) with very sharp absorption peaks. Its fluorescence is extremely strong (absolute fluorescence quantum yield, $\Phi = 0.79$) and the red color emission could even be seen under room light. Transient absorption measurements revealed stimulated emission signals at 700 nm both in toluene solution and polystyrene (PS) matrix, which means that this molecule could be potentially used as optical gain material. Amplified stimulated emission (ASE) could also be seen for the 1w% DBOV doped PS film with relatively low irradiation energy of $60 \mu\text{J cm}^{-2}$. However, increasing the concentration of DBOV molecules to 3w% requires much higher laser energy ($150 \mu\text{J cm}^{-2}$) to see PL narrowing due to aggregation induced quenching of PL. In addition, after irradiation at high intensity ($320 \mu\text{J cm}^{-2}$) for 30 minutes, only a 30% decay was observed on the emission spectra, indicating the high stability of the DBOV core. These results characterize DBOV as a promising dye molecule, which might find applications in light-emitting devices or organic lasers.

In the future, one possible direction of the DBOV projects might be to prolong the length of its zigzag edges and study the properties of these short 5-ZGNR segments (Figure 8-2). I expect that these extended versions (**8-3** and **8-4**) will have much longer UV-vis absorption and emission wavelength, which might appear in the NIR region. On the other hand, extending the length of the zigzag edges will also have a chance to result in open-shell biradicaloids or tetraradicaloids, which is being fiercely chased by chemists today for their role as elements of spintronics.

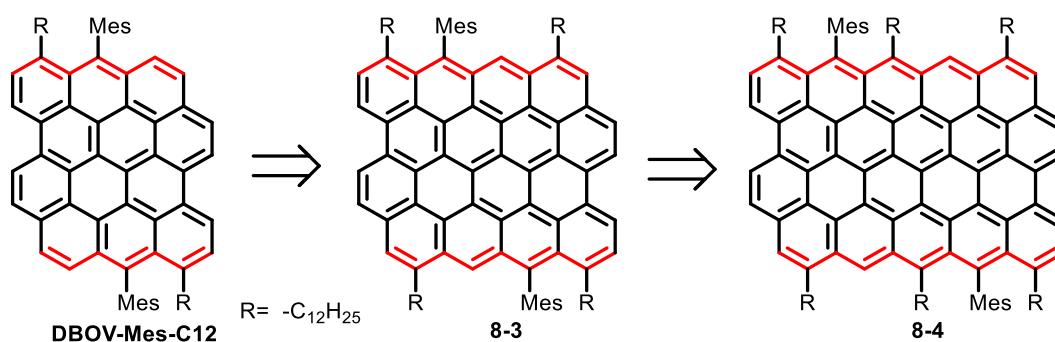


Figure 8-2. Extension of DBOV along its zigzag edges.

The synthesis of DBOV described in Chapter 2 requires many steps (12) and the total yield is very low (<2%). This hinders further investigation into DBOV's properties. In Chapter 3, I improved the synthetic method toward DBOV and found that the key dialdehyde intermediate could be efficiently synthesized using a combination of ICl promoted iodobenzannulation and photochemical cyclodehydroiodination (PCDHI). Compared with the previously used method, the new protocol avoids the application of expensive PtCl_2 and tedious synthetic steps and has chances to be used as a Scholl reaction-free method for making other GMs. The total yield to DBOV was improved from less than 2% up to 23-41% with only 7 steps. Different functional groups could be introduced to the *meso*-positions, for example, alky chains (**DBOV-C12**), phenyl groups with electron withdrawing (**DBOV-CF3**) or electron donating groups (**DBOV-DMEP** and **DBOV-TMOP**) and alkynyl groups (**DBOV-TIPS**). The optical properties could be tuned by these attached substitution groups, for example, by introducing TIPS-ethynyl groups, the maximum UV-vis absorption wavelength was red shifted to the NIR region. By using the sterically hindered **DBOV-DMEP** molecule, which efficiently prevented intermolecular π - π stackings, we studied the single-molecular spectroscopy of DBOV at both room and low temperature. It is found that the triplet decay rate of DBOV does not change with temperature, while the ISC at low temperature is decreased by more than one order of magnitude. The high ISC rate at room temperature might result from the thermal population of higher vibrational levels of S_1 , which decreases the energy gap to higher-lying triplet states T_n ($n > 1$) and accelerates the ISC. High-contrast photon antibunching and intense ZPLs were observed, together with high fluorescence quantum yield and high stability, making **DBOV-DMEP** a promising single quantum emitter, which is ideally suited for high-resolution, frequency-resolved single-molecule spectroscopy.

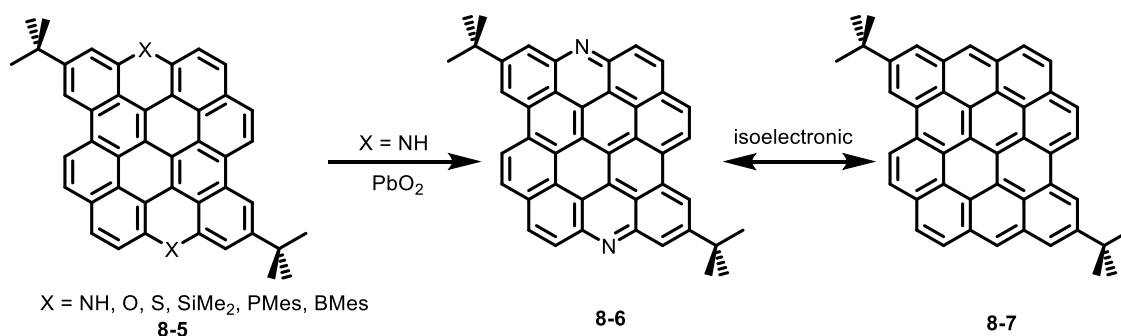


Figure 8-3. Structures of heteroatoms doped DBOVs.

By using the improved synthetic method described above, we will be able to easily make different heteroatoms doped DBOVs, such as O, S, Si, B, etc (8-5). These heteroatoms have different electronegativity and electronic structures to carbon atoms and can effectively tune the electron distribution on the DBOV core and its optical properties. After oxidation or reduction (8-6), they will become isoelectronic to the all carbon based DBOV (8-7). Among them, boron-doped GMs are attracting more and more interests in recent years and some of them show very strong light emitting properties and high chemical stability. On the other hand, the B and N doped DBOV molecules hold promise to respond to outer stimulus, such as pH value, and can be used as chemical sensors.

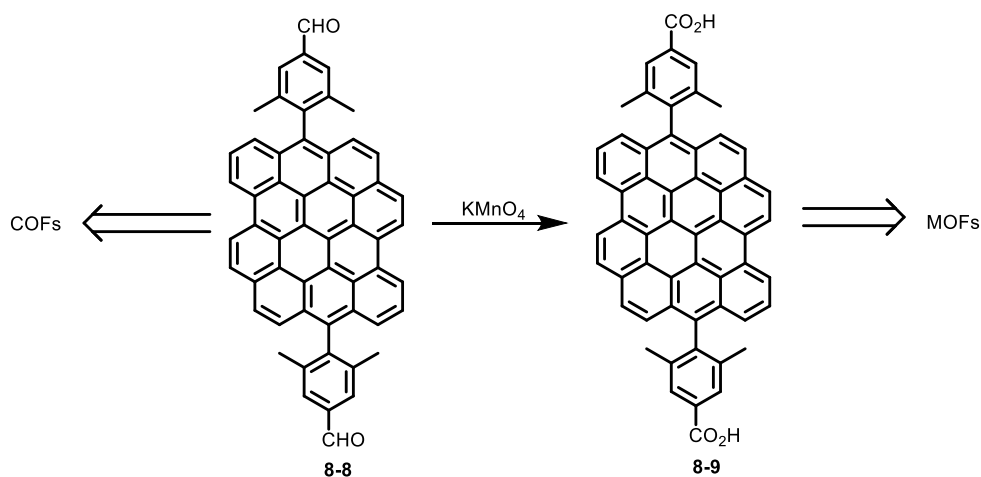


Figure 8-4. Syntheses of COFs and MOFs using dialdehyde DBOV (8-8) and dicarboxylic acid DBOV (8-9) derivatives as building blocks.

The DBOV core could also be introduced into 2D materials, such as COFs and MOFs, to take advantage of the attractive light emitting properties. Two possible DBOV based building blocks can be easily synthesized using our improved method (8-8 and 8-9). Thereby, the dimethylphenyl groups should be used to suppress the intramolecular π - π aggregation and to

improve solubility. The dialdehyde and dicarboxylic acid DBOV can react with amines or Zn^{2+} to give COFs and MOFs with different topologies.

In Chapter 4, I introduced two 3,4,5-tris(dodecyloxy)phenyl (TDOP) groups at the *meso*-positions of the DBOV core for making **DBOV-TDOP**. The TDOP groups significantly increased the solubility of this molecule. In the liquid crystal phase, the rigid DBOV cores and soft TDOP groups attached at the periphery result in phase separation between these two components. **DBOV-TDOP** forms very long self-assembled columns, in which the molecules are stacked in a helical fashion because of the repulsion between the TDOP groups. The distance between two DBOV cores is 0.33–0.37 nm, which is similar to the layer-to-layer distance in graphite. The self-assembly behavior on the interface of HOPG and PO was studied by STM. A self-assembled bilayer was formed even at very low concentration of 10^{-6} M, because of the strong intermolecule π - π stacking. The long alkyl chains are protruding from the surface to the solution, preventing the formation of more layers.

Although the above mentioned method can provide many different *meso*-substituted DBOVs, it only allows to change the functional groups at the 5-, 6-, 13-, and 14- positions. What's more, because the synthesis involves using excess amount of highly nucleophilic Grignard reagents and organo lithium reagents, it cannot be used to synthesize DBOVs with reactive functional groups, such as hydroxyl or carboxylic acids. In Chapter 5, I found that the DBOV core could be selectively brominated at its 3- and 11- positions. This provides an access to DBOVs with various types of functional groups. Our preliminary results realized Suzuki coupling and Sonogashira coupling reactions with aryl boronic acid and substituted ethynyls. The functionalized DBOVs possess largely red shifted UV-vis absorption and emission up to NIR region with higher fluorescence quantum yield as compared to their precursor **DBOV-Mes**. Also these new DBOV derivatives could be oxidized easily to stable radical cation using SbCl_5 and reduced back by Zn powder.

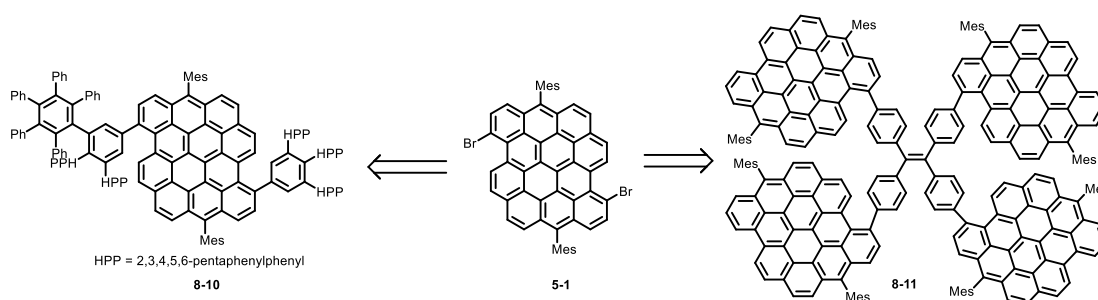


Figure 8-5. Two strategies to achieve solid state emission.

This selective functionalization method will promote the application of DBOV in the future by many ways. For example, in order to prevent the aggregation of DBOV cores (Figure 8-5), one can introduce bulky functional groups to the periphery by appropriate coupling reactions, like polyphenylene dendrimers (**8-10**), or introducing tetraphenyl ethylene (**8-11**) to achieve aggregation induced emission (AIE) in the solid state.

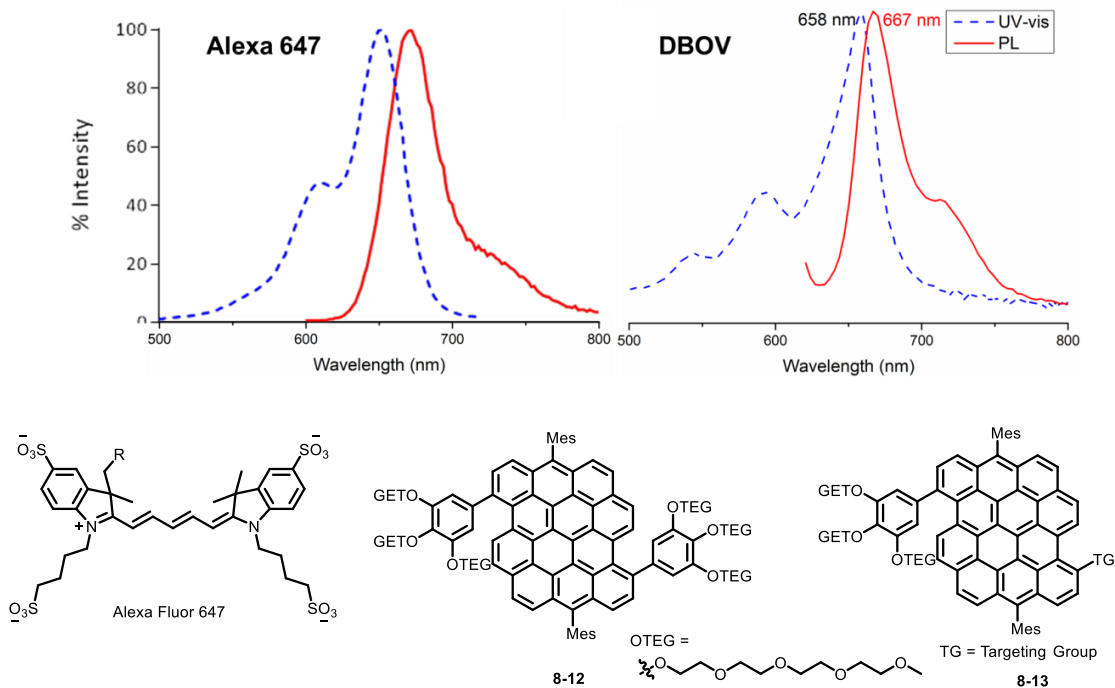


Figure 8-6. Comparison between UV-vis/fluorescence spectra of Alexa 647 and water soluble DBOV.

The other promising application of DBOV is as dye molecule in biological imaging because of its sharp absorption and emission in the long wavelength region. The spectra are very similar to Alexa 647 (Figure 8-6), which has been widely used as dyes in super-resolution bioimaging. In addition, DBOV also revealed blinking properties, with high stability to air and light when compared to Alexa 647. To use this molecule in biosystems, we can take advantage of the functionalization method described above to introduce both water-soluble functional groups (**8-12**) and targeting groups (**8-13**) to its periphery.

In Chapter 6, I mainly worked on the syntheses of full zigzag edged GMs, namely circumpyrene. The synthetic strategy is to selectively fill the bay regions of DBOV by two C=C bonds, without affecting the structure of the zigzag edges. Here I used two methods. One is based on PtCl₂ promoted benzannulation of ethynyl bond connected to the 3- and 11-positions of DBOV and the other is direct benzannulation of dibrominated **DBOV-Mes** with diphenylacetylene. Single-crystal structure analysis unambiguously proved its ring-in-ring

backbone structure. Compared with its DBOV precursor, the UV-vis and fluorescence signal are largely blue shifted, indicating increased energy gap. This can be explained by a simple MO perturbation model. By using the dimethylphenyl substituted circumpyrene precursor, I will be very interested in the synthesis of the full zigzag edged GM **8-15** using the surface promoted C-H activation and dehydrogenation. This molecule might show open-shell biradical or tetraradical properties.

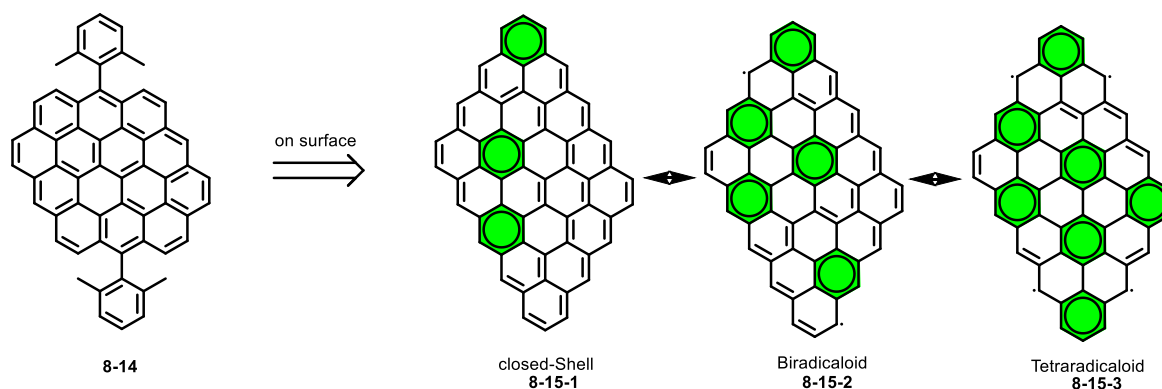


Figure 8-7. On-surface synthesis of full zigzag edged GM **8-15** using dimethylphenyl circumpyrene.

In Chapter 7, I synthesized two nanographene-porphyrin conjugates, in which the porphyrin and nanographene parts are completely conjugated, allowing for efficient electron delocalization through the whole aromatic system. This design is completely different from the previously reported examples, which mostly used single C-C bond to connect nanographenes to porphyrin. In those systems, the electron communication between porphyrin and nanographene is weak. For my design, the key step is to synthesize a benzo[*m*]tetraphene building block, which can be coupled to porphyrin using Suzuki reaction. After a Scholl reaction under optimized conditions, the target product could be obtained in good yield and unambiguously characterized. Intense and broad NIR absorptions were observed in the UV-vis spectra, making it very promising for NIR detectors. The four coordinated Ni porphyrin is low spin. However, when it is coordinated with a ligand, it will become high spin. Using this property, we can try to control the magnetism of nanographene-porphyrin conjugates with an axial ligand.

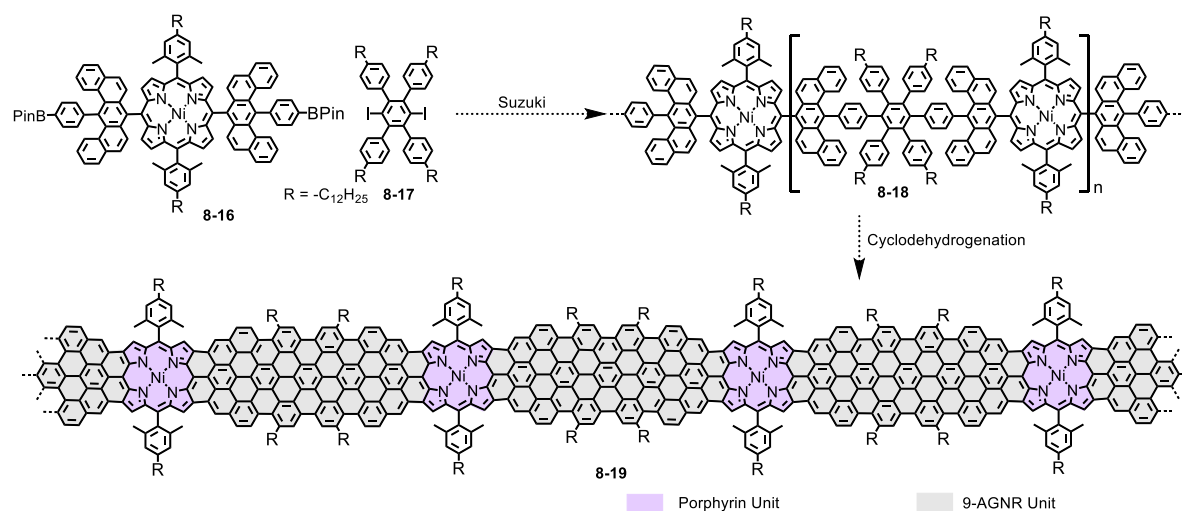


Figure 8-8. Synthesis of porphyrin doped 9AGNR.

Following this step, I will extend the size along one dimension for making porphyrin doped 9AGNR (Figure 8-8). The trick is that the porphyrin core in the backbone of GNR can be used to coordinate metal ions. This will allow us to see how the porphyrins and metal centers affect the charge and spin transport property of the new GNR.

Acknowledgements

Here, I would like to acknowledge all the people who have kindly helped me during my PhD study and contributed to my PhD thesis.

First and foremost, I would like to express my greatest gratitude to my supervisor Prof. Dr. [REDACTED] for his continuous guide and support. Prof. [REDACTED] has profound knowledge not only in organic chemistry but also in many other fields, such as material science, polymer chemistry. I have always been impressed by his interdisciplinary thinking and intensive research capacity. He kept on encouraging and supporting me to explore new scientific things in the free environment he provided for me. He also greatly contributed to build up my scientific point of view to think independently and enriched my research directions. I am deeply impressed by his curiosity to chemistry and open mind to different ideas. His constant guide has significantly influenced me through my whole PhD study and will be a great treasure for my future life.

I would like to cordially thank my project leader, Dr. [REDACTED], with whom I often discuss the problems I encountered while working on my projects. He can always give me a lot of useful suggestions based on his rich experiences, with which I can solve all of my problems. He also helped me a lot to correct my reports and papers and trained my writing skills. In addition, he also offered me a lot of chances to participate in international conferences and exchange ideas with different people. His profound knowledge and rich professional experience are very valuable for my development. He is a very nice person, easy to get along with. He can always give me suggestions and help when I am in need.

I also would like to thank Prof. Dr. [REDACTED], who provided me a lot of help and inspiring discussions at the very beginning of my PhD study. He is a very good chemist and a nice person. We all take him as our spiritual idol.

I want to thank all the members in the analysis department from MPIP, especially the NMR and MS group, who provided nice and timely analysis results for me and helped me with special measurements.

Furthermore, I am truly grateful to all the past and current members in Prof. [REDACTED]'s group:

Prof. Dr. [REDACTED], Dr. [REDACTED], Prof. Dr. [REDACTED], Prof. Dr. [REDACTED], Prof. Dr. [REDACTED], Dr. [REDACTED], Dr. [REDACTED], Prof. Dr. [REDACTED], Dr. [REDACTED], Prof. Dr. [REDACTED], Dr. [REDACTED], Dr. [REDACTED], Dr. [REDACTED], Dr. [REDACTED]

██████████, Dr. ██████████, Dr. ██████████, Ms. ██████████, Ms. ██████████
██████████, Mr. ██████████, Mr. ██████████, Mr. ██████████, Dr. ██████████
Dr. ██████████, Dr. ██████████, Dr. ██████████, Dr. ██████████, Dr. ██████████, Mr.
██████████, for their kind help and accompany.

In addition, I would like to sincerely thank our collaborators:

Prof. Dr. ██████████ and Dr. ██████████ in Politecnico di Milano; Prof.
Dr. ██████████ and ██████████ in University of Sheffield; ██████████, Prof. Dr.
██████████, Dr. ██████████, and ██████████ in Mainz University; Prof. Dr.
██████████, Prof. Dr. ██████████, Dr. ██████████, Dr. ██████████ in
MPIP; Prof. Dr. ██████████, Dr. ██████████, Dr. ██████████, Dr. ██████████
██████████ in KU Leuven; Dr. ██████████ in Politecnico di Milano,
and Prof. ██████████, Dr. ██████████, who provided me with fruitful results
and broadened my horizons.

Last but not least, I would like to thank my family for giving me unconditional, long-term and
considerable support to pursue my dream; and my girlfriend, who shared my happiness and
sadness, success and fail, and encouraged me all the time.

Many thanks also to everybody I might have unintentionally forgotten to mention here.

List of Publications

20. Giovannantonio M., Urgel I. J., **Chen Q.**, Ruffieux C., Pignedoli C., Müllen K., Narita A., Fasel R., “Poly(indenoindene)(p) ladder polymer grown on Au(111) via post-polymerization ladderization”, **2019**, under preparation.
19. **Chen Q.**, Schollmeyer D., Müllen K., Narita A., “Synthesis of Pentagon Fused Hexabenzocoronene (HBC) with Open Shell Characters”, under preparation
18. Cotella G.F., Minotto A., Carnicella G., **Chen Q.**, Paterno G.M., Scotognella F., Müllen K., Narita A., and Cacialli F., “Efficient Red-NIR Light-Emitting Diode Based on Atomically Defined Nanographene Quantum Dots”, under preparation.
17. Liu X., Chen S., **Chen Q.**, Gelleri S., Ritz S., Kumar S., Cremer C., Landfester K., Müllen K., Parekh S., Narita A., Bonn M., “Nanographene-based dyes as stable, high-brightness probes for super-resolution microscopy”, *Angew. Chem. Int. Ed.*, 2019, in press, doi: 10.1002/anie.201909220.
16. Fantuzzi P., Candini A., **Chen Q.**, Dumsclaff T., Müllen K., Narita A., Affronte M., “Colour sensitive response of graphene-graphene quantum dot photo-transistor”, *J. Phys. Chem. C*, **2019**, 123, 26490–26497.
15. **Chen Q.**, Schollmeyer D., Müllen K., Narita A., “Synthesis of Circumphyrene: Nanographene with a Full Zigzag Periphery”, *J. Am. Chem. Soc.*, **2019**, accepted.
14. **Chen Q.**,[#] Thoms S.,[#] Stöttinger S., Schollmeyer D., Müllen K., Narita A., Basché T., “Dibenzo[hi,st]ovalene as Highly Luminescent Nanographene: Efficient Synthesis via Photochemical Cyclodehydroiodination, Opto-electronic Properties and Single Molecule Spectroscopy perties”, *J. Am. Chem. Soc.*, **2019**, 141, 16439–16449.
13. **Chen Q.**,[#] Zajaczkowski W.,[#] Seibel J.,[#] Stöttinger S., Feyter S., Pisula W., Müllen K., Narita A., “Synthesis and Supramolecular Organization of Discotic Liquid Crystalline Dibenzo[hi,st]ovalene with Long-Range Helical Packing”, *J. Mater. Chem. C*, **2019**, 7, 12898–12906.
12. Urgel I. J., Giovannantonio Di M., Gandus G., **Chen Q.**, Liu X., Hayashi H., Ruffieux P., Decurtins S., Narita A., Passerone D., Yamada H., Liu S.X., Müllen K., A. C., Fasel R., “Overcoming Steric Hindrance in Aryl-Aryl Homocoupling via On-Surface Copolymerization”, *ChemPhysChem*, **2019**, 20, 2360–2366
11. Hu Y., Paterno M. G., Wang X. -Y., Wang X. -C., Guizzardi M., **Chen Q.**, Schollmeyer D., Cao X. -Y., Cerullo G., Scotognella F., Müllen K., Narita A., “ π -Extended Pyrene-Fused

Double [7]Carbohelicene as a Chiral Polycyclic Aromatic Hydrocarbon”, *J. Am. Chem. Soc.*, **2019**, 141 (32), 12797–12803.

10. Giovannantonio M., Eimre K., Yakutovich A., **Chen Q.**, Mishra S., Urgel J., Pignedoli C., Ruffieux C., Müllen K., Narita A., Fasel R., “On-surface synthesis of indeno[2,1-b]fluorene polymers with antiaromatic and open-shell characters”, *J. Am. Chem. Soc.*, **2019**, 141 (31) 12346–12354.

9. **Chen Q.**, Wang D., Baumgarten M., Schollmeyer D., Müllen K., Narita A., “Regioselective Bromination of Dibenzo[hi,st]ovalene and Its Post-Synthetic Functionalization”, *Chem. Asian J.*, **2019**, 14(10), 1703–1707. (Highlighted in ChemistryViews, 23, MAR, 2019).

8. Narita A., Chen Z. P.,# **Chen Q.**,# Müllen K., “Solution and On-Surface Synthesis of Structurally Defined Graphene Nanoribbons as a New Family of Semiconductors”, *Chem. Sci.*, **2019**, 10, 964–975. (# equal contribution)

7. G. M., Moretti L., Barker J. A., **Chen Q.**, Müllen K., Narita A., G. Cerullo, Scotognella F., Lanzani G., “Pump–Push–Probe for Ultrafast All-Optical Switching: The Case of a Nanographene Molecule”, *Adv. Funct. Mater.*, **2019**, 29, 1805249

6. G. M., Nicoli L., **Chen Q.**, Müllen K., Narita A., Lanzani G., Scotognella F., “Modulation of the Nonlinear Optical Properties of Dibenzo[hi,st]ovalene by Peripheral Substituents”, *J. Phys. Chem. C*, **2018**, 122, 25007–25013.

5. **Chen Q.**, Brambilla L., Daukiya L., Mali K. S., De Feyter S., Tommasini M., Müllen K., Narita A. “Synthesis of Triply Fused Porphyrin-Nanographene Conjugates” *Angew. Chem. Int. Ed.*, **2018**, 57, 11233–11237. (Highlighted by Synfacts 2018; 14(10): 1032)

4. Coles D. M.,# **Chen Q.**,# Flatten L.C., Smith J.M., Müllen K., Narita A., Lidzey D.G., “Strong Exciton-Photon Coupling in a Nanographene Filled Microcavity”, *Nano Lett.*, **2017**, 17, 5521–5525. (# equal contribution)

3. Liu Z., Wang H. I., Narita A., **Chen Q.**, Mics Z., Turchinovich D., Kläui M., Bonn M., Müllen K., “Photoswitchable Micro-Supercapacitor Based on a Diarylethene-Graphene Composite Film” *J. Am. Chem. Soc.*, **2017**, 139, 9443–9446.

2. G. M.,# **Chen Q.**,# Wang X. Y., Liu J., Motti S. G., Petrozza A., Feng X., Lanzani G., Müllen K., Narita A., Scotognella F., “Synthesis of Dibenzo[hi,st]ovalene and Its Amplified Spontaneous Emission in a Polystyrene Matrix Paternò ”, *Angew. Chem. Int. Ed.*, **2017**, 56, 6753–6757. (# equal contribution)

1. **Chen Q.**, Zhu Y. Z., Fan Q. J. , Zhang S. C., Zheng J. Y., “ Simple and Catalyst-Free Synthesis of meso-O-, -S-, and -C-Substituted Porphyrins”, *Org. Lett.* **2014**, 16, 1590–1593.

Patents:

1. Liu X., Narita A., Parekh S. **Chen Q.**, Cremer C., Landfester K., Müllen K., Bonn M.: Use of a substituted or unsubstituted polycyclic aromatic hydrocarbon compounds for high-resolution microscopy. Submitted as EP (Application No. 18199451.8 – EPO, filed in October 2018)
2. **Chen Q.**, Narita A., Müllen K., Liu X., Parekh S., Bonn M.: Hydrophilic and particularly water soluble DBOV-derivatives. Submitted as EP (Application No. 18199447.6 - EPO, filed in October 2018)

Curriculum Vitae

Personal Details

Name: Qiang Chen

Gender: Male

Place of birth: Shandong, China

Nationality: Chinese

Marital status: Single

University Education

05.2015-11.2019 **PhD** studies, Max Planck Institute for Polymer Research, Mainz, Germany

Research advisor: [REDACTED]

09.2011-06.2014 **M.Sc.**, State Key Laboratory of Elemento-Organic Chemistry, Nankai University, Tianjin, China

Research advisor: [REDACTED]

Thesis title: Post-Functionalization of Porphyrin Periphery by S_NAr Reaction

09.2007-06.2011 **B.A.**, College of Chemistry and Material Science, Shandong Agricultural University, Shandong, China

Research advisor: [REDACTED]

Thesis title: Synthesis of Benzoimidazole Oxime Ethers and Their Fungicidal Activity Study

School Education

09.2004-06.2007 Wei-shan Second High School, Shandong, China

09.2001-06.2004 Huan-cheng Second Middle School, Shandong, China

09.1996-05.2001 Su-zhuang Primary School, Shandong, China

Tutorial Jobs

2017-2018 Assistant tutor in supervising undergraduate students in organic chemistry experiment courses in Johannes Gutenberg University of Mainz.

Awards and Fellowships

2018 Prestigious Chinese Government Award for Outstanding Self-Financed Students Abroad

2014 Excellent Master Thesis Award, Nankai University

2011 Outstanding Graduate Student, Shandong Agricultural University, Shandong, China